JSST2021

The 40th JSST Annual International Conference on Simulation Technology

Conference Proceedings

同志社大学
Doshisha University

Doshisya University

Kyoto, JAPAN

September 1–3, 2021

Supporting Companies

Session Schedule

Day 1 (Wednesday, 1st September, 2021)					
Time	**Hall A**	**Hall B**	**Hall C**	**Hall D**	**Hall E**
09:30 – 09:45	Opening Ceremony (Hall A)				
09:45 – 10:45	Plenary Talk 1 (Symposium 1, Hall A)				
10:45 – 11:00	Group Photo (Hall A)				
11:00 – 12:15	Symposium 1 ① Invited Talk 1 Tutorial Talk 1 Session 1 (2)	OS8 ① Session 5 (4)	OS3 + OS9 ① Session 8 (3)	OS2 ① Session 12 (3)	OS7 ① Session 16 (3)
12:15 – 13:30	Lunch Time				
13:30 – 14:15	Corporate Seminar ① (Hall A) Differential equations and machine learning/neural networks *Koji Maruyama* (*Wolfram Research*)				
14:30 – 15:30	Symposium 1 ② Session 2 (3)	OS8 ② Session 6 (3)	OS3 + OS9 ② Session 9 (3)	OS2 ② Session 13 (3)	OS7 ② Session 17 (3)
15:45 – 16:45	Symposium 1 ③ Session 3 (3)	OS8 ③ Session 7 (3)	OS3 + OS9 ③ Session 10 (3)	OS6 ① Session 14 (3)	OS11 ① Session 18 (3)
17:00 – 18:00	Symposium 1 ④ Session 4 (3)		Symposium 2 ① Session 11 (3)	OS6 ② Session 15 (2)	OS11 ② Session 19 (2)

Day 2 (Thursday, 2nd September, 2021)					
Time	**Hall A**	**Hall B**	**Hall C**	**Hall D**	**Hall E**
09:00 – 10:00	Plenary Talk 2 (Symposium 2, Hall A)				
10:15 – 11:15	Symposium 1 ⑤ Session 20 (3)	Symposium 2 ② Invited Talk 2 Invited Talk 3 Session 22 (2)	Symposium 3 ① Session 24 (3)	OS11 ③ Session 26 (3)	OS1 ① Session 28 (3)
11:30 – 12:30	Symposium 1 ⑥ Session 21 (3)	Symposium 2 ③ Session 23 (2)	Symposium 3 ② Session 25 (3)	OS10 ① Session 27 (3)	OS1 ② Session 29 (3)
12:30 – 13:30	Lunch Time				
13:30 – 14:15	Corporate Seminar ② (Hall A) The Trends of Latest Personal Supercomputer: Performance and App Support Status *Keiou Nishimura and Rika Yamashita* (*Visual Technology*)				
14:30 – 15:00	Plenary Talk 3 (Symposium 3, Hall A)				
15:00 – 15:05	Announcement about JSST2022 (Hall A)				
15:15 – 16:15	Shotgun Presentations of Student Session (Hall A)				
16:30 – 18:00	Student Session (Poster Session, Remo)				

Day 3 (Friday, 3rd September, 2021)					
Time	**Hall A**	**Hall B**	**Hall C**	**Hall D**	**Hall E**
09:00 – 10:00	Plenary Talk 4 + Invited Talk 4 (Symposium 3, Hall A)				
10:15 – 11:15	OS4 ① Session 30 (3)	RS ① Session 33 (3)	Symposium 3 ③ Tutorial Talk 2 Session 36 (2)	OS10 ② Session 39 (3)	OS5 ① Session 42 (3)
11:30 – 12:45	OS4 ② Session 31 (2)	RS ② Session 34 (2)	Symposium 3 ④ Session 37 (3)	OS10 ③ Session 40 (3)	OS5 ② Session 43 (3)
12:45 – 13:30	Lunch Time				
13:30 – 14:15	OS4 ③ Session 32 (2)	Symposium 2 ④ Session 35 (2)	Symposium 3 ⑤ Session 38 (2)	OS10 ④ Session 41 (2)	OS5 ③ Session 44 (2)
14:15 – 14:30	Break				
14:30 – 15:00	Closing Ceremony (Hall A)				

Symposium1

Plenary Talk

Presenter:

Prof. Hiroaki Natsukawa

Academic Center for Computing and Media Studies,
Kyoto University

Title:

Understanding System Dynamics by Combining Data-Driven Analysis and Information Visualization

Abstract:

Natural systems are often complex and dynamic. Reductionism is not universally applicable for natural complex systems found in biology and elsewhere where behavior is driven by complex interactions between many components acting together in time nonlinear dynamic systems. In this talk, I will introduce a minimalist paradigm, empirical dynamic modeling (EDM), for studying non-linear systems. It is a data-driven approach that uses time-series information to study a system by reconstructing its attractor (a geometric object) that embodies the rules of a full set of equations for the system. Particularly, I will introduce a few recent works of visual analytics to support the identification and mechanistic interpretation of system states using integration EDM with visualization techniques, leads to our understanding of complex dynamics.

Biography:

Hiroaki Natsukawa is a junior associate professor / senior lecturer in Academic Center for Computing and Media Studies, Kyoto University. He received a Ph.D. in engineering from Kyoto University in 2013. Although formally trained as a researcher in the field of biomedical engineering at Kyoto University, He has successfully crossed fields into other areas such as information visualization, neuroscience, and more recently into nonlinear dynamics. Currently, he has worked in the field of information visualization and his work focuses on developing visual analytics systems enabling data-

driven analytical reasoning by empirical dynamic modeling in collaboration with UC San Diego. He is currently an associate editor of Journal of Visualization, was a The 36th Annual Meeting of Japan Biomagnetism and Bioelectromagneics Society Local Committee, IEEE PacificVis 2019 Poster Co-chairs, IEEE PacificVis 2018 Publication Chair, The 47th Symposium of Visualization Society of Japan Organizer, NICOGRAPH International 2017 Local Committee Chair, JSST2016 Publication Chair, JHBM18 Local Committee.

Invited Talk

Presenter:

Prof. Tomohiro Sogabe

Department of Applied Physics, Nagoya University

Title:

Computation of Singular Values for Generalized Tensor Sum

(Joint work with Asuka Ohashi (National Institute of Technology, Kagawa)

Abstract:

We consider computing singular values of the generalized tensor sum of the form

$$T := I_n \otimes I_m \otimes A + I_n \otimes B \otimes I_\ell + C \otimes I_m \otimes I_\ell, \tag{1}$$

where I is the $n \times n$ identity matrix and $A \in R^{\ell \times \ell}, B \in R^{m \times m}, A \in R^{n \times n}$. The mathematical symbol $\otimes$ denotes tensor product (or Kronecker's product). A simple example of the tensor product is given below.

$$A \otimes B := \begin{bmatrix} a_{11}B & a_{12}B \\ a_{21}B & a_{22}B \end{bmatrix} = \begin{bmatrix} a_{11}b_{11} & a_{12}b_{11} & a_{11}b_{12} & a_{12}b_{12} \\ a_{21}b_{11} & a_{22}b_{11} & a_{21}b_{12} & a_{22}b_{12} \\ a_{11}b_{21} & a_{12}b_{21} & a_{11}b_{22} & a_{12}b_{22} \\ a_{21}b_{21} & a_{22}b_{21} & a_{21}b_{22} & a_{22}b_{22} \end{bmatrix}$$

where $A := \begin{bmatrix} a_{11} & a_{12} \\ a_{21} & a_{22} \end{bmatrix}$. Similarly, $A \otimes B \otimes C$ is calculated recursively by $(A \otimes B) \otimes C$ or $(A \otimes B) \otimes C$. The size of the generalized tensor sum T in (1) is of $n^3 \times n^3$, which can be extremely large even if matrices A, B, C are small. Indeed, for A, B, C being $1{,}000 \times 1{,}000$ matrices, the generalized tensor sum T can be a $1{,}000{,}000{,}000 \times 1{,}000{,}000{,}000$ matrix.

Though the generalized tensor sum T can be very large, it is easy to compute some fundamental quantities of linear algebra, such as determinant and eigenvalues. In fact, the eigenvalues of T can be written as the sum of eigenvalues of relatively much smaller matrices A,B, and C than T. On the other hand, unlike eigenvalues, it is difficult to compute the singular values of T since there is no such a simple relation between the singular values of T and the singular values of A,B, and C.

In this talk, we present recent progress on efficient computational algorithms [1,2,3] for some specific singular values of the generalized tensor sum T, which are based on the use of the notion of numerical multilinear algebra.

References

[1] A. Ohashi, T. Sogabe, On computing maximum/minimum singular values of a generalized tensor sum, Electronic Transaction on Numerical Analysis, 43 (2015), pp. 244-254.

[2] A. Ohashi, T. Sogabe, On computing the minimum singular value of a tensor sum, Special Matrices, 7 (2019), pp. 95-106.

[3] A. Ohashi, T. Sogabe, On computing an arbitrary singular value of a tensor sum, in preparation.

Biography:

Tomohiro Sogabe was graduated from the department of Applied Physics, the University of Tokyo in 2001 and received Ph.D. from the same university in 2006. He worked at Nagoya university as an assistant professor, and Aichi prefectural university as an associate professor. He is currently an associate professor at the department of Applied Physics, Nagoya University, Japan. He served as editors of JSIAM Letters, the Transactions of JSIAM, and currently he serves as an editor of JJIAM journal, Springer. He will be a member of the board of directors of JSIAM from June 2021. His research interests include numerical linear algebra, numerical multilinear algebra, and scientific computing. He published more than 70 international journal papers and 15 domestic journal papers include applied mathematics journals, computational physics journals and quantum computing journal, such as AMC, AML, ETNA, JCAM, JJIAM, NLAA for applied mathematics; IEEE TMTT, JCP, PRB, PRE for computational physics; QIC for quantum computing journal.

Tutorial Talk

Presenter:

Prof. Kuniyoshi Abe

Faculty of Economics and Information, Gifu Shotoku Gakuen University

Title:

A Numerical Study of Parallel Variants of GPBiCG Method with Stabilization Strategy for Solving Linear Equations

(Joint work with Soichiro Ikuno and Gerard L.G. Sleijpen)

Abstract:

The hybrid Bi-conjugate gradient (Bi-CG) methods such as Bi-CG stabilized (Bi-CGSTAB), Generalized Product-type based on Bi-CG (GPBiCG) are well-known for efficiently solving linear equations, but we have seen the convergence behavior with a long stagnation phase. In such cases, it is important to have Bi-CG coefficients that are as accurate as possible. We introduce the stabilization strategy for improving the accuracy of the Bi-CG coefficients.

On present petascale high-performance computing hardware, the main bottleneck for efficient parallelization is the inner products which require a global reduction. The parallel variants of Bi-CGSTAB reducing the number of global communication phases and hiding the communication latency have been proposed. In this paper, therefore, following the analogy of Cools et al., we design parallel variants of GPBiCG, and examine the convergence speed of the parallel variants with the stabilization strategy.

Biography:

Kuniyoshi Abe obtained Ph. D at Nagoya University in 1999. He began his career as Assistant professor at Anna National College of Technology in 1998. He moved to Advanced Computing Center, RIKEN as a Contract researcher in 1999. He was associate professor at Faculty of Economics and Information, Gifu Shotoku University in 2003, and is professor from 2012. His research field is numerical linear algebra, especially, he is interested in fast and iterative solvers for linear equations.

Symposium2

Plenary Talk

Presenter:

Prof. Hajime Ishihara

Department of Materials Engineering Science, Osaka University

Title:

Interaction of Optical Vortex and Matter Systems: from Microscopic to Macroscopic Regimes and Linkage between Them

Abstract:

A remarkable effect in the interaction between the optical vortex and matter systems is the transfer of the orbital angular momentum. A lot of theoretical and experimental demonstrations have been conducted for macroscopic rotational manipulation of matters from microscale to nanoscale objects. On the other hand, in the microscopic regime, the optical vortex changes the selection rule of electronic transitions, which induces unconventional spin dynamics in solids. Interestingly, the macroscopic and microscopic degrees of freedom are sometimes linked to each other in a unique way via linear and nonlinear optical responses. In this talk, I will present some examples of the above topics and puzzling aspects about them.

Biography:

Hajime Ishihara is a Professor in Graduate School of Engineering Science at Osaka University. Since 2016, he has been the project representative of JSPS Grand-in Aid for Scientific Research on Innovative Area “Nano-Material Manipulation and Structural Order Control with Optical Forces”. His research interests are the microscopic interaction between light and nanostructures and the optical functionalities arising from their interaction. He is the fellow of the Japan Society of Applied Physics.

Invited Talk

Presenter:

Prof. Yoshiki Kohmura

RIKEN SPring-8 Center

Title:

Generation of X-ray Vortices by Bragg Reflection from Crystals and Microscopy to Diagnose Topological Charge Distribution

Abstract:

We developed a method to transfer the structure of dislocation in a crystal to the Bragg X-ray wave front and performed a phase measurement that could diagnose the dislocation. This method helps to enhance the functionality of materials affected by dislocations. The two-beam X-ray interferometry was performed to measure the Bragg reflected X-ray wave front from a spiral dislocation area in a SiC crystal. As a result, a pair of fork patterns was observed. The number of fringes changed by +1 and -1 at the phase anomalies due to generation of an X-ray vortex with the topological charge of +1. Kinematic diffraction simulation showed that X-ray vortices are generated on Bragg reflected X-rays from spiral dislocation areas. This result is realized by using sufficiently large spatial coherence of the irradiated X-rays.

Biography:

Yoshiki Kohmura is currently a Team Leader of Synchrotron Radiation Imaging Instrumentation Team at SPring-8 facility, Japan. He received his PhD in the Department of Physics, Graduate School of Science, the University of Tokyo in 1994. He has been working for RIKEN SPring-8 Center since 1996. He is involved in developing various x-ray optical elements and methodologies for synchrotron radiation experiments. In the past ten years, he studied the novel waveguiding phenomenon of x-rays occurring inside slightly deformed crystals and its application to fast switching of x-rays.

Invited Talk

Presenter:

Dr. Toru Tsujimura

National Institute for Fusion Science, National Institutes of Natural Sciences

Title:

Propagation Properties of Optical Vortex in Magnetized Plasma

Abstract:

We investigated theoretically propagation properties of an optical vortex with a helical wavefront in cold uniform magnetized plasmas in an electron cyclotron (EC) range of frequencies. We describe the effects of the helical wavefront of the vortex EC wave on the wave fields in magnetized plasmas as anisotropic media. These effects become significant as the topological charge of the vortex EC wave increases or the distance from the phase singularity becomes small. The different propagation properties are also confirmed in the propagation of Laguerre–Gaussian beams on three-dimensional simulations with the finite element method. We found a remarkable phenomenon on mode conversion in the vortex EC wave propagation, which suggests an optical vortex can be a new tool to heat high-density plasmas.

Biography:

Toru Ii Tsujimura received the B.Eng., M.Eng., and D.Eng. Degrees from the University of Tokyo in 2009, 2011, and 2014, respectively. Since 2014, he has been working as an assistant professor at National Institute for Fusion Science, National Institutes of Natural Sciences (NINS). His current research focuses on wave heating in fusion plasma at the Large Helical Device. He was a representative of NINS programs for cross-disciplinary study in 2018 and 2019, leading the program on helical wavefront measurements of optical vortices emitted by high-energy electrons.

Symposium3

Plenary Talk

Presenter:

Prof. Kenichi Yoshikawa

Self-organization Science Research Center, Doshisha University / Institute for Advances Study, Kyoto University

Title:

Cooperation of Real-World Modeling with Simulation toward the Problem “What is Life?”

Abstract:

Living matter is manipulating large number of different molecules to create spatio-temporal self-organization. Currently, many numerical studies have been carried out to shed light on the underlying mechanisms of life. Sometimes, these studies remain as a possible explanatory interpretation because of the complexity of actual living systems. In the present talk, I would like to show some examples of real-world modeling, which help us to obtain deeper understanding in biological systems. 1) Emergence of cell-like structure and function under crowding condition with macromolecules. 2) Self-organization of cellular assembly. 3) Self-generation of macroscopic regular motion for the assembly of nano-scaled self-propelling objects.

Biography:

Name
Kenichi Yoshikawa
URL: http://dmpl.doshisha.ac.jp/
Academic Degree
PhD, Physical Chemistry, Graduate School of Engineering, Kyoto University (1976)

Professional Appointments
1998 – 2012
Professor, Department of Physics, Graduate School of Science, Kyoto University
2011 – 2014
Chair, Commission of Biological Physics C6, IUPAP
2012 –
Professor, Faculty of Life and Medical Sciences, Doshisha University
2019-
Specially Appointed Prof., Institute for Advances Study, Kyoto University

Plenary Talk

Presenter:

Prof. Helmut Schiessel

Cluster of Excellence Physics of Life, Technical University Dresden

Title:

The mechanical genome

Abstract:

In addition to the classical layer of genetic information, DNA molecules also carry other layers of information. Two possible layers are discussed. One is a mechanical layer, namely that the base pair sequence influences the mechanical and geometrical properties of the DNA molecules which in turn might guide their packing inside the cell. A second possible layer is the speed of translation in the protein-producing ribosomes where the speed influences the quality of the protein product. We demonstrate that the degeneracy

Biography:

Helmut Schiessel studied physics in Freiburg where he did his Ph.D. in theoretical polymer physics in 1997. He then worked as a postdoc at two Universities of California, in Santa Barbara and in Los Angeles. In 2000 he joined the MPI for Polymer Research in Mainz where he was in charge of a biophysics research project. From 2005 to 2020 Schiessel headed the chair of Theoretical Physics of Life Processes at the Lorentz Institute, Leiden University. Since January he heads the group Theoretical Physics of Living Matter at the Cluster of Excellence Physics of Life.

Invited Talk

Presenter:

Prof. Yoshiteru Yonetani

National Institute for Quantum and Radiological Science and Technology

Title:

Water on the DNA Surface: Microscopic Insight from Molecular Dynamics Simulations

Abstract:

Water on the DNA surface exhibits characteristic behavior such as ice-like water network along the narrow groove of DNA. By using molecular dynamics simulations, we obtained detailed picture for such water; our characterization fully describes the water network patterns and their sequence variation [Biophys. J. 97, 1138 (2009)]. Analysis on such water network further revealed microscopic origin of the slow water-exchange kinetics [Biophys. Chem. 160, 54 (2012)]. As another relevant topic, I will also mention a relation with DNA damage production. Our recent study [Chem. Phys. Lett. 749, 137441 (2020)] found that site-dependent water accessibility for DNA backbone is well correlated with the probabilities of DNA damage production by OH radical attacking. This suggests that the site-dependent hydration property is a key factor for DNA damage production.

Biography:

Yoshiteru Yonetani received B.E. and Dr. degrees from Keio University in 1998 and 2002, respectively. He worked as a postdoctoral researcher at Nara Women's University (2002-2003) and Japan Atomic Energy Agency (2004-2008). He is currently a senior researcher in National Institutes of Quantum and Radiological Science and Technology. His current interests include molecular dynamics and quantum dynamics in biological and chemical physics.

Tutorial Talk

Presenter:

Dr. Miyuki Sasaki

Collaborative Laboratories for Advanced Decommissioning Science, Japan Atomic Energy Agency

Title:

Visualization of Dose Rate Distribution around Fukushima Daiichi Nuclear Power Plant using Artificial Neural Networks.

Abstract:

This study proposes a method of visualizing the ambient dose rate distribution using artificial neural networks (ANN) from airborne radiation monitoring results. The ANN method was applied to the results of the airborne radiation monitoring which was conducted around the Fukushima Daiichi Nuclear Power Plant by an unmanned aerial vehicle. The ANN was constructed by training data consisting of input variable dataset (radiation count rate, altitude, topographic data, photographic RGB data) and objective variable dataset (the air dose rate data at 1 m above the ground level). The reliability of the ANN method was evaluated by comparison with the ground-based survey data. The dose rate map created by the ANN method reproduced ground-based survey results better than traditional methods.

Biography:

Miyuki Sasaki received Dr. Eng. degrees from the University of Nagoya, Japan, in 2021. She became a researcher at the Japan Atomic Energy Agency in 2015. Her current research interests include radiation measurement.

Committee

General Chair:
Hiroaki Nakamura (National Institute for Fusion Science)

Conference Chair:
Takahiro Kenmotsu (Doshisha University)

Conference Co-Chair:
Susumu Fujiwara (Kyoto Institute of Technology)
Katsuhiko Yamaguchi (Fukushima University)

Program Chair:
Seiki Saito (Yamagata University)
Hiroshi Tamura (Chuo University)

Program Co-Chair:
Nobuaki Ohno (University of Hyogo)
Yoshihide Shibata (National Institute of Technology, Gifu College)
Yoshihisa Fujita (Ritsumeikan University)

Post-Conference Chair:
Susumu Fujiwara (Kyoto Institute of Technology)

Post-Conference Co-Chair:
Tomoko Mizuguchi (Kyoto Institute of Technology)
Hiroaki Ohtani (National Institute for Fusion Science)
Daisuke Ishihara (Kyushu Institute of Technology)

Publication Chair:
Taku Itoh (Nihon University)

Publication Co-Chair:
Hiroto Tadano (University of Tsukuba)
Soichiro Ikuno (Tokyo University of Technology)

Finance Chair:
Hiroki Sakuta (Doshisha University)

Publicity Chair:
Satoshi Takatori (Doshisha University)

Exhibition Chair:
Yoji Matsumoto (Cybernet Systems Co., Ltd.)

Conference Adviser:
Amane Takei (University of Miyazaki)
Takuo Yasunaga (Kyushu Institute of Technology)
Motoi Wada (Doshisha University)

Table of Contents

Day 1 (Wednesday, 1st September, 2021)

Plenary Talk 1 (Numerical Simulation and Visual Analytics of Nonlinear Problems) 9:45 – 10:45, Hall A

Symposium 1 on Numerical Simulation and Visual Analytics of Nonlinear Problems, Session 01, Invited and Tutorial Talks, 11:00 – 12:00, Hall A

OS8: Numerical Harmonic Analysis and Signal Processing, Session 05, 11:00 – 12:20, Hall B

OS3+OS9: Complex and Ultimate Systems (OS3), Complex Networks and Complex Systems (OS9),Session 08, 11:00 – 12:00, Hall C

OS2: Simulation Technology in Origami, Session 12, 11:00 – 12:00, Hall D

OS7: Advanced Numerical Analysis and Software Technology, Session 16, 11:00 – 12:00, Hall E

Symposium 1 on Numerical Simulation and Visual Analytics of Nonlinear Problems, Session 02, 14:30 – 15:30, Hall A

OS8: Numerical Harmonic Analysis and Signal Processing, Session 06, 14:30 – 15:30, Hall B

OS3+OS9: Complex and Ultimate Systems (OS3), Complex Networks and Complex Systems (OS9), Session 09, 14:30 – 15:30, Hall C

OS2: Simulation Technology in Origami, Session 13, 14:30 – 15:30, Hall D

OS7: Advanced Numerical Analysis and Software Technology, Session 17, 14:30 – 15:30, Hall E

Symposium 1 on Numerical Simulation and Visual Analytics of Nonlinear Problems, Session 03, 15:45 – 16:45, Hall A

OS8: Numerical Harmonic Analysis and Signal Processing, Session 07, 15:45 – 16:45, Hall B

OS3+OS9:Complex and Ultimate Systems (OS3), Complex Networks and Complex Systems (OS9), Session 10, 15:45 – 16:45, Hall C

OS6: Multi Dimensional Communication Networks, Session 14, 15:45 – 16:45, Hall D

OS11: Simulation in Nuclear Fusion, Session 18, 15:45 – 16:45, Hall E

Symposium 1 on Numerical Simulation and Visual Analytics of Nonlinear Problems, Session 04, 17:00 – 18:00, Hall A

Symposium 2 on Analysis of Optical Vortex Field and Applications, Session 11, 17:00 – 18:00, Hall C

OS6: Multi Dimensional Communication Networks, Session 15, 17:00 – 17:40, Hall D

OS11: Simulation in Nuclear Fusion, Session 19, 17:00 – 17:40, Hall E

Day 2 (Thursday, 2nd September, 2021)

Plenary Talk 2 (Analysis of Optical Vortex Field and Applications), 9:00 – 10:00, Hall A

Symposium 1 on Numerical Simulation and Visual Analytics of Nonlinear Problems, Session 20, 10:15 – 11:15, Hall A

Symposium 2 on Analysis of Optical Vortex Field and Applications, Session 22, Invited Talks, 10:15 – 11:15, Hall B

Symposium 3 on Advanced Concept and Methodology in Bioscience, Session 24, 10:15 – 11:15, Hall C

OS11: Simulation in Nuclear Fusion, Session 26, 10:15 – 11:15, Hall D

OS1: Verified Numerical Computations, Session 28, 10:15 – 11:15, Hall E

Symposium 1 on Numerical Simulation and Visual Analytics of Nonlinear Problems, Session 21, 11:30 – 12:30, Hall A

Symposium 2 on Analysis of Optical Vortex Field and Applications, Session 23, 11:30 – 12:10, Hall B

Symposium 3 on Advanced Concept and Methodology in Bioscience, Session 25, 11:30 – 12:30, Hall C

OS10: Computational Electromagnetics and Its Applications, Session 27, 11:30 – 12:30, Hall D

OS1: Verified Numerical Computations, Session 29, 11:30 – 12:30, Hall E

Plenary Talk 3 (Advanced Concept and Methodology in Bioscience), 14:30 – 15:00, Hall A

Day 3 (Friday, 3rd September, 2021)

Plenary Talk 4 and Invited Talk 4 (Advanced Concept and Methodology in Bioscience), 9:00 – 10:00, Hall A

OS4: Design and Simulations for System Integration, Session 30, 10:15 – 11:15, Hall A

RS1, Session 33, 10:15 – 11:15, Hall B

RS2, Session 34, 11:30 – 12:10, Hall B

Symposium 3 on Advanced Concept and Methodology in Bioscience, Session 37, 11:30 – 12:30, Hall C

OS10: Computational Electromagnetics and Its Applications, Session 40, 11:30 – 12:30, Hall D

OS5: Coupled-Simulation and Co-Simulation, Session 43, 11:30 – 12:30, Hall E

OS4: Design and Simulations for System Integration, Session 32, 13:30 – 14:10, Hall A

Symposium 2 on Analysis of Optical Vortex Field and Applications, Session 35, 13:30 – 14:10, Hall B

Understanding system dynamics by combining data-driven analysis and information visualization

Hiroaki Natsukawa

Academic Center for Computing and Media Studies, Kyoto University

natsukawa.hiroaki.3u@kyoto-u.ac.jp

Abstract. Natural systems are often complex and dynamic. Reductionism is not universally applicable for natural complex systems found in biology and elsewhere where behavior is driven by complex interactions between many components acting together in time nonlinear dynamic systems. In this talk, I will introduce a minimalist paradigm, empirical dynamic modeling (EDM), for studying non-linear systems. It is a data-driven approach that uses time-series information to study a system by reconstructing its attractor (a geometric object) that embodies the rules of a full set of equations for the system. Particularly, I will introduce a few recent works of visual analytics to support the identification and mechanistic interpretation of system states using integration EDM with visualization techniques, which leads to our understanding of complex dynamics.

Keywords: Visual analytics, Nonlinear dynamics

1. Introduction

Natural systems are often complex and dynamic; therefore, relationships between measured time series variables are generally not static; instead, these relations dynamically change in either a nonlinear or state-dependent manner. For example, in ecology, competition between small desert mammals changes with the amount of rainfall [1]; or predation on insect herbivores varies with vegetation structure [2]. To achieve sustainable use of natural resources and conservation of ecosystems, such as those listed in the sustainable development goals (SDGs) [3], it is necessary to monitor the abundance of species included in the ecosystem and understand the interspecies relationship, which changes depending on the state of the system. Moreover, we must understand what type of state the ecosystem has and how this state changes over time.

Because it is difficult to accurately quantify these time-varying interspecies relationships using a conventional linear approach, Deyle et al. proposed a state-of-the-art method that specifically measures relationships changing in a state dependent manner between time series variables; this method is one element of empirical dynamic modeling (EDM) [4]. EDM is a collection of methods to study systems using attractors reconstructed from time series data based on nonlinear state space reconstruction. Specifically, this is an equation-free approach with minimal assumptions for inductive data-science explorations of natural complex systems.

2. visEDM

A core strength of data-driven nonlinear analysis, such as EDM, is that system dynamics are not prescribed a priori, but inferred from empirical evidence. A fundamental weakness can be the overwhelming task of interpreting results and identifying intersystem drivers. Therefore, in order to overcome the weaknesses of EDM and to better understand dynamic systems, we propose visEDM that integrates methods that appropriately characterize these dynamics (i.e., EDM) with visualization techniques that can help analyze the behavior of the system [5].

As illustrated in Figure 1, we developed a visual analytics system that links the construction of dynamic networks, state identi- fication, annotation, and the construction of a state transition graph (STG) by summarizing 2D trajectories. The proposed system supports the identification and interpretation of the system state using EDM-constructed dynamic graphs.

In this talk, I present the methodology of EDM and report a case study of ecosystem analysis by visEDM. I also introduce the latest researches on data-driven analysis using EDM, and discuss future prospects.

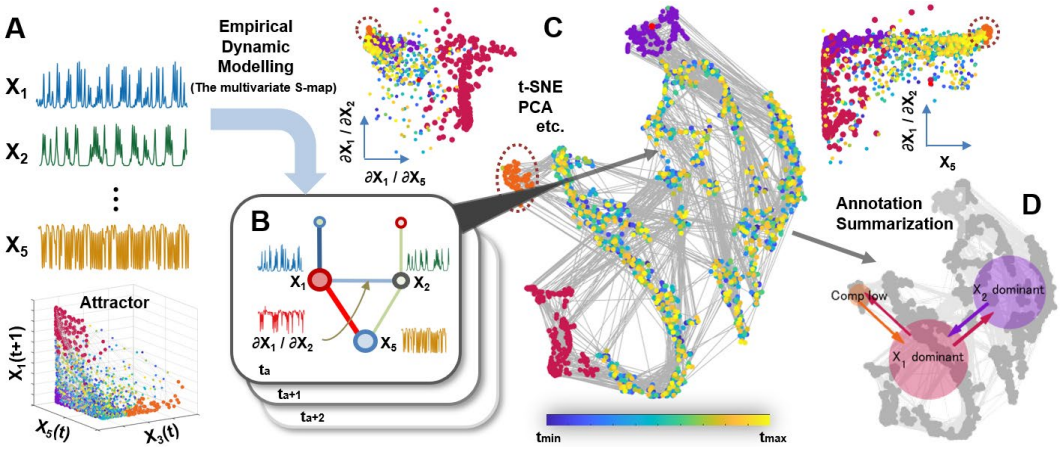

Figure 1. Schematic of visual analytics to study nonlinear interactions with empirical dynamic modeling (EDM)

References

[1] M. Lima, SKM. Ernest, JH. Brown, A. Belgrano, NC. Stenseth: Chihuahuan desert kangaroo rats: Nonlinear effects of population dynam- ics, competition, and rainfall, *Ecology*, 89:9 (2008), 2594-2603.

[2] C. Gratton, RF. Denno: Seasonal shift from bottom-up to top-down impact in phytophagous insect populations, *Oecologia*, 134:4 (2003),487-495.

[3] United Nations. Transforming our world: the 2030 agenda for sustain- able development., 2015.

[4] ER. Deyle, RM. May, SB. Munch, G. Sugihara: Tracking and forecasting ecosystem interactions in real time, *Proceedings of the Royal Society B: Biological Sciences*, 283:1822 (2016), 20152258.

[5] H. Natsukawa, ER. Deyle, GM. Pao, K. Koyamada, G. Sugihara: A visual analytics approach for ecosystem dynamics based on empirical dynamic modeling, *IEEE Transactions on Visualization and Computer Graphicsc*, 27:2 (2021), 506-516.

JSST 2021

Computation of singular values for generalized tensor sum

Tomohiro Sogabe[1,*] and Asuka Ohashi[2]

[1]Department of Applied Physics, Nagoya University, Japan
[2]National Institute of Technology, Kagawa College, Japan

[*]sogabe@na.nuap.nagoya-u.ac.jp

The full paper of this paper has been published in Journal of Advanced Simulation in Science and Engineering (JASSE).

DOI: https://doi.org/10.15748/jasse.9.136

JSST 2021

A Numerical Study of Parallel Variants of GPBiCG Method with Stabilization Strategy for Solving Linear Equations

Kuniyoshi Abe[1,*], Soichiro Ikuno[2], Gerard L.G. Sleijpen[3]

[1]Faculty of Economics and Information, Gifu Shotoku University
[2]School of Computer Science, Tokyo University of Technology
[3]Department of Mathematics, Utrecht University

[*]abe@gifu.shotoku.ac.jp

Abstract. The hybrid Bi-conjugate Gradient (Bi-CG) methods such as Bi-CGSTAB and GPBiCG are well-known for efficiently solving linear equations, but we have seen the convergence behavior with a long stagnation phase. In such cases, it is important to have Bi-CG coefficients that are as accurate as possible. We introduce the strategy for stabilizing the Bi-CG coefficients. On present petascale high-performance computing hardware, the main bottleneck for efficient parallelization is the inner products which require a global reduction. The parallel variants of Bi-CGSTAB reducing the number of global communication phases and hiding the communication latency have been proposed. In this paper, therefore, following the analogy proposed by Cools et al., we design parallel variants of GPBiCG. Then we examine the convergence speed of the parallel variants with the stabilization strategy.

Keywords: linear equations, Krylov subspace methods, Generalized Product-type Bi-CG, parallel variants, stabilization strategy

1. Introduction

The hybrid Bi-conjugate Gradient (Bi-CG) methods such as Bi-CG STABilized (Bi-CGSTAB), BiCGstab(ℓ), BiCG×MR2 and Generalized Product-type Bi-CG (GPBiCG) methods are well-known for efficiently solving linear equations $\boldsymbol{Ax} = \boldsymbol{b}$, for $\boldsymbol{x}$, where $\boldsymbol{A}$ is a given n-by-n matrix, and $\boldsymbol{b}$ is a given n-vector. The convergence of GPBiCG/BiCG×MR2 and BiCGstab(ℓ) is faster and more robust than that of Bi-CGSTAB. We have sometimes seen the convergence behavior with a long stagnation phase. In such cases, it is important to have Bi-CG coefficients that are as accurate as possible. The stabilization strategy [4] for the Bi-CG coefficients is as accurate as possible has been proposed.

On present petascale high-performance computing hardware, the main bottleneck for efficient parallelization is the inner products which require a global reduction. The resulting global synchronization phases cause communication overhead on parallel computers. The

reduction of the synchronization bottleneck, i.e., the idea of reducing the number of global communication phases and hiding the communication latency in the Krylov subspace methods has been presented for the Conjugate Gradient (CG) and Generalized Minimal RESidual (GMRES) methods [1, 3, 5]. In addition to reducing the number of global synchronization points, the idea of hiding global communication latency by overlapping communication with computations has been proposed. Cools et al. have developed a parallel variant of Bi-CGSTAB which is referred to as the pipelined Bi-CGSTAB method [2]. In our talk of JSST 2019 we have proposed the parallel variants of Bi-CGSTAB, which have faster convergence speed than the pipelined Bi-CGSTAB method proposed by Cool et al.

In this paper, therefore, we design the pipelined variants of GPBiCG. We examine the convergence behavior of the pipelined variants and the effectiveness when applying the stabilization strategy by numerical experiments.

2. Parallel variants of GPBiCG method

The standard GPBiCG has three global reduction steps for the inner products required in the computations of α_k, β_k, and ζ_k and η_k. First, the inner product for the computation of α_k is merged with that of β_k to reduce the number of global communication phases. Then the denominator of α_k is computed by the inner products between an initial shadow vector and a recurrence for vector updates. The inner products for the computation of α_{k+1} can be moved above that of β_k, i.e., the communication avoiding variant is derived. In the communication avoiding variant, the first computation of the matrix-vector multiplication (abbreviated as MV) is separated from the first reduction phase.

Next, the first computation of MV is moved below the first global reduction phase for overlapping communication with computation. Thus the MVs are computed below the inner products. After the local computation of the inner products has been executed on each worker, each global reduction can be overlapped with the computation of the corresponding MV. This overlap hides the communication latency behind the computation of the explicit MV, i.e., the pipelined variant is obtained.

This research was partly supported by JSPS KAKENHI Grant Number 19K12008.

References

[1] Chronopoulos, A.T., Gear, C.W.: s-step iterative methods for symmetric linear systems. J. Comput. Math. 25, 153–168 (1989)

[2] Cools, S., Vanroose, W.: The communication-hiding pipelined BiCGStab method for the parallel solution of large unsymmetric linear systems. Parallel Comput. 65, 1–20 (2017)

[3] Erhel, J.: A parallel GMRES version for general sparse matrices. ETNA 3, 160–176 (1995)

[4] Sleijpen, G.L.G., van der Vorst, H.A.: Maintaining convergence properties of BiCGstab methods in finite precision arithmetic. Numer. Algorithms 10, 203–223 (1995)

[5] Sturler, E.D.: A parallel variant of GMRES(m). In: Proceedings of the 13th IMACS World Congress on Computational and Applied Mathematics. vol. 9. IMACS, Criterion Press (1991)

JSST 2021

Feature Extraction of Distorted Sound Waveforms and Estimation of Distortion Effects and Their Settings

Taiga Ishida[1,*], Toshio Suzuki[2], Emiko Ishiwata[2]

[1]Graduate School of Science, Tokyo University of Science
[2]Faculty of Science Division I, Tokyo University of Science

[*]1420504@ed.tus.ac.jp

Abstract. In this study, we improve the formulas for previously reported features extracted from distorted sound waveforms using a wavelet transform. By replacing integration with a difference scheme, the computation time is reduced. Experiments show that using the proposed features makes it easier for a person with no guitar experience to estimate a target guitar sound.

Keywords: Distorted sound, Wavelet transform, Sound approximation, Feature extraction

1. Introduction

Distorted sound is used in various types of music. In general, distortion on a guitar is created by using distortion pedals. To produce the desired sound, guitarists must select the appropriate type of distortion effect and tune its parameters, Drive, Tone and so on. This is difficult even for experienced guitarists.

A previous study [1] extracted features from a waveform of distorted sound using a wavelet transform. In the present study, we improve the formula for calculating the values of these features and reduce the computation time. Moreover, we conduct experiments to determine whether a person with no guitar experience can produce a desired sound by selecting a distortion effect and estimating its settings using the values of the proposed features.

2. Improvement of features

A previous study [1] on amplification and clipping defined two features that represent the distortion level using the Haar wavelet. Now, we improve the formulas for these two features regarding the distortion level to reduce computation time.

Let $f(t)$ be the signal from an electric guitar. We assume that $f(t)$ is normalized such that $\max_t |f(t)| = 1$. Distorted sound is created in two steps. In the first step, the signal is amplified. It is transformed from $f(t)$ to $\check{f}(t) = Cf(t)$ for some constant $C > 1$.

In the second step, the signal is clipped using a clipping transform, such as $\tilde{f}(t) = \max\left\{-1, \min\left\{1, \check{f}(t)\right\}\right\}$, as shown in Figure 1. Different combinations of the constant C and the type of clipping transform produce different sounds, making it difficult to select a distortion effect and estimate its settings.

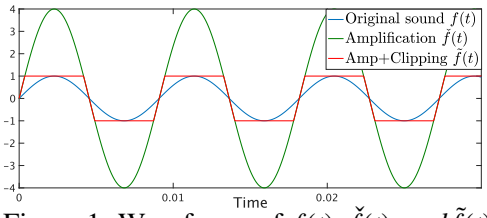

Figure 1: Waveforms of $f(t)$, $\check{f}(t)$, *and* $\tilde{f}(t)$

The feature that represents amplification is defined as follows [1]:

$$E_1(a) = \max_b \frac{1}{a}\left|\int_{-\infty}^{\infty} f(t)\psi_{\mathrm{H}}\left(\frac{t-b}{a}\right)dt\right|, \tag{1}$$

where $\psi_{\mathrm{H}}(t)$ is the Haar wavelet. $\psi_{\mathrm{H}}(t)$ equals 1 for $0 \le t < 1/2$, -1 for $1/2 \le t < 1$ and 0 for the other points. The value of this feature increases with increasing distortion level. If $|a|$ is sufficiently small, E_1 can be approximated as $\frac{a}{4}\max_b\left|f'\left(b+\frac{a}{2}\right)\right|$ by using the second-order central difference formula. E_1 represents the maximum variation of f. To obtain the gradient of f, we consider $\tilde{E}_1(a) = \max_b \frac{4}{a^2}\left|\int_{-\infty}^{\infty} f(t)\psi_{\mathrm{H}}\left(\frac{t-b}{a}\right)dt\right|$ instead of E_1. In the same way, $\tilde{E}_1$ can be approximated as $\max_b\left|f'\left(b+\frac{a}{2}\right)\right|$. By using the first-order central difference formula, we define the feature that represents amplification as follows:

$$D_A = \max_b\left|\frac{f(b+a)-f(b)}{a}\right|. \tag{2}$$

With this improved formula, where D_A denotes the maximum gradient of f, the computation time is reduced by a factor of $2000 \sim 3500$ by replacing integration with a difference scheme.

The feature that represents clipping is defined as follows [1]:

$$E_2(a) = \int_{-\infty}^{\infty}\left|\int_{-\infty}^{\infty}|f(t)|^{\frac{1}{4}}\psi_{\mathrm{H}}\left(\frac{t-b}{a}\right)dt\right|db. \tag{3}$$

When the Haar wavelet ψ_{H} completely overlaps the clipped part of the distorted sound $f(t)$, the integral of (3) with respect to t becomes zero. Hence, the value of this feature decreases with increasing distortion level. However, this feature has irregular behavior when the distortion level is small because $E_2(a)$ indirectly measures the amount of clipping. We thus improve the formula for E_2, and consider $e_2(a,b) = \frac{a^2}{4}\left|\int_{-\infty}^{\infty}|f(t)|^{\frac{1}{4}}\psi_{\mathrm{H}}\left(\frac{t-b}{a}\right)dt\right|$. For $b \in \mathbb{R}$ and $a > 0$ is sufficiently small, e_2 can be approximated as $\left|g'\left(b+\frac{a}{2}\right)\right|$ if $g(t) = |f(t)|^{\frac{1}{4}}$. Moreover, let $D = \left|\frac{g(b+a)-g(b)}{a}\right|$. We define $D_C = \mathrm{card}(\mathrm{clip}(D))$ for $\mathrm{clip}(D) = \{b \in \mathbb{R} \mid D \le \varepsilon\}$, where $\varepsilon > 0$ is a constant for detecting clipped parts and $\mathrm{card}(A)$ denotes the number of elements if A is a finite set or the cardinality if it is an infinite set. D_C directly measures the amount of clipping.

D_A or D_C is computed from the discretized signal with a sampling rate Fs. Therefore, we set $a = 2/Fs$. To verify the benefit of D_C, we prepared ten kinds of distorted sounds with different distortion levels. The association between the distortion level and the value of

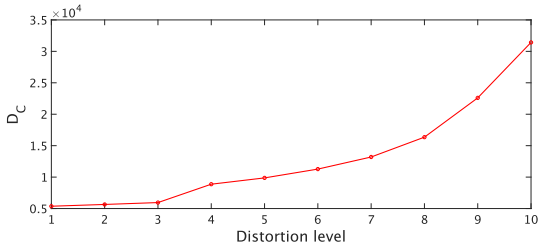

Figure 2: Behavior of D_C

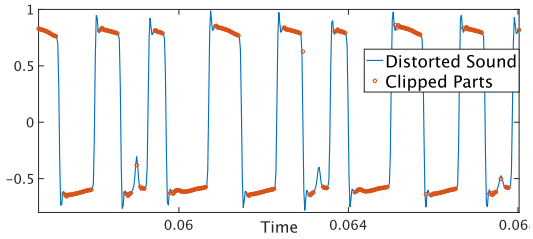

Figure 3: Clipped parts of a waveform

D_C is shown in Figure 2. The clipped parts can be clearly extracted, as shown in Figure 3. We can reduce the computation time by a factor of $100 \sim 200$ by replacing integration with a difference scheme.

Moreover, in [1], not only the feature of distortion level, the feature that represents the brightness of timbre is defined as follows:

$$E_0 = \frac{1}{S} \int_{-\infty}^{\infty} \omega \left| \hat{f}(\omega) \right|^2 d\omega, \tag{4}$$

where $\hat{f}(\omega)$ is the Fourier transform of $f(t)$ and $S = \int_{-\infty}^{\infty} |\hat{f}(\omega)|^2 d\omega$, which is the average of the frequency components of the distorted sound f.

3. Experiments on distortion effects

We conducted an experiment with 11 participants to evaluate our formulas. We created a target sound and six comparison sounds, I-VI, which have different values for features D_A, D_C, and E_0. The features of the target sound are denoted as D_A^*, D_C^*, and E_0^*. Table 1 shows the ratios of the feature values for the six comparison sounds. The participants first listened to the target sound and sounds I-VI. They then scored sounds I-VI on a scale of 0 to 5 on how similar they are to the target sound.

The results show that 82% of the participants gave sound V, whose values for the three features are closest to those for the target sound, the highest score (i.e., it was the most similar to the target sound). None of the participants identified sounds I and IV as most similar to the target sound. These results show that sounds with similar D_A, D_C, and E_0 values sound similar to the human ear.

Table 1: Ratio of feature values for six comparison sounds

	D_A/D_A^*	D_C/D_C^*	E_0/E_0^*
I	0.75	0.55	0.82
II	0.93	0.50	1.12
III	0.90	0.50	1.01
IV	1.08	1.12	2.01
V	1.01	1.07	1.09
VI	0.42	1.07	0.97

We also conducted an experiment with three participants to verify the utility of using D_A, D_C, and E_0. These participants had never played an electric guitar. In this experiment, the target sound was recorded using an effect called "Distortion", a built-in distortion effect of the BOSS Micro BR BR-80 digital recorder. The parameters for this effect were set to Drive=55 and Tone=30. The participants were instructed on how to make a sound using an electric guitar and the BR-80 digital recorder.

Table 2: Estimated effect and settings based on feature values

Participant	Effect	Drive	Tone
A	Distortion	100	30
B	Lead	90	40
C	Distortion	55	50

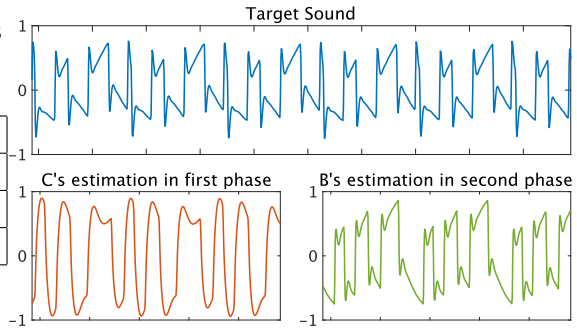

Figure 4: Waveforms of target and estimated sounds

In the first phase, participants were not given the D_A^*, D_C^*, and E_0^* values. They selected one of the twenty built-in distortion effects and estimated the values of Drive and Tone by comparing the target sound with the sound produced by the guitar. In the second phase, they were given the D_A^*, D_C^*, and E_0^* values. They selected the distortion effect and estimated the values of Drive and Tone by comparing D_A^*, D_C^*, and E_0^* values to the D_A, D_C, and E_0 values for the sound produced by the guitar.

Table 2 is the estimation results in the second phase by three participants. We recorded the sounds obtained with the estimated values and analyzed their waveforms. None of the participants could identify the built-in effect without the D_A^*, D_C^*, and E_0^* values. The waveform obtained without using the feature values (orange line) is quite different from that for the target sound (blue line) in Figure 4. The sounds estimated without using feature values are not similar to the target sound. In contrast, two participants identified the effect "Distortion" based on the feature values, but they could not estimate the values of Drive or Tone. This may be due to the differences in the force and angle of picking the strings. Participant B selected a different built-in effect; nevertheless, the waveform for the estimated sound (green line) for this participant is similar to that for the target sound, as shown in Figure 4.

4. Conclusion

In this study, we improved the formulas for two features for distorted sounds defined in a previous study. The computation time is reduced by replacing integration with a difference scheme. We showed that sounds with similar D_A, D_C, and E_0 values sound similar to the human ear. A person with no guitar experience can create a sound close to the target sound by using these features. In the future, we will collect more experimental data and analyze the correlation among feature values using multidimensional scaling.

References

[1] Toshio Suzuki, Keiichi Zempo, Tamotu Kinoshita: *Approximation of Distortion Sound via Fourier and Wavelet Transform*, 25th International Congress on Sound and Vibration (ICSV25), Hiroshima, Japan, 9, July, (2018).

JSST 2021

A digital image watermarking based on high-frequency components with additive low-frequency of the dual-tree complex discrete wavelet transform

MASAYUKI SHIMOSHIMBARA[1,*] and TERUYA MINAMOTO[1]

[1]Graduate School of Science and Engineering, Saga University, Saga, Japan

[*]simosimm@ma.is.saga-u.ac.jp

Abstract.

We propose a digital watermarking method based on the dual-tree complex discrete wavelet transform (DT-CDWT), which enables us to obtain 16 frequency components. In our previous work, we proposed the watermarking method based on the dyadic wavelet transform (DYWT) which enables us to obtain only four frequency components and interval arithmetic (IA). Our new method is the modified version of the previous one. We embed a watermark into the high-frequency components with additive low-frequency components obtained by the DT-CDWT, whereas we do not use IA. The experimental results show that the proposed method has the better image quality of a watermarked image than the previous one and is more robust against some attacks.

Keywords: Wavelet transform, Dual-tree complex discreate wavelet transform, Watermark

1. Introduction

Many digital watermarking methods using wavelet transform have been developed [1],[2], [3],[4],[5]. In our previous study [4], we developed the blind digital image watermarking method based on the dyadic wavelet transform(DYWT) and interval arithmetic(IA). We also proved that the high-frequency components obtained by the DYWT and IA contain the low-frequency component. Our previous results in [5] showed that the high-frequency components containing the low-frequency components played an important role to develop a robust watermarking against several attacks. On the other hand, we also developed the digital watermarking based on the dual-tree complex discrete wavelet transform (DT-CDWT) and IA. However, we did not discuss the high-frequency component's properties obtained by the DT-CDWT and IA.

The aim of this study is to develop a digital watermarking method based on the high-frequency components containing the low-frequency components obtained by the DT-CDWT

and investigate its robustness. Applying the DT-CDWT to an image, we obtain four low-frequency components and 12 high-frequency components. We intentionally add the four low-frequency components to 12 high-frequency components at each. Experimental results demonstrate that the addition of the low-frequency and high-frequency components play an important role to develop the robust digital watermarking.

This paper proceeds as follows. We first present our watermarking embedding and extraction procedure. Next, the experimental results are presented in Section 3 and a summary and discussion are given in Section 4.

2. Watermarking algorithm

The algorithm for embedding and extraction of a watermark is in a similar manner as in [5]. The embedding procedure is as follows:

1. Apply the DT-CDWT to a host image. Then, 16 frequency components C_{RR}, C_{RI}, C_{IR}, C_{II},$D_{RR}, D_{RI}, D_{IR}, D_{II}, E_{RR}, E_{RI}, E_{IR}, E_{II}, F_{RR}, F_{RI}, F_{IR}$ and F_{II} are obtained, where I and R stand for imaginary and real, respectively. Here, C, D, E and F represent the low-frequency components and high-frequency components in the vertical, horizontal, and diagonal directions, respectively.

2. Select one component from the D, E, and F components to embed the watermark (for simplicity, we assume that the D component is selected).

3. Add the low-frequency components $C_{RR}, C_{RI}, C_{IR}, C_{II}$ multiplied by a factor β to the components $D_{RR}, D_{RI}, D_{IR}, D_{II}$, respectively. We set $S \leftarrow D + \beta C$.

4. The sliding window is applied to the component S. The formula for the sliding window is shown below.

$$\underline{S}(m,n) = \mathrm{sgn}(S(m,n)) \cdot \frac{1}{2K+1}\frac{1}{2L+1}\sum_{k=-K}^{K}\sum_{l=-L}^{L}|S(m+k,n+l)|,$$

   where K and L are natural numbers and constants. Also, $\mathrm{sgn}(x)$ is a sign function like

$$\mathrm{sgn}(x) = \begin{cases} 1 & (x > 0) \\ 0 & (x = 0) \\ -1 & (x < 0) \end{cases}.$$

5. Embed the watermark into the 4 components obtained above. The embedding formula is shown below.

$$WM(i,j) = \underline{S}(i,j) \times (1 + W(i,j) * \alpha)$$

   where WM is the high-frequency component after embedding the watermark, and W is the watermark to be embedded. The quantity α is a hiding factor that adjusts the robustness.

6. Choose WM instead of D, use other components, and then apply the inverse DT-CDWT. The watermarked image K is thus obtained.

The extraction algorithm is as follows:

1. Decompose the watermarked image K into the 16 components using the DT-CDWT and choose the watermarked components $\widetilde{WM}$.

2. Extract the binary-valued watermark by computing:

$$\widetilde{W}_i = |\widetilde{WM}_i| - |\underline{S}_i|, i \in \{RR, RI, IR, II\}$$
$$\widetilde{W}_e = \sum_{i=1}^{4} \widetilde{W}_i,$$
$$\widetilde{W} = \mathrm{sgn}(\widetilde{W}_e).$$

3. Experimental results

In this experiment, we confirmed that adding the low frequency component to the high frequency component of the DT-CDWT improves the noise tolerance. Table 1 shows the peak signal-to-noise ratios (PSNR) of the watermarked image and the extracted watermark after adding a Gaussian noise to the watermarked image with the different values of β. We embedded a watermark into the four D components. The PSNR of the watermarked image in the conventional method [5] is 33.7075 and the PSNR of the extracted watermark is 5.0202. Figure 1 shows that the watermarked images and extracted watermarked images by the method [5] and the proposed method when $\beta = 4$.

β	4	4.4	4.6	4.8	5
PSNRs of the watermarked image	33.7932	33.4419	33.2729	33.0959	32.9217
PSNRs of extracted watermark	5.0371	5.2017	5.2316	5.2636	5.3690

Table 1: The PSNRs of the watermarked images and watermarks extracted from the watermarked ones subjected to a Gaussian noise with the different values of β.

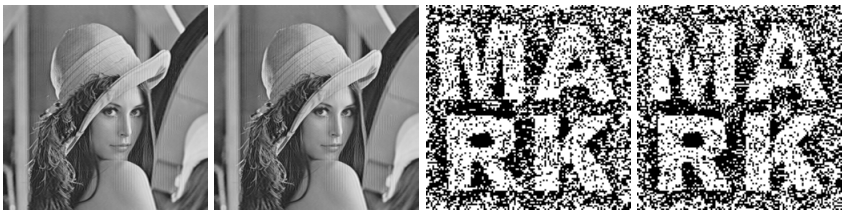

Figure 1: The watermarked images subjected to a Gaussian noise and extracted watermarks by the method [5] (first and third form the left) and the proposed method (second and fourth from the left) when $\beta = 4$.

Figure 1 shows that the watermark is extracted by the proposed method and the conventional method. Although both extracted watermarks are degraded, we can identify the

watermark at a single glance. It seems that the quality of these images are almost the same at a single glance, however, the PSNR of the extracted watermark by the proposed method is slightly larger than the one by the conventional method. In fact, the former is 5.0371 and the latter is 5.0202 when the PSNRs obtained by the conventional and proposed method are 33.7075 and 33.7932, replectively In this experiment, the watermark was embedded into the D components, whereas similar results as in Figure 1 and Table 1 can be obtained by embedding it into the E or F components. Adding low-frequency components to high-frequency components makes the watermarking more robust against attacks, however, this leads to an image quality degradation of the watermarked image.

4. Conclusion

We proposed a watermarking method using the high-frequency components with additive low-frequency components obtained by the DT-CDWT. We have confirmed that this method is more robust against attacks than the conventional method. In the future, we have to further investigate the robustness against other attacks. We also need to figure out why the high-frequency components with additive low-frequency components make the watermarking better resistant to attacks.

Acknowledgements

This work was partially supported by JSPS KAKENHI Grant Number 19K03623.

References

[1] Jing Liu, Jingbing Li, Jieren Cheng, Jixin Ma, Naveed Sadiq,Baoru Han, Qiang Geng and Yang Ai: A Novel Robust Watermarking Algorithm for Encrypted Medical Image Based on DTCWT-DCT and Chaotic Map, *Computers,Materials & Continua*, Vol. 61,(2019), 889–910.

[2] Nadhir Nouioua, Ali Seddiki, Abdelkrim Ghaz: Blind Digital Watermarking Framework Based on DTCWT and NSCT for Telemedicine Application, *Traitement du Signal*, Vol. 37,(2020), 955–964.

[3] Mohamed Lebcir, Suryanti Awang, Ali Benziane: Robust Blind Watermarking Technique Against Geometric Attacks for Fingerprint Image Using DTCWT-DCT, *Iraqi Journal of Science*, Vol. 61,(2020), 2715–2739.

[4] Teruya Minamoto, Ryuji Ohura: A blind digital image watermarking method based on the dyadic wavelet transform and interval arithmetic, *Applied Mathematics and Computation*, Vol. 226,(2014), 306–319.

[5] Teruya Minamoto,Ryuji Ohura: A digital image watermarking for authentication based on the dual-tree complex discrete wavelet transform and interval arithmetic, *International Journal of Wavelets, Multiresolution and information Processing*, Vol. 11,Issue 4, (2013), 1360005, 19pages.

JSST 2021

Detection of maliciously image blurred portions using dyadic wavelet transform

TAKAKI HIRAMATSU[1*] and TERUYA MINAMOTO[1]

[1]Graduate School of Science and Engineering , Saga University, Japan

[*]hiramatt@ma.is.saga-u.ac.jp

Abstract. We propose a detection technique to find maliciously blurred portions in images using the dyadic wavelet transform (DYWT). In recent years, the widespread use of image editing software has made it easy for anyone to alter images. Blurring is one of the most common image tampering and is used to delete small details from an image. Since noise properties in tampered images may change, the development of a blur tampering method will lead to the development of a fake image detection method. In our method, we apply the DYWT to an image and then obtain one low-frequency and three high-frequency components. Using the difference between the low-frequency component and its original image, we detect the blurred portions by thresholding. Our experimental results show that the proposed method can detect the portions suspected of maliciously blurred ones.

Keywords: Wavelet transform, Dyadic wavelet transform, Image forgery detection

1. Introduction

In recent years, the rapid spread of electronic devices has made it easy for anyone to edit digital image content and the number of image tamperings has been increasing on the web. The image tamperings are sometimes used to spread fake news. To prevent malicious image manipulations, many image tampering detection technologies have been actively developed.

Image tampering detection techniques can be divided mainly into two categories. One is to detect tampering by embedding a digital watermark or signature in advance. The other is to detect tampering only from the tampered image [1]. The former method requires a certain image processing in advance, while the latter does not. Up to now, image tampering detection techniques have been studied mainly for copy and paste and splicing tampering [2][3]. However, retouching tampering detection techniques, such as image blurring, are rare [4].

The purpose of this study is to develop a new method to detect maliciously blurred portions in images based on the dyadic wavelet transform (DYWT) without any requirements of prior image processing.The DYWT decomposes the original image into one low-frequency component and three high-frequency components. Since the low-frequency components is

an approximation to its original image with the same size of the original one, the difference between the original image and its low-frequency component is expected to extract a certain information for the image containing some blurred portions. Our experimental results show that the proposed method can detect the portions suspected of maliciously blurred ones.

2. DYWT

The DYWT has multiscale and shift-invariant properties and decomposes an image into its one low-frequency component and three high-frequency components. The size of all four ones is the same as the original one [5]. Setting S as an original image and applying the DYWT to S, we obtain the low-frequency component C, the vertical high-frequency component D, the horizontal high-frequency component E, and the diagonal high-frequency component F [6]. Figure 1 shows the frequency components obtained by applying the DYWT to Lenna.

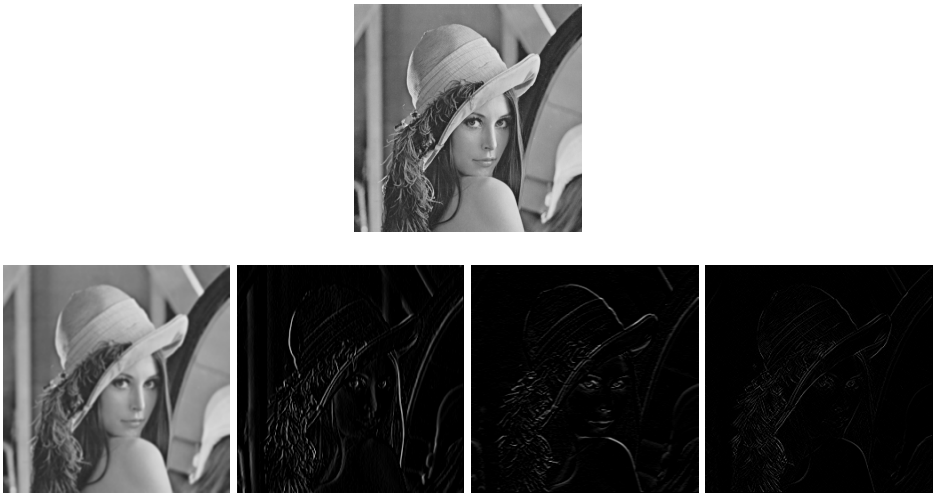

Figure 1: Lenna image S (top) , low-frequency component C, vertical high-frequency component D, horizontal high-frequency component E, and diagonal high-frequency component F (from left to right).

3. Blurred portions detection method

The procedure for blurred portions detection is as follows:

1. Apply the DYWT to the original image S. Then, the one low-frequency component C, three high-frequency component D, E, and F are obtained.

2. Compute the component H by using the following expression.

$$H[i, j] = |S[i, j] - C[i, j]|$$

3. Compute the median value Me from H.

4. Generate the component O using the following expression.

$$O[i, j] = \begin{cases} 1 & \text{When } H[i, j] < Me \\ 0 & \text{Others} \end{cases}$$

Since the blurred portion in the components H has extremely small values from our experience, the region satisfying $O[i, j] = 1$ can be judged as the blurred one by the naked eye.

4. Experimental results

The experiment was conducted using partially blurred images and its original image. Some of the experimental results are shown in Figure 2. It can be seen that the non-forgery image has flickering throughout the image, whereas the forgery image has non-flickering portion in the blurred area. The right cheek region is unnaturally flat in comparison to the left one.

Figure 2: Untampered Lenna image (top left), the component O obtained by the proposed method (top right), partially blurred images where the blurred portion is marked (first and third from the left at the bottom) and the component O obtained by the proposed method (second and fourth from the left at the bottom).

5. Conclusion

In this paper, we proposed a method for detecting maliciously blurred portions in images using the DYWT. Using the difference between the original image and its low-frequency

component, we detect the maliciously blurred portion by the naked eye. This method does not require any image processing in advance such as watermarking method and does not depend on the file format. Up to now, our method is only able to detect partially blurred region. Therefore, it is necessary to improve our method so as to detect other tampered regions automatically.

Acknowledgements

This work was partially supported by JSPS KAKENHI Grant Number 19K03623.

References

[1] Dittmann, J., Steinmetz, A., and Steinmetz, R. : Content-based digital signature for motion pictures authentication and content-fragile watermarking, International Conference on Multimedia Computing and Systems -Proceedings 2, pp. 209-213 (1999)

[2] Anuja Dixit, R. K. Gupta: Copy-Move Image Forgery Detection a Review, International Journal of Image, Graphics and Signal Processing, 8(6), pp.29-40 (2016)

[3] Jwaid, M.F., Baraskar, T.N. : Study and analysis of copy-move & splicing image forgery detection techniques, Proceedings of the International Conference on IoT in Social, Mobile, Analytics and Cloud, I-SMAC 2017, 8058268, pp. 697-702 (2017)

[4] Hashem, F.S., Sulong, G. : Passive aproaches for detecting image tampering: A review, Jurnal Teknologi, 73(2), pp. 31-36 (2015)

[5] Mallat, S. : A Wavelet Tour of Signal Processing:The Sparse Way. Third Edition. Academic Press (2008)

[6] T. Minamoto, K. Tsuruta and S. Fujii : Edge-preserving image denoising methods based on dyadic lifting schemes, IPSJ Transactions on Computer Vision and Applications, Vol.2, pp. 48-58 (2010)

JSST 2021

Feature Extraction Method for Detecting Early Stage Colorectal Cancer from Endoscopic Images Using Dual-Tree Complex Wavelet Packet Transform

Daigo Takano[1,*] and Teruya Minamoto[1]

[1]Graduate School of Science and Engineering, Saga University, Saga, Japan

[*]takanod@ma.is.saga-u.ac.jp

Abstract. Colorectal cancer is one of the most common and deadly types of cancer in Japan, and many methods to detect early colorectal cancer from endoscopic images have been developed. Most modern methods are based on machine learning methods, especially deep learning (DL). These methods can detect the cancer with high accuracy, but a large number of data is required and we don't know how these methods detect cancers. We propose a feature extraction method for detecting early stage colorectal cancer from endoscopic images using the Dual-Tree Complex Wavelet Packet Transform (DT-CWPT). Our method does not require a large amount of data and can explain the reason for detecting early colorectal cancers.

Keywords: Wavelet Transform,Dual-Tree Complex Wavelet Transform,Wavelet Packet

1. Introduction

In recent years, deep learning techniques have been used in many cases and can detect early cancer with high accuracy from endoscopic images. However, there are mainly two defects. One is that these techniques require a large number of data, the other is a "black box" problem in machine learning, that is, humans cannot understand the reason why these techniques have come to a specific decision.

We aim to propose a new feature extraction method for detecting early-stage colorectal cancer from endoscopic images. The features can be extracted from a small amount of data and can be interpreted by humans. To achieve our aim, we use the Dual-Tree Complex Wavelet Transform (DT-CWT) [1] and Wavelet Packet [2]. According to our interview with doctors, they focus on the normal regions and determine the regions that are different from the normal ones as the abnormal regions when they try to detect early-stage colorectal cancers. Since the DT-CWT has the directional selectivity, it is expected to detect the difference between abnormal and normal regions based on the DT-CWT. To obtain more detail features from endoscopic images, we use the Dual-Tree Complex Wavelet Packet Transform (DT-CWPT) which decompose not only the low-frequency components but also the

high-frequency components, whereas the DT-CWT decompose the low-frequency component only[3] . We then apply PCA to the components obtained by the DT-CWPT and make a graph depending on the first and second principal components of PCA. Experimental results show that the graph depicts the difference between the abnormal and normal regions.

2. Proposed method

The proposed method is described as follows:

1. Apply the DT-CWPT to colonoscopy images to obtain multiple frequency components.

   Applying the DT-CWT to an image, we obtain four components depending on real (R) and imaginary (I) filters such as, $D_{RR}, D_{RI}, D_{RI}, D_{II}$ for the component D, for example. In this study, only use the D_{RI}.Here, $d^{RI,(n,m)}_{j,n_y,n_x}$ in (1) represents the frequency components obtained by applying the real (R) filter in the vertical direction and the imaginary (I) filter in the horizontal direction to the input image at level j. The notations n_y and n_x indicate the locations in the horizontal and vertical directions, respectively. We distinguished the frequency components by labeling them with m and n.

$$D^{R,(n,m)}_{j,n_x,n_y} = \frac{d^{RR,(n,m)}_{j,n_y,n_x} + d^{II,(n,m)}_{j,n_y,n_x}}{2} \tag{1}$$

$$D^{I,(n,m)}_{j,n_x,n_y} = \frac{d^{IR,(n,m)}_{j,n_y,n_x} + d^{RI,(n,m)}_{j,n_y,n_x}}{2} \tag{2}$$

2. Compute the variance from the obtained frequency components at each and perform PCA on all variances.

   Applying the Wavelet Packet transform at level j to an image, we obtain 4^j components. Therefore, the total number of components obtained by the DT-CWPT at level j is 4^{j+1}. For example, we obtain 64 components at level2. but, We don't use low frequency components. Figure 1 shows the components obtained by applying the DT-CWPT at level 2 for endoscopic image. The blue dots in the figure represent normal images, and the red dots represent abnormal images. The x-axis is the value in (1), and the y-axis is the value in (2). As can be seen from Figure 1, the points in the normal image are concentrated in the center, while those in the abnormal image are relatively scattered. Therefore, We compute variances of 63 components, and use like 63-dimensional vector. Finally, we performed PCA on these vectors.

3. Draw a scatterplot between the first and second principal components.

   We make scatterplot between the first (x-axis) and second (y-axis) principal components.

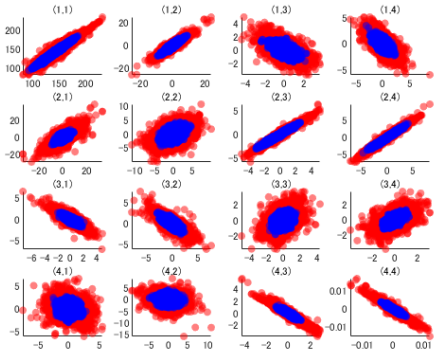

Figure 1: Examples of the frequency components obtained by the DT-CWPT at level 2

3. Experimental results

We define ”normal images” as images that do not contain any abnormal regions, and ”abnormal images” as images that contains abnormal regions. Figure 2 shows an actual endoscope image. The marked region in the image is early stage colon cancer. 800 images were cre-

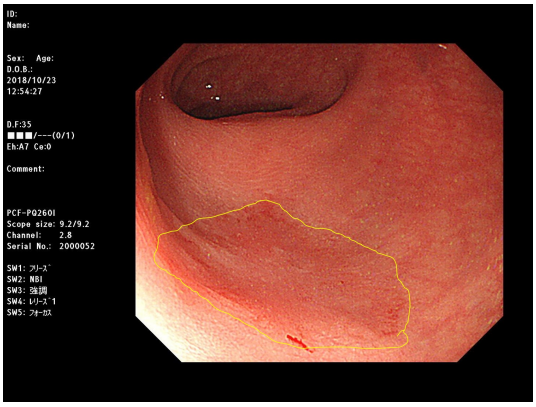

Figure 2: An endoscopic image where the region of early-stage colon cancer was marked by a doctor.

ated by cropping 400 normal and 400 abnormal images in 64×64 size. We converted all images to CIE L*a*b* color space and apply our method to the a* and b* components of the images.

The scatterplot obtained by proposed method are shown in Figure 3. Again, blue dots indicate normal images, and red dots indicate abnormal images. Figure 3 shows that we can almost distinguish between normal and abnormal regions.

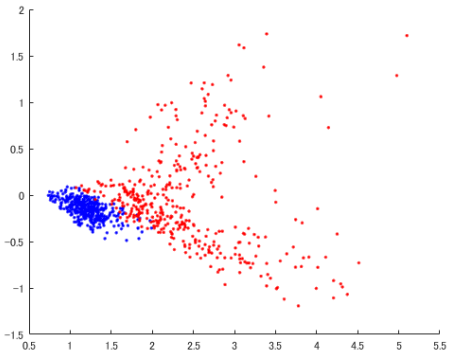

Figure 3: The value of the first and second principal components calculated from the variance of frequency components

4. Conclusion

From the experimental results, we confirmed that the DT-CWPT is useful for extracting the features of early-stage colorectal cancer from endoscopic images. However, we have not been able to completely separate normal and abnormal regions. In future work, we want to reveal the property of images that cannot be correctly classified and develop a method to classify normal and abnormal regions with high accuracy.

Acknowledgements

This work was partially supported by JSPS KAKENHI Grant Number 19K03623.

References

[1] Kingsbury, Nick.: ”Complex Wavelets for Shift Invariant Analysis and Filtering of Signals”, Applied and Computational Harmonic Analysis, 10, no.3 (2001), pp.234–53.

[2] R. R. Coifman,Y. Meyer, and M. V. Wickerhauser.: ”Wavelet analysis and signal processing.” Wavelets and Their Applications, pp.153–178,1992.

[3] Bayram I., SelesnickW. I., “ On the Dual-tree Complex Wavelet Packet and M-band Transform ”, ”IEEE Transactions on Signal Processing”, Vol.56, no.6 (2008), pp.2298-2310.

Computation of Compressive Flow in Pulsed Focusing Engine (Fugine) Set in Shock Tube

Daiki Okada[1*], Hiroki Kijima[1], Tomotaka Kobayashi[1], Ken Naitoh[1]

[1]Faculty of Science and Engineering, Waseda University, Japan

*okapy_ilsag@suou.waseda.jp

Abstract. In order to realize high thermal efficiency, in our previous research, we proposed a new engine concept based on pulsed supermulti-jets colliding at a single point around the chamber center through a focusing process [1]. The shock tube experiments were conducted for supermulti-jets colliding in the reaction chamber of a prototype engine with 14 jet-nozzles and side-passages [2]. The present report shows the first computational result for the new engine including all of the jet-nozzles and side-passages installed in the shock tube. Computed pressure on a sensor installed near the collision point of jets can be quantitatively compared with the experiment.

Keywords: Pulsed supermulti-jets colliding, 14 jet-nozzles and side-passages, Shock tube, Pressure on a sensor

1. Introduction

The engine which uses a new compressive combustion principle based on supermulti-jets colliding was proposed [1]. This principle generates strong single point compression and leads to single-point auto ignition, due to supermulti-jets colliding with a pulse (Fig. 1). It has the potential of high thermal efficiency of low exhaust gas because of its high point compression and low heat loss on the wall due to the effect of burned gas encased by supermulti-jets colliding, with additional compression due to position or rotating cascades. The jets also encase the combustion noise, leading to less noise.

Based on the principle, the engine which has 14 jet-nozzles and side-passages having curved pipes between nozzles and straight passages was created and has experimented to be set in the shock tube on the condition that the high pressure domain is 310[kPa] and the low pressure domain is 40[kPa] [2] (Fig. 2). Computations focused around the collision point with no side-passages including curved pipes were conducted [2] (Fig. 3).

In this paper, unsteady three-dimensional computation for the engine with 14 jet-nozzles and side-passages set in the shock tube was conducted, which corresponds to the shock tube experiment (Fig. 4). Computed pressure on a sensor installed near the collision point of jets was compared with the experimental results.

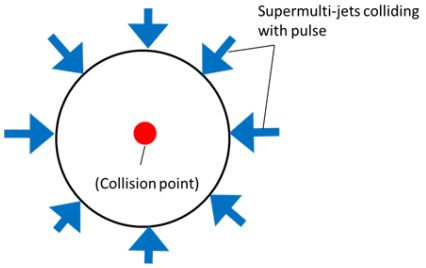

Fig. 1. A diagram of a new compressive combustion principle

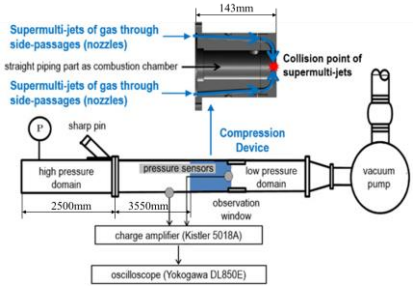

Fig. 2. A diagram of the experiment set in shock tube

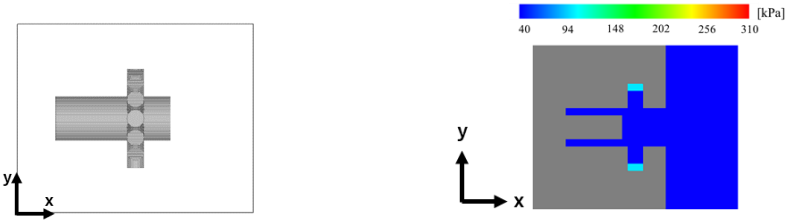

Fig. 3. The analytical subject of the computation focused around the collision point

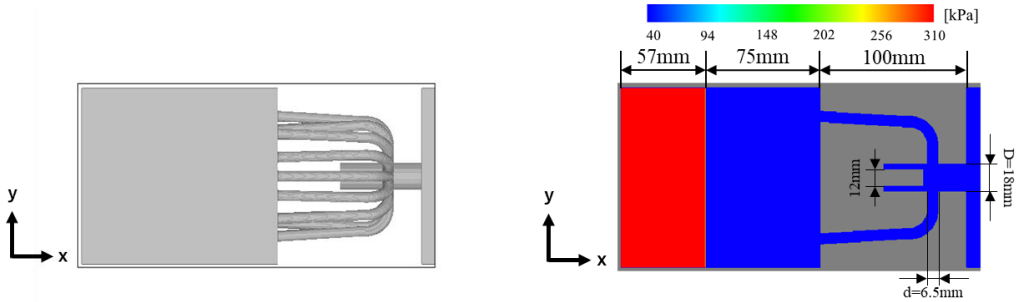

Fig. 4. The analytical subject of the engine with 14 jet-nozzles and side-passages set in the shock tube

2. Simulation method

The simulation method is to be solved the unsteady compressible Navier-Stokes equation in three-dimensional space which is described in a non-conservative form by using the BI-SCALES method [3] including the CIP method [4] and the SOR method.

In the experiment set in the shock tube, the length of the compression device including the nozzles and side-passages for supermulti-jets colliding with pulse is 143[mm], the shock tube length of the high pressure domain is 2500[mm], and the shock tube length of the low pressure domain in front of the compression device is 3550[mm] (Fig. 2). (For the analytical subject of computation (Fig. 4), the analytical domain is shortened to reduce CPU time and memory. The length of the compression device is 100[mm], the length of the high pressure domain is 57[mm], and the length of the low pressure domain in front of the compression device is 75[mm].) Nozzle diameter d=6.5[mm], Chamber diameter D=18[mm], D/d ratio=2.7, and Sensor diameter=12[mm] are same for both computation and experiment. As the initial conditions, the temperature and the velocity are 298.2[K] and 0[m/s]. The high pressure domain is 310[kPa] and the low pressure domain is 40[kPa] (Fig. 4). Grid sizes are 0.25[mm] in the compression device and 0.50[mm] in the shock tube. Number of grid points is 131 million (400x492x492, 500x258x258 points)

3. Computational result and experiment evaluation

Fig. 5 presents computational results of pressure and temperature time histories. The pressure and temperature at the geometrical collision point of jets firstly rise to 626.8[kPa] and 656.4[K] at about 395[μs]. The pressure and temperature secondly rise more when supermulti-jets collide with the pressure sensor surface at about 400[μs]. The peak value of computed pressure on the center of the sensor is 1003[kPa] (Fig. 6). The peak value of pressure measured in shock tube experiment was about 726.7[kPa] [2]. This difference between computational and experimental pressures is attributable to the fact that the pressure obtained from the sensor is averaged on the sensor surface. Thus, the computed pressure should be averaged on the sensor surface while changing the number of grid points for averaging (Fig. 6). The peak value (802.7[kPa]) of computed pressure averaged with the sensor surface diameter 0.5[mm] is the closest to the experiment. However, as the pressure sensor used in the experiment may detect the pressure averaged by the sensor surface diameter 2.0~4.0[mm], the computed pressure is smaller than the experiment. In case of computation for the engine with 14 jet-nozzles and side-passages set in the shock tube (Fig. 4), the pressure just before entering the chamber is 88.89[kPa], and the pressure at collision point is 626.8[kPa]. In case of computation in which there are no side-passages (Fig. 3), the pressure just before entering the chamber was 102.6[kPa], and the pressure at collision point was 963.1[kPa] [2]. Comparing two computations in Figs. 3 and 4, difference of the pressure just before entering the chamber is 13.71[kPa] (102.6[kPa]–88.89[kPa]). Combined pressure difference due to 14 jet-nozzles is 191.9[kPa] (13.71[kPa]x14). Additionally, combined momentum energy difference due to 14 jet-nozzles just before entering the chamber between Figs. 3 and 4 is 161.3[kPa]. The value 353.2[kPa] (191.9[kPa]+161.3[kPa]) is close to the difference of pressure at collision point, 336.3[kPa] (963.1[kPa]–626.8[kPa]). Computational pressure loss by pipe friction in a jet-nozzle and side-passage (15.86[kPa]) which is larger than the theoretical value (6.562[kPa]) may bring the difference of pressure at collision point between Figs. 3 and 4, also the difference of pressure on the sensor between experiment and Fig. 4.

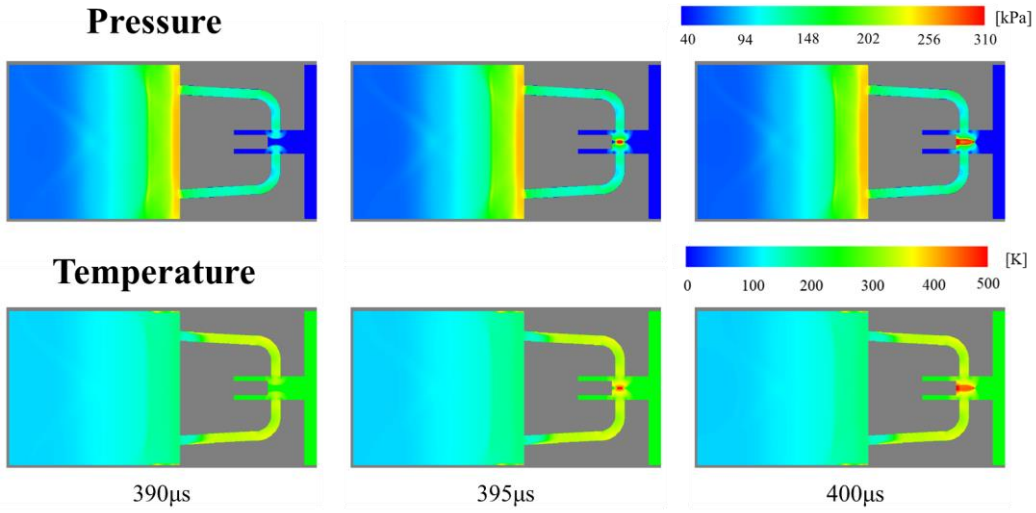

Fig. 5. Computational results of pressure and temperature time histories

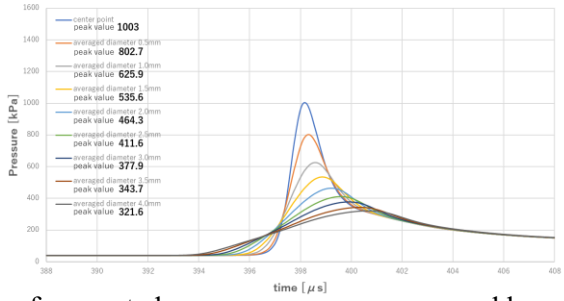

Fig. 6. Time histories of computed pressure on sensor averaged by sensor surface diameter

4. Conclusion

Computation with the added shape of 14 side-passages and shock tube was conducted, which corresponds to the shock tube experiment. Computational results of pressure on the sensor were lower than the experiment. To evaluate pressure loss in jet-nozzles and side-passages accurately, multi-grid systems [5] may be useful.

References

[1] K. Naitoh, K. Nakamura, T. Emoto: *A New Cascade-Less Engine Operated from Subsonic to Hypersonic Conditions*, Journal of Thermal Science, 19-6 (2010), pp.481-485.

[2] R. Konagaya: *Principle Study on the Compression Combustion Engine Based on Supermulti-jets Colliding with Pulse*, Doctoral Dissertation of Waseda University (2020).

[3] K. Naitoh, K. Kuwahara: *Large eddy simulation and direct simulation of compressible turbulence and combusting flows in engines based on the BI-SCALES method*, Fluid Dynamics Research 10 (1992), 299-325.

[4] H. Takewaki, T. Yabe: *The Cubic-Interpolated Pseudo Particle (CIP) Method: Application to Nonlinear and Multi-dimensional Hyperbolic Equations*, JOURNAL OF COMPUTATIONAL PHYSICS 70 (1987), 355-365

[5] H. Suzuki, H. Kijima, D. Igarashi, T. Kobayashi, R. Konagaya, and K. Naitoh: *Multigrid numerical analysis on principle of collision of pulsed supermulti jets*, JSASS 64 (2020).

[6] Yakhot, V. and Orszag, S.A.: *Renormalized group analysis of turbulence I. Basic theory*, J. Sci. Computing 1 (1986), pp. 3-51

Appendix

The three-dimensional unsteady compressible Navier-Stokes equation is basically employed as the governing equation. The boundary conditions of velocity and thermodynamic quantities at the downstream are given by the Thompson non-reflection condition (the method of characteristics) and those at the wall is given by the Neumann condition and non-Slip condition [3]. The computation set in shock tube (Fig. 2) is in the laminar flow because supermulti-jets collide before turbulence transition. However, for straight pipe flows, there was very little difference in computational results between the turbulence model and the laminar flow model [2]. Then, vortices and turbulence will appear in the combustion chamber [6]. Thus, as a subgrid turbulence model, the Yakhot-Orszag model simplified for a large eddy simulation (LES) was added in this study.

Computations on high efficiencies of pulsed focusing engine for rocket

Tomotaka Kobayashi[1*], Hayato Suzuki[1], Hiroki Kijima[1], Ken Naitoh[1]

[1]Faculty of Science and Engineering, Waseda University, Japan

*winningshot1996@asagi.waseda.jp

Abstract. We proposed a new engine concept based on pulsed supermulti-jets colliding at a single point around the chamber center through a focusing process, in order to realize high thermal efficiency due to nearly-complete insulation effect and relatively-silent high compression (Naitoh, et al. 2010). This engine concept can be applied for various usages including automobiles, power generation, aircrafts, and rockets. As the evidence for air-breathing conditions such as aircraft and automobiles, we principally performed some fundamental combustion experiments for a prototype engine with 14 jet-nozzles, which indicate the potential of high thermal efficiency and insulation effect (Konagaya, et al. 2020). However, at very high altitude of rockets, free redundant dense atmospheric air cannot be used as insulation gas layer around reaction chamber wall, i.e., hydrogen or oxygen must be used for insulation gas, which may lead to waste of unburned gases. The present report proposes a novel way for overcoming this problem.

Keywords: Pulsed supermulti-jets colliding, Combustion and Thermal efficiencies, Rocket

1. Introduction

A new compressive combustion principle based on supermulti-jets colliding with pulse was proposed for combustion engines [1]. Strong compression is caused by the collision of the jets and auto ignition occurs around the combustion chamber center (Fig. 1).

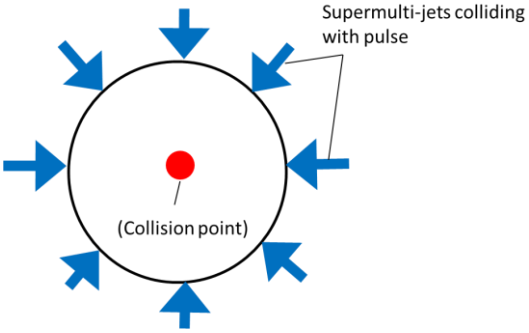

Fig. 1. A diagram of a new compressive combustion principle

It has the potential of high thermal efficiency because of chamber-center high compression and low heat loss on the wall due to the encasing of burned gas by the supermulti-jets, in cases with additional compression due to position or rotating cascades. The jets also encase the combustion noise, leading to less noise.

This engine concept can be applied for various usages including automobiles, power generation, aircrafts, and rockets.

As the evidence for air-breathing conditions such as aircraft and automobiles, we principally performed some fundamental combustion experiments for a prototype engine with semi-spherical 14 jet-nozzles, which indicate the potential of high thermal efficiency and insulation effect [2].

2. Our previous computation at startup of pulsed focusing engine for rocket

However, at very high altitude of rockets, free redundant dense atmospheric air cannot be used as insulation gas layer around reaction chamber wall, i.e., hydrogen or oxygen must be used for insulation gas, which may lead to waste of unburned gases.

Let us see Fig. 2 (left), which shows computational results of reacting flow during the first engine cycle (at startup) for semi-spherical distributions of 14 jets, which shows lots of unburned hydrogen gas wasted from the nozzles close to the external area (close to lower part of the combustion chamber). [3] The present waste of unburned gas has no problem for atmospheric air breathing engines such as those installed in aircrafts and automobiles, because atmospheric air is redundant and free. However, this problem must be overcome for rockets. Thus, we add more jets for enclosing the jets more as shown in Fig. 2 (right). We qualitatively confirmed that the number of jets increasing brings higher thermal efficiency, higher combustion efficiency, and higher power (thrust). [3] [See the governing equation and computational methods in appendix.]

However, we found that the efficiencies and power are still insufficient.

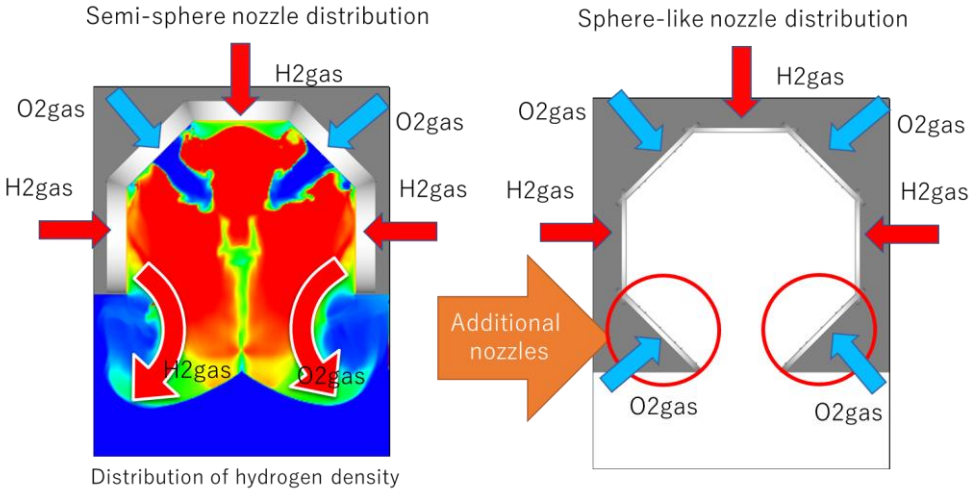

Fig. 2. Computation of reacting flow in primitive pulsed focusing engine for rocket [3]

3. Further analysis at startup of pulsed focusing engine for rocket

In the present section, we set two new improvements for obtaining higher efficiencies. First is increase in the number of jets, i.e., 24-jets corresponding to that in Fig. 2 (right), although the number of jets was 14 in the primitive computation of Fig. 2 (left). Second is supply of premixed gas of hydrogen and oxygen through each jet nozzle, although oxygen and hydrogen are separately supplied, which leads to less mixing and also the amount of combustible gases.

Figure 3 demonstrates the computational result during the first engine cycle, while the combustion chamber is initially filled with atmospheric air (not pure oxygen and including no hydrogen). From the temperature distribution in Fig.3 (left), this figure is at the timing that all of the shock fronts at the head of 24-jets collide. We can see a high temperature and high pressure around the reaction chamber center. However, Figure 3 (right) indicates no mixture of hydrogen and oxygen around the chamber center, because initial atmospheric air still remains around the chamber center. [See the governing equation and computational methods in appendix.]

We should find the reason of no hydrogen and oxygen around the chamber center, whereas high temperature and high pressure appear at the chamber center. The reason is very simple. As textbooks on compressible fluid dynamics [4] explain for students, shock front proceeds ahead of gas injected from the nozzles, i.e., only pressure wave such as shock wave proceeds inside the gas at upstream of the shock front. Thus, high temperature gas around chamber center without hydrogen and oxygen cannot burn, which results in combustion at the region with pressure lower than relatively high pressure region around combustion chamber center, i.e., the contact surface between hot gas of air and cool gas of H2+O2 entering from the nozzles shown in Fig. 3 (right). The present combustion occurrence at lower compression condition results in lower thermal efficiency and also no ignition of lower temperature O2+H2 mixture around chamber wall, leading to low combustion efficiency.

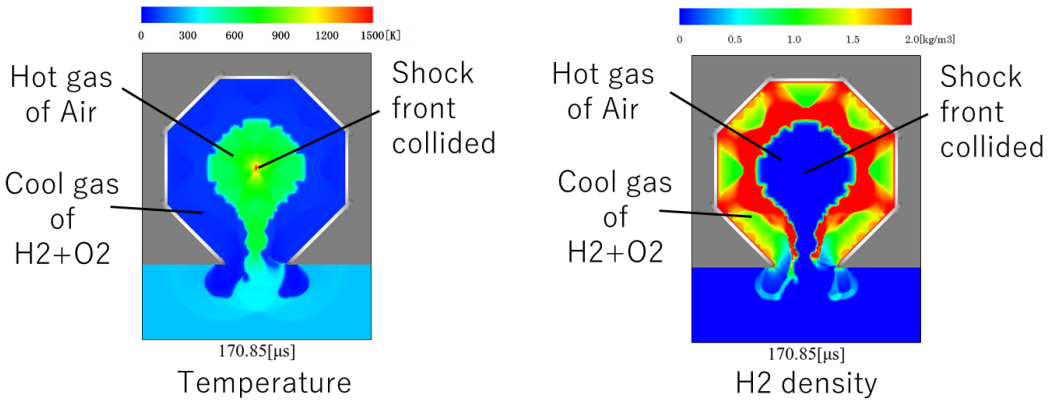

Fig. 3. Computational result of reacting flow at first engine cycle for premixed gas of oxygen and hydrogen (24-jets)

However, we find that this computational result has no problem for obtaining high thermal and combustion efficiencies for the second engine cycle. It is stressed that unburned mixture gas of hydrogen and oxygen at the end of the first engine cycle moves to the chamber center in the second engine cycle, because the new jet flow pushes the unburned mixture gas toward

the chamber center.

4. Conclusion

Computation and theoretical consideration shown above bring that the sphere-like distribution of jets will lead to high thermal and high combustion efficiencies after the second engine cycle, if further fine optimizations are done on details of jet nozzles distribution and also period of pulse.

References

[1] K. Naitoh, K. Nakamura, T. Emoto: *A New Cascade-Less Engine Operated from Subsonic to Hypersonic Conditions*, Journal of Thermal Science, 19-6 (2010), pp.481-485.

[2] R. Konagaya, K. Naitoh, T. Kobayashi, Y. Isshiki, et al.: *Two Prototype Engines with Colliding and Compression of Pulsed Supermulti-Jets through a Focusing Process, Leading to Nearly Complete Air Insulation and Relatively Silent High Compression for Automobiles, Motorcycles, Aircrafts, and Rockets*, SAE Technical Paper 2020-01-0837 (2020). doi:10.4271/2020-01-0837

[3] S. Kawaguchi, R. Konagaya, K. Tsuru and K. Naitoh: *Computations for Improving the Performance of a New Hydrogen-Oxygen Rocket Engine Based on Supermulti-jets Colliding with Pulse*, 2018 AIAA Aerospace Sciences Meeting, AIAA 2018-0668 (2018). doi:10.2514/6.2018-0668 (Also in S. Kawaguchi, master thesis (directed by Ken Naitoh, Waseda University), 2018)

[4] T. Ikui and K. Matsuo, Compressible Fluid Mechanics, Rikougakusha, (2001).

[5] H. Takewaki, T. Yabe: *The Cubic-Interpolated Pseudo Particle (CIP) Method: Application to Nonlinear and Multi-dimensional Hyperbolic Equations*, JOURNAL OF COMPUTATIONAL PHYSICS 70 (1987), 355-365

[6] K. Naitoh and K. Kuwahara, Large eddy simulation and direct simulation of compressible turbulence and combusting flows in engines based on the BI-SCALES method. J. of Fluid Dynamics Research, Vol. 10, pp. 299-325. (1992).

[7] K. Naitoh, Y. Takagi, and K. Kuwahara, Cycle-resolved computations of compressible vortical flows in automotive engines. Computers and Fluids, Vol. 22, pp. 623-648 (1993).

[8] Yakhot, V. and Orszag, S.A.: *Renormalized group analysis of turbulence I. Basic theory*, J. Sci. Computing 1 (1986), pp. 3-51.

Appnendix: Governing equation and computational method

The unsteady compressible Navier-Stokes equation in the three-dimensional space which is described in a non-conservative form with the BI-SCALES method [6,7,8] is solved by using the CIP method [5] and SOR method. As a subgrid turbulence model, the Yakhot-Orszag model simplified for a large eddy simulation (LES) was used [8]. The boundary conditions of velocity and thermodynamic quantities at the downstream are given by the Thompson non-reflection condition (the method of characteristics) and those at the wall is given by the Neumann condition and non-slip condition. [6]

JSST 2021

A simple model of on–demand transporter

Yuhei Okubo[1,*], Takashi Shimada[2], Toru Ohira[1]

[1]Nagoya University, Japan
[2]The University of Tokyo, Japan

[*]d20001h@math.nagoya-u.ac.jp

Abstract. We consider a theoretical model of a "transporter" in two dimensions. We define "town" by square 2-D grids. In the town, we place multiple "parcels" with randomly chosen specified pick-up and delivery addresses. The transporter goes around these addresses to deliver parcels. We observe the transporter's total traveling distance for the delivery of all the parcels. We find that it can be approximately obtained by the number of parcels and the size of the town.

Keywords: Transporter, Delivery, Traveling distance

1. Introduction

Delivery services let us increasingly enjoy the purchase of goods and foods without physically moving. It has also become an important service under the current situation with the COVID-19. Increasing demand, on the other hand, has caused shortages of delivery personnel and vehicles, which is leading to increasing delivery costs. It is, therefore, crucial that we allocate appropriate resources that match the volume of delivery as well as the size of the area without reducing the level of service for customers.
Against this background, we consider a theoretical model of delivery or transporting problem in two–dimensions. In this work, we studied the properties of delivery when the transporter has the following strategy: a transporter moves to the nearest point, which either has a parcel to pick up or is one of the delivery locations among parcels that the transporter currently holds. In particular, we analyze by measuring the total distance of delivery paths.

2. Model

We construct a theoretical model of a transporter. On the "town" with square grid streets, "parcels" are placed randomly each of which has its delivery location. A "transporter" goes around to pick up and deliver parcels. He/She can hold multiple parcels and move north-south and east-west directions. Let a transporter move according to the following rule:

1. Determine the first destination to the closest point of pick-up addresses from the current transporter ' s position.

2. Let the transporter go to the destination, then pick up the parcel.

3. Determine the next destination to the closest point of delivery addresses or the other pick–up ones.

4. Go back to step (2) until all parcels have been picked up and delivered.

3. Simulations and Analysis

We analyze the behavior of the model mainly by computer simulations. We set the size of the town as $M \times M$ grid points and the number of parcels as C. We have simulated 10,000 statistical samples for each parameter pair of (M, C) with $M = 20, 30, 40, 50$, and $C = 3n(n = 1, 2, ...40)$.
We have computed the average total traveling distance $\langle L \rangle$ for the entire delivery for each parameter set. (We estimate average error is of the order of 1 %).

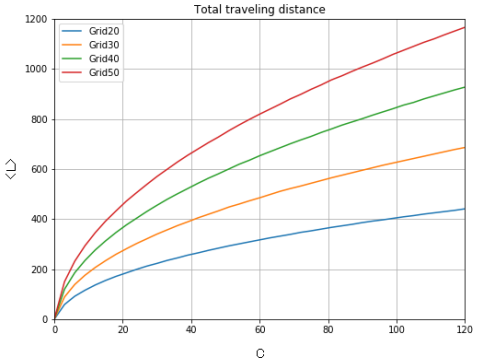

Figure 1: Total travelling distance

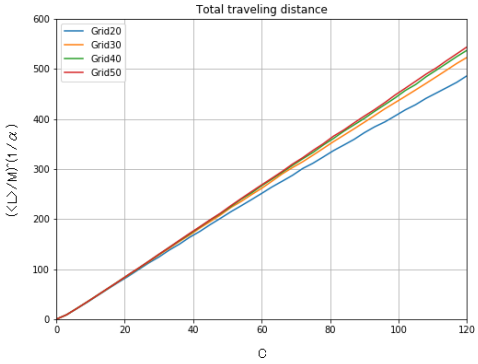

Figure 2: Scaled total travelling distance

The results are shown in **Fig. 1**. To investigate the functional relations, we scale our results. The result is shown in **Fig. 2** and we have found

$$\langle L \rangle \simeq 2M\sqrt{C} \tag{1}$$

which is estimated from the slope of the lines in **Fig. 2**.
This relation can be described approximately with the following theoretical explanation. We consider the case of large M and C so that we can argue that related variables are continuous. Let $n(t)$ be the number of parcels still to be delivered at time t. Considering the density of parcels at t is $n(t)/M^2$, we can roughly estimate the average traveling distance to pick up and deliver the current parcel $l(t)$ as

$$\frac{n(t)}{M^2} \approx \frac{1}{l(t)^2}, \tag{2}$$

which leads to

$$l(n(t)) \approx \frac{M}{\sqrt{n(t)}}. \tag{3}$$

The total average traveling distance $\langle L \rangle$ can be obtained by summing (integrating) $l(t)$ for all the parcels starting from $n(t = 0) = C$ to the last one:

$$\langle L \rangle \approx \int_C^1 l(n)(-dn) = \int_1^C \frac{M}{\sqrt{n}} dn \approx 2M\sqrt{C} \tag{4}$$

This agrees approximately our estimation of the parameters above through simulations.

4. RELATED TOPICS AND OUTLOOK

We have investigated related topics such as models of computer packet congestions, 1-dimensional foraging process, and group chase and escapes, where there are agents involved that have the purpose of picking up and/or delivering objects [1, 2, 3, 4]. Here, we have presented yet another model that belongs to the same category.
We have found numerically that we can approximate the average travel length of delivery trips give the size of the town and the total number of parcels.
As future investigations, we can consider the effect of multiple transporters. By changing and/or mixing of strategies (movement rules of normal/express delivery apply to all transporters or allocate), we would like to investigate a way to deliver all parcels with a minimum traveling distance with moderate load.

References

[1] Ohira T, Sawatari R (1998), Phase transition in a computer network traffic model. *Physical Review E*, **58**:193-196

[2] Shimada T, Ohira T (2019), Diffusion constant of a forager on a one-dimentional periodic system, in the 25th *Proceedings of Traffic Symposium*, Nagoya Japan

[3] Kamimura A, Ohira T (2010), Group chase and escape. *New Journal of Physics*, **12**:053013

[4] Masuko M, Hiraoka T, Ito N, Shimada T (2017), The effect of laziness in group chase and escape. J. of *Physical Society of Japan*, **86**:085002

Numerical evaluation on the out-of-plane properties of bio-inspired honeycomb cores with extra hollows

Mudong Li[1*], Sachiko Ishida[1], Kazuya Saito[2]

[1] Department of Mechanical Engineering, Meiji University

[2] Faculty of Design, Kyushu University

*ce202076@meiji.ac.jp

Abstract. In this study, we designed new bio-inspired honeycomb cores with extra hollows inspired by a microstructure which can be seen in beetle elytron plates. The new cores can be fabricated as the conventional corrugated method. We numerically confirmed that the extra hollows contribute to enhance the compressive strength of the honeycomb cores, compared with the equivalent-volumed conventional hexagonal honeycomb cores.

Keywords: Honeycomb cores, Structural material, Composite material, Finite element analysis, Biomimetics

1. Introduction

Honeycomb cores are widely used as core material of sandwich panels in aerospace applications and transportation systems because of its light weight, high compressive strength and high energy absorbing capacity [1]. Previous studies showed that cylindrical hollow trabeculae in beetle elytron plates (BEPs), which are placed at the vertexes of primary hexagonal honeycomb cores, are contributed to increase the compressive strength of BEPs [2]. This study implies the possibility of designing stronger structural materials by adding the extra hollows in conventional hexagonal cores. However, this original geometry can only be 3D-printed, which is not suitable for high-speed manufacturing. In this study, we revised the original geometry to apply the corrugated method. Through theoretical estimations and finite element analyses, the new geometry enhanced compressive properties in out-of-plane direction.

2. Design and theoretical estimation

Corrugated method is one of the conventional fabrication methods of honeycomb cores. Thin-walled materials are folded into corrugated shapes, stacked and glued together. We arranged the new geometry of honeycomb cores by arraying square hollows between adhesive surfaces shown in Fig. 1. The size of the square hollows x is derived by $x = 1 / \sqrt{3}\left(2 + \sqrt{2}\right)a$, where a is the size of primary core. The thickness of adhesive surfaces is expressed as $2t$, where t is the thickness of the single surface. Axis z represents the out-of-plane direction of honeycomb

cores. This revised model shown in Fig.1, which includes eight primary cores, and seven square hollows, was used on the following analysis.

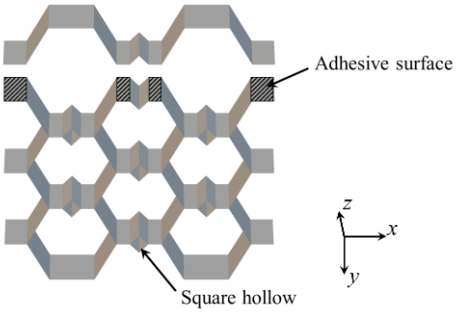

Fig. 1 Honeycomb cores with extra hollows

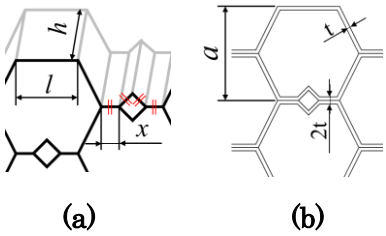

Fig. 2 Design details

Following the theory by Timoshenko *et al.* [3], the elastic buckling load P_{cr} of a simple supported rectangular plate is described in the following equation:

$$P_{cr} = \frac{k\pi^2 E}{12(1-\nu^2)}\frac{t^3}{l} \tag{1}$$

where E is Young's modulus of the material, ν is Poisson's ratio, t and l represent the thickness and width of the rectangle (see Fig. 2), respectively. Factor k is determined by the shape of the rectangle, but we approximate it as a constant value $k = 4.0$ here. As these material properties are fixed, the buckling load of honeycomb cores is determined by the core thickness and the core size, which does not depend on the core height. The square hollow consists of four rectangular plates, each side of the plates is shorter than one side of hexagonal primary cores. In a quick estimation, when the thickness t is doubled, the buckling load increses by eight times; when the width l is halved, the buckling load is doubled. This is the reason why the extra square hollows can increase the compressive strength.

3. Finite element analysis

We numerically performed compressive simulation by finite element analysis application, ANSYS. The material properties of aluminum which we set up for analysis are shown in Table. 1. Out-of-plane displacements with the constant speed at 1.0 mm/s were given on the upper sides of the analysis models, and the lower sides were simply supported. The dynamic analysis was carried out, but the speed was sufficiently slow to ignore the effect of strain rate. To evaluate the increase rate of ultimate compressive strength, we made comparison between the revised model with hollows and the conventional hexagonal model which has equivalent volume. Figure 3 describes that the revised model enhanced compressive strength by approximately 45%, but the amount of enhancement was lower than the expectation by Eq. 1. The gaps between theoretical estimated buckling load and analyzed ultimate strength were possibly caused by the effect of elastic buckling modes appeared in the analysis, which are not considered in the theory. Figure 4 shows the elastic buckling modes before plastic collapse. The deformation by elastic buckling in the primary cores was larger than that in the extra hollows, but the larger number of the buckling waves was observed in the extra hollows. Different buckling modes in primary cores and extra hollows interfered each other across the adhesive surface. Thus, the model with extra hollows reached its elastic limit sooner than expected due to the complex buckling phenomenon. Moreover, we prepared two other analysis

models whose core size was the same with different core heights and thicknesses. All of these results showed the same tendency.

4. Conclusions

Table. 1 Material properties

Material	A3003-H19
Young's modulus	70 GPa
Poisson's ratio	0.33
Yield strength	210 MPa
Elongation	1.1%
Tensile strength	240 MPa

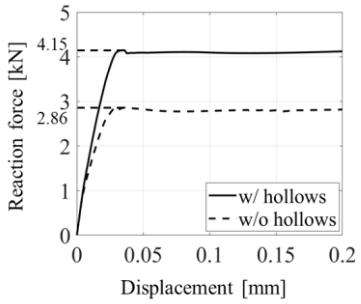

Fig. 3 Force-displacement diagram of honeycomb cores with and without extra hollows

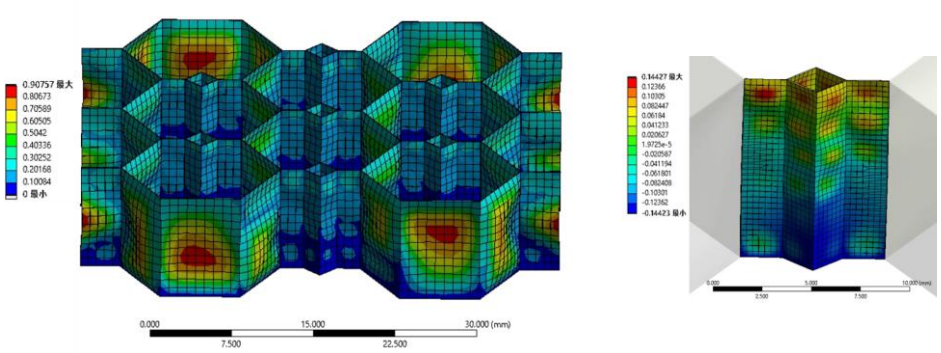

Fig. 4 Elastic buckling modes of primary cores (left) and the extra hollow (right) before plastic collapse.

In this study, the revised geometry of honeycomb cores inspired by BEPs was proposed. It consisted of primary cores and square hollows in adhesive surfaces. The buckling mode and the compressive strength were investigated through theoretical estimation and finite element analysis. The simulation result showed the out-of-plane compressive strength of the revised model increased 45% compared to the conventional cores. The mechanical properties of the revised model will be investigated experimentally in our future work.

Acknowledgement

This study is financially supported by JSPS KAKENHI Grant No. 21K03755.

References

[1] T. Sato (2002), *Development and application of honeycomb core materials and sandwich structures*, CMC Publishing (in Japanese).

[2] J. Chen, X. Zhang, Y. Okabe, K. Saito, Z. Guo, L. Pan: The deformation mode and

strengthening mechanism of compression in the beetle elytron plate, *Material and Design*, 131 (2017), 481-486.

[3] S. Timoshenko & J. Gere (1988), *Theory of elastic stability* (2nd ed.), McGraw-Hill Book Company.

Sound Insulation Simulations focusing on Height of Origami Core

Aya Abe[1*], Ichiro Hagiwara[1]

[1] Meiji Institute for Advanced Study of Mathematical Sciences, Meiji University

*aya_abe@meiji.ac.jp

Abstract. We have developed a new truss core panel by origami forming to get the higher aspect ratio than that by multi-stage press molding. Our object is to apply the new origami truss core to the train floor. Whether or not this goal can be achieved depends on whether this new origami truss core with a high aspect ratio has excellent sound insulation characteristics. Therefore, as a development of the analysis technology by FEM which accurately estimates the sound insulation characteristics, at first, the relation between the aspect ratio and the sound insulation performance is discussed in the flat plate with one core.

Keywords: Origami forming, Finite element method, Helmholtz equation

1. Introduction

As a part of our origami engineering approach to sound insulation, our group has been performing research with the aim of industrializing octet truss-type cores (truss cores) that use space filling structures composed of regular tetrahedrons and half regular octahedrons. Truss cores were expected to be used as flooring for trains, but both good sound insulation characteristics and bending stiffness are required for this application. It has been reported that a longer core height produces better sound insulation characteristics. However, there is a limit to the core height available in the multi-stage pressing approach[1]. Therefore, we developed the origami engineering method to solve the core height problem and then decided to reexamine the sound insulation properties of these cores.

2. Calculation Method for Sound Insulation Characteristic Evaluation

2.1 Examination of sound insulation calculations

The definition of the transmission loss (TL) used in sound insulation calculations is the ratio of the energy of the incident sound wave to the energy of the transmitted sound wave. The equation (1) is used in this paper. p_{in} is the incident sound pressure, and p_{out} is the transmitted sound pressure.

$$TL = 20\log_{10}\frac{|p_{in}|}{|p_{out}|} \quad (1)$$

In the previous paper[2], the problem is solved when the specimen was a rigid body, and the magnitudes of the incident and reflected waves are equal. However, this method cannot be applied when the specimen cannot be clearly regarded as a rigid body, e.g., when the effect of attaching a sound absorbing material is to be analyzed. Therefore, a method to obtain the transmission loss by separating the incident sound pressure from the reflected sound pressure theoretically is studied here.

2.2 Incident sound pressure calculation method in sound insulation characteristic simulation method

Helmholtz's equation (2) holds in the acoustic tube model[3].

$$\frac{\partial^2 u}{\partial x^2} = \frac{1}{c^2}\frac{\partial^2 u}{\partial t^2} \quad (2)$$

Here, u is the particle velocity, x is the one-dimensional position coordinate, and t is the time. The solution of Eq. (2) can be obtained by Eq. (3). Assuming a harmonic motion for the particle velocity,

$$u(x,t) = Ae^{j(\omega t - kx)} + Be^{j(\omega t + kx)} \quad (3)$$

From the boundary conditions calculated by FEM, the solution u becomes Eq. (4). Here, ω is the angular frequency, e is Napier's constant, k is the wave number, and j is the imaginary unit. u_0, D are the amplitude of the particle velocity of the excitation plate, and of the sound insulation plate, respectively. This model is one-dimensional, and l is the length of the tube.

$$u(x,t) = \frac{u_0 e^{j2kl} - De^{jkl}}{e^{j2kl}-1} e^{j(\omega t - kx)} + \frac{De^{jkl} - u_0}{e^{j2kl}-1} e^{j(\omega t + kx)} \quad (4)$$

The incident sound pressure $p_{in}|_{x=l}$ is obtained by multiplying the first term of the particle velocity $u(l,t)$ in Eq. (4) by the air density ρ and the sound velocity c, so it becomes Eq. (5).

$$p_{in}|_{x=l} = \rho c \cdot \frac{u_0 e^{jkl} - D}{e^{j2kl}-1} e^{j\omega t},\ p_{reflct}|_{x=l} = \rho c \frac{u_0 e^{jkl} - De^{j2kl}}{e^{j2kl}-1} e^{j\omega t} \quad (5)$$

Here, D is obtained from Eq. (6).

$$D = \frac{2u_0 e^{jkl}}{1+e^{j2kl}} + p_{x=l} \cdot \frac{1-e^{j2kl}}{\rho c\left(1+e^{j2kl}\right)} \quad (6)$$

3. Comparison of The Two Methods for Flat Plate Transmission Loss

3.1 Analysis model

Fig.1 shows the simulation model. A flat plate is used as the test piece. It is calculated by COMSOL Multiphysics®[4]. The boundary condition between the acoustic tube and the test piece is free. The total number of elements is 640 (comprising 624 solid elements and 16 shell elements) and the number of nodes is 1025. The sound insulation plate is a steel plate with a thickness of 0.8 mm and the plate's material properties are listed in Table 1. The sound pressure observation point is located 1 mm in front of the sound insulation plate in the x-axis direction.

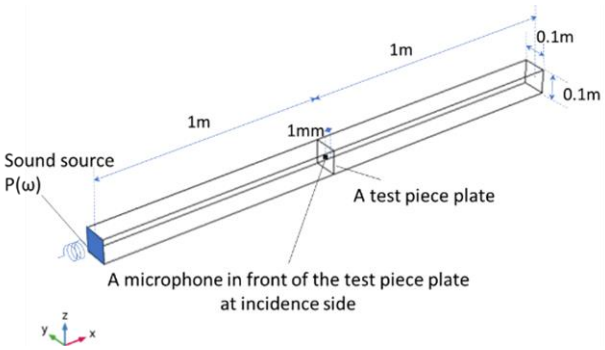

Fig.1 Simulation model and a microphone position in case of a test piece plate

Table 1 Specification of material of the panels

Material	Young's modulus [N/m^2]	Density [kg/m^3]	Poisson ratio
Steel	2.05×10^{11}	7.85×10^{3}	0.28

3.2 Comparison of the transmission loss

The transmission loss obtained by two(the previous and the proposed) methods are compared in Fig.2. In the transmission loss obtained based on the theoretical value (green line), the local value increases occur. With the exception of these points, transmission loss values from both methods are almost identical at each frequency. Therefore, in the flat plate model, the validity of the method proposed in this paper is verified.

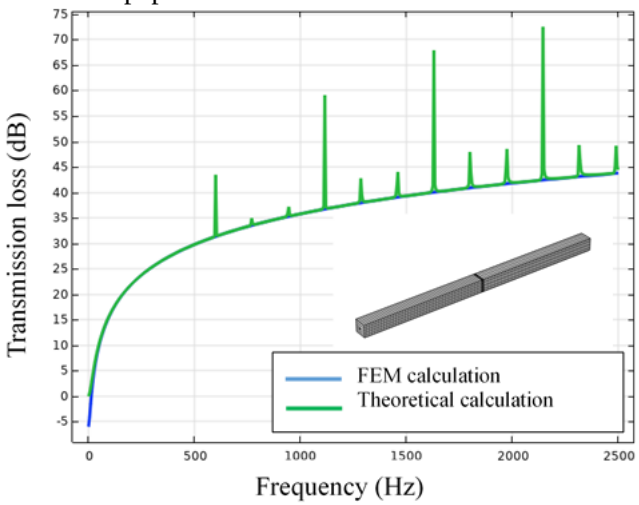

Fig.2 Comparison of transmission loss between FEM and theoretical calculation

4. Differences in Sound Insulation Characteristics Depending on The Aspect Ratio of Flat Plate With a Vertical Core

The following three different shapes of core are used as test pieces. The weight is set to be the same as that of the flat plate with the thickness of 0.8 mm. It can be said that the thinner the plate thickness and the higher the core height (the higher the aspect ratio), the more likely it is to have high peaks in the low frequency range.

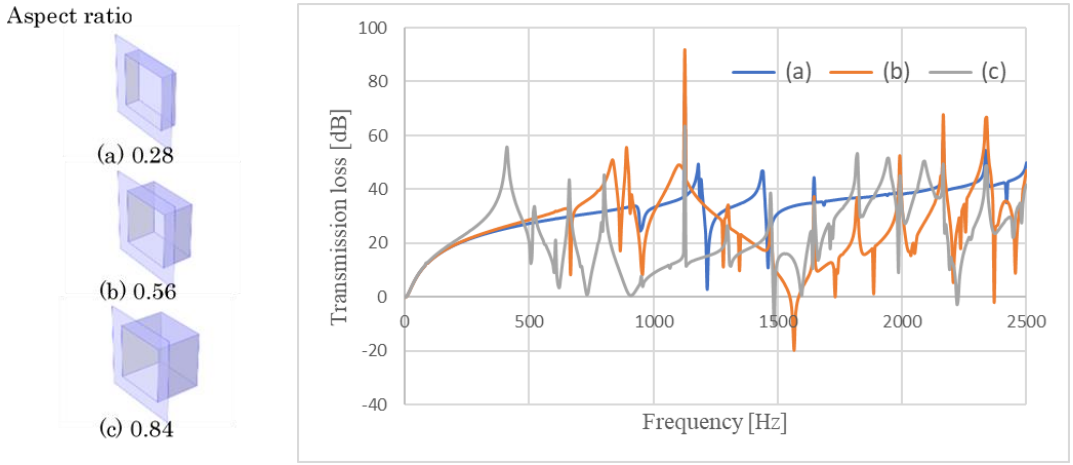

Fig.3 Differences in transmission loss depending on the aspect ratio

5. CONCLUSION

We have developed a new method for sound insulation analysis by using the differential solution of Helmholtz equation which is expressed using the sum of the forward and the backward waves explicitly with the boundary condition given by FEM.This new method give the same result for a flat plate as the previous method. Furthermore, we have new findings such as the longer aspect ratio gives more gathering sound effect by this new method using several flat panels with single cores including long aspect ratio core generated by origami forming. In the future work, we would apply this method to the flooring in trains which is necessary to have good sound insulation characteristics.

References

[1] S.Tokura and I.Hagiwara: Forming process simulation of truss core panel, Journal of Computational Science and Technology, Vol.4, No.1 (2010), pp.25-35. DOI: 10.1299/jcst.4.25

[2] A.Abe, H.Yashiro, and I.Hagiwara: Development of vertical incident sound insulation simulation technology using finite element method and application to lightweight core, Transactions of the JSME (in Japanese), Vol.86, No.891 (2020), DOI: 10.1299/transjsme.20-00126.

[3] Y.Suzuki, M.Akagi, A.Ito, H.Sato, A.Yuki and K.Nakamura: The Acoustical Society of Japan ed., Introduction to acoustics (2011), pp. 170-191, Corona Publishing (in Japanese).

[4] COMSOL Multiphysics® v. 5.5. www.comsol.com. COMSOL AB, Stockholm, Sweden.

Application to anti-vibration table of two-layered origami structures

Yingxue Bai[1], Sachiko Ishida[1*]

[1] Department of Mechanical Engineering, Meiji University, Kanagawa, Japan

*sishida@meiji.ac.jp

Abstract. In this study, we numerically investigated spring properties and isolation performances of an anti-vibration table using four two-layered origami structures as feet. The two-layered structure was designed exactly as the cylindrical foldable structure with a torsional buckling pattern in order to simplify construction of our one-layered isolator and to cancel a twisting motion while folded and deployed. Transient response analysis revealed that the resonance frequency of the anti-vibration table was sufficiently low as long as the weight applied on the top of the table was reasonably tuned and the table vibrated within the quasi-zero-stiffness region.

Keywords: Vibration control, Nonlinear vibration, Quasi-zero-stiffness spring, High-static-low-dynamic-stiffness spring, Structure design, Bistability, Origami

1. Introduction

In this study, an application of a cylindrical foldable structure with the torsional buckling pattern to an anti-vibration table is considered. The cylindrical foldable structure with the torsional buckling pattern is known as a bistable structure, which has only two stable states; an initial spatial state and a flat folded state. By combining the bistable structure to a linear compressive spring in parallel, the combined spring stiffness can be designed to be zero. Since a resonant frequency of a zero-stiffness spring is zero theoretically, vibration can be isolated in a wide frequency range. According to the theory, Ishida et al. [1] and Inamoto et al. [2] investigated the vibration isolator consisting of the foldable structure with a quasi-zero stiffness, and numerically and experimentally evaluated the isolation performance. However, the foldable structure was remodeled as a truss structure and twisting motion during folding and deployment was not considered. In this study, the original foldable structure is focused again for simplification and users' convenience, and devised to cancel the twisting motion for application to an anti-vibration table. The spring properties and isolation performances of the devised structures are numerically analyzed.

2. Modeling

A two-layered foldable structure was modelled by combining two one-layered foldable structures in the Z direction in a way such that the inclined fold lines were distributed symmetrically. The height of the structure was simply doubled. Since the upper and lower layers required separate linear

Fig. 1 Side views of a two-layered foldable structure (left) and a vibration isolator (right)

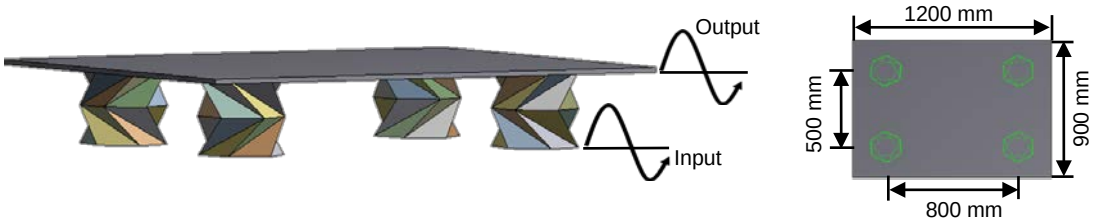

Fig. 2 Analytical model of an anti-vibration table

springs at center (Fig. 1), the relationship between the stiffnesses of the two springs in series K' and of each spring K, was obtained by $K' = K/2$.

Next, a board was placed on the four two-layered isolators, which worked to make the four isolators vibrate together to Z direction and also play a role as a display board of the anti-vibration table. The positions and the directions of the inclined fold lines were symmetric as shown in Fig. 2. Finally, an anti-vibration table was obtained by combining the four two-layered vibration isolators and the board (Fig. 2). The relationship among stiffnesses of eight springs K_{sys}, the two springs K' and the one spring K was given by $K_{sys} = 4K' = 2K$. The stiffness K_{sys} was adjusted to suppress the total stiffness of the four two-layered structures at given displacement range.

3. Results

3.1 Spring properties

The bottom surfaces of the four two-layered isolators were fixed and a compressive displacement was quasi-statically applied on the board from 0 mm to 155 mm to Z direction. Then, the reaction force generated was measured. In the folding process, the lower layer was twisted in clockwise; while, the upper layer in counterclockwise. As this motion was symmetric between the lower and top layers, the torsion was cancelled. Figure 3 shows the spring property of the anti-vibration table. Quasi-zero stiffness appeared in a range from 110 mm and 130 mm in height, which corresponds to a weight of 93 kg to 90 kg to be applied.

3.2 Transmissibilities

Transient response analysis was executed on the anti-vibration table to evaluate transmissibilities of the system. Sinusoidal signal was applied on the bottom surfaces of the four two-layered isolators and output signal was measured on the top board with regards to a single frequency as shown in Fig. 2. Thus, the transmissibility was calculated as an amplification ratio; i.e., the amplitude of the output signal over that of the input signal.

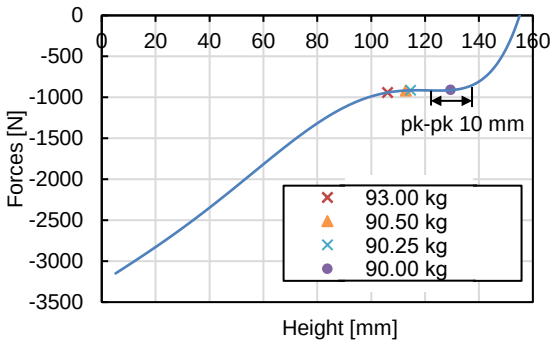

Fig. 3 Spring property of the anti-vibration table consisting of the four two-layered foldable structures

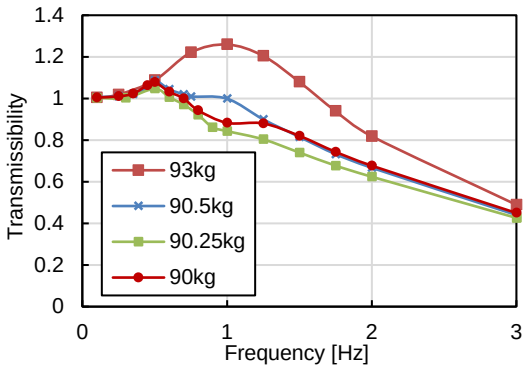

Fig. 4 Transmissibility of the anti-vibration table with vibration amplitude of A_{in} = 5 mm

Figure 4 shows the transmissibility of the anti-vibration table in case of input vibration amplitude $A_{in} = 5.0$ mm with a weight of 90.00 kg, 90.25 kg, 90.50 kg, and 93.00 kg. Resonance was slightly observed at 0.5 Hz with a weight of 90.00 kg, 90.25 kg, and 90.50 kg, because the stiffness was considerably close to but not exactly zero. This small resonance can be negligible as the resonance frequency was sufficiently low and the transmissibility decreased sharply at higher frequencies. However, with a weight of 93.00 kg, the anti-vibration table clearly resonated at 1.0 Hz. It was supposed to possess a quasi-zero stiffness as shown in Fig. 3, but the equillibrium position was close to the boundary of the quasi-zero stiffness so that dynamic oscillations possibly moved out of the quasi-zero-stiffness range.

4. Conclusions

In this study, an anti-vibration table using the four two-layered foldable structures was numerically designed and the performance on vibration isolation was investigated by transient response analysis. The torsional motion of the one-layered foldable structure was suppressed on the anti-vibration table. The resonance frequency of the anti-vibration table was sufficiently low as long as the weight applied on the board was reasonably tuned.

Acknowledgement

This research was financially supported by a grant-in-aid for scientific research from Japan Society for the Promotion of Science under no. 17K18166.

References

[1] S. Ishida, K. Suzuki, and H. Shimosaka: Design and Experimental Analysis of Origami-inspired Vibration Isolator with Quasi-zero-stiffness Characteristic, ASME Journal of Vibration and Acoustics, 139 (5), 051004.

[2] K. Inamoto, and S. Ishida: Improved Feasible Load Range and Its Effect on the Frequency Response of Origami-Inspired Vibration Isolators With Quasi-Zero-Stiffness Characteristics, ASME Journal of Vibration and Acoustics, 141 (2), 021004.

JSST 2021

Application of Ordinary State-based Peridynamics in Bimaterial Modeling

Huy Anh Nguyen[1], Hanlin Wang[1], Satoyuki Tanaka[1,*]

[1]Graduate School of Advanced Science and Engineering, Hiroshima University, Japan

[*]satoyuki@hiroshima-u.ac.jp

Abstract. This study presents the application of ordinary state-based peridynamics (OSB-PD) in the treatment of the bimaterial interface. OSB-PD offers an effective approach to model a structure with multiple interfaces because of its simplicity and ease of computer implementation. In the current study, a multi-inclusion unit cell model is used to investigate the accuracy of the OSB-PD as compared to the finite element method (FEM). The OSB-PD shows a close agreement with FEM in terms of deformation response.

Keywords: Peridynamics, Bimaterial, Inclusion

1. Introduction

Peridynamics (PD) is a reformulation of the classical continuum mechanics (CCM) introduced by Silling [1] to overcome the difficulties of CCM in modeling discontinuities such as cracks. PD is a purely nonlocal theory which takes into account the nonlocal interactions between material points, and its governing equation is an integro-differential equation which does not contain any spatial derivatives as oppsed to CCM. Therefore, the PD equation is valid everywhere in the domain regardless of whether the discontinuities exist or not. There are three main types of PD formulations in the literature, i.e. bond-based PD (BB-PD), ordinary state-based PD (OSB-PD), and non-ordinary state-based PD (NOSB-PD). In this paper, we focus on investigating the capabilities of OSB-PD in modeling bimaterial structures. The remainder of the paper is organized as follows. In Section 2, the OSB-PD formulation and bimaterial modeling are presented. Finally, an analysis of a structure with multiple inclusions is carried out to demonstrate the effectiveness of OSB-PD in Section 3.

2. Ordinary state-based peridynamic formulation

In PD, a material point is considered to interact with other points within a finite distance δ. As shown in Fig. 1, a material point, initially located at $\boldsymbol{x}$, is associated with its own family $H_{\boldsymbol{x}}$, and it interacts with other family members $\boldsymbol{x}'$ through bonds. Similarly, material points $\boldsymbol{x}'$ also interacts with other material points in their own families $H_{\boldsymbol{x}'}$. The relative position

vector between $\boldsymbol{x}$ and $\boldsymbol{x'}$ is defined as $\boldsymbol{\xi} = \boldsymbol{x'} - \boldsymbol{x}$. During the deformation, the material points $\boldsymbol{x}$ and $\boldsymbol{x'}$ undergo displacements $\boldsymbol{u}$ and $\boldsymbol{u'}$, respectively. Furthermore, the positions of $\boldsymbol{x}$ and $\boldsymbol{x'}$ in the deformed state can be specified as $\boldsymbol{y} = \boldsymbol{x} + \boldsymbol{u}$ and $\boldsymbol{y'} = \boldsymbol{x'} + \boldsymbol{u'}$.

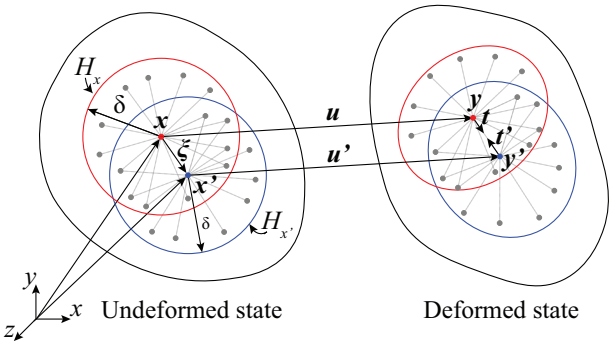

Fig. 1 Nonlocal interactions between material points $\boldsymbol{x}$ and $\boldsymbol{x'}$, and the resulting force density vectors

The PD equations of motion at a material point, $\boldsymbol{x}$, at any instant of time t, can be expressed as [1–3]

$$\rho(\boldsymbol{x})\ddot{\boldsymbol{u}}(\boldsymbol{x},t) = \int_{H_{\boldsymbol{x}}} (\boldsymbol{t}(\boldsymbol{u'}-\boldsymbol{u},\boldsymbol{x'}-\boldsymbol{x},t) - \boldsymbol{t'}(\boldsymbol{u}-\boldsymbol{u'},\boldsymbol{x}-\boldsymbol{x'},t))dH + \boldsymbol{b}(\boldsymbol{x},t), \tag{1}$$

where ρ is the mass density, $\ddot{\boldsymbol{u}}$ is the acceleration, $\boldsymbol{b}$ is the body force density vector. $H_{\boldsymbol{x}}$ denotes the horizon of a material point at position $\boldsymbol{x}$. The shape of a family is represented by a circle with a radius of δ. The force density vector $\boldsymbol{t}$ can be formulated by Madenci and Oterkus [3] as

$$\boldsymbol{t}(\boldsymbol{u'}-\boldsymbol{u},\boldsymbol{x'}-\boldsymbol{x},t) = \left(2ad\delta\frac{\theta}{|\boldsymbol{\xi}|}\Lambda + 2\delta b\frac{|\boldsymbol{y'}-\boldsymbol{y}|-|\boldsymbol{\xi}|}{|\boldsymbol{\xi}|}\right)\frac{\boldsymbol{y'}-\boldsymbol{y}}{|\boldsymbol{y'}-\boldsymbol{y}|}, \tag{2}$$

where $\Lambda = \frac{\boldsymbol{y'}-\boldsymbol{y}}{|\boldsymbol{y'}-\boldsymbol{y}|}\cdot\frac{\boldsymbol{x'}-\boldsymbol{x}}{|\boldsymbol{x'}-\boldsymbol{x}|}$ and θ is the dilatation at point $\boldsymbol{x}$ [3].

The PD parameters a, b, and d in Eq. (2) can be expressed in terms of bulk modulus κ and shear modulus μ as derived by Madenci and Oterkus [3] for plane stress as

$$a = \frac{1}{2}(\kappa - 2\mu), \quad b = \frac{6\mu}{\pi h\delta^4}, \quad d = \frac{2}{\pi h\delta^3}. \tag{3}$$

For a bond extending across the interface, the average material properties of the bond can be achieved as

$$\alpha = \frac{L}{\frac{L_1}{\alpha_1} + \frac{L_2}{\alpha_2}}, \tag{4}$$

where α is the material property, L_1 denotes the length of the bond in material 1, L_2 denotes the length of the bond in material 2, and $L = L_1 + L_2$ is the total length of the bond.

3. Application

A square unit cell containing four equal circular inclusions as shown in Fig. 2 is analyzed. The model is fixed on the left side and is subjected to a uniform tensile loading on the right side. The positions of the four inclusions are symmetrical to the axes, and each inclusion has a radius of $r = 0.1$ m. As depicted in Figs. 3 and 4, there is a good agreement between FEM and PD results. The displacement distributions smoothly vary at the interfaces in x and y directions, and the deformation of the plate is symmetrical to the axes. However, the deformation variation is irregular due to the presence of inclusions.

The contours of strain in PD are shown in Fig. 5. It can be seen from the figure that the distributions are symmetrical to the axis. Furthermore, the concentrations of strain due to the mismatch deformation between the inclusion and matrix occur at the interface as expected.

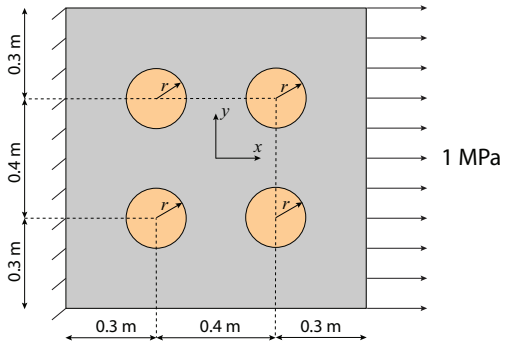

Fig. 2 Geometry and BCs for the plate with four inclusions problem

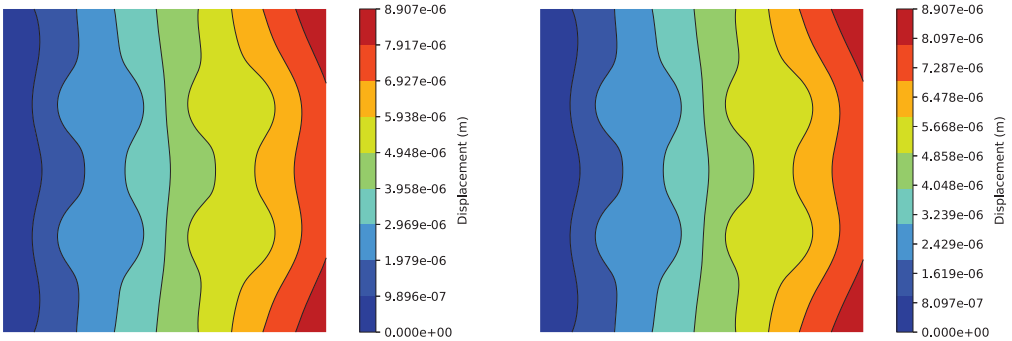

a) **b)**

Fig. 3 Horizontal displacement **a)** PD **b)** FEM

4. Conclusion

In this study, OSB-PD is used to investigate a structure with multiple material interfaces. In general, there is a good agreement in predictions between FEM and OSB-PD. OSB-PD

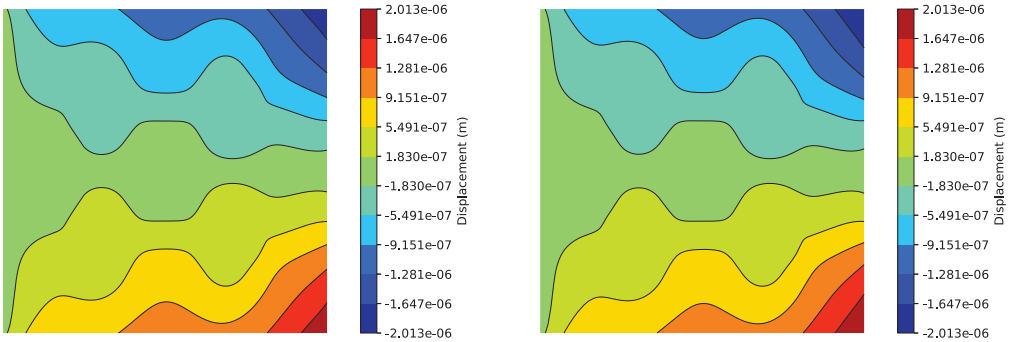

Fig. 4 Vertical displacement **a)** PD, **b)** FEM

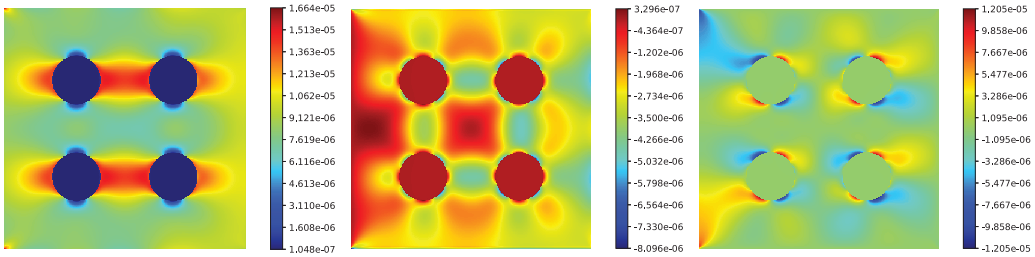

Fig. 5 Contour of strain **a)** x-normal strain , **b)** y-normal strain, **c)** shear strain

provides the flexibility in modeling structures with multiple inclusions. Although not being shown in this present study, the crack modeling is another feature of PD. As a result, PD is extremely appropriate for problems involving the presence of different types of defects including inclusions, voids, or cracks.

References

[1] S. A. Silling: Reformulation of elasticity theory for discontinuities and long-range forces, *Journal of the Mechanics and Physics of Solids*, 48:1 (2000), 175–209.

[2] S. A. Silling, M. Epton, O. Weckner, J. Xu, E. Askari: Peridynamic states and constitutive modeling, *Journal of Elasticity* 88:2 (2007), 151–184.

[3] E. Madenci, E. Oterkus: Peridynamic theory and its applications, *Springer New York*, (2014).

[4] H. A. Nguyen, H. Wang, S. Tanaka, S. Oterkus, E. Oterkus: An in-depth investigation of bimaterial interface modeling using ordinary state-based peridynamics, *Journal of Peridynamics and Nonlocal Modeling*, (2021).

JSST2021

Accurate and Fast Electrostatic Field Analysis with Unstructured Numerical Human Body Model Using Parallel Geometric Multi-Grid Method

Masamune Nomura[1*], Amane Takei[2]

[1] University of Miyazaki, Interdisciplinary Graduate School of Agriculture and Engineering
[2]University of Miyazaki, Faculty of Engineering
*hl13034@student.miyazaki-u.ac.jp

Abstract. In electrostatic field analysis using a numerical human body model constructed with voxels, the electric field strength is overestimated near the staircase boundary of different materials (called staircasing errors). To reduce this staircasing errors, mesh smoothing based on the marching cubes method is developed and applied to a part of the numerical human body model. In addition, to reduce the increase in computational time for electrostatic field analysis due to this mesh smoothing using unstructured lattices, the geometric multi-grid method dealing with unstructured lattices is applied. As a result, this mesh smoothing method reduces the stair casing errors and this geometric multi-grid method takes up to 1/3 of the computation time of a general linear algebra solver.

Keywords: Electrostatic analysis, Geometric multigrid method, Numerical human body model, Mesh Smoothing

1. Introduction

To reduce the staircasing errors, mesh smoothing based on the marching cube method [1] is applied to the numerical human body model constructed with voxels. The visualization result of the mesh applied to a part of the human body model is shown in the figure below. From the visualization results, it can be seen that the 90° angle of the voxel model is removed by mesh smoothing. The results of the electrostatic field analysis also show that the overestimation of the electric field strength due to the staircase approximation at the boundaries of dissimilar materials is reduced by smoothing. Mesh smoothing is effective for this model, but elements in this model using mesh smoothing is huge, and the computation time increases significantly.

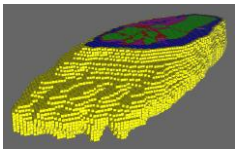

a. Mesh

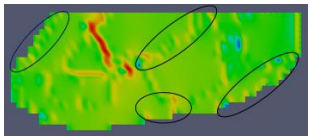

b. Electrostatic analysis

Figure 1. Voxel model(Left ankle)

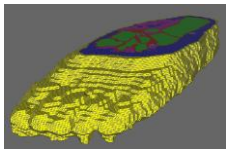

a. Mesh

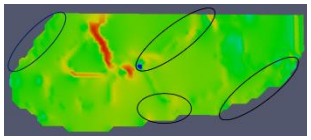

b. Electrostatic analysis

Figure 2. Smoothing model(Left ankle)

To address this problem, the unstructured multigrid method based on the refinement algorithm of UG4 is used in this study. As a result, this Geometric Multi-Grid method (GMG) takes up to 1/3 of the computation time of a general linear algebra solver.

2. Electrostatic field analysis with unstructured GMG

Electrostatic field analysis is performed on the voxel model and smoothing model in Fig. 1, and the iteration count and computation time for the GMG and the preconditioned CG method (ILUCG) are compared. As boundary conditions for this numerical analysis, electrodes are attached to the heel and toe parts of the model, and a voltage difference of 1 V is set. Table 1 shows the iteration count and computation time (72 cores) of GMG and ILUCG for each model. The voxel model and smoothing model are refined until the number of elements reaches several hundred million elements. The maximum refinement levels of the voxel model and smoothing model are 4 and 3, respectively. Table 1 shows that the GMG on the smoothing model requires fewer iterations than the voxel model. This is because smoothing reduces staircassing errors at the boundary of dissimilar materials and improves the accuracy of the interpolation in the geometric multigrid method. It is also found that the voxel model takes up to 1/6 of the computation time of ILUCG and the smoothing model takes up to 1/3 of that. Figure 3 shows that the Computation time of ILUCG and GMG for each refinement level. From Fig. 3, it can be seen that the increasing rate of computation time due to refinement of GMG is much smaller than that of ILUCG. This shows the effectiveness of the unstructured geometric multigrid method for mesh-smoothed, high-accuracy, large-scale human body models.

Table 1 Iteration counts and computation time (72cores) of GMG and ILUCG for each model

Model	Ref.	GMG		ILUCG	
		Iter.	Time	Iter.	Time
Voxel	1	NaN	NaN	506	3
	2	63	34	970	43
	3	36	163	1,858	490
	4	32	1,060	3,671	6,532
Smooth	1	25	86	621	93
	2	27	240	1,237	409
	3	28	1,518	2,342	4,957

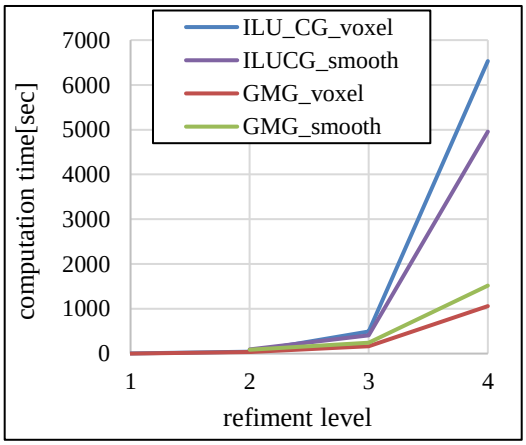

Figure 3. Computation time for each refinment level

3. Conclusion

We infer that the difference in the convergence of the multigrid method between the voxel model and the smoothing model is remarkable for the whole human body model. We will discuss the calculation results for the whole human body model in the JSST2021 conference.

References

[1] A. Takei, et al, “High-Accuracy Electromagnetic Field Simulation Using Numerical Human Body Models” *IEEE Trans. on Mag.* , Vol. 52, No. 3, 2016.

High Performance Implementation of Skyline Solver for Many Core Environment

Hiroshi Kawai[1*]

[1]Faculty of Information Systems and Arts, Toyo University

[*]kawai063@toyo.jp

Abstract. ADVENTURE AutoLinAS (pronounced as 'O-to-li-na-shi') is a linear algebraic solver library, dedicated for simulation-based research and development. It is designed for the simulation users to develop their own solvers. Currently, the library is used among many researchers and simulation users, mainly in universities and national research centers. Its functionalities and supported platforms are explained. AutoLinAS applications of various kinds of simulation methods are demonstrated also.

Keywords: Skyline Solver, Direct Solver, High Performance Computing, Supercomputing, Many core, HPC

1. Introduction

To build your own simulation code, its linear algebraic solver, either direct or iterative, is very important for the performance of the code. Therefore, HPC (High Performance Computing) is the key technology to accelerate the linear algebraic solver part. Modern HPC environment, however, is getting more and more complicated, and it might have already been very difficult for an ordinary researcher or a software developer to utilize them effectively.

ADVENTURE AutoLinAS is a simple and handy linear algebraic solver library. AutoLinAS is dedicated for basic vector / matrix operations and linear algebraic solvers used in the continuum mechanics field, is now under development. It covers both direct solvers and iterative solvers. It also contains basic building blocks for making a linear algebraic solver itself, such as dense and sparse matrix operations. Interface to other HPC-related libraries, such as BLAS / LAPACK / Intel MKL, Fujitsu SSL, are also provided. Implementations of the library for various kinds of high performance computing platforms, such as Intel x86 (Skylake-SP) and Fugaku/Fujitsu PRIMEHPC FX-1000, are available. Each of them is highly tuned for the underlying hardware architecture. Based on AutoLinAS library, a high performance implementation of skyline solver is developed. Its performance evaluation will be done on various multi-core / many core CPU architectures.

References

[1] ADVENTURE project HP: http://adventure.sys.t.u-tokyo.ac.jp/

JSST 2021

High-Performance Solver for EFG-Type Saddle-Point Problem: Improved Variable-Reduction Method

Atsushi Kamitani[1,*], Teruou Takayama[1], Ayumu Saitoh[1]

[1]Graduate School of Science and Engineering, Yamagata University

[*]kamitani@yz.yamagata-u.ac.jp

Abstract. Discretization of an elliptic boundary-value problem with the extended element-free Galerkin method yields a saddle-point problem. For the purpose of fast solving the problem, the improved Variable-Reduction Method (iVRM) is developed. All projectors are determined without the *QR* decomposition in the iVRM and, hence, the computational cost of the iVRM can be suppressed to $O(N)$. Here, N is the number of nodes.

Keywords: Element-free Galerkin method, Krylov space method, Saddle-point problem

1. Introduction

In order to remove the concept of elements from the finite element method, the Element-Free Galerkin (EFG) method [1] and the eXtended Element-Free Galerkin (X-EFG) method [2] have been so far proposed. However, application of either method to an elliptic boundary-value problem yields a saddle-point problem that is extremely difficult to solve numerically. Throughout the present study, the problem is called an EFG-type saddle-point problem. Although the Variable-Reduction Method (VRM) [3] was developed for solving the problem, it contains the costly *QR* decomposition.

The purpose of the present study is to reformulate the VRM without using the *QR* decomposition and to investigate applicability of the obtained method to an EFG-type saddle-point problem.

2. EFG-Type Saddle-Point Problem

If a two-dimensional (2D) Poisson problem is discretized by use of the X-EFG method with N nodes and k boundary nodes, we get the following linear system:

$$\begin{bmatrix} A & C \\ D^T & O \end{bmatrix} \begin{bmatrix} \boldsymbol{x} \\ \boldsymbol{\lambda} \end{bmatrix} = \begin{bmatrix} \boldsymbol{b} \\ \boldsymbol{c} \end{bmatrix}. \tag{1}$$

Here, $A \in \mathbb{R}^{N\times N}$ is positive semidefinite and $C, D \in \mathbb{R}^{N\times k}$ are full-column rank. Furthermore, the coefficient matrix in (1) is nonsingular. Besides, both $\boldsymbol{x} \in \mathbb{R}^N$ and $\boldsymbol{\lambda} \in \mathbb{R}^k$ are unknown vectors.

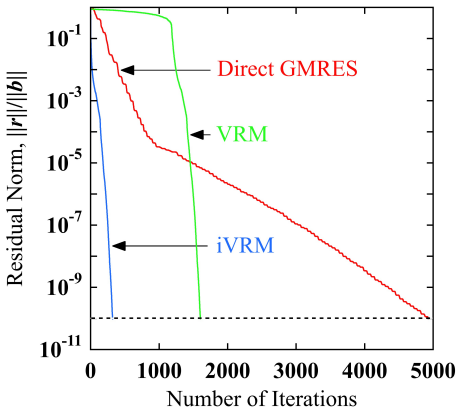

Figure 1: Residual histories of direct GMRES, VRM and iVRM for the case with $N = 66049$.

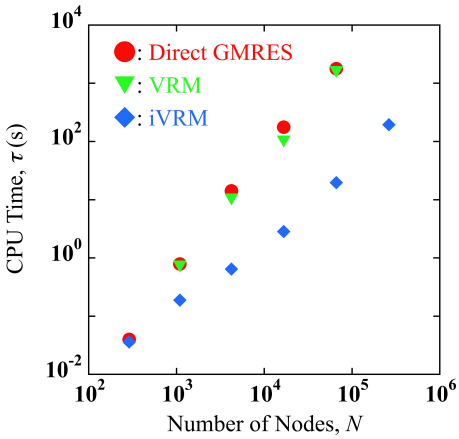

Figure 2: Dependence of the CPU time τ on the number of nodes N.

In order to solve (1) numerically, Krylov space methods have been so far applied directly to (1). In the present study, direct application of GMRES to (1) is called direct GMRES.

3. Improved Variable-Reduction Method

For the purpose of solving (1) for the case where A is dense, the authors proposed the VRM. In the VRM, after C and D are first QR factorized, $\boldsymbol{\lambda}$ is eliminated from (1). Next, the resulting linear system is solved with GMRES. However, even for the case where A is sparse, the computational cost of the VRM amounts to $O(N^2)$ due to the QR decomposition.

To overcome this difficulty, we have developed the improved VRM (iVRM). In the iVRM, the linear system, $A^\dagger \boldsymbol{x} = \boldsymbol{b}^\dagger$, is solved for $\boldsymbol{x}$ with GMRES, where $A^\dagger \equiv UAU + F$, $\boldsymbol{b}^\dagger \equiv U(\boldsymbol{b} - A\boldsymbol{c}^*) + \boldsymbol{c}^*$ and $U \equiv I - F$. Here, I and F denote an identity matrix and a projector onto $\mathrm{Im}\, C$ along $(\mathrm{Im}\, D)^\perp$, respectively, and $\boldsymbol{c}^* \in \mathbb{R}^N$ is a vector calculated from $\boldsymbol{c}$. Note that the iVRM does not require the QR decomposition. Hence, if A is sparse, its computational cost can be reduced to $O(N)$.

An EFG-type saddle-point problem originating from a 2D Poisson problem is solved with direct GMRES/VRM/iVRM. The residual histories and the dependence of the CPU time on the number of nodes are depicted in Figures 1 and 2, respectively.

References

[1] T. Belytchko *et al.*: *Int. J. Numer. Mech. Eng.*, Vol. 37 (1994) 229-256.

[2] A. Kamitani *et al.*: *Plasma Fusion Res.*, Vol. 6 (2011) Art. No. 2401074.

[3] A. Kamitani *et al.*: *Int. J. Appl. Electromagn. Mech.*, Vol. 59 (2019) 157-163.

JSST 2021

Parallel implementation of the approach for solving saddle point problems using block structure

Hiroto Tadano[1,*]

[1]Center for Computational Sciences, University of Tsukuba

[*]tadano@cs.tsukuba.ac.jp

Abstract. Saddle point problems arise in many scientific applications. Recently, we have proposed an efficient approach for solving saddle point problems using block structure. The main computation part of our approach is the solution of a linear system with multiple right-hand sides. Since the multiple right-hand sides of the linear system are mutually independent, the linear system can be solved in parallel by distributing the right-hand sides in a parallel computing environment. In this presentation, a parallel implementation of our approach is presented, and its parallel performance is evaluated.

Keywords: Saddle point problems, Block Krylov subspace methods, Parallelization

1. Introduction

This paper focuses on saddle point problems of the form:

$$\begin{bmatrix} A & B \\ C^{\mathsf{T}} & O \end{bmatrix} \begin{bmatrix} \boldsymbol{x} \\ \boldsymbol{y} \end{bmatrix} = \begin{bmatrix} \boldsymbol{f} \\ \boldsymbol{g} \end{bmatrix}, \tag{1}$$

where $A \in \mathbb{R}^{n \times n}$ is a nonsingular matrix, $B \in \mathbb{R}^{n \times m}$ and $C \in \mathbb{R}^{n \times m}$ $(n > m)$ are full rank matrices, $\boldsymbol{x}, \boldsymbol{f} \in \mathbb{R}^n$ and $\boldsymbol{y}, \boldsymbol{g} \in \mathbb{R}^m$. The saddle point problems (1) arise in many scientific applications such as structural analysis, fluid dynamics, and so on. Since the solution of (1) is the time-consuming part of the applications, it is desired to solve (1) as fast as possible.

Recently, we have proposed an approach for solving the saddle point problems using block structure [1] to solve (1) efficiently. The main computation part of this approach is the solution of a linear system with the matrix A and multiple right-hand sides. In [1], it is shown that Block Krylov subspace methods can solve this linear system more efficiently than Krylov subspace methods. Since the multiple right-hand sides are mutually independent, this linear system can be solved in parallel by distributing the right-hand sides in a parallel computing environment.

In this presentation, a parallel implementation of our approach is presented. In addition, its performance in a parallel computing environment is evaluated through numerical experiments.

2. The approach for solving saddle point problems using block structure

In this section, the approach for solving the saddle point problems (1) using block structure [1] is briefly described. The saddle point problems (1) is expressed as follows:

$$\begin{cases} A\boldsymbol{x} + B\boldsymbol{y} = \boldsymbol{f}, \\ C^{\mathsf{T}}\boldsymbol{x} = \boldsymbol{g}. \end{cases} \tag{2}$$

From Eq. (2), the solution vectors $\boldsymbol{x}$ and $\boldsymbol{y}$ of (1) can be computed as follows:

$$\begin{aligned} \boldsymbol{x} &= A^{-1}\boldsymbol{f} - A^{-1}B\boldsymbol{y}, \\ \boldsymbol{y} &= \left(C^{\mathsf{T}}A^{-1}B\right)^{-1}\left(C^{\mathsf{T}}A^{-1}\boldsymbol{f} - \boldsymbol{g}\right). \end{aligned}$$

Hence, the matrix $U \equiv A^{-1}B \in \mathbb{R}^{n\times m}$ and the vector $\boldsymbol{v} \equiv A^{-1}\boldsymbol{f} \in \mathbb{R}^n$ are required to compute the solution vectors.

By defining the matrices $\hat{X} \equiv [U \ \ \boldsymbol{v}] \in \mathbb{R}^{n\times(m+1)}$ and $\hat{B} \equiv [B \ \ \boldsymbol{f}] \in \mathbb{R}^{n\times(m+1)}$, the linear system with multiple right-hand sides:

$$A\hat{X} = \hat{B} \tag{3}$$

can be obtained. By solving the linear system (3), the solution vectors $\boldsymbol{x} = \boldsymbol{v} - U\boldsymbol{y}$ and $\boldsymbol{y} = \left(C^{\mathsf{T}}U\right)^{-1}\left(C^{\mathsf{T}}\boldsymbol{v} - \boldsymbol{g}\right)$ can be computed.

3. Parallel implementation

In this section, a parallel implementation of our approach is presented. Throughout this paper, P denotes the number of MPI processes. In addition, for simplicity, it is assumed that n and m are divisible by P.

3.1. Preconditioning for the linear system $A\hat{X} = \hat{B}$

Since the solution of the linear system with multiple right-hand sides (3) is the most time-consuming part of our approach, it is essential to apply a preconditioner to (3) to reduce the computation time of iterative methods. Although it is known that the incomplete LU factorization preconditioner is efficient, the most computation part of this preconditioner is sequential computation. Hence, it is difficult to bring out the computation performance of this preconditioner in a parallel computing environment.

To compute a preconditioning matrix efficiently in a parallel computing environment, the sparse approximate inverse (SAI) preconditioner [2] is employed. The SAI preconditioner generates a preconditioning matrix $M \in \mathbb{R}^{n\times n}$ such that $M \approx A^{-1}$ by solving the n least square problems $\min_{\boldsymbol{m}_j} \|A\boldsymbol{m}_j - \boldsymbol{e}_j\|_2$ $(j = 1, 2, \ldots, n)$, where $\boldsymbol{m}_j$ and $\boldsymbol{e}_j$ are jth column vector of M and the identity matrix I, respectively. The nonzero structure of the matrix M is specified by the user. Since these least square problems are mutually independent, the preconditioning matrix M can be computed in parallel by assigning n/P problems to each MPI process.

3.2. Solution of the linear system $A\hat{X} = \hat{B}$

Let us consider solving the linear system (3) in parallel. Since the column vectors of matrix $\hat{B}$ are mutually independent, it is easy to parallelize the solution of (3). The matrices $\hat{X}$ and $\hat{B}$ are split as follows:

$$\hat{X} = \left[\hat{X}^{(0)}\ \hat{X}^{(1)}\ \ldots\ \hat{X}^{(P-1)}\right],\ \ \hat{B} = \left[\hat{B}^{(0)}\ \hat{B}^{(1)}\ \ldots\ \hat{B}^{(P-1)}\right],$$

where $\hat{X}^{(p)},\ \hat{B}^{(p)} \in \mathbb{R}^{n\times(m/P)}$ $(p = 0, 1, \ldots, P-1)$. By splitting the matrices $\hat{X}$ and $\hat{B}$, the following P linear systems with multiple right-hand sides can be obtained.

$$A\hat{X}^{(p)} = \hat{B}^{(p)},\ p = 0, 1, \ldots, P-1. \tag{4}$$

The linear system $A\hat{X}^{(p)} = \hat{B}^{(p)}$ with m/P right-hand sides is assigned to the pth MPI process. Hence, the number of right-hand sides when using OpenMP/MPI Hybrid parallelization is relatively larger than that when using Flat MPI parallelization. Although the Block Krylov subspace methods are efficient methods for linear systems with multiple right-hand sides in terms of the number of iterations, the computation complexity of most computing kernels is proportional to the square of the number of right-hand sides. Therefore, a long computation time may be required to solve (4) when the number of MPI processes is small and OpenMP/MPI Hybrid parallelization is used.

3.3. Computation of the solution vectors

To compute the solution vector $\boldsymbol{y}$, the linear system with the coefficient matrix $C^{\mathsf{T}}U$ needs to be solved. After that, the solution vector $\boldsymbol{x}$ can be computed by using $\boldsymbol{y}$. At this time, in our implementation, these computations are performed by a single MPI process. Parallelization of this computation phase is our future work.

4. Performance evaluation

The computation performance of our implementation is evaluated through numerical experiments. As the matrix A of (1), torso3 from the SuiteSparse Matrix Collection [3] is used. The size n and the number of nonzero elements of A are 259,156 and 4,429,042, respectively. The number m of columns of B and C is set as $3,000$. The elements of these matrices are given by a random number generator. The nonzero structure of the preconditioning matrix M computed by the SAI preconditioner is the same as that of A. The Block GWBiCGSTABrQ method [4] is adopted to solve the linear systems with multiple right-hand sides (4).

Computations are carried out on the Cygnus Supercomputer operated at the Center for Computational Sciences, University of Tsukuba. Each compute node is equipped with two sockets of Intel Xeon Gold 6126 2.6GHz (12 cores). The number of MPI processes per compute node is 24 when Flat MPI is used. When OpenMP/MPI Hybrid is used, each MPI process is assigned to a socket, and the computations in each MPI process are parallelized by OpenMP with 12 threads. The compiler and MPI library used in numerical experiments are Intel Fortran ver. 19.1.3 and OpenMPI ver. 4.0.3, respectively. The used compile option is `-axCORE-AVX512 -align array64byte`.

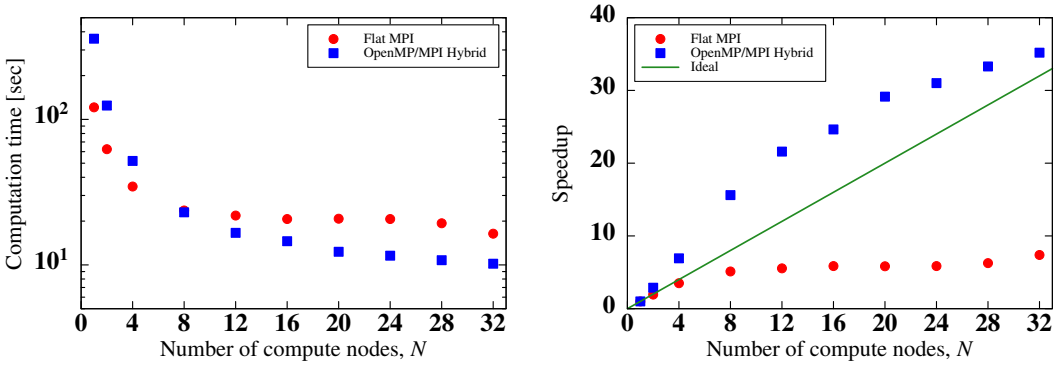

(a) Computation time.

(b) Speedup.

Figure 1: Computation time and speedup as a function of the number of compute nodes.

Figure 1 shows the computation time and speedup as a function of the number of compute nodes. Here, N denotes the number of used compute nodes. As shown in Fig. 1 (a), for $N < 8$, the computation time when using Flat MPI was shorter than that when using OpenMP/MPI Hybrid. On the other hand, for $N > 8$, the computation time when using OpenMP/MPI Hybrid was shorter than that when using Flat MPI. Figure 1 (b) shows the speedup as a function of N. The speedup of OpenMP/MPI Hybrid was superior to that of Flat MPI. Moreover, the speedup of OpenMP/MPI Hybrid exceeded the ideal speedup. When $N = 32$, the speedup of OpenMP/MPI Hybrid and Flat MPI were 35.2 and 7.39, respectively. The detailed results will be shown at the Conference.

Acknowledgement

This research was supported by JSPS KAKENHI Grant Number JP20K11840. This research used computational resources of the Cygnus Supercomputer provided by Multidisciplinary Cooperative Research Program in Center for Computational Sciences, University of Tsukuba.

References

[1] H. Tadano, S. Ishikawa: An efficient approach for solving saddle point problems using block structure, *J. Adv. Simulat. Sci. Eng.*, 8:1 (2021), 114–127.

[2] M. Benzi, M. Tůma: A sparse approximate inverse preconditioner for nonsymmetric linear systems, *SIAM J. Sci. Comput.*, 19:3 (1998), 968–994.

[3] T. A. Davis, Y. Hu: The university of Florida sparse matrix collection, *ACM Trans. Math. Software*, 38 (2011). (`https://sparse.tamu.edu`)

[4] H. Tadano, R. Kuramoto: Accuracy improvement of the Block BiCGSTAB method for linear systems with multiple right-hand sides by group-wise updating technique, *J. Adv. Simulat. Sci. Eng.*, 6:1 (2019), 100–117.

JSST 2021

A Paralellization Strategy for Incomplete Decomposition-based Preconditioning for Solving Linear Systems

Taiga Yamashita[1,*], Taku Itoh[2], Hiroto Tadano[3]

[1]Graduate School of Industrial Technology, Nihon University, Japan
[2]College of Industrial Technology, Nihon University, Japan
[3]Center for Computational Sciences, University of Tsukuba, Japan

*cita20015@g.nihon-u.ac.jp

Abstract. To efficiently solve linear systems by Krylov subspace methods, an incomplete decomposition-based strategy with parallel processing has been proposed. Basically, the incomplete decomposition-based Krylov subspace methods are not very suitable for parallel processing, since sequential process is contained in their algorithms. In the proposed method, the algorithms are transformed so that they consist only of inner products and matrix-vector products by excluding the sequential process. Hence, the incomplete decomposition-based Krylov subspace methods may be more easily parallelized than those of the original ones.

Keywords: Krylov subspace methods, Incomplete decomposition, Parallel processing, Linear systems, Preconditioning

1. Introduction

This paper focuses on linear systems:

$$A\boldsymbol{x} = \boldsymbol{b}, \tag{1}$$

where $A \in \mathbb{R}^{N\times N}$ is a given matrix, $\boldsymbol{x} \in \mathbb{R}^N$ is an unknown vector, and $\boldsymbol{b} \in \mathbb{R}^N$ is a given vector. To solve the linear systems, many kinds of Krylov subspace methods have been applied [1]. In addition, incomplete decomposition methods such as IC and ILU have employed for accelerating solving the linear systems by Krylov subspace methods. Note that the incomplete decomposition methods are basically sequential algorithms. For this reason, the incomplete decomposition-based Krylov subspace methods are not very suitable for parallel processing.

The purpose of this study is to propose an incomplete decomposition-based strategy for solving linear systems in parallel processing. To this end, the sequential process in the incomplete decomposition is excluded from the iteration process of Krylov subspace methods.

2. Incomplete Decomposition Methods

In what follows, we especially focus on incomplete LDU decomposition (iLDU) based Krylov subspace methods for solving asymmetric linear systems. We employ an algorithm described in [2] as iLDU. In the algorithm, the preconditioning matrices L, D and U are composed so that $A \simeq LDU$ is satisfied. Note that the non-zero structures of L and U are the same as those of A in the algorithm. In addition, D is a diagonal matrix.

In the iteration process of iLDU based Krylov subspace methods, calculating such as $\boldsymbol{v} = (LDU)^{-1}\boldsymbol{r}_k$ is required for each iteration, where $\boldsymbol{r}_k$ is the residual vector for the kth iteration. The vector $\boldsymbol{v}$ can be obtained by solving the following two equations.

$$\begin{cases} L\boldsymbol{y} = \boldsymbol{r}_k, \\ DU\boldsymbol{v} = \boldsymbol{y}. \end{cases} \tag{2}$$

Since they are sequential process, the performance of parallel processing for iLDU based Krylov subspace methods deteriorates.

3. Parallelization Strategy for Incomplete Decomposition-based Preconditioning

In this section, we consider excluding the sequential process (2) in the iteration process. To this end, we explicitly obtain $M = (LDU)^{-1}$ by solving

$$LDUM = E, \tag{3}$$

before the iteration step of iLDU based Krylov subspace methods is started, where $E \in \mathbb{R}^{N\times N}$ is the identity matrix. By obtaining the matrix M, the algorithms of iLDU based Krylov subspace methods are transformed so that they consist only of inner products and matrix-vector products. Namely, iLDU based Krylov subspace methods may be more easily parallelized than those of the original ones.

Note that the matrix M may become a dense one, if (3) is solved exactly. Since dense matrices are sometimes difficult to retain on the memory, we obtain a sparse matrix $\hat{M}$ by the following procedures so that $\hat{M} \simeq M$.

1. Solve $L\boldsymbol{y}_j = \boldsymbol{e}_j$.
2. Solve $DU\boldsymbol{m}_j = \boldsymbol{y}_j$.
3. Compose $\hat{\boldsymbol{m}}_j$ by extracting some non-zero components of the vector $\boldsymbol{m}_j$ based on some criteria. The non-zero components of $\hat{\boldsymbol{m}}_j$ are retained based on the CCS (compressed column storage) format [3].
4. Delete the memory allocated to $\boldsymbol{m}_j$.

Here, $E = [\boldsymbol{e}_1, \boldsymbol{e}_2, \ldots, \boldsymbol{e}_N]$, $M = [\boldsymbol{m}_1, \boldsymbol{m}_2, \ldots, \boldsymbol{m}_N]$ and $\hat{M} = [\hat{\boldsymbol{m}}_1, \hat{\boldsymbol{m}}_2, \ldots, \hat{\boldsymbol{m}}_N]$. In addition, $\boldsymbol{e}_j$, $\boldsymbol{m}_j$ and $\hat{\boldsymbol{m}}_j$ are the jth vectors of the matrices E, M and $\hat{M}$, respectively ($j = 1, 2, \ldots, N$). Note that $\hat{\boldsymbol{m}}_j$ can be determined in parallel, although the procedures 1–4 are sequential.

As examples of the criteria for the procedure 3, the following may be considered.

1. If $a_{ij} \neq 0$ then $\hat{m}_{ij} = m_{ij}$, else $\hat{m}_{ij} = 0$ $(i = 1, 2, \ldots, N)$.

2. If $|m_{ij}| > c_j$ then $\hat{m}_{ij} = m_{ij}$, else $\hat{m}_{ij} = 0$ $(i = 1, 2, \ldots, N)$.

Here, a_{ij} is the (i, j)-element of the matrix A, and m_{ij} and $\hat{m}_{ij}$ are ith components of $\boldsymbol{m}_j$ and $\hat{\boldsymbol{m}}_j$, respectively. In addition, c_j is a parameter that may be determined as

$$c_j = \frac{\sum_{i=0}^{N} |m_{ij}|}{N}. \tag{4}$$

Note that the above criteria are separately employed.

4. Numerical Experiments

In this section, numerical experiments are conducted to investigate the performance of the strategy. To this end, linear systems based on `poisson3Db` [4] as a coefficient matrix together with `poisson3Db_b` [4] as a right-hand side vector are solved by BiCGStab [5] with preconditioning. The preconditioning matrices are generated by an incomplete LDU decomposition [2] or the strategy described in Section 3. Here, $N = 85623$. In what follows, we refer to BiCGStab with the incomplete LDU decomposition as iLDU-BiCGStab, and BiCGStab with the strategy as M-BiCGStab.

Computations were performed on Cygnus at the CCS (Center for Computational Sciences), University of Tsukuba. Cygnus for each node equips dual 12-core Intel Xeon Gold 6126 2.6 GHz processors, 192 GB RAM, CentOS, and Intel C++ Compiler ver. 19.0.5 with double-precision arithmetic. In addition, parallelization is performed by OpenMP on one node, and optimize options for all codes are `-O3 -axCORE-AVX512`. Besides, we set an environment variable, `KMP_AFFINITY=scatter`.

First, the dependence of execution time and speed-up ration on the number T of threads for generation of preconditioning matrices is shown in Fig. 1(a). In this figure, 'iLDU + M' denotes the proposed strategy. We see from Fig. 1(a) that the speed-up ratio of proposed strategy is about 16.8 for $T = 24$ in comparison with $T = 1$. In addition, the speed-up ratio of iLDU is almost the same for all numbers of threads. Hence, the algorithm of the proposed strategy is suitable for parallelization in comparison with the original incomplete LDU decomposition. Note that the execution time of the proposed strategy is larger than that of iLDU for all numbers of threads.

Next, for iteration process, the dependence of execution time and speed-up ration on the number T of threads is shown in Fig. 1(b). We see from this figure that the speed-up ratio of M-BiCGStab is about 4.86 for $T = 24$ in comparison with $T = 1$. Besides, the speed-up ratio of iLDU-BiCGStab is about 1.51 for $T = 24$ compared with $T = 1$. Thus, M-BiCGStab is more suitable for parallelization than iLDU-BiCGStab. However, the total execution time of M-BiCGStab is greater than that of iLDU-BiCGStab. Note that the number of iterations for M-BiCGStab and that for iLDU-BiCGStab are 796 and 113 for $T = 24$, respectively. Namely, the execution time for each iteration of M-BiCGStab and that of iLDU-BiCGStab

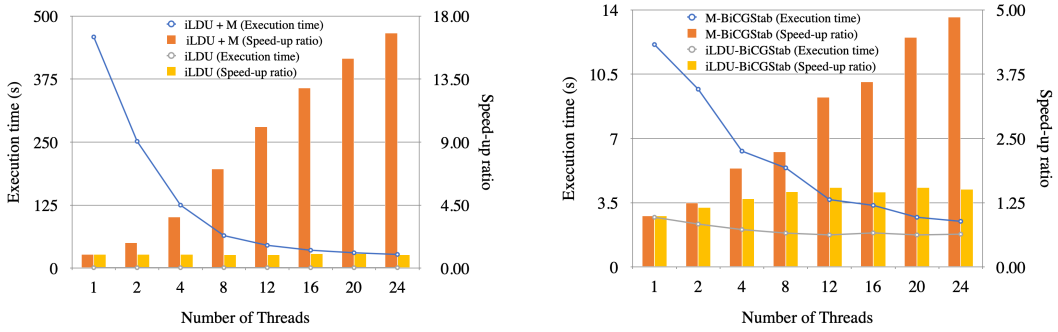

Figure 1: Dependence of Execution time and speed-up ratio on the number of threads for (a) generation of preconditioning matrices and (b) iteration process.

are about 0.00313 s and 0.0158 s. Hence, the the execution time for each iteration of M-BiCGStab is about 5.06 times faster than that of iLDU-BiCGStab.

From the results, although the speed-up ratio of M-BiCGStab is higher than that of iLDU-BiCGStab, the total execution time of M-BiCGStab is greater than that of iLDU-BiCGStab, for this case. We consider that the performance of M-BiCGStab may be more efficient for larger cases. In addition, there is a possibility that the algorithm for generating the preconditioning matrices may be improved, by utilizing the structures of matrices. Other results and further details will be presented at the conference.

Acknowledgement

Numerical calculations were performed using Cygnus at the CCS, University of Tsukuba.

References

[1] Y. Saad: Iterative Methods for Sparse Linear Systems (2nd Edition), SIAM, Philadelphia, PA (2003).

[2] K. Murata, M. Natori, Y. Karaki: Large-scale Numerical Simulations, Iwanami Shoten, Tokyo (1990) (in Japanese).

[3] I. S. Duff, R. G. Grimes, J. G. Lewis: Sparse matrix test problems, *ACM Trans. Math. Soft.*, 15:1 (1989), 1–14.

[4] *SuiteSparse Matrix Collection, Formerly the University of Florida Sparse Matrix Collection*, accessed on Aug. 2, 2021. [Online]. Available: https://sparse.tamu.edu/

[5] H. A. van der Vorst: Bi-CGSTAB: A Fast and Smoothly Converging Variant of Bi-CG for the Solution of Nonsymmetric Linear Systems, *SIAM J. Sci. Stat. Comput.*, 13:2 (1992), 631–644.

An analysis of electrocardiograms through the wavelet transform with pseudo differential operator like operators

M. Rahman[1,*], T. Kagawa[2], S. Kawasaki[3], S. Nagai[2], T. Okai[4], H. Oya[4], Y. Yahagi[5], M.Yoshida[1]

[1]Graduate School of Engineering, Kanagawa Univ.
[2]Faculty of Engineering, Kanagawa Univ.
[3]Faculty of Science and Engineering , Iwate Univ.
[4]Faculty of Information Engineering, Tokyo City Univ.
[5]Dept.of Mathematical informatics, Tokyo Univ. of Information Science

[*]masudur_2006@yahoo.com

The full paper of this paper has been published in Journal of Advanced Simulation in Science and Engineering (JASSE).

DOI: https://doi.org/10.15748/jasse.9.96

Application of Wavelet-Taylor-Galerkin method to the 1D Euler equations

[1]Yamamoto Kyosuke and [2]Matsuura Taishi

[1]Faculty of Engineering, Information and Systems, University of Tsukuba

[2]Sumitomo Heavy Industries, Ltd (Research while in Univ. of Tsukuba)

[1]yamamoto_k@kz.tsukuba.ac.jp, [2]taishi.matsuura@shi-g.com

Abstract. In the present study, the Euler equation is numerically solved by the Wavelet-Taylor-Galerkin (WTG) method and its effectiveness is confirmed; it is found that the WTG method can obtain a numerical solution with high accuracy, while suppressing numerical oscillations compared with popular finite difference methods, such as the Lax Wendroff method.

Keywords: Wavelet-Taylor-Galerkin method, Euler equations

1. Introduction

The finite element method (FEM) is the most popular method for numerically solving partial differential equations (PDE), as well as the finite differential method (FDM). Since almost all mechanical and social systems can be described by PDE, we can apply FEM to them. It enables us to solve various problems of modern society by computers. FEM has been generalized by the weighted residual method (WRM). The most common scheme of WRM is called the Galerkin method. Suppose that a PDE is given by $R(u) = 0$. If the given PDE is an advection equation, in which t, x, $u(t, x)$ and c denote the time, position, physical quantity and advection velocity, respectively, we have

$$\frac{\partial u}{\partial t} + c\frac{\partial u}{\partial x} = R,$$

where R is also called residual. The approximate solution of the analytical solution for $u(t, x)$ is expressed by the following equation:

$$u(t, x) = \boldsymbol{u}(t) \cdot \boldsymbol{N}(x),$$

where $\boldsymbol{N}(x)$ is the basis function vector and $\boldsymbol{u}(t)$ is the numerical solution vector. This operation is called interpolation. Since we cannot always set the residual *R* nor the average of the residuals $\int R\mathrm{d}x$ to zero, we instead make the assumption that the average of the weighted residuals is always zero, for any weight $\omega(x)$:

$$\int_0^L \omega R\mathrm{d}x = 0,$$

where $[0, L]$ is the defined area. Substituting the approximate solution $\boldsymbol{\omega} \cdot \boldsymbol{N}(x)$ of the analytical solution $\omega(x)$ into this equation, we obtain the finite element equation. For example, the

above advection equation can be transformed into the following equation

$$\boldsymbol{\omega}^{\mathrm{T}} \int_0^L \boldsymbol{N}(x) R(u) \mathrm{d}x = \boldsymbol{\omega}^{\mathrm{T}} \left(\left[\int_0^L \boldsymbol{N}\boldsymbol{N}^{\mathrm{T}} \mathrm{d}x \right] \{\dot{\boldsymbol{u}}\} + \left[\int_0^L \boldsymbol{N} \frac{\partial \boldsymbol{N}^{\mathrm{T}}}{\partial x} \, \mathrm{d}x \right] \{\boldsymbol{u}\} \right) = 0.$$

Putting $\mathbf{M} = \left[\int_0^L \boldsymbol{N}\boldsymbol{N}^{\mathrm{T}} \mathrm{d}x\right]$ and $\mathbf{C} = \left[\int_0^L \boldsymbol{N} \frac{\partial \boldsymbol{N}^{\mathrm{T}}}{\partial x} \, \mathrm{d}x\right]$, the finite element formula is as follows:

$$\mathbf{M}\dot{\boldsymbol{u}} + \mathbf{C}\boldsymbol{u} = \mathbf{0}.$$

This kind of operation is general and can be applied to any PDE. For the basis functions, Lagrange or Hermite interpolation functions are common. In the case of the Discontinuous Galerkin (DG) method, the Legendre interpolation function is used. On the other hand, a scaling function, which is used in the wavelet transform[1], is also an orthonormal basis and can be used as the basis function vector $\boldsymbol{N}(x)$. When a scaling function is used for the basis function $\boldsymbol{N}(x)$, the geometry matrix $\mathbf{M}$ becomes an unitary matrix, which makes the calculation very efficient. If the scaling function is applied to Taylor-Galerkin method[2], we call it Wavelet Taylor Galerkin (WTG) method[3]-[4].

When $\phi(x)$ denotes the scaling function, $\phi_{j,k}(x)$ is defined as the following:

$$\phi_{j,k}(x) = 2^{-\frac{j}{2}} \phi(2^{-j}x - k),$$

where both j and k are integers. j indicates the approximate resolution and k represents the corresponding node number. In other words, the node position must be $x_k = k\Delta x$.

2. Basic Theory

Let ρ, u, p and e be the fluid's density, flux, pressure, and total energy per unit volume, respectively. The Euler equation is given by

$$\frac{\partial \boldsymbol{Q}}{\partial t} + \frac{\partial \boldsymbol{E}}{\partial x} = \mathbf{0}.$$

where $\boldsymbol{Q} = [\rho \ \rho u \ e]^{\mathrm{T}}$ is the conserved quantity and $\boldsymbol{E} = [\rho u \ p + \rho u^2 \ (e+p)u]^{\mathrm{T}}$ is the flux.

The second-order Taylor expansion of the conserved quantity $\boldsymbol{Q}$ is given by

$$\boldsymbol{Q}^{n+1} = \boldsymbol{Q}^n + \Delta t \frac{\partial \boldsymbol{Q}}{\partial t} + \frac{1}{2}\Delta t^2 \frac{\partial^2 \boldsymbol{Q}}{\partial t^2}.$$

where n is the time step. The second-order term in this equation can be transformed, using the Jacobi matrix $\mathbf{A} \equiv \frac{\partial \boldsymbol{E}}{\partial \boldsymbol{Q}}$, as

$$\frac{\partial^2 \boldsymbol{Q}}{\partial t^2} = \frac{\partial}{\partial t}\left(\frac{\partial \boldsymbol{Q}}{\partial t}\right) = \frac{\partial}{\partial t}\left(-\frac{\partial \boldsymbol{E}}{\partial x}\right) = -\frac{\partial}{\partial x}\frac{\partial \boldsymbol{E}}{\partial t} = -\frac{\partial}{\partial x}\left(\mathbf{A}\frac{\partial \boldsymbol{Q}}{\partial t}\right) = \frac{\partial}{\partial x}\left(\mathbf{A}\frac{\partial \boldsymbol{E}}{\partial x}\right),$$

where

$$\mathbf{A} = \begin{bmatrix} 0 & 1 & 0 \\ \frac{1}{2}(\gamma-3)\rho u^2 & -(\gamma-3)u & \gamma - 1 \\ -\gamma\frac{e}{\rho}u + (\gamma-1)u^3 & \gamma\frac{e}{\rho} - \frac{3}{2}(\gamma-1)u^2 & \gamma u \end{bmatrix}.$$

γ is the heat capacity ratio. Thus, we obtain

$$\boldsymbol{Q}^{n+1} = \boldsymbol{Q}^n - \Delta t \frac{\partial \boldsymbol{E}^n}{\partial x} + \frac{1}{2}\Delta t^2 \frac{\partial}{\partial x}\left(\mathbf{A}^n \frac{\partial \boldsymbol{E}^n}{\partial x}\right),$$

Let $\boldsymbol{Q}_i^n$ be the conserved quantity at i-th node: $\boldsymbol{Q}_i^n = [\rho_i(n\Delta t)\ \rho_i(n\Delta t)u_i(n\Delta t)\ e_i(n\Delta t)]^{\mathrm{T}}$. When we now apply WRM with the scaling function as the basis, we further obtain

$$\boldsymbol{Q}_i^{n+1} = \boldsymbol{Q}_i^n - \frac{\Delta t}{\Delta x}\sum_{k=-L+1}^{L-1} \boldsymbol{E}_{i+k}^n a_k^{(1)} + \frac{1}{2}\frac{\Delta t^2}{\Delta x^2}\sum_{k=-L+1}^{L-1}\sum_{l=-L+1}^{L-1}\left(\mathbf{A}_{i+k}^n \boldsymbol{E}_{i+l}^n b_{kl}^{(1,1)} + \mathbf{A}_{i+k}^n \boldsymbol{E}_{i+l}^n b_{kl}^{(0,2)}\right),$$

where k and l are integers. Also, the coefficients $a_k^{(p)}$ and $b_k^{(p.q)}$ are

$$a_k^{(p)} = \int_{-\infty}^{+\infty} \phi_{0,0}(x)\frac{\partial^p \phi_{0,k}}{\partial x^p}(x)\mathrm{d}x\,,$$

$$b_{kl}^{(p,q)} = \int_{-\infty}^{+\infty} \phi_{0,0}(x)\frac{\partial^p \phi_{0,k}}{\partial x^p}(x)\frac{\partial^q \phi_{0,l}}{\partial x^q}(x)\mathrm{d}x,$$

respectively. If $\boldsymbol{Q}_i^n$ is known, we can solve this equation to obtain $\boldsymbol{Q}_i^{n+1}$, though we need to introduce the artificial viscosity.

In order to suppress the numerical oscillations, the obtained velocity u_i^{n+1} should be replaced by $\bar{u}_i^{n+1}$ as following:

$$\bar{u}_i^{n+1} = u_i^{n+1} + \varepsilon\frac{|u_{i+1}^{n+1} - 2u_i^{n+1} + u_{i-1}^{n+1}|}{|u_{i+1}^{n+1} + 2u_i^{n+1} + u_{i-1}^{n+1}|}(u_{i+1}^{n+1} - 2u_i^{n+1} + u_{i-1}^{n+1}).$$

However, this formula is derived from the idea based on FDM. Thus, in this study, novel artificial viscosity of which based idea comes from WTG method is also introduced and compared with the former:

$$\bar{u}_i^{n+1} = u_i^{n+1} + \varepsilon\frac{\left|\sum_{l=-L+1}^{L-1} u_i^{n+1}a_l^{(2)}\right|}{\left|\sum_{l=-L+1}^{L-1} u_i^{n+1}\left|a_l^{(2)}\right|\right|}\sum_{l=-L+1}^{L-1} u_i^{n+1}a_l^{(2)}.$$

3. Numerical Simulation

A one-dimensional shock tube problem is set up as shown in **Fig.1**, and applied WTG and FDM methods for comparing the numerical solutions. As the WTG, we prepare two types: one is the As the FDM in this study, Lax-Wendroff method[5] is applied.

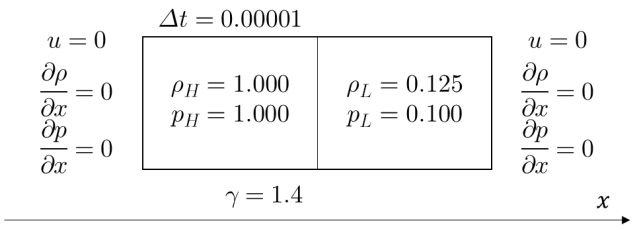

Fig.1 The initial condition / boundary condition of Shock Tube Problem

The results obtained by the WTG method using Coiflet's scaling function and the finite difference method (FDM, Lax-Wendroff method) are shown in **Fig. 2**. When calculating

the results of the WTG method, two cases are prepared: one where the artificial viscosity is calculated in the same way as in FDM, and another where the artificial viscosity is done in the same way as in WTG. The results show that the numerical solution obtained by the WTG method with the WTG-type artificial viscosity is the closest to the analytical solution: the amplitude of the numerical oscillations is sufficiently suppressed by the WTG method compared to FDM, and the positions of the shock wave surfaces are calculated at near positions as in FDM. Although further improvement is still needed, it is confirmed that the WTG method is an effective numerical analysis method for the Euler equation.

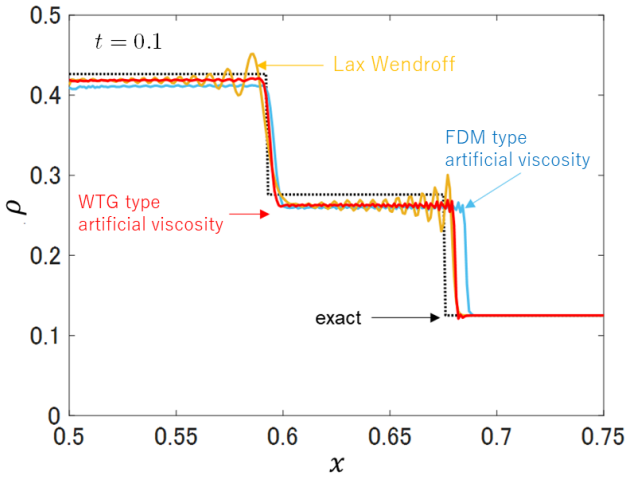

Fig. 2 The results of WTG simulation

The WTG method with WTG type artificial viscosity is a better option for numerically solving the Euler equation. This scheme can suppress the amplitude of numerical oscillations well. However, a technical issue that we must set all nodes in regular distance still remains.

References

[1] Liandrat, J. and Tchamitchian, Ph., "Resolution of the 1D regularized Burgers equation using a spatial wavelet approximation," *ICASE Report* (1990), pp.90-83.

[2] Donea, J., "A Taylor-Galerkin method for convective transport problems," *International Journal for Numerical Methods in Engineering*, **20** (1984), pp.101-119.

[3] Kumar, B. R. and Mehra, M., "A Wavelet-Taylor Galerkin method for parabolic and hyperbolic partial differential equations," *International Journal of Computational Methods*, **2** (1) (2005), pp.75-97.

[4] Kumar, B. R. and Mehra, M., "Wavelet-Taylor Galerkin method for the Buegers Equation," *BIT Numerical Mathmatics*, 45 (2005), pp.543-560.

[5] Peter D. Lax, Burton Wendroff, "Systems of Conservation Laws," *Communications on Pure and Applied Mathematics*, **17** (1964), pp.381-398.

JSST 2021

Wavelet Galerkin method for three-dimensional boundary value problems with MPC technique

Satoyuki Tanaka[1,*], Thin Thin Htut[1], Hanlin Wang[1], Hiroshi Okada[2]

[1]Graduate School of Advanced Science and Engineering, Hiroshima University
[2]Department of Mechanical Engineering, Faculty of Science and Technology, Tokyo University of Science

[*]satoyuki@hiroshima-u.ac.jp

The full paper of this paper has been published in Journal of Advanced Simulation in Science and Engineering (JASSE).

DOI: https://doi.org/10.15748/jasse.9.78

JSST 2021

Driving forces for structural transitions in atomic clusters in collective eigen-time-delay coordinates

Yusuke Ogasawara[1] and Tomohiro Yanao[1,*]

[1]Department of Applied Mechanics and Aerospace Engineering, Waseda University

[*]yanao@waseda.jp

Abstract. This study explores driving forces for structural transitions in atomic clusters using collective eigen-time-delay coordinates. Hyperspherical radius of an atomic cluster serves as a collective coordinate characterizing structural transitions between two distinct structures. We apply a time series of the hyperspherical radius to the Hankel alternative view of Koopman analysis to construct a reduced-order linear system of eigen-time-delay coordinates with an intermittent forcing. This intermittent forcing can signify precursors to structural transitions in a probabilistic manner. We argue the similarity between this intermittent forcing and the mechanical driving forces for structural transitions in clusters.

Keywords: Driving forces, Hankel alternative view of Koopman, Eigen-time-delay coordinates, Atomic clusters, Structural transitions, Hyperspherical radius

1. Introduction

Prediction of abrupt state transitions in chaotic dynamical systems attracts significant interest in nonlinear dynamics and data science. Examples are abundant in celestial mechanics, turbulent dynamics, biological systems, and molecular dynamics. For an accurate prediction of state transitions, identification of precursors is important. Precursors are sometimes associated with driving forces. This study thus explores driving forces for structural transitions in atomic clusters based on the methods of time series analysis [1, 2] and geometric mechanics [3].

2. Methods and results

Structural transitions of six-atom Lennard-Jones clusters in vacuum serve as a prototypical model of abrupt state transitions in chaotic dynamical systems throughout this study. This cluster has two geometrically distinct local equilibrium structures, called OCT and CTBP, corresponding to the minima of the total potential energy. When the total energy is sufficiently high, the cluster undergoes structural transitions between the two equilibrium structures.

We apply the hyperspherical coordinates and take the largest hyperspherical radius among the three, $a_1 (\geq a_2 \geq a_3)$, as the collective variable that can characterize structural transitions in the six-atom cluster. We then input the time series of the hyperspherical radius $a_1(t)$, where t is time, into the procedure of the Hankel alternative view of Koopman (HAVOK) analysis [1], and obtain a reduced-order linear model of differential equations,

$$\frac{d}{dt}\begin{pmatrix} v_1 \\ v_2 \end{pmatrix} = \mathbf{A}\begin{pmatrix} v_1 \\ v_2 \end{pmatrix} + \mathbf{B}v_3, \tag{1}$$

where v_1 and v_2 are eigen-time-delay coordinates. v_3 is an intermittent forcing derived from the data. The coefficients $\mathbf{A}$ and $\mathbf{B}$ are 2×2 and 2×1 matrices respectively, which are determined by a regression method called the sparse identification of nonlinear dynamical systems [2]. The intermittent forcing v_3 showed some characteristic behaviors right before structural transitions. For example, the signal of v_3 tends to be strong in OCT right before transitions into CTBP, and the signal of v_3 tends to be weak in CTBP right before transitions into OCT. These characteristic behaviors could serve as precursors to the structural transitions in a probabilistic sense since they are faint requiring a statistical characterization.

We also argue the similarity and correspondence between v_3 in Eq. (1) and mechanical forces [3] in the classical (Euler-Lagrange) equations of motion for a_1,

$$\frac{d^2 a_1}{dt^2} = \Gamma(a_1, a_2)\omega_{12}^2 + \Gamma(a_1, a_3)\omega_{13}^2 + a_1 \sum_{k=4}^{n-1} \gamma_{1k}^2 - \frac{\partial V_{\mathrm{LJ}}}{\partial a_1}, \tag{2}$$

where $\Gamma(a_i, a_j)$ is a function of hyperspherical radii, ω_{ij} and γ_{1k} are internal angular velocities, $n = 6$ is the number of atoms, and V_{LJ} is the interatomic Lennard-Jones potential. Physically, the first three terms on the right hand side of Eq. (2) are internal centrifugal forces and the forth term is the potential force. We have evidenced that these mechanical forces in Eq. (2) can drive structural transitions of clusters in a probabilistic sense. Moreover, behaviors of these forces were very similar to those of v_3 in Eq. (1), indicating that v_3 could also be interpreted as a driving force mediating structural transitions. We finally present an analytical account for the similarity between v_3 and the mechanical driving forces.

In summary, we have first reduced the dynamics of atomic clusters into a linear system of eigen-time-delay coordinates with an intermittent forcing using HAVOK. We have then evidenced the similarity between the intermittent forcing and the mechanical driving forces for structural transitions in atomic clusters.

References

[1] S. L. Brunton, B. W. Brunton, J. L. Proctor, E. Kaiser, J. N. Kutz: Chaos as an intermittently forced linear system, *Nature Communications*, 8:1 (2017), 1–9.

[2] S. L. Brunton, J. L. Proctor, J. N. Kutz, Discovering governing equations from data by sparse identification of nonlinear dynamical systems, *Proceedings of the National Academy of Sciences*, 113 (2016), 3932–3937.

[3] T. Yanao, W. S. Koon, J. E. Marsden, Intramolecular energy transfer and the driving mechanisms for large-amplitude collective motions of clusters, *J. Chem. Phys.*, 130 (2009) 144111.

[4] J. F. Gibson, J. Doyne Farmer, M. Casdagli, S. Eubank, An analytic approach to practical state space reconstruction, *Physica D*, 57 (1-2) (1992) 1–30.

JSST 2021

Multiagent simulation of infectious propagation of COVID-19

Jin Suzuki[1] and Atsushi Tanaka[2,*]

[1,2]Graduate School of Science and Engineering, Yamagata University

[*]tanaka@yamagata-u.ac.jp

Abstract. In this paper it is investigated how the COVID-19 infectious disease spread using multiagent simulation. Simulation spaces are a building for a closed space and a park for an open space. And three kinds of infectious forms, air, contact and droplet are compared. As a result, it is confirmed that the more the density of people is higher, the more the infection increases significantly. The consideration of effective vaccination of COVID-19 is expected in the future.

Keywords: COVID-19, Infection, Multiagent simulation

1. Introduction

The fury of COVID-19 originated in Wuhan, China in November 2019 has been spread rapidly all over the world and we can say it is the pandemic situation without no doubt. Recently some vaccines have been developed and vaccinations in many countries have started though, they are not enough yet and the emergence of some strong variant strains stir up our anxiety. It is well-known that infections of COVID-19 spread mainly by air, contact and droplet, and some aspects of droplet have been visualized by supercomputer "FUGAKU"[1]. In addition, studies of COVID-19 have been very active and wide-ranging, they include not only viruses themselves but also information propagation of them[2, 3]. Though Japanese government is stepping up efforts to stem the tide of people for the prevention of infection, the situation has not been made the desired progress and the state of emergency has been invoked three times so far. Thus it is investigated how the infection spread by the flow of people using multiagent simulation. From the simulation results, it is verified the higher human density becomes, the higher the risk of infection arises.

2. Simulation procedure

2.1. Simulation framework

Multiagent simulation is a framework which consider a lot of moving around particles as autonomous agents. It can enumerate human activities and many behaviors of things in

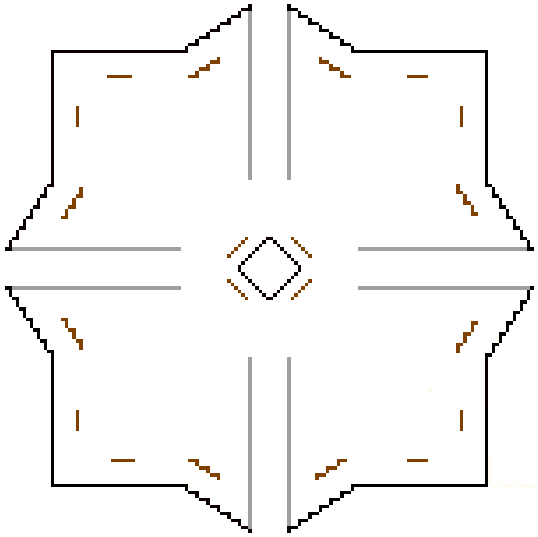

Figure 1: Overview of the park space. There locates a monument at the center. There are also some chairs in the park.

broad perspective, so it is one of the powerful simulation methods. Its applications cover a broad range of topics like traffic congestion, evacuation behaviors, offensive strategy etc. The more precisely we describe it, the more complicated its coding tends to be. Therefore we make use of time-tested multiagent simulation framework called as “Artisoc” in this study[2]. Though it is free software, we can describe the situation very precisely and carry out simulation easily.

2.2. Simulation settings

We consider three kinds of virus infection modes, air contact and droplet. Here we enumerate simulation settings roughly as follows.

- 20 % of infected person spread virus all over.
- For every agent its age and immunizing power are configured. Its power and whether they notice symptom or not depend on their ages.
- In contact infection case, the infection rate arises when the agent contacts infected one.
- In air and droplet infections, the infection rate arises when there exits virus at the position of the agent.

We study two models for simulation spaces, a building and a park. The former is a three-story closed space without any obstacles. The later is an open space though, there locates a monument and some chairs everywhere(Fig.1). We carry out all simulations 10 times and average them.

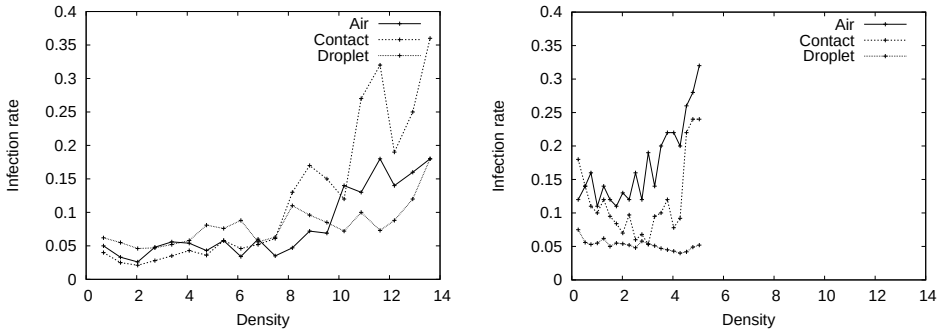

(a) Building model (b) Park model

Figure 2: Density correlation of infection rate. We can easily find the more density is high, the more the infection rate will arise.

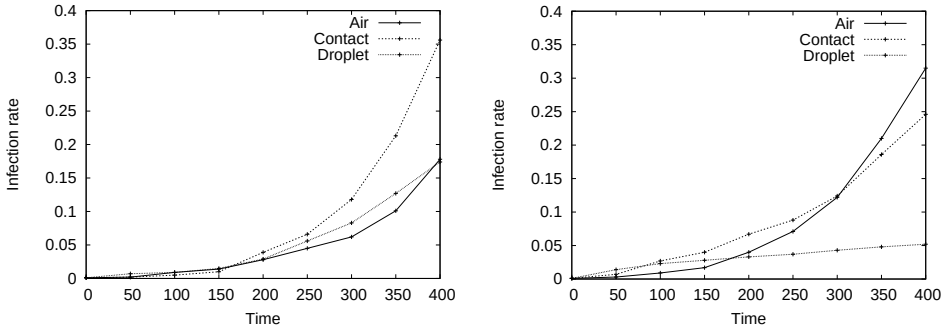

(a) Building model (b) Park model

Figure 3: Time evolution of infection rate. In the building, the infection by touch spread widely, while in the park, the infection through air spread significantly.

3. Numerical results

Since the risk of infection is said to become higher if many people pack at some place, we investigate the relation of packing density and infection rate in detail at first(Fig.2). In this figure, the horizontal and vertical axes show the number of persons in 100 cells and the infection rate respectively. For both building and park models, we investigate infection rates in three kinds of infection modes.

Then we show time evolutions of infection rates for each case in Fig.3. Here time means computational steps in simulation, and corresponds to the speed of human walk.

4. Discussion

4.1. Correlation between density and infection rate

In the contact mode, the infection rate is higher for high human density. In the air mode, is is relatively higher for high human density in the park model. That is because they always spread virus to the space, then the area of high virus density become large. On the contrary in the droplet mode, it is relatively low comparing with other two modes, and its fluctuation

is also small all over. That is because viruses in the space are localized, and so they are hard to spread.

4.2. Time evolution of infection

In the contact mode, the increasing rate is high in the building model, while it is low in the park model. That is because in the latter case, the human population increases and decreases, and so most contacts relatively new ones and the infection probability is hard to increase. In the air mode, the increasing rate of infected person is high in the park model. That is because the infection probability of newly entered agents becomes higher because the area of viruses in the space becomes larger. At last in the droplet mode, it increases slightly in the building model, while it is almost constant in the park model. That is because uninfected agents rarely pass through infected area because virus becomes more localized and some infected agents go out naturally. On the contrary, in the building mode, the space is closed, so it increases a little higher.

5. Summary

In this paper it is investigated how the COVID-19 infectious disease spread using multiagent simulation. Simulation spaces are a building for a closed space and a park for an open space. And three kinds of infectious forms, contact, air and droplet are compared. As a result, it is confirmed that the more the density of people is higher, the more the infection increases significantly. For the future work, we would like to investigate several other spacial models and take the diversity of agents into account. Moreover since the vaccinations of COVID-19 have started in many countries, we will investigate which agent is the most effective to be vaccinated for the control of virus diffusion.

References

[1] Makoto Tsubokura: Droplet/Aerosol Dispersion Simulation on Supercomputer Fugaku for the Fight against COVID-19, *IPSJ MAGAZINE*, 62:2 (2021), 64–66.

[2] J. Zarocostas: WHO's newly launched platform aims to combat misinformation around COVID-19, *www.thelancet.com*, 395 (2020), 676.

[3] Atsushi Tanaka and Fujio Toriumi: Characteristics of Information Propagation in COVID-19 Crisis, *Proc. Int. Symp. on Nonlinear Theory and its Application*, (2020), 54–57.

[4] https://mas.kke.co.jp/en/.

JSST 2021

A prediction algorithm of drosophila lifespan toward high-throughput screening in genetic research

Masaya Hata[1], Ki-Hyeong Seong[2], Siu Kang[1*]

[1] Department of Bio-Systems Engineering, Graduate School of Science and Engineering, Yamagata University

[2] RIKEN cluster for Pioneering Research, RIKEN Tsukuba Institute (Current affiliation: Insect Design Technology Group Division of Insect Advanced Technology Institute of Agrobiological Sciences, NARO)

*siu@yamagata-u.ac.jp

Abstract. Drosophila has been often used in genetic research field. We tried to predict lifespan of individual drosophila through the combination of image processing and deep learning by convolutional neural network. As a result, 68% of flies predicted by the algorithm showed 10% consistency compared with manual detection of actual lifetime measured by an experimental expert. It is expected that the present result contributes to high-throughput screening in gene- and drag-discovery related with the extend of lifespan.

Keywords: Biological image analysis, Machine learning, Deep neural network

1. Introduction

Drosophila is model animal in genetic research filed and the insect has been frequently used in screening through several gene manipulation such as gene knock-in/out, etc. It has been well known that drosophila preserve many parts of disease-related genomic sequences same as the ones in human being. So, searching and examining the disease-related phenotype in drosophila directly contributes to human health and promotion of quality of life in human society.

We previously developed the drosophila individual activity monitoring and detection system (DIAMonDs) toward high-throughput screening related with drosophila life-events [1]. The system provides automatic and high-accurate detection of drosophila life-events such as pupariation, eclosion, and death with single animal resolution.

In the present study, we tried to develop an prediction algorithm of drosophila life-span just through the time-lapse images of drosophila population.

2. Method

2.1. Time lapse images of drosophila population

We scanned the drosophila population images on the plate in an incubator. Sequential images were obtained with 1 minute intervals for about 40 hours. An image includes 288 wells with adult drosophila (Fig 1a). All the image acquisition process was performed at RIKEN

Tsukuba Institute.

2.2. Pre-processing for learning

Pre-process for the learning of life-span prediction is as follows:

First, all the images are separated into patch images with 56 x 56 pixel including an adult drosophila in a well (Fig 1b).

Second, all animal bodies were detected as binary labeling through the animal body detection algorithm we previously developed (Fig 1c, [1]).

Third, as training/test data for learning, the image subsets of 50 frames were prepared with sliding window without overlapping (Fig 2). The extraction in all the animals was performed until just before the death timing of an individual showing a minimum lifespan.

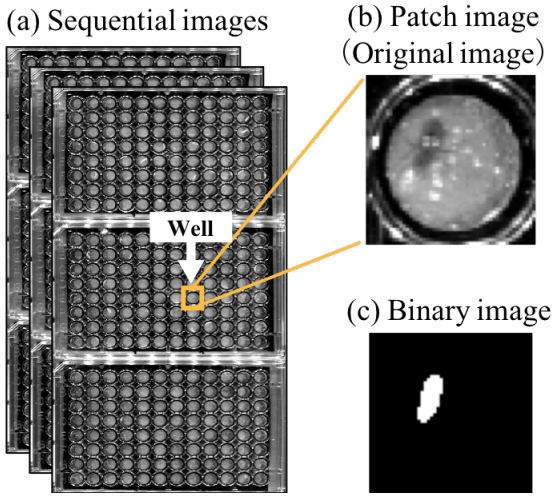

Fig 1 Time lapse image of drosophila population and an example of binary label

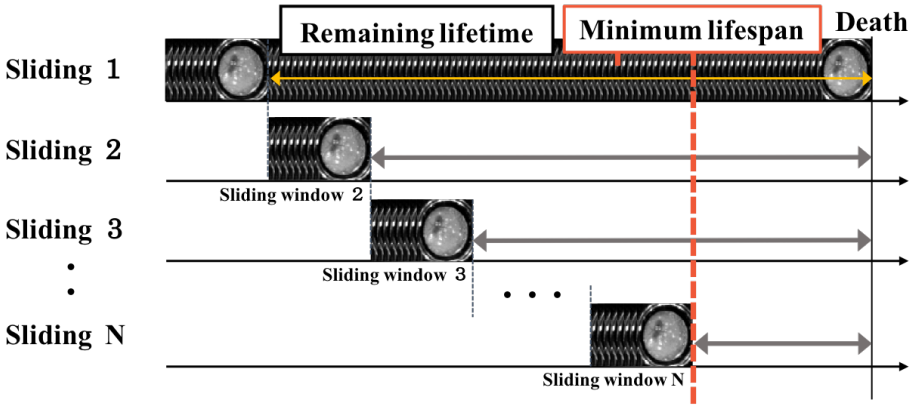

Fig 2 Extraction of subset images as training data

2.3. Learning for prediction

The deep neural network was trained for the image subsets described in previous section. The structure of the network was shown in Fig 3. Animal population was separated into train and test data with 9:1. Each animal has 4,420 image sequences and each sequences includes 50 frames. Training was performed for 1,500 epochs with 128 batch size, Adadelta as optimizer, and Huber loss function. In inference phase after the training, the network predicted the remaining lifetime of individual drosophila.

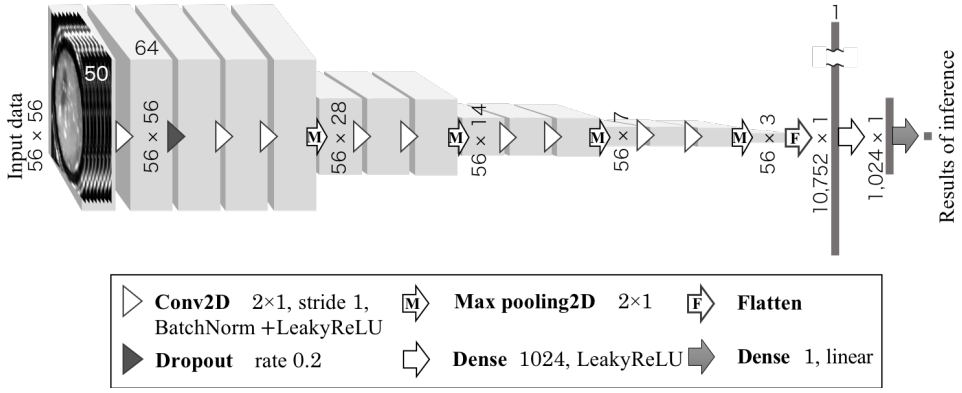

Fig 3 Network architecture for lifespan prediction

3. Results

Fig 4-6 show scatter plots for comparison between actual- and predicted-lifespans obtained by binary-, segmented- and original-images, respectively. Segmented images were obtained by convolution between binary- and original-images. A prediction accuracy was characterized as root mean square error (RSME) between actual- and predicted-lifespans. An accuracy of predictions from original image showed higher accuracy than the prediction from binary image.

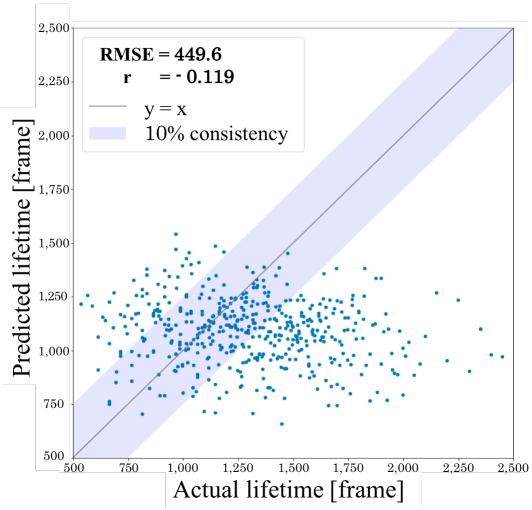

Fig 4 Prediction from binary images

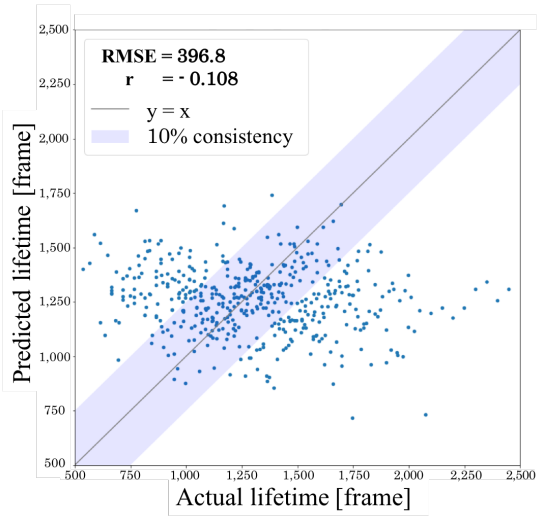

Fig 5 Prediction from segmented images

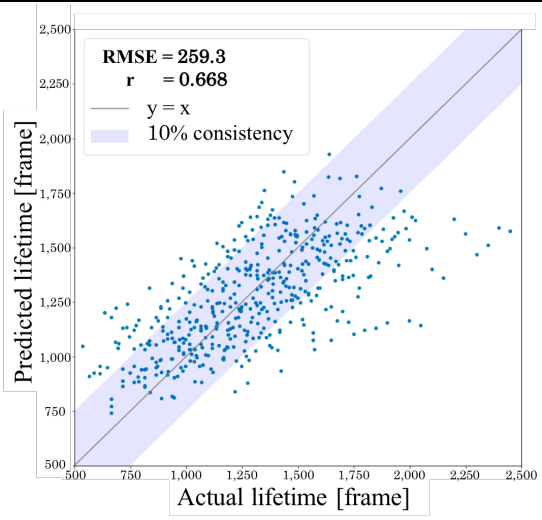

Fig 6 Prediction from original images

4. Conclusions

In the present study, we tried to predict drosophila lifespan by performing image analysis and deep learning onto the time lapse image of drosophila population. As a result, more than half percent of individuals was predicted with high accuracy compared with actual lifespans. It was also revealed that segmentation before learning leads to the decrease of accuracy of lifespan prediction. In order to improve the prediction accuracy, network architecture and pre-processing should be modified in future study.

Reference

[1] K.H. Seong, T. Matsumura, Y. Shimada-Niwa, R. Niwa, S. Kang (2020) “The Drosophila Individual Activity Monitoring and Detection System (DIAMonDS)”, *eLife*, DOI: 10.7554/eLife.58630

New semi origami structure for collision energy absorption and its manufacturing method

Yang Yang[1*], Ichiro Hagiwara[1]

[1]Institute for Advanced Study of Mathematical Sciences, Meiji university, Japan University

*piscesyy0227@gmail.com

Abstract. FCM(Full cut member) is shown to have splendid performance for the truck crash box and the simulation method is developed for its devised manufacturing method. Applying this simulation model to the crash model with 3mm thickness shows the thickness distribution is very small. The performance for the collision energy absorption from the model gained by manufacturing simulation is better than the one from the model with constant plate thickness gained by CAD in terms of much lower initial peak load and almost same energy absorption.

Keywords: Full cut member, Half cut member, Crash box, Liquid press manufacturing method

1. Introduction they work effectively

Origami structures are splendid also for collision energy absorption and there are 3 types of origami structures. One is 4 folding lines such as bellows fold which are studied by Zhong group. On the other hand, 6 folding lines such as RSO and RTO which are studied by Hagiwara group. The 3rd one is semi origami structures such as HCM and FCM which are studied also by Hagiwara group. Although origami structure such as RSO (Reversed Spiral Origami structure) has splendid performance also for crash energy absorption [1], it is difficult to develop inexpensive and excellent manufacturing technology for the origami structure. We have developed the inexpensive and excellent manufacturing technology named “Partially heated torsion manufacturing method” for RTO (Reversed Torsion Origami structure” [2] which has been developed to imitate RSO. It has also shown the excellent absorption performance with a half cut type member (HCM) [3] which can be placed as a semi origami structure of which reason will be described below. Here full cut type member (FCM) is developed by extending the HCM and is discussed how FCM works effectively to the truck crash box. And, it is discussed about the manufacturing technique for the FCM.

2. Truck crash box

The vehicle crash boxes are set between the bumper and side members so that only bumper and crash boxes are deformed for the light collision. In this case, the bumper and the crash boxes are replaced which leads an advantage over automobile insurance. The performance expected for the crash box is that over a certain limit energy absorption, below a certain level initial peak

load and it is collapsed from the tip to the back in order. Beads which consist of cut and protrusion structures are properly placed on the crash boxes so that it can be elapsed in the axis direction without bending. However even though this ideal collapsed mode is achieved, it is collapsed only 70% of its length due to its bulkiness and the initial peak load is too high which brings sometimes the dangerous situation to the passengers. It is very effective the origami structures to solve these problems where most of researchers use the 4 folding lines such as bellows fold with 4 lines at every intersection on the other hand our group uses the 6 folding ones such as RSO and RTO with 6 ones at every intersection. The advantages of origami structures especially with RSO and RTO are as follows;1) folding lines on the side of the column which guides to the collapse in the axial direction,2) receiving vertical loads diagonally which guides initial peak load below a level,3) setting the layers which prevents the lowered cross section size too large,4) keeping the foldable condition at each intersection. The FCM shown in Fig.1 to consider here does not charge only No.4) as well as the HCM so that they are positioned to be semi origami structures. As shown in Fig.1, the cross section is symmetry and it is shown that centered angle of quarter section is divided n equally for n=6 in Fig.1. The radii $(r_1, r_2, r_3, r_4, r_5)$ from the center to the key points are selected as shape parameters. The column is divided N equally along the axis direction and for segment difference on even number cross sections the radii have different Δ each from $(r_1, r_2, r_3, r_4, r_5)$ as shown in Fig.2. The targets are as follows; 1) weight to be below 5.04Kg for current weight 5.6Kg 10% or less),2) crush mode: collapse from the tip,3) energy absorption: 70KJ or more for current 76KJ,4) peak load:335KN or less for current 10% or less.

3. Study on collision simulation

3・1 Simulation method

Rectangular shell elements are used for crash box, the number of nodes is 5836 and the number of elements is 6178. The rigid wall is fixed completely and the frontend cross section has only degree of freedom perpendicular to rigid wall. The initial velocity is 56km/h. Vehicle weight 3000kg is given on the rear end face. The contact surface with coefficient of friction 0.1 is defined between crash box model and the rigid wall. The material of crash box is SPCE cold rolled steel sheet of which density is $7.85*10^{-6}$kg/mm3, Young modulus is 206Gpa, Poisson ratio is 0.3 and yield stress is 215Mpa. LS-DYNA is used for the simulation.

3・2 Simulation results

3・2・1 Study on cross section shape

Fig. 1(a) shows FCM with 7 layers and $\Delta = 0$. Fig.1(b) shows the Model (1) of cross section shape is controlled by changing $(r_1, r_2, r_3, r_4, r_5)$. $(r_1 = 50.92mm, r_2 = 44.39mm, r_3 = 35.27mm, r_4 = 32.56mm, r_5 = 28.61mm)$ and volume reduction rate is 20%. With this model, it is collapsed from the tip.

3・2・2 Study on segment difference

Based on FCM, the nodes on the odd cross sections are constant and the segment differences $\Delta = 10\%$ of each radius length are given to the nodes on the even cross sections. As a result, the shape along the axis direction is valley-mountain-valley as shown in Fig.2 where the segment difference on the 2nd and 4th cross sections. Weight, collision energy absorption and initial peak load are summalized for each case in Table1. This concludes segment difference is effective to collapse mode control and gives good influence for reaction load.

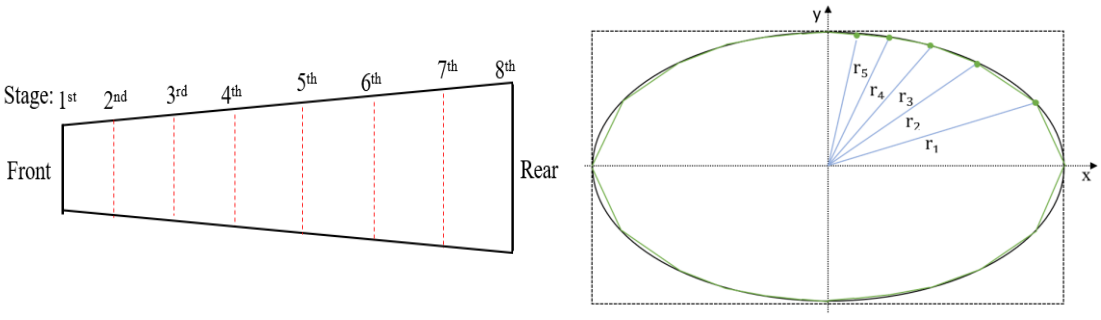

(a) Axial direction (b) Cross section

Fig.1 Different cross-section shapes by changing the lengths of $r_1, r_2, r_3, r_3, r_4, r_5$.

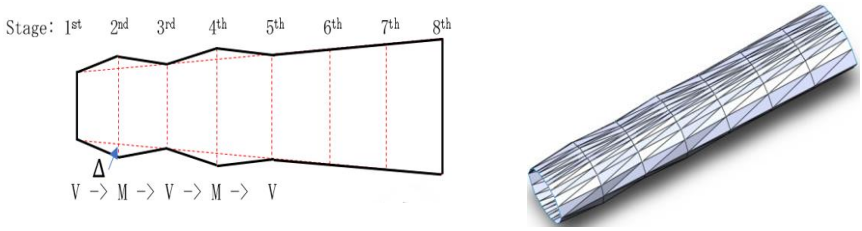

Fig.2 Model (2) of different section shapes by setting the division section along the axial direction. V means valley and M means mountain.

Table 1 Comparison results of different cross-section shapes

Structure	Thickness [mm]	Mass [kg]	Peak force[kN]	Energy absorption [KJ]	Energy absorption/Mass[KJ/kg]	Front collapse
Original (1)/CAD data	3.5	5.6	372	76	13.5	○
Original (2)/ CAD data	3.0	4.8	320(○)	64	11.9	○
Model (1)/ CAD data	3.0	4.1(○)	286(○)	72(○)	17.5	○
Model (2)/ CAD data	3.0	4.2(○)	294(○)	75(○)	17.9	○
Model (3)/Simulation data	3.0	4.2(○)	272(○)	70(○)	16.7	○

4. Liquid press manufacturing method

FCM can be manufactured by liquid press manufacturing method in the flow of the following (1) to (4)as shown in Fig.3.

（1）Square pillar material is closed on both sides by round core bar and fixing metal fittings. Liquid is filled in the square pillar material through the centered hole of the round core bar.

（2）Square pillar material filled with liquid is installed on the mold and it is molded by press.

（3）The mold is opened. The molded material is pulled out and the liquid inside is taken out.

（4）At last, unnecessary parts of both ends of the forming product are cut and crush box is generated.

We have developed the simulation technique for the liquid press manufacturing method [14]. Using this technique to the model in Fig.2. As a result, the maximum and the minimum thickness are 3.5mm and 2.5mm so that plate thickness change is within 16.7%. The FCM of Model (3) based on the manufacturing results has the almost same performance as the one based on CAD as shown in Table1.

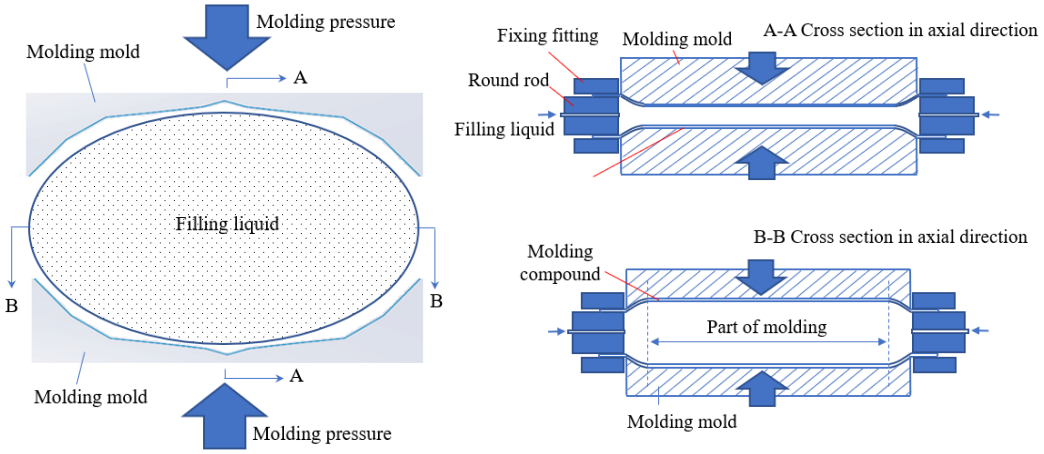

Fig.3 The proposed manufacturing method.

5. Conclusion

Here FCM is shown to have splendid performance for the truck crash box and the simulation method is developed for its devised manufacturing method. Applying this simulation model to the crash model with 3mm thickness shows the thickness distribution is within 16.7%. The performance for the collision energy absorption from the model gained by manufacturing simulation is better than the one from the model with constant plate thickness gained by CAD in terms of much lower initial peak load and almost same energy absorption. In the near future the manufacturing equipment will be developed based on this manufacturing method.

References

[1] I. Hagiwara, S.Nadayosi, Folding Process of Cylindrical Structures Using Origami Model., International Journal of Automotive Engineering, Vol.34, No.4 (2003), pp.145-149 (in Japanese).
[2] D. Liang, Y. Yang, C. Kong, Y. Jing, W. Zhao, X. Zhao, I. Hagiwara, Reversed Torsion Type Crash Energy Absorption Structure and Its Inexpensive Partially Heated Torsion Manufacturing Method, Transactions of the JSME, Vol.87, No.895 (2021-3), p. 20-00425.
[3] X. Zhao, ,Y. Hu, I. Hagiwara, Study on Crash Characteristics of Energy Absorption Ability of Half Cut Type Vehicle Side Member Structure by Using Origami Engineering, Transactions of the JSME, Series A,Vol.76, No.769 (2010-9), pp.1131-1138.
[4] Hagiwara, I., M., Tsuda, M. and Kitagawa, Y., Method of Determining Positions of Beads, Japanese Patent, Patent Number JP2727680B2 (1991).

JSST 2021

Development of a Pattern for Continuous Manufacturing of Complex 3D Shapes with Kirigami Honeycombs

Luis Diago[1,2,*], Junichi Shinoda[2], Ichiro Hagiwara[1]

[1]MIMS, Meiji University
[2]Interlocus Inc

[*]luis_diago@meiji.ac.jp

Abstract. Recent developments show that honeycomb structures built by a continuous production process can be successful in industrial applications at different scales (from nanosciences to aerospace applications) because of their material savings and low weight; while maintaining the mechanical properties required in the application. However, these properties cannot be well exploited when the three-dimensional shapes to be built have complex geometries because the theory supporting the production process is centered on an axial slice and two two-dimensional curves for the representation of the three-dimensional shapes. This work extends the range of applications of the technology by means of a new design methodology based on the constructive geometry of solids that allows combining the hexagonal honeycomb cell into complex three-dimensional structures by means of boolean operations while maintaining an optimal utilization of the material within a continuous production process.

Keywords: Kirigami honeycombs, manufacturing, constructive solid geometry

1. Introduction

The term ”kirigami honeycomb” was introduced by Nojima and Saito in [1] where they use the cross section of the 3D shape to describe the panel and include cuts in the pattern to obtain its 3D structure. Then, they generalized the method ([2], and [3]) from the representation of 3d shapes by means of two curves in the cross section of the shape ([2]) and with a mapping to polar coordinates ([3]) to represent curved shapes in the direction perpendicular to the cross section. Recently, Caslish and Gershenfeld ([4]) designed a continuous folding machine to construct the Kirigami patterns obtained by the previous method. However, the use of the two curves in the cross section of the shape limits the representation of more complex shapes. In our proposal, the design method is generalized for more complex shapes based on 3 fundamental contributions: 1) the need to represent the shape by 2 curves in the cross section to represent any 3D shape is eliminated, 2) the ”honeycomb cores” are

embedded in the 3D shape by means of boolean operations on the 3D shape and 3) an optimal method of assigning folding lines, cutting and gluing areas was developed for the manufacturing of the panel. In the following the main approach is detailed.

2. Materials and Methods

In [3], Saito, Fujimoto, and Okabe tried to expand the number of shapes to represent by transforming the coordinates from the pattern to the polar system. In this way they could scale the width and height of the pattern in the direction perpendicular to the cut cross section of the shape. However they can only represent scaled versions of the 2 curves of the cross section. Saito, Peregrino and Nojima [2], said that it is impossible to fold non-convex unit cells from a single paper because the total angles surrounding a slit edge are over 360 degrees, so the slit with has a negative value and the paper will overlap at the slits. Similar to Caslish and Gershenfeld ([4]), to ensure that no sections of the folding pattern overlap, we first calculate the height values (max-min) $a'_{i,j}$, $b'_{i,j}$, $c'_{i,j}$, $d'_{i,j}$ based on the five faces of the unit cell. Then we calculate column-wise shifts w_i and v_i such that $a_{i,j} = a'_{i,j} + w_i$, $b_{i,j} = b'_{i,j} + w_i$,$c_{i,j} = c'_{i,j} + v_i$, and $d_{i,j} = d'_{i,j} + v_i$ determine a non-overlapping pattern. To guarantee no overlaps occur in the pattern, Caslish and Gershenfeld ([4]) set $v_0 = w_0 = 0$ and calculate recursively:

$$w_i = max(d'_{i1,j} - a_{i,j}) + w_{i1} \tag{1a}$$

$$v_i = max(b_{i,j} - c_{i,j}) + w_i \tag{1b}$$

Instead of using above equations, in our approach we use the following two-step algorithm to avoid overlap and minimize the amount of un-used materials in the final pattern. The algorithm 1 can work with any solid model and the pattern is

Algorithm 1 Two-step Algorithm to minimize the amount of un-used materials

```
1:  procedure createPattern(model, C, Dir)   ▷ The 3D model, cell size and direction
2:      bbox ← model.BoundBox
3:      nx ← bbox.XLength/C
4:      ny ← √3 * bbox.YLength/(3 * C)
5:      for i = 0 to nx do
6:          for j = 0 to ny do                                          ▷ First pass
7:              Compute min-max of 5 faces in Cell_j (a',b',c',d')
8:              Compute Cell_j.BoundBox
9:              Update Column_i.BoundBox with Cell_j.BoundBox
10:         for j = 0 to ny do                                          ▷ Second pass
11:             F_k ← Create 5 faces in Cell_j
12:             P_k ← model.common(F_k)                                 ▷ Boolean operation
13:             Pattern ← P_k.rotate(Dir)                               ▷ Update the pattern
14:     Optimize Pattern with Pattern.BoundBox, Glue, Mountain & Valley lines
```

automatically computed by the boolean and rotation operations in steps 12 and 13.

3. Preliminary Results

The proposed Algorithm 1 have been programmed in Python version 3.8.6 within FreeCAD Version 0.19.23578 and macOS High Sierra (10.13). Figure 1 shows and example of a honeycomb created with the Stanford Bunny[1] using 3 diferent directions (x, y, z). The dimensions of the model are 86.33mm x 66.71mm x 85.21mm and the size of the file is 25.3MB. The cell size used for the experiment was 10mm. The upper panels show the top view of the model and the lower part shows the isometric view of the created honeycomb model for each direction. Figure 2 shows the pattern generated for Z direction.

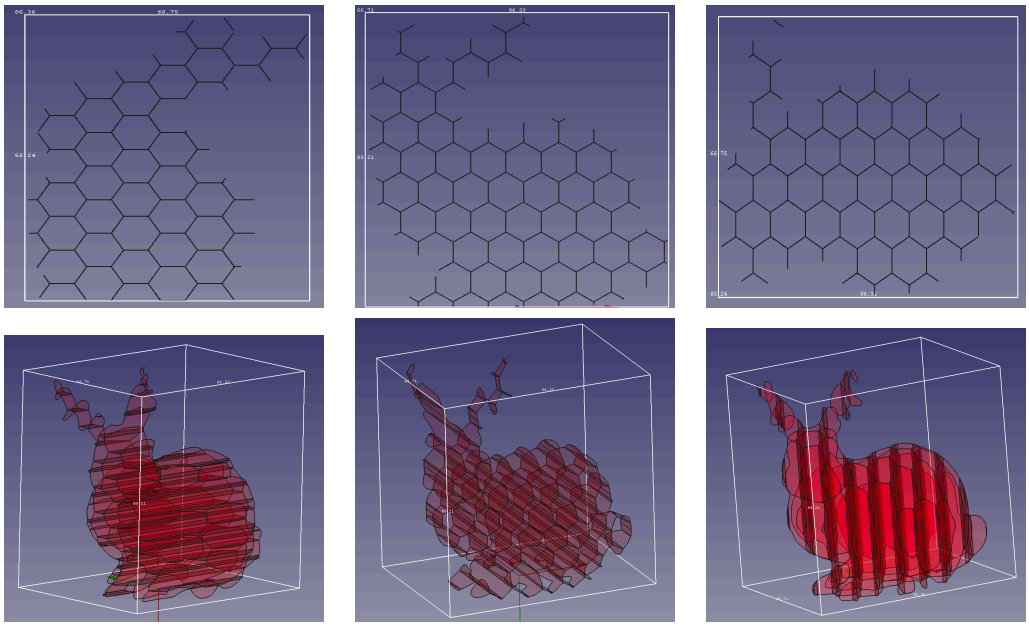

x y z

Figure 1: Example of Bunny in 3 directions.

4. Conclusions and Future works

Kirigami, a traditional Japanese paper-cutting art, has also proven its worth in origami engineering by cutting a portion of the paper to increase the degree of freedom in molding. Honeycomb has been recognized as an excellent structure since the times of Greece and Rome, but the method of mass production of honeycomb was developed in England during WWII with a touch of Japanese Tanabata decoration, sparking the birth of origami engineering. The degree of freedom of molding increased, and if a complex structure could be formed continuously, a strong structure was possible, but there was a problem. This work showed that any structure can

[1]the solid model is avalilable at https://grabcad.com/library/stanford-bunny-solid-model/files

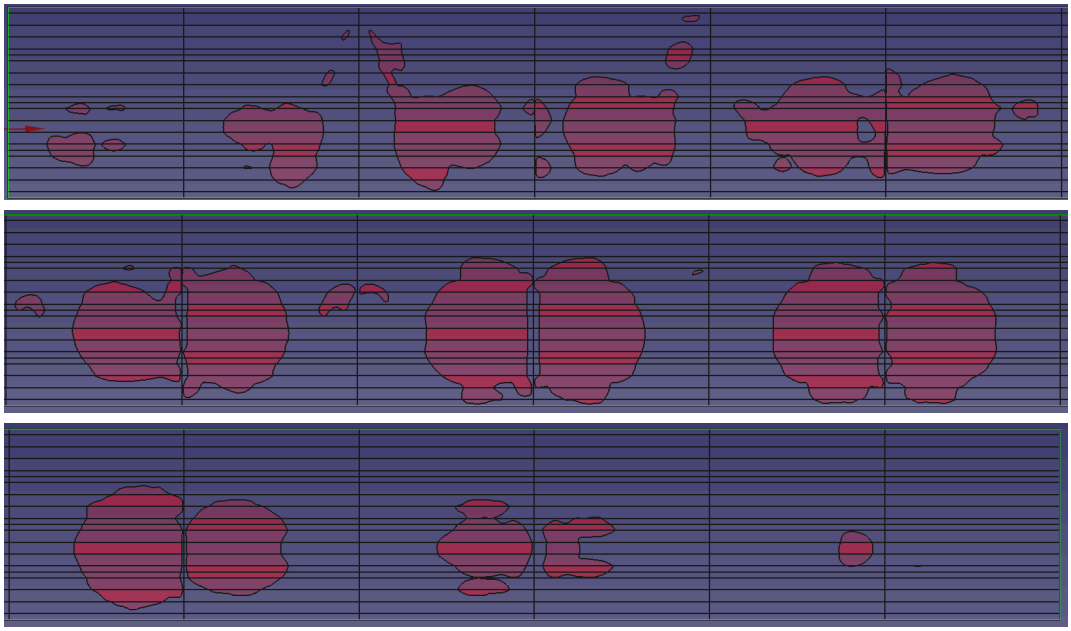

Figure 2: Example of pattern generated for Z direction.

be made in one piece, which can be called a meta-material thanks to the solution proposed in this paper. Currently, a continuous cutting, gluing and folding machine is under development for manufacturing the designed patterns.

References

[1] Nojima, T., and Saito, K. Development of Newly Designed Ultra-Light Core Structures, JSME Int. A 2006, 49(1), pp. 38–42. doi:10.1299/jsmea.49.38

[2] Saito, K., Pellegrino, S., and Nojima, T. Manufacture of Arbitrary Cross-Section Composite Honeycomb Cores Based on Origami Techniques. ASME. J. Mech. Des. May 2014; 136(5): 051011. doi:10.1115/1.4026824

[3] Saito, K, Fujimoto, A, and Okabe, Y. Design of a 3D Wing Honeycomb Core Based on Origami Techniques. Proc. of the ASME IDETC/IEC. Volume 5B: 40th Mechanisms and Robotics Conference. Charlotte, North Carolina, USA. August 21–24, 2016. V05BT07A026. ASME. doi:10.1115/DETC2016-60419

[4] Calisch, SE, and Gershenfeld, NA. Towards Continuous Production of Shaped Honeycombs. Proceedings of the ASME 2018 13th International Manufacturing Science and Engineering Conference. Volume 3: Manufacturing Equipment and Systems. College Station, Texas, USA. June 18–22, 2018. V003T02A007. ASME. doi:10.1115/MSEC2018-6646.

3D structural form creation of earwig fan using the algorithmic design tool

Kazuya Saito[1*], Chisaki Kitajima[2]

[1]Faculty of Design, Kyushu University
[2] Graduate School of Human-Environment Studies, Kyushu University
*k-saito@design.kyushu-u.ac.jp

Abstract. Earwigs can fold their wings most compactly among insects, therefore have the large potential for engineering applications. The previous study has clarified the method of designing the crease pattern of this earwig fan. Here we show the method to create new three-dimensional forms of the earwig fan by simulating their folding process with the algorithmic design tool. The result enabled to create a compact deployment structure with a frame and hinges, and to design dome shape structures based on earwig fan folding.

Keywords: Algorithmic design, Biomimetics, Folding Simulation, Origami

1. Introduction

Technology used to fold large structures into compact shapes are needed in a variety of products from daily use articles like umbrellas and folding fans to solar battery panels on satellites. In nature, various organisms have been tackling the same problem as represented by insect wing folding. These naturally developed structures are interesting research targets from the viewpoint of biomimetics. There is a wide variety of ways that insects store their wings, but the most compact and complex folding patterns can be founded in the hind wings of earwigs. The special folding process reduces surface area ten to 15 times or more depending on the species [1]. Authors revealed that the complex folding pattern of these earwig fans can be reconstructed by very simple geometric rules [2]. The proposed design software enables to customize the fan shape into various shapes [3]. However, to apply the earwig fan to the actual deployed structures, it is necessary to correctly design not only the crease pattern but also the shape and arrangement of the hinge and frame. In addition, the proposed design software could only output 2D crease patterns, and expansion to 3D structures such as domes or parabolic surfaces was a challenge.
Here we show the method to design earwig-fan based 3D deployable structures by using the algorithmic design tool. The proposed software can simulate the 3D shape in the folding process, enabling to design shapes and positions where the frame and hinges do not interfere, and to customize the pattern to the dome shapes.

2. Folding Simulation of Earwig Fan

We developed the design software using Rhino 7 (Robert McNeel & Associates) and Grasshopper [3]. A customized code was used to simulate the folding process of the input crease pattern. By placing the hinge parts on the simulated fold lines, it is possible to prevent the hinges from colliding during the folding process (Fig. 1).

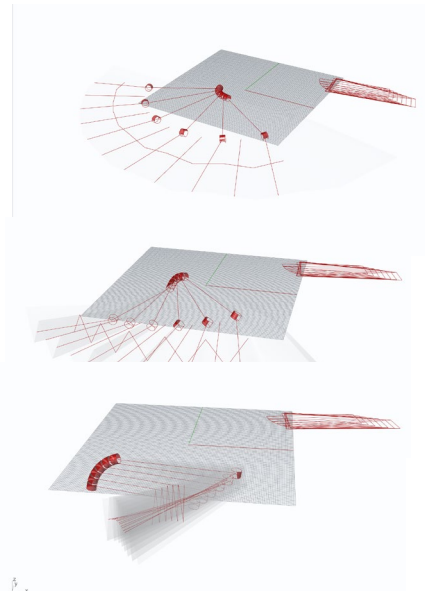

Fig. 1 Folding simulation of the earwig fan.

3. Earwig Fan Dome

By cutting out a part of the crease pattern and introducing vertices smaller than 360 degrees, it is possible to give a positive curvature to the earwig fan and make it a dome shape. Here, by cutting out so that the folding conditions are maintained, it is possible to construct the deployable dome structure. We improved the design software and made a code to design the shape of this earwig fan dome (Fig. 2). By using this software, it is possible to design a deployment dome with a specified diameter and height.

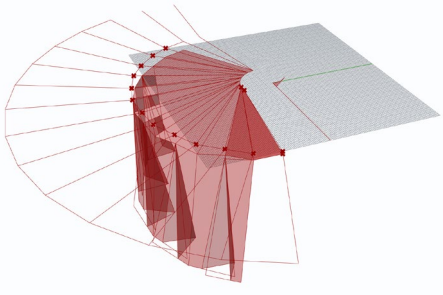

Fig. 2 Designing of Earwig fan dome.

4. Conclusion

We created a new three-dimensional form of the earwig fan by simulating the folding process of the earwig wing fan with the algorithmic design tool. The result enabled to create a compact deployment structure with a frame and hinges, and to design a dome shape based on earwig fan folding.

Acknowledgements

This work has been partially supported by JST FOREST (Grant Number JPMJFR203E4).

References

[1] K. Saito, et al.: Earwig fan designing: Biomimetic and evolutionary biology applications, *Proceedings of the National Academy of Sciences,* 117(2020), 17622-17626.

[2] K. Saito et al.: Earwig fan designing: biomimetic and evolutionary biology applications, *Open Science Framework*. https://osf.io/j9ufg/. Accessed 25 June 2020.dd

[3] R. McNeel, Grasshopper (2014). https://www.grasshopper3d.com/. Accessed 18 May 2020.

JSST 2021

Performance evaluation of wave-sound analysis code: ADVENTURE_Sound

Akihiro Kudo, Amane Takei[2]

[1]Department of Engineering for Innovation, Tomakomai Collage, Japan

[2]Faculty of Engineering, University of Miyazaki, Japan

[*]**kudo@tomakomai-ct.ac.jp**

Abstract. In this presentation, a performance evaluation of a wave-sound analysis code based on an iterative domain decomposition method is explained that is named ADVENTURE_Sound. A wave-equation for the wave-sound analyses is solved taking a speed potential as an unknown function. In this code, an iterative domain decomposition method is employed as a parallel technique. To solve subdomain problems by the direct method, the direct method based on the LDL^T decomposition method is introduced . In this paper, some numerical results are discussed in the view point of a performance for parallel computing environments.

Keywords: wave-sound analysis, Parallelized finite element method, Domain decomposition method, ADVENTURE_Sound.

1. Introduction

A wave-sound analysis based on a numerical analysis method, such as the finite element method, has become widespread due to recent improvements in computer performance and numerical calculation technology. In the case of accurately reproducing an analysis model of complicated shape, it is necessary to use many small the elements. In the case of analyzing the state of wave-sound propagation in a wide range, a wide analysis domain is examined. Furthermore, to perform a high-accuracy analysis, it is necessary to model the analysis domain with a sufficiently small element for the wavelength, and, in this case, the number of elements also increases. Increasing the number of elements increases the scale of the problem. Therefore, a method that can calculate large-scale problems has come to be demanded. Moreover, large-scale problems must be solved with high accuracy. In the presentation, a large-scale analysis code: ADVENTURE_Sound is introduced, and some numerical result in the performance evaluation for the parallel computing environment: Workstation Cluster is shown.

2. Governing equations and algorithm for parallel computing

In ADVENTURE_Sound, the wave-sound analysis is considered. To derive a weak form, the Galerkin method is applied to the Helmholtz equation [1]. The finite element approximation and discretized, the following equation is obtained:

$$\iiint_{\Omega_e} \nabla\Phi_h \cdot \nabla{\Phi_h}^* d\Omega_e - \frac{j\omega\rho}{Z_n} \iint_{\Gamma_e} \Phi_h {\Phi_h}^* d\Gamma_e - k^2 \iiint_{\Omega} \Phi_h {\Phi_h}^* d\Omega_e = 0. \quad (1)$$

where Φ is the speed potential that is the unknown function. k and ω are the wave

number and angular frequency, ρ is the medium density, and Z_n is the specific acoustic impedance.

The equation contains complex numbers and becomes a complex symmetric matrix. In the present study, the speed potential Φ is obtained using the conjugate orthogonal conjugate gradient (COCG) method. The finite element approximation (1) is rewritten as $Ku = f$ by the coefficient matrix K, the unknown vector u, and the right-hand side vector f. Next, Ω is divided into N subdomains (Eq. (2)). Eq. (3) and (4) are obtained from Eq. (2) [2].

$$\begin{bmatrix} K_{II}^{(1)} & 0 & 0 & K_{IB}^{(1)}R_B^{(1)\mathrm{T}} \\ 0 & \ddots & 0 & \vdots \\ & & K_{II}^{(N)} & K_{IB}^{(N)}R_B^{(N)\mathrm{T}} \\ 0 & 0 & & \\ R_B^{(1)}K_{IB}^{(1)\mathrm{T}} & \cdots & R_B^{(N)}K_{IB}^{(N)\mathrm{T}} & \sum_{i=1}^{\mathrm{N}} R_B^{(i)}K_{BB}^{(i)}R_B^{(i)\mathrm{T}} \end{bmatrix} \begin{bmatrix} u_I^{(1)} \\ \vdots \\ u_I^{(N)} \\ u_B \end{bmatrix} = \begin{bmatrix} f_I^{(1)} \\ \vdots \\ f_I^{(N)} \\ f_B \end{bmatrix} \tag{2}$$

$$K_{II}^{(i)}u_I^{(i)} = f_I^{(i)} - K_{IB}^{(i)}u_B^{(i)} \quad (i = 1, \ldots, N) \tag{3}$$

$$\left\{\sum_{i=1}^{\mathrm{N}} R_B^{(i)}\left\{K_{BB}^{(i)} - K_{IB}^{(i)\mathrm{T}}\left(K_{II}^{(i)}\right)^{-1}K_{IB}^{(i)}\right\}R_B^{(i)T}\right\}u_B = \sum_{i=1}^{\mathrm{N}} R_B^{(i)}\left\{f_B^{(i)} - K_{IB}^{(i)T}\left(K_{II}^{(i)}\right)^{-1}f_I^{(i)}\right\} \tag{4}$$

where ${f_B}^{(i)}$ is the right-hand vector for u_B, and $\left(K_{II}^{(i)}\right)^{-1}$ is the inverse matrix of $K_{II}^{(i)}$. Equation (4) is referred to as an interface problem and is an equation for satisfying the continuity between domains in the domain decomposition method. For simplicity, rewrite equation (5) as follows:

$$Su_B = g, \qquad S = \sum_{i=1}^{N} R_B^{(i)}S^{(i)}R_B^{(i)T}, \quad S^{(i)} = K_{BB}^{(i)} - K_{IB}^{(i)T}\left(K_{II}^{(i)}\right)^{-1}K_{IB}^{(i)}. \tag{5}$$

3. Numerical example

For examining ADVENTURE_Sound on a real-world problem, we model the environment of acoustic experiments. The computations are performed on a 16-node (62-core) PC cluster (Intel(R) Xeon(R) CPU E5-2650L; 1.80 GHz; L2 20480 KB) with 32 GB RAM per node. The simulation statistics and the numerical are shown in Table 1 and 2, respectively. More detail thins will be shown at the conference.

Table 1 Simulation Statistic

Frequency	442[Hz]
No. of Elements	911,133
No. of DOF	1,249,959
Platform	10-node workstation cluster with Intel(R) Xeon(R) CPU E5-2650L, 1.8 GHz
No. of cores per node	16
No. of nodes	8
Main memory per node	32 [GB/node]

Table 2 Numerical result

Elapsed time	509.153 [s]
Memory requirements	0.26 [GB/node]

References

[1] A. Takei, A. Kudo: Over 100 million degrees of freedom scale wave sound analysis based on parallel finite element method, JSST, 12:2 (2020), 76-84.

[2] A. Takei, S. Sugimoto, M. Ogino, S. Yoshimura, H. Kanayama: Full wave analyses of electromagnetic fields with an iterative domain decomposition method, *IEEE Trans. on Magn.*, 46:8 (2010), 2860-2863.

JSST 2021

Development of Huge-Scale Microwave analysis code: ADVENTURE_Fullwave

Amane Takei[1]

[1]Faculty of Engineering, University of Miyazaki, Japan

*takei@cc.miyazaki-u.ac.jp

Abstract. In this presentation, a huge-scale microwave analysis code based on an iterative domain decomposition method is explained that is named ADVENTURE_Fullwave. A stationary vector wave equation for the high-frequency electromagnetic field analyses is solved taking an electric field as an unknown function. Then, to solve subdomain problems by the direct method, the direct method based on the LDL^T decomposition method is introduced in subdomains. The simplified Berenger's PML is introduced which these eight corners are given the average value of all PML's layers.

Keywords: Microwave analysis, E method, Parallelized finite element method, Domain decomposition method, ADVENTURE_Fullwave.

1. Introduction

Electromagnetic field analysis based on a numerical analysis method, such as the finite element method, has become widespread [1] due to recent improvements in computer performance and numerical calculation technology. In the case of accurately reproducing an analysis model of complicated shape, it is necessary to use many small the elements. In the case of analyzing the state of electromagnetic waves propagation in a wide range, a wide analysis domain is examined. Furthermore, to perform a high-accuracy analysis, it is necessary to model the analysis domain with a sufficiently small element for the wavelength, and, in this case, the number of elements also increases. Increasing the number of elements increases the scale of the problem. Therefore, a method that can calculate large-scale problems has come to be demanded. Moreover, large-scale problems must be solved with high accuracy. In the presentation, a large-scale analysis code: ADVENTURE_Fullwave is introduced, and detail of the parallel algorism is shown.

2. Governing equations and algorithm for parallel computing

In ADVENTURE_Fullwave, the full-wave analysis based on an E method [1] is considered. $\mathbf{E}_\mathrm{h}$ and $\mathbf{J}_h$ are finite element approximations of electric field $\mathbf{E}$ [V/m] and current density $\mathbf{J}$ [A/m^2], respectively. The permeability is given by $\mu = \mu_0\mu_r$ [H/m], μ_0 is the vacuum permeability [H/m], and μ_r is the relative permeability. The complex permittivity is given by $\varepsilon = \varepsilon_0\varepsilon_r - \sigma/j\omega$ [F/m], ε_0 is the vacuum permittivity [F/m], ε_r is the relative permittivity, and ω is the angular frequency [rad/s]. The following equation is the finite element equation to be solved:

$$\iiint_\Omega (1/\mu)\mathrm{rot}\mathbf{E}_\mathrm{h} \cdot rot\mathbf{E}_\mathrm{h}{}^* dv - \omega^2 \iiint_\Omega \varepsilon\mathbf{E}_\mathrm{h} \cdot \mathbf{E}_\mathrm{h}{}^* dv = j\omega \iiint_\Omega \mathbf{J}_h \cdot \mathbf{E}_h{}^* dv. \quad (1)$$

The equation contains complex numbers and becomes a complex symmetric matrix. In the present study, the electric field **E**, which is unknown, is obtained using the conjugate orthogonal conjugate gradient (COCG) method. The finite element approximation (1) is rewritten as $Ku = f$ by the coefficient matrix K, the unknown vector u, and the right-hand side vector f. Next, Ω is divided into N subdomains (Eq. (2)). Eq. (3) and (4) are obtained from Eq. (2).

$$\begin{bmatrix} K_{II}^{(1)} & 0 & 0 & K_{IB}^{(1)}R_B^{(1)\mathrm{T}} \\ 0 & \ddots & 0 & \vdots \\ & & K_{II}^{(N)} & K_{IB}^{(N)}R_B^{(N)\mathrm{T}} \\ 0 & 0 & & \\ R_B^{(1)}K_{IB}^{(1)\mathrm{T}} & \cdots & R_B^{(N)}K_{IB}^{(N)\mathrm{T}} & \sum_{i=1}^{\mathrm{N}} R_B^{(i)}K_{BB}^{(i)}R_B^{(i)\mathrm{T}} \end{bmatrix} \begin{bmatrix} u_I^{(1)} \\ \vdots \\ u_I^{(N)} \\ u_B \end{bmatrix} = \begin{bmatrix} f_I^{(1)} \\ \vdots \\ f_I^{(N)} \\ f_B \end{bmatrix} \tag{2}$$

$$K_{II}^{(i)}u_I^{(i)} = f_I^{(i)} - K_{IB}^{(i)}u_B^{(i)} \quad (i = 1, \dots, N) \tag{3}$$

$$\left\{\sum_{i=1}^{\mathrm{N}} R_B^{(i)}\left\{K_{BB}^{(i)} - K_{IB}^{(i)\mathrm{T}}\left(K_{II}^{(i)}\right)^{-1}K_{IB}^{(i)}\right\}R_B^{(i)T}\right\}u_B = \sum_{i=1}^{\mathrm{N}} R_B^{(i)}\left\{f_B^{(i)} - K_{IB}^{(i)T}\left(K_{II}^{(i)}\right)^{-1}f_I^{(i)}\right\} \tag{4}$$

where ${f_B}^{(i)}$ is the right-hand vector for u_B, and $\left(K_{II}^{(i)}\right)^{-1}$ is the inverse matrix of $K_{II}^{(i)}$. Equation (4) is referred to as an interface problem and is an equation for satisfying the continuity between domains in the domain decomposition method. For simplicity, rewrite equation (5) as follows:

$$Su_B = g, \qquad S = \sum_{i=1}^{N} R_B^{(i)}S^{(i)}R_B^{(i)T}, \quad S^{(i)} = K_{BB}^{(i)} - K_{IB}^{(i)T}\left(K_{II}^{(i)}\right)^{-1}K_{IB}^{(i)}. \tag{5}$$

3. Numerical example

For examining ADVENTURE_Fullwave on a real-world problem, we model the environment of a commuter train, including 48 human bodies placed inside it. In such a commuter train, dielectrics, such as reflecting barriers, walls, handrails, etc. and human bodies exist. The electromagnetic field distribution may change with the differences of geometric arrangement between these materials. Therefore, when developing the numerical environmental model use for calculation, it is necessary to perform the modeling in such a way that the real environment may be reproduced correctly. The train plan is referred for the modeling of the train. The computations are performed on a 20-node (160-core) PC cluster (Intel(R) Core(TM) i7-9700K, 3.60 GHz) with 36 GB RAM per node. The simulation statistics are shown in Table 1.
More detail thins will be shown at the conference.

Table 1 Simulation Statistic

Analysis Frequency	1.0 GHz
No. of Elements	15,712,684
No. of DOF	15,599,463
Platform	20-node PC cluster with Intel Core i7-9700K 3.60 GHz
No. of cores	160
Main memory per node	32 GB
Elapsed Time [s]	1,998

References

[1] A. Takei, S. Sugimoto, M. Ogino, S. Yoshimura, H. Kanayama: Full wave analyses of electromagnetic fields with an iterative domain decomposition method, *IEEE Trans. on Magn.*, 46:8 (2010), 2860-2863.

Heat Transfer Analysis with Uncertainty Using Non-Statistical Uncertainty Quantification Method and Parallelized Heat Transfer Analysis Tool

Sota Goto[1*], Amane Takei[2], Shigeki Kaneko[1], Shinobu Yoshimura[1]

[1]Department of Systems Innovation, School of Engineering, The University of Tokyo
[2]Faculty of Engineering, University of Miyazaki
*goto-sota0926@g.ecc.u-tokyo.ac.jp

Abstract. Uncertainty Quantification (UQ) is a research field that has been used for the reliability design of devices and systems, and has been attracting interest in recent years. In this research, we utilized non-intrusive method, which is one of UQ methods that have very high computational efficiency and then integrated it with ADVENTURE_Thermal, a large-scale heat transfer analysis software. Also, using the integrated analysis method, we analyze the steady-state heat conduction equation in which heat conductivity is regarded as a random field, and the validity of the proposed method is shown by comparing its analysis results with those of Monte Carlo simulation.

Keywords: Uncertainty Quantification, Probabilistic Collocation, Non-Intrusive method, Karhunen-Loeve expansion, Polynomial Chaos expansion

1. Introduction

In numerical analysis, it is essential to analyze stochastically when the geometric structure, physical properties as represented by Young's modulus, and boundary conditions of the analysis objects. The field of evaluating uncertainties of input parameters in simulation is called Uncertainty Quantification (UQ). UQ is a field that has attracted more attention in recent years because it is used for reliability evaluation, optimization, and safety evalua-tion in the design of systems and devices.

One of the most common and widely used methods for uncertainty quantification is the Monte Carlo method [1]. Monte Carlo method evaluates probability distributions of output parameters by generating random numbers that follow a specific probability distribution of input parameters with uncertainty, and then calculating the response value for each random number. Monte Carlo method makes it possible to use a deterministic simulator as a black box, it is computationally expensive because the accuracy depends on the sampling size. Therefore, it may cause difficulties in large-scale analysis such as seismic wave analysis.

On the contrary, Spectral Stochastic Finite Element Method (SSFEM) [2], which is a

method for evaluating uncertainty without sampling, was devised by Ghanem and Spanos. In this method, the input and response probability fields are functionally expanded in probability space using two spectral expansions, and the probability distribution of the response value can be evaluated in a single matrix calculation. Although this method has high computational efficiency, it is not easy and takes much labor to construct a reliable simulator that can handle large-scale problems because it requires modifying the existing deterministic simulator.

In this study, we apply the uncertainty quantification method which has the advantages of both Monte Carlo method and SSFEM, that is reusability of deterministic codes and high computational efficiency, to the numerical solution of the steady-state and nonsteady-state heat conduction equation where the thermal conductivity is assumed as a stochastic field, and evaluate its effectiveness by comparing it with Monte Carlo method. We utilized ADVENTURE_Thermal code [3] as a large-scale heat transfer analysis software. Some numerical examples will be shown and discussed at the JSST2021 conference.

References

[1] Christopher Z Mooney, "Monte carlo simulation", No. 116. Sage, 1997.

[2] A.Lehikoinen, "Spectral Stochastic Finite Element Method for Electromagnetic Problems with Random Geometry", Electrical, Control and Communication Engineering, Vol. 6, pp.5-12, 2014

[3] "ADVENTURE Project Homepage:" https://adventure.sys.t.u-tokyo.ac.jp/ (accessed Jun. 24, 2021).

Photonic Crystal Frequency Demultiplexer Design for Electromagnetic Wave using FDTD and MEMD

Ran Dong[1,*], Daisuke Shigeta[1], Yoshihisa Fujita[2], Soichiro Ikuno[1]

[1]School of Computer Science, Tokyo University of Technology
[2]College of Information Science and Engineering, Ritsumeikan University

[*]randong@stf.teu.ac.jp

The full paper of this paper has been published in Journal of Advanced Simulation in Science and Engineering (JASSE).

DOI: https://doi.org/10.15748/jasse.9.65

JSST 2021

Numerical Investigation on Superconducting Linear Acceleration System: Shape Optimization of Current Distribution in Electromagnet

Teruou Takayama[1,*], Takazumi Yamaguchi[2], Ayumu Saitoh[1], Atsushi Kamitani[1]

[1]Graduate School of Science and Engineering, Yamagata University, Japan
[2]School of Physical Sciences, The Graduate University for Advanced Studies, SOKENDAI, Japan

[*]takayama@yz.yamagata-u.ac.jp

Abstract. The enhancement of the acceleration performance of a superconducting linear acceleration (SLA) system to inject the pellet container has been investigated numerically. To this end, a numerical code used in the FEM has been developed for analyzing the shielding current density in high-temperature superconducting films. In addition, the normalized Gaussian network (NGnet) method and the non-dominated sorting genetic algorithms-II has been implemented in the code for the shape optimization of an acceleration electromagnet. The results of the computations show that the speed of the pellet container for the current profile of the optimized coil is significantly faster than that for the homogeneous current distribution in the electromagnet. Moreover, it is found that the NGnet method is an effective tool for improving the acceleration performance of the SLA system.

Keywords: Finite element analysis, Genetic algorithm, Linear accelerator, Nuclear fuel, Thin film

1. Indroduction

Recently, a high-temperature superconducting (HTS) linear acceleration system has been proposed for injecting pellets into the plasma core. Hereinafter, this system is referred to as the superconducting linear acceleration (SLA) system. This system can electromagnetically accelerate containers with frozen hydrogen pellets by using an HTS film, such as a linear motor car. In the system, two types of films are used for acceleration and levitation. Although the estimated required speed of the SLA system to reach the plasma core is more than 5 km/s, it is not clear how much pellet speed can be obtained experimentally since the SLA system has not yet been applied to pellet injection.

In order to simulate an SLA system we have developed a numerical code for analyzing a shielding current density in an HTS film. In the present study, we try to implement the genetic algorithm (GA) to improve the acceleration performance of the SLA system. The

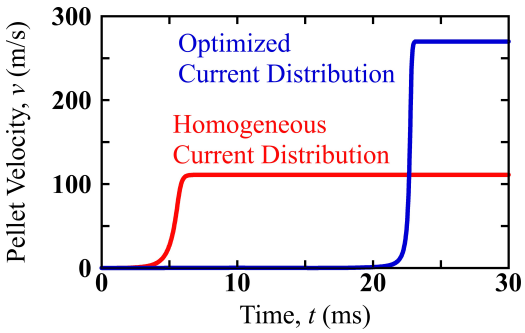

Figure 1: Time dependence of the pellet velocity v.

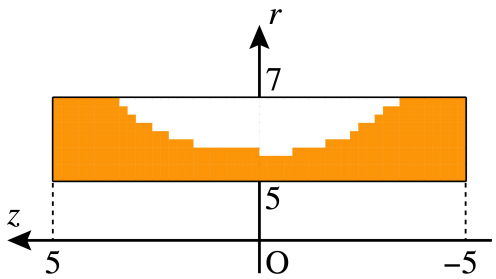

Figure 2: Current distribution in the electromagnet for the NGnet method. Here, the orange area indicates the on-state of the filament. The inner and outer radii of the electromagnet are 5 cm and 7 cm, and the length of the electromagnet is given by 10 cm.

GA has been used for the design optimization of electromagnetic devices because of the recent improvements in computing performance.

The purpose of the present study is to enhance the acceleration performance for the SLA system numerically. To this end, we implement the non-dominated sorting genetic algorithm II (NSGA-II) of the multi-objective optimization in the FEM code for analyzing the shielding current density in an HTS film. Moreover, we adopt the normalized Gaussian network (NGnet) method [1] for the shape optimization of the acceleration electromagnet.

2. Numerical Results

In this section, we optimize the current distribution of the acceleration electromagnet to increase the pellet speed on the basis of the NGnet method for the shape optimization of the electromagnet. In Fig. 1, we show the time dependence of the pellet velocity v. The figure shows that the pellet velocity estimated by the NGnet method is much higher than the value of v obtained by the homogeneous current distribution in the electromagnet.

In Fig. 2, we show the current distribution of the filaments for the NGnet method. We see from this figure that the electromagnet becomes a concave shape. Consequently, the NGnet method is an effective tool for improving the acceleration performance of the SLA system. This reason that the maximum value of the optimized current distribution using the NGnet method is larger than that for the conventional electromagnet.

In future works, to further investigate the validity of the optimal solution in the above results, we increase the number of the filaments and change the parameters of the NGnet method and the NSGA-II.

References

[1] J. Moody and C. J. Darken: Fast learning in networks of locally-tuned processing units. *Neural Comput.*, 1:2 (1989), 281–294.

JSST 2021

Three-Dimensional Analysis of Magnetic Shielding Current in High-Temperature Superconducting Tape

Takazumi Yamaguchi[1,*], Hiroaki Ohtani[1,2], Shinsuke Satake[1,2], Nagato Yanagi[1,2]

[1]School of Physical Sciences, The Graduate University for Advanced Studies, Japan
[2]National Institute for Fusion Science, Japan

[*]yamaguchi.takazumi@nifs.ac.jp

Abstract. The shielding current in the high-temperature superconducting (HTS) tape has been investigated by using the edge-based finite element method (FEM). The time evolution of the shielding current distribution can be determined by solving the Maxwell equation with the edge-based FEM. The numerical result shows that the shielding current concentratedly flows in the HTS layer.

Keywords: Edge-based finite element method, high-temperature superconductor, shielding current density.

1. Introduction

A high-temperature superconducting (HTS) tape [1] is used for developing a linear motorcar, an MRI, and a fusion reactor. In the HTS tape, an HTS layer is piled with a stabilizing layer on a material substrate. The material substrate is made of Hastelloy, and the stabilizing layer is made of Cu and/or Ag. When an electric current is applied to the HTS tape, it flows only in the HTS layer. However, in the place where the superconducting characteristics of the HTS tape are deteriorated locally, the electric current flows from the HTS layer into the stabilizing layer. Because the deterioration of the superconducting characteristics is caused by defects such as small holes and cracks, it is necessary to clarify the influence of the defects on the superconducting characteristics. The purpose of the present study is to three-dimensionally analyze the electromagnetic field in the HTS tape with considering the spatial distribution of the electric conductivity.

2. Numerical Simulation

In the present study, it is assumed that an HTS tape is composed of an HTS layer and a Cu stabilizing layer (see Fig. 1). For simplicity, a material substrate is not taken into consideration. This is because the interface between the material substrate and the stabilizing layer is insulated. In addition, an electromagnet in which an AC current $\boldsymbol{j}_0$ flows is placed above the

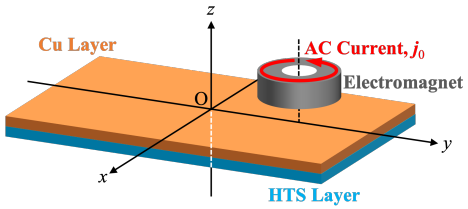

Figure 1: A schematic view of the numerical model.

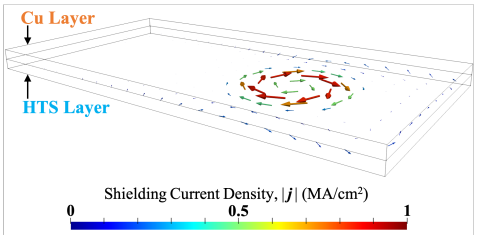

Figure 2: The typical distribution of the shielding current density (the tape size is 10 mm × 20 mm × 1 mm).

HTS tape. A shielding current density $\boldsymbol{j}$ is generated in the HTS tape by an applied magnetic flux density $\boldsymbol{B}_0$ generated by the electromagnet. The shielding current density $\boldsymbol{j}$ is governed by the following Maxwell equation:

$$\nabla \cdot \boldsymbol{B} = 0, \quad \nabla \times (\mu^{-1}\boldsymbol{B}) = \boldsymbol{j}, \quad \nabla \times \boldsymbol{E} = -\frac{\partial}{\partial t}(\boldsymbol{B} + \boldsymbol{B}_0), \quad \boldsymbol{j} = \sigma \boldsymbol{E}. \tag{1}$$

Here, $\boldsymbol{B}$ is a magnetic flux density generated by $\boldsymbol{j}$, and $\boldsymbol{E}$ is an electric field in the HTS tape. Furthermore, μ and σ are a magnetic permeability and an electric conductivity, respectively. Note that, in the HTS layer, σ is a non-linear function of $\boldsymbol{j}$. The value of σ is determined by using the critical-state model [2]. By using the A-method [3], Eq. (1) becomes equivalent to the following equation:

$$\nabla \times (\mu^{-1}\nabla \times \boldsymbol{A}) = -\sigma \frac{\partial}{\partial t}(\boldsymbol{A} + \boldsymbol{A}_0), \tag{2}$$

where $\boldsymbol{A}$ and $\boldsymbol{A}_0$ are a vector potential of $\boldsymbol{B}$ and that of $\boldsymbol{B}_0$, respectively. Equation (2) with the natural boundary condition is discretized by using the edge-based finite element method [3] to obtain the following equation:

$$\frac{d\boldsymbol{a}}{dt} = -\left\{ C^{-1}(K\boldsymbol{a}) + \frac{d\boldsymbol{a}_0}{dt} \right\}, \tag{3}$$

where K and C are finite element matrixes corresponding to μ and σ, respectively. In addition, $\boldsymbol{a}$ and $\boldsymbol{a}_0$ are vectors corresponding to $\boldsymbol{A}$ and $\boldsymbol{A}_0$, respectively. Both the spatial distribution and the time evolution of $\boldsymbol{j}$ can be determined by solving Eq. (3).

The typical distribution of the shielding current density in the HTS tape is shown in Fig. 2. The shielding current density concentratedly flows in the HTS layer. In the future work, an electromagnetic field in HTS tapes with defects will be investigated.

References

[1] Y. Shiohara *et al.*: *J. Japan Inst. Met. Mater.*, 80:7 (2016), 406–419.

[2] H. Ueda *et al.*: *J. Cryo. Super. Soc. Jpn.*, 48:9 (2013), 472–484.

[3] R. Albanese *et al.*: *Advances in Imaging and Electron Physics*, 102 (1997), 1–86.

JSST 2021

Some suitable settings for Haar-like four-point orthogonal transform

Kensuke Fujinoki[1,*] and Yuji Senda[1]

[1]Department of Mathematical Sciences, School of Science, Tokai University

[*]fujinoki@tokai-u.jp

Abstract.

In this paper, some settings for the Haar-like four-point orthogonal transform are considered. We show that two custom settings are available to realize the transform, which are a combination of taking the disjoint subsets and the design of an orthonormal matrix. Exploring suitable conditions for these settings, some numerical results for nonlinear approximation of images are presented.

Keywords: Linear orthogonal transform, Haar transform, Image processing, Nonlinear approximation

1. Introduction

In conventional wavelet analysis of a tensor product of Haar wavelets in two dimensions, a digital image is divided into 2×2 blocks and the four points of each block are decomposed into the average and the three differences [1]. As an alternative, we have presented a method of dividing an image into disjoint subsets of four points that are not 2×2 blocks and performing the same orthogonal transform as the Haar transform for each subset [2, 3].

Our previous study showed that there are several ways of taking disjoint subsets of an image, and that different combinations of the subsets result in performance differences in some image processing tasks [3]. We also showed how to design coefficients of an orthonormal matrix to be used in the transform. Assembling the orthonormal matrix involves some parameters, so we also investigated an optimal pair of parameters for nonlinear image approximation [2].

In this paper, we report our further study of the case where the two independent conditions for the Haar-like four-point orthogonal transform are combined, which are the selections of the disjoint subsets and the coefficients. We explore some suitable conditions for these settings through an application to nonlinear image approximation.

2. Haar-like transform

We begin with a brief introduction of the Haar-like four-point orthogonal transform. Let $A \in \mathbb{Z}^{2\times 2}$ and $m = |\det A|$. A scaling function and wavelets associated with a lattice $(\mathbb{Z}^2, A)$ satisfy the dilation equation and the wavelet equation, respectively:

$$\phi(x) = |\det A|^{1/2} \sum_{k\in\mathbb{Z}^2} h_k \phi(Ax - k),$$
$$\psi_\ell(x) = |\det A|^{1/2} \sum_{k\in\mathbb{Z}^2} g_{\ell,k} \phi(Ax - k), \quad \ell = 1, \ldots, m-1,$$

where $\{h_k\}_{k\in\mathbb{Z}^2}$ and $\{g_{\ell,k}\}_{k\in\mathbb{Z}^2, 1\le\ell\le m-1}$ are sequences for $\ell^2(\mathbb{Z}^2)$.

We consider $A = \begin{pmatrix} 2 & 0 \\ 0 & 2 \end{pmatrix}$, and $m = |\det A| = 4$. Let $\{x_k\}_{k\in\mathbb{Z}^2}$ be a signal. The Haar-like four-point orthogonal transform of the signal corresponds to a linear orthogonal transform with the sequences of the scaling function and wavelets, which is defined by

$$\begin{pmatrix} y_{2k+k_0} \\ y_{2k+k_1} \\ y_{2k+k_2} \\ y_{2k+k_3} \end{pmatrix} = M \begin{pmatrix} x_{2k+k_0} \\ x_{2k+k_1} \\ x_{2k+k_2} \\ x_{2k+k_3} \end{pmatrix},$$

where $\{k_\ell \in \mathbb{Z}^2\}_{0\le\ell\le m-1}$ is translation vectors and

$$M = \begin{pmatrix} h_0 & h_1 & h_2 & h_3 \\ g_{1,0} & g_{1,1} & g_{1,2} & g_{1,3} \\ g_{2,0} & g_{2,1} & g_{2,2} & g_{2,3} \\ g_{3,0} & g_{3,1} & g_{3,2} & g_{3,3} \end{pmatrix}. \tag{1}$$

The inverse transform is realized using M^*, which is the complex conjugate transpose of M because we assume that the matrix $M \in \mathbb{R}^{4\times 4}$ is an orthonormal matrix, i.e., $MM^* = M^*M = I_4$, where I_4 is the fourth-order identity matrix.

From these formulas, this transform yields the correlation of four points for each disjoint subset of an image $\{x_{2k+k_\ell}\}_{k\in\mathbb{Z}^2, 0\le\ell\le m-1}$ with an orthonormal matrix M. Thus, we have two options to design the transform. One is the combination of the four subsets $\{x_{2k+k_\ell}\}_{k\in\mathbb{Z}^2, 0\le\ell\le m-1}$ taken in the transform, and here we fix $k_0 = (0,0)^T$, $k_1 = (1,0)^T$ and select each translation vector from

$$k_2 \in \left\{ \begin{pmatrix} 0 \\ 1 \end{pmatrix}, \begin{pmatrix} 0 \\ -1 \end{pmatrix} \right\}, \quad k_3 \in \left\{ \begin{pmatrix} 1 \\ 1 \end{pmatrix}, \begin{pmatrix} -1 \\ 1 \end{pmatrix}, \begin{pmatrix} 1 \\ -1 \end{pmatrix}, \begin{pmatrix} -1 \\ -1 \end{pmatrix} \right\}. \tag{2}$$

The second option is the design of the orthonormal matrix M. There are many parameters to design the matrix (1), but according to the results of Rosca [4, 5], these parameters of 4×4 entries reduce to only two parameters α_1 and α_2 as

$$M = \begin{pmatrix} h_0 & h_1 & h_2 & h_3 \\ g_{1,0} & g_{1,1} & g_{1,2} & g_{1,3} \\ g_{2,0} & g_{2,1} & g_{2,2} & g_{2,3} \\ g_{3,0} & g_{3,1} & g_{3,2} & g_{3,3} \end{pmatrix} = \begin{pmatrix} \frac{1}{2} & \frac{1}{2} & \frac{1}{2} & \frac{1}{2} \\ \alpha_1 & \frac{1}{2} & \alpha_2 & -\left(\frac{1}{2} + \alpha_1 + \alpha_2\right) \\ \alpha_2 & \frac{1}{2} & -\left(\frac{1}{2} + \alpha_1 + \alpha_2\right) & \alpha_1 \\ -\left(\frac{1}{2} + \alpha_1 + \alpha_2\right) & \frac{1}{2} & \alpha_1 & \alpha_2 \end{pmatrix}, \tag{3}$$

where $\alpha_1 \in [-5/6, 1/2]$ and $\alpha_2 \in [-1/2, 5/6]$. Furthermore, thanks to the orthonormal conditions, we can derive α_2 from α_1, so we only need to fix one or the other to assemble an orthonormal matrix M for the transform [2].

3. Numerical results

We carried out numerical experiments to find suitable settings for the Haar-like four-point orthogonal transform. In these experiments, we applied the transform to some images and then reconstructed the transformed images from a few of the largest coefficients. At the same time, we changed the translation vectors and the coefficients defined by (2) and (3), respectively, in order to observe the behavior of the transform.

Figure 1 shows the results of the peak signal-to-noise ratio (PSNR) for Lenna. The percentages of the largest coefficients used for the reconstruction are $1[\%], 2[\%], 3[\%], 4[\%]$, and $5[\%]$. We observe that there is a periodic behavior in the relationship between α_1 and its PSNR value for all the cases. While this periodicity was also observed in our previous study [2], we see in Figure 1 that it is reversed when we set $k_3 = (-1, \cdot)^T$. Furthermore, we can expect better performance with $k_3 = (1, \cdot)^T$ rather than with $k_3 = (-1, \cdot)^T$. From these results, k_3 is the most important among the translation vectors, and $\{k_2 = (0, \pm 1)^T, k_3 = (1, 1)^T\}$ and $\{k_2 = (0, -1)^T, k_3 = (1, -1)^T\}$ are suitable combinations which provide relatively high performance. Similar results were confirmed for other types of images.

4. Conclusion

In this paper, we investigated some properties of the Haar-like four-point orthogonal transform. We considered two settings of the transform, which are the combination of translation vectors and the selection of coefficients, through an application to nonlinear image approximation. Although these settings are minor, experimental results showed that changing these settings has a considerable effect on the performance of reconstructing images.

References

[1] S. Mallat: A Wavelet Tour of Signal Processing, 3rd ed., *Academic Press*, 2008.

[2] K. Fujinoki: Nonlinear approximation of images with Haar-like four-point orthogonal transforms, *Proceedings of the 16th IEEE International Conference on Wavelet Analysis and Pattern Recognition (ICWAPR 2019)*, Kobe, Japan, 110–115 (2019).

[3] K. Fujinoki: Properties of Haar-like four-point orthogonal transforms for image processing, *in: S. Latifi (eds) 17th International Conference on Information Technology–New Generations (ITNG 2020), Advances in Intelligent Systems and Computing*, 1134, Springer, Cham, 233–239 (2020).

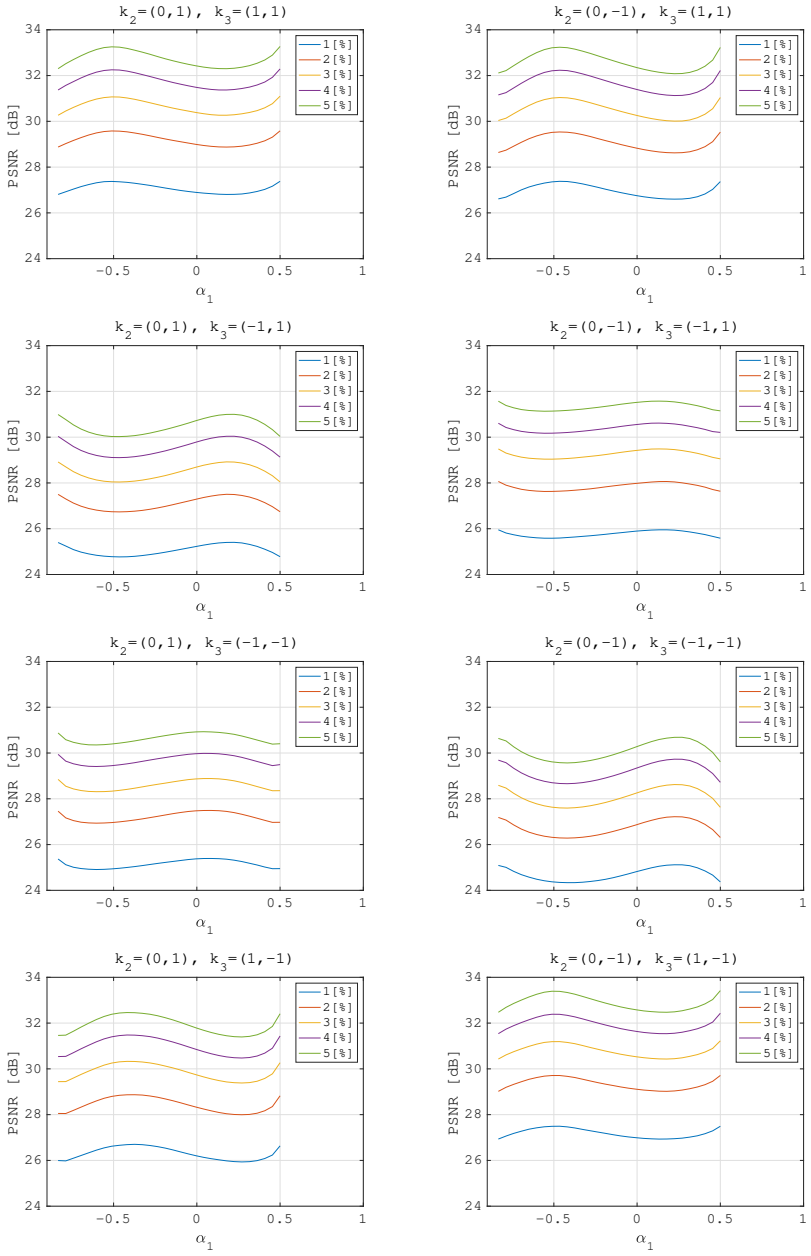

Figure 1: PSNR for Lenna with different choices of translation vectors k_2 and k_3, and parameter α_1. Left column: $k_2 = (0, 1)^T$. Right column: $k_2 = (0, -1)^T$.

[4] D. Rosca: Haar wavelets on spherical triangulations, *in: N. A. Dogson, M. S. Floater, M. A. Sabin (Eds.), Advances in Multiresolution for Geometric Modelling, Springer, Berlin*, 407–419 (2005).

[5] D. Rosca: Optimal Haar wavelets on spherical triangulations, *Pure Math. Appl.*, 15:4 (2006), 429–438.

JSST 2021

Estimation method for scale-shift relationship between two speech signals based on Fourier-Mellin transform

Akira Morimoto[1,*], Ryuichi Ashino[1], Takeshi Mandai[2]

[1]Mathematics and Informatics, Osaka Kyoiku University
[2]Center for Physics and Mathematics, Osaka Electro-Communication University

[*]morimoto@cc.osaka-kyoiku.ac.jp

Abstract. An algorithm, which estimates scale, gain, shift parameters among two speech signals with a scale-shift relationship, is proposed. Several experiments show the usefulness of the algorithm.

Keywords: Fourier-Mellin transform, scale-shift relationship, scale parameter, shift parameter

1. Introduction

The Mellin transform [1, 2] is well known as a scale invariant transform. The Fourier-Mellin transform has a scale-shift invariant property. It is widely applied in various fields, for example, mammalian hearing [3], rhythm description [4], gray-Level image description [5], etc. We [6] proposed an algorithm to decide whether two speech signals have a scale-shift relationship. In this talk, we present an algorithm which evaluates scale, gain, shift parameters for two speech signals with a scale-shift relationship.

2. The Fourier-Mellin transform

The Fourier transform of $f(t) \in L^1(\mathbb{R})$ is

$$\widehat{f}(\xi) = \mathcal{F}[f](\xi) = \int_{\mathbb{R}} f(t)\, e^{-i\xi t}\, dt.$$

The Fourier-Mellin transform of $f(t) \in L^1(\mathbb{R})$ is

$$\mathcal{FM}[f](p, \omega) = \int_{\mathbb{R}} \left|\widehat{f}(\xi)\right|^p\, |\xi|^\omega\, d\xi,$$

where $p \geq 1$ and $\omega > 0$.

For scale parameter $\alpha > 0$, gain parameter $\beta > 0$, and shift parameter $\gamma \in \mathbb{R}$, we define

$$f_{\alpha,\beta,\gamma}(t) = \beta f(\alpha t - \gamma).$$

The Fourier transform of $f_{\alpha,\beta,\gamma}$ is

$$\widehat{f_{\alpha,\beta,\gamma}}(\xi) = \frac{\beta}{\alpha} e^{-i\frac{\gamma}{\alpha}\xi} \widehat{f}\left(\frac{\xi}{\alpha}\right).$$

The Fourier-Mellin transform of $f_{\alpha,\beta,\gamma}$ is

$$\mathcal{FM}[f_{\alpha,\beta,\gamma}](p,\omega) = \alpha^{(\omega+1-p)} \beta^p \mathcal{FM}[f](p,\omega). \tag{1}$$

Taking the logarithm of (1), we have

$$\log\left(\mathcal{FM}[f_{\alpha,\beta,\gamma}](p,\omega)\right) - \log\left(\mathcal{FM}[f](p,\omega)\right) = (\omega + 1 - p)\log\alpha + p\log\beta. \tag{2}$$

3. Estimation algorithm for α, β, γ

For two speech signals $f(t)$ and $g(t)$, we would like to know whether two signals have a scale-shift relationship $g(t) = \beta f(\alpha t - \gamma)$. The following algorithm 1 checks the scale-shift relationship. If the relationship exists, the algorithm evaluates scale, gain and shift parameters.

Algorithm 1. *For two speech signals, we do the following steps.*

1. *Set $p = 4$. Calculate the Fourier-Mellin transforms of f and g.*
2. *Set*
$$R(p,\omega) = \log\left(\mathcal{FM}[g](p,\omega)\right) - \log\left(\mathcal{FM}[f](p,\omega)\right).$$
3. *Plot a graph of $R(p,\omega)$ against ω.*
4. *If the graph is a linear function of ω, then calculate α and β which satisfy the equation*
$$R(p,\omega) = (\omega + 1 - p)\log\alpha + p\log\beta$$
in the sense of the least squares, else two speech signals do not have a scale-shift relationship.
5. *Make $h(t) = \beta f(\alpha t)$.*
6. *Calculate a correlation between $h(t)$ and $g(t-s)$:*
$$C(s) = \frac{\int_{\mathbb{R}} h(t)\, g(t-s)\, dt}{\|h\|\,\|g\|},$$
where $\|g\|$ is the $L^2(\mathbb{R})$ norm of g.
7. *Set $Q = max_s |C(s)|$. If Q is large enough, then two speech signals have the relationship $g(t) = \beta f(\alpha t - \gamma)$, where $C(s)$ attains its maximum at $s = \gamma$, else two speech signals do not have a scale-shift relationship.*

We give numerical experiments as Figure 1. These experiments show the usefulness of the algorithm.

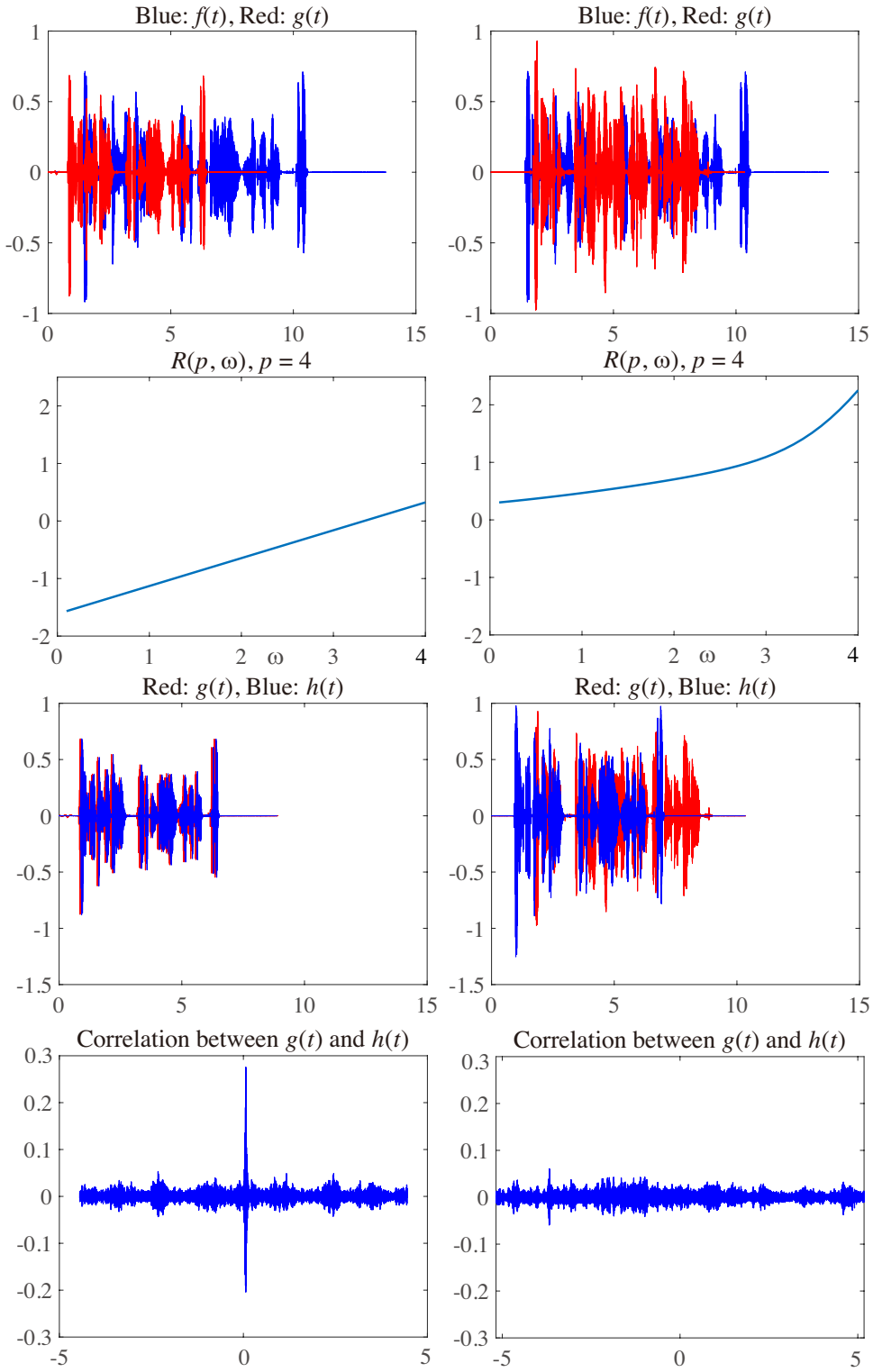

Figure 1: Numerical experiments. Left: two speech signals with scale-shift relationship. Right: two speech signals without scale-shift relationship. First row: $f(t)$ and $g(t)$. Second row: $R(p, \omega)$, $p = 4$. Third row: $g(t)$ and $h(t)$, Fourth row: Correlation between $g(t)$ and $h(t)$.

Acknowledgement

This work was partially supported by JSPS KAKENHI Grant Numbers 20K03653 and 21K03351. We use speech signals provided by NII-SRC: PASL-DSR [7] and AIJ-SMLE [8].

References

[1] R. Godement: Analysis III, "Analytic and Differential Functions, Manifolds and Riemann Surfaces", Springer, 2015.

[2] L. Cohen: The scale representation. *IEEE Transactions on Signal Processing*, 41(1993), 3275–3292, doi: 10.1109/78.258073.

[3] R. A. Altes: The Fourier-Mellin transform and mammalian hearing, *J Acoust Soc Am.*, 63(1978), 174–183, doi: 10.1121/1.381708.

[4] U. Marchand and G. Peeters: Scale and shift invariant time/frequency representation using auditory statistics: Application to rhythm description, *2016 IEEE 26th International Workshop on Machine Learning for Signal Processing (MLSP)*, (2016), 1–6, doi: 10.1109/MLSP.2016.7738904.

[5] S. Derrode and F. Ghorbel: Robust and Efficient Fourier-Mellin Transform Approximations for Gray-Level Image Reconstruction and Complete Invariant Description, *Computer Vision and Image Understanding*, 83(2001), 57–78, doi: 10.1006/cviu.2001.0922.

[6] A. Morimoto: An Estimation of a Scale Parameter Based on the Fourler- Mellin Transform, *Proceedings of the Tenth International Conference on Information*, (2021), 11–15.

[7] Speech Resources Consortium, National Institute of Informatics: PASL-DSR (dataset). https://doi.org/10.32130/src.PASL-DSR

[8] Architectural Institute of Japan: Sound Material in Living Environment (Gihodoshuppan, Chiyodaku, Tokyo, Japan, 2004).

JSST 2021

Some properties of fractional wavelet transform

Mawardi Bahri[1] and Ryuichi Ashino[2,*]

[1]Department of Mathematics, Hasanuddin University, Makassar 90245, Indonesia
[2]Mathematics and Informatics, Osaka Kyoiku University, Osaka 582-8582, Japan

*ashino@cc.osaka-kyoiku.ac.jp

Abstract. The fractional wavelet transform can be interpreted as a generalization of the classical wavelet transform in the the fractional frequency domain. The direct relation between the fractional Fourier transform and classical wavelet transform is presented. Some general properties of the fractional wavelet transform are presented.

Keywords: fractional wavelet transform, fractional Fourier transform, reproducing kernel

1. Introduction

It is known that the classical wavelet transform (WT) is a useful mathematical tool, which has been broadly implemented in quantum physics, signal processing and many other fields of science and engineering [1, 2, 3]. In recent years, a number of efforts have been increasing interest in generalizing the classical wavelet transform using the fractional Fourier transform (FRFT). As for recent applications of the fractional Fourier transform to speech enhancement, see [4]. In [5, 6, 7], the authors have studied an extension of the WT in the FRFT domain, the so-called the fractional wavelet transform (FRWT). The generalized transform is constructed by including the Fourier kernel with the FRFT kernel in the definition of the WT. They also have derived its essential properties like linearity, orthogonality relation, reconstruction formula and the inequalities.

In [8, 9], the author has derived some properties of the fractional Fourier transform utilizing the direct interaction between the classical Fourier transform and the fractional Fourier transform. Based on this idea, we can obtain some properties of the fractional wavelet transform using the basic relation between the fractional wavelet transform and the classical wavelet transform. This work is intended as a mathematical overview of general properties of the fractional wavelet transform such as the orthogonality relation and inversion formula and the other properties.

2. Continuous fractional wavelet transform (CFRWT)

We start by introducing the wavelet transform. Let the shifting parameter be $b \in \mathbb{R}$ and scaling parameter be $a \in \mathbb{R}_+$. We denote the shifting and scaling of the function f by

$\tau_b f(t) = f(t-b)$ and $f_a(t) = a^{-1/2} f(t/a)$, respectively. The family of wavelets are functions of the form:

$$\Psi_{a,b}(t) = \tau_b \Psi_a(t) = \frac{1}{\sqrt{a}} \Psi\left(\frac{t-b}{a}\right), \tag{1}$$

that are generated from the mother (basic) wavelets $\Psi \in L^2(\mathbb{R})$. This leads to the definition of the continuous wavelet transform of $f \in L^2(\mathbb{R})$ with respect to the mother wavelet Ψ as

$$\begin{aligned} T_\Psi f(a,b) &= \int_{\mathbb{R}} f(t) \overline{\Psi_{a,b}(t)}\, dt \\ &= \frac{1}{\sqrt{a}} \int_{\mathbb{R}} f(t) \overline{\Psi\left(\frac{t-b}{a}\right)} dt. \end{aligned} \tag{2}$$

Let us consider the family of fractional mother wavelets described by

$$\begin{aligned} \Psi_{a,b,\theta}(t) &= \frac{1}{\sqrt{a}} \Psi\left(\frac{t-b}{a}\right) e^{-\frac{i}{2}(t^2-b^2)\cot\theta} \\ &= \Psi_{a,b}(t) e^{-\frac{i}{2}(t^2-b^2)\cot\theta}. \end{aligned} \tag{3}$$

The most important property of family of fractional mother wavelets (3) is the admissibility condition as follows.

Definition 2..1. *We call a mother wavelet $\Psi \in L^2(\mathbb{R})$ associated with the FRFT is admissible if and only if the following admissibility condition is satisfied:*

$$C_{\Psi,\theta} = \int_{\mathbb{R}^+} \left| \mathcal{F}^\theta\{e^{-\frac{i}{2}(\cdot)^2 \cot\theta} \Psi\}(a\xi) \right|^2 \frac{da}{a} < \infty. \tag{4}$$

In this case, $C_{\Psi,\theta}$ is a real positive constant independent of ξ satisfying $|\xi| = 1$.

Lemma 1. *Suppose that*

$$C_\Psi = \int_{\mathbb{R}^+} |\mathcal{F}\{\Psi\}(a\xi)|^2 \frac{da}{a} < \infty. \tag{5}$$

is the admissibility condition for the conventional wavelet transform. The relationship between (4) *and* (5) *is described by*

$$C_\Psi = \sin\theta\, C_{\Psi,\theta}. \tag{6}$$

Note that the Fourier transform of (1) takes the form

$$\hat{\Psi}_{a,b}(\xi) = \sqrt{a}\, e^{-ib\xi} \mathcal{F}\{\Psi\}(a\xi). \tag{7}$$

The following Lemma 2 gives a relationship between (3) and its FRFT.

Lemma 2. *Let Ψ be a mother wavelet. Then, the family of the fractional mother wavelets* (3) *can be expressed in terms of the FRFT as*

$$\begin{aligned} \mathcal{F}^\theta\{\Psi_{a,b,\theta}\}(\xi) &= \hat{\Psi}^\theta_{a,b,\theta}(\xi) \\ &= \sqrt{a}\, e^{\frac{i}{2}(b^2+\xi^2)\cot\theta - ib\xi\csc\theta - \frac{i}{2}a^2\xi^2\cot\theta} \mathcal{F}^\theta\{e^{-\frac{i}{2}(\cdot)^2\cot\theta}\Psi\}(a\xi). \end{aligned} \tag{8}$$

Let us define the continuous fractional wavelet transform (CFRWT).

Definition 2..2 (CFRWT)**.** *The CFRWT of $f \in L^2(\mathbb{R})$ with respect to mother wavelet $\psi \in L^2(\mathbb{R})$ associated with the FRFT is defined by*

$$T^{\theta}_{\Psi} f(a,b) = \int_{\mathbb{R}} f(t)\overline{\psi_{a,b,\theta}(t)}\, dt = \frac{1}{\sqrt{a}} \int_{\mathbb{R}} f(t)\overline{\Psi\left(\frac{t-b}{a}\right)} e^{\frac{i}{2}(t^2-b^2)\cot\theta}\, dt. \tag{9}$$

The following lemma explains an interesting connection between the CFRWT and the CWT.

Lemma 3. *Let Ψ, $f \in L^2(\mathbb{R})$. Then,*

$$T^{\theta}_{\Psi} f(a,b) = e^{-\frac{i}{2}b^2\cot\theta} T_{\Psi}\tilde{f}(a,b), \tag{10}$$

where

$$\tilde{f}(t) = f(t)e^{\frac{i}{2}t^2\cot\theta}. \tag{11}$$

Lemma 4. *Let $\Psi \in L^2(\mathbb{R})$. Then, the CFRWT* (9) *has a fractional Fourier representation form*

$$T^{\theta}{}_{\Psi} f(a,b) = \sqrt{a} \int_{\mathbb{R}} e^{-\frac{i}{2}(b^2+\xi^2)\cot\theta + ib\xi\csc\theta + \frac{i}{2}a^2\xi^2\cot\theta} \overline{\mathcal{F}^{\theta}\{e^{-\frac{i}{2}(\cdot)^2\cot\theta}\Psi\}(a\xi)}\hat{f}^{\theta}(\xi)\, d\xi. \tag{12}$$

The inverse FRFT of $\hat{f}^{\theta} \in L^1(\mathbb{R})$ is defined by the integral

$$(\mathcal{F}^{\theta})^{-1}\{\hat{f}^{\theta}\}(t) = \int_{\mathbb{R}} \hat{f}^{\theta}(\xi)\overline{K^{\theta}(t,\xi)}\, d\xi, \tag{13}$$

where $\overline{K^{\theta}(t,\xi)}$ is the complex conjugate of $K^{\theta}(t,\xi)$. Then, we have

$$\mathcal{F}^{\theta}_{b}\{T^{\theta}_{\Psi} f(a,b)\}(\omega) = \frac{\sqrt{a}}{\overline{C^{\theta}}}\, e^{\frac{i}{2}a^2\omega^2\cot\theta} \overline{\mathcal{F}^{\theta}\{e^{-\frac{i}{2}(\cdot)^2\cot\theta}\Psi\}(a\omega)}\hat{f}^{\theta}(\omega). \tag{14}$$

The next results provide the fundamental properties of the CFRWT such as the inversion theorem and orthogonality relation. They are generalizations of corresponding properties of the WT.

Theorem 1. *Let $\Psi \in L^2(\mathbb{R})$ satisfy the admissibility condition defined by* (4)*. Then, for $f \in L^2(\mathbb{R})$, the following inversion formula holds:*

$$f(t) = \frac{1}{2\pi\sin\theta\, C_{\Psi,\theta}} \int_{\mathbb{R}^+}\int_{\mathbb{R}} \Psi_{a,b,\theta}(t)\, T^{\theta}_{\Psi} f(a,b)\, db\, \frac{da}{a^2}. \tag{15}$$

Theorem 2. *Assume that the basic wavelet $\varphi \in L^2(\mathbb{R})$ related to the FRFT satisfies the admissibility condition* (4)*. For f, $g \in L^2(\mathbb{R}) \cap L^1(\mathbb{R})$ we have*

$$\int_{\mathbb{R}^+}\int_{\mathbb{R}} T^{\theta}_{\Psi} f(a,b)\, \overline{T^{\theta}_{\Psi} g(a,b)}\, db\, \frac{da}{a^2} = 2\pi\sin\theta\, C_{\Psi,\theta}(f,g)_{L^2(\mathbb{R})}, \tag{16}$$

and

$$\int_{\mathbb{R}^+}\int_{\mathbb{R}} \left|T^{A}_{\Psi} f(a,b)\right|^2 db\, \frac{da}{a^2} = \int_{\mathbb{R}^+} \|T^{\theta}_{\Psi} f(a,b)\|^2_{L^2(\mathbb{R})}\, \frac{da}{a^2} = 2\pi\sin\theta\, C_{\Psi,\theta}\|f\|^2_{L^2(\mathbb{R})}. \tag{17}$$

The next result is reproducing kernel related to the FRWT, which is an extension of the reproducing kernel of the classical wavelet transform (see Mallat [2]).

Theorem 3 (Reproducing kernel)**.** *Let* Ψ *be an admissible wavelet. If*

$$K_\Psi(a,b,\theta;a',b',\theta') = \frac{1}{2\pi\sin\theta\, C_{\Psi,\theta}}(\Psi_{a,b,\theta},\psi_{a',b',\theta'})_{L^2(\mathbb{R})}, \tag{18}$$

then $K_\Psi(a,b,\theta;a',b',\theta')$ *is a reproducing kernel, i.e.,*

$$T^{\theta'}_\psi f(a',b') = \int_0^\infty \int_{-\infty}^\infty T^\theta_\psi f(a,b) K_\Psi(a,b,\theta;a',b',\theta')\, db\, \frac{da}{a^2}. \tag{19}$$

References

[1] K. Gröchenig, Foundation of Time-Frequency Analysis, Birkhäuser, Boston, MA, 2001.

[2] S. Mallat, A Wavelet Tour of Signal Processing, Academic Press, San Diego, CA, 2001.

[3] R. Ashino, S. Kataoka, T. Mandai and A. Morimoto, Blind image source separations by wavelet analysis, Appli. Anal., **91**(4), 617–644, 2012.

[4] P. Kunche, N. Manikanthababu, Fractional Fourier Transform Techniques for Speech Enhancement, Springer, 2020.

[5] J. Shi, N. Zhang, X. Liu, A novel fractional wavelet transform and its applications, Sci. China Inf. Sci, **55**(6), 1270–1279, 2012.

[6] A. Prasad, S. Manna, A. Mahato, and V. K. Singh, Generalized continuous wavelet transform associated with the fractional Fourier transform, J. Comput. Appli. Math., **259**, 660–671, 2014.

[7] A. Prasad and P. Kumar, The continuous fractional wavelet transform on generalized weighted Sobolev spaces, Asian-European Journal of Mathematics, **8**(3), 11 pages, 2015.

[8] Z. I. Zayed, On the relationship between the Fourier and fractional Fourier transforms, IEEE Signal Processing Letters, **3**(12), 310–311, 1996.

[9] Z. I. Zayed, A convolution and product theorem for the fractional Fourier transform, IEEE Signal Processing Letters, **5**(4), 101–103, 1998.

A Study on Tracking Individual Pedestrian Trajectories in a Walking Crowd Using Openpose

Minagi Miyokawa[1], Hideo Miyachi[2]

[1] Graduate School of Environmental And Information Studies, Tokyo City University

[2]Department of Informtion Systems, Tokyo City University

[1]g2183130@tcu.ac.jp

Abstract. In urban design, it is important to study the behavior of pedestrians. In the past, measurement of the amount of walking in the field was the mainstream for such research, but in recent years, analysis using image processing has been progressing. However, it is difficult to analyze video images directly due to restrictions on personal information protection. Therefore, we propose a two-step human behavior analysis method that extracts posture information of a person from a video image and then tracks the person. In this paper, we conducted a rudimentary experiment to verify the validity of the method.We acquired a video of three people walking crossways from the side, and obtained a reasonable plane trajectory. .

Keywords: Pedestrian Trajectory, Multi objects detection, Openpose, Pose Estimation

1. Introduction

Studying pedestrian behavior not only contributes to safe traffic, but also makes a significant contribution to urban design [1]. For example, when people walk through a shopping district, it is difficult to cross the flow of passing traffic to enter a store. To solve this problem, the area can be designed to slow down the flow of people in front of the store [2]. Usually, the design starts with knowing the current flow of people. To do so, a field survey is indispensable. For that field survey, image analysis of surveillance cameras installed in the city is effective, but due to privacy protection issues, we are not allowed to analyze the videos while visually checking them. However, it is allowed to analyze the video after primary image processing to make it non-personally identifiable. In this research, we are investigating the use of machine learning to track the trajectory of individual people by applying primary image processing, thereby overcoming the privacy protection issue. In this paper, as a first step, we tried to acquire skeletal information with a machine learning software called Openpose as a primary processing, and track the walking trajectory of an individual person from it.

2. Related works and the purpose of this study

Since the success of deep learning, there have been significant advances in object detection techniques and a lot of research has been done to track people. However, learning images of different people to identify them requires a huge amount of training data, and dynamic tracking

requires high-performance GPUs [3]. Benchmark tests have also been designed to compete for efficiency improvements in multiple person detection [4]. Research has also been conducted to improve detection accuracy and speed at limited shooting angles [5]. In this study, we propose a two-stage approach, where instead of directly tracking people using machine learning, we first detect people from videos with Openpose [6], which extracts skeletal information of people, and then use the skeletal information to track people. We believe that t8is approach solves the problem of personal information protection and separates the learning algorithm for extracting skeletal information from the tracking algorithm, thus enabling efficient analysis of human flows. Our goal is not to track a specific person (e.g., a criminal) completely, but to know the behavior of each person in order to understand the complex flow of people.

3. Experimental method

Three people crossing each other were video-recorded from the side. The experiment took place in a space of about 8m square in front of the elevator hall on the 7th floor of the Tokyo City University Building No. 3. Two pedestrians walked from the right side of the camera facing left and one from the left side facing right, crossing each other in the center. The walking paths were not set explicitly, but the starting positions were set to the front, middle, and back so that the walkers could reach the other side without any movement to avoid. A smartphone was used to capture 30 frames per second. Figure 1 shows an image taken at the beginning of the walk. The skeleton information detected by Openpose is superimposed on the image.

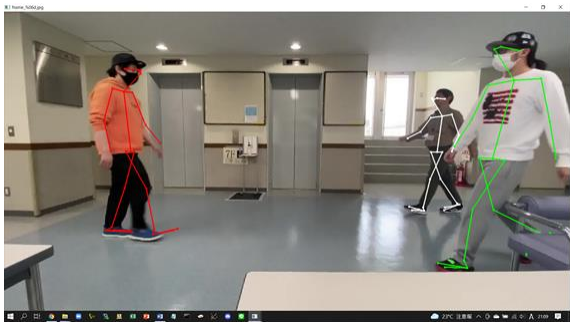

Fig.1 Snapshot of the experiment

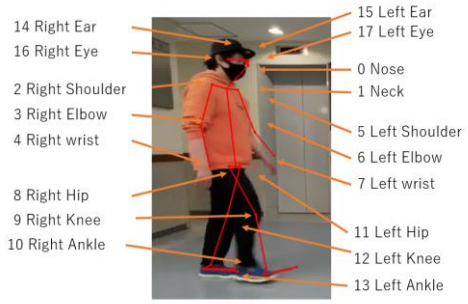

Fig.2 18 keypoints detected by Openpose

Openpose uses a non-parametric method called Part Affinity Fields (PAF) on 2D images to learn associations between individuals and body parts. This allows for fast and accurate estimation of human posture regardless of the number of people in the image. However, it can only estimate the posture of an individual person from a 2D image, and cannot estimate the position or track the person in 3D. Openpose detects 18 nodes such as head, neck, and left and right shoulders, elbows, wrists, knees, and ankles, as shown in Fig. 2, and outputs them as a file in JSON format.

In this case, we are examining the flow of human tracking, which does not require accuracy. Therefore, we used approximate numbers to calculate the conversion from 2D images to 3D coordinates. The camera was set at a height of about 1m, the number of pixels per frame was 2000x1000, and the angle of view was 60 degrees. Since a person moves up and down while walking, it is not possible to convert all the key points into 3D coordinates, but considering the walking style, the height of the ankle when the foot touches the ground can be set as Z coordinate = 0. In this study, the ground contact point was identified visually using the

knowledge of the gait pattern from the two-dimensional trajectory of the ankle. From one person's walking data, we calculated the 3D coordinates of three or four ground contact points, and approximated them with a cubic function, which we used as the walking trajectory.

In this experiment, occlusion occurs when people starting from the left and right intersect. However, the trajectories of the three people do not intersect in a complicated way. Therefore, we used the approximate linear prediction from the trajectory before the occlusion occurred (10 points) to predict the person belonging to the point where the occlusion was resolved and became detectable.

4. Experimental results

Figure 3 shows the time-series variation of the XY coordinate values in the 2D image of the keypoint "neck". The horizontal axis shows the X coordinate values and the vertical axis shows the Y coordinate values. Both are shown as the number of pixels with the lower left as the origin. From this, it can be seen that the top line has no occlusion it indicates front person, the next line is the center person, and the bottom line is the back person.

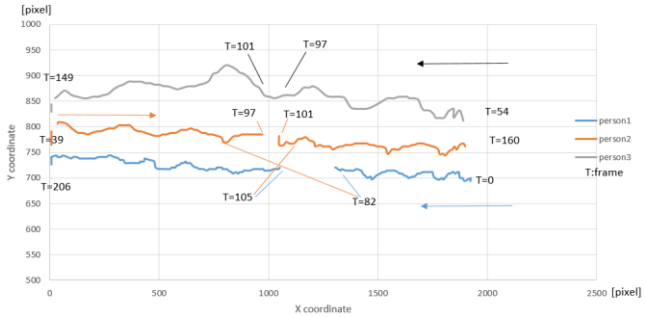

Fig.3 Movement of the detected neck position

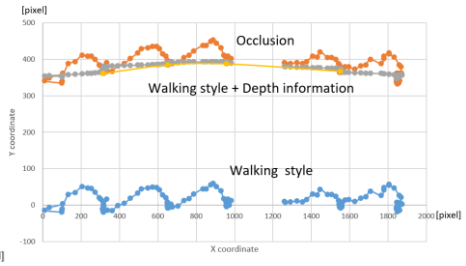

Fig.4 Extraction of depth information

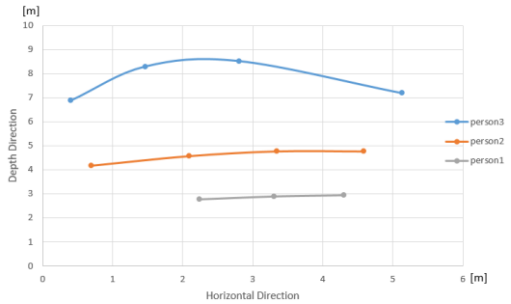

Fig.5 Walking trajectories of three people seen from above.

As an example of coordinate transformation, we show the coordinate transformation procedure for the farthest pedestrian. Figure 4 shows the XY coordinate values of the right heel. Five large waves are measured, which is considered to be one step. In general, the movement of the heel during walking is a rapid rise when stepping out, followed by a gradual fall, and finally a sliding contact with the ground. The heel then remains grounded while the opposite foot is stepped forward. Therefore, it can be seen that the person is walking from right to left, and the group of plots that are solid in Figure 4 shows the grounded state of the heel. Five of these ground points are extracted and approximated by a cubic function to show the change in depth direction. The change in the XY coordinate, which is obtained by subtracting this depth

variation from the Y coordinate value, indicates the walking style of the person.The results of calculating the walking trajectories of three people using the procedure described in the previous section are shown in Fig.5, with the XY axis in meters. In this case, it was a simple problem, so a simple linear prediction was enough to avoid mistaking the person before and after the occlusion. The trajectory shows that the person who walked at the far end changed his walking direction toward the front because he hit a wall due to the limitation of the space, and it was visually verified by video and confirmed to be a reasonable walking trajectory.

5. Conclusion

We proposed a two-step person tracking method that extracts skeletal information from walking videos using Openpose (machine learning), and then tracks people based on this information. As a result of a verification experiment of the proposed method, we were able to calculate a reasonable movement trajectory for each of the three persons. In the future, we plan to verify the effectiveness of the proposed method for complex walking situations, such as tracking of four or more people in a crowded situation.

References

[1] Takaaki Furukawa and Hideaki Takayanagi: A Pedestrian Flow Survey Using Proportional Distribution Origin-Destination Method, *Journal of Civil Engineering and Architecture* ,14(2020),537-546

[2] Takeuchi, M., Yoshida, T., and Kaneda, T.: A Transition Analysis of Shopping Street Complex from the Viewpoint of Shop-Around Behavior, *J. Archit. Plan. AIJ*, 76:660(2011),361-368

[3] Personal Information Protection Commission Secretariat: Report by the Personal Information Protection Commission Secretariat: Anonymously Processed Information, *Towards Balanced Promotion of Personal Data Utilization and Consumer Trust*, (2017)

[4] S.-H. Bae and K.-J. Yoon: Confidence-based data association and discriminative deep appearance learning for robust online multiobject tracking, *IEEE transactions on pattern analysis and machine intelligence*, 40:3(2018), 595–610

[5] K. Fang, Y. Xiang, and S. Savarese: Recurrent autoregressive networks for online multi-object tracking, *arXiv preprint arXiv:1711.02741*, (2017)

[6] Milan, A., Leal-Taixé, L., Reid, I., Roth, S., & Schindler, K.: MOT16: A Benchmark for Multi-Object Tracking, *ArXiv, abs/1603.00831*, (2016)

[7] R. Chandra, U. Bhattacharya, A. Bera and D. Manocha: DensePeds: Pedestrian Tracking in Dense Crowds Using Front-RVO and Sparse Features, *2019 IEEE/RSJ International Conference on Intelligent Robots and Systems*, (2019),468-475

[8] Z. Cao, G. Hidalgo, T. Simon, S. -E. Wei and Y. Sheikh: OpenPose: Realtime Multi-Person 2D Pose Estimation Using Part Affinity Fields, in *IEEE Transactions on Pattern Analysis and Machine Intelligence*, 43:1(2021),172-186

Transient Trajectories on Chaotic and Random Neural Network (CRNN)

Hitoaki YOSHIDA[1*], Takeshi MURAKAMI[2], Zhongda LIU[3], Satoshi KAWAMURA[4]

[1]Faculty of Education, Iwate University, Japan

[2]Technical Division, Iwate University, Japan

[3]Faculty of Science and Engineering, Ishinomaki Senshu University, Japan

[4]Super-Computing and Information Sciences Center, Iwate University, Japan

*hitoaki@iwate-u.ac.jp

Abstract. The information security of IoT devices and embedded systems have rapidly increased in importance. We have studied the pseudo-random-number series (PRNS) that are extracted from outputs of the chaotic and random neural network (CRNN). In particular, it had been applied to the Controller Area Network (CAN) bus in modern vehicles. The behavior of transient trajectories has been studied in detail by using *a junction diagram* and the security has been confirmed by *a secure interval* in this work.

Keywords: Random number, Neural network, Information security, Controller area network

1. Introduction

The information security of IoT devices and embedded systems have rapidly increased in importance year by year. We have studied the computer-generated pseudo-random-number series (PRNS) extracted from outputs of the chaotic and random neural network (CRNN) with fixed-point arithmetic (Q5.26) and the asymmetric piecewise-linear-function (APLF) as an activation function [1-4]. In particular, it had been applied to the Controller Area Network (CAN) bus in modern vehicles [5]. The aim of this study is how to prevent the prediction of the time series from CRNN outputs, and keep the security of systems. For this purpose, the behavior of transient trajectories has been studied in detail and the security of PRNS has been confirmed in this work.

2. Transient Trajectory

Result in precedent works [3,4] suggests that the time series generated from CRNN is random and non-deterministic, and the lower bits show better randomness for security applications. The closed trajectory from CRNN is periodic but isn't a limit cycle, therefore the closed trajectory is called a non-attractive periodic trajectory (NPT). Most trajectories started from an initial point move through a transient trajectory (TT) and eventually reach one of NPTs (Figure 1), where an arrow shows a direction of the time course. Mainstream is the longest TT within

an experimental result. *Transient time* is the time from an initial point to a fusion point (FP) that is the fused point of NPT and TT. *Branch Time* is the time from an initial point of a branch to a junction on a mainstream (JM). TTs appear as if they joined at JM, but TTs are independent trajectories, therefore JM is just a hypothetical point. NPT generally contains more than one FP that is always accompanied by transient trajectories (Figure 1).

The experimental condition is fixed as an external input $I = 0.000001$ and a perturbation $I_D = 0.119725$ in this work. The preliminary results are summarized as follows [3,4]: The points in NPT are not appropriate for security applications because NPT has a period that is about 9.5×10^8 on average. The number of points in the domain is $2^{64} \approx 1.8\times10^{19}$, and the total number of points in NPTs is just $\approx1.8\times10^{10}$, therefore the possibility of the point in NPT is only 10^{-7} %. On the other side, 42.7% of initial points join into the mainstream and finally join into the NPT through the FP, and 23.8% of initial points join into the NPT through other FPs.

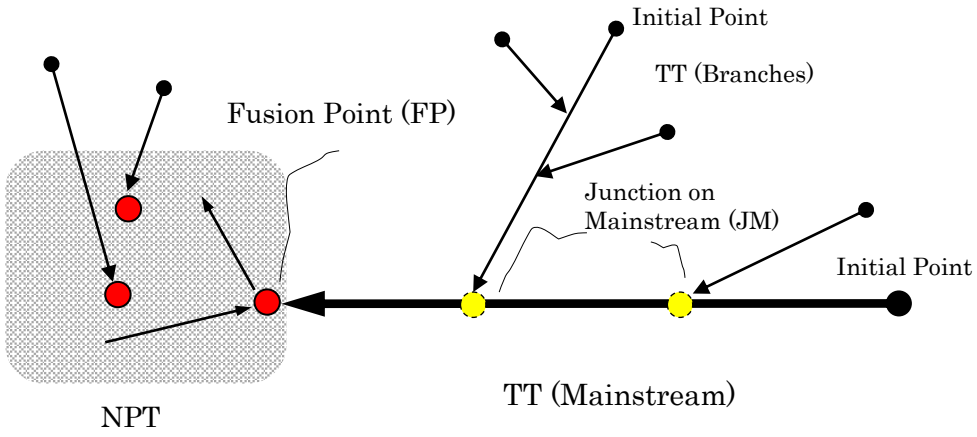

Figure 1: Non-Attractive Periodic Trajectory (NPT) and Transient Trajectory (TT).

3. Junction Diagram and Secure Interval

A junction diagram is useful to observe how to join branches of transient trajectories into the mainstream and to find JMs, graphically (Figure 2, 3). In the junction diagram, a length of a transient trajectory (t) and a length of a branch (b) is plotted as a point s (t, b), which represents an initial point. The abscissa of the graph is the transient time axis, and the ordinate represents the branch time. Here, ($t - b$) gives the coordinate of JM, and time started from an initial point of the mainstream to JM is called *junction time*. The points sharing the same JM form a line that typically draws a same-angle-line towards the abscissa ($\theta = \pi/3$ in Figure 2, and if the scale of abscissa and ordinate is the same then $\theta = \pi/4$). The line is called *a portion* because it is a part of TTs and sounds like pouring rain. The trajectories of all branches are too complicated to observe junctions, yet the diagram makes it simple owing to vanishing junctions between branches shown in Figure 1 except for JM. The distribution of portions and maximal length of portions are random, which will be discussed in detail in further study. The portion isn't a trajectory itself, it is just a point-set of initial points. As for the relatively larger portion, it seems to consist of many initial points. Let us think about ith portion ($S_i = \{s_1, s_2, \cdots, s_{max}\}$), and let the maximum length of a branch be $b_{\max}$, and let the number of initial points be n_i, the correlation analysis shows the positive correlation between $b_{\max}$ and n_i (R^2 =

0.829). Analysis of the diagram also shows the minimal interval of portions is 20978 (the average interval is 2.94×10^7), therefore any neighboring portions are independent of each other.

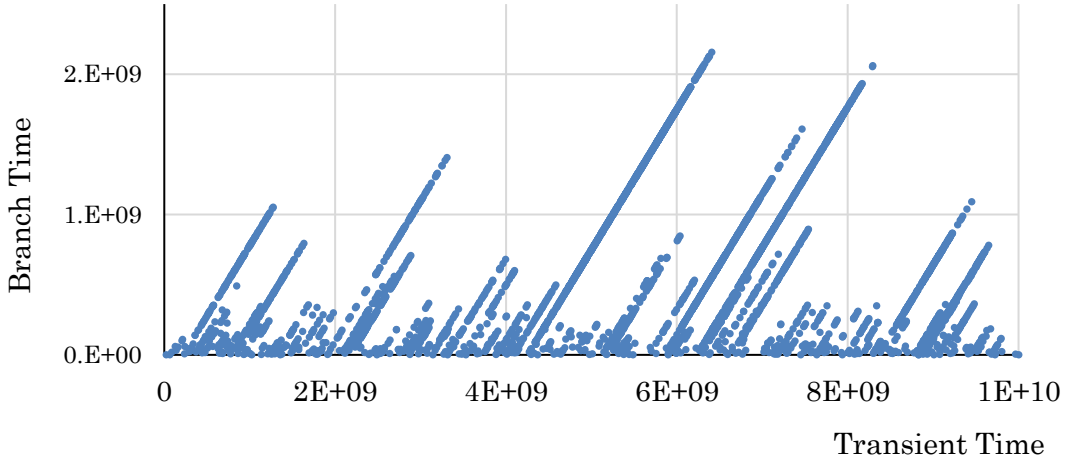

Figure 2: Junction Diagram (Consists of 4266 Initial Points).

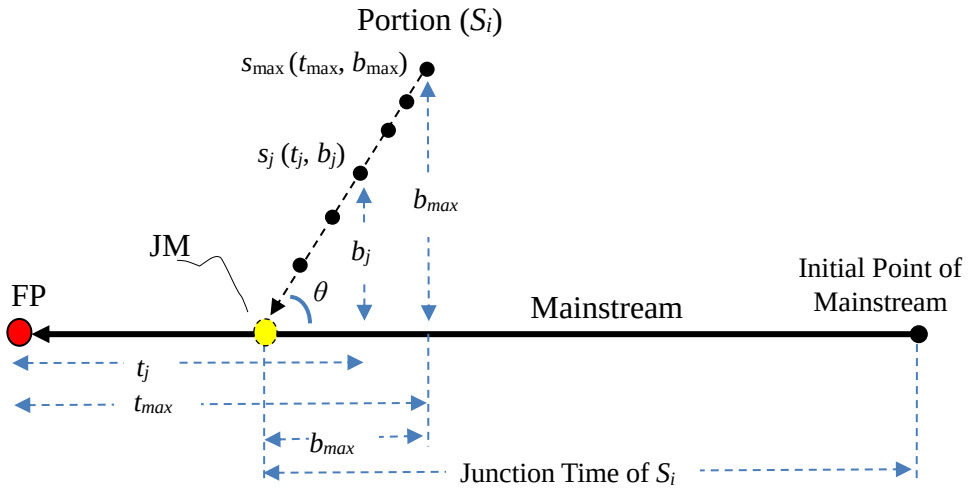

Figure 3: Schema of Junction Diagram.

Frequencies of JMs (equal to the number of initial points, s) are listed in Table 1 to estimate the secure interval that hardly has JM (Table 1). The result suggests that the minimum cardinality of NPTs (p_{min}) can be adopted as the secure interval; $p_{min} \approx 5.155852\times10^6$ (empirical value) [4]. The securer interval (p_{sec}) has been obtained as 5.74×10^5, in which interval there is no JM. If an initial value is reset at every p_{min}, fusion point formation is probably interrupted and consequently, TT may extend to $(2^{64}\times p_{min})^2 \approx 10^{51}$-$10^{52}$. If an initial value is reset at every securer interval (5.74×10^5) it will be securer and TT may extend to $(2^{64}\times p_{sec})^2 \approx 10^{50}$. Moreover, if another parameter (*e.g.* an external input or a perturbation) is slightly changed at the interval, NPTs will completely change and as a result, TT may extend furthermore.

Table 1: Frequency of Junction on Mainstream (JM) [a].

Interval of Branch Time	Interval of Junction Time			
	$0.00 – 5.16\times10^{6}$	$5.16\times10^{6} – 4.14\times10^{7}$	$4.14\times10^{7} – 5.47\times10^{8}$	$5.47\times10^{8} – 1.00\times10^{10}$
$0.00 – 5.74\times10^{5}$	0	0	0	0
$5.74\times10^{5} – 5.16\times10^{6}$	0	0	2 (0.0469%)	34 (0.797%)
$5.16\times10^{6} – 1.00\times10^{10}$	0	0	30 (0.703%)	4199 (98.5%)

a) The cardinality of the mainstream is $9.999433773\times10^{9} \approx 1.00\times10^{10}$ in this work.

4. Conclusion and Future Study

To prevent prediction of the time series the transient trajectory should be restarted with a new initial value within the secure interval that hardly has a junction on a mainstream (JM). The secure interval has been estimated the same as the minimum frequency of NPTs ($p_{\min}$) and the securer interval ($p_{\sec}$) has been estimated as 5.74×10^{5}. In the proposed method the length of the transient trajectory is expected to reach 10^{50}–10^{52}. The detailed result on the security of the PRNS will be discussed in the further publication.

Acknowledgments

Part of the experimental results in this research was obtained using supercomputing resources at Cyberscience Center, Tohoku University. This work was supported by KAKENHI Grant Numbers JP16K00180. Special thanks to the staff members of Iwate University Super-Computing and Information Sciences Center.

References

[1] H. Yoshida, Y. Akatsuka and T. Murakami: Implementation of High-Performance Pseudo-Random Number Generator by Chaos Neural Networks using Fix-Point Arithmetic with Perturbation, *Proceedings of Papers, NOLTA 2018*, 2018, pp46-49.

[2] H. Yoshida, H. Fukuchi and T. Murakami: Implementation of High-Speed Pseudo-Random-Number Generator with Chaotic and Random Neural Networks, *Proceedings of Papers, HICSS53 2020*, 2020, pp.6418-6425.

[3] H. Yoshida and T. Murakami: Non-Attractive Periodic Trajectory Formation Mechanism on Random and Chaotic Time Series, *Knowledge Innovation Through Intelligent Software Methodologies, Tools and Techniques*, H. Fujita et al. (Eds.), IOS Press, 327 (2020), pp.197-208.

[4] H. Yoshida and T. Murakami: Non-Attractive Periodic Trajectory Formation Mechanism on Random and Chaotic Time Series PART II, *Proceedings of Papers, NOLTA 2020*, 2020, pp.25-28.

[5] Zhongda Liu, Takeshi Murakami, Satoshi Kawamura, and Hitoaki Yoshida: Fast Stream Cipher based Chaos Neural Network for Data Security in CAN Bus, *Advances in Science, Technology and Engineering Systems Journal*, 5:5(2020), pp.63-68.

JSST 2021

Performance evaluation of collaboration networks by simulations of interacting discovery processes

Tetsuo Imai[1]

[1]Graduate School of Information Sciences, Hiroshima City University

*imai@hiroshima-cu.ac.jp

Abstract. In resent research and problem solving, there are many collaboration activities among expert researchers in multiple fields. Their individual collaborative activities form a network which shows the nature of collaboration among researchers, there have not been many efforts to measure the performance of collaboration networks, however. There is a mathematical model which represents knowledge discovery as an iterative process of extracting balls from urns and the model also represents information exchange with neighbors. The social network structure seems to strongly affects to the performance of the collaboration on it, actual amount of its affection is not clarified yet. In this article, I attempt to evaluate the performance of collaboration networks by simulating the model of discovery process with interaction. Specifically, I executed simulations on a nursing research coauthor network, which is a sample of the collaboration networks, to investigate how the efficiency of knowledge discovery is affected by the structure of the collaboration network.

Keywords: Discovery processes, Urn model with triggering, Coauthor network, Nursing research, Computer simulation

1. Introduction

Since academia has been divided into many special fields, in resent research and problem solving, there are many collaboration activities among expert researchers in multiple fields. By accumulating a large number of such collaborations among researchers, a network is constructed with researchers as nodes and collaboration relationships as edges, which is a structure that shows the nature of collaboration among researchers. A typical example of collaboration networks is the coauthor network. This is a network that considers the coauthor relationship in academic articles as a collaboration relationship, with the author as the node and the coauthor relationship as the edge. The characteristics of the structure of coauthor networks have been a research subject since early times in the field of network science and various analyses have been done so far, there have not been many efforts to measure the *goodness* or *badness* of coauthorship networks, however.

One of the methods to measure the *goodness* of collaboration networks is how well the collaboration in that network produces outcomes. Iacopini et al. mathematically modeled

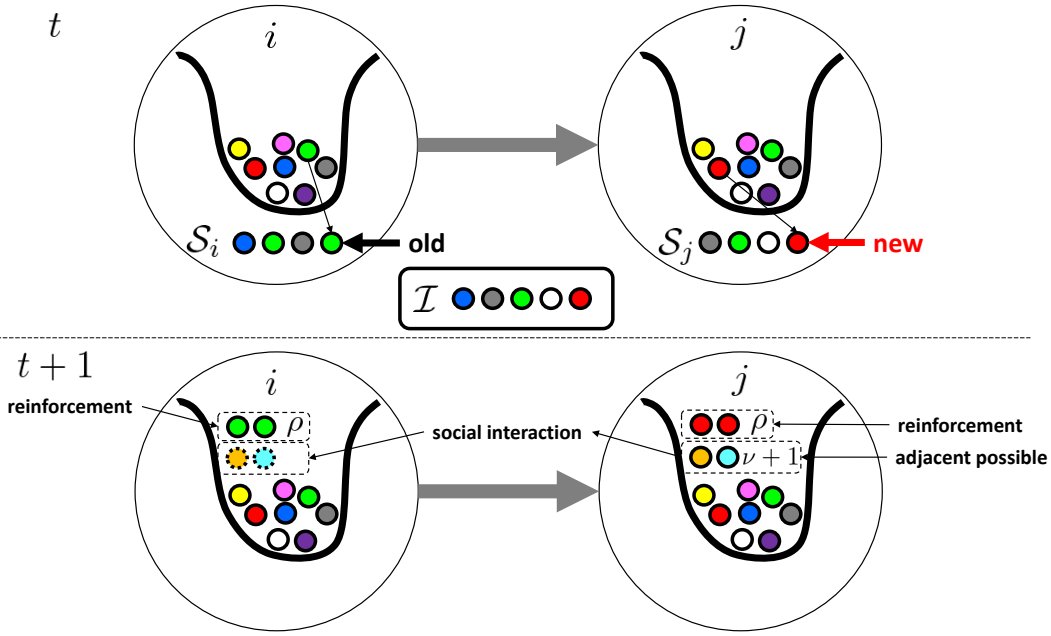

Figure 1: Behavior of socially interacting UMT in the case of a network with two nodes. Each node is equipped with an urn obeying the UMT with the parameters $\rho = 2$, $\nu = 1$. At the time t, node i, j extracts a ball (i:Green, j : Red) respectively, then ρ additional balls of the same colors are added to the its urns (*reinforcement*). In addition since for node j the color of drawn ball (Green) is a new one for it, $\nu+1$ balls of brand new colors are also added (discovery from the concept space of *adjacent possible*). At $t+1$, node i has access to all of its balls plus two extra ones which are discovered by its neighbor j (*social interaction*) without an addition to i's urn. $\mathcal{I}$ represents a sequence of *innovations*.

the knowledge discovery process in human intellectual activity [1]. In their work, they used a model of UMT(Urn Model with Triggering), which models intellectual search as an iterative process of extracting balls from urns. Furthermore they added to this model an element of interaction with neighbors in a human social network to represent the knowledge exchange activities that take place in the network. Moreover, they focused on the pace of individual discoveries (they called it as *novelty*) made by each individual(node) in the network, and clarified that it obeys the law called Heaps' law, and they investigated the actual value of the power-index of the law and the ralationships among it and several network centralities by mathematical analysis and computer simulations. On the other hand, in their work they did not specifically mention the amount of discoveries for the world (they called it as *innovation*) that whole individuals in the network generates.

In this arcidle, I investigated the amount of intellectual discoveries generated by the entire network by computer simulations based on their model, and how it differs depending on the network structure(topology). Specifically I investigated the pace of innovation of the coauthor network on nursing research which I and coauthors had previously constructed.

2. Model

In this section, I describe a model of the intelligent discovery process by Iacopini et al. [1] (Fig. 1) I call their model as socially interacting UMT.

Let us consider an unweighted directed graph. Each node of the graph represents an individual/agent, while a link (i, j) denotes the existence of a directed social relation from individual i to j (such that i can benefit from j). Each node i is equipped with an UMT that describes the discovery process of the individual i. A state of the urn i at time t is described as an ordered multiset $\mathcal{S}_i(t)$ which denotes the sequence of balls generated up to time t. At time t each individuals extract a ball from there own urns, then ρ balls of the same color are added to the urn (*reinforcement*). In addition if a color of the extracted ball is the first time for node i, $\nu_i + 1$ balls of brand new colors are added to the urn of node i (*adjacent possible*). Moreover, at each time t, the individual i draws a ball from an socially enriched urn, which is composed by its own urn plus the additional balls present at time t in the urns of its neighbors, without an addition(*social interaction*). By these procedures, new colors for everybody, which is called as *innovations*, increase at each time. In this article I investigate the pace of innovations and how it is affected by a structure of network.

3. Coauthor network of nursing research

I used a coauthor network on nursing research as a sample of collaboration networks. The coauthor network is constructed by assigning edges between nodes when there is a coauthor relationship between two authors. If there are multiple coauthored articles between the two authors, the number of assigned edges is as same number as articles, and if there are more than three authors in an article, edges are assigned between all related authors. The target articles are about nursing research, specifically, all original articles published from 1982 to 2018 in journals (including predecessor journals) published by the 44 member societies of the Japan Association of Nursing Academies (JANA) are included. The bibliography was obtained from the Ichushi database provided by the Japan Medical Abstracts Society (JAMAS). The total number of extracted articles is 9 700. There are 8 835 nodes and 96 556 directed edges in the constructed network.

4. Evaluation

To evaluate the performance of the nursing research network as a collaboration network, I simulate the socially interacting UMT on the network and measure the pace of innovations. To evaluate the performance of the nursing research coauthor network, the same simulations are executed on networks randomly generated by the configuration model and the pace of innovations are measured. Here the configuration model [3] is one of the network generation models, it can generate randomly reconnected networks while maintaining its degree dictribution of the specific network(the nursing research coauthor network in this article).

Figure 2 shows the basic result of the simulations. It is shown that the pace of innovations of the nursing research coauthor network is slightly faster than those of each

configurations model networks.

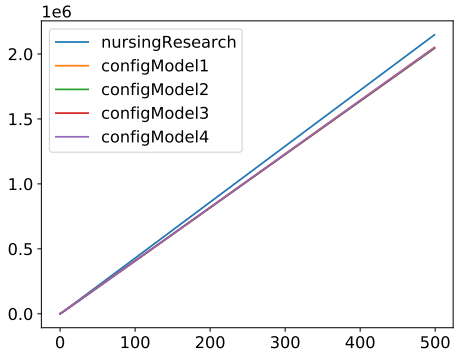

Nursing research	Config model 1	Config model 2	Config model 3	Config model 4
2147634.4	2050659.6	2042647.2	2046173.2	2048776.6

Figure 2: The basic results of the discovery process simulations by socially interacting UMT. A plot shows the pace of innovations in each network and a table shows the number of innovations at $t = 500$. All values are average of 5 trials. In the plot horizontal axis indicates time step and vertical axis indicates the number of innovations. Each line for configuration model networks are almost overlapping, because paces of those were almost equal. Simulations were continued up to $t = 500$ and parameters of the socially interacting UMT were $\rho = 6, \nu = 3$, respectively.

References

[1] Iacopini, Iacopo and Di Bona, Gabriele and Ubaldi, Enrico and Loreto, Vittorio and Latora, Vito, "Interacting Discovery Processes on Complex Networks", Physical Review Letters, Vol. 125, No. 24, 248301, 2020.

[2] Francesca Tria, Vittorio Loreto, Vito D. P. Servedio, Steven H. Strogatz, "The dynamics of correlated novelties," Scientific Reports, Vol. 4, 5890, 2014.

[3] Mark E. J. Newman, Steven. H. Strogatz, and Duncan J. Watts, "Random graphs with arbitrary degree distributions and their applications," Physical Review E, Vol. 64, No. 2, 026118, 2001.

[4] Tetsuo Imai and Takayasu Kawaguchi, "Clustering of nursing research journals based on co-occurrences in co-author relationships," Proceedings of the 38th JSST Annual International Conference on Simulation Technology (JSST2019), pp. 133–136, 2019.

[5] Tetsuo Imai and Takayasu Kawaguchi, "Analysis of a co-author network of nursing research," Abstract collection of the 2018 International Symposium on Nonlinear Theory and its Applications (NOLTA2018), A1L-B5, 2018.

JSST 2021

Analysis of information floating at an intersection considering traffic lights

Kazuyuki Miyakita[1,*], Naoyuki Karasawa[2], Hiroshi Tamura[3], Keisuke Nakano[4]

[1]Niigata University of International and Information Studies
[2]Kaishi Professional University
[3]Chuo University
[4]Niigata University

[*]miyakita@nuis.ac.jp

Abstract. In information floating (IF), mobile nodes transmit information to other nodes by direct wireless communication only in transmittable areas to prevent unnecessary information diffusion. In this paper, we theoretically analyze the mean IF lifetime considering the effect of traffic lights, which had not been considered in past IF researches to simplify the analysis. From the numerical and simulation results, we discuss how the traffic lights affect the IF performance.

Keywords: information floating, traffic lights, theoretical analysis

1. Introduction

Information floating (IF) is a type of epidemic communication in which direct transmissions to other mobile nodes is permitted only in a limited area (transmissible area: TA). It is a technology for keeping information in a specific area while preventing unnecessary information diffusion, and has been studied in recent years[1, 2, 3, 4].

In past IF researches, the performance of IF for various road models such as straight roads, crossroads, and lattice roads has been analyzed[1, 2, 3, 4]. In these analyses, the effects of traffic lights have not been considered for simplicity. In this paper, we analyze IF performance considering the effects of traffic lights. Specifically, we theoretically analyze the mean IF lifetime at an intersection with traffic lights. From the numerical and simulation results, we discuss how the traffic lights affect the IF performance.

2. Definitions and assumptions

We consider a crossroad network model as shown in Fig. 1. Nodes flow in from each of the W, E, N, and S directions according to a Poisson process with intensity λ. At the intersection, there are traffic lights for vehicles. Suppose that the green light and the red light are switched

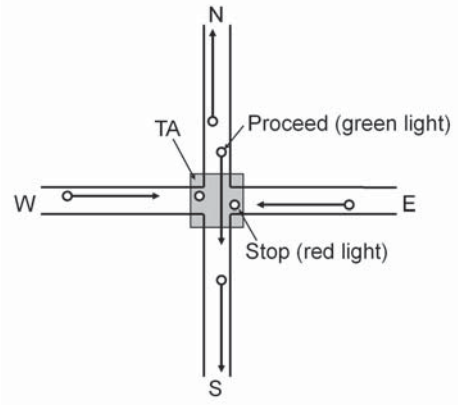

Figure 1: The model of an intersection.

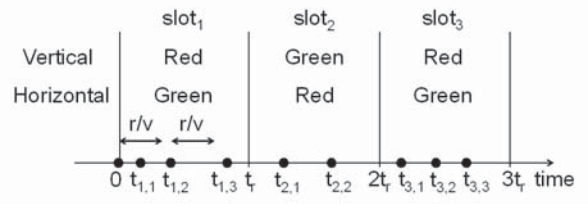

Figure 2: Time slots and arrival time at the intersection of each node.

alternately at time interval t_r in the horizontal and vertical directions. Nodes move at velocity v. If a node encounters a red light at the intersection, then the node stops at the intersection and starts moving after the traffic light turns green.

TA is set only at the intersection for simplifying the analysis. Communication range of a node is r. If a node having information is in the TA, the node transmits the information to other nodes within the communication range of the node. Note that the node receiving information does not have to be in the TA. We ignore the width of the road, the length of a vehicle, and the distance between stopped vehicles at the intersection because these are considered to be much smaller than r.

In the initial time, the first node having information arrives at the intersection from direction W, and the traffic light for the horizontal direction just turns green. IF continues while the nodes arriving at the intersection can deliver information to other nodes. If a node having information leaves the intersection without delivering the information to other node, the IF ends. Denote the time duration from the initial time to the end of IF by T_f. To evaluate the IF performance, we use $E(T_f)$, where $E(\cdot)$ means the mean of $\cdot$.

In the above model, the direction of a node after passing the intersection does not affect the IF performance obviously. Therefore, we do not consider the direction of a node after passing the intersection in this paper.

3. Analysis

In this section, we theoretically analyze $E(T_f)$. Because precisely analyzing $E(T_f)$ is difficult, we use an approximation. In the analysis, we consider time slots whose length is t_r as shown in Fig. 2 and consider in which time slot the IF ends. In Fig. 2, black points represent the times when nodes arrive at the intersection.

Here, we define the following symbols.

- $slot_i$: ith time slot. Namely, $slot_i$ corresponds to time interval $[(i-1)t_r, it_r)$.
- $t_{i,j}$: Time when the jth node arrives at the intersection after time $t = (i-1)t_r$.

- N_i: Set of nodes that arrive at the intersection at $t_{i,1}, t_{i,2}, \cdots, t_{i,k}$, where k is an integer that satisfies $t_{i,1} \leq \frac{r}{v}, t_{i,2} \leq t_{i,1} + \frac{r}{v}, t_{i,3} \leq t_{i,2} + \frac{r}{v}, \cdots, t_{i,k} \leq t_{i,k-1} + \frac{r}{v}, t_{i,k+1} > t_{i,k} + \frac{r}{v}$.
- A_i: Event where there is at least one node that stops at the intersection due to a red light in N_i.
- M: Random variable representing the number of A_is that continuously occur. Namely, if A_1, A_2, $\cdots$, A_i, and $\overline{A_{i+1}}$ occur, then $M = i$, where $\overline{A_{i+1}}$ means the complementary event of A_{i+1}.

If A_1 occurs, then the IF continues until the start of the next time slot $slot_2$ because at least one node having information stops at the intersection. Here, even if A_1 does not occur, the IF may continue until the start of the next time slot. Such a case occurs if the last node of N_i arrives at the intersection after time $t = t_r$. However, such a case rarely occurs especially for a large t_r. Therefore, we approximately assume that the IF continues until the start of $slot_2$ if and only if A_1 occurs. In the same manner, we approximately assume that the IF continues until the start of $slot_{i+1}$ if and only if $A_1, A_2, \cdots, A_i$ occur. Under this assumption, if $A_1, A_2, \cdots, A_i, \overline{A_{i+1}}$ occur, we have $it_r \leq T_f < (i+1)t_r$ because the IF will end in the middle of $slot_{i+1}$. Therefore, we have $E(M)t_r \leq E(T_f) < \{E(M)+1\}t_r$. Here, as a lower bound approximation, we approximately compute $E(T_f)$ by $E(M)t_r$.

$E(M)$ can be represented as

$$E(M) = \sum_{i=0}^{\infty} \Pr(A_1)\Pr(A_2)\cdots\Pr(A_i)\Pr(\overline{A_{i+1}})i, \tag{1}$$

where

$$\Pr(A_i) = \sum_{n=0}^{\infty} \Pr(|N_i| = n)\Pr(A_i||N_i| = n), \tag{2}$$

$$\Pr(|N_i| = n) = (1 - e^{-4\lambda r})^n e^{-4\lambda r}, \tag{3}$$

$$\Pr(A_i||N_i| = n) = 1 - \left(\frac{1}{2}\right)^n. \tag{4}$$

From these equations, we finally have

$$E(T_f) = \frac{e^{4\lambda r}-1}{2} t_r. \tag{5}$$

Note that this formula does not include the factor of v, which is contrary to intuition. This is because $E(T_f)$ depends only on how many times A_i occurs, and the probability that A_i occurs depends only on λ and r.

4. Results and discussions

Figure 3 shows the numerical and simulation results of $E(T_f)$. Parameters are as follows: $r = 100$ m, $v = 10$ m/s $= 36$ km/h, $\lambda = 0.01$ m^{-1} in (a), and $\lambda = 0.005$ m^{-1} in (b). The horizontal axis means t_r. From this figure, the numerical results agree well with the simulation results, which means that the analysis in the preceding section is valid. We can also see that $E(T_f)$ linearly increases with t_r.

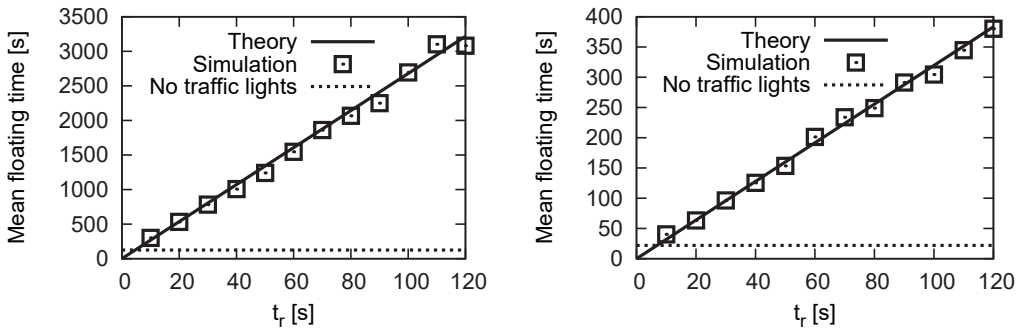

(a) $\lambda = 0.01$ m^{-1} (b) $\lambda = 0.005$ m^{-1}

Figure 3: Results of $E(T_f)$.

Figure 3 also includes the numerical results of $E(T_f)$ in the case where there are no traffic lights for comparison. $E(T_f)$ without traffic lights can be precisely computed by $E(T_f) = \frac{e^{4\lambda r}-1}{4\lambda v} - \frac{r}{v}$. This formula can be easily derived from the formula for a random clump[5].

Comparing the $E(T_f)$ values for these cases, we can confirm that $E(T_f)$ with traffic lights is significantly larger than that without traffic lights. For example, if $t_r = 120$ s, $E(T_f)$ with traffic lights is about 15 to 25 times that without traffic lights. However, when $\lambda = 0.005$ m^{-1}, $E(T_f)$ with traffic lights is only about 400 s even when $t_r = 120$ s. In order to further increase the $E(T_f)$, it is necessary to extend the TA outside the intersection.

Future works include the analyses of IF for extended TA and for more complicated road models, movement models, and communication models. This work is partially supported by JSPS KAKENHI Grant Number 19K04371.

References

[1] A. V. Castro, G. Di Marzo Serugendo, et al., "Hovering Information - Self-organising Information that Finds its Own Storage," *Technical Report, School of Computer Science and Information Systems, Birkbeck College, London, UK*, BBKCS-07-07 (2007).

[2] K. Nakano, "Epidemic Communication, Information Floating and Safety/Security," *IEICE Fundamentals Review*, vol. 10, no. 4, pp. 282–292, April 2017.

[3] K. Nakano, K. Miyakita, "Information Floating on a Road with Different Traffic Volumes Between Opposite Lanes," *Journal of Advanced Simulation in Science and Engineering*, vol. 3, no. 1, pp. 97–113, Aug. 2016.

[4] K. Miyakita, N. Karasawa, Y. Inagawa, K. Nakano, "A Consideration on Traffic Guidance by Information Floating," *IEICE Transactions on Communications (Japanese Edition)*, vol. J101-B, no.8, pp. 603–618, Aug. 2018.

[5] P. Hall, Introduction to the theory of coverage processes, John Wiley & Sons, 1988.

JSST 2021

Effects of human body shadowing and entering and leaving of mobile nodes on information floating in a one-dimensional street

Naoyuki Karasawa[1], Kazuyuki Miyakita[2], Hiroshi Tamura[3], Keisuke Nakano[4]

[1]Kaishi Professional University
[2]Niigata University of International and Information Studies
[3]Chuo University
[4]Niigata University

*karasawa.naoyuki@kaishi-pu.ac.jp, miyakita@nuis.ac.jp,
tamura@elect.chuo-u.ac.jp, nakano@ie.niigata-u.ac.jp

Abstract. In epidemic communication, mobile nodes such as vehicles and pedestrians spatially distribute and deliver information by direct wireless communication between themselves and their movement with information. Epidemic communication has a problem that information is disorderly spread. To overcome this problem, information floating, which permits mobile nodes to transmit information only in transmittable areas, has been proposed and discussed. In this paper, we evaluate performance of information floating by pedestrians walking toward opposite directions along a one-dimensional street considering effects of human body shadowing on communication range. In this performance evaluation, we suppose that pedestrians enter and leave the street while doing information floating, and show effects of such behavior of mobile nodes on performance of information floating.

Keywords: information floating, epidemic communication, human body shadowing, alley

1. Introduction

In epidemic communication, mobile nodes such as vehicles and pedestrians spatially distribute and deliver information by direct wireless communication between themselves and their movement with information. Epidemic communication has a problem that information is disorderly spread. To overcome this problem, information floating (IF), which permits mobile nodes to transmit information only in transmittable areas (TAs), has been proposed and discussed[1, 2, 3, 4, 5, 6, 7, 8]. We consider IF by pedestrians walking toward opposite directions along a one-dimensional street. We also consider the difference of densities of pedestrians between both directions. In such IF, information exchanges between two mobile nodes moving in same direction are required for continuing IF. In such situation, shadowing caused by the pedestrians' body occurs because pedestrians often hold or carry user

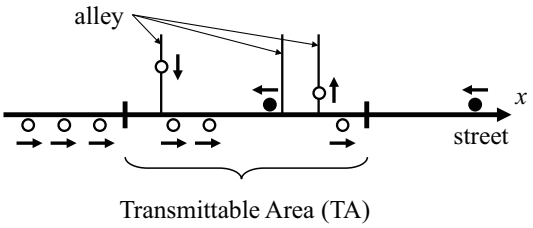

Figure 1: Network Model.

equipment in close proximity to the own body[9, 10]. Then, we need to assume that the communication range is different according to directions of two mobile nodes that information exchanges.

In [8], we evaluate effects of human body shadowing on IF in a street assuming that mobile nodes move along the street. In this paper, we consider the same problem in a more complicated mobility model because performance of IF is affected by the mobility characteristics of the mobile nodes. Here, we assume that pedestrians enter and leave the street while doing IF. We evaluate performance of IF under these assumptions to explore the both of the effect of human body shadowing and the effects of such behavior of mobile nodes.

2. Assumptions and Models

In this paper, we consider a network model in Fig. 1. The nodes entering from left side of TA and the nodes entering from right side of TA are distributed based on a Poisson process with intensities λ_w and λ_b, respectively. Each node moves on a street at constant velocity v. We consider the following two models. In Model 1, nodes do not enter and leave the street at any point in TA. In Model 2, nodes can enter and leave the street at some point in TA. Here, the points at which nodes enter and leave the street are randomly distributed for simplicity. Let X be the distance from the point that a node enters TA from alley to the point that the node enters another alley in Model 2. Assume that X obeys an exponential distribution of mean x_m. In order to compare Models 1 and 2 under the same node density, we assume the following for node arrival in Model 2. In Model 2, nodes enter the service area randomly with intensity $\frac{(\lambda_w+\lambda_b)v}{x_m}$. Each node that enters the service area moves to the right with probability $\frac{\lambda_w}{\lambda_w+\lambda_b}$ and moves to the left with probability $\frac{\lambda_b}{\lambda_w+\lambda_b}$.

In both of Model 1 and Model 2, the communication range of a node is r. A node having information in TA can transmit information to other node if the distance between these nodes is not longer than r. In this paper, we consider human body shadowing. We assume that the value of r is different according to the directions of sender and receiver. If the sender and receiver face each other, $r = r_a$. If the sender and receiver move toward the same direction, $r = r_b$. Due to the effect of human body shadowing, we assume that $r_a \geq r_b$.

3. Simulation results and discussions

In this paper, we evaluate mean lifetime of IF, denoted by $E(T_f)$, by computer simulations. In the computer simulations, $\lambda_w = 0.03\text{m}^{-1}$, the length of TA is 500m, $v = 1$m/sec, $x_m =$ 2000, 1000, 500, 250m. $r_a = 100$m, and $r_b = 100$m, 50m, 25m. Note that the parameter $r_b = 100$m means the case without human body shadowing, and the parameters $r_b = 50$m and $r_b = 25$m mean the case with human body shadowing.

The simulation results of Model 1 and Model 2 are shown in Fig.2. The horizontal axis represents λ_b, and the vertical axis represents $E(T_f)$. From these results, if there is no human body shadowing (i.e., $r_b = 100$m), $E(T_f)$ in Model 2 is larger than that in Model 1. On the other hand, if the effect of human body shadowing is large (i.e., $r_b = 25$m), $E(T_f)$ in Model 2 is smaller than that in Model 1. We consider the reason of these results as follows. The effect of nodes entering and leaving the street has both advantage and disadvantage in terms of continuation of IF. The advantage is that the topology of nodes can be rapidly changed, which may contribute to delivering information to nodes that do not have information. The disadvantage is that nodes having information may suddenly disappeared, which causes a smaller $E(T_f)$. We consider that the advantage outweighs the disadvantage in the case of no human body shadowing, and that the disadvantage outweighs the advantage in the case where the effect of human body shadowing is large.

This work was partially supported by JSPS KAKENHI Grant Number 19K04371.

References

[1] K. Nakano, "Epidemic Communication, Information Floating and Safety/Security," *IEICE Fundamentals Review,* vol. 10, no. 4, pp.282–292, April 2017. (in Japanese)

[2] A. V. Castro, et al., "Hovering Information - Self-Organising Information that Finds its Own Storage," *BBKCS-07-07, Technical Report, School of Computer Science and Information Systems,* Birkbeck College, London, UK, Nov. 2007.

[3] B. Liu, et al., "Analysis of the information storage capability of VANET for highway and city traffic," *Transportation Research Part C: Emerging Technologies,* vol.23, pp.68–84, 2012.

[4] J. Virtamo, et al., "Criticality condition for information floating with random walk of nodes," *Performance Evaluation,* Volume 70, Issue 2, pp.114–123, Feb. 2013.

[5] K. Nakano, K. Miyakita, "Information floating on a road with different traffic volumes between opposite lanes," *Journal of Advanced Simulation in Science and Engineering,* vol.3, no.1, pp.97–113, Aug. 2016.

[6] K. Nakano, K. Miyakita, "Analysis of information floating with a fixed source of information considering behavior changes of mobile nodes," *IEICE Trans. Fundamentals,* vol.E99-A, no.8, pp.1529–1538, Aug. 2016.

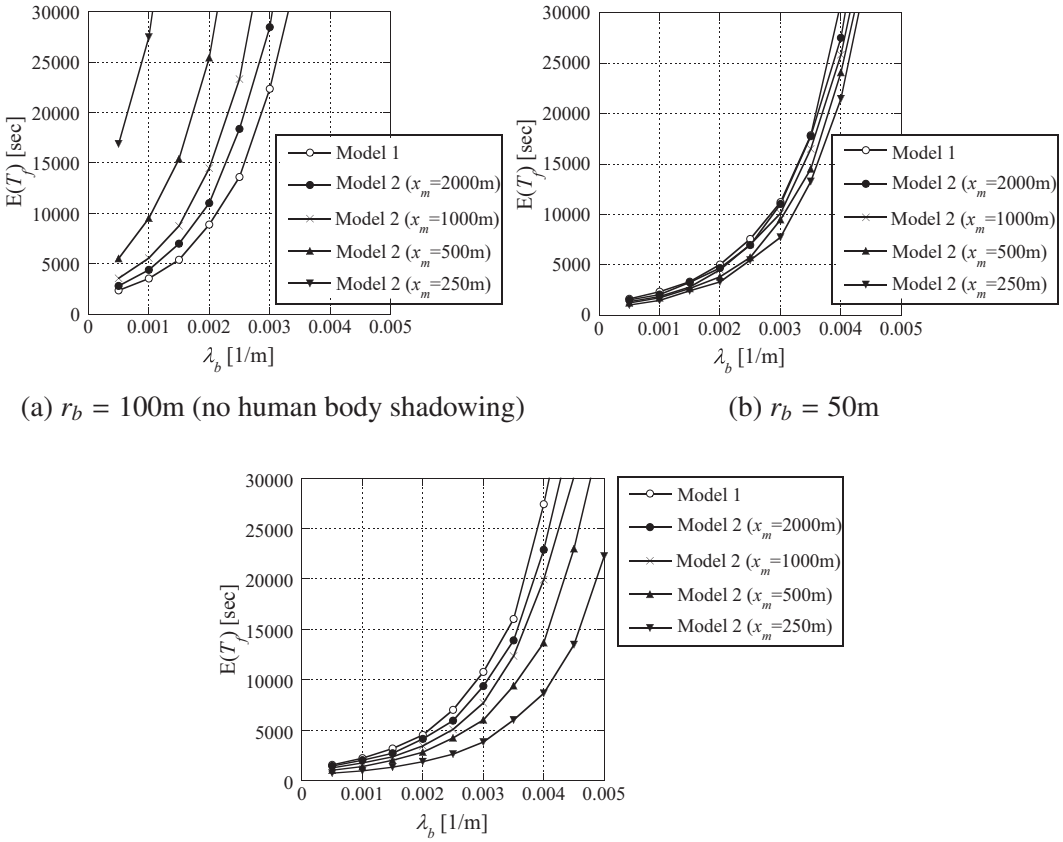

(a) $r_b = 100$m (no human body shadowing) (b) $r_b = 50$m

(c) $r_b = 25$m

Figure 2: Simulation results of $E(T_f)$, where $r_a = 100$m and $\lambda_w = 0.03\text{m}^{-1}$.

[7] K. Miyakita, N. Karasawa, Y. Inagawa, K. Nakano, "A consideration on traffic guidance by information floating," *IEICE Trans. Comm. (Japanese Edition),* vol.J101-B, no.8, pp.603–618, April 2018. (in Japanese)

[8] N. Karasawa, K. Miyakita, H. Tamura, K. Nakano, "Theoretical Analysis of Information Floating Considering Effects of Human Body Shadowing of Mobile Nodes," *JSST Technical Report,* JSST-MDMC2021-1-02, pp.13–20, April 2021. (in Japanese)

[9] D. Kotz, et al., "Experimental evaluation of wireless simulation assumptions," *Proc. of the 7th ACM Int. Symp. on Modeling, analysis and simulation of wireless and mobile systems (MSWiM),* pp.78-82, Oct. 2004.

[10] C. Bettstetter, C. Hartmann, "Connectivity of Wireless Multihop Networks in a Shadow Fading Environment," *Wireless Networks 11,* pp.571–579, Sept. 2005.

On the edge Grundy number and the number of vertices in grid graphs

Hiroshi Tamura[1*], Keisuke Nakano[2]

[1]Faculty of Science and Engineering, Chuo University, Japan
[2]Graduate School of Science and Technology, Niigata University, Japan
[*]**tamura@elect.chuo-u.ac.jp**

Abstract. Relationship between graph coloring and channel assignment in wireless communication is well known. However, almost studies are about the minimum number of colors despite the difficulty of optimum coloring. In the previous study, we paid attention to graph coloring assigned maximum number of colors called Grundy coloring. In this paper, we pick up the grid graphs that are applicable to topologies of sensor networks. For edge colorings, we consider the grid graph that achieves the maximum number of colors.

Keywords: Wireless communication, Channel Assignment, Graph coloring, Edge Grundy coloring

1. Introduction

Relationship between graph coloring and channel assignment in wireless communication is well known. However, almost studies are about the minimum number of colors. This number is called the chromatic number of the graph and the problem of finding the chromatic number is NP hard. In the previous study[1], we paid attention to graph coloring assigned maximum number of colors called Grundy coloring. Because, it is important to find the required number of channels. In [1], we showed some graphs expected to be assigned many colors theoretically. In this paper, we pick up the grid graphs that are applicable to topologies of sensor networks. For edge colorings, we consider the grid graph that achieves the maximum number of colors.

2. Assumptions and definitions

First of all, we define greedy coloring[2]. A ***greedy coloring*** is a coloring of the elements (vertices or edges) of a graph formed by a greedy algorithm that considers the elements of the graph in sequence and assigns each element its first available color. The number of colors produced by the greedy coloring for the worst ordering of a given graph G is called its ***Grundy number***[3] and its coloring is called ***Grundy coloring***. The vertex Grundy coloring is

popular. The conventional edge coloring version called ***edge Grundy number*** and ***edge Grundy coloring*** is discussed in [4].

We explain edge Grundy coloring. We consider a path graph(Fig.1(a)). In Fig.1(a), the number with parenthesis represents edge ordering. The edge greedy coloring of Fig.1(a) is Fig.1(b).

(a) (b)

Fig.1 An edge ordering and coloring.

(a) (b)

Fig.2 An edge ordering and coloring.

Another case is in Fig.2. The number of colors is 2 in Fig.1(b) and 3 in Fig.2(b). Since the edge Grundy number is the maximum number of colors, the edge Grundy number of the path graph is 3.

In [1], we showed the graphs assigned many colors theoretically and vertex/edge ordering of coloring.

[Theorem 1][1]

Let G be a graph. For a greedy coloring, the number of colors is not greater than

max {deg(u) +1 | u is a vertex of G}, in case of vertex coloring,

max{deg(u)+deg(v) -1| (u,v) is an edge of G}, in case of edge colorings,

where deg(u) is the degree of vertex u.

Theorem 1 shows the upper bounds of colors for Grundy number/ edge Grundy number.

3. Results

In this section, we consider grid graphs (Fig.3)

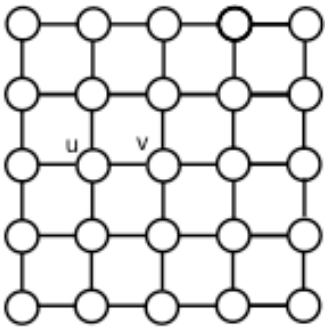

Fig.3 A grid graph G.

In the grid graph, the maximum number of colors in edge Grundy coloring

deg(u)+deg(v) - 1=4+4-1=7

from Theorem1. In this paper, a grid graph means graph G of Fig.3 or a subgraph of G,

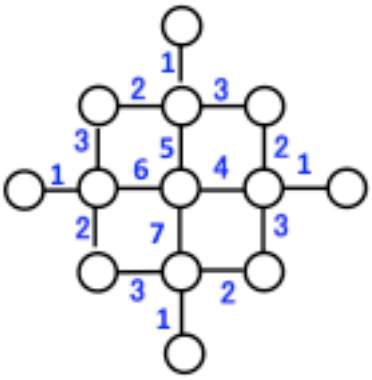

Fig.4(a) A colored grid graph G.

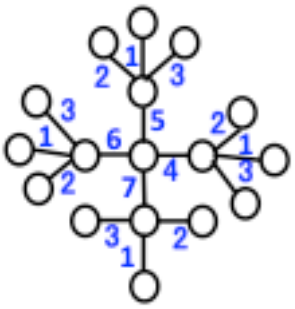

Fig.4(b) A tree T whose edge Grundy number is 7.

Graph G of Fig.4(a) is a colored grid graph and the edge Grundy number is 7. From the discussion of [1], in case of deg(u)=deg(v)=4, the number of vertices of T in Fig.4(b) is minimum of all trees whose edge Grundy number are 7. We obtain graph G by embedding T to a grid graph.

In the assumption above, a color is assigned to an edge once, the color remains on the edge. Hereafter, we adopt an operation to delete a color once assigned. Because, in communication networks, when communication is terminated, the corresponding edge should be decolored. Therefore, in a graph coloring, we assume the deleting operation of color on an edge. For example, the edge Grundy number of G in Fig.5 is 2. However, in the following ordering, the number of colors is 3.

e2, e3, e2(x), e1, e2

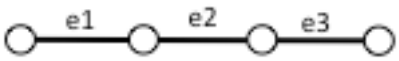

Fig.5 A graph G.

Here, e2(x) represents deletion of the color of e2. This coloring is called ***Edge Grundy coloring with decoloring***. Since Grundy coloring with decoloring is a generalized Grundy coloring, the number of colors may increase. However, it is easy to show that Theorem 1 holds.

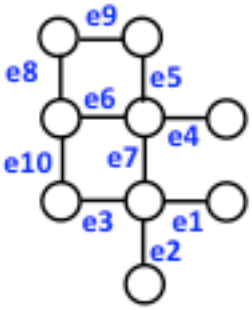

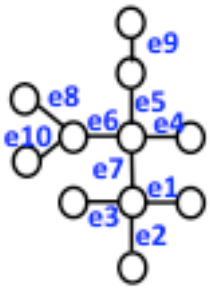

Fig.6(a) A grid graph G. Fig.6(b) A tree T whose edge Grundy number is 7.

In G of Fig.6(a), the edge ordering for coloring is the follows.

e5,e6,e7,e4,e5(x),e9,e5,e6(x),e8,e10,e6,e7(x),e3,e2,e1,e7

Finally, color 7 is assigned to e7. In edge Grundy coloring with decoloring, the number of vertices of G of Fig.6(a) is minimum of all graphs whose edge Grundy number are 7. Because from the discussion of [1], in case of deg(u)=deg(v)=4, the number of vertices of T in Fig.6(b) is minimum of all trees whose edge Grundy number are 7. Therefore we obtain graph G by embedding T to a grid graph.

Conclusions

In this paper, we show the graph, where the edge Grundy number is maximum and the number of vertices is minimum. Although the size of the graph is small, it is unclear whether the maximum number of colors will actually be used in some cases. So, verification with computer simulation is necessary.

References

[1] H. Tamura, S. Matsumoto, K. Nanano, M. Sengoku, On Graph Coloring with Relation to Channel Assignment in Wireless Networks, IEICE Trans. Fundamentals, Vol.J102-A,No.7,pp.214-223,Jul. 2019.

[2] Tommy R. Jensen, Bjarne Toft: Graph Coloring Problem, John Wiley & Sons,1994.

[3] P. M. Grundy:"Mathematics and games", Eureka, 2: 6–8, 1939.

[4] Leizhen Cai and Xuding Zhu: "Game Chromatic Index of k-Degenerate Graphs, J. Graph Theory, Vol.36, 3, pp.144-155, 2001.

Simulation of GAMMA 10/PDX plasmas by a plasma fluid model based on the anisotropic ion pressure (AIP model)

Satoshi Togo[1,*], Naomichi Ezumi[1], Mizuki Sakamoto[1], Md. Shahinul Islam[1], Tsukasa Sugiyama[1], Kosuke Takanashi[1], Tomonori Takizuka[2], Kenzo Ibano[2]

[1]Plasma Research Center, University of Tsukuba
[2]Graduate School of Engineering, Osaka University

[*]togo@prc.tsukuba.ac.jp

The full paper of this paper has been published in Journal of Advanced Simulation in Science and Engineering (JASSE).

DOI: https://doi.org/10.15748/jasse.9.185

Detached helium plasma simulation with collisional-radiative model

Hirohiko Tanaka[1*], Isaya Saeki[1], Noriyasu Ohno[1], Shin Kajita[2], Taichi Ido[1], Hiroki Natsume[1], Akiyoshi Hatayama[3], Kazuo Hoshino[3], Keiji Sawada[4], Motoshi Goto[5]

[1]Graduate School of Engineering, Nagoya University
[2]Institute of Materials and Systems for Sustainability, Nagoya University
[3]Faculty of Science and Technology, Keio University
[4]Institute of Engineering, Shinshu University
[4]National Institute for Fusion Science, National Institutes of Natural Sciences

*h-tanaka@ees.nagoya-u.ac.jp

Abstract. To improve the accuracy of the detached helium plasma simulation, effective rate coefficients obtained from the collisional-radiative (CR) model were introduced in the plasma fluid code LINDA. The CR-based and the empirical source terms for the simulation have finite differences, and computed detached plasmas using these source terms show qualitatively the same but quantitatively different parameter profiles. This study also suggests the importance of the choice of source terms particularly in future fusion devices.

Keywords: Detached plasma, Fluid simulation, Collisional-radiative model

1. Introduction

To realize the neuclear fusion reactor, sufficient reduction of the heat load toward the plasma-facing material (“divertor plate”) is an essential issue. For this purpose, the formation of the detached plasma utilizing the plasma-neutral gas interactions is expected as a promising method. However, the reliability of the detached plasma simulation is still insufficient possibly due to simplified models related to atomic and molecular processes. To deal the detaild atomic processes, this study focused on the collisional-radiative (CR) model in helium plasmas [1,2]. The effective rate coefficients were evaluated with the CR model and then applied to the one-dimensional (1D) detached helium plasma simulation using the LINDA code [3,4,5].

2. Results and discussion

In the plasma fluid simulation, the rate coefficients are used to calculate the plasma particle, momentum, and energy source terms. At first, we compared the rate coefficients and related source terms obtained from the CR model and the empirical databases. As a result, differences

between several CR-based and empirical source terms were found to be more significant in higher plasma density case. Detached plasma simulations with CR-based and empirical source terms showed qualitatively similar but quantitatively different parameter profiles, e.g., the density-peak amplitudes at the highly volume-recombining region ("recombination front"). To validate the simulation, parametric study under various calculation conditions and comparison with experimental results are needed. Furthermore, because the impact attributed to the different source terms becomes stronger in higher density condition, the choice of source terms is more important for simulations of future fusion devices with higher density plasmas in front of the divertor plate.

References

[1] T. Fujimoto: A collisional-radiative model for helium and its application to a discharge plasma, *Journal of Quantitative Spectroscopy and Radiative Transfer*, 21 (1979) 439-455.

[2] M. Goto: Collisional-radiative model for neutral helium in plasma revisited, *Journal of Quantitative Spectroscopy and Radiative Transfer*, 76 (2003) 331-344.

[3] T. Furuta, H. Takeda, M. Toma, W. Sato, Y. Homma, Y. Sawada, Y. Nakashima, A. Hatayama: Modeling of Plasma Transport in the Magnetic Mirror Configuration (GAMMA 10), *Fusion Science and Technology*, 63 (2013) 411-413.

[4] M.S. Islam, Y Nakashima, A Hatayama: Investigation of plasma behavior during noble gas injection in the end-cell of GAMMA 10/PDX by using the multi-fluid code 'LINDA', *Plasma Physics and Controlled Fusion*, 59 (2017) 125010.

[5] H. Tanaka, I. Saeki, N. Ohno, S. Kajita, T. Ido, H. Natsume, A. Hatayama, K. Hoshino, K. Sawada, M. Goto: Detached helium plasma simulation by a one-dimensional fluid code with detailed collisional-radiative model, *Physics of Plasmas*, 27 (2020), 102505.

JSST 2021

Development of the efficient electrostatic plasma particle simulation code for the study of fusion boundary layer plasmas

Hiroki Hasegawa[1,2*] and Seiji Ishiguro[1,2]

[1]National Institute for Fusion Science, National Institutes of Natural Sciences
[2]Department of Fusion Science, The Graduate University for Advanced Studies, SOKENDAI

[*]hasegawa.hiroki@nifs.ac.jp

Abstract. The three-dimensional (3D) electrostatic particle-in-cell (PIC) simulation code has been developed with the domain decomposition, in which the field and particle data are distributed to domains on processes, in the basis of our original 3D-PIC code in which only the particle data are distributed to processes. In an electrostatic plasma particle code, the Poisson's equation should be solved in order to obtain the electric potential. In our original code, the fast Fourier transform (FFT) is used for this purpose. However, FFT needs all-to-all communication. Thus, in the code developed in this study, the subroutine which provides the simple interface to the FFT libraries adaptable to the domain decomposition is applied. The code verification has been performed on FUJITSU FX100. We have obtained better scalability and performance with the developed code than the original code.

Keywords: particle-in-cell, domain decomposition, fast Fourier transform, fusion boundary layer plasma

1. Introduction

The simulations on supercomputers are one of powerful tools to investigate plasma phenomena in the fusion magnetic confinement devices. Although there are many numerical method to study the fusion plasmas, a particle-in-cell (PIC) simulation [1] is used to reveal the kinetic, i.e., microscopic, dynamics in various plasma phenomena. We have also developed the three-dimensional (3D) electrostatic PIC simulation code called "p3bd" code [2] in order to investigate the kinetic dynamics in the fusion boundary layer plasma and we have shown the significant discoveries regarding the non-diffusive radial plasma transport in the fusion boundary layer plasma, e.g., Ref. [3]. Our future works regarding those topics need larger scale simulations than that in our previous studies.

However, the p3bd code cannot calculate huge systems because only the particle data are distributed to processes and all field data are copied to each process in the p3bd code. That

is, in the simulations of huge systems, the field data cannot be stored in shared memories on each processor with the distribution method used in the p3bd code. Thus, in this study, we have developed the upgraded 3D-PIC code called "up3bd" code in which both the field and the particle data are distributed to domains on processes.

2. Outline of the up3bd Code

In this section, we briefly explain the calculation flow of the up3bd code, the domain decomposition, the Poisson solver with the fast Fourier transform (FFT), and the particle data sort applied in the up3bd code.

2.1. Calculation Flow

First, the initial positions and velocities of all simulation particles are set (in other words, particle loading) by the subroutine "init".

Next, the charge density on the grids is calculated from the particle positions, i.e., the charges of particles are assigned to the grids by the subroutine "charge".

Using the charge density on the grid, the electric potential is calculated by the Poisson's equation. In the subroutine "field", applying the finite difference equation of the Poisson's equation, the electric potential is solved with the FFT [4]. The electric field is obtained from the difference of electric potential.

The acceleration of a particle is computed by the equation of motion in the subroutine "accel" and the position of a particle is developed in the subroutine "move" by means of the leap frog method [1]. Although the force affecting the charged particle is the Coulomb force which needs N^2 computation, the plasma particle simulation needs only N computation because the Coulomb force between individual particles is neglected due to the Debye shielding [5]. After the new positions of particles are calculated, the charge density is computed again.

2.2. Domain Decomposition

In the p3bd and up3bd codes, particles are absorbed at some boundaries [2] and the time developments of absorbed particles are not calculated. Thus, the subroutine "pact" stores the numbers of particles which are out of the system, i.e., have been absorbed. Also the subroutine "pact" keeps the numbers of particles moved to the next domains in other arrays. In the up3bd code, the domains are aligned in the z direction, that is, the system is decomposed one-dimensionally.

In the subroutine "adjust", the data of non-active particles which are out of the system and the domain are deleted and the empty arrays caused by the deletion of non-active particle data is stuffed with the active particle data. Furthermore the data of particles moved to the next domains is transferred to the next domains by the message passing interface (MPI) communications. Before the data transfer, the data buffer array is prepared temporally and the data of particles moved to the next domains is stored in this array. After that, the data in this array are transferred to the processes in which the next domains exist.

2.3. Poisson Solver with FFT

In our original code p3bd, the FFT subroutine for the single-process computation has been used to solve the Poisson equation. Thus, the whole field data are copied to all processes in the p3bd code. However, because the field data are distributed to processes with the domain decomposition in the up3bd code, we should apply a FFT code adaptable to the domain decomposition. Thus, in this study, we have developed the subroutine called "PoissonFFT2" which provides the simple interface to the FFT libraries P3DFFT [6] and 2Decomp&FFT [7] in which FFTW [8] is used.

2.4. Sorting the Particle Data

In PIC simulations, the charge assignment needs large computer resource. If the numbers of the particles in the same cell are aligned continuously, the computation time is saved because the frequency of loading the charge density array on cache memory becomes small. Thus, in the subroutine "bsort", the particle data are sorted by the in-place bucket sorting method. The subroutine "bsort" is called once every several tens of time steps.

3. Code Verification

The verification of the up3bd code has been performed on FUJITSU FX100 of National Institute for Fusion Science (NIFS). As a result, the calculation shows that the performance of the up3bd code is about twice as high as that of the p3bd code. Figure 1 presents the weak scaling of the up3bd code. From these results, we obtain the effective parallelism ratio as 99.959 %. Although the simulations shown in above do not include the sorting, Table 1 shows the comparison between the codes without or with the sorting and indicates that the performance of the code with sorting is about 1.4 times as high as that of the code without the sorting. As described above, we have obtained better scalability and performance with the developed code than the original code.

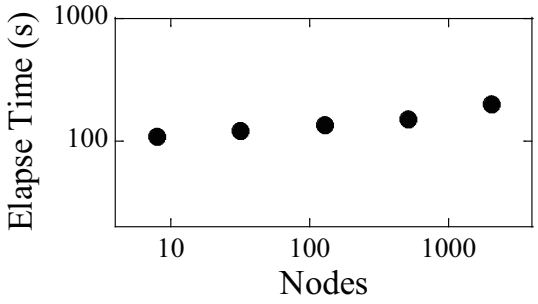

Figure 1: Relation between the number of nodes and the elapse time. Here, the system size per 8 nodes is $64 \times 64 \times 256$. The average number of particles per 1 cell is 144.

Table 1: Comparison between the codes w/o or with the sorting. Each simulation uses 8 nodes.

	Elapse time [s]	Ratio to peak performance [%]
w/o bsort	110	2.14
with bsort (once every 40 times)	77.1	2.84

Acknowledgments

The simulations were carried out on the "Plasma Simulator (PS)" (FUJITSU FX100) of NIFS. This work is performed with the support and under the auspices of the NIFS Collaboration Research programs (NIFS15KNSS058, NIFS17KNSS086, NIFS19KNSS119, and NIFS21KNSS155) and supported by JSPS KAKENHI Grant Numbers JP23740411 and JP19K03787. Development of some numerical codes used in this work was supported in part by the "Code development support program" of Numerical Simulation Reactor research Project (NSRP), NIFS.

References

[1] C.K. Birdsall, A.B. Langdon: *Plasma Physics via Computer Simulation*, McGraw-Hill, New York (1985).

[2] Hiroki Hasegawa, Seiji Ishiguro: Development and Verification of the Three-dimensional Electrostatic Particle Simulation Code for the Study of Blob and Hole Propagation Dynamics, *Plasma and Fusion Research*, volume:12 (2017), 1401044–1–1401044–9.

[3] Hiroki Hasegawa, Seiji Ishiguro: Three-dimensional effect of particle motion on plasma filament dynamics, *Physics of Plasmas* volume:26 (2019), 062104–1–062104–5.

[4] W.H. Press et al.: *Numerical recipes in Fortran 77 : The art of scientific computing* (2nd ed.), Cambridge University Press, New York (1996).

[5] Francis F. Chen: *Introduction to Plasma Physics and Controlled Fusion* (3rd ed.), Springer International Publishing, Switzerland (2016).

[6] D. Pekurovsky: P3DFFT: a framework for parallel computations of Fourier transforms in three dimensions, *SIAM Journal on Scientific Computing*, volume:34(4) (2012), C192–C209.

[7] N. Li, S. Laizet: 2DECOMP&FFT - A highly scalable 2D decomposition library and FFT interface, *Cray User Group 2010 conference* (2010).

[8] Matteo Frigo, Steven G. Johnson: The Design and Implementation of FFTW3, *Proceedings of the IEEE*, volume:93(2) (2005), 216–231.

Improved linear notch mechanics based on congruent condition of stress distribution for all notched materials

Wataru Fujisaki[1*], Ryunosuke Sakamoto[2], Yuto Shikata[2]

[1]Department of Mechanical Engineering, Kyushu Sangyo University
[2]Undergraduate school of Kyusyu Sangyo University

***fujisaki@ip.kyusan-u.ac.jp**

Abstract. This is a study on a new method to evaluate the brittle fracture strength of the all notched materials correctly. The physical meaning of this fracture mechanics for notch problems is same as the one for crack problems. We discuss the application limit of conventional linear notch mechanics, and clarify the effectiveness of the improved method through calculations and tensile tests.

Keywords: Linear notch mechanics, Estimation method, Brittle fracture strength, FEM

1. Application limit of conventional linear notch mechanics

One of the authors has proposed a generalized fracture criterion to predict the brittle fracture strength of the notched materials with from a small hole to a big hole [1],[2]. Here, we call it the improved linear notch mechanics. It is useful to reduce the weight of products which contributes on effective utilization of earth resources and energy conservation. For plane materials, the fracture criteria is based on one parameter, like as a maximum shear stress or a maximum von Mises stress. On the other hand, for notched materials, Nisitani had proposed the linear notch mechanics (conventional LNM) using σ_{max} and ρ [3]. For example, the relationship between the notch radius ρ and the maximum stress σ_{max} at fracture of a glass fiber reinforced polycarbonate composite material [4] is shown in Fig.1.

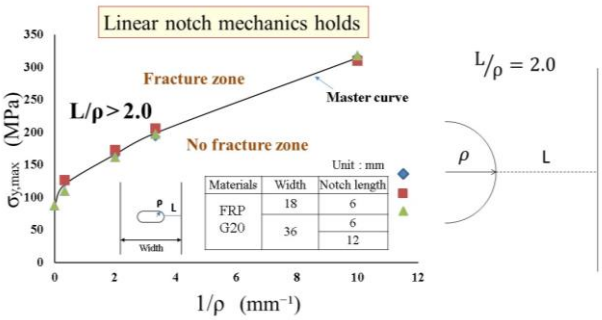

Fig.1 Clear master curve in LNM

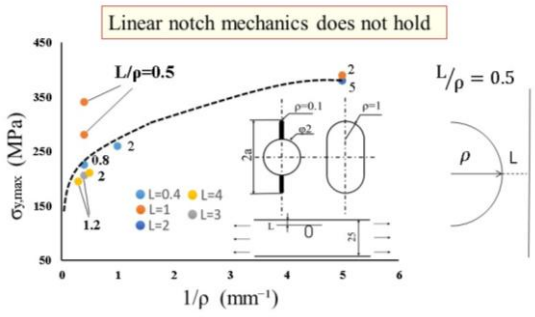

Fig.2 Unclear master curve in LNM

Here, σ_{max} is the maximum stress on the notch root, ρ is the curvature radius of the notch, and the parameter $1/\rho$ is almost proportional to the stress gradient χ at the notch root for various size of notches from a small notch to a medium notch. In this case, the conventional LNM holds under the condition $L/\rho>2.0$. Here, L is the length of the ligament of the plate. On the other hand, Noguchi et.al. reported the case in which the conventional LNM does not hold [5] as shown in Fig.2. You can see the values of $L/\rho=0.5$ apart from other points, and we cannot make a clear master curve of the conventional LNM.

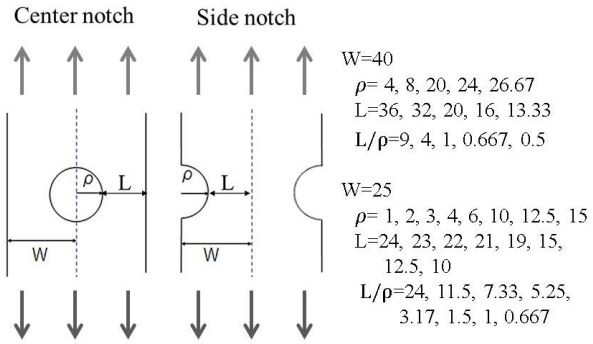

Fig3 Two types of test pieces

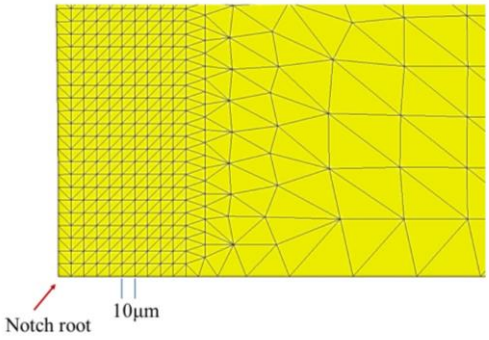

Fig.4 Mesh pattern of the notch root

The question is, to how much value of L/ρ, does the conventional LNM hold? The past studies do not reveal it. In recent years, we have systematically calculate the relative stress gradients of center notches and side notches[2] using the test pieces as shown in Fig.3. To calculate the accurate stress gradient, the finite element method (SolidWorks simulation) with 0.3～1.4 million D.O.F and also the method of fundamental solutions[6] are used. For FEM. The mesh pattern of the notch root is shown in Fig.4. The length of the one element near the notch root is 0.01 mm which is nearly equal to the grain size of common metal. The reason we choose these two types of test pieces is, when ρ becomes bigger, the difference of the stress gradients becomes bigger. Therefore, it is ease to evaluate the application limit of conventional LNM using 1/ρ which is the shortcut parameter of the real stress gradient χ.

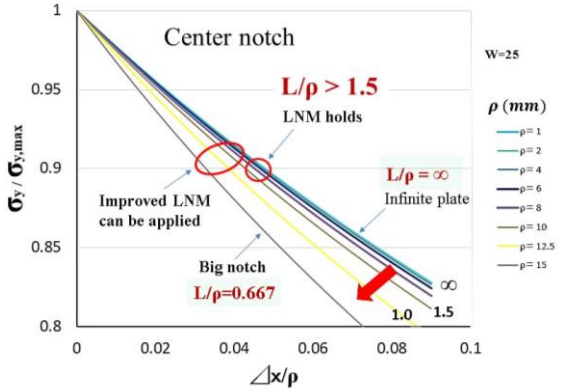

Fig.5 Stress gradients of center notches

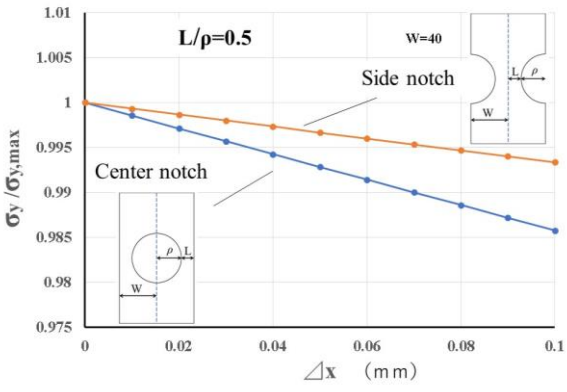

Fig.6 Stress gradient of big notch

We summarized the relative stress gradients of the center notches from L/ρ=0～0.667 in Fig.5. Here, ⊿x is the distance from the notch root, and ⊿x/ρ means the relative distance. Therefore, if the relative stress gradients is same, the stress distribution is controlled by 1/ρ. As a result, for the center notch, the limitation of application limit of 1/ρ can be distinguished as shown in Fig.5. We can see the conventional LNM can be hold in case of L/ρ>1.5. As ρ becomes bigger in L/ρ<1.5, the stress gradient changes rapidly and the conventional LNM cannot be applied. This is the same in the case of the side notches [2].

2. Usefulness of improved LNM

Therefore, for a big notch problem, we cannot use ρ as the shortcut parameter anymore. For example,

the comparison of the stress gradients of a big center notch and a big side notch (L/ρ=0.5) is shown in Fig.6 using the test pieces as shown in Fig.3 . In this case, you can see the large difference of the relative stress gradient appears, and this means that congruent condition of the stress distribution cannot be assured by 1/ρ. Therefore, we have to apply the improved LNM which uses a stress gradient χ directly.

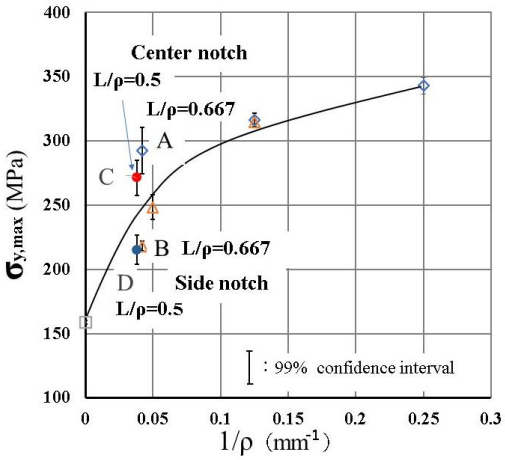

Fig.7 Conventional LNM

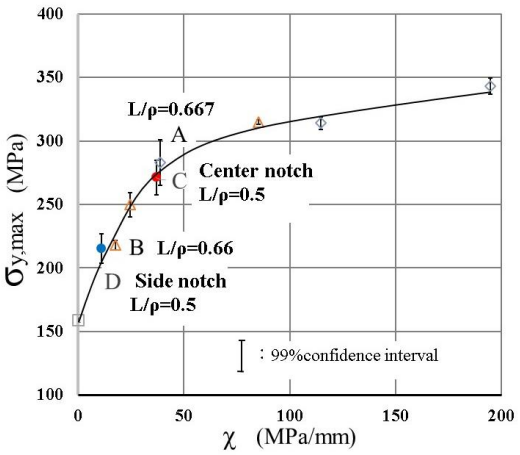

Fig. 8 Improved LNM

We have conducted some tensile tests of Cu sheet specimens (W=40mm) systematically. Firstly, we made the master curve of our experimental results based on the conventional LNM in Fig.7. Each condition of the tensile tests is repeated 6 times and the bar represents a 99% confidence interval. The data of small circular notch size are on the master curve, while the data of the bigger circular notches (L/ρ=0.667; A, B and L/ρ=0.5; C and D) are apart from the master curve. Therefore, we cannot accurately estimate the fracture strength of A～D by the conventional LNM. On the other hand, the new master curve based on the improved LNM is shown in Fig.8. Here, the stress gradient χ is $\Delta\sigma_y/\Delta x$. It is clear that the data of A ～D are on the master curve. Therefore, we can correctly evaluate the fracture strength of notched materials with most size by using the improved LNM.

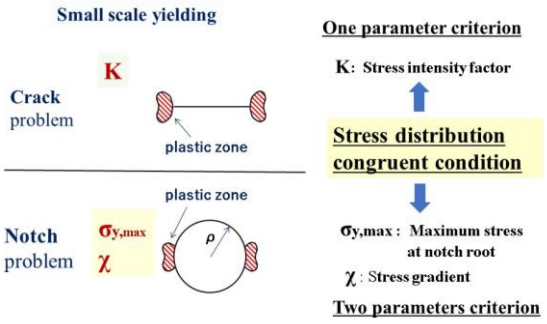

Fig.9 Physical background of improved LNM

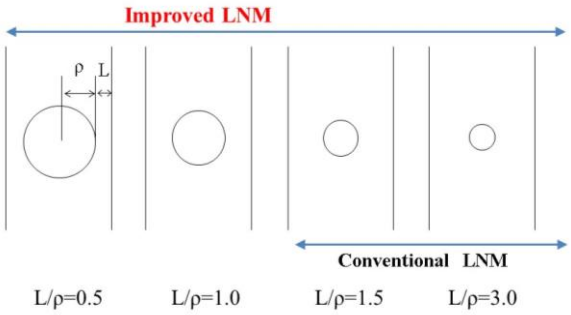

Fig.10 Comparison of application limit

The physical background of the improved LNM is shown in Fig.9. Upper part is the linear crack mechanics using the stress intensity factor K. These two criteria are based on a congruent condition of the stress distribution. If we would like to estimate the brittle fracture strength of the real product from

the test piece, what we should do is to make the two stress distributions same. For crack problems, one parameter K guarantees the same stress distribution. On the other hand, for notch problems, the two parameters σ_{max}, χ guarantee the same stress distribution. The application ranges of the two LNMs are illustrated in Fig.10. The conventional LNM can only be used above $L/\rho>1.5$. On the other hand, up to now, it turned out that we can apply the improved LNM to the very big notch with $L/\rho=0.5$.

3. Conclusion

We clarified that the conventional LNM can be applied to the medium size of notch ($> L/\rho=1.5$) and the improved LNM which can be applied to the bigger size of notch. Up to now, we have conducted systematic tensile tests and found this improved LNM can be applied to the very big notch problem with $L/\rho=0.5$. This improved LNM is based on the stress congruent condition like as the stress intensity factor K. For the notch problems, the two parameters, namely the maximum stress σ_{max} and the stress gradient χ at the notch root, assure the same stress distribution under small scale yielding condition. This improved LNM is effective to design the lightweight products including a big notch.

References

[1] W.Fujisaki, Y.Takamiya,: Generalized Linear Notch Mechanics for Strength Evaluation, *Proc. Inter. Conf. Japan Society of Simulation and Technology,JSST2017*,pp.1-4,2017.

[2] W.Fujisaki, H.Iwatsubo, Y.Takamiya : Effectivness of Generalized Linear Notch Mechanics in View of Stress Gradient, *Proc. Inter. Conf. Japan Society of Simulation and Technology,JSST2018*,pp.1-4,2018.

[3] H.Nisitani: Linear Notch Mechanics as an Extention of Linear Fracture Mechanics, *Proc. Inter. Conf. Role of Fracture Mechanics in Modern Technology,* (Eds; Sih,G.C. and Nisitani,H.), pp.23-37,Elsevier,1987.

[4] Y.H. Kim, H.Nisitani: Fracture Criterion in Tension Test of Center Notched Plates of GFRP, *Journal of Japan Society of Mechanical Engineering*,Vol.56, pp.582-588,1990.

[5] H.Noguchi, Y.Aono: Application Limit of Linear Notch Mechanics, *Journal of Japan Society of Mechanical Engineering,* Vol.61, No,589, pp.2044-2051, 1995.

[6] W.Fujisaki: Recent Studies in Meshless & Other Novel Computational Methods, pp.57-69, Tech Science Press, 2010.

[7] W.Fujisaki, R.Yamasaki : Estimation of fracture strength using improved linear notch mechanics for notched materials, *Proc. 3rd. Inter. Conf. on Comp. Engineering and Science for Safe and Environmental Problems, COMPSAFE 2020*,pp.1-4,2020.

JSST 2021

Fully explicit computational method for gas-solid two-phase flow with large temperature variation

Daisuke Toriu[1,*] and Satoru Ushijima[1]

[1]Academic Center for Computing and Media studies, Kyoto University

[*]toriu.daisuke.8v@kyoto-u.ac.jp

The full paper of this paper has been published in Journal of Advanced Simulation in Science and Engineering (JASSE).

DOI: https://doi.org/10.15748/jasse.9.170

Radiation field analysis using deep learning algorithms

Katsuhiko Yamaguchi*, Masaharu Matsumoto, Yuto Kondo, Kenji Suzuki, Jun Kinugawa

Faculty of Symbiotic Systems Science, Fukushima University

*yama@sss.fukushima-u.ac.jp

Abstract. The spatial intensity distribution of γ-rays emitted from radionuclides was analyzed using the deep Galerkin method, which is one of the deep learning algorithms, and compared with the conventional results by the particle transport Monte Carlo method. The results of both methods showed good agreement when the effect of the shield was small. This method can be expected to speed up the calculation by using a deep learning machine equipped with GPUs.

Keywords: deep Galerkin method, γ-rays, radiation field analysis

1. Introduction

Calculating the spatial intensity distribution of γ-rays emitted from radionuclides is a necessary technology in various fields such as medical treatment and nuclear power plants. Therefore, many simulations using the particle transport Monte Carlo method have been performed until now. However, Monte Carlo simulation requires placing meshes in each region of space, and also a long calculation time. Recently, the deep Galerkin method (DGM), which can be calculated mesh-free, has attracted attention as one of the differential equation solving methods using a deep learning algorithm [1]. In this study, we propose a new radiation field simulation using DGM, which has the potential to overcome the difficulties of the Monte Carlo method.

2. Calculation Method

Poisson's equation was assumed as the basic equation of the radiation field in the two-dimensional region shown in Fig. 1. The radiation source was set in a circle with a radius of 0.1 centered on the positions of x = 0.5 and y = 0.5, and the other areas were set as vacuum regions. First, two points, one coordinate point (x1, y1) inside the calculation area and one coordinate point (x2, y2) on the boundary, are randomly selected. Next, using these two points as the input of the DNN, the outputs f (x1, y1) and f (x2, y2) are obtained, and the parameters of the DNN are optimized so that the following loss function *L* becomes zero.

$$L=\left\{\frac{\partial^2 f(x_1,y_1)}{\partial x^2}+\frac{\partial^2 f(x_1,y_1)}{\partial y^2}+\rho(x_1,y_1)\right\}^2+\left\{f(x_2,y_2)-\varphi(x_2,y_2)\right\}^2 \quad (1).$$

In addition, the radiation intensity distribution was calculated when there is a shield using the radiation transfer equation [2] as below,

$$cos\,\theta\frac{\partial I_v}{\partial x} + sin\,\theta\frac{\partial I_v}{\partial y} - S(x,y,\theta) + \mu_a(x,y,\theta)I_v(x,y,\theta) = 0 \qquad (2).$$

Here, I_v means the radiation intensity at each position. In addition, S indicates the production term and μ_a indicates the absorption coefficient. Calculation results by DGM were compared the ones by a Monte Carlo simulation code (PHITS) [3].

3. Results and Discussion

Figure 2 shows the results of the radiation intensity distribution calculated by DGM based on (1). The two-dimensional map (left) draws that the radiation intensity is symmetrical from the center. The radiation intensity distribution on y = 0.5 (right) shows a graph that is inversely proportional to the distance from the center. This result is in good agreement with the result calculated by the Monte Carlo method for the radiation intensity distribution emitted from the point source placed in vacuum. Furthermore, it should be noted that this calculation result is expressed as a continuous value that does not depend on the mesh.

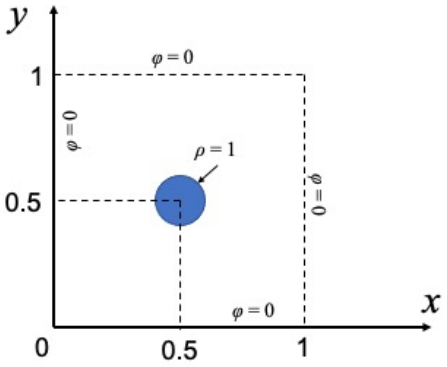

Fig.1 Computational area set in 2D.

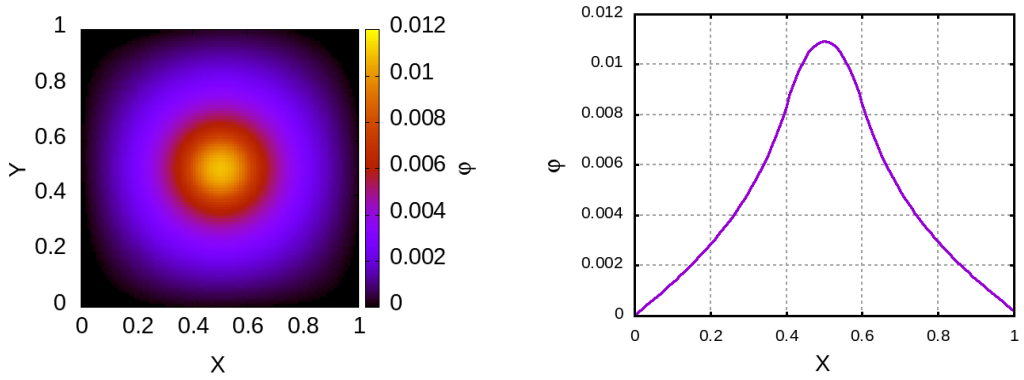

Fig.2 Calcuration results of the radiation intensity distribution by DGM.

Figure 3 shows the radiation intensity calculation result when the shield is placed near the radiation source. Figure 3(a) shows the calculation result by the Monte Carlo simulation, and aluminum is arranged as a shield at the position indicated by the white frame. Figure 3(b) is the result by DGM, and it can be seen that it corresponds well with Figure 3 (a). As described above, since the results can be obtained without arranging the mesh in the calculation by DGM, it is highly expected as a new simulation method.

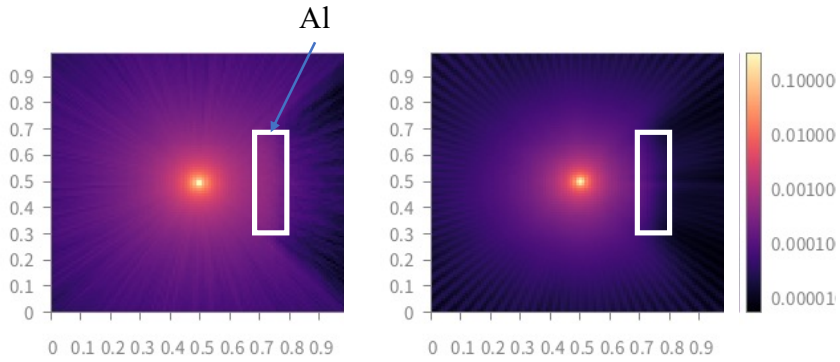

(a) MC (b) DGM

Fig.3 Calcuration results of the radiation intensity distribution when there is a shield.

References

[1] Sirignano and Konstantinos Spiliopoulos, “DGM: A deep learning algorithm of solving partial differential equations”, Journal of Computational Physics, Vol.375, pp.1339-1364, 2018.

[2] D. Mihalas and B. Weibel-Mihalas: Foundations of Radiation Hydrodynamics, Dover, 1999.

[3] Yosuke Iwamoto, Tatsuhiko Sato, Shintaro Hashimoto, Tatsuhiko Ogawa, Takuya Furuta, Shin-ichiro Abe, Takeshi Kai, Norihiro Matsuda, Ryuji Hosoyamada and Koji Niita Benchmark study of the recent version of the PHITS code, J. Nucl. Sci. Technol. 54, 617-635 (2017)

JSST 2021

Laguerre-Gaussian beam formation by spatiotemporal coherent motion of electrons

Shin Kubo[1,*], Yuki Goto[2], Toru I. Tsujimura[2], Toru Kobayashi[3]

[1]College of Engineering, Chubu University
[2]National Institute for Fusion Science
[3]Department of Applied Energy, Nagoya University

[*]kuboshin@isc.chubu.ac.jp

Abstract. The radiation from single electron in circular motion is shown to have a helical phase structure. Such radiation from multi-electron system is expected to form a Laguerre-Gaussian (LG) beam which is identified as an optical vortex and proved to have an orbital angular momentum (OAM). Spatiotemporal coherence of the electrons in circular motion would be the key to form a LG beam with high purity and high efficiency. This paper describes the method to clarify the effect of spatiotemporal coherence to form LG beam with OAM.

Keywords: Laguerre-Gaussian beam, orbital angular momentum, vortex, coherence

1. Introduction

Optical vortex is recognized by Allen *et al.*[1] as one of the characteristic feature of Laguerre-Gaussian (LG) beam. They demonstrated LG beam carries orbital angular momentum(OAM). Since then, optical vortex has been intensively investigated in both characterization and application of OAM. There the Laguerre-Gaussian beam are generated from normal Gaussian beam utilizing optical converters, such as grating or phase plate. M. Katoh *et al.* demonstrated an electron in circular motion emits a radiation with twisted phase front[2, 3]. They also indicated that electrons in cyclotron motion exist anywhere in the universe and optical vortex should be associated with the ubiquitous electron cyclotron emission (ECE). A question arises why such ubiquitous optical vortex was not observed so far? One of the reasons is that the theoretical and experimental investigations had been focused mainly on the intensity characteristics of the ECE and dedicated investigation had not been performed in view of OAM. The other important reason would be ECE from thermal electrons have random gyro-phases and the vortex feature will be cancelled out. This point had been partly clarified by Goto [4] by calculating far field phase structure of the summation of several electrons distributed homogeneously confined in a finite area but with partly coherent gyro-phase. An experiment to control the gyro-phase by accelerating electron cyclotron motion

by an externally applied resonant electromagnetic wave is underway. It is worth investigating the condition of the spatiotemporal coherence to form LG beam. Far field calculation can be performed just like Fresnel-Kirchoff integral of the radiation from each electron with given spatiotemporal coherence. The amount or the purity of the LG beam can be estimated by utilizing the orthogonality of the Laguerre function. This paper describes how spatiotemporal coherence and structures of source density and phase of the radiating electrons affects the LG beam efficiency. Clarifying this condition leads to an active control of vortex ECE or interpretation of forced vortex ECE by a resonant electromagnetic field.

2. Acceleration of electrons in a static magnetic field by externally applied RF and radiation from them

If an electron moves in a propagating electro-magnetic wave with the electric field $\boldsymbol{E}_{\rm ext} = E_{\rm ext}\exp[-i(\omega_{\rm ext}t - \boldsymbol{k}_{\rm ext}\cdot\boldsymbol{r})]$, $\boldsymbol{B}_{\rm ext} = (\boldsymbol{k}_{\rm ext}/\omega_{\rm ext})\times\boldsymbol{E}_{\rm ext} = \frac{\boldsymbol{n}}{c}\times\boldsymbol{E}_{\rm ext}$, in a static magnetic field $\boldsymbol{B}_0 = B_0\hat{\boldsymbol{z}}$, the motion of electrons can be described by a relativistic equation of motion[5],

$$\dot{\boldsymbol{\beta}} = \underbrace{\frac{e}{m_{\rm e0}c\gamma}\Big(\underbrace{\overleftrightarrow{\boldsymbol{I}} - \boldsymbol{\beta}\diamond\boldsymbol{\beta}}_{\textit{electric field contribution}} + \underbrace{\boldsymbol{\beta}\times\boldsymbol{n}\times}_{\textit{magnetic field contribution}}\Big)\cdot\tilde{\boldsymbol{E}}_{\rm ext}}_{\textit{acceleration by oscillating external field}} + \underbrace{(\boldsymbol{\beta}\times\hat{\boldsymbol{z}})\frac{\Omega_{\rm e0}}{\gamma}}_{\textit{Lorentz force}} \tag{1}$$

Here, e is electron charge with negative sign, $\Omega_{\rm e0}$ is an electron cyclotron angular frequency of electron rest mass m_{e0} ($\equiv eB_0/m_{e0}$).

The electric field radiated from accelerated electron at distance R can be described by $R = |\boldsymbol{r}-\boldsymbol{r'}|$ is a distance between the charged particle (position $\boldsymbol{r'}$) and observer (position $\boldsymbol{r}$), $\hat{\boldsymbol{q}} = (\boldsymbol{r}-\boldsymbol{r'})/|\boldsymbol{r}-\boldsymbol{r'}|$ is a unit vector in the direction from particle to the observer, $t' = t - R(t')/c$ defines a retarded time, $\boldsymbol{\beta} = \frac{\boldsymbol{v}}{c}$ is a normalized velocity of particle by light velocity c, and $g = (1-\hat{\boldsymbol{q}}\cdot\boldsymbol{\beta})$ defines a longitudinal relativistic Doppler factor. After some manipulations, the electric field at far-field region $\boldsymbol{r}$ radiated from an accelerated electron at $\boldsymbol{r'}$ can be described as

$$\boldsymbol{E}_{\rm rad}(\boldsymbol{r},t) = \frac{e}{4\pi\varepsilon_0}\Big[\underbrace{\frac{(1-\beta^2)(\hat{\boldsymbol{q}}-\boldsymbol{\beta})}{g^3R^2}}_{near-field} + \underbrace{\frac{\hat{\boldsymbol{q}}\times(\hat{\boldsymbol{q}}-\boldsymbol{\beta})\times\dot{\boldsymbol{\beta}}}{g^3cR}}_{far-field}\Big]_{t'} \tag{2}$$

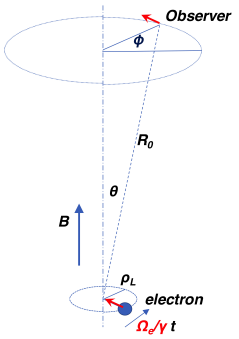

The idea here comes that applying resonant external field at electron cyclotron frequency, intensify the perpendicular energy of electrons and increases phase and space coherence of gyro-motion. Actually, in the non-relativistic regime, $\dot{\boldsymbol{\beta}}$ is proportional to the external electric field and gyration phase should become highly coherent in time and space with external wave field[4, 5]. Furthermore the trial to detect the optical vortex feature is underway. Here, the electrons in a magnetic field are accelerated by externally applied high power right hand circularly polarized resonant wave and phase and intensity structure at far field of second harmonic radiation from these

electrons. Due to the non-linear dependence of $\dot{\boldsymbol{\beta}}$ on $\boldsymbol{E}_{\rm ext}$ and $\boldsymbol{E}_{\rm rad}$ on $\dot{\boldsymbol{\beta}}$ as shown in Eqns. (1) and (2). Therfore, it is important to know how the spatiotemporal coherence of electron motion affects the total radiation as a LG beam. This investigation may indicate the way to control or optimize the quality of the generated LG beam.

3. Spatiotemporal coherence and LG beam formation

Given calculated far-field $\boldsymbol{E}_{\rm rad}(\boldsymbol{r})$ pattern using formula (2) on some target plane assuming spatiotemporal coherence , one can estimate the $\mathrm{LG}_{\ell,p}$ beam purity $\eta_{\ell,p}$ using the formula

$$\eta_{\ell,p} \equiv \frac{\int_S \boldsymbol{E}_{\rm rad}(\boldsymbol{r}) \cdot \boldsymbol{E}^*_{\mathrm{LG}_{\ell,p}}(\boldsymbol{r},\omega)\mathrm{d}S}{\sqrt{\int_S \boldsymbol{E}_{\rm rad}(\boldsymbol{r}) \cdot \boldsymbol{E}^*_{\rm rad}(\boldsymbol{r})\mathrm{d}S}\sqrt{\int_S \boldsymbol{E}_{\mathrm{LG}_{\ell,p}}(\boldsymbol{r},\omega) \cdot \boldsymbol{E}^*_{\mathrm{LG}_{\ell,p}}(\boldsymbol{r},\omega)\mathrm{d}S}} \tag{3}$$

Here,

$$\boldsymbol{E}_{\rm rad}(\boldsymbol{r},\omega) = \sum_{i=1}^{n}\int_{-\infty}^{\infty}\frac{e}{4\pi\varepsilon_0}\left[\frac{\hat{\boldsymbol{q}}_i \times (\hat{\boldsymbol{q}}_i - \boldsymbol{\beta}_i)\times\dot{\boldsymbol{\beta}}_i}{g_i^3 cR}\right]_{t'} e^{-i\omega t}\mathrm{d}t \tag{4}$$

is a summation of radiation field from n electrons. Here, LG beam is defined by

$$\begin{aligned}\boldsymbol{E}_{\mathrm{LG}_{\ell,p}}(\boldsymbol{r},\omega) &= \boldsymbol{e}_{\rm p}\sqrt{\frac{2p!}{\pi(p+|\ell|)!}}\left(\frac{\sqrt{2}r}{w(z)}\right)^{|\ell|}\frac{w_0}{w(z)}L^p_{|\ell|}\left(\frac{2r^2}{w(z)^2}\right)\exp\left[-\frac{r^2}{w_(z)^2}\right] \\ &\quad\times\exp[i\ell\phi]\cdot\exp\left[-ik_0\frac{r^2}{2R(z)}\right]\exp\left[-i(|\ell|+2p+1)\eta\right]e^{-i\omega t}dt\end{aligned} \tag{5}$$

here, $\boldsymbol{e}_{\rm p}$ is a unit vector expressing a polarization, $w(z)^2 = w_0^2\left[1+\left(\frac{\lambda(z-z_0)}{\pi w_0^2}\right)^2\right]$, $R(z) = (z - z_{0,\sigma})\left[1+\left(\frac{\lambda(z-z_0)}{\pi w_0^2}\right)^2\right]$ and $\eta(z) = \tan^{-1}\left(\frac{\lambda(z-z_0)}{\pi w_0^2}\right)$ $L^n_m$is Laguerre function defined by

$$L^n_m = \frac{\exp[r]r^{-n}}{m!}\frac{\mathrm{d}^m}{\mathrm{d}r^m}\left(\exp[-r]r^{n+m}\right) \tag{6}$$

The spatiotemporal coherence here can be interpreted as the distribution of electrons in real and velocity space relative to externally applied RF field, for example.

References

[1] L. Allen, M. W. Beijersbergen, R. J. C. Spreeuw, and J. P. Woerdman, Orbital angular momentum of light and the transformation of Laguerre-Gaussian laser modes, *Phys. Rev. A* **45** *(1992) 8185-8189.*

[2] M. Katoh, M. Fujimoto, H. Kawaguchi *et al.* Angular Momentum of Twisted Radiation from an Electron in Spiral Motion, *Physical Review Letters* **118** (2017) 094801–.

[3] M. Katoh, M. Fujimoto, N. S. Mirian, T. Konomi *et al.*, Helical Phase Structure of Radiation from an Electron in Circular Motion, *Scientific Reports* **7** (2017) 6130–.

[4] Yuki Goto, Shin Kubo and Toru Ii Tsujimura, Coherent Cyclotron Emission with a Helical Wavefront from Multi-electron System Accelerated by the Circularly Polarized Wave, *New Journal of Physics*, in press (2021).

[5] Yuki Goto, Shin Kubo and Toru Ii Tsujimura, Cyclotron Emission with a Helical Wavefront from an Electron Accelerated by the Circularly Polarized Wave *Journal of Advanced Simulation Science and Engineering* **7** (2020) 34-50.

Application of optical vortex to laser-induced fluorescence velocimetry of ions in a plasma

Shinji Yoshimura[1,*], Kenichiro Terasaka[2], Mitsutoshi Aramaki[3]

[1]National Institute for Fusion Science
[2]Kyushu University
[3]Nihon University

[*]yoshimura.shinji@nifs.ac.jp

The full paper of this paper has been published in Journal of Advanced Simulation in Science and Engineering (JASSE).

DOI: https://doi.org/10.15748/jasse.9.150

FDTD analysis of propagation of millimeter wave vortex in magnetized cold-plasma

Kazuki Chiba[1*] and Hideki Kawaguchi[**]

Division of Information and Electronic Engineering, Muroran Institute of Technology.

*20043037@mmm.muroran-it.ac.jp

**Kawa@mmm.muroran-it.ac.jp

Abstract. Since it was pointed out that an optical vortex carries orbital angular momentum in 1992, various kinds of research works on the optical vortex have been performed actively. In addition, it was found that the vortex phenomena can exist in other frequency ranges such as X-ray, ultraviolet, millimeter and so on. Recently it was theoretically shown that the millimeter wave vortex can propagate in magnetized cold plasma where plane wave is blocked by cut-off condition. In this study, we present the FDTD simulation of the propagations of the milli-meter vortex wave in the magnetized cold plasma.

Keywords: FDTD method, nuclear fusion plasma, optical vortex, milli-meter wave, magnetized cold plasma

1. Introduction

An optical vortex has its proper characteristics of a spiral structure wavefront and transportation of orbital angular momentum[1]. Various applications such as large capacity optical communication and optical tweezers have been considered to employ these special characteristics. Recently the vortex phenomenon in milli-wave frequency range was applied to a plasma heating in a nuclear fusion device and it was found from theoretical discussions that the vortex milliwave may propagate in magnetized cold plasma in which a plane wave with the same frequency can not propagate[2]. In this work, the propagation properties of the milli-wave vortex in the magnetized cold plasma are investigated by using numerical simulation of the FDTD method.

2. FDTD simulation of millimeter in magnetized cold plasma

In the FDTD simulation of the magnetized cold plasma, the plasma is considered as a dispersive medium described by the following Lorentz-Drude model,

$$\frac{d\boldsymbol{J}}{dt} + \nu\boldsymbol{J} + \omega_0^2\mathbf{P} = \varepsilon_0\omega_p^2\left(\boldsymbol{E} + \frac{\boldsymbol{J}}{en_e} \times \boldsymbol{B_0}\right), \ \boldsymbol{J} = \frac{d\boldsymbol{P}}{dt} \tag{1}$$

Then the electric field $\boldsymbol{E}$ in (1) is calculated by the following Maxwell's equations,

$$\nabla \times \boldsymbol{H} = \boldsymbol{J} + \varepsilon_0 \frac{\partial \boldsymbol{E}}{\partial t}, \nabla \times \boldsymbol{E} = -\mu_0 \frac{\partial \boldsymbol{H}}{\partial t} \quad (2)$$

On the other hand, the current density $\boldsymbol{J}$ in (2) is provided from the calculation of (1). That is, the time-domain calculation of (1) and (2) are carried out simultaneously.

3. Numerical example

Numerical model of the FDTD simulation of the milli-wave vortex in the magnetized cold plasma is depicted in Fig.1. Circularly polarized HE_{11} mode with 84GHz frequency generated in the corrugated wavegate is passed through the spiral dielectric plate at the downstream end of waveguide and transformed to the milli-wave vortex field on the another side of the spiral dielectric plate[3]. And the milliwave vortex is injected into the cold plasma region in which the external magnetic field $\boldsymbol{B_0}$ is applied. In Fig.2, distributions of intensity of electric field of x-z vertical cross-section are depicted for two kinds incident waves of the HE_{11} plane milli-wave (a) and milli-wave vortex (b). It is found that the milli-wave vortex can propagate the magnetized cold plasma which has cut-off condition for plane wave.

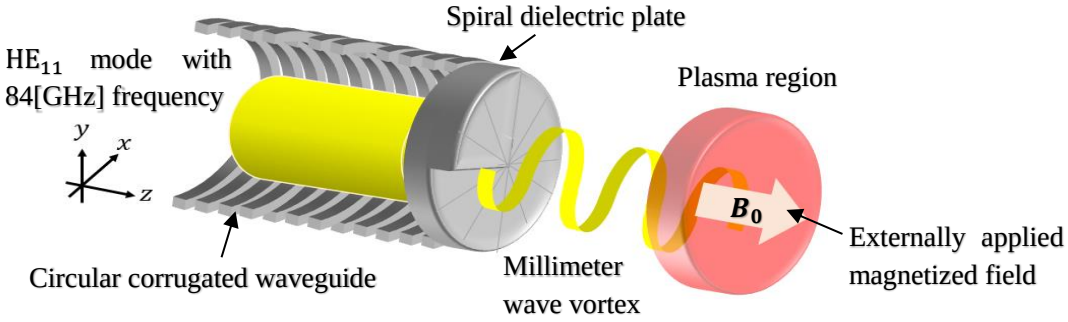

Fig.1 Numerical model of FDTD simulation of vortex wave in magnetized cold plasma.

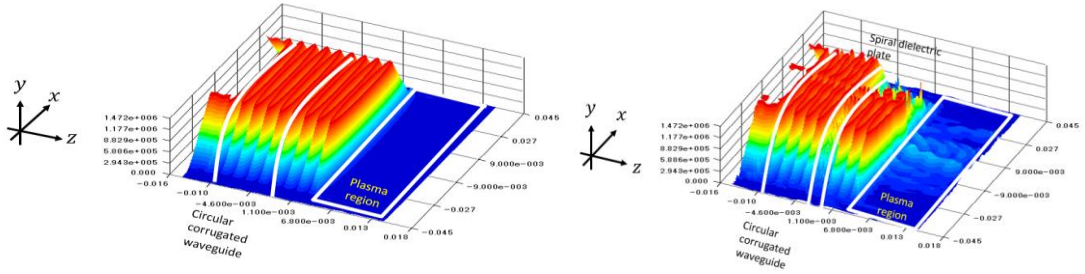

Fig.2. (a) Propagation of plane wave. (b) Propagation of vortex wave.

References

[1] L.Allen, M.W. Beijersbergen, R.J.C. Spreeuw and J.P. Woerdman, Orbital angular momentum of light and the transformation of Laguerre-Gaussian laser modes, Phys. Rev. A., Vol.45, No.2 (1992), pp.8185-8189.

[2] T.Tsujimura and S,Kubo, Propagation properties of electron cyclotron waves with helical wavefronts in magnetized plasma, Phys.Plasmas Vol.28,012502(2021).

[3] H.Kawaguchi, H.Nakamura, Evaluation of Mechanical Torque Acting on Scatterer in Microwave Vortex Fields, IEEE Microwave and Wireless Components Letters, Vol.29, Issue 7, pp.504-506, July (2019).

Various characteristic evaluation on magnetically-coupled intra-body communication using three-dimensional finite element modeling of a human upper-body

Kenichi Ito[1*]

[1] Niigata Institute of Technology

*itoh@iee.niit.ac.jp

Abstract. This study examined the signal transmission loss characteristic, biosafety criteria, and transmitting and receiving power efficiency on magnetically-coupled intra-body communication through computer simulation using three-dimensional finite element modeling (FEM) of a human upper body. The transmitter and receiver were placed on the chest and upper arm, respectively, and their coils were arranged at right angles to establish their positional relationship. Three types of coupling were chosen as the magnetic coupling methods: non-resonant inductive, low-Q resonant, and high-Q resonant. The signal transmission loss for each coupling method was 12~13 dB worse than the previous results on condition that their transmitter and receiver coils were linearly arranged in parallel on both arms. When the coil was placed on the chest, the biosafety was as high as it was in the previous results. In addition, we have shown the possibility that the power efficiencies of the two resonant couplings were higher than that of the non-resonant inductive coupling.

Keywords: intra-body communication, signal transmission loss, biosafety, power efficiency

1. Introduction

Intra-body communication (IBC) is a new transmission method that uses a human body as the transmission medium. Generally, although capacitive and galvanic coupling methods have been utilized [1], magnetic-coupling was recently proposed as the third method [2], which uses coils as the antennas of the transmitters and receivers. The transmitter generates a magnetic field signal by adding an alternating current to the transmitting coil, and the receiver detects this signal as the current signal using the receiving coil. The signal transmission loss characteristic of this magnetically-coupled method relies heavily on adopted coupling methods. So far, we have analyzed the characteristics of several magnetic-coupling methods in an attempt to minimize signal loss [3]. In this study, we examined a general inductive (non-resonant) coupling method, and two types of resonant (low-Q and high-Q) coupling methods. Low-Q resonant coupling is a method in which the transmitting and receiving coils are resonated by adding capacitances to them, whereas high-Q resonant coupling is a method in which the added coils are resonated by placing the coils and capacitances in the vicinity of transmitting and receiving coils.

Although previous studies analyzed inter-coil distances of up to 100 cm (the communication range for IBC), their transmitting and receiving coils were linearly arranged in parallel on both arms. This study analyzed a more practical situation, in which the transmitting coil was placed on the chest in such a way that the direction of both transmitting and receiving coils would be at right angles. The items that had to be analyzed were the signal transmission loss characteristic, biosafety criteria (internal electric field intensity and localized specific absorption rate (SAR)) based on the international commission on non-ionizing radiation protection, and transmitting and receiving power efficiency.

2. Three-dimensional finite element modeling of a human upper body

Figure 1 illustrates the circuit-coupled FEM models, which are designed using COMSOL 5.5 software. The models mainly consist of air, an upper body, and transmitter and receiver circuits. The model in Fig. 1(a) is used for non-resonant and low-Q resonant couplings, whereas the model in Fig. 1(b) is used for high-Q resonant coupling. Coil 1 and coil 4 denote the transmitting and receiving coils, respectively, whereas, coil 2 and coil 3 represent the resonance coils for high-Q resonant coupling. The turn number of coil 1 and coil 4 was set to 1, whereas it was set to 2.5 for coil 2 and coil 3. The transmitter and receiver circuits (except for the coils) were incorporated as the electric circuit elements.

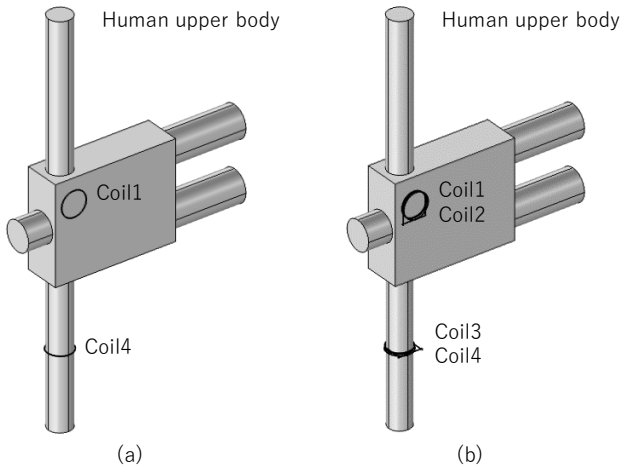

Figure 1. Three-dimensional FEM of a human upper body.

3. Computer simulation

3.1. Simulation conditions

The signal loss quantity for each coupling method was evaluated at several inter-coil distances. For both non-resonant and low-Q resonant couplings, the distance between coil 1 and coil 4 was set to 40, 50, and 60 cm (Fig. 1(a)). For high-Q resonant coupling, the distance between coil 2 and coil 3 was set to the same previous values, and coil 1 and coil 4 were arranged in closer proximity to coil 2 and coil 3, respectively (Fig. 1(b)). The variable range of the measurement frequency was approximately 300 kHz– 10 MHz and the resonant frequency was set to 2 MHz. The internal electric field intensity, localized SAR, and transmitting and receiving power were computed at an inter-coil distance of 60 cm, and the internal electric field intensity and localized SAR were compared to the basic restrictions for public exposure.

3.2. Signal transmission loss frequency characteristic

The signal loss frequency characteristics at each inter-coil distance is depicted in Fig. 2. Frequency characteristics showed the same tendency as they did in the previous results [3]. In short, for non-resonant coupling, the signal loss quantity at each inter-coil distance was minimum at $2-3$ MHz; whereas, for low-Q and high-Q resonant couplings it was respectively improved by 10 and 20 dB at the resonant frequency. Compared to the previous results [3] on condition that the transmitter and receiver coils were linearly arranged in parallel on both arms, the signal loss quantity at the same inter coil distance was approximately $12-13$ dB worse for each coupling method.

3.3. Internal electric field intensity and localized SAR characteristics

The maximum values of the internal electric field intensity and localized SAR for each coupling method at an inter-coil distance of 60 cm is depicted in Fig. 3. The maximum values of both criteria were the largest for high-Q resonant coupling compared to those of other couplings at a resonant frequency of 2 MHz. The maximum values of both criteria were 1 V/m and 0.001 W/kg, respectively, and as before [3], they were two or four orders of magnitude smaller than the basic restrictions for general public exposure: $1.35 \times 10^{\wedge 4} f$ V/m and 2 W/kg, respectively. This indicated that biosafety was sufficiently high even though the coil was placed on the chest.

3.4. Transmitting and receiving power characteristics

The transmitting and receiving power characteristics at an inter-coil distance of 60 cm are depicted in Fig. 4. As shown in Fig. 4(a), the transmitting power for non-resonant coupling decreased as the frequency increased. On the other hand, the transmitting powers for low-Q and high-Q resonant couplings were minimum at the resonant frequency, and these values were relatively smaller than those for non-resonant coupling (2.5 % and 4 %). As shown in Fig. 4(b), the receiving powers for low-Q and high-Q resonant couplings showed nearly opposite characteristics, and these values were relatively larger than those for non-resonant coupling (12 times and 200 times). This indicated that low-Q and high-Q resonant couplings had higher power efficiencies than non-resonant coupling.

References

[1] M. Seyedi, B. Kibret, D. T. H. Lai and M. Faulkner: A survey on intrabody communications for body area network applications, *IEEE Trans. Biomed. Eng.*, 60:8 (2013), 2067-2079.

[2] J. park, P. Mercier: Magnetic human body communication, *EMBC2015*, (2015), 1841-1843.

[3] K. Ito: Signal transmission characteristic and biosafety evaluation on magnetically coupled intra-body communication, *JSST2019 Oral*, (2019), 178-181.

[4] Y. M. Gao, H. f. Zhang, et al.: Electrical exposure analysis of galvanic-coupled intra-body communication based on the empirical arm models, *BioMed Eng OnLine*, 17:71 (2018).

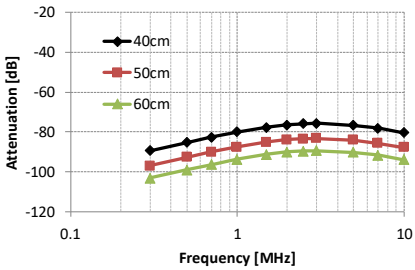

(a) Non-resonant coupling

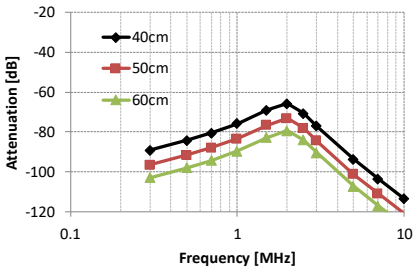

(b) Low-Q resonant coupling

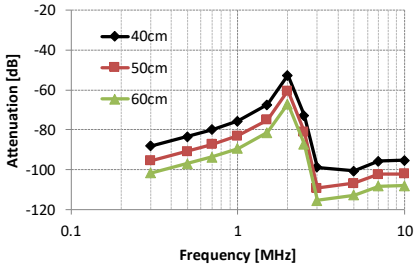

(c) High-Q resonant coupling

Figure 2. Signal loss frequency characteristics.

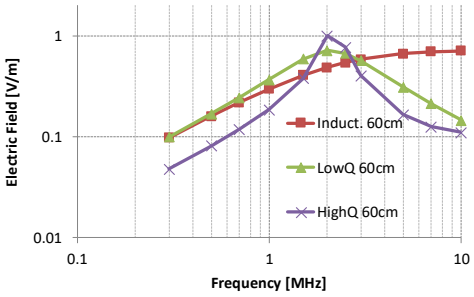

(a) Internal electric field intensity

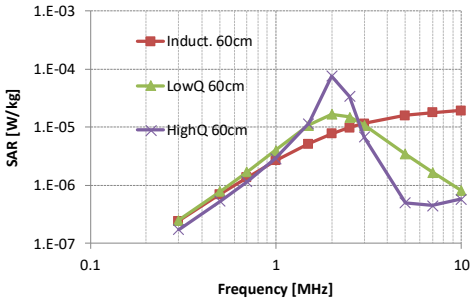

(b) Localized SAR

Figure 3. Internal electric field intensity and localized SAR characteristics.

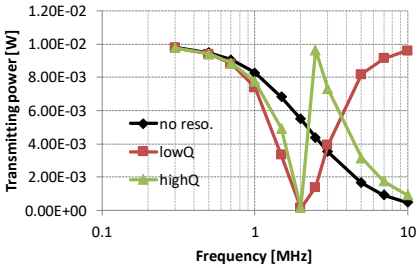

(a) Transmitting power

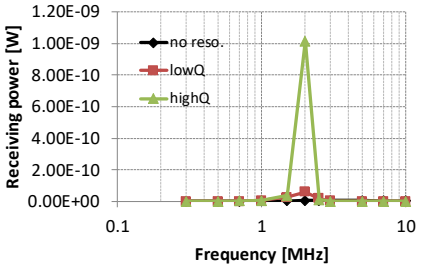

(b) Receiving power

Figure 4. Transmitting and receiving power characteristics.

JSST 2021

Excitation of Metal Plate Using Folded Dipole Antenna

Takumi Nishime*, Hiroshi Hashiguchi , Naobumi Michishita , Hisashi Morishita

Graduate School of Science and Engineering, National Defense Academy

*ed21001@nda.ac.jp

The full paper of this paper has been published in Journal of Advanced Simulation in Science and Engineering (JASSE).

DOI: https://doi.org/10.15748/jasse.9.128

Development of hydrogen recycling model on carbon divertor by molecular dynamics simulation

Yuki Kojima [1], Hiroaki Nakamura [2,3], Keiji Sawada [4], Gakushi Kawamura[2,5], Masahiro Kobayashi [2,5], Masahiro Hasuo [6], Masato Iida [1], Mayuko Miura [1], Seiki Saito [1*]

[1] Department of Information and Electronics, Faculty of Engineering, Yamagata University

[2] Department of Helical Plasma Research, National Institude for Fusion Science

[3] Department of Electrical Engineering, Graduate School of Engineering, Nagoya University

[4] Department of Material System Engineering, Faculty of Engineering, Shinsyu University

[5] Department of Fusion Science, Physical Sciences Research Section, The Graduate University for Adcanced Studies

[6] Department of Mechanical Engineering and Science, Graduate School of Engineering, Kyoto University

*saitos@yz.yzmagata-u.ac.jp

Abstract.

We develop a hydrogen recycling model on carbon divertor by molecular dynamics simulation. In this model, neumerical simulation of one hydrogen atom injection into a carbon material is performed. NVE ensemble is adapted for calculation of motion of atoms in the center of the carbon material. As a result, the hydrogen molecules in relatively high state is observed.

Keywords: Molecular dynamics simulation, Recycling, Neuclear fusion.

1. Introduction

Plasma facing materials are bombarded by hydrogen plasma in magnetic confinement plasma devices such as Large Helical Device (LHD) in National Institute for Fusion Science, Japan. In the case of LHD, the divertor which directly contacts to plasma is made of carbon materials. When the divertor plates are irradiated by hydrogen ions, some hydrogen atoms reflect and back to the plasma while the other hydrogen atoms retain in the divertor. The investigation of this recycling of hydrogen ions at the divertor is an important issue because this recycled hydrogen atoms or molecules affects the plasma parameter by the charge exchange recombination and dissociative recombination. Therefore, in order to obtaine information of recycled hydrogen atoms and molecules on the divertor, we developed a hydrogen recycling model [1-4] by molecular dynamics (MD) simulation of a hydrogen atom injection into a carbon material is

performed to investigate the distribution of the rovibrational states, translational energy and emission angle of emitted hydrogen molecules in addition to atoms.

2. Simulation Model [1, 2]

A carbon amorphous structure consisting of 3872 carbon atoms and 2080 hydrogen atoms shown in Fig. 1 is prepared for the target material. The size of the target material is 40Å ×40Å ×30Å. The unit structure is determined by two steps as follows: an amorphous carbon structure which containing excess hydrogen atoms is prepared; excess hydrogen atoms are removed by annealing the structure in Langevin thermostat using Molecular Dynamics (MD) simulations to creat stable structure. The density of carbon atoms are fixed at density which is determined by another MD simulation by depositing carbon atoms on a diamond substrate. The initial material temparture is set to 300K. Brenner's potential is employed for the interatomic potential between carbon and hydrogen atoms. One hydrogen atom is injected into the target material with incident energy 100 eV. The incident angle is set to parallel to *z*-axis. The *x* and *y*-coordinates of the starting position of the incident hydrogen atom are set randomly in the range of -5Å<x<5Å, -5Å<y<5Å as shown in Fig. 2. The simulation time is set to 50 ps. Angular and energy distridutions of recycled and reflected hydrogen atoms are calculated. The atomic motions are solved under the NVE ensemble where the number of particles (N), volume (V), and total energy (E) are conserved. To obtain statistical data, 1500 simulations are performed for the same condition with changing the *x* and *y*-coordinates of the incident positions by random numbers. The thermostat is attached the edge hatched region in Fig. 2.

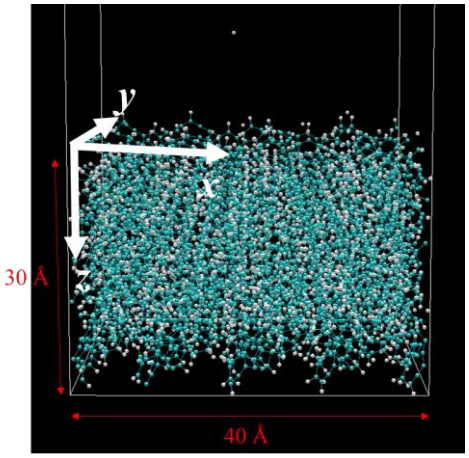

Fig. 1: Simulation system.

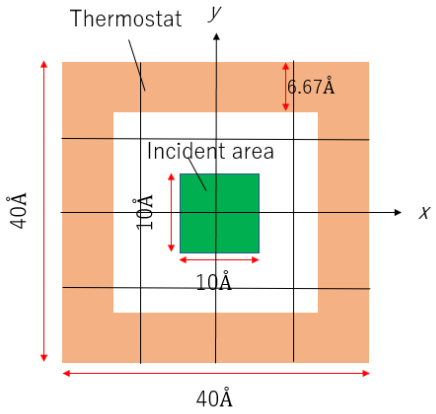

Fig. 2: Surface of the target material.

3. Simulation Result [1]

Figure 3 shows the distriburion of rotational state *J* of emitted hydrogen molecules. It is found that the hydrogen molecules in relatively high state exist. We would like to discuss the results in detail at the presentation. Please refer the reference [1] for the results of vibrational states of emitted hydrogen molecules.

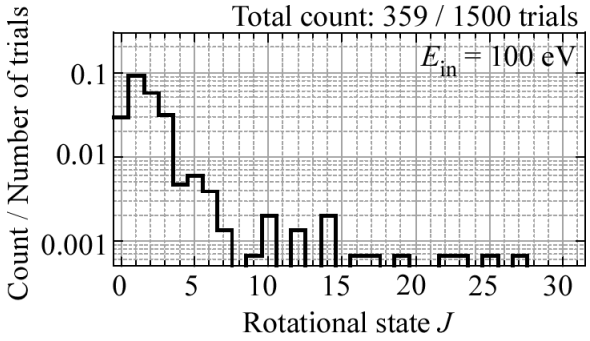

Fig. 3: Distribution of rotational state *J*.

Reference

[1] Seiki Saito, Hiroaki Nakamura, Keiji Sawada, Gakushi Kawamura, Masahiro Kobayashi, Masahiro Hasuo: Molecular dynamics simulation model of hydrogen recycling on carbon divertor for neutral transport analysis in large helical device, *Contribution to Plasma Physics*, e201900152 (2020).

[2] S. Saito, H. Nakamura, K. Sawada, G. Kawamura, M. Kobayashi, and M. Hasuo: Development of a Molecular Dynamics Method with Heat Transfer into Bulk for Ion Injection into Materials, *Plasma Fusion Res*, 15:2403073 (2020).

[3] K. Sawada, H. Nakamura, S. Saito, G. Kawamura, M. Kobayashi, K. Haga, T. Sawada, and M. Hasuo: Neutral transport code for rovibrational population calculation of molecular hydrogen in large helical device plasmas, *Contrib. Plasma Phys*, 60:e201900153 (2020).

[4] Seiki Saito, Hiroaki Nakamura, Keiji Sawada, Masahiro Kobayashi, Gakushi Kawamura, Masahiro Hasuo: Molecular dynamics simulation for hydrogen recycling on tungsten divertor for neutral transport analysis, *Japanese Journal of Applied Physics,* SAAB08 (2021), SAA08-1 – SAA08-11.

Investigation of hydrogen recycling process on tungsten divertor

Seiki Saito [1], Mayuko Miura [1], Hiroaki Nakamura [2,3], Keiji Sawada [4], Gakushi Kawamura[2,5], Masahiro Kobayashi [2,5], Masahiro Hasuo [6]

[1] Department of Information and Electronics, Faculty of Engineering, Yamagata University

[2] Department of Helical Plasma Research, National Institude for Fusion Science

[3] Department of Electrical Engineering, Graduate School of Engineering, Nagoya University

[4] Department of Material System Engineering, Faculty of Engineering, Shinsyu University

[5] Department of Fusion Science, Physical Sciences Research Section, The Graduate University for Adcanced Studies

[6] Department of Mechanical Engineering and Science, Graduate School of Engineering, Kyoto University

*saitos@yz.yzmagata-u.ac.jp

Abstract.

We develop a hydrogen recycling model on carbon divertor by molecular dynamics simulation. In this model, neumerical simulation of one hydrogen atom injection into a carbon material is performed. NVE ensemble is adapted for calculation of motion of atoms in the center of the carbon material. As a result, the hydrogen molecules in relatively high state is observed.

Keywords: Molecular dynamics simulation, Recycling, Neuclear fusion.

1. Introduction

Tungsten divertor is exposed by hydrogen plasma in nuclear fusion device such as ITER. Some hydrogen ions are recycled at the divertor. The recycled hydrogen atoms and molecules affect the plasma parameter of core plasma by the variety of reactions such as excitation, ionization, recombination, and dissociation caused during their transportation in the edge plasma.

The transport of hydrogen atoms and molecules emitted from the wall can be calculated by the neutral transport code [1]. For the boundary condition of the calculation, the emission angle and energy distribution are necessary. Moreover, the reaction rate of molecular assisted recombination (MAR) depends on the rotational and vibrational energies of hydrogen molecules. Therefore, the distributions of rotational and vibrational energies are also necessary for the calculation.

In this study, therefore, molecular dynamics (MD) simulation model [2-4] of hydrogen recycling at tungsten divertor is developed to analize the recycling process in atomic scale.

2. Simulation Model and Results

Figure 1 (a) shows the system of our MD simulation. Hydrogen-containing bcc tungsten

structure is prepared as a target material. One hydrogen atom is injected into the target material with the incident energy of 100 eV. For the interaction between hydrogen and tungsten atoms, an EAM potential is employed.

The simulation results show the number of emitted hydrogen molecules increases as the ratio of the number of hydrogen and tungsten atoms (H/W) in the material increases, although the H/W dependence of the number of emitted hydrogen atoms is not significant in the range of our simulation $0.49 < H/W < 1.37$. The analysis reveals that the hydrogen atom travels on the surface of the tungsten material and remains there for a while because it is trapped on the surface of the tungsten material as shown in Fig. 1 (b).

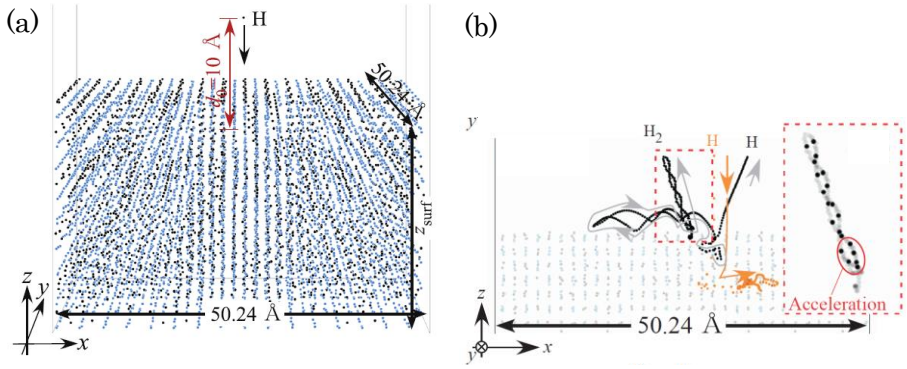

Fig. 1 (a) MD model of hydrogen recycling on tungsten wall. Black and blue balls denote hydrogen and tungsten atoms respectively. (b) An example of formation process of hydrogen molecules at the tungsten wall. [4] (Copyright: The Japan Society of Applied Physics)

Reference

[1] K. Sawada, H. Nakamura, S. Saito, G. Kawamura, M. Kobayashi, K. Haga, T. Sawada, M. Hasuo: Neutral transport code for rovibrational population calculation of molecular hydrogen in large helical device plasmas, *Contrib. Plasma Phys*, 60:e201900153 (2020).

[2] S. Saito, H. Nakamura, K. Sawada, G. Kawamura, M. Kobayashi, M. Hasuo: Molecular dynamics simulation model of hydrogen recycling on carbon divertor for neutral transport analysis in large helical device, *Contrib. Plasma Phys*, 60:e201900152 (2020).

[3] S. Saito, H. Nakamura, K. Sawada, G. Kawamura, M. Kobayashi, M. Hasuo: Development of a Molecular Dynamics Method with Heat Transfer into Bulk for Ion Injection into Materials, *Plasma Fusion Res*, 15:2403073 (2020).

[4] S. Saito, H. Nakamura, K. Sawada, G. Kawamura, M. Kobayashi, T. Sawada, M. Hasuo: Molecular dynamics simulation for hydrogen recycling on tungsten divertor for neutral transport analysis, *Jpn. J. Appl. Phys.* 60 SAAB08 (2020).

JSST 2021

Interaction of optical vortex and matter systems: from microscopic to macroscopic regimes and linkage between them

Hajime Ishihara[1,*]

[1]Department of Materials Engineering Science, Osaka University

[*]ishi@mp.es.osaka-u.ac.jp

Abstract. Characteristic features of optical vortices are its unique spatial structures and orbital angular momentum (OAM). Typical applications of the former are those to achieve spatial resolution beyond normal diffraction limits. The latter aspect manifests as OAM transfer from light to matter systems. In the OAM transfer, the microscopic light-matter interaction causes macroscopic motions of matter systems. Thus, the macroscopic and microscopic degrees of freedom are sometimes linked to each other in a unique manner via linear and nonlinear optical responses. In this talk, characteristic effects of the optical vortex are discussed showing some theoretical studies of light-matter interaction.

Keywords: Optical vortex, Optical manipulation, Chiral interaction, Chiral helimagnet

1. Introduction

The emergence of optical vortices has greatly widened the light-matter interaction scheme and promoted our understanding of chirality-related interactions. One of the characteristic features of the optical vortex is its unique spatial structure. The field intensity is low near the singularity in the center of the beam, and the span length of this area is shorter than the light wavelength. This feature is used in various applications to achieve spatial resolution beyond normal diffraction limits. More importantly, the optical vortex has orbital angular momentum (OAM), which is the origin of a variety of light-matter interactions. OAM of the optical vortex is transferred to the matter system through their microscopic interaction. In this talk, we introduce the theoretical proposal of super-resolution trapping of nanoparticles as an example of a study using the former feature of the optical vortex. As the latter issue, some transfer schemes of OAM are presented with discussing their macroscopic and microscopic aspects. Presented examples show some kinds of linkage between microscopic and macroscopic degrees of freedom through the OAM transfer by the optical vortex.

2. Super-resolution trapping of nanoparticles

Flexible optical manipulation of nanoparticles is now still challenging. A strategy to realize it is to use a light frequency that is resonant with a transition energy between the electronic levels quantized in nanostructures. Such resonance processes often cause a nonlinear optical effect. We have revealed that the attractive force near the metallic nanogaps becomes inverted when the optical nonlinearity is strong. This phenomenon can be used to realize super-resolution trapping of nanoparticles [1][2]. If we irradiate nanoparticles trapped at nanogap array with the usual Gaussian beam and optical vortex beam simultaneously, particles at the overlapped area of two beams are repulsed due to the force inversion, and only those around the beam center are kept trapped (Fig. 1). Thus, the trapping area of the particles becomes very narrow beyond the diffraction limit, which has a good analogy with STED microscope [4] based on the unique spatial structure of the optical vortex.

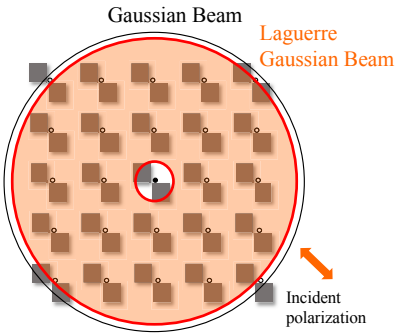

Figure 1: Schematic image of the super-resolution trapping. Nanoparticles at the overlapped area of the optical vortex and Gaussian beam are repulsed due to the force inversion, and only those around the beam center are kept trapped.

3. OAM transfer to matter system: macroscopic and microscopic aspects

A typical phenomenon caused by OAM transfer is the rotational manipulation of absorptive micro-particles [3]. This effect is understood as macroscopic OAM transfer through the microscopic photon absorption processes.

If nanoparticles are rotated by the electronic resonance, more elaborate roles of microscopic electronic transition are clearly seen. Figure 2 shows the results of theoretical demonstrations of nanoparticle rotation. We assumed the aggregated three-level molecules as nanoparticles. The irradiation of the optical vortex with a frequency resonant with $1 \rightarrow 2$ transition induces the rotation of nanoparticles. Interestingly, if the particles are irradiated with another beam for pumping to make occupation probability of the level 2

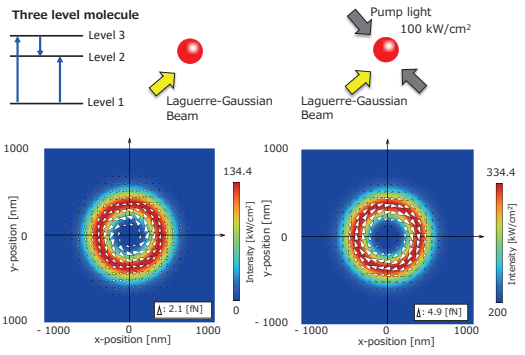

Figure 2: The three-level molecular aggregate (see inset) is rotated by an optical vortex. If the aggregated particle is pumped and the occupation probability of the level 2 becomes over 0.5, the rotation direction becomes inverted.

above 0.5, a stimulated emission occurs, and the rotational direction becomes inverted (Fig. 2)[5]. This indicates that nonlinear optical processes based on the quantum mechanical properties affect macroscopic OAM transfer. Thus, microscopic and macroscopic degrees of freedom of motion are linked to each other in a unique manner through OAM transfer.

The other example of OAM transfer is also associated with microscopic electronic transitions. Photons with OAM can change the optical selection rule of electronic transitions from the standard one. This effect causes novel types of spin-spin interactions and induces peculiar spin textures in solid states. In particular, we have demonstrated that this effect leads to modulation of the chiral magnetic order to the unconventional phase structure[6]. This is an interesting example of microscopic OAM transfer that produces unconventional macroscopic spin structures.

References

[1] M. Hoshina, N. Yokoshi, H. Okamoto and H. Ishihara, "Super-Resolution Trapping: A Nanoparticle Manipulation Using Nonlinear Optical Response", ACS Photonics **5**, 318–323 (2018)

[2] H. Ishihara, "Optical manipulation of nanoscale materials by linear and nonlinear resonant optical responses", Adv. in Phys.: X, **6**, 1885991 (2021)

[3] H. He, M. E. J. Friese, N. R. Heckenberg, and H. Rubinsztein-Dunlop, "Direct observation of transfer of angular momentum to absorptive particles from a laser beam with a phase singularity", Phys. Rev. Lett. **75**, 826–829 (1995).

[4] S. W. Hell and J. Wichmann, "Breaking the diffraction resolution limit by stimulated emission: stimulated-emission-depletion fluorescence microscopy", Opt. Lett. **19**, 780–782 (1994)

[5] M. Hoshina, N. Yokoshi and H. Ishihara, "Nanoscale rotational optical manipulation", Opt. Exp. **28**, 14980–14994 (2020)

[6] Y. Goto, H. Ishihara and N. Yokoshi, "Twisted light-induced spin–spin interaction in a chiral helimagnet", New J. Phys. **23**, 053004 (2021)

Improvement of Visibility in Feature Emphasis Visualization of 3D Measured Point Cloud

Mizuki Katahira[1*], Kyoko Hasegawa[2*], Liang Li[2*], Satoshi Tanaka[2*]

[1]Graduate School of Information Science & Engineering, Ritsumeikan University
[2]College of Information Science & Engineering, Ritsumeikan University

*is0349ve@ed.ritsumei.ac.jp

Abstract. In recent years, the development of laser measurement technology has made it possible to measure a variety of objects without any physical contact. The laser measured data are large 3D point clouds, and many of them contain complex structures in detail. In order to accurately visualize objects with complex structures, it is necessary to visualize the internal and external structures simultaneously. Therefore, in this paper, we propose a method that combines " transparent visualization," which can visualize both internal and external structures simultaneously, and "feature enhancement visualization," which improves visibility. In our method, feature-enhanced visualization compensates for the decrease in visibility caused by the increase in the amount of information, which is a drawback of transparent visualization, and 3D visualization results can be displayed more clearly. In addition, the effectiveness of the proposed method is verified by visualizing using actual 3D measurement point clouds.

Keywords: Transparent visualization, Laser-scanned large-scale point cloud, Feature extraction

1. Introduction

The development of laser measurement technology has made it possible to measure various objects, such as historically important buildings and historical documents, without directly touching the objects. This has led to more active digital archiving of cultural assets. The data obtained by laser measurement is a large 3D measurement point cloud, which often has a complex internal and external structure. When both internal and external structures are presented, the complexity of the 3D structure becomes more pronounced. In the past, stochastic point-based rendering (SPBR) [1, 2], a rendering method using a stochastic algorithm, was used for visualization, but the problem was the blurring of the shape due to the decrease in opacity. To solve this problem, we used feature-enhanced visualization, which emphasizes the edges of the object. Using feature-enhanced visualization, we can improve the visibility of the target object, which has been a problem in visualization using SPBR. However, in conventional

feature-enhanced visualization, the visibility of the original point cloud is sometimes degraded by overemphasizing the 3D edges. In this paper, we propose a method to improve the overall visibility of the object by transparently visualize the original point cloud and emphysising the 3D edge region at the same time.

2. Highlighting of feature region based on curvature

In this research, we use principal component analysis (PCA) to extract feature regions. This algorithm of extracting feature regions is as follows:

1. Perform PCA on the coordinate values of the 3D point cloud in the sphere of optional radius r centered on the point $P^{(i)}$. r is a parameter determined by the user.
2. Calculate eigenvalues($\lambda_1 \geq \lambda_2 \geq \lambda_3$) from the covariance matrix obtained by PCA.
3. Caluculate feature value $F^{(i)}$ by combining the eigenvalues.
4. Emphasize points with $F^{(i)}$ greater than a threshold t. t is a parameter determined by the user.

Feature value $F^{(i)}$ is calculated as follows [3]:

$$F^{(i)} = \frac{\lambda_3}{\lambda_1 + \lambda_2 + \lambda_3} \quad (1)$$

In our method, feature extraction and enhancement are the same as the conventional method, but the visualization method is different. In the conventional method, the entire point cloud is used as the visualization target, and the points of the feature extracted by the above method are highlighted by changing the color of the points. However, the emphasis is too conspicuous and spoils the visibility of the original point cloud. On the other hand, the proposed method visualizes both the entire point cloud and the point cloud from which the feature parts are extracted. This means that the color of the point cloud to be emphasized is a fusion of the conventional emphasized color and the color of the original point cloud. In the feature regions, two points are visualized simultaneously, one from the original point data and one from the feature point data. Therefore, we can emphasize the point cloud with a color close to the color of the original point cloud and solve the visibility problem.

3. Experimental results

In this section, we demonstrate the effectiveness of our proposed method by reporting the results of case studies performed on the data of Kyoto Women's University. Fig. 1(a) shows the visualization results with highlighting feature regions by the conventional method, in which red points are feature regions. On the other side, in Fig. 1(b), the visibility of the original point clouds has been improved by merging the emphasis color with the color of the original point clouds. In both results, feature emphasis visualization improves the visibility which was the problem of transparent visualization. In the case of Fig. 1(a), only one point

cloud is drawn in the feature regions, and the emphasis color is too conspicuous, so the visibility of the original point cloud is reduced by transparent visualization. In the case of Fig. 1(b), the visibility of the original point cloud is improved because both the original and the feature point clouds are drawn simultaneously in the feature region.

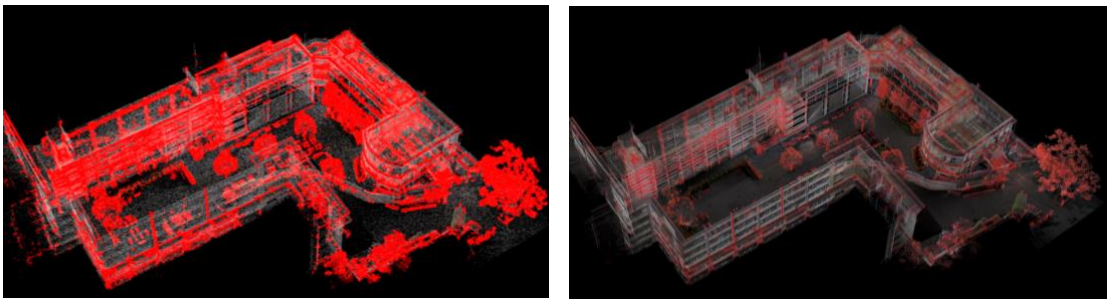

(a) Visualization result of the conventional method[3] (b) Visualization result of the proposal method

Figure 1: Visualization results with highlighting feature regions on the point cloud data of Kyoto Women's University.

4. Conclusion

In this paper, we proposed a method for feature enhancement visualization in transparent visualization using stochastic point-based rendering. Using the proposed method, we were able to improve the visibility of both the original point cloud and the 3D edge region.

References

[1] S. Tanaka, K. Hasegawa, N. Okamoto, R. Umegaki, S. Wang, M. Uemura, A. Okamoto, and K. Koyamada: See-Through Imaging of Laser-scanned 3D Cultural Heritage Objects based on Stochastic Rendering of Large-Scale Point Clouds, ISPRS Ann. Photogramm. Remote Sens. Spatial Inf. Sci., III-5, pp. 73-80, 2016.

[2] Tomomasa Uchida, Kyoko Hasegawa, Liang Li, Motoaki Adachi, Hiroshi Yamaguchi, Fadjar I. Thufail, Sugeng Riyanto, Atsushi Okamoto, Satoshi Tanaka: Noise-robust transparent visualization of large-scale point clouds acquired by laser scanning, ISPRS Journal of Photogrammetry and Remote Sensing, vol. 161, pp.124-134, March 2020.

[3] Martin Weinmann, Boris Jutzi, Cle´ment Mallet: Semantic 3D scene interpretation: A framework combining optimal neighborhood size selection with relevant features, ISPRS Ann. Photogramm. Remote Sens. Spatial Inf. Sci., II-5/W2 (2013), 313–318.

Improving Depth Perception of Transparent Objects in Stereoscopic Vision using Ambient Occlusion

Kota KATAOKA[1*], Yuichi SAKANO[2], Naohisa SAKAMOTO[3]

Kyoko HASEGAWA[4], Liang LI[4], Satoshi TANAKA[4]

[1]Graduate School of Information Science and Engineering, Ritsumeikan University
[2] National Institute of Information and Communications Technology: NICT
[3] College of Engineering, Kobe University
[4]College of Information Science and Engineering, Ritsumeikan University

*is0349er@ed.ritsumei.ac.jp

Abstract. We utilize transparent visualization that allows better visibility of the internal structure of 3D data in stereoscopic vision. Transparent visualization is expected to make it possible to perceive the object structure more intuitively, even for complex solids. However, when 3D data are rendered transparently, the depth cues change and the positional relationship becomes ambiguous. This paper investigates the effect on depth perception of combining transparent stereoscopic vision and ambient occlusion, which has high depth representation capability, to improve transparent stereoscopic depth perception. Ten participants were asked to evaluate the distance of an object from a reference point. The experimental results confirmed that depth perception was improved by combining two types of depth cues, binocular disparity and ambient occlusion.

Keywords: Ambient occlusion, Autostereoscopic, Transparent visualization

1. Introduction

In the field of cultural assets and medical care, 3D data visualization has been actively performed. To understand the internal structure of complex 3D data, transparent visualization is used, which can visualize the appearance and internal structure simultaneosly. However, it is difficult to perceive 3D information correctly when using transparent visualization, and it is known that depth is often under estimated. Humans use various imformation to perceive depth, and it is necessary to provide more depth cues to achieve accurate depth perception. One of these depth cues is the perception of shape-from-shading. When estimating depth from shading, the human visual system is considered to have two assumptions: “light-from-above,” which assumes a sole light source and recognizes depth from shading, and “dark-is-deep,” which recognizes dark areas as deep. In addition, it is known that we perceive depth by switching between these two assumptions depending on the situation[1]. In this study, we examine how to

make the perceived depth closer to the actual depth by providing information on the perception of depth shape by shading using ambient occlusion (AO) for transparent stereopsis.

2. Ambient Occlusion

In this study, we use screen-space AO to provide shading. The algorithm to calculate the shading rate of the ambient occlusion is as follows [2]:

1. Generate N_s sampling points randomly in a sphere of arbitrary radius r centered at point P according to the following equation (1). In equation (1), x, y and z are the coordinates of the sampling point, u, v, and w are uniform random numbers with ranges of $[0,\ 1]$, $[-1,\ 1]$, and $[0,\ 1]$, R is a sampling radius.

$$\begin{cases} x = r\sqrt{1-v^2}\cos(2\pi u) \\ y = r\sqrt{1-v^2}\cos(2\pi u) \end{cases} \qquad (1)$$
$$z = vr$$
$$r = wR$$

2. Compare the depth values at the sampling points in the screen space with the depth values at the points in the data, and count the number of sampling points N_p that are smaller than the depth value.

3. The ambient light coefficient *occlusion* is calculated as shown in equation (2) below.

$$occlusion = \frac{N_p \times 2}{N_s} \qquad (2)$$

3. Experimental results

In this section, the effectiveness of AO is shown in an experiment to verify the depth obtained from images with and without AO displayed on a naked-eye 3D display. Surface data with depressed square weights were used for the experiment. Figures 1(a) and 1(b) are images without AO applied, showing depressions with small depth and large depth, respectively. The light source located slightly to the upper left casts a shadow on the image to the extent that the shape of the depression of the square can be recognized. Figures 1(c) and 1(d) show images with AO applied, showing small and large depth depressions, respectively. Here, in addition to the shadows described above, shadows are cast on the center and the tip of the depression by AO. A light shadow is cast when the depression is small, and a dark shadow is cast when the depression is large. As a result of the dark-is-deep property, Figs. 1(c) and 1(d) show greater depth than Figures. 1(a) and 1(b) where AO is not applied.

4. Conclusion

In this paper, we proposed a depth enhancement method using AO to make the perceived depth in transparent stereopsis closer to the actual depth. This proposed method enables more accurate depth perception in transparent stereopsis.

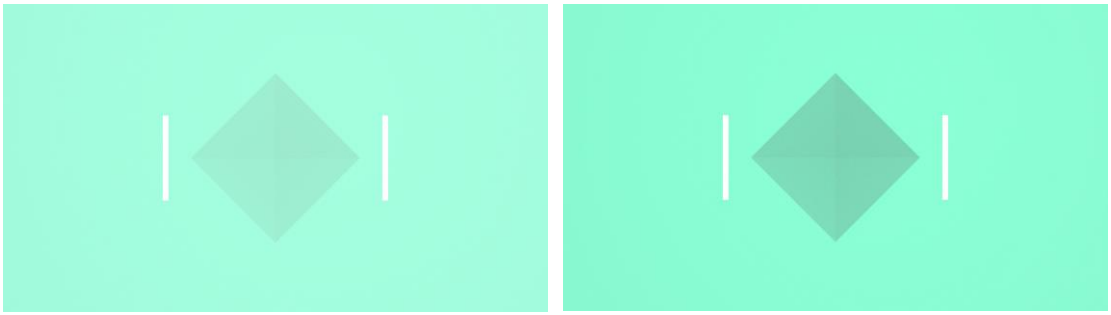

(a) without ambient occlusion, depth = 1.0 (b) without ambient occlusion, depth = 2.5

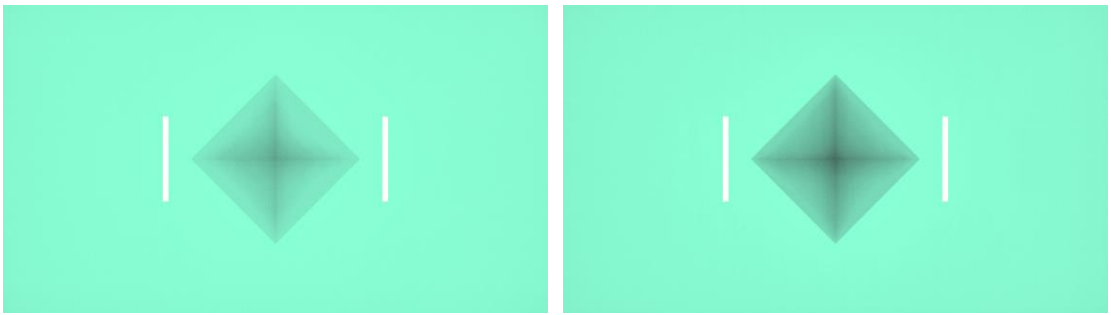

(c) with ambient occlusion, depth = 1.0 (d) with ambient occlusion, depth = 2.5

Figure 1: Visualization results of transparent objects using ambient occlusion, $\alpha = 0.9$.

References

[1] Sakano,Y.: Quantitative evaluation of perceived depth of transparently-visualized medical 3D data presented with a multi-view 3D display, *International Journal of Modeling, Simulation, and Scientific Computing* Vol. 09, No. 03, 1840009 (2018).

[2] Fujita,Y.,Sakamoto,N.: Ambient occlusion for semitransparent streamlines with stochastic rendering technique, *The 2nd Visualization Workshop*, (2019).

Adaptive Opacity Control using Implicit Function for Visualizing Large-Scale 3D Measurement Point Clouds

Masaya Kishimoto[1*], Motoaki Adachi[2], Kyoko Hasegawa[3], Liang Li[3], Satoshi Tanaka[3]

[1]Graduate School of Information Science & Engineering, Ritsumeikan University
[2]Shrewd Sekkei Inc.
[3] College of Information Science & Engineering, Ritsumeikan University

*is0352rr@ed.ritsumei.ac.jp

Abstract. Stochastic point-based rendering (SPBR) is one of the methods for transparent visualization of 3D measurement point clouds, and it allows us to grasp the structure of the visualization target easily. However, the visibility of the structure is degraded when the internal structure is intricate because the spatial relationship becomes unclear. In this paper, we propose a method for easily grasping the internal structure and appearance of large-scale measurement point cloud data obtained by 3D measurement by adaptively controlling the opacity using a hyperquadric function. Using this method, we were able to visualize the internal structure and external shape with high resolution.

Keywords: Implicit function, Adaptive opacity control, Large-scale 3D measurement point cloud data

1. Introduction

Recent improvements in computer processing speed and the development of laser measurement technology have made it possible to store cultural properties as large-scale 3D measurement point cloud data. Stochastic point-based rendering (SPBR) has been shown to be useful as a visualization method for large-scale 3D point cloud data [1,2]. This visualization method is a method to realize transparent visualization of measured point cloud data according to the point density, and it is also a method to visualize the structure of buildings with high precision and accuracy [3]. Since the recorded points in a point cloud are often unevenly distributed, it is possible to achieve high-definition visualization by using Poisson disk sampling (PDS) [4] to make the point distribution of the point cloud uniform and then visualize it with SPBR. However, when the structure is complex, problems such as visibility reduction may occur due to the obscuration of the front-back relationship. This research aims to propose a method to adaptively

change the point density between the exterior and interior of a building in order to understand its structure. For this purpose, we use implicit functions to achieve non-uniform point densities that take into account the shape of the building. The proposed method makes it possible to improve the visibility of the interior structure and the exterior by controlling the opacity.

2. Non-uniform opacity control using hyperquadric functions

In SPBR, the density of the point cloud determines the uniform opacity. The number of points n required to achieve opacity α is:

$$n = \frac{\ln(1-\alpha)}{\ln(1-\frac{s}{S})} L_{\mathrm{R}}. \tag{1}$$

Here, s is the cross-sectional area of the point, S is the area of the great circle of the measurement sphere, and L_{R} is the parameter that adjusts the image quality. However, because generating new points in a measurement point cloud is complex in practice, its opacity is increased or decreased by copying the points to achieve the opacity. The rate of increase or decrease in the number of points r is calculated from the ratio of the total number of measurement points n_0 as follows:

$$r = \frac{n}{n_0}. \tag{2}$$

Therefore, in this study, we define a new non-uniform point increase/decrease rate by multiplying the point increase/decrease rate r by hyperquadric functions f in the implicit function according to the shape of the measured point cloud. If the $x, y,$ and z coordinates of the center point of the hyperquadric function in the point cloud are $x_{\mathrm{c}}, y_{\mathrm{c}},$ and z_{c}, respectively, and the radii of the $x, y,$ and z axes of the hyperquadric function to be set are $a, b,$ and c, respectively, then the hyperquadric function to be used is:

$$f(x,y,z) = \left(\frac{x-x_{\mathrm{c}}}{a}\right)^{\frac{2}{\varepsilon}} + \left(\frac{y-y_{\mathrm{c}}}{b}\right)^{\frac{2}{\varepsilon}} + \left(\frac{z-z_{\mathrm{c}}}{c}\right)^{\frac{2}{\varepsilon}} - 1. \tag{3}$$

In addition, in order to visualize the structure in an easy-to-understand manner, two types of visualization, one focusing on the internal structure and the other focusing on the external appearance, are used: the rate of increase/decrease r_{in} for focusing on the internal structure and the rate of increase/decrease r_{out} for focusing on the external appearance:

$$r_{\mathrm{in}} = f^d \frac{n}{n_0}, \tag{4}$$

$$r_{\mathrm{out}} = (1-f)^d \frac{n}{n_0}. \tag{5}$$

Here, d is a parameter that controls the changing rate of the increase or decrease. By changing the point density based on the position as described above, it is possible to achieve an opacity that depends on the shape of the function.

3. Experimental results

In this chapter, we show the results of using the proposed method on the measured point cloud data of a red brick warehouse in Maizuru City, Kyoto prefecture, and a factory. First, Figure 1

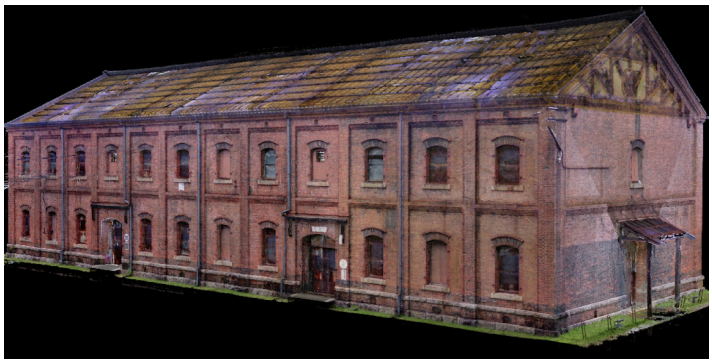

(a) The conventional method

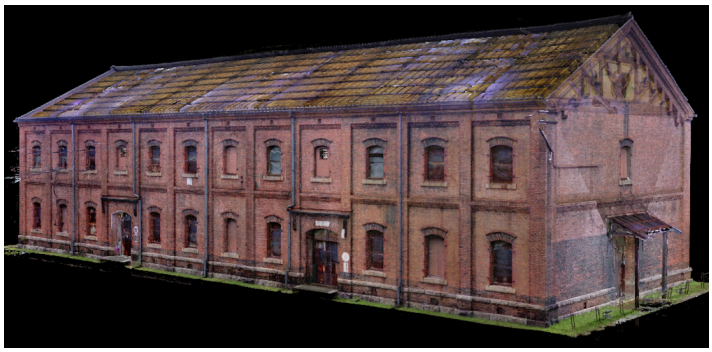

(b) The proposed method

Figure 1: Comparison of transparent visualization results in external appearance on the point cloud data of red brick warehouse. The values used are $\boldsymbol{L_R = 50}$, $\boldsymbol{\alpha = 0.8}$, $\boldsymbol{d}$ (on the roof area) $= \boldsymbol{30}$, and $\boldsymbol{d}$ (on the first and second floors) $= \boldsymbol{5}$.

shows the comparison between the conventional method and the proposed method for visualizing the external appearance of the red brick warehouse. Figure 1(a) shows the data visualized with the conventional uniform opacity and the total number of points is 755,531,703, while Figure 1(b) shows the data visualized with the newly set non-uniform opacity and the total number of points is 430,956,554. Comparing the results of Figure 1(a) and Figure 1(b), it can be seen that the appearance of the appearance-oriented visualization does not change much because the external appearance is emphasized even if both opacities are used, but the total number of points in Figure 1(b) using the proposed method is greatly reduced by outputting points only in the external appearance using non-uniform opacity.

Figure 2 shows the comparison between the conventional method and the proposed method for visualizing the internal structure of the point cloud data of the factory. In addition, when visualizing the internal structure of the building, we processed it so that the visibility of the internal structure of the building surrounded by the red circle in Figure 2(a) would be high. Figure 2(a) shows the visualization using the conventional method with uniform opacity, which shows that it is not easy to grasp the internal structure because it is blocked by the external appearance. On the other hand, Figure 2(b) was visualized using non-uniform opacity using equation (4), and the internal structure can be grasped because only the internal structure has a high point density. These results indicate that the method is useful for improving the visibility of the internal structure and the external appearance of the complex structure of the

visualization target in transparent visualization of 3D measurement point clouds.

References

[1] S. Tanaka, K. Hasegawa, N. Okamoto, R. Umegaki, S. Wang, M. Umemura, A. Okamoto, and K. Koyamada: *See- Through Imaging of Laser-scanned 3D Cultural Heritage Objects based on Stochastic Rendering of Large-Scale Point Clouds*, ISPRS Ann. Photogramm. Remote Sens. Spatial Inf. Sci., III-5, (2016) pp. 73-80.

[2] S. Tanaka, K. Hasegawa, Y. Shimokubo, T. Kaneko, T. Kawamura, S. Nakata, S. Ojima, N. Sakamoto, H. Tanaka, and K. Koyamada: *Particle-Based Transparent Rendering of Implicit Surfaces and its Application to Fused Visualization*, EuroVis 2012, (2012) pp. 25- 29.

[3] T. Uchida, K. Hasegawa, L. Li, M. Adachi, H. Yamaguchi, Fadjar I. Thufail, S. Riyanto, A. Okamoto, S. Tanaka: *Noise- robust transparent visualization of large-scale point clouds acquired by laser scanning,ISPRS Journal of Photogrammetry and Remote Sensing*, vol. 161, (2020) pp.124-134.

[4] T. Wang, U. Kiichi: *Stippling by Poisson Disk Sampling with Grayscale Ordering of Pixels*, The IEICE transactions on information and systems (Japasene edition), vol. 96(1), pp.262-265.

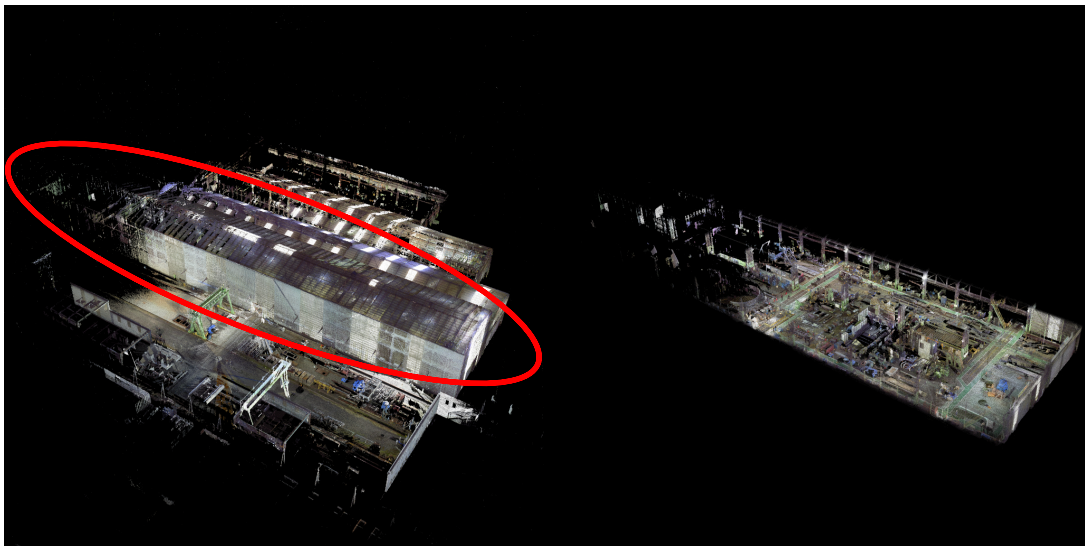

(a) The conventional method (b) The proposed method

Figure 2: Comparison of transparent visualization results in internal structure on the point cloud data of the factory. The values used are $\boldsymbol{L_R = 50}$, $\boldsymbol{\alpha = 0.8}$, and $\boldsymbol{d = 5}$.

Generation of X-ray vortices by Bragg reflection from crystals and microscopy to diagnose topological charge distribution

Yoshiki Kohmura[1*], Kei Sawada, Kenji Ohwada[2], Masaichiro Mizumaki[3], Tetsu Watanuki[2], Tetsuya Ishikawa[1]

[1]RIKEN SPring-8 Center

[2]National Institutes for Quantum and Radiological Science and Technology

[3]Japan Synchrotron Radiation Research Institute

*yoshiki.kohmura@riken.jp

Abstract. Two experiments were performed to generate X-ray vortices by the Bragg reflection from crystalline materials. We tried two kinds of crystals having completely different lattice planes. One is a perfect crystal with a depth distribution at surface which generated an X-ray vortex with a fixed topological charge regardless of X-ray energy as predicted by the past theory. The other has a staircase lattice plane with a truncated spiral dislocation which generated wave fields. We also demonstrated our novel method to diagnose the topological charge distribution of X-ray vortices by utilizing a Radial Hilbert Transform X-ray microscope.

Keywords: X-ray vortex formation, Bragg reflection by crystals, X-ray photonics

1. Introduction

As for the wave control at X-ray wavelength scale, we have verified the Berry phase theory that predicted the X-ray wave guiding effect by anomalous X-ray translation inside a deformed crystal [1-3]. These results imply that crystals with deformed atomic configurations will be potential basis for the near future X-ray photonics. In this talk, we will summarize our results on X-ray wave control using two different kinds of crystals, one with a modified surface depth distribution on a perfect crystal and the other with a defect on a lattice plane. Some progess on simulation studies, which takes into account of diffraction of x-rays, will be presented for the understanding of the X-ray properties in reflection.

2. Experimental Results for Generating X-ray Vortices using Bragg Reflection on crystals.

For generating X-ray vortices in the Bragg reflected wave, we have tried two crystals having completely different lattice planes. Experimental setup and result for each crystal are shown below.

As for the first crystal, lattice planes are perfectly periodic but the surface is deformed from the flat shape with a depth distribution. We will show that the X-ray wave fields having arbitrary and energy independent phase distribution can be generated by the Bragg reflection on the crystal, verifying the theory predicting that this phase is proportional to depth on crystal surface and lattice spacing. A two-beam interferometer with a plane reference wave clearly visualized X-ray vortices generated in the reflected wave downstream of a spiral phase plate on a silicon crystal. A fixed topological charge was observed from a fixed lattice plane regardless of X-ray energy. This result is a further development from the previous work that achieved the X-ray focusing using Bragg Fresnel zone plates [4]. Such energy tunable X-ray phase plates would be ideal for the future phase-shifting elements in white-light interferometers or Zernike phase-contrast microscopes. First note is that phase-shifting in visible white-light interferometers uses the translation of optical elements which is impossible in X-ray wavelength. Second note is that the phase shift by the transmissive optical element is inversely proportional to the X-ray energy and cannot be used for such an energy independent phase plate.

As for the second crystal, lattice planes having staircase structures known as the truncated spiral dislocations (TSDs) are used. TSDs are found ubiquitously in various industrial functional devices such as in silicon carbide (SiC) crystal. Dot like structures from TSDs were observed at the surfaces of the SiC crystal using the X-ray topography [5]. We here tried to diagnose the phase distribution after Bragg reflection from a SiC crystal. We performed a kinematical diffraction simulation indicating that X-ray vortices are generated on Bragg reflected X-rays from TSDs when the spatial coherence length of the irradiating X-rays is sufficiently large. A two-beam X-ray interferometry, with a plane reference wave and an object wave passing through the TSD area, was carried out which manifested a pair of fork patterns indicating that wave fields resembling X-ray vortices were generated with the topological charge of +1 or -1. We regard that this is a novel and promising technique for discriminating TSDs and their topological charges in functional devices. Our future research will increase the precision of such discrimination by measuring a very thin crystal containing TSDs with the thickness of 1 micrometer or so, comparable to or thinner than the extinction depth, to avoid the effect of multiple diffraction effects.

3. Experimental Results for Diagnosing Topological Charge Distribution of X-ray Vortices.

Next topic is on a diagnosis of the topological charge distribution of the X-ray vortices using Radial Hilbert Transform (RHT) X-ray Microscope. Our microscope used the Spiral Fresnel zone plate (SFZP) as the objective lens to modify the wave front downstream of objects and to add vorticity with the topological charge of $l = -1$ & $+1$ [6]. We also prepared a silicon demonstration specimen containing multiple spiral phase plates that transfers vorticity to the wave fields with the topological charge of $m = -1$ and $+1$. We successfully proved our theoretical finding that the vorticity cancellation occurs to form a bright spot in the microscope image when $l + m = 0$. RHT microscope enables us to sensitively derive the two-dimensional map of

X-ray vortices transferred from the spiral structures.

We plan to apply RHT microscope to observe X-ray vortices formed by Bragg refection from crystalline specimens. This research will help us to accelerate the evaluation of defects and thus improve the quality of the next-generation functional materials, such as semiconductor power devices, light-emitting devices and high-rigidity metals.

References

[1] K. Sawada, S. Murakami and N. Nagaosa: *Physical Review Letters*, **96** (2006), 154802-1-4.

[2] Y. Kohmura, K. Sawada and T. Ishikawa: *Physical Review Letters,* **104** (2010), 244801-1-4.

[3] Y. Kohmura, K. Sawada, S. Fukatsu and T. Ishikawa: *Physical Review Letters,* **110** (2013), 057402-1-4.

[4] V. V. Aristov, Yu. A. Basov, G. N. Kulipanov, V. F. Pindyurin, A. A.Snigirev and A. S. Sokolov: *Nucl. Instr. And Meth.* **A 274** (1989), 390-393.

[5] Y. Yamaguchi and H. Matsuhata: *J. Electron. Mater.* **39** (2010), 715-.

[6] Y. Kohmura, K. Sawada, K. Ohwada, M. Mizumaki, T. Watanuki, T. Ishikawa: *Optics Express*, **28, 16** (2020), 24115-24122.

Propagation properties of optical vortex in magnetized plasma

Toru I. Tsujimura[1,*] and Shin Kubo [2]

[1]National Institute for Fusion Science, National Institutes of Natural Sciences
[2]College of Engineering, Chubu University

[*]tsujimura.tohru@nifs.ac.jp

Abstract. The propagation properties of optical vortices with helical wavefronts in cold uniform magnetized plasmas in the electron cyclotron (EC) frequency range are investigated theoretically. The effects of helical wavefronts of vortex EC waves on the wavefield in magnetized plasma as an anisotropic medium are described. These effects become more prominent when the topological charge of the vortex EC wave becomes larger or the distance from the phase singularity becomes smaller. Different propagation properties were also observed in the propagation of a Laguerre-Gaussian beam in a three-dimensional simulation using the finite element method. These results suggest that optical vortices can be a new tool for heating high-density plasmas.

Keywords: Electron cyclotron wave, Optical vortex, Magnetized plasma, Laguerre-Gaussian beam

Radiofrequency (RF) waves are widely used for heating, current drive, and diagnostics in magnetically confined fusion plasmas. Knowing the propagation properties of RF waves in magnetized plasmas is fundamental for designing RF systems such as launch antennas. The propagation properties of RF waves conventionally originate from a plane wave, where the phase of the wavefields is assumed to be $\boldsymbol{k} \cdot \boldsymbol{r} - \omega t$. Here, $\boldsymbol{k}$, $\boldsymbol{r}$, ω, and t denote the wave vector, the position vector, the angular frequency, and time. Recently, it has been theoretically and experimentally shown that a single free electron in circular or spiral motion radiates twisted photons with orbital angular momentum (OAM) along the electron circulation axis in addition to spin angular momentum [1, 2]. It is found that the emitted wavefield has a phase term expressed as $l\varphi + k_z z - \omega t$, where l is the topological charge and φ is the azimuthal angle around the optical axis z. A wave with a helical wavefront is commonly called an optical vortex. Figure 1 is a schematic diagram showing the propagation of an optical vortex. Optical vortices were initially discussed in terms of a particular mode of electromagnetic waves called the Laguerre-Gaussian (LG) mode, which was conventionally thought to be artificially generated using optical elements. However, twisted photons are

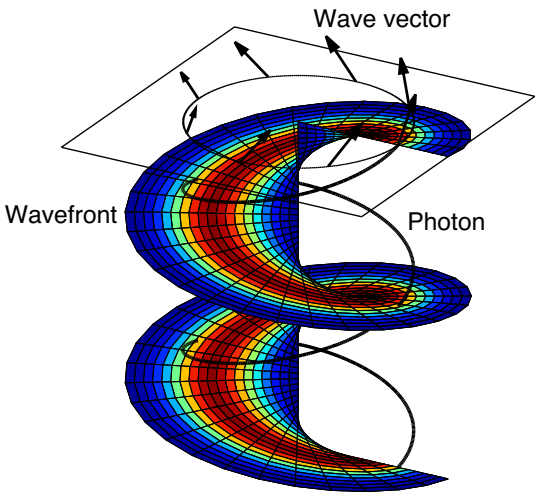

Figure 1: Schematic representation of the propagation of an optical vortex with a helical wavefront together with a photon with OAM.

emitted naturally by the cyclotron motion of electrons and are more ubiquitous in laboratories and nature. Naturally, the question arises as to how the optical vortex propagates in an anisotropic medium, the magnetized plasma, and whether the unique property of the helical wavefront is beneficial for heating, current drive, and diagnostics in magnetic fusion plasmas.

In this work [3], the propagation properties of optical vortices with helical wavefronts in a cold uniform magnetized plasma were theoretically investigated in the frequency range of an electron cyclotron (EC) wave. The effect of the helical wavefront of the optical vortex on the wavefield in the magnetized plasma is explained. A detailed description of the theory will be given at the conference. It was found that these effects become larger when the topological charge of the optical vortex becomes larger or the distance from the phase singularity becomes smaller. Different propagation properties were also observed in the propagation of a Laguerre-Gaussian beam in a three-dimensional simulation using the finite element method with the commercial software COMSOL Multiphysics. It was found that a part of the ordinary-mode LG beam with topological charge l excited in the region of lower electron density is converted into a high wavenumber extraordinary-mode LG beam with $l - 1$ at the upper hybrid resonance layer. Then, it propagates to the region with a higher electron density.

In order to demonstrate the new propagation properties of vortex EC waves in heating and current-drive experiments, it is necessary to generate optical vortices with the desired l in the millimeter-wave transmission system and launch them into the magnetic fusion plasma. A spiral phase mirror has been developed to generate optical vortices with the designed l in the millimeter-wave frequency range [4]. Therefore, the optical vortex can be generated by instrumenting the spiral phase mirror between the gyrotron and the launch antenna mirror in the existing transmission line for EC heating and current drive. This modified system will allow us to verify whether optical vortices can be a new tool for efficient heating of

high-density plasmas.

This work was supported by the NINS program for cross-disciplinary study (Grant Nos. 01311802 and 01311903), JSPS Grants-in-Aid for Scientific Research (Grant No. JP19K14687), and NIFS Grant Nos. ULRR703 and ULRR036.

References

[1] M. Katoh *et al*., Phys. Rev. Lett. **118**, 094801 (2017).

[2] M. Katoh *et al*., Sci. Rep. **7**, 6130 (2017).

[3] T. I. Tsujimura and S. Kubo, Phys. Plasmas **28**, 012502 (2021).

[4] Y. Goto, T. I. Tsujimura, and S. Kubo, J. Infrared Milli. Terahz. Waves **40**, 943 (2019).

JSST2021

Possibility of Visualisation of electrostatic potential by electron microscopy

Takuo Yasunaga[1*], Yasuhisa Honda[1]

[1]Department of Simulation, School of Technology, Kyushu Institute of Technology

*yasunaga@phys.kyutech.ac.jp

Abstract.

Keywords: Electron microscopy, Electrostatic potential,

1. Introduction

In electron microscopy, the contrast of images is generated by the phase shift of electron waves when electrons interact electrostatically with a sample. In other words, the image contrast reflects the electrostatic potential where the electron cloud shields the positive charge of the atomic nucleus. Electron microscopy thus has the potential to capture the ionic nature and polarization of the electron cloud. Previous researches have proposed that it is possible to visualize partially charged atoms. The recent Mirco-ED (electron diffraction) method can provide us structural information with a resolution of over 1 Å and capture the polarization of this electron cloud. Here, by quantum chemical calculations, we compared the calculated electrostatic potentials of molecules with experimental results by micro ED. Thus we show the possibility of detection of the polarization of the electron cloud.

2. Results and Discussion

We detected diffraction patterns of acetaminophen by micro-ED and could solve the three-dimensional structure except for hydrogen atoms at the atomic levels. However, the R-factor was not good in case of using conventional methods. We considered that this should be due to the electron density maps for reconstruction.

Thus, we automatically set the atomic coordinates of hydrogen atoms and calculated the electrostatic potential of acetaminophen quantum chemically by GAMESS and Gaussian [1]. Fig 1 shows the density map and electrostatic potentials calculated by Gaussian. Indeed, an oxygen atom of hydroxyl residue (left in Fig 1) was negatively charged, and a hydrogen atom was positively charged and slightly polarized. Then we compared the structural factors of diffraction patterns with the simulated one from the electrostatic potentials, and the R-factor improved to show good fitness. This fitness offers the possibilities to elucidate the polarization.

Furthermore, we could move the hydrogen atom of the hydroxyl residue so as to show better fitness to decrease the R-factor. This situation offers the possibility of refinement of atomic coordinates using quantum chemical calculations. At present, the calculation time of quantum chemical calculation is too long to refine the coordinates precisely. Still, we think the analysis is helpful to consider the validity of the hydrogen coordinates etc.

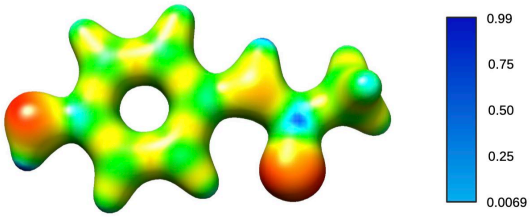

Fig. 1. Calculated electrostatic potential of acetoaminophen. The surface shows the iso-density surface and the colours indicate the electrostatic potential (red: negative potential, green: 0, and blue: positive).

References

[1] 巨大システムとしてのクライオ電子顕微鏡法の自動化から自働化への展開
安永 卓生, 田中 康太郎, 岩嵜 彩夏, 塚本 崇文, 本多 康久, 顕微鏡、2021 年 56 巻 1 号 p. 43-47 https://doi.org/10.11410/kenbikyo.56.1_43

Linear response theory applied to molecular dynamics simulations

Kazumi Omata[1,2*], Ryuta Kawanami[3], Hiroaki Nakamura[4,5], Susumu Fujiwara[6]

[1]Clinical Research Center, National Center for Global Health and Medicine
[2]Departments of Hematology, Rheumatology, and Infectious Diseases, Kumamoto University
[3]Graduate School of Science and Technology, Kyoto Institute of Technology
[4]Department of Helical Plasma Research, National Institute for Fusion Science
[5]Department of Energy Engineering and Science, Nagoya University
[6]Faculty of Materials Science and Engineering, Kyoto Institute of Technology

[*]komata@hosp.ncgm.go.jp

Abstract. We show that the linear response theory is applicable to molecular dynamics simulations in which sudden change in an external force plays a role for relaxation of a system. As one of such systems, we focus on the structural change of tritium-substituted polyethylene induced by beta decays of substituted tritium, and derive the time derivative of the dynamical quantity, which is conjugate to the force applied as perturbation in the framework of the linear response theory, required to calculate the response function.

Keywords: Linear response theory, Molecular dynamics simulation, Structural change, Polymer, Substituted tritium, Decay effect

1. Introduction

The linear response theory [1,2,3] describes the input-output relationship of a system in which the intensity of input is so small that the output can be described approximately with a linear function. The origin of this theory lies in studies of Brownian motion or Johnson–Nyquist noise: the former is the random motion of a suspended particle which is driven by a random force and the frictional force for a forced motion due to molecular collisions; the latter is the electronic noise generated by the thermal agitation of electrons inside an electrical conductor at equilibrium. A general proof of these phenomena is known as the fluctuation–dissipation theorem. After 1950s, formal descriptions were given to the linear response theory through analyses of irreversible processes or nonequilibrium systems, and especially, Kubo developed the method of a response function for this theory [1,2,3].

The present study shows that the linear response theory is applicable to molecular dynamics simulations in which sudden change in an external force plays a role for relaxation of a system. We review the linear response theory [1,2,3] in Sec.2, and in Sec.3, delineate the calculations

practical for application of the linear response theory to the molecular dynamics simulations for the structural change of tritium-substituted polyethylene induced by beta decays of substituted tritium [4,5,6,7].

2. Linear response theory

For the density function f representing a statistical ensemble, the equation of motion is given by

$$\frac{\partial f}{\partial t} = i\mathcal{L}f = [\mathcal{H}, f], \qquad i\mathcal{L} = \left[\mathcal{H}, \right] = \frac{\partial \mathcal{H}}{\partial q}\frac{\partial}{\partial p} - \frac{\partial \mathcal{H}}{\partial p}\frac{\partial}{\partial q} \tag{2.1}$$

where $\mathcal{H}$ denotes the Hamiltonian, and $i\mathcal{L}$ is the Liouville operator. When the system is under an external force $F(t)$, the Hamiltonian is written as the sum of non-perturbed part H and perturbed part H':

$$\mathcal{H} = H + H', \qquad H' = -A\big(q(t), p(t)\big) \cdot F(t), \tag{2.2}$$

and the corresponding density function

$$f = f_0 + \Delta f, \tag{2.3}$$

changes according to eq.(2.1):

$$\frac{\partial f_0}{\partial t} = [H, f_0] = 0, \qquad \frac{\partial \Delta f}{\partial t} = [H, \Delta f] - F(t)\big[A,\ f_0\big] = i\mathcal{L}\Delta f - F(t)\big[A,\ f_0\big]. \tag{2.4}$$

The solution of Eq.(2.4) for Δf is

$$\Delta f = -\int_{-\infty}^{t} dt'\, e^{i(t-t')\mathcal{L}}\big[A,\ f_0\big]F(t'). \tag{2.5}$$

Because $f_0 \sim e^{-\beta H}$, we obtain

$$[f_0, A] = -\beta f_0 [H, A] = \beta f_0 \dot{A}, \tag{2.6}$$

where $\beta = 1/k_B T$, k_B is the Boltzmann constant, and T is the absolute temperature. The ensemble average $\langle \Delta B \rangle$ of the deviation in a physical quantity B is given by

$$\langle \Delta B \rangle = \int B \Delta f d\Gamma = \int_{-\infty}^{t} dt'\, \Phi_{BA}(t - t')F(t'), \tag{2.7}$$

where $\Phi_{BA}(t)$ is the response function which is defined as

$$\Phi_{BA}(t) = \int \big[f_0, A\,\big]B(t)d\Gamma = \beta\big\langle \dot{A}(0)B(t)\big\rangle. \tag{2.8}$$

3. Application to molecular dynamics simulations

To apply the linear response theory to the molecular dynamics simulations of the structural change of tritium-substituted polyethylene induced by beta decays of substituted tritium [4,5,6,7], we derive the time derivative $\dot{A}$ of the dynamical quantity A, which is conjugate to the force applied, required to calculate the response function [7]. The dynamical quantity in this study is the total potential energy difference of hydrogen-removed polyethylene before and after beta decays of substituted tritium.

This time derivative has three terms,

$$\dot{A}_B = \dot{E}_{\mathrm{B}}^{\mathrm{before}} - \dot{E}_{\mathrm{B}}^{\mathrm{after}}, \tag{3.1}$$

$$\dot{A}_A = \dot{E}_{\mathrm{A}}^{\mathrm{before}} - \dot{E}_{\mathrm{A}}^{\mathrm{after}}, \tag{3.2}$$

$$\dot{A}_T = \dot{E}_{\mathrm{T}}^{\mathrm{before}} - \dot{E}_{\mathrm{T}}^{\mathrm{after}}, \tag{3.3}$$

where, $E_{\mathrm{B}}^{\mathrm{before}}$, $E_{\mathrm{B}}^{\mathrm{after}}$, $E_{\mathrm{A}}^{\mathrm{before}}$, $E_{\mathrm{A}}^{\mathrm{after}}$, $E_{\mathrm{T}}^{\mathrm{before}}$, and $E_{\mathrm{T}}^{\mathrm{after}}$ represent the bond-stretching, bond-bending and torsional potentials before and after beta decays of substituted tritium, respectively. We arrive at the following expressions for $\dot{A}_B$, $\dot{A}_A$, and $\dot{A}_T$ after simple but cumbersome calculation.

$$\dot{A}_B = K_B \sum_{i=1}^{N-1} \left(d_{i,i+1}^{0\prime} - d_{i,i+1}^{0}\right) \hat{\boldsymbol{d}}_{i,i+1} \cdot \dot{\boldsymbol{d}}_{i,i+1}, \tag{3.4}$$

where $\boldsymbol{d}_{i,i+1} = \boldsymbol{r}_{i+1} - \boldsymbol{r}_i$ is the bond vector between the i-th united atom and the $(i+1)$-th united atom, $\boldsymbol{r}_i$ is the position vector of the i-th united atom, $\hat{\boldsymbol{d}}_{i,i+1}$ is the unit vector of $\boldsymbol{d}_{i,i+1}$, and $d_{i,i+1}^{0}$, $d_{i,i+1}^{0\prime}$ are the equilibrium bond lengths before and after beta decays of substituted tritium, respectively. As for $\dot{A}_A$, we have

$$\dot{A}_A = K_A \sum_{i=2}^{N-1} \left(\theta_i^{0\prime} - \theta_i^{0}\right) \dot{\theta}_i, \tag{3.5}$$

$$\dot{\theta}_i = \frac{\left(\frac{\dot{\boldsymbol{d}}_{i-1,i}}{d_{i-1,i}} \cdot \hat{\boldsymbol{d}}_{i,i+1} + \hat{\boldsymbol{d}}_{i-1,i} \cdot \frac{\dot{\boldsymbol{d}}_{i,i+1}}{d_{i,i+1}}\right) - \hat{\boldsymbol{d}}_{i-1,i} \cdot \hat{\boldsymbol{d}}_{i,i+1} \left(\hat{\boldsymbol{d}}_{i-1,i} \frac{\dot{\boldsymbol{d}}_{i-1,i}}{d_{i-1,i}} + \hat{\boldsymbol{d}}_{i,i+1} \cdot \frac{\dot{\boldsymbol{d}}_{i,i+1}}{d_{i,i+1}}\right)}{\sqrt{1 - \hat{\boldsymbol{d}}_{i-1,i} \cdot \hat{\boldsymbol{d}}_{i,i+1}^2}}, \tag{3.6}$$

where θ_i^0 and $\theta_i^{0\prime}$ represent the equilibrium bond angles before and after beta decays of substituted tritium, respectively. $\dot{A}_T$ is expressed as the following equations:

$$\dot{A}_T = \frac{1}{2} \sum_{i=2}^{N-2} \{ n_{i,i+1} V_{i,i+1} \sin\left[n_{i,i+1}\left(\phi_{i,i+1} - \phi_{i,i+1}^{0}\right)\right] - n_{i,i+1}' V_{i,i+1}' \sin\left[n_{i,i+1}'\left(\phi_{i,i+1} - \phi_{i,i+1}^{0\prime}\right)\right] \} \dot{\phi}_{i,i+1}, \tag{3.7}$$

$$\dot{\phi}_{i,i+1} = \frac{C - D}{\sin \phi_{i,i+1}}, \tag{3.8}$$

$$C = \frac{1}{\left|\boldsymbol{d}_{i-1,i} \times \boldsymbol{d}_{i,i+1}\right| \left|\boldsymbol{d}_{i,i+1} \times \boldsymbol{d}_{i+1,i+2}\right|} \times \left\{ \left(\boldsymbol{d}_{i-1,i} \times \boldsymbol{d}_{i,i+1}\right) \cdot \left(\dot{\boldsymbol{d}}_{i-1,i} \times \boldsymbol{d}_{i,i+1} + \boldsymbol{d}_{i-1,i} \times \dot{\boldsymbol{d}}_{i,i+1}\right) + \left(\boldsymbol{d}_{i,i+1} \times \boldsymbol{d}_{i+1,i+2}\right) \cdot \left(\dot{\boldsymbol{d}}_{i,i+1} \times \boldsymbol{d}_{i+1,i+2} + \boldsymbol{d}_{i,i+1} \times \dot{\boldsymbol{d}}_{i+1,i+2}\right) \right\}, \tag{3.9}$$

$$D = \frac{\left(\boldsymbol{d}_{i-1,i} \times \boldsymbol{d}_{i,i+1}\right) \cdot \left(\boldsymbol{d}_{i,i+1} \times \boldsymbol{d}_{i+1,i+2}\right)}{\left|\boldsymbol{d}_{i-1,i} \times \boldsymbol{d}_{i,i+1}\right|^2 \left|\boldsymbol{d}_{i,i+1} \times \boldsymbol{d}_{i+1,i+2}\right|^2} \times \left\{ \frac{\left|\boldsymbol{d}_{i,i+1} \times \boldsymbol{d}_{i+1,i+2}\right|}{\left|\boldsymbol{d}_{i-1,i} \times \boldsymbol{d}_{i,i+1}\right|} \left(\boldsymbol{d}_{i-1,i} \times \boldsymbol{d}_{i,i+1}\right) \cdot \left(\dot{\boldsymbol{d}}_{i-1,i} \times \boldsymbol{d}_{i,i+1} + \boldsymbol{d}_{i-1,i} \times \dot{\boldsymbol{d}}_{i,i+1}\right) + \frac{\left|\boldsymbol{d}_{i-1,i} \times \boldsymbol{d}_{i,i+1}\right|}{\left|\boldsymbol{d}_{i,i+1} \times \boldsymbol{d}_{i+1,i+2}\right|} \left(\boldsymbol{d}_{i,i+1} \times \boldsymbol{d}_{i+1,i+2}\right) \cdot \left(\dot{\boldsymbol{d}}_{i,i+1} \times \boldsymbol{d}_{i+1,i+2} + \boldsymbol{d}_{i,i+1} \times \dot{\boldsymbol{d}}_{i+1,i+2}\right) \right\}, \tag{3.10}$$

$$\left|\sin \phi_{i,i+1}\right| = \sqrt{1 - \left\{ \frac{\left(\boldsymbol{d}_{i-1,i} \times \boldsymbol{d}_{i,i+1}\right) \cdot \left(\boldsymbol{d}_{i,i+1} \times \boldsymbol{d}_{i+1,i+2}\right)}{\left|\boldsymbol{d}_{i-1,i} \times \boldsymbol{d}_{i,i+1}\right| \left|\boldsymbol{d}_{i,i+1} \times \boldsymbol{d}_{i+1,i+2}\right|} \right\}^2}, \tag{3.11}$$

where $\phi_{i,i+1}^0$ and $\phi_{i,i+1}^0{}'$, $n_{i,i+1}$ and $n_{i,i+1}'$, $V_{i,i+1}$ and $V_{i,i+1}{}'$ denote the equilibrium dihedral angles, the periodicities and the energy barriers to rotation before and after beta decays of substituted tritium, respectively. The sign of $\sin \phi_{i,i+1}$ is decided by that of $\left(\boldsymbol{d}_{i-1,i} \times \boldsymbol{d}_{i,i+1}\right) \times \left(\boldsymbol{d}_{i,i+1} \times \boldsymbol{d}_{i+1,i+2}\right) \cdot \boldsymbol{d}_{i,i+1}$.

References

[1] R. Kubo: Statistical-Mechanical Theory of Irreversible Processes. I. General Theory and Simple Applications to Magnetic and Conduction Problems, *J. Phys. Soc. Jpn.*, 12:6 (1957), 570-586.

[2] R. Kubo: The fluctuation-dissipation theorem, *Rep. Prog. Phys*., 29 (1966) 255-284.

[3] R. Kubo, M. Toda, N. Hashitsume: Statistical Physics II, Springer-Verlag Berlin Heidelberg (1985).

[4] S. Fujiwara, H. Nakamura, H. Li, H. Miyanishi, T. Mizuguchi, T. Yasunaga, T. Otsuka, Y. Hatano, S. Saito: Computational strategy for studying structural change of tritiumsubstituted macromolecules by a beta decay to helium-3, *J. Adv. Simulat. Sci. Eng.*, 6:1 (2019) 94-99.

[5] H. Li, S. Fujiwara, H. Nakamura, T. Mizuguchi, T. Yasunaga, T. Otsuka, T. Kenmotsu, Y. Hatano, S. Saito: Structural change of tritium-substituted polymeric materials by a beta decay: A molecular dynamics study, *Plasma Fusion Res.*, 14 (2019) 3401106.

[6] H. Li, S. Fujiwara, H. Nakamura, T. Mizuguchi, A. Nakata, T. Miyazaki, S. Saito: Structural change of damaged polyethylene by beta-decay of substituted tritium using reactive force field, *Jpn. J. Appl. Phys.*, 60 (2021) SAAB06.

[7] S. Fujiwara, R. Kawanami, H. Li, H. Nakamura, K. Omata, A theoretical approach to structural change of a polymer induced by beta decays of substituted tritium based on the linear response theory, in submission.

JSST 2021

Molecular simulations on dynamics of lipid bilayers and water molecules

Yuji Higuchi[1,*], Hiroaki Ito[2], Naofumi Shimokawa[3], Yuta Asano[1], Takuya Kuwahara[4], Mafumi Hishida[5]

[1]Institute for Solid State Physics, The University of Tokyo
[2]Department of Physics, Chiba University
[3]School of Materials Science, Japan Advanced Institute of Science and Technology
[4]Fraunhofer IWM, MicroTribology Center μTC
[5]Department of Chemistry, Faculty of Pure and Applied Sciences, University of Tsukuba

[*]yuji.higuchi@issp.u-tokyo.ac.jp

Abstract. We studied the structure and dynamics of a phospholipid bilayer and water by molecular dynamics simulations. We revealed the dependency of water dynamics on the chemical structure of lipid heads by all-atomic molecular dynamics simulations. When water molecules are strongly attracted to the positively charged group, hydrogen bond networks in water molecules are broken. In contrast, weak hydration does not break the hydrogen networks. Next, we studied the morphological change of vesicles composed of neutral and charged lipids by coarse-grained molecular dynamics simulations. We revealed the large deformation process from the vesicle to the disk shape. The flip of the lipids initiates the pore formation in the charged-lipid-rich domain.

Keywords: Molecular simulation, Phospholipid, Biomembrane

1. Introduction

The phospholipid bilayer is the main component of the cell membrane, and therefore its structures and properties are actively studied. Charged lipids are contained in biomembrane and play important roles such as protein adsorption and phase separation of lipids. However, the effect of charges on the structure and dynamics of lipids is still controversial. Thus, we focus on charges of lipids and have studied the effect of charges on the bilayer structures. The interactions between charged lipid and water are also crucial for the self-assemble structures of phospholipid. The dynamics of water molecules around the hydrophilic head groups in phospholipids are investigated by all-atomic molecular dynamics (MD) simulations [1]. Then, we perform coarse-grained (CG) MD simulations to reveal the effect of the charge on the phase separation and structure in phospholipid vesicle [2, 3, 4].

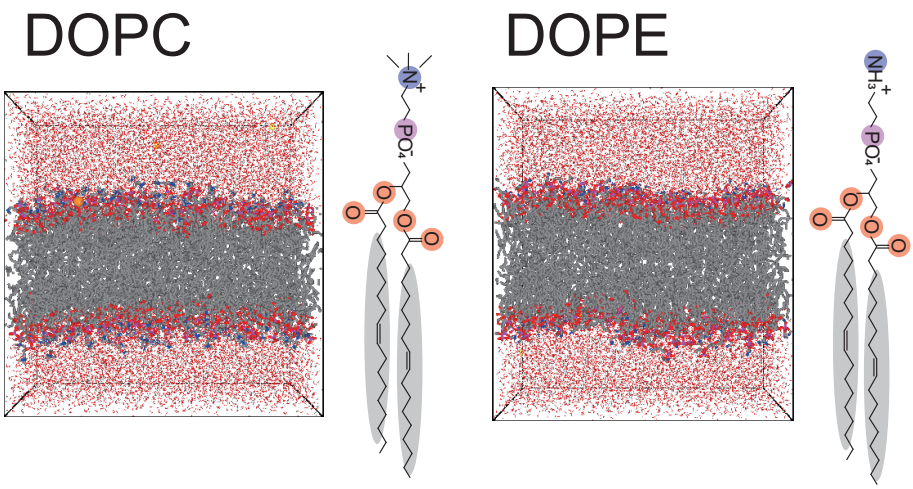

Figure 1: Snapshots of molecular dynamics simulations and molecular structures of 1,2-dioleoyl-*sn*-glycero-3-phosphocholine (DOPC) and 1,2-dioleoyl-*sn*-glycero-3-phosphoethanolamine (DOPE).

2. Results

We perform all-atomic MD simulations using LAMMPS [5] and DFTB+ [6] to reveal the water dynamics around the phosphatidylcholine (PC) and phosphatidylethanolamine (PE) head group. Figure 1 shows typical snapshots of MD simulation. Molecular structures of DOPC and DOPE are also shown, where the only difference is the ammonium group in the head groups. The rotation relaxations of water are faster in PE than that in PC. This is consistent with a previous experimental study using terahertz spectroscopy [7], confirming the validity of the simulation results. Radial distribution functions (RDF) show that the PE lipid with NH_3^+ is strongly hydrated by water molecules, whereas PC lipid with $N(CH_3)_3^+$ is weakly hydrated. Interestingly, strong hydration enhances the rotation of water molecules. To reveal the mechanism, we compare the numbers of hydrogen bonds (HBs) between water molecules around the head group. The HBs in PE are less than that in PC. Thus, we suggest that the strong hydration in PE breaks the HB network and enhances the rotation of water molecules.

Next, we study the morphological change in charged lipid bilayer vesicles by CG MD simulation. We adopt the model by Cooke *et al.* for the CG model of the lipid membrane and use the Debye-Hückel potential to include the electrostatic interaction. Two kinds of lipids are composed of the vesicle, and the attractive interaction among them is set to separate each other. When both lipids are neutral, phase separation is observed. When the vesicle consists of negatively charged and neutral lipids, phase separation is delayed due to the repulsive interaction between charged lipids. Figure 2 shows a morphological change of the vesicle. After the phase separation, the pore is formed in the charged-lipid-rich domain. Then, the vesicle changes to the disk shape. Remarkably, some lipid molecules flip, and then a pore is formed. The morphologies are summarized with the salt concentration, which

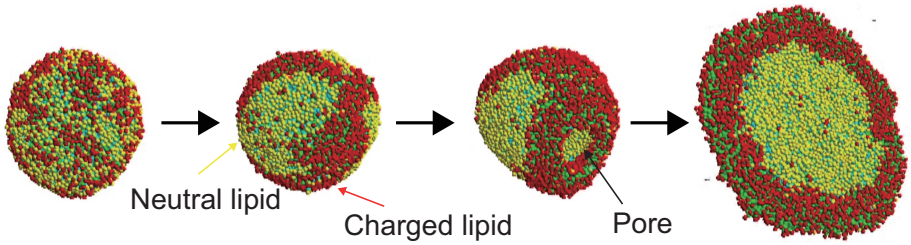

Figure 2: Morphological change of lipid bilayers from vesicle to disk by coarse-grained molecular dynamics simulation.

is consistent with the experiment. This confirms the validity of our CG MD simulations. Thus, we successfully revealed the structure and dynamics of lipid bilayers in multi-scale.

References

[1] Y. Higuchi, Y. Asano, T. Kuwahara, M. Hishida: Rotational Dynamics of Water at the Phospholipid Bilayer Depending on the Head Groups Studied by Molecular Dynamics Simulations, *Langmuir*, 37 (2021), 5329–5338.

[2] H. Himeno, H. Ito, Y. Higuchi, T. Hamada, N. Shimokawa, M. Takagi: Coupling between pore formation and phase separation in charged lipid membranes, *Phys. Rev. E*, 92 (2015), 062713.

[3] H. Ito, Y. Higuchi, N. Shimokawa: Coarse-grained molecular dynamics simulation of charged lipid membranes: Phase separation and morphological dynamics, *Phys. Rev. E*, 94 (2016), 042611.

[4] N. Shimokawa, H. Ito, Y. Higuchi: Coarse-grained molecular dynamics simulation for uptake of nanoparticles into a charged lipid vesicle dominated by electrostatic interactions, *Phys. Rev. E*, 100 (2019), 012407.

[5] S. Plimpton: Fast Parallel Algorithms for Short-Range Molecular Dynamics, *J. Comput. Phys.*, 117 (1995), 1–19.

[6] B. Hourahine, et al.: DFTB+, a software package for efficient approximate density functional theory based atomistic simulations, *J. Chem. Phys.*, 152 (2020), 124101.

[7] M. Hishida, K. Tanaka, Y. Yamamura, K. Saito: Cooperativity between Water and Lipids in Lamellar to Inverted-Hexagonal Phase Transition, *J. Phys. Soc. Jpn.*, 83 (2014), 044801.

[8] I. R. Cooke, K. Kremer, M. Deserno: Tunable generic model for fluid bilayer membranes, *Phys. Rev. E*, 72 (2005), 011506.

JSST 2021

Molecular Dynamics Simulation on Hydrogen Isotope Molecules Emitted from Amorphous Carbon

Hiroaki Nakamura[1,2,*], Seiki Saito[3], Keiji Sawada[4], Masahiro Kobayashi[1,5], Masahiro Hasuo[6]

[1]National Institute for Fusion Science
[2]Nagoya University
[3]Yamagata University
[4]Shinshu University
[5]The Graduate University for Advanced Studies, SOKENDAI
[6]Kyoto University

[*]hnakamura@nifs.ac.jp

Abstract. We have been developing the hybrid code between molecular dynamics and heat conduction solver (MD-HC), which drive the hydrogen emission rate from amorphous carbon. From our previous work, the emission rate strongly depends on the structure of the amorphous carbon. In the present paper, we show the target-structure dependence of the hydrogen emission rate by the MD-HC code.

Keywords: Molecular dynamics simulation, heat conduction equation, amorphous carbon, hydrogen emission, rotational state, vibrational state

1. Introduction

Detached plasma is one of candidates to decrease the heat load to the divertor to realize nuclear fusion generation. Some portion of the detached plasma is generated by the Molecular Assisted Recombination (MAR) process, where the population of the neutral particles has a strong influence the reaction rate[1, 2]. Therefore, the information of the neutral particles emitted from the wall is essential for accurate estimation of the MAR[3]. In order to achieve this goal, we've been developing the hybrid code between molecular dynamics and heat conduction solver (MD-HC), which drive the hydrogen emission rate from amorphous carbon[4].

In our previous work[4], we concentrate on the isotopic hydrogen molecules which are emitted from the divertor plate, which is made of amorphous carbon. There, it was found that the emission rate strongly depends on the structure of the amorphous carbon. In the present paper, we show the target-structure dependence of the hydrogen emission rate by the MD-HC code.

2. Simulation model and method

We performed the MD simulation which are the same method as our previous work[2, 4]. The initial target of the amorphous carbon is made by the same way as the previous works. However the configuration is different from the previous works, because the random numbers to distribute the velocity to all atoms is different from that of the previous works. Using a few random numbers, we prepare the various initial configurations of the amorphous carbon.

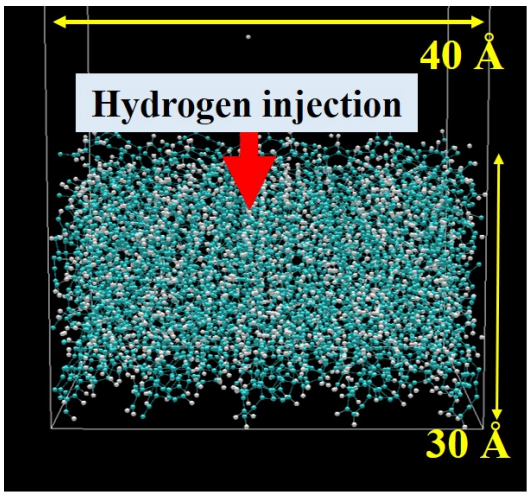

Figure 1: Simulation model of MD simulation. A hydrogen atom is injected to the amorphous carbon.

3. Results and Discussions

The rovibrational energy of hydrogen molecules is determined from kinetic energy, potential energy, and angular momentum of the two atoms in the center-of-mass system. We obtain the information of the emitted hydrogen atom and molecules from the carbon. In Fig.2, we also obtain the hydrogen distributions in the target and the initial depth distribution of the emitted hydrogen.

Acknowledgments

The research was supported by Grants-in-Aid for Scientific Research (C), Nos.18K11416, 19K03802 and 19K03800 from the Japan Society for the Promotion of Science, and by the NIFS Collaborative Research Programs NIFS20KNTS066, NIFS20KKGS028 and NIFS20KNSS150. The computations were performed using the JFRS-1 supercomputer system at Computational Simulation Centre of International Fusion Energy Research Centre

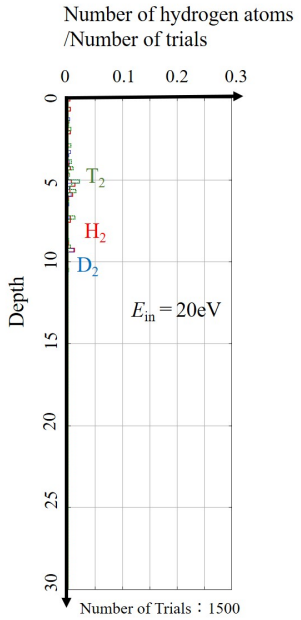

Figure 2: Hydrogen distributions in the target and the initial depth distribution of the emitted hydrogen.

(IFERC-CSC) in Rokkasho Fusion Institute of QST, Japan, Research Center for Computational Science, Okazaki, Japan and Plasma Simulator of NIFS, Japan.

References

[1] K. Sawada, H. Nakamura, S. Saito, G. Kawamura, M. Kobayashi, K. Haga, T. Sawada, M. Hasuo, Contrib. Plasma Phys., **60**(2020) e201900153, doi:10.1002/ctpp.201900153.

[2] S. Saito, H. Nakamura, K. Sawada, G. Kawamura, M. Kobayashi and H. Hasuo, Contrib. Plasma Phys., **60**(2020) e201900152, doi:10.1002/ctpp.201900152.

[3] S. Saito, H. Nakamura, K. Sawada, M. Kobayashi, G. Kawamura and H. Hasuo, Plasma Fus. Res., **15**(2020) 240307, doi:10.1585/pfr.15.2403073.

[4] H. Nakamura,S. Saito, T. Sawada, K. Sawada, G. Kawamura, M. Kobayashi and H. Hasuo, Jpn. J. Appl. Phys. submitted.

Studies on ion heating through the merging of spherical tokamaks by means of particle simulations

Shunsuke Usami[1,2*], Ritoku Horiuchi[1], Toseo Moritaka[1], Yasushi Ono[2]

[1]National Institute for Fusion Science, National Institute of Natural Sciences
[2]The University of Tokyo

*usami.shunsuke@nifs.ac.jp

Abstract. The ion heating through the merging of spherical tokamaks is investigated by means of particle simulations. Simulations show that part-of-circle structures of velocity distributions are formed, and thus effective heating by the Pick-Up-Like process occurs. Also, part-of-circle structures are seen during merging and for long periods of time after merging.

Keywords: Particle simulation, Spherical tokamak, Heating, Magnetic reconnection

1. Introduction

Spherical tokamaks (STs) can confine higher-β plasmas than standard tokamaks or helical devices. In merging of STs, in which two STs are merged through magnetic reconnection, a case for β~40% was reported. The heating mechanism, however, remains to be unsolved. The elucidation of heating mechanism can lead to the higher performance of future ST reactors. We investigate ion heating processes by means of particle simulation.

2. Simulation results

Figure 1 shows the spatial profiles of the ion temperature at various times. At the initial time (Fig. 1(a)), the temperature is low and uniform. At $\omega_{ce}t$=1445 (Fig. 1(b)), the two STs are being merged at the central position and magnetic reconnection takes place. The temperature becomes high in parts of the downstream. At $\omega_{ce}t$=1807 (Fig. 1(c)), the merging process is completed, and high-temperature regions are expanded. Also, a new high-temperature region is generated around the central position. At $\omega_{ce}t$ =2045 (Fig. 4(d)), 2581 (Fig. 4(e)), and 3097 (Fig. 4(f)), high-temperature ions are further expanded to wider regions.

In Fig. 2 we show ion velocity distributions at A1, B1, B2, C1, C2, D1, E1, and F1 designated in Fig. 1. Figure 2(a) displays that initially a Maxwellian distribution holds. Figure 2(b) shows that the distribution is clearly spread compared with Fig. 2(a), nearly keeping a Maxwellian distribution, which means that genuine compression acts on ions. Figure 2(c) shows that the distribution consists of three parts and the distribution shape is a part of a circle. This

feature indicates that ions are effectively heated by the Pick-Up-Like process [1,2], which is similar to the Pickup [3,4]. Furthermore, ion velocity distributions at $\omega_{ce}t$ =1807, 2045, 2581, and 3097 are depicted in Figs. 2 (d), (f), (g), and (h), which show that part-of-circle structures are maintained during long periods of time after merging. In contrast, at C2, viscous heating also occurs. Figure 2 (e) displays that a different type of effective heating acts on ions at C2.

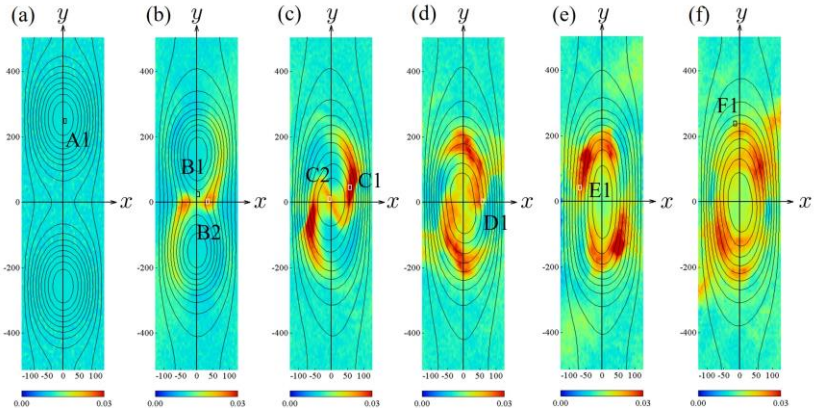

Figure 1: Spatial profiles of the ion temperature at various times.

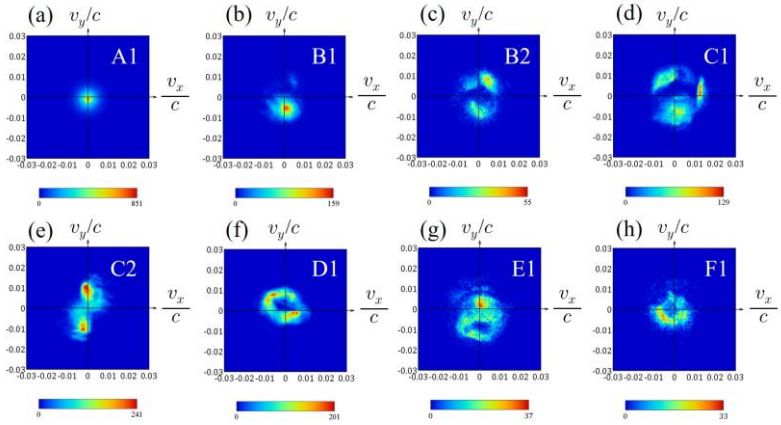

Figure 2: Ion velocity distributions at A1, B1, B2, C1, C2, D1, E1, and F1 in Fig. 1

References

[1] S. Usami R. Horiuchi, H. Ohtani: Effective heating of nonadiabatic protons in magnetic reconnection with a guide field, *Phys. Plasmas*, 24 (2017) 092101.

[2] S. Usami et al.: Dependence of the pickup-like ion effective heating on the poloidal and toroidal magnetic fields during magnetic reconnection, *Phys. Plasmas*, 26 (2019) 102103.

[3] E. Möbius, et al.: Direct observation of He^+ pick-up ions of interstellar origin in the solar wind, *Nature*, 318 (1985) 426-429.

[4] J. F. Drake, et al.: A magnetic reconnection mechanism for ion acceleration and abundance enhancements in impulsive flares, *Astrophys. J.*, 700 (2009) L16-L20.

Visualization analysis of intersection points of energetic tritons and plasma facing wall in LHD by virtual-reality system

Hiroaki Ohtani[1,2*], Suguru Masuzaki[1,2], Kunihiro Ogawa[1,2], Seiji Ishiguro[1,2]

[1]National Institute for Fusion Science
[2]The Graduate University for Advanced Studies, SOKENDAI
*ohtani.hiroaki @nifs.ac.jp

Abstract. We evaluated the trajectories of the energetic tritons from the triton generation distribution in Large Helical Device (LHD) by means of the collisionless Lorentz orbit code, and we calculated the intersection points of the tritons and the plasma facing wall. The intersection points were visualized in the virtual-reality world as spheres with the rendered internal vacuum wall and the divertor plates. It became possible to directly observe the points distributed on the wall. This visualization played an important role in determination of the appropriate positions of the material probes on the wall in the real LHD to observe the accumulated tritium on the wall experimentally.

Keywords: Virtual-reality visualization, Intersection points, Tritons, plasma facing wall

1. Introduction

Tritium recycle in the fuel system is one of the important issues in realization of a fusion power generation system. Tritium inventory is the amount of accumulated tritiums which stay in the shadow area and do not circulate in the tritium circulation system [1]. One of the shadow areas is the plasma facing wall where the tritium approaches directly. Therefore, there is concern over the increase of the inventory at the wall [2,3,4]. To investigate the energetic triton accumulation experimentally on the vacuum wall, we planned to put material probes on the vacuum vessel of the Large Helical Device (LHD). Since the size of the probe is much small compared with that of the wall, it is necessary to place the probe on the appropriate position on the wall. For deciding specifically the position of the material probe, the intersection point of energetic triton and the plasma facing wall is visualized in the vacuum vessel of the LHD with the divertor plates in the virtual-reality (VR) system [5]. The researcher can directly check the distribution of the intersection points on the plasma facing wall to decide where the probes should be placed at the positions on the wall, watching many tritons collide on the wall and so many tritons did not strike with the wall. In this paper, we report the calculation method of the triton trajectory and the collision point, the VR visualization method of the triton intersection points,

and the visualization results.

2. Trajectory and intersection point of triton[6]

The initial position of the triton by DD fusion reaction is determined from the neutron generation distribution calculated by FIT3D-DD code [7], and the trajectory of the triton with 1MeV energy from the initial position is evaluated by the LORBIT code in which the Newtonian equation of motion is solved without any collision effect [8]. The magnetic field in a vacuum calculated from the coil current of LHD is used and no electric field is assumed in this paper. The divertor plate and the vacuum vessel are represented by the triangle and polygons, respectively, based on the design data which was used in the installation and construction of the real LHD. We calculate whether the triton trajectory exists inside or outside the triangles and the polygons, and we detect the intersection point of the triton and the plasma facing wall. The coordinate point of the intersection point is stored in the Cartesian coordinate system.

3. VR visualization method

We use CAVE-type VR system [9] called CompleXcope. A modified virtual-LHD [10,11] based on C++, OpenGL and CAVELib library visualizes the intersection points of the tritons and the wall as spheres by the point-sprite method with the interface routine of reading the coordinate points of the intersection points, while the plasma interface wall, such as internal vacuum wall and divertor plates, is rendered by Unity [12]. The commercial software, FusionSDK [13,14,15], superimposes and displays the spheres and the internal components of LHD in the one VR world.

4. Visualization results

A viewer watches the intersection points (red spheres) of the tritons and the plasma facing wall in the vacuum of LHD in CompleXcope as shown in Fig. 1. The viewer is surrounded by stereoscopic images with a high immersion feeling, and he can look at the objects he is interested in with enlarging the images and from any viewpoints It is found that many tritons collide with the divertor plates, while some tritons strike the vacuum vessel wall.

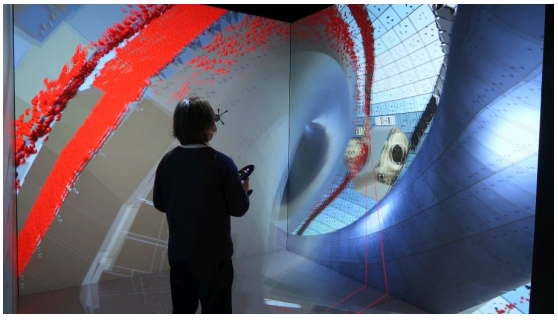

Figure 1: A viewer watches the intersection points of the tritons and the wall in the LHD by VR system.

5. Conclusion

We calculated the trajectories of energetic tritons which were generated in the deuterium operations in LHD, and we found the intersection points of the tritons and the plasma facing wall by using VR system “CompleXcope”. It was possible to analyze the collision point distribution on the vacuum wall and the divertor plates. This visualization helped the experiment researcher who planned to put the material probes on the plasma facing wall in the real LHD to determine

the appropriate positions of the material probes.

Acknowledgements

This work is performed with the support and under the auspices of the NIFS Collaboration Research program (NIFS19KNTS057, NIFS20KKGS026, NIFS20KOAH037), and by the LHD project budget (NIFS20ULHH003, NIFS20ULHH034).

References

[1] For example, https://www.iter.org/mach/FuelCycle.

[2] S. Masuzaki et al: Physica Scripta T170 (2020) 014068.

[3] M. Yajima et al.: Nuclear Materials Energy, 27 (2021) 100906.

[4] S. Masuzaki et al., Nuclear Materials and Energy, 26 (2021) 100884.

[5] H.Ohtani et al., submitted to J. Visualization (2021).

[6] K. Ogawa, et al.: Plasma Science and Technology, 21 (2019) 025102 (5pp).

[7] R.Seki, et al.: Plasma Fusion Res., 14, (2019), 3402126.

[8] M. Isobe, et al.: J. Plasma Fusion Res. SERIES, 8, (2009), 330.

[9] C. Cruz-Neira, et al.: SIGGRAPH'93: Proc. 20th Ann. Conf. Comp. Graphics Interactive Tech. pp.135-142, (1993).

[10] A. Kageyama et al. Proc. ICNSP, 138 (1998).

[11] H. Ohtani, et al: Contrib. Plasma Phys. Vol.56, No.6-8, (2016) 692-697.

[12] https://unity.com/

[13] https://www.fiatlux.co.jp/product/virtual/easyvr/

[14] H. Miyachi et al: IEEE Comp. Soc. (2005) 530.

[15] H. Miyachi et al: IEEE Comp. Soc. (2007) 536.

JSST 2021

Constructive a priori error estimates for Poisson's equation with discontinuous coefficients

Kazuaki Tanaka[1,*] and Mitsuhiro T. Nakao[2]

[1]Institute for Mathematical Science, Waseda University
[2]Waseda Research Institute for Science and Engineering, Waseda University

[*]tanaka@ims.sci.waseda.ac.jp

Abstract. Our objective is the Dirichlet boundary value problem of Poisson's equation with discontinuous coefficients. We provide explicit a priori error estimates for solutions of the problem and apply these to finite element approximations.

Keywords: A priori error estimates, Computer-assisted proofs, Numerical Verification, Poisson's equation with discontinuous coefficients, Rigorous computations

1. Introduction

We consider the boundary value problem of Poisson's equation

$$\begin{cases} -\nabla \cdot \lambda \nabla u = f & \text{in } \Omega, \\ u = 0 & \text{on } \partial\Omega \end{cases} \tag{1}$$

with $\Omega = (0,1)^3 \subset \mathbb{R}^3$ and $f \in L^2(\Omega)$. The coefficient λ discontinuous over Ω is defined as follows. We divide Ω into the three parts $\Omega_1 = (0,a)\times I^2$, $\Omega_2 = (a,b)\times I^2$, and $\Omega_3 = (b,1)\times I^2$ with the inner boundaries $\Gamma_a = \{a\} \times I^2, \Gamma_b = \{b\} \times I^2$ as displayed in Fig. 1. The coefficient $\lambda \in L^\infty(\Omega)$ is piecewise constant that satisfies $\lambda = \lambda_k > 0$ in Ω_k for $k = 1, 2, 3$.

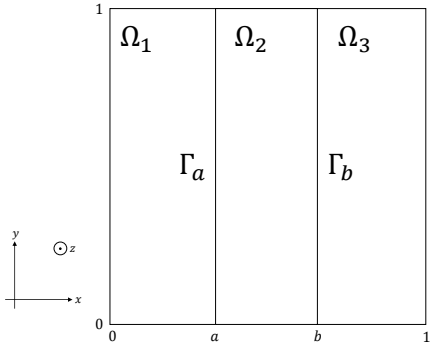

Figure 1: Domain Ω for a fixed z.

The weak form of (1) is written as the following form

$$(u, v)_\lambda = \int_\Omega f(x)v(x)dx \quad \forall v \in H_0^1(\Omega), \tag{2}$$

where

$$(u, v)_\lambda := (\lambda\nabla u, \nabla v)_{L^2(\Omega)} = \sum_{k=1,2,3} \lambda_k(\nabla u, \nabla v)_{L^2(\Omega_k)}, \quad u, v \in H_0^1(\Omega). \tag{3}$$

We look for a solution $u \in H_0^1(\Omega)$ of (2). The bilinear form $(\cdot, \cdot)_\lambda$ is continuous and coercive. Therefore, the Lax-Milgram theorem ensures that the problem (2) has a unique solution $u \in H_0^1(\Omega)$ for each $f \in H^{-1}$ (the dual space of $H_0^1(\Omega)$). Generally, solutions of (2) do not belong to $H^2(\Omega)$ but have H^2-regularity in each subdomain Ω_k. Therefore, $u \in H_0^1(\Omega) \cap (\bigcap_{k=1,2,3} H^2(\Omega_k))$.

Let V_h be a finite dimensional subspace of $H_0^1(\Omega)$ that depends on a parameter h, and let Π be some interpolation that maps $H_0^1(\Omega) \cap (\bigcap_{k=1,2,3} H^2(\Omega_k))$ into V_h. Suppose that there exists positive constants $C(h)$ that satisfies

$$\|\nabla(v - \Pi v)\|_{L^2(\Omega_k)} \leq C(h)|v|_{H^2(\Omega_k)} \tag{4}$$

for all $v \in H_0^1(\Omega) \cap (\bigcap_{k=1,2,3} H^2(\Omega_k))$. This interpolation constant $C(h)$ exists such as when we use the tri-linear interpolation $\Pi = P_z P_y P_x$. We define the orthogonal projection $R_h^\lambda : H_0^1(\Omega) \to V_h$ by

$$(v - R_h^\lambda v, v_h)_\lambda = 0 \ \text{ for all } \ v \in H_0^1(\Omega) \text{ and } v_h \in V_h. \tag{5}$$

Then, R_h^λ coincides with the solution u_h of

$$(u_h, v_h)_\lambda = (f, v_h)_{L^2(\Omega)} \quad \forall v_h \in V_h. \tag{6}$$

We report the following estimation result:

Theorem 1. *Let $u \in H_0^1(\Omega)$ be the solution of* (2) *and $R_h^\lambda u\ (= u_h) \in V_h$ a solution of* (6)*. For some interpolation Π that maps $H_0^1(\Omega) \cap (\bigcap_{k=1,2,3} H^2(\Omega_k))$ into V_h, suppose that there exists a positive constant $C(h)$ satisfying* (4)*. Then, we have the following a priori estimates:*

$$\|u - R_h^\lambda u\|_\lambda \leq C(h)|||f|||_\lambda \leq M_\lambda C(h)\|f\|_{L^2(\Omega)} \tag{7}$$

and

$$\|u - R_h^\lambda u\|_{L^2(\Omega)} \leq M_\lambda C(h)^2|||f|||_\lambda \leq M_\lambda^2 C(h)^2\|f\|_{L^2(\Omega)}, \tag{8}$$

where $M_\lambda := \max_{k=1,2,3} \lambda_k^{-1/2}$.

By applying Theorem 1 to the tri-linear interpolation with a uniform mesh size h, we have the following a priori estimates.

Example 1. *When $\min_k \lambda_k = 10^{-3}$ and $h = 2^{-7}$, we have*

$$\begin{aligned}
&\|u - R_h^\lambda u\|_\lambda / |||f|||_\lambda \leq 2.49 \times 10^{-3}, \\
&\|u - R_h^\lambda u\|_\lambda / \|f\|_{L^2(\Omega)} \leq 7.87 \times 10^{-2}, \\
&\|u - R_h^\lambda u\|_{L^2(\Omega)} / |||f|||_\lambda \leq 1.96 \times 10^{-4}, \\
&\|u - R_h^\lambda u\|_{L^2(\Omega)} / \|f\|_{L^2(\Omega)} \leq 6.19 \times 10^{-3}.
\end{aligned}$$

Numerical verification for positive solutions of the Hénon equation on bounded domains

Taisei Asai[1,*], Kazuaki Tanaka[2], Shin'ichi Oishi[3]

[1]Graduate School of Fundamental Science and Engineering, Waseda University, Japan
[2]Institute for Mathematical Science, Waseda University, Japan
[3]Faculty of Science and Engineering, Waseda University, Japan

*captino@fuji.waseda.jp

Abstract. For the Hénon equation, it is known that if the potential index is zero, then there is no asymmetric positive solution, and if the potential index is sufficiently large, then there are some asymmetric positive solutions. However, the symmetry-breaking bifurcation point and the total number of multiple solutions branching from its bifurcation point are not known completely. In this talk, we introduce the numerical verification method for the Hénon equation's multiple solutions and present several numerical results on some bounded domains.

Keywords: Hénon equation, Numerical verification method, Symmetry-breaking

1. Introduction

We consider the Hénon equation which is the boundary value problem

$$\begin{cases} -\Delta u = |\boldsymbol{x} - \boldsymbol{x_0}|^l |u|^{p-1} u & \text{in} \quad \Omega, \\ u = 0 & \text{on} \quad \partial\Omega, \end{cases} \tag{1}$$

where $\Omega \subset \mathbb{R}^N (N \geq 1)$ is a bounded domain, and $\boldsymbol{x_0}$ is set at the center of the domain if Ω be a symmetric convex domain. The parameter $l \geq 0$ is the potential index, and the parameter $2 \leq p < p^*$ ($p^* = \infty$ if $N = 1, 2$ and $p^* = (N+2)/(N-2)$ if $N \geq 3$) is the polytropic index. It is known that if $l = 0$, then there is no asymmetric positive solution, and if $l > 0$ is sufficiently large, then there are some asymmetric positive solutions even if there is some symmetry in the domain. Its symmetry-breaking phenomena is forcused, and the importance of the Hénon equation has led to active mathematical study on it over last decade. For example, Tanaka [1] considered one-dimensianal problem, and he proved that if $l(p-1) \geq 4$, the Morse index of the positive least energy solution equals 1 and the Morse index of the positive symmetric solution equals 2, and hence the positive least energy solution is asymmetric and symmetry-breaking phenomena occur. It is also shown that if l and p are sufficiently small, then there is no positive asymmetric solution and the Morse index of the symmetric positive solution equals 1. In another study, Shioji [2, 3] found the

minimum number of asymmetric positive solutions where $\Omega = \{\boldsymbol{x} \in \mathbb{R}^N : |\boldsymbol{x}| < 1\}$ $(N = 2, 3)$. However, the exact symmetry-breaking bifurcation point and the total number of multiple solutions branching from its point are still not known completely.

The purpose of this study is to prove the existence of each multiple solutions of (1) using a numerical verification method. Then, we also present a discussion of the correlation between the symmetry of the solution and the domain by verifying on several bounded domains.

2. Numerical verification

We first define the operator f as

$$f : \begin{cases} u(\cdot) & \mapsto |\cdot - \boldsymbol{x_0}|^l |u(\cdot)|^{p-1} u(\cdot), \\ H_0^1(\Omega) & \to H^{-1}, \end{cases}$$

where $2 \le p < p^*$ ($p^* = \infty$ if $N = 1, 2$ and $p^* = (N+2)/(N-2)$ if $N \ge 3$). Furthermore, we define the nonlinear operator $F : H_0^1(\Omega) \to H^{-1}$ by $F(u) := -\Delta u - f(u)$, which is given by

$$\langle F(u), v\rangle = (\nabla u, \nabla v)_{L^2} - \langle f(u), v\rangle \quad \text{for all} \quad v \in H_0^1(\Omega),$$

where $\langle f(u), v\rangle = \int_\Omega (|\boldsymbol{x} - \boldsymbol{x_0}|^l |u(\boldsymbol{x})|^{p-1} u(\boldsymbol{x}))v(\boldsymbol{x})d\boldsymbol{x}$. The Fréchet derivatives of f and F at $\varphi \in H_0^1(\Omega)$ are denoted by f'_φ and F'_φ, respectively, and given by

$$\left\langle f'_\varphi u, v\right\rangle = \int_\Omega (p|\boldsymbol{x} - \boldsymbol{x_0}|^l |\varphi(\boldsymbol{x})|^{p-1}) u(\boldsymbol{x}) v(\boldsymbol{x}) d\boldsymbol{x} \quad \text{for all} \quad u, v \in H_0^1(\Omega), \tag{2}$$

$$\left\langle F'_\varphi u, v\right\rangle = (\nabla u, \nabla v)_{L^2} - \left\langle f'_\varphi u, v\right\rangle \quad \text{for all} \quad u, v \in H_0^1(\Omega). \tag{3}$$

Then, we consider the following problem:

$$\text{Find} \quad u \in H_0^1(\Omega) \quad \text{s.t.} \quad F(u) = 0, \tag{4}$$

which is the weak form of the problem (1). Then, we apply the Newton–Kantorovich theorem [4], which enables us to prove the existence of a true solution u near a numerically computed approximate solution $\hat{u}$.

In this talk, we will present the results of verifying the existence of true solutions u near approximate solutions $\hat{u}$ such as shown in Tables 1 to 3.

Table 1: Approximate solutions on $\Omega = (-1, 1)$ with $p = 3, l = 1, 1.75$.

l	1	1.75		
$\hat{u}$	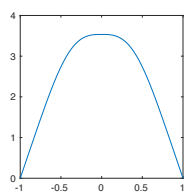	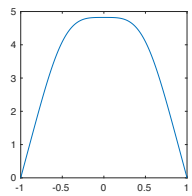	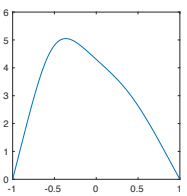	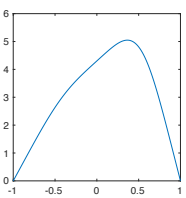

Table 2: Approximate solutions on $\Omega = (-1, 1)^2$ with $p = 3, l = 0, 2$.

l	0	2		
$\hat{u}$	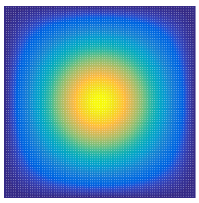	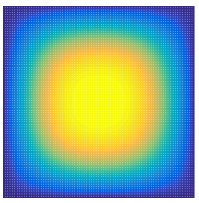	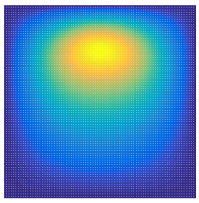	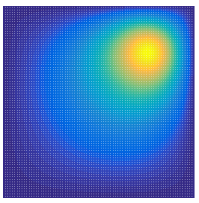

Table 3: Approximate solutions on $\Omega = \{\boldsymbol{x} \in \mathbb{R}^2 : |\boldsymbol{x}| < 1\}$ with $p = 3, l = 0, 6$.

l	0	6		
$\hat{u}$	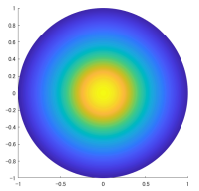	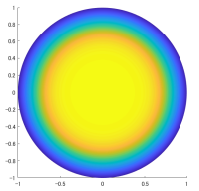	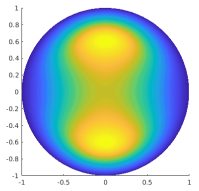	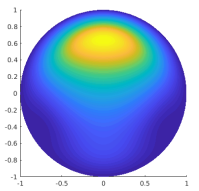

References

[1] S. Tanaka: Morse index and symmetry–breaking for positive solutions of one–dimensional Hénon type equations, *Journal of Differential Equations*, 255:7 (2013), 1709–1733.

[2] N. Shioji, K. Watanabe: Radial symmetry of n-mode positive solutions for semilinear elliptic equations in a disc and its application to the Hénon equation, *Topological Methods in Nonlinear Analysis*, 43:1 (2014), 269–285.

[3] N. Shioji: Existence of Many Nonradial Positive Solutions of the Hénon Equation in $\mathbb{R}^3$, *Journal of Convex Analysis*, 22:1 (2015), 61–80.

[4] P. Deuflhard, G. Heindl: Affine invariant convergence theorems for Newton's method and extensions to related methods. *SIAM Journal on Numerical Analysis*, 16:1 (1979), 1–10.

JSST 2021

Acceleration of Error-Free Transformation of Matrix Multiplication using GPU Tensor Cores

Katsuhisa Ozaki[1,*], Daichi Mukunoki[2], Takeshi Ogita[3]

[1]Department of Mathematical Sciences, Shibaura Institute of Technology
[2]Riken Center of Computational Science
[3]Division of Mathematical Sciences, Tokyo Woman's Christian University

[*]ozaki@sic.shibaura-it.ac.jp

Abstract. This study aims to provide an accurate numerical result of matrix multiplication using floating-point arithmetic. An error-free transformation of matrix multiplication is proposed, which is very useful for proposing accurate numerical algorithms for matrix multiplication. We improve the original error-free transformation by reducing the number of matrix multiplications in the transformation. Numerical results on a recently provided GPU by NVIDIA illustrate the efficiency of the proposed method.

Keywords: Matrix Multiplication, Graphics Processing Unit, Tensor Core, Accurate Numerical Algorithms

1. Introduction

Floating-point arithmetic [1] is widely used in scientific computing due to its impressive performance. Matrix multiplication plays a crucial role in numerical linear algebra. However, if a problem is ill-conditioned, heavy cancellation occurs in the dot product; a computed result may be inaccurate due to the accumulation of rounding errors. In the worst case, a relative error is greater than one; the computed result has no correct digit. There have been many discussions for improving the accuracy of numerical results, e.g., multiple-precision arithmetic [2, 3, 4], double word arithmetic [5], and accurate numerical computations [6].

An error-free transformation for matrix multiplication has been proposed [7]. The method is used for proposing accurate algorithms for matrix multiplication. Its performance is exceptional due to the dependency of GEMM on basic linear algebra subprograms. Single precision arithmetic is much faster than double-precision arithmetic on some GPUs, e.g., the RTX series by NVIDIA. Using such GPUs, Mukunoki et al. [8] proposed an error-free transformation. Especially, the Tensor Core is efficiently used in computations. In this study, we reduce the number of matrix multiplications and accelerate the error-free transformation. Numerical results shown in the presentation illustrate the efficiency of the proposed method.

2. Error-free Transformation using Tensor Core

Let $\mathbb{F}_w$ be a set of w-bit floating-point numbers, e.g., $\mathbb{F}_{64}$ is a set of floating-point numbers represented by binary64. Denote $\mathtt{fl}_w(\cdot)$ as a computed result using w-bit floating-point arithmetic. For $A \in \mathbb{F}_w^{m\times n}$ and $B \in \mathbb{F}_w^{n\times p}$, we aim to obtain an accurate approximation of AB.

We briefly introduce the error-free transformation proposed in [7]. Matrices A and B are split such that

$$\begin{aligned} A &= A_1 + A_2 + \cdots + A_k, \quad A_i \in \mathbb{F}_w^{m\times n},\ 1 \le i \le k, \\ B &= B_1 + B_2 + \cdots + B_\ell, \quad B_j \in \mathbb{F}_w^{n\times p},\ 1 \le j \le \ell \end{aligned}$$

to satisfy

$$\mathtt{fl}_w\left(A_iB_j\right) = A_iB_j$$

for all (i, j) pairs. Then, AB can be transformed into an unevaluated sum of $k\ell$ floating-point matrices such that

$$AB = \sum_{i=1}^{k}\sum_{j=1}^{\ell} A_iB_j.$$

In the original paper, numerical examples with $w = 64$ were presented.

Mukunoki et al. exploited fast low-precision arithmetic on GPUs [8]. The matrices $A \in \mathbb{F}_{64}^{m\times n}$ and $B \in \mathbb{F}_{64}^{n\times p}$ are split such that

$$\begin{aligned} A = &\quad P_1^{-1}P_1A_1 + P_2^{-1}P_2A_2 + \cdots + P_{k'}^{-1}P_{k'}A_{k'}, \quad P_iA_i \in \mathbb{F}_{32}^{m\times n},\ 1 \le i \le k', \\ B = &\quad B_1Q_1Q_1^{-1} + B_2Q_2Q_2^{-1} + \cdots + B_{\ell'}Q_{\ell'}Q_{\ell'}^{-1}, \quad B_jQ_j \in \mathbb{F}_{32}^{n\times p},\ 1 \le j \le \ell' \end{aligned} \tag{1}$$

to satisfy

$$\mathtt{fl}_{32}\left((P_iA_i)(B_jQ_j)\right) = P_iA_iB_jQ_j,$$

where P_i and Q_j are diagonal matrices. Here, k' and ℓ' are larger than k and ℓ, respectively. Then, we have

$$AB = \sum_{i=1}^{k'}\sum_{j=1}^{\ell'} P_i^{-1}(P_iA_i)(B_jQ_j)Q_j^{-1}.$$

Besides,

$$P_iA_i \in \mathbb{F}_{16}^{m\times n}, \quad B_jQ_j \in \mathbb{F}_{16}^{n\times p}$$

holds true for $n \ge 2$, and we can exploit the Tensor Core for $(P_iA_i)(B_jQ_j)$.

First, we apply the technique [9] to the original error-free transformation. Next, we focus on the sparsity of A_i and B_j. In the original error-free transformation, $\lceil \log_2 n \rceil$ bit carrying is assumed in a dot product in matrix multiplication. We consider the number of non-zero elements for the splitting. Combing these strategies, we can effectively reduce k' and ℓ' in (1). The detailed algorithm and numerical results will be shown in the presentation in JSST 2021.

References

[1] IEEE standard for floating-point arithmetic. ANSI/IEEE Std 754-2008, 1–70.

[2] The GNU Multiple Precision Arithmetic Library, https://gmplib.org/.

[3] The GNU MPFR Library, https://www.mpfr.org/.

[4] exflib - extend precision floating-point arithmetic library, http://www-an.acs.i.kyoto-u.ac.jp/~fujiwara/exflib/.

[5] High-Precision Software Directory, https://www.davidhbailey.com/dhbsoftware/.

[6] T. Ogita, S.M. Rump, and S. Oishi: Accurate sum and dot product, *SIAM Journal on Scientific Computing (SISC)*, 26:6 (2005), 1955–1988.

[7] K. Ozaki, T. Ogita, S. Oishi, and S.M. Rump: Error-free transformations of matrix multiplication by using fast routines of matrix multiplication and its applications, *Numerical Algorithms*, 59: 1 (2012), 95–118.

[8] D. Mukunoki, K. Ozaki, T. Ogita, and T. Imamura: DGEMM Using Tensor Cores, and Its Accurate and Reproducible Versions, *In: Sadayappan P., Chamberlain B., Juckeland G., Ltaief H. (eds) High Performance Computing. ISC High Performance 2020. Lecture Notes in Computer Science*, 12151 (2020), 230–248.

[9] A. Minamihata, K. Ozaki, T. Ogita, and S. Oishi: Improved extraction scheme for accurate floating-point summation, *In: The 35th JSST Annual Conference International Conference on Simulation Technology*, 2016.

JSST 2021

Generation of Implicit Surface Based on Isoparametric Elements

Taku Itoh[1,*]

[1]College of Industrial Technology, Nihon University, Japan

*itoh.taku@nihon-u.ac.jp

Abstract. To decrease the memory cost of volume data-based method for generating an implicit surface $g(\boldsymbol{x}) = 0$, a method based on isoparametric elements has been proposed, where $g(\boldsymbol{x})$ is a scalar field generated from surface points obtained from three-dimensional scanning devices. In this method, $g(\boldsymbol{x})$ can be generated from volume data directly. Namely, since the piecewise polynomials are not employed, their coefficients do not need to retain in the proposed method. Numerical experiments show that the result of the proposed method is visually almost the same with that of the conventional one. In addition, the memory cost of the proposed method can be decreased to 1/27 in comparison with that of the conventional one.

Keywords: Implicit surface, Isoparametric elements, Volume data

1. Introduction

This paper focuses on generation of a scalar field $g(\boldsymbol{x})$ for implicit surface. The scalar field has been employed for surface reconstruction from a set of surface points $\mathcal{X} = \{\boldsymbol{x}_1, \boldsymbol{x}_2, \ldots, \boldsymbol{x}_n\}$ obtained from three-dimensional scanning devices. In addition, many methods have been proposed for generating the scalar field $g(\boldsymbol{x})$ [1, 2, 3, 4]. An implicit surface is represented as $g(\boldsymbol{x}) = 0$. Note that the rendering cost for extracting $g(\boldsymbol{x}) = 0$ tends to be high usually.

A method described in [3] has enabled to render $g(\boldsymbol{x}) = 0$ in real-time on graphics processing unit (GPU). In this method, a set of field values $f_{i,j,k}$ (volume data) on N^3 uniform grid points $\boldsymbol{x}_{i,j,k}$ are required for generating $g(\boldsymbol{x})$. In addition, piecewise polynomials based on the B-spline are constructed from the field values [3]. The field values $f_{i,j,k}$ are obtained by evaluating another scalar field $f(\boldsymbol{x})$ generated from $\mathcal{X}$ by such as multi-level partition of unity implicits (MPU) method [2]. Namely, $f(\boldsymbol{x})$ is indispensable as an intermediate for generating $g(\boldsymbol{x})$.

A method for determining $f_{i,j,k}$ without the intermediate has been proposed [4]. In the method, $f_{i,j,k}$ can be determined from $\mathcal{X}$ directly. Note that some coefficients for constructing piecewise polynomials have to be retained as well as [3], although the intermediate is not required in [4]. Hence, the memory cost becomes large for the case where a complex-shaped object is represented.

On the other hands, isoparametric elements have been employed in the finite element analysis [5]. The isoparametric elements are employed for interpolating values between nodes in the analysis. If the isoparametric elements are embedded to the method in [4], the memory cost of [4] may be decreased.

The purpose of this study is to propose a method for generating an implicit surface based on the isoparametric elements. To this end, the method described in [4] is modified so that $g(\boldsymbol{x})$ can be generated from $f_{i,j,k}$ directly. Namely, since the piecewise polynomials are not employed, their coefficients do not need to retain in the proposed method.

2. Implicit Surface Based on Isoparametric Elements

By the method described in [4], the field values $f_{i,j,k}$ can directly be determined from the given point data $\mathcal{X} = \{\boldsymbol{x}_1, \boldsymbol{x}_2, \ldots, \boldsymbol{x}_n\}$ together with normals $\mathcal{N} = \{\boldsymbol{n}_1, \boldsymbol{n}_2, \ldots, \boldsymbol{n}_n\}$, where n is the number of given points. We employ the field values $f_{i,j,k}$ in the proposed method. Figure 1 shows an example of a set of field values $f_{i,j,k}$ on $\boldsymbol{x}_{i,j,k}$ $(1 \leq i, j, k \leq N)$ in a cubic domain Ω. In this figure, the red and blue nodes are large and small field values, respectively. The detail procedures for obtaining the field values $f_{i,j,k}$ are shown in [4].

Here, 8-nodes three-dimensional (3D) isoparametric elements are written as follows:

$$
\begin{aligned}
N_1(\boldsymbol{t}) &= \frac{1}{8}(1-\xi)(1-\eta)(1-\zeta), & N_2(\boldsymbol{t}) &= \frac{1}{8}(1+\xi)(1-\eta)(1-\zeta),\\
N_3(\boldsymbol{t}) &= \frac{1}{8}(1+\xi)(1+\eta)(1-\zeta), & N_4(\boldsymbol{t}) &= \frac{1}{8}(1-\xi)(1+\eta)(1-\zeta),\\
N_5(\boldsymbol{t}) &= \frac{1}{8}(1-\xi)(1-\eta)(1+\zeta), & N_6(\boldsymbol{t}) &= \frac{1}{8}(1+\xi)(1-\eta)(1+\zeta),\\
N_7(\boldsymbol{t}) &= \frac{1}{8}(1+\xi)(1+\eta)(1+\zeta), & N_8(\boldsymbol{t}) &= \frac{1}{8}(1-\xi)(1+\eta)(1+\zeta),
\end{aligned}
$$

where $\boldsymbol{t} = [\xi, \eta, \zeta]^{\mathrm{T}}$, $\xi \in [-1, 1], \eta \in [-1, 1]$ and $\zeta \in [-1, 1]$. Here, a scalar value function $g(\boldsymbol{x})$ is represented as

$$
g(\boldsymbol{x}) = \sum_{i=1}^{N-1} \sum_{j=1}^{N-1} \sum_{k=1}^{N-1} g_{ijk}(\boldsymbol{t}(\boldsymbol{x})), \tag{1}
$$

where $g_{ijk}(\boldsymbol{t}(\boldsymbol{x}))$ is a local scalar value function in (i, j, k)-th cubic subdomain $\Omega_{i,j,k}$ constructed by $\{\boldsymbol{x}_{i,j,k}, \boldsymbol{x}_{i+1,j,k}, \boldsymbol{x}_{i+1,j+1,k}, \boldsymbol{x}_{i,j+1,k}, \boldsymbol{x}_{i,j,k+1}, \boldsymbol{x}_{i+1,j,k+1}, \boldsymbol{x}_{i+1,j+1,k+1}, \boldsymbol{x}_{i,j+1,k+1}\}$, as shown in Fig. 2. Here, $g_{ijk}(\boldsymbol{t}(\boldsymbol{x}))$ $(1 \leq i, j, k \leq N-1)$ is represented as

$$
\begin{aligned}
g_{ijk}(\boldsymbol{t}(\boldsymbol{x})) &= N_1(\boldsymbol{t}) f_{i,j,k} + N_2(\boldsymbol{t}) f_{i+1,j,k} + N_3(\boldsymbol{t}) f_{i+1,j+1,k} + N_4(\boldsymbol{t}) f_{i,j+1,k}\\
&+ N_5(\boldsymbol{t}) f_{i,j,k+1} + N_6(\boldsymbol{t}) f_{i+1,j,k+1} + N_7(\boldsymbol{t}) f_{i+1,j+1,k+1} + N_8(\boldsymbol{t}) f_{i,j+1,k+1},
\end{aligned}
$$

where $f_{i,j,k}$ is a field value on $\boldsymbol{x}_{i,j,k}$ $(1 \leq i, j, k \leq N)$. Note that $g_{ijk}(\boldsymbol{t}(\boldsymbol{x})) = 0 \notin \Omega_{i,j,k}$.

To evaluate $g(\boldsymbol{x})$, a subdomain $\Omega_{i,j,k}$ that contains $\boldsymbol{x}$ is first searched, and $g_{ijk}(\boldsymbol{t}(\boldsymbol{x}))$ is evaluated. Here, $\boldsymbol{t}(\boldsymbol{x}) = [\xi(x), \eta(y), \zeta(z)]^{\mathrm{T}}$ is determined by

$$
\boldsymbol{t}(\boldsymbol{x}) = \frac{2}{\Delta d}(\boldsymbol{x} - \boldsymbol{x}_{i,j,k}) - [1, 1, 1]^{\mathrm{T}} \in \Omega_{i,j,k}, \tag{2}
$$

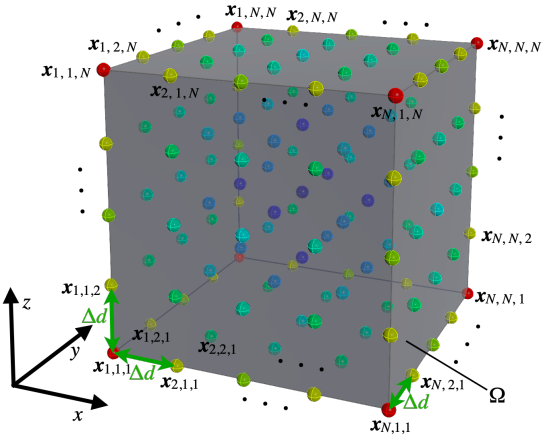

Figure 1: An example of a set of field values $f_{i,j,k}$ on $\boldsymbol{x}_{i,j,k}$ $(1 \leq i, j, k \leq N)$ in a cubic domain Ω. The red and blue nodes are large and small field values, respectively.

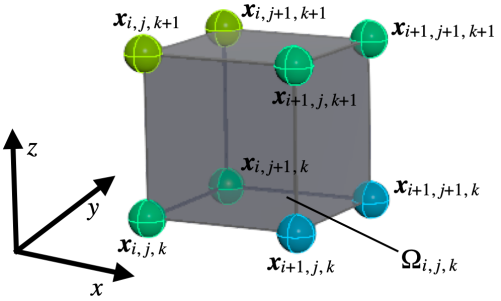

Figure 2: Enlarged view of (i, j, k)-th cubic subdomain $\Omega_{i,j,k}$ constructed by $\{\boldsymbol{x}_{i,j,k}, \boldsymbol{x}_{i+1,j,k}, \boldsymbol{x}_{i+1,j+1,k}, \boldsymbol{x}_{i,j+1,k}, \boldsymbol{x}_{i,j,k+1}, \boldsymbol{x}_{i+1,j,k+1}, \boldsymbol{x}_{i+1,j+1,k+1}, \boldsymbol{x}_{i,j+1,k+1}\}$.

where $\boldsymbol{x} = [x, y, z]^{\mathrm{T}}$, $\boldsymbol{x}_{i,j,k} = [x_i, y_j, z_k]^{\mathrm{T}}$, and $\Delta d = |x_{i+1} - x_i| = |y_{j+1} - y_j| = |z_{k+1} - z_k|$ as shown in Fig. 1. An implicit surface $g(\boldsymbol{x}) = 0$ can be extracted by ray-marching method [3], marching-cubes method [6], or Bloomenthal's polygonizer [7].

3. Numerical Experiments

In this section, numerical experiments are conducted to evaluate the proposed method by employing Bunny model ($n = 34834$) [8]. This model is first rescaled so that the given points are lie in a unit cube $[0, 1) \times [0, 1) \times [0, 1)$.

As results of implicit surfaces of Bunny model obtained by conventional method [4] and proposed one are shown in Figs. 3(a) and 3(b), respectively ($N = 400$). We see from these figures that Bunny models are reconstructed by both methods. Although these results are visually almost the same, the accuracy of the conventional method may be better than that of the proposed one. This is because the conventional method employs the quadratic polynomials for interpolating the field values $f_{i,j,k}$. Note that, by employing the 8-points 3D isoparametric elements, the field values $f_{i,j,k}$ are interpolated as linear function in the proposed method. However, to represent the piecewise polynomial, 27 coefficients have to be retained for each subdomain, in the conventional method. In the proposed method, to evaluate $g(\boldsymbol{x})$, $f_{i,j,k}$ on $\boldsymbol{x}_{i,j,k}$ $(1 \leq i, j, k \leq N)$ are required. Note that retaining $\boldsymbol{x}_{i,j,k}$ $(1 \leq i, j, k \leq N)$ is not required, since $\boldsymbol{x}_{i,j,k}$ can be calculated as $\boldsymbol{x}_{i,j,k} = [(i-1)\Delta d, (j-1)\Delta d, (k-1)\Delta d]^{\mathrm{T}}$. Hence, in the proposed method, retaining the field values $f_{i,j,k}$ $(1 \leq i, j, k \leq N)$ is only required. Since the number of piecewise polynomials in the conventional method and that of field values in the proposed one are the same, N^3, the memory cost of proposed method can be decreased to 1/27 in comparison with that of conventional one.

Other results and further details will be presented at the conference.

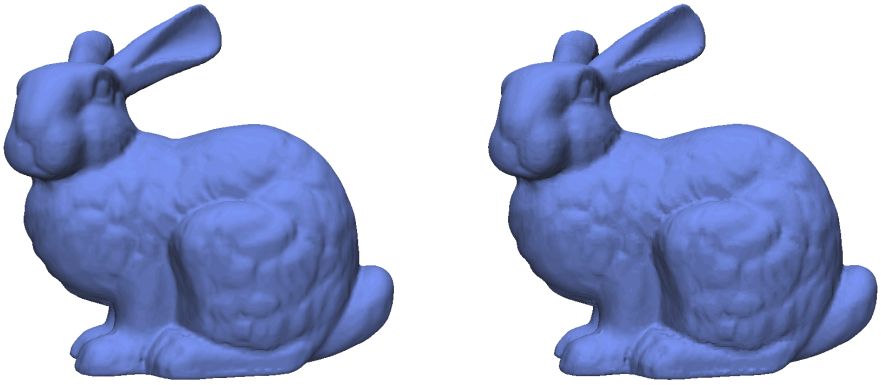

(a) (b)

Figure 3: Results of implicit surfaces of Bunny model obtained by (a) conventional method and (b) proposed method, respectively.

References

[1] G. Turk, J. F. O'Brien: Modelling with Implicit Surfaces that Interpolate, *ACM Transactions on Graphics*, 21:4 (2002), 855–873.

[2] Y. Ohtake, A. Belyaev, M. Alexa, G. Turk, H.-P. Seidel: Multi-level partition of unity implicits, *ACM Transactions on Graphics*, 22:3 (2003), 463–470.

[3] S. Nakata, S. Aoyama, R. Makino, K. Hasegawa, S. Tanaka: Real-time isosurface rendering of smooth fields, *Journal of Visualization*, 15:2 (2012), 179–187.

[4] T. Itoh, S. Nakata: Fast generation of smooth implicit surface based on piecewise polynomial, *Computer Modeling in Engineering & Sciences*, 107:3 (2015), 187–199.

[5] D. V. Hutton: Fundamentals of Finite Element Analysis, McGraw-Hill, Boston (2004).

[6] W. E. Lorensen, H. E. Cline: Marching cubes: A high resolution 3D surface construction algorithm, *Computer Graphics* , 21:4 (1987), pp. 163–169.

[7] J. Bloomenthal, C. Bajaj, J. Blinn, M.-P. Cani-Gascuel, A. Rockwood, B. Wyvill, G. Wyvill: Introduction to Implicit Surfaces, Morgan Kaufmann Publishers, Inc., San Francisco (1997).

[8] *The Stanford 3D Scanning Repository*, accessed on Jun. 24, 2021. [Online]. Available: http://www.graphics.stanford.edu/data/3Dscanrep/

JSST2021

A Study for Recognizing and Simulating Deliberate Emotional Expressions in Japanese Speech

Chihiro Asada[1*], Yuichi Tamura[2], Ryo Nagata[2], Katsunari Sato[1]

[1]Major in Human Centered Engineering, Nara Women's University
[2]Department of Intelligence and Informatics, Konan University
*chihiro.asada.mmg@gmail.com

Abstract. In this study, a classification method for Japanese utterances with deliberate emotional expressions was investigated. We generated annotation data for deliberate emotional expressions using existing speech data. From the classification results, using a support vector machine, we found that our method could classify deliberate emotional expressions contained in utterances with a micro-averaged F1 score of 0.47.

Keywords: Affective computing, Speech emotion recognition, Support vector machine

1. Introduction

Although emotions are an essential part of human communication, it is difficult for a listener to accurately recognize a speaker's intended emotions. This problem can be reduced if a speaker realizes that the intentions contained in their emotional expressions are not conveyed based on the objective emotion recognition results of systems that help human– human interaction. Users of such computer systems can learn deliberate emotional expressions that are comprehensible by others, and they can acquire a common understanding for communication.

In this study, we investigated a method for classifying deliberate emotional expressions that are commonly recognized by a certain number of people in a conversation to develop such systems. We aimed to achieve the following objectives.

1. Creation of annotation data for deliberate emotional expression using existing speech data.
2. Construction of a system to classify deliberate emotional expressions from non-verbal information using a support vector machine (SVM).
3. Analysis of the classification results to reveal the features of speech including deliberate emotional expressions.

Because Japanese people tend to recognize emotions using sounds rather than their content [2], we developed an emotion classification method using utterances. Furthermore, for the classification of emotions, we focus on a part of "emotion regulation" [3], which can change the behavior of others. IHASZ et al. [4] used an emotion model that resembled emotion regulation for classification; however, systems that objectively classify emotions to help users communicate with each other have not yet been researched. Therefore, this study examined the expansion of emotion recognition and simulation technologies.

2. Creation of training data

First, we created the annotated "Utsunomiya University Spoken Dialogue Database (UUDB)" [5] with deliberate emotional expressions. A total of 27 Japanese female undergraduate and

graduate students participated in the annotation exercise. They listened continuously to the speech of one person in a dialogue between two people and marked the parts where they perceived deliberate emotional expressions. The participants used two types of marks that we defined as "positive" and "negative," which conveyed the intention to encourage and inhibit a person's conduct, respectively. We did not define the length of the mark because the length to which people perceive deliberate emotional expressions is unclear. We used 1,433 utterances by two Japanese females and 1,134 utterances by two Japanese males, for a total of 2,567 Japanese utterances from the UUDB. Due to missing annotation data, the actual number of participants who annotated varied for each speech, with a maximum of 26, a minimum of 24, and an average of 25.

In the second step, we allocated labels to the utterance segments based on the marked results of the participants. The label was determined using the following process.

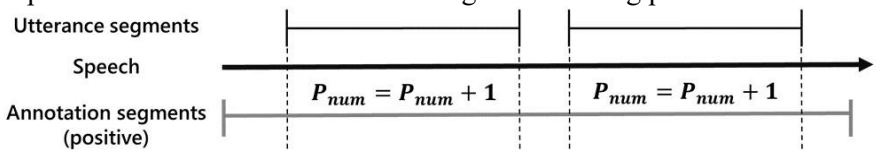

Fig.1. Matching the utterance segments in UUDB with the segments where the participants perceived the specified deliberate emotional expression

1. We matched the marked results with the utterance segments in UUDB (Fig.1). Subsequently, we counted the following numbers based on the matching results — P_{num}: number of positive marks, I_{num}: number of negative marks, S_{num}: number of participants in the annotation, and N_{num}: number of neutral (no deliberate emotional expression) for each utterance were calculated.

2. To determine the label, we calculated "the degree of intention," which indicates the tendency of the intentions (positive, negative, or neutral) in utterances. Positive and negative degrees of intention in an utterance were respectively defined as

$$P_{\mathrm{degree}} = P_{\mathrm{w}} P_{\mathrm{num}} \; and \; I_{\mathrm{degree}} = -I_{\mathrm{w}} I_{\mathrm{num}}.$$

P_{w} and I_{w} are parameters that can change the weight of the intentions. Because negative utterances receive more attention than positive ones [6], we experimentally set the parameters P_{w} to 1.0, and I_{w} to 2.0 to reduce the pattern of the trained model that misclassified the negative intentions. Furthermore, we calculated L_{degree}, which represents the degree (encouraging or inhibiting trend) of the intention in an utterance. We also calculated N_{ratio}, which is the percentage of participants who did not perceive deliberate emotional expressions for an utterance. The calculations for L_{degree}, and N_{ratio} are as follows:

$$L_{\mathrm{degree}} = \frac{(P_{\mathrm{degree}} + I_{\mathrm{degree}})}{S_{\mathrm{num}}}, N_{\mathrm{ratio}} = \frac{N_{\mathrm{num}}}{S_{\mathrm{num}}}.$$

3. We assigned labels to the utterances based on L_{degree}, and N_{ratio}. "Positive" and "negative" were assigned for the cases where $L_{\mathrm{degree}} \geq T$ and $L_{\mathrm{degree}} \leq -T$, respectively. For other utterances, "neutral" was assigned for the case where $N_{\mathrm{ratio}} \geq T$. The threshold T was set to 0.6. When none of the above conditions were satisfied, "unknown" was assigned so that the system could recognize "some intention" that was not "neutral," although the participants' judgments differed.

In the third step, we created 386-dimensional feature vectors consisting of 384 dimensions of acoustic features, which were extracted using the feature set IS09 of open SMILE [7], and two dimensions of timeline data of the start and end times of utterances from UUDB. The latter two

were included assuming a relationship between the timeline of the utterance and the strength of the deliberate emotional expression.

3. Classification method

Considering that people approximately guess deliberate emotions, a linear soft-margin SVM method was adopted as the classification method. In addition, the binary classification SVM was extended to multiclass classification using a one versus other method. The ratio of training data to test data was 7:3. The regularization parameter C was set to 0.00039 using the Bayesian optimization with 10-fold cross-validation. The trained model was evaluated based on a micro-averaged F1 score, confusion matrix, and recall score for each deliberate emotional expression.

4. Results and discussion

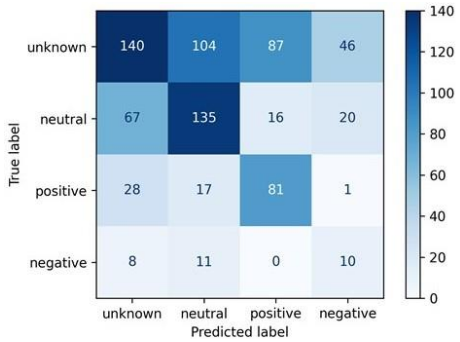

Fig.2 Confusion matrix of the test data

Table.1: (i) Number of each label and average of each label's L_{degree}. (ii) Average and standard deviation of marks for each label. (iii) Recall score for each deliberate emotional expression. (iv) Average of L_{degree}, and decision function score (unknown). (v) Average of L_{degree}, and decision function score (neutral).

(i)

		The number of labels	Percentage of each label (%)
The number of labels	Unknown	1254	48.85
	Neutral	793	30.89
	Positive	422	16.44
	Negative	98	3.82
		average	Standard deviation
L_{degree} Average	Unknown	0.23	0.28
	Neutral	0.18	0.16
	Positive	0.71	0.09
	Negative	-0.93	0.27

(ii)

labels		Annotation marks		
		Positive	Negative	Neutral
Positive	Average	19.00	0.30	6.69
	Standard deviation	2.17	0.50	2.21
Negative	Average	3.98	13.85	7.84
	Standard deviation	1.87	2.97	2.92
Neutral	Average	7.36	1.35	17.13
	Standard deviation	1.69	1.38	1.17
Unknown	Average	11.68	2.82	11.52
	Standard deviation	3.31	2.51	2.85

(iii)

Labels	Unknown	Neutral	Positive	Negative
Recall (%)	38.46	55.46	62.20	34.48

(iv)

Misclassified labels			Decision function score	
		L_{degree}	Positive	Negative
Positive n = 86	Average	0.39	0.22	-0.72
	Standard deviation	0.22	0.25	0.24
Negative n = 46	Average	0.12	-0.64	0.09
	Standard deviation	0.29	0.24	0.24

(v)

Misclassified labels			Decision function score	
		L_{degree}	Positive	Negative
Positive n = 16	Average	0.15	0.14	-0.74
	Standard deviation	0.17	0.24	0.26
Negative n = 22	Average	0.10	-0.63	0.06
	Standard deviation	0.18	0.26	0.17

Table. 1-(i) shows that more utterances were labeled as unknown or neutral than positive or negative. Table. 1-(ii) shows that approximately 50% of the participants commonly perceived negative, although there was more variability than the other labeled data. The micro-averaged F1 score was 0.47, and approximately half of the test data was classified correctly. Table. 1-(iii) shows that the recall score of the negative group was 34.48%. Fig. 2 shows the confusion matrix of the test data. The darker the color of the color bar, the more data there is. This result

suggests that there was no error in misclassifying negative as positive in the confusion matrix. Based on these results, our system can facilitate communication by estimating the deliberate emotional expressions from utterances.

For the analysis of unknown and neutral labeled data, we used the average of L_{degree} and decision function scores of the unknown and neutral data that were misclassified as positive or negative. The decision function score is a metric of the distance between the predicted data and hyperplane, where the highest score is the predicted value. Table.1-(iv) and (v) show the results of the analysis. The data that were misclassified as positive had the following characteristics: the average of L_{degree} tended to be positive for the smallest negative decision function score. The data that were misclassified as negative had the following characteristics: the average L_{degree} was approximately zero for the smallest positive decision function score. These results imply that some of the data misclassified as positive or negative were judged as positive or negative, respectively. Therefore, better classification results can be obtained by changing the criteria for labeling the training data.

5. Conclusion

In this study, a classification method for Japanese utterances with deliberate emotional expressions was investigated. Our method could classify intentions contained in utterances with a micro-averaged F1 score of 0.47. In addition, utterances labeled as negative were commonly perceived as containing negative intentions by approximately 50% of the participants.

6. Acknowledgements

This work was supported by JSPS KAKENHI Grant Number JP18K11416.

References

[1] B. Carlos, et al.: “Analysis of emotion recognition using facial expressions, speech and multimodal information,” *Proceedings of the 6th international conference on Multimodal interfaces*, (2004), pp. 205-211.

[2] K. Shinobu, et al.: “Word and voice: Spontaneous attention to emotional utterances in two languages,” *Cognition & Emotion*, volume:16.1, (2002), pp. 29-59.

[3] G. James J.: “Emotion regulation,” *Handbook of emotions*, (2008), pp. 497-513.

[4] P. L. IHASZ, et al.: “Emotion Recognition through Intentional Context-Towards Advancing In-game Affect Awareness,” *International Journal of Affective Engineering*, volume:18.1, (2019), pp. 17-25.

[5] M. Hiroki, et al.: “Constructing a spoken dialogue corpus for studying paralinguistic information inexpressive conversation and analyzing its statistical/acoustic characteristics,” *Speech Communication*, volume:53, (2011), pp. 36-50.

[6] R. F. Baumeister, et al.: “Bad is Stronger than Good,” Review of General Psychology, volume:5, (2001), pp. 323-370.

[7] F. Eyben, et al.: “openSMILE - The Munich Versatile and Fast Open-Source Audio Feature Extractor,” *Proc. ACM Multimedia (MM)*, Florence: Italy, (2010), pp. 1459-1462.

Continuous collision avoidance model between pedestrians

Kotori Tsutsumi[1*], Yuichi Tamura[2], Katsunari Sato[1]

[1] Nara Women's University
[2] Konan University
*uak_tsutsumi@cc.nara-wu.ac.jp

Abstract. The phenomenon whereby pedestrians who are facing each other continuously avoid one another in the same direction and cannot move forward is known as "continuous collision avoidance." We propose a model for continuous collision avoidance based on the pedestrian walking velocity. The simulation results demonstrated that the proposed model was effective and could reproduce the phenomenon of continuous collision avoidance.

Keywords: Simulation of human flow, avoidance model

1. Introduction

While walking, it is likely that a pedestrian will collide with another oncoming pedestrian. Both parties attempt to avoid the other, but if avoidance occurs in the same direction the first time, this will be repeated the next time and thereafter. This phenomenon is known as continuous collision avoidance (Fig. 1).

This study's purpose is to simulate continuous collision avoidance. By simulating this phenomenon, it can be used in advance for designs such as walkways, corridors, and station gates. Furthermore, by implementing it in a virtual reality (VR) environment as well as by acquiring human behavioral data in the VR environment and providing feedback to the simulation parameters, it is possible to represent a more natural gait for the avatar. The social force model (SFM) proposed by Helbeing et al. [1] is a method for reproducing the flow of people. In our proposed model in this study, a new equation is added and implemented so that continuous collision avoidance would occur based on the SFM.

2. Algorithm of Continuous-avoidance Simulation

We propose an algorithm for continuous collision avoidance. The current position of the pedestrian (at a certain time $t - \Delta t$) and the predicted position of the pedestrian Δt later (t) were indicated by the black circle and dotted virtual circle (hereinafter referred to as "ghost") in Fig. 2. The SFM was used to determine the predicted position. As Fig. 2 illustrates, the position of the ghost was derived from $\boldsymbol{v}_i(t)$, which was the sum of the velocity vector ($\boldsymbol{v}_i$ $(t - \Delta t)$) of the pedestrian at a certain time $(t - \Delta t)$ and the velocity ($\frac{\boldsymbol{f}i(t)}{2m}\Delta t$), which was calculated

from the average acceleration vector originating from external forces, which was derived from $\boldsymbol{v}_i(t)$.

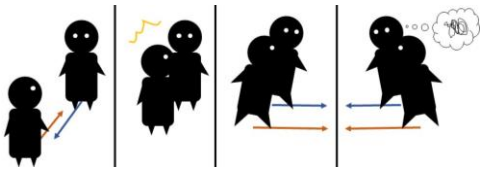

Fig. 1: Continuous collision avoidance

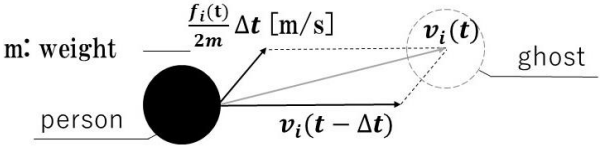

Fig. 2: Decision of predicted position

The external force was determined by the total force of the repulsive force received from other pedestrians and the attractive force received from the destination, which was expressed by Eqs. (1) and (2) [2– 4]. In our proposed simulation model, when two pedestrians were about to collide with one another, the external force was determined by Eq. (3).

$$\frac{d\boldsymbol{v}_i}{dt} = \boldsymbol{f}_i(t) + \boldsymbol{\xi}_i \tag{1}$$

$$\boldsymbol{f}_i(t) = \boldsymbol{f}_i^0(t) + \sum_{j\neq i}\boldsymbol{f}_{ij}^{soc}(t) + \sum_{j\neq i}\boldsymbol{f}_{iW}^{wall}(t) \tag{2}$$

(Dis $>$ thr : Dis is the distance between ghosts and thr is the decision threshold)

$$\boldsymbol{f}_i(t) = \boldsymbol{f}_{ij}^{sig}(t)(\text{Dis} \leq \text{thr}) \tag{3}$$

where $\boldsymbol{\xi}_i$ was the fluctuation term, $\boldsymbol{f}_i^0(t)$ was the attractive force that pedestrian i experienced from the destination, i.e., the propulsive force to the destination, and $\boldsymbol{f}_{ij}^{soc}(t)$ was the social repulsive force that caused pedestrian i to maintain a distance from another pedestrian j. Moreover, $\boldsymbol{f}_{iW}^{wall}(t)$ was the repulsive force of pedestrian i attempting to maintain a distance from the wall, and $\boldsymbol{f}_{ij}^{sig}(t)$ was the force experienced by pedestrian i when a collision with another pedestrian j was about to occur. In this case, $\boldsymbol{f}_i^0(t), \boldsymbol{f}_{ij}^{soc}(t)$, and $\boldsymbol{f}_{iW}^{wall}(t)$ were represented by Eqs. (4), (5), and (6), respectively, whereas the added $\boldsymbol{f}_{ij}^{sig}(t)$ was represented by Eq. (7).

$$\boldsymbol{f}_i^0(t) = \frac{v_i^0\boldsymbol{e}_i - \boldsymbol{v}_i}{\tau_i} \tag{4}$$

$$\boldsymbol{f}_{ij}^{soc}(t) = A_i \exp\left(\frac{r_{ij}-d_{ij}}{Bi}\right)\boldsymbol{n}_{ij} \tag{5}$$

$$\boldsymbol{f}_{iW}^{wall}(t) = C_i \exp\left(-\frac{d_{iW}}{Di}\right)\boldsymbol{n}_{iW} \tag{6}$$

$$\boldsymbol{f}_{ij}^{sig}(t) = E_i\boldsymbol{m}_{ij} \tag{7}$$

In the above, $\boldsymbol{v}_i^0$ was the desired walking speed of pedestrian i; $\boldsymbol{e}_i$ was the unit direction vector to the destination observed from pedestrian i, $\boldsymbol{v}_i$ was the current speed of pedestrian i, τ_i was the relaxation time for pedestrian i to recover the original walking path; r_{ij} was the sum of the body radii of pedestrians i and j; d_{ij} was the distance between the centers of pedestrians i and j; $\boldsymbol{n}_{ij}$ was the unit direction vector from pedestrians j to pedestrian i; d_{iW} was the distance between pedestrian i and the wall; $\boldsymbol{n}_{iW}$ was the unit vector in the normal direction from the wall that was received by pedestrian i, $\boldsymbol{m}_{ij}$ was the normal vector of $\boldsymbol{n}_{ij}$; and A_i, B_i, C_i, D_i , and E_i were model parameters : $A_i = 18.66, B_i = 0.69, C_i = 500, D_i = 0.08, E_i = 0.2$. We determined these values from a previous study [3]. The relaxation time τ_i = 0.5, and the human body radius was set to 30 cm.

The distance between the ghosts was used for evaluation prior to a collision. When the position of the ghost of pedestrian i and the ghost of the oncoming pedestrian j were closer than 20 cm, the collision process was performed as per Eq. (3). If pedestrians i and j collided for the first time, they avoided one another in either direction according to the vector perpendicular to

the vector connecting their centers. As Fig. 3 illustrates, the direction in which they avoided one another was set randomly and distinguished by the $\boldsymbol{m}_{ij}$ symbol. For the second and subsequent collisions, the avoidance occurred in the direction of the vector opposite to the avoidance of the previous collision or stopped at this point. We referred to this algorithm as the "basic avoidance algorithm".

However, in the real world, a pedestrian might avoid a collision by maintaining a distance and avoiding the other pedestrian before the other party notices. We believe that this would be the case for people whose ghosts were located farther away; i.e., people who walk faster would notice the other party at an earlier stage and avoid a collision. Therefore, in this study, we improved the simulation by adding the condition whereby the collision was avoided at the pedestrian speed to the basic avoidance algorithm. As Fig. 4 illustrates, if the opponent was more than twice the distance between ghost position and current position, avoidance was performed. In this case, faster pedestrian movement resulted in earlier noticing of the other party and the ability to perform avoidance behavior processing. We referred to this algorithm as the "improved avoidance algorithm".

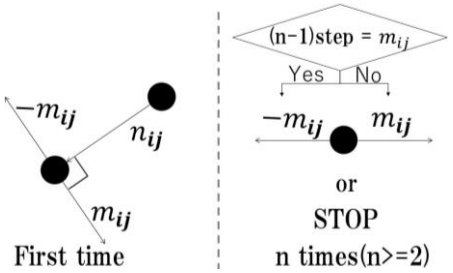

Fig. 3: Collision processing

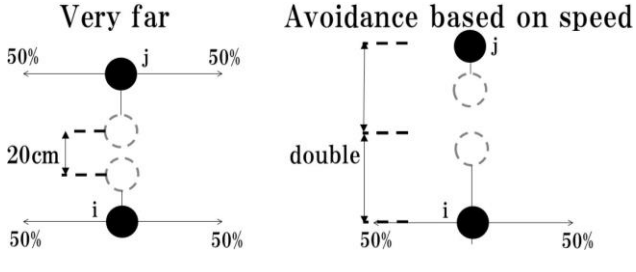

Fig. 4: Algorithm based on walking speed

3. Experiments and results

We evaluated the number of collisions and the continuous collision avoidance that were obtained by simulation using the basic and improved avoidance algorithms. The width of the path was assumed to be 2 m for the school corridor and 3.5 m for the sidewalk, which was necessary for traffic. In both cases, the length of the path was set to 15 m. Furthermore, the number of people walking on the path was set to be within the range of 5 to 15 for every two people. Moreover, males or females were randomly selected. The initial velocity was randomly set between 0.91 and 1.6 [m/s] for males and between 0.85 and 1.31 [m/s] for females, and the simulation was repeated 10 times for each condition in Python. Fig. 5 shows an example of the simulation run. Pedestrians who avoided collisions are indicated in red. Fig. 6 presents the results of the data acquisition with the improved avoidance algorithm.

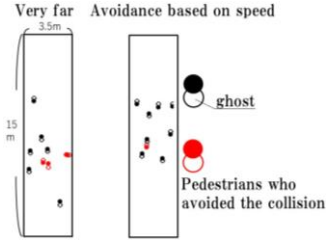

Fig. 5: Example of walking state

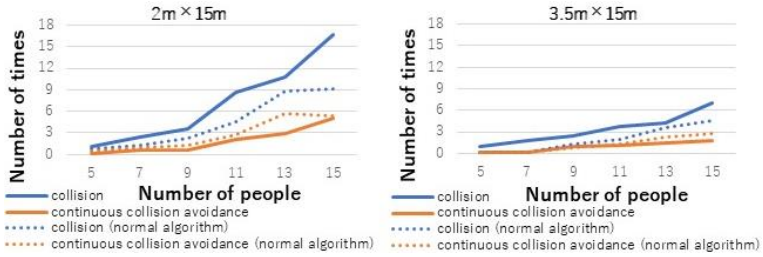

Fig. 6: Results of collision judgement using proposed model

The number of consecutive collision avoidance processes increased as population density

increased. Moreover, in some cases, the number of collision processes of the improved avoidance algorithm increased by more than 30% compared to the basic avoidance algorithm, but the number of continuous collision avoidance processes was the same or lower.

4. Discussion

We found that the number of collisions and continuous collision avoidances tended to increase according to the number of people and the width of the road, i.e., the population density. This result was as we expected, and we believed that the simulation worked correctly.

The improved avoidance algorithm resulted in a higher number of collisions. We consider this to be because the improved avoidance model avoided collisions based on the position of the pedestrian ghost and the position of the other party, rather than waiting until the two ghosts were close to one another. If the position of the ghost was far from that of the pedestrian itself, i.e., if the ghost moved rapidly, the number of collisions would increase because the avoidance process started in advance. Moreover, if only one of them took avoidance action, the other had not yet taken avoidance action, so continuous collision avoidance did not develop and the collision could be avoided successfully. For this reason, the number of collisions was higher than that of the basic avoidance algorithm, but the number of continuous collision avoidance was lower. We consider that the improved avoidance algorithm could reproduce the walking of a real human compared with the basic avoidance algorithm.

5. Conclusion

We proposed a simulation model for continuous collision avoidance. We included an algorithm in which a person walked more rapidly; as a result, it could notice the oncoming party earlier and exhibit avoidance behavior. As a result, it was confirmed that the higher the density of people, the higher the number of collisions and continuous collision avoidance actions between people. Furthermore, the number of collisions of the improved avoidance algorithm increased compared to that of the basic avoidance algorithm, but the number of continuous collision avoidances tended to decrease. We expect that the improved avoidance algorithm reproduces a more appropriate and realistic situation of continuous collision avoidance in terms of the incidence of one.

References

[1] D.Helbing and P.Molnar,“Social Force model for pedestrian dynamics, ” Physical Review E, vol. 51, no.5, pp.4282-4286, 1995

[2] H. Fujii, "Simulation of Human Flow," incorporated association Japan academic conference of simulation, Vol. 38 No3, pp. 42-46, 2019-09.

[3] Hitomi Iori, Satoru Fujita, and Toshio Hirotsu, "Two-phase simulation of crowds incorporating gait prediction," in Proc. of Multimedia, Distributed Coordination and Mobile Symposium 2017, 263-269, 2017-06-21

[4] PDF document "Simulation of Congestion in Souvenir Shops Based on Social Forces Model."
http://www.msi.co.jp/s4/solution/userscase_pdf/tmu_fukuoka.pdf (Ref: 2021.7.31)

Creation of hexagonal close-packed photonic-ring with optical vortex

Kanta Takahashi[1], Haruki Kawaguchi[1], Kei Umesato[1], Yoshihiko Arita[2,6], Keisaku Yamane[3], Ryuji Morita[3], Ken-ichi Yuyama[4], Satoyuki Kawano[5], Katsuhiko Miyamoto[1,6], Takashige Omatsu[1,6*]

[1]Graduate School of Engineering, Chiba University, Japan
[2]School of Physics and Astronomy, University of St Andrews,United Kingdom
[3]Department of Applied Physics, Hokkaido University, Japan.
[4]Department of Chemistry, Osaka City University, Japan.
[5]Graduate School of Engineering Science, Osaka University, Japan.
[6]Molecular Chirality Research Center, Chiba University, Japan
*omatsu@faculty.chiba-u.jp

Abstract. We demonstrate, for the first time, the direct print of photonic-microrings formed of dielectric nanoparticles on a receiver substrate by optical vortex laser induced forward transfer. Such exotic phenomenon is discussed by numerical analysis of optical force acting on the dielectric nanoparticles under optical vortex.

Keywords: Optical vortex, Laser induced forward transfer, Optical force, Nanopartciles, Printed nanophotonics

1. Introduction

Photonic-nanostructures enable us to manipulate light fields at the sub-wavelength scale, beyond the diffraction limit, to exploit new fundamental sciences and advanced technologies through exotic light-matter interactions unattainable in nature [1].
An optical vortex possesses a ring-shaped spatial profile and an orbital angular momentum (OAM) owing to its helical wavefront, and it has currently been leading to new fundamental physics and applications, such as optical manipulation, optical free-space telecommunications, quantum optics, and super-resolution microscopes. The optical vortex also opens the door towards advanced laser materials processing, including helical nanostructures fabrication [2,3].
In this paper, we here report on the first demonstration, to the best of our knowledge, of the direct print of a monolayered photonic-microring with a hexagonal close-packed structure, made of dielectric nanoparticles, on a receiver substrate simply by deposition of a single optical vortex pulse. Such exotic phenomenon will offer advanced nanofabrication technologies and provide new physical insights for light-matter interaction.

2. Result

A colloidal suspension of the monodisperse polystyrene nanoparticles (diameter: ca. 250 nm, density: 1.57 wt%) was used as a donor material, and it was dropped on a glass substrate to

form a 40 μm thick liquid film. A nanosecond laser (a wavelength of 532 nm, a pulse duration of 10 ns, and pulse energy of ca. 160 μJ) was employed as a laser source. Its output was converted to an optical vortex with ℓ=1 and loosely focused to be an annular spot with a diameter of ca. 50 μm on the film from the backside. A pL-scale single microdroplet was ejected from an irradiated film, and it was printed on a glass receiver substrate located 1 mm away from the donor film.

Figure 1 (a) shows the images of the printed dot. Intriguingly, a hexagonal close-packed, monolayered (ca. 250 nm thick) and ring-shaped microstructure (diameter: 58-60 μm, width: 2.7-4.0 μm) (referred to here as a photonic-ring) made of dielectric nanoparticles was formed in the printed dot, which reflected the ring-shaped spatial form of the irradiated optical vortex.

These results manifest that the nanoparticles are trapped at high density within the irradiated optical vortex field and they are then packed to form a photonic-ring in the microdroplet owing to OAM transfer effects.The trapping potential depth for the nanoparticles under optical vortex illumination can be also numerically estimated to be (~ -2260 k_BT) by the surface integration of Maxwell's stress tensor on the nanoparticle, and it supports well the experiments.

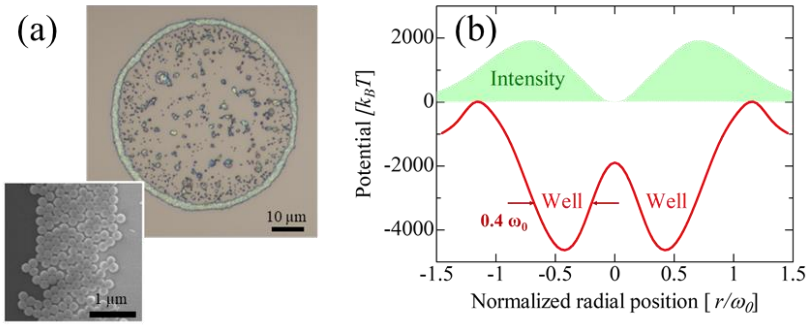

Fig. 1 (a)Optical and scanning electron microscope images of a fabricated photonic-microring. (b) Numerically simulated optical trapping potentials.

3. Conclution

We have demonstrated the direct print of a hexagonal close-packed and monolayered photonic-microring, formed of nanoparticles, on a receiver substrate without any additional processes simply by employing the optical vortex induced forward transfer. This exotic nanostructuring in microdroplet can be well supported by the numerical simulation based on the surface integration of Maxwell's stress tensor on the nanoparticle.

References

[1] V. M. Shalaev, W. Cai, U. K. Chettiar, H. Yuan, A. K. Sarychev, V. P. Drachev, and A. V. Kildishev: Negative index of refraction in optical metamaterials," *Opt. Lett*. 30 (2005), 3356-3358

[2] K. Toyoda, F. Takahashi, S. Takizawa, Y. Tokizane, K. Miyamoto, and T. Omatsu: Transfer of Light Helicity to Nanostructures. *Phys. Rev. Lett.* 110 (14) (2013), 143603

[3] R. Nakamura, H. Kawaguchi, M. Iwata, A. Kaneko, R. Nagura, S. Kawano, K. Toyoda, K. Miyamoto, and T. Omatsu: Optical vortex-induced forward mass transfer: manifestation of helical trajectory of optical vortex. *Opt. Express* 27 (2019), 38019-38027

Quantum interference of spontaneous optical vortex photon emission in a cylindrical waveguide

Satoshi Tanaka[1,*], Kazuki Kanki[1], Yuki Goto[2], Shin Kubo[2,3], Tomio Petrosky[4,5]

[1]Department of Physical Science, Osaka Prefecture University, Japan
[2]National Institute for Fusion Science, National Institutes of Natural Sciences, Japan
[3]College of Engineering, Chubu University, Japan
[4]Center for Complex Quantum System, University of Texas at Austin, USA
[5]Institute of Industrial Science, The University of Tokyo, Japan

[*]stanaka@p.s.osakafu-u.ac.jp

Abstract. We have studied a spontaneous photon emission from a molecular exciton in a cylindrical waveguide in terms of the complex spectral analysis. The mode density of the Bessel beam in a cylindrical waveguide exhibits the Van Hove singularity at the bottom of each continuum. The interaction of the dipole and the radiation field is enhanced by the Van Hove singularity when the exciton energy is close to the band edges, where the ordinary perturbation analysis breaks down. We have obtained the complex eigenstates of the total Hamlitonian in the form of the entangled states of the matter and single photon states with different angular momenta. We have found that a quantum interference causes Fano gap structure in the emission spectrum. This Fano gap can be understood as the ingterfernce between the Markovian and the non-Markovian decays in the single photon emission processes.

Keywords: Spontaneous photon emission, Van Hove singularity, Angular momentum

Recent advances in photonics technology make it possible to control optical processes in the light and matter interactions with a single quantum level precision. The mode density of the radiation field in photonic crystals is designed so that the optical absorption, emission, and scattering processes are arbitrarily controlled in spatially confined systems, such a cavity QED and waveguide QED. In addition, spatial confinement of radiation fields causes strong coupling of light and matter to yield an entangled state exhibiting the quantum features, such as the formation of polariton, vacuum Rabi oscillation and squeezed states[1].

In the present work, we study a spontaneous photon emission of a molecular exciton dipole in a cylindrical waveguide. The radiation field in the waveguide is two-dimensionally confined in the plane perpendicular to the axis, while it can propagate freely in the axis direction. As a result, the eigenmodes of the radiation field are classified by the longitudinal

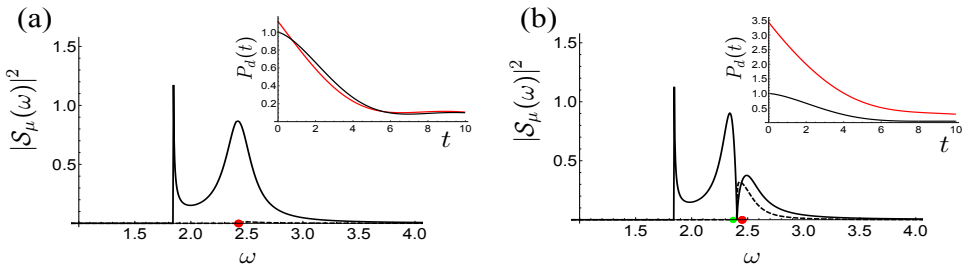

Figure 1: Spontaneous photon emission of a molecular exciton in a cylindrical waveguide. (a) The molecular dipole is in the perpendicular plane, and (b) it has an axial component. The transitions to the $TE_{\pm1,1}$ and $TM_{0,1}$ bands are drawn by the solid and dotted lines, respectively, and the resonant state energies are plotted by the dots. The surviving probabilities (black line) are also shown in the inset, where the Markovian components are depicted by the red lines.

total angular momentum and the linear momentum along the cylinder axis[2]. The mode density diverges at the photon band edges due to the one-dimensional Van Hove singularity resulting in the strong coupling between the exciton and the radiation field.

In this work, we consider a spontaneous photon emission of a molecular exciton positioned in a cylindrical waveguide. The eigenmodes of a cylindrical waveguide has been known as the Bessel modes[2], which are classified by the total angular momentum, translational momentum along the axis, and the helicity. The eigenmodes exhibits the Van Hove singularity at each band edges. We have solved the complex eigenvalue problem of the total Hamiltonian and obtained the dressed exciton and the dressed photon modes which are represented as the quantum entanglement states of the exciton and the multiple single photon states.

In Fig.1, we show the calculated spontaneous emission spectrum for different molecular orientations: In (a) the dipole is oriented in the orthogonal plane to the axis, and in (b) it is tilted toward the axis. The photon emissions are attributed to the transitions to $TE_{\pm1,1}$ mode in (a), while the transition to $TM_{0,1}$ is mixed in (b). In the latter, we find the distinct dip structure in the spectrum which is due to the quantum interference of the single photon emission to both modes. We found that the large non-Markovian decay process due to the Van Hove singularity contributes to the quantum interference as shown in the insets[3, 4].

References

[1] R. Loudon, *The Quantum Theory of Light* (OUP Oxford, Oxford, 2000).

[2] J. D. Jackson, *Classical electrodynamics*, 3rd ed. ed. (Wiley, New York, {NY}, 1999).

[3] S. Tanaka, S. Garmon, and T. Petrosky, Phys. Rev. B **73**, 115340 (2006).

[4] T. Fukuta, S. Garmon, K. Kanki, K.-i. Noba, and S. Tanaka, Phys. Rev. A **96**, 52511 (2017).

Numerical Simulation and Experiments of Intermittent Camphor Boats

Takatoshi Ichino[1*]

[1]Department of Computational Systems Biology, Faculty of Biology-Oriented Science and Technology, Kindai University

*ichino@waka.kindai.ac.jp

Abstract. The camphor boats moved spontaneously on the water surface. When a camphor disk was connected to the inside of a larger plastic plate, intermittent motion (alternating between rest and rapid motion) was observed. In this presentation, we show the mathematical model and numerical results of intermittent motion of camphor boat, and experimental results of collective motion of intermittent camphor boats.

Keywords: camphor boat, collective motion, numerical simulation

1. Introduction

The collection of self-propelled particles has rich variety behavior, such as nonequilibrium phase transition, and are observed in a wide range of biological system, such as human crowed, fish schools, bird flocks, associated motor proteins. The experimental investigation of collective motion has already reported, e.g., granular system driven by vibrating plate, multiple robot system. In the theoretical studies, Vicsek et al. has proposed simple model. The camphor boats moved spontaneously on the water surface and interact with one another through the concentration of the camphor molecules on the water. When a camphor disk was connected to the edge of a larger plastic plate, continuous motion was observed. The camphor molecules dissolved from camphor disk diffuse to the edge of the boat and are supplied constantly; thus, the driving force is kept constant. On the other hands, when a camphor disk was connected to the inside of a larger plastic plate, intermittent motion (alternating between rest and rapid motion) was observed. In the resting state, the molecules dissolved from the camphor disk and diffuse to the edge of the boat. After the molecules reach the edge, the camphor molecules are developed on water, and as a result, the boat accelerated. The molecules accumulated under the plate are spread out on water and disappear. Then, the boat rapidly stops due to the viscous resistance.

2. Numerical Section

Heisler et al. reported and reproduced in the numerical simulation based on reaction-diffusion equations, and we adopted the modified it's mathematical model. The dimentionless model is as follows:

$$\frac{\partial^2 x_i}{\partial t^2} = -\mu\frac{\partial x_i}{\partial t} + \Gamma\left[\frac{1}{c(x_i + l_f)^2 + 1} - \frac{1}{c(x_i - l_b)^2 + 1}\right] \quad (1)$$

$$\frac{\partial c}{\partial t} = \frac{\partial^2 c}{\partial x^2} - kc + a\sum_{i=1}^{N} F(x - x_i) \quad (2)$$

$$F(x) = \begin{cases} 1 & for|x| < r_0 \\ 0 & otherwise \end{cases}$$

Here, x_i is the dimensionless position of the camphor disk, μ is the dimensionless viscosity constant of the water, c is the dimensionless concetration of camphor, k is a constant combining the effect of evaporation and dissolution, and aF represents the addition of camphor by camphor disk, which is centered at the point x_i and has half-length r_0. l_f and l_b are the right- and left-side length of boat from the camphor disk, respectively.

3. Experimental Section

A camphor disk (diameter: 3mm, thickness: 1mm, mass: 5mg) was prepared using a pellet die set for Fourier transform infrared spectroscopy (FTIP). A plastic boat was made by cutting a polyester film (thickness: 1mm) into a discoid shape (diameter: 20mm).

4. Results

Figure 1 (a) and (b) showed the time series of the velocity of intermittent motion using numerical simulation and experiments, respectively.

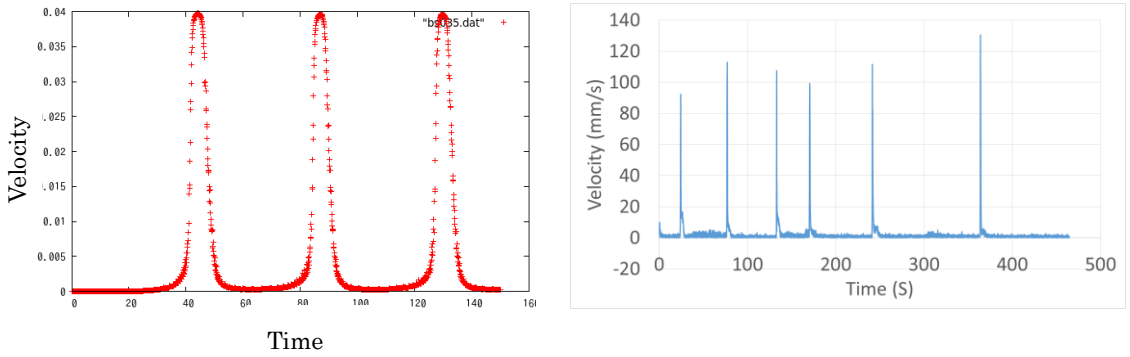

Fig. 1. Time series of the velocity in intermittent motion.(a) numerical simulation. (b) experiment.

When several camphor boats floated in water circular container (diameter: 160mm), as a result, two types of states were observed with varying the number of the boats. One is an individual motion, the other is stationary state. The results of the collective motion as follows: the number of boats, N, was changed from 5 to 45. The collective motion of camphor boats exhibited two different motions depending on N, which were (i) an individual motion and (ii) stationary state. When N was less than 25, the boats moved individually, when N was greater than 25, all boats stopped and became stationary.

References

[1] E. Heisler, et. al.: Swarming of self-propelled camphor boats, *Phys. Rev. E*, 85 (2012), 055201(R).

[2] N. J. Suematsu, et al.: Mode –Switching of the Self-Motion of a Camphor Boat Depneding on the Diffusion Distance of Camphor Molecules, *J. Phys. Chem. C,* 114 (2010), 9876-9882.

[3] S. Soh, et al.: Dynamic Self-Assembly in Ensembles of Camphor Boats, *J. Phys. Chem. B*, 112 (2008), 10848-10853.

[4] N. J. Suematsu, et al.: Collective Behavior of Inanimate Boats, *Phys. Rev. E*, 81 (2010), 056210.

[5] E. Heisler et al.: Collective Motion and Phase Transitions of Symmetric CamphorBoats, *J. Phys. Soc. Jpn*., 81 (2012), 074605.

Particle layer effect of liquid marble on Belouzov–Zhabotinsky reaction

Yasunao Okamoto[1*1], Jun'ya Tanoue[1], Daigo Yamamoto[1], Akihisa Shioi[1*2]

[1]Department of Chemical Engineering and Materials Science, Doshisha University, Japan

*[1]yaokamot@mail.doshisha.ac.jp

*[2]ashioi@mail.doshisha.ac.jp

Abstract. In the Belouzov–Zhabotinsky (BZ) reaction with malonic acid, carbon dioxide gas is generated, which sometimes causes difficulties during observation of the BZ reaction, particularly in a small space. Our previous study showed that the bubble accumulation of the generated carbon dioxide was suppressed within a liquid marble. Therefore, in this report, the role of the particle layer surrounding a droplet is discussed. We assume that the particle layer provides the nuclei for gas generation and as well as the paths for the carbon dioxide and oxygen gases, which are the product and inhibitor of the BZ reaction, respectively. Based on this assumption, a mathematical model of the BZ reaction in a liquid marble using the reaction–diffusion equation is proposed. The result suggests that the period of chemical oscillation depends on the local density of particles in the particle layer surrounding the liquid marble.

Keywords: Belouzov–Zhabotinsky reaction, Liquid marble, Chemical oscillation, Gas permeation

1. Introduction

The Belouzov–Zhabotinsky (BZ) reaction is a typical chemical oscillation that has garnered significant research attention; the BZ reaction in a small reactor is one such example. Liquid marble (LM) can be utilized for the design of small reactors. LM is a liquid droplet stabilized by a particle layer and has been used in various applications owing to its unique characteristics. One application involves the BZ reaction in LM (BZLM), for which the communication of the BZ reaction between multiple LMs [1], the size-dependency of the period [2], and the control of a robot [3] have been reported. The results of our previous study indicated that the oscillation period changed with LM size and that the accumulation of carbon dioxide (CO_2) gas in the droplet was not observed in BZLM [2]. These can be caused by the diffusion of oxygen (O_2) from air and by the presence of a particle layer on the BZLM surface, respectively. However, the effect of the gas permeability through the particle layer on the BZLM was not discussed. In this study, the role of the particle layer on BZLM was examined using a mathematical model with regard to the gas transfer rate. Assuming that the particle surface in the layer provides the nuclei for the gas generation, i.e., no bubble formation, then CO_2 gas is continuously discharged from the liquid droplet through the layer. A mathematical

model based on this assumption was proposed, and the calculated results were compared with the experimental results.

2. Method

2.1 Experiment

The BZ solution includes 0.20 M $NaBrO_3$, 0.072 M NaBr, 0.40 M malonic acid, 1.00 M H_2SO_4, and 2.00 mM ferroin. All chemicals were purchased from Fujifilm Wako Pure Chemical Corporation. Thirty microliters of the solution were dropped onto hydrophobic silica powder (Aerosil, RY-300) to form BZLM. Three types of BZLMs were produced: one was named full-coated BZLM, where all droplet surfaces were covered with the powder; the second was prepared with approximately half the surfaces coated with the powder; and the third was thinly coated with the powder. The latter was achieved by partially removing the powder using a blower after the powder was fully coated. Each BZLM was placed in an O_2 atmosphere, and the period of chemical oscillation was measured. The O_2 atmosphere was established in a closed Petri dish via the decomposition of H_2O_2 catalyzed by $FeCl_3$.

2.2 Model of reaction kinetics

For the calculation, an Oregonator that incorporated O_2 as an inhibitor was used [4]. Eqs. (1)–(5) are the reaction–diffusion equations for the following components: bromous acid (U), ferriin (V), bromide ion (W), CO_2, and O_2, respectively. Here, the one-dimensional coordinate that corresponds to the diameter line of the BZLM is applied.

$$\partial[\mathrm{U}]/\partial t = D_\mathrm{U}\partial^2[\mathrm{U}]/\partial x^2 + k_1[\mathrm{A}]_0[\mathrm{W}] - k_2[\mathrm{U}][\mathrm{W}] + k_3[\mathrm{A}]_0[\mathrm{U}] - 2k_4[\mathrm{U}]^2 \quad \ldots(1)$$

$$\partial[\mathrm{V}]/\partial t = D_\mathrm{V}\partial^2[\mathrm{V}]/\partial x^2 + 2k_3[\mathrm{A}]_0[\mathrm{U}] - k_5[\mathrm{B}]_0[\mathrm{V}] \quad \ldots(2)$$

$$\partial[\mathrm{W}]/\partial t = D_\mathrm{W}\partial^2[\mathrm{W}]/\partial x^2 + k_1[\mathrm{A}][\mathrm{W}] - k_2[\mathrm{U}][\mathrm{W}] + k_6[\mathrm{R}]^2 + 2k_8[\mathrm{Q}]^2 \quad \ldots(3)$$

$$\partial[\mathrm{CO_2}]/\partial t = D_{\mathrm{CO2}}\partial^2[\mathrm{CO_2}]/\partial x^2 + k_6[\mathrm{R}]^2 \quad \ldots(4)$$

$$\partial[\mathrm{O_2}]/\partial t = D_{\mathrm{O2}}\partial^2[\mathrm{O_2}]/\mathrm{d}x^2 - k_7[\mathrm{R}][\mathrm{O_2}] + k_8[\mathrm{Q}]^2 \quad \ldots(5)$$

$$[\mathrm{R}] = \left(\sqrt{(k_7[\mathrm{O_2}])^2 - 8k_5k_6[\mathrm{B}]_0[\mathrm{V}]} - k_7[\mathrm{O_2}]\right)/(4k_6) \quad \ldots(6)$$

$$[\mathrm{Q}] = \sqrt{k_7[\mathrm{R}][\mathrm{O_2}]/(2k_8)} \quad \ldots(7)$$

[j] expresses the concentration of chemical component, j. $[\mathrm{A}]_0$ and $[\mathrm{B}]_0$ represent the initial concentrations of sodium bromate and malonic acid, respectively. R and Q denote the malonyl/bromomalonyl radical and corresponding peroxyl radicals, respectively. For these radicals, the diffusion terms are ignored, and the reaction rates are much higher than those of the other chemical components; then, steady-state approximations are applied. The generation rate of CO_2 was calculated using the reaction term $k_6[\mathrm{R}]^2$.

As the BZ reaction is inhibited by oxygen, the previous experimental results suggesting that BZLM can prevent oxygen inlet [2] seem to indicate that oxygen transport into the BZLM is disturbed by the particle layer. It is reasonable to consider that the layer physically blocks oxygen transport owing to its thick and condensed packing of the powder. However, because CO_2 generated by the BZ reaction seems to be discharged easily, the particle layer does not block CO_2 transport. This indicates that the role of the particle layer in oxygen transport is not a simple physical wall effect as CO_2 transport would also be blocked. CO_2 is continuously generated by the BZ reaction, and thus accumulates inside the particle layer, which increases the pressure. The generated CO_2 did not form bubbles in the droplet, suggesting that CO_2 gas was probably formed at the droplet surface with the help of the particle layer. The accumulation rate of CO_2 on the particles was determined using the mass balance between the generation and discharge rates. When the latter is lower than the former, a high-pressure zone forms locally

due to the accumulated CO_2, producing gas flow from the BZLM to the outside. This gas flow intercepts the oxygen inlet from the outside and prevents oxygen from entering the BZLM. As shown in Fig. 1, these processes may be modeled using the fluxes of CO_2 and O_2 at the liquid surface, as shown in Eqs. (8) and (9).

$$N_{CO2,\,xmax} = K_{CO2}(p_{CO2} - p_{CO2,\,liq}) - v[CO_2]_{xmax} \quad \ldots(8)$$

$$N_{O2,\,xmax} = K_{O2}(p_{O2} - p_{O2,\,liq}) - v[O_2]_{xmax} \quad \ldots(9)$$

$$1/K_i = 1/k_{i,\,gas} + 1/k_{particle} + 1/k_{i,\,liq} \quad \ldots(10)$$

$$v = \alpha RT\,[CO_2]_{xmax} / (\pi d^2) \quad \ldots(11)$$

Here, x_{max} indicates the surface of the bulk liquid (Fig. 1); $N_{i,\,xmax}$ and K_i represent the flux at x_{max} and the overall mass transfer coefficient, respectively; the first term on the right-hand side in both Eqs. (8) and (9) indicates the diffusion flux between the liquid and gas phases through the particle layer; $k_{i,\,gas}$, $k_{particle}$, and $k_{i,\,liq}$ represent the mass transfer coefficients in the gas boundary, particle layer, and liquid boundary, respectively; subscript i denotes the chemical components, O_2 or CO_2; p_i expresses the partial pressure of the i-th component in the gas; $p_{i,\,liq}$ is the partial pressure that is in equilibrium with the i-th component concentration in the liquid at the same position (Fig. 1); the second term is the advection term by CO_2 convection, as discussed in the previous paragraph; v, R, and T denote the advection velocity, gas constant, and absolute temperature, respectively; πd^2 is the surface area of a droplet in BZLM; and α is a proportionality constant. As mentioned above, we assume that CO_2 flows through the particle layer to the gas phase. This flow is driven by a pressure increase due to CO_2 accumulation, which should appear more remarkably when the particle layer is thicker. Therefore, the flow rate increases with increasing thickness of the particle layer. Following this assumption, it is expected that a thicker particle layer corresponds to a larger value of α.

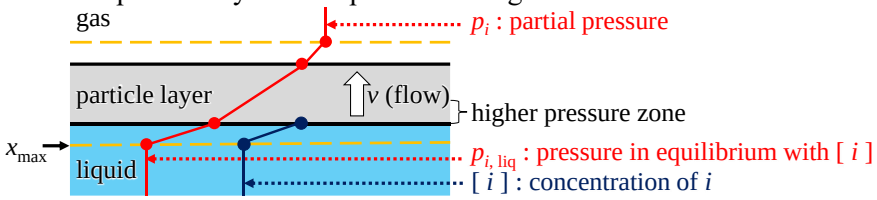

Fig. 1 Gas transfer model through the particle layer with advection.

3. Results and Discussions

In the experiment, the solution color fluctuates between red and blue. Fig. 2 shows the blue-colored component estimated using the brightness of each BZLM over time, which was extracted using image analysis software, Image J. The larger the brightness value, the bluer the solution. The frequency of color change decreased in the order of full-coated, half-coated, and thin-coated BZLM, finally disappeared in the thin-coated BZLM. Because O_2 (inhibitor) should theoretically elongate the period, the results demonstrate that the O_2 transfer rate is the lowest for the full-coated BZLM. Interestingly, the O_2 transfer rate of the half-coated (half-exposed) BZLM is considered to be lower than that of the thin-coated one.

Fig. 3 shows the oscillation period results obtained from the experiment and calculation. The period of the experiment was the average of periods for 2,000 s. As shown in Fig. 3a, the experimental period increased in the order of full-coated, half-coated, and finally disappeared in the thin-coated BZLM. Meanwhile, as shown in Fig. 3b, the calculated period increased with a decrease in α and finally diverged. Because the full-coated BZLM has a thicker particle layer than the thin-coated one, the line symmetry-like pattern seen in Figs. 3a and b indicates that

the present model can reproduce the experimental results qualitatively.

Almost half the area of the half-coated BZLM surface is exposed to air. Based on the present model, it is expected that the oscillation of the half-coated BZLM would not be active compared to that of the thin-coated BZLM. However, the experimental results demonstrate that the oscillation of the half-coated BZLM is more active than that of the thin-coated BZLM. A thick particle layer in the local area of the half-coated BZLM may contribute to the generation of a high pressure zone by CO_2 accumulation. Then, the oscillation is locally activated on the surface of the half-coated BZLM to produce a chemical wave. The wave propagation can be seen as a red–blue oscillation, as the droplet is very small. In the thin-coated BZLM, a high pressure zone is not produced at any location on its surface because the barrier effect is too weak. This causes a smooth CO_2 discharge and the disappearance of the high pressure zone, resulting in easier penetration of O_2 into the BZLM. Thus, the oscillation disappeared. Even though the LM is a small reactor, the present results suggest that the heterogeny cannot be ignored.

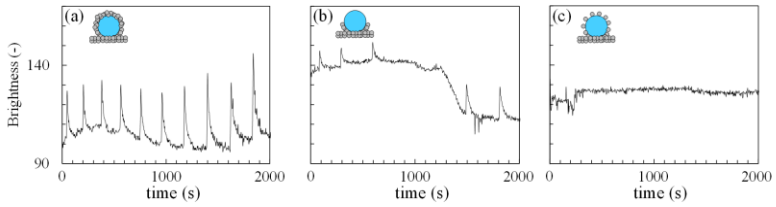

Fig. 2 Brightness changes over time in (a) full-coated, (b) half-coated, and (c) thin-coated BZLMs.

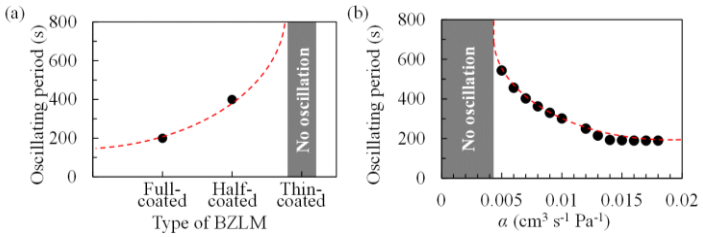

Fig. 3 Oscillation period of BZLM obtained through (a) experiment and (b) model. The period in the model was calculated from the concentration of V at the center corresponding to BZLM.

4. Conclusion

The present study suggests the interesting role of the particle layer of LM when it is applied to the BZ reaction. The layer controls the gas transport through two unique characteristics: The particle surface provides the nuclei of CO_2, which enables its discharge without bubble formation. The particles also provide a barrier for gas transport, causing a pressure difference and resulting flow. This flow prevents oxygen from entering the droplet. Consequently, the BZ reaction continued in LM for a long time without the inhibition of oxygen.

References

[1] C. Fullarton et al., *J. Phys. Mater.*, 2, 015005 (2019)

[2] Y. Okamoto et al., *J. Soc. Powder Technol. Jpn.*, 57, 2 (2019), 74-79

[3] M. A. Tsompanas et al., *Sens. Actuators B*, 295 (2019), 194-203

[4] O. Steinbock et al., *J. Phys. Chem. A,* 104, 27 (2000), 6411-6415

Numerical calculation for near-wall accumulation of swimming microorganism

Takuya Ohmura[1*], Yukinori Nishigami[2], Masatoshi Ichikawa[3]

[1]Biozentrum, University of Basel
[2]Research Institute for Electronic Science, Hokkaido University
[3]Department of Physics, Kyoto University

*takuya.ohmura@mpi-marburg.mpg.de

Abstract. Swimming microorganisms play a crucial role in aquatic ecosystems. Identification of mechanisms under their behaviors is necessary to understand those ecosystems quantitatively. One class of swimming microorganisms, ciliates, lives in water environments and tends to accumulate close to solid-liquid interfaces to obtain sedimented nutrients. Considering this accumulation as a physical phenomenon like self-assembly of microswimmers, the dynamics can be approached with a theoretical model. We performed numerical calculations with a hydrodynamic model for swimming microorganisms, and compared the numerical results with experiments. As a result, interestingly, the dynamics of the accumulation was described only by two physical factors. Our simulations revealed the simple mechanism governs the microorganism's complicated behavior to survive efficiently.

Keywords: Fluid dynamics, Swimming microorganism, Numerical calculation, Boundary element method

1. Introduction

Microorganisms maintain ecosystems where they live. To understand detailed ecosystems, we should know why and how the microorganisms behave in environments. Ciliates is a class of single-celled microorganisms and lives in aquatic environments [1,2]. Although ciliates propel freely in bulk water by beating cilia around their body, they tend to accumulate close to a liquid-solid interface, such as the bottom of a lake or a pond, the surface of waterweed or stones, etc. [3,4,5]. Nutrient sediments at the interfaces, where ciliates can grow efficiently. While the ethological reason for the accumulation has been clear, the physical dynamics was not unclear. To clarify the dynamics for the accumulation of ciliates, we performed a numerical calculation with a hydrodynamic model for swimming microorganisms [6,7].

2. Methods

To calculate swimming motion of ciliates close to a wall, the boundary element method (BEM) was used in 3D. The BEM is appropriate for a moving object at low Reynolds number. An initial model that we used to describe swimming ciliates was the squirmer model, which is one of the simplest models for swimming microorganisms [8]. To develop the model more realistically, we compared the numerical results with experiments of microscope observation of swimming ciliates and updated the model iteratively from the feedback of the difference.

3. Results

We calculated a numerical swimmer approaching a solid wall. To simplify the dynamics, two simple parameters are changed in this calculation. One parameter is a cell shape, spherical and ellipsoidal shape. While the spherical shape has been generally used for numerical research of

swimming microorganisms, the ellipsoidal shape approximately corresponds to actual ciliates. Another parameter is an asymmetricity of swimming thrust force around the swimmer's body. When the ciliates swim in bulk water, the swimming thrust force is rotational symmetry. However, our experiments indicated that the cilia attaching the wall didn't beat and the swimming trust force became asymmetry.

A spherical swimmer and an ellipsoidal swimmer with the symmetry force repelled away from the wall due to hydrodynamic interaction, which means the swimmers cannot accumulate near the wall. A spherical swimmer with the asymmetry force did not go away from the wall but stopped on the wall, which means that the swimmer can accumulate but cannot move on the wall. An ellipsoidal swimmer with the asymmetry force slid along the wall, which corresponds to the experiments. In addition, the sliding speed and the contacting angle of the ellipsoidal swimmer with asymmetry force also correspond to the experimental results. The key factors for the ciliates accumulation are the cell shape and the asymmetricity of thrust force.

In conclusion, we identified that the dynamics for the complicated behavior of the microorganism can be described by the two simple physical parameters.

References

[1] T. Weisse, R. Anderson, H. Arndt, A. Calbet, P.J. Hansen, D.J.S. Montagnes: *Eur. J. Protistol.* 55 (2016), 50-74.

[2] T. Weisse: *Eur. J. Protistol.* 61 (2017), 331-358.

[3] H.S. Jennings: *J. Comp. Neurol. Psychol.* 14 (1904), 441-510.

[4] T. Fenchel: *Ecology of Protozoa* (1987), Springer, Berlin.

[5] T. Fenchel: *Funct. Ecol*. 6 (1992), 499-507.

[6] T. Ohmura, Y. Nishigami, A. Taniguchi, S. Nonaka, J. Manabe, T. Ishikawa, M. Ichikawa: *Proc. Natl. Acad. Sci. USA*, 115 (2018), 3231-3236.

[7] Y. Nishigami, T. Ohmura, A. Taniguchi, S. Nonaka, J. Manabe, T. Ishikawa, M. Ichikawa: *Commun. Integr. Biol.*, 11 (2018), e1506666.

[8] T. Ishikawa, M.P. Simmonds, T.J. Pedley: *J. Fluid Mech.* 568 (2006), 119-160.

[9] M. J. Lighthill: *Commun. Pure Appl. Math.* 5 (1952) , 109-118.

JSST 2021

Analysis of Foreign Object Detection for Wireless power transfer Using Differential Coils

Yunyi Gong[1,*], Yoshitsugu Otomo[1], Hajime Igarashi[1]

[1]Graduate School of information Science and Technology, Hokkaido University

[*]gongyunyi@em.ist.hokudai.ac.jp

The full paper of this paper has been published in Journal of Advanced Simulation in Science and Engineering (JASSE).

DOI: https://doi.org/10.15748/jasse.9.20

JSST2021

On Equivalent Circuit Representation of Transformer Considering Eddy Currents

Qiao Liu[1], Yoshitsugu Otomo[1], Hajime Igarashi[1]

[1]Graduate School of Information Science and Technology, Hokkaido University

*liuqiao@em.ist.hokudai.ac.jp

Abstract: In the transformers working at a high frequency, the resistance and leakage inductance depend on frequency because of eddy currents. This paper presents an equivalent circuit representation of the high frequency transformer considering eddy currents in the windings. The Cauer equivalent circuit, which can easily be coupled with the external systems, is numerically obtained from the frequency characteristics of the input impedance of the transformer. What's more it is shown that the inrush current can be analyzed using the Cauer circuit.

Keywords: Eddy current, Transformer, Cauer circuit, Inrush current

1. Introduction

The operating frequency of power electronics circuits has been increased for reduction of device size. In the transformers working at high frequencies, the effect of eddy currents especially in the windings become prominent [1]. Although the eddy current can be analyzed by using finite element method (FEM), it would not be effectively coupled with power circuit and systems because of the large computing cost. For the design of power electronics systems, we need accurate and fast models of high frequency transformers [2].

In this work, we build the Cauer equivalent circuit from the impedance in frequency domain of a high-frequency transformer using the method based on the adjoint variable method [3]. The equivalent circuit can easily be coupled with the power circuits in both frequency and time domain. We analyze the inrush current of the transformer in time domain using the proposed method. It is shown that the results obtained from the proposed method are consistent with the results obtained from the theoretical method [4] and FEM.

2. Model of transformer

a) Leakage Inductance

We consider the leakage flux in the transformer shown in Fig.1. Let us assume that the secondary side is short. In this situation, the main flux is canceled out so that the leakage flux is dominant. We also assume that the permeability of the core is infinite, and the magnetic field is negligible. Although the permeability of the steel sheet would be reduced as frequency increases, it is still much larger than the air. Moreover, we assume that the winding is sufficiently long in y and z directions so that the magnetic and electric fields are represented by $\boldsymbol{H} = H(x)\boldsymbol{z}$ and $\boldsymbol{E} = E(x)\boldsymbol{y}$, respectively. By solving the one-dimensional magnetic diffusion equation derived from the Maxwell equations under the quasi-static approximation

$$\frac{d^2H}{dx^2} - \gamma^2 H = 0 \tag{1}$$

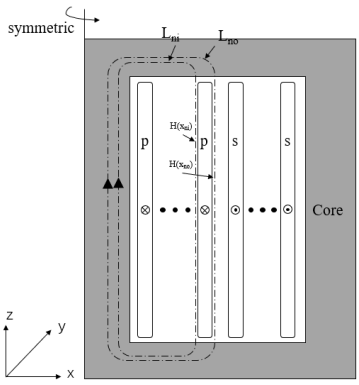

Figre.1 Leakage inductance

Where $\gamma = \sqrt{j\omega\mu_0\sigma}$, we obtain

$$H(x) = H_1 e^{\gamma x} + H_2 e^{-\gamma x} \tag{2}$$

Applying the boundary condition into (2), we obtain [4]

$$H(x) = H_0 \frac{nsinh(\gamma x) + (n-1)sinh\,(\gamma t - \gamma x)}{sinh\,(\gamma t)} \tag{3}$$

Where n and t are the layer number and is layer thickness, and x begins from the inner side of each layer. The magnetic field in the air gap and insulation layer, which are constant, can also be obtained. From the stored magnetic energy in the winding and insulation layers, we find that the inductance is represented by

$$L_{lk} = \frac{2}{2I^2}\int \mu HH^*\, dV$$

$$= \frac{\mu_0 l_w n_p}{6h_w}\left(\frac{2{n_p}^2(k_1+2k_2)(p+1)}{a\,(\cosh(2at)-\cos(2at))} + \frac{(p+1)(k_1-4k_2)}{pa\,(\cosh(2at)-\cos(2at))} + \left(2{n_p}^2 + 2p{n_p}^2 + \frac{1}{p} + 1\right)t_i\right) \tag{4}$$

Where $k_1 = \sinh(2at) - \sin(2at)$ $k_2 = \sin(at)\cosh(at) - \cos(at)\sinh(at)$ $a = \sqrt{\frac{wu_0\sigma}{2}}$ $l_w, h_w, n_p,$

$p,\ t_i$ denote the length and height of the windings, the number of turns of the primary winding, the ratio of the primary and secondary number of turns and thickness of the insulation layer.

b) AC Resistance

We also can evaluate the AC resistance of the transformer from

$$R_{ac}I^2 = \int \sigma EE^*\, dV \tag{5}$$

where we obtain $E(x)$ from (3). By performing integration in (5), we have

$$R_{ac} = \frac{l_w a n_p}{3\sigma h_w(\cosh(2at)-\cos(2at))}\left(2{n_p}^2(k_3-2k_4)(p+1) + \frac{(p+1)(k_3+4k_4)}{p}\right) \tag{6}$$

where $k_3 = \sinh(2at) + \sin(2at)$, $k_4 = \sin(at)\cosh(at) + \cos(at)\sinh(at)$.

We obtain the frequency-dependent impedance $Z(\omega) = R_{ac} + j\omega L$ from (4) and (6).

c) Equivalent circuit

We derive the Cauer equivalent circuit shown in Fig.2 which has the impedance consistent with the above results. By finding the poles and residues of, we would be able to derive the Cauer circuit. Here, we derive it using the numerical approach [3] in which we compute the resistance and inductance in the Cauer circuit so that its impedance coincides with the impedance computed from the above formulas in frequency domain.

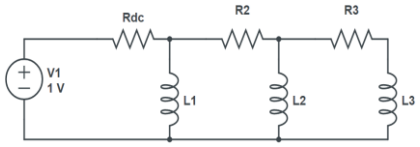

Figure.2 Structure of the Cauer circuit

The impedance of the Cauer circuit is given by the continued fraction as

$$Z(\omega) = R_{dc} + \cfrac{1}{\cfrac{1}{j\omega L_1} + \cfrac{1}{R_2 + \cfrac{1}{\cfrac{1}{j\omega L_2} + \cdots}}} \tag{7}$$

3. Numerical Result

a) Construction of Cauer circuit

The parameters of the transformer are summarized in Table.1 where the permeability of the core is assumed to be 2200. The circuit parameters of the Cauer circuit we derived from the results given in the previous section are summarized in Table.2. We also compute $Z(\omega)$ using FEM in which the two-dimensional quasi-static Maxwell equations are solved. The resistance and reactance are plotted against frequency in Fig.3 and 4. It' concluded all the results are consistent.

Table.1 Transformer parameters

μ_r	h_w	l_w	n_p/n_s	t/t_i
2200	26mm	62.8mm	6/6	0.2/0.25mm

Table.2 Circuit parameters in Cauer circuit

	R_{DC}, L_1	R_2, L_2	R_3, L_3	R_4, L_4
$R(\Omega)$	2.08E-03	1.79E+00	5.51E+01	1.82E+02
L(H)	1.98E-07	3.43E-07	1.70E-06	4.93E-07

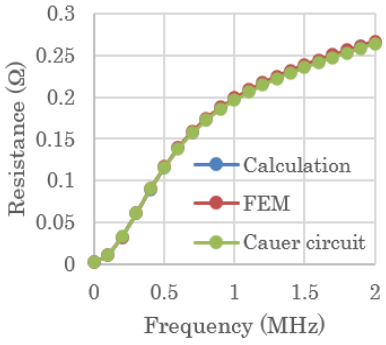

Figure.3 AC Resistance

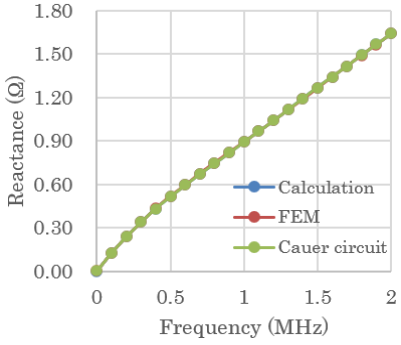

Figure.4 Reactance

b) Analysis of Inrush current

By using the Cauer circuit, we analyze the inrush currents at 0.1 and 1 MHz. For the time-domain analysis of the Cauer circuit, we use the circuit simulator, SPICE. In addition, we carry out the time-domain analysis of the R-L circuit which has the frequency characteristics derived in section 2 using SPICE. For comparison, we compute the inrush currents by FEM for which we use JMAG. The results are shown in Figs. 5 and 6, from which it is seen that the results are consistent. The error in SPICE(Calculation) at 1MHz, computed from the formulas in Section 2, is due to the fact that only the fundamental mode is considered. The results computed by the Cauer circuit in SPICE(Cauer) agree well with those computed by FEM.

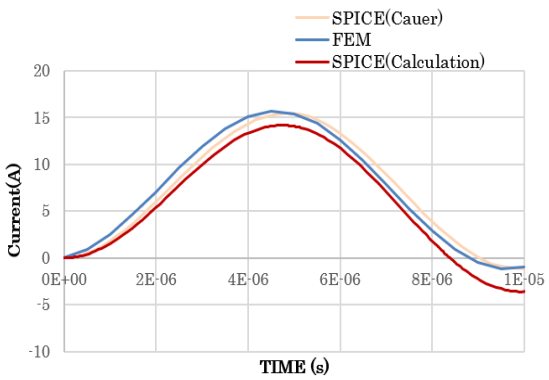

Figure.5 Inrush current at 0.1MHz

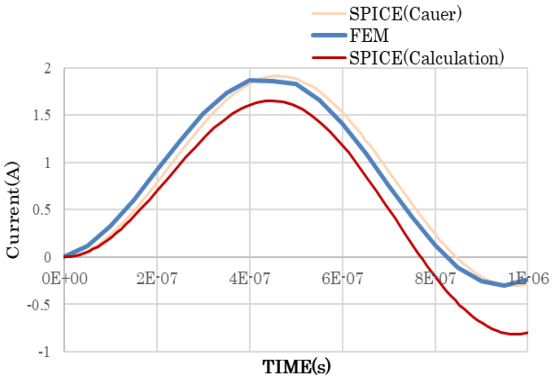

Figure.6 Inrush current at 1MHz

4. Conclusions

We have derived the Cauer circuit from the frequency-dependent impedance of the high-frequency transformer considering the eddy currents in the winding. The transformer impedance represented in a closed form is obtained by solving the one-dimensional magnetic diffusion equation. The circuit parameters in the Cauer circuit are determined so that its impedance is consistent with that of the transformer model. The frequency characteristics of the impedance computed from the Cauer circuit agree well with that of the transformer model. We have also analyzed the inrush current of the transformer considering the eddy currents using the Cauer circuit. Although the computed inrush currents by FEM are not consistent with those computed from the calculated impedance. In particular, the inrush currents computed from the Cauer circuit agree well with those computed by FEM.

References

[1] S. Zhao, Q. Li, F. C. Lee, B. Li, High-Frequency Transformer Design for Modular Power Conversion from Medium-Voltage AC to 400 VDC, *IEEE Transactions on Power Electronics*, vol.33, no. 9, pp.7545-7557, 2018.

[2] D. Fu, F. C. Lee, S. Wang, Investigation on transformer design of high frequency high efficiency dc-dc converters, 2010 Twenty-Fifth Annual IEEE Applied Power Electronics Conference and Exposition (APEC), pp. 940-947, doi: 10.1109/APEC.2010.5433391, 2010.

[3] Y. Otomo, H. Igarashi, Synthesis of Cauer Equivalent Circuit for Electric Devices from Computed and Measured Data, *IEEE Transactions on Power Electronics*, vol.36, no. 4, 10.1109/TPEL.2020.3022167, 2021.

[4] Z. Ouyang, J. Zhang, W. G. Hurley, Calculation of Leakage Inductance for High-Frequency Transformers, *IEEE Transactions on Power Electronics*, vol. 30, no.10, pp.5769-5775, 2015.

JSST 2021

Numerical Optical Modeling of Nanostructures using Fractal Dimension

Yoshihisa Fujita[1,*], Hiroaki Nakamura[2], Soichiro Ikuno[3], Susumu Nakata[1]

[1]College of Information Science and Engineering, Ritsumeikan University
[2]National Institute for Fusion Science, National Institute of Natural Science
[3]School of Computer Technology, Tokyo University of Technology

[*]yfujita@fc.ritsumei.ac.jp

Abstract. Even a complicated structure can easily represent by the fractal dimension. Hence, the fractal dimension can be expected to apply to the investigation of the optical properties of a nanostructure such as a photocatalyst. In this paper, optical modeling with the fractal dimension is proposed and is improved using the evanescent field.

Keywords: Fractal structure, FDTD method, Evanescent field

1. Introduction

It has been reported that the fuzzy nanostructure is generated by high-temperature helium irradiation [1]. The geometric characteristics of fuzzy nanostructure suggest a high absorptance. At the moment, large-scale equipment is necessary in order to generate the fuzzy nanostructure. In addition, it is difficult to handle numerically the fuzzy nanostructure because the geometric scale is smaller than the wavelength. For that reason, the optical property of the fuzzy nanostructure has not become clear. The fractal dimension is a solution in order to handle numerically the complex geometric structure. In fact, the fractal dimension of the fuzzy nanostructure is estimated [2]. However, the relationship between the optical properties and the fractal dimension is not clear. The optical modeling using fractal dimension contributes largely since fractal patterns appear widely in nature.

An arbitrary fractal surface can be generated by the random fractal theory. The mid-point algorithm is known as an implementation of the random fractal [3]. The optical properties can be calculated using the finite-difference time-domain (FDTD) method. We already know that the fractal dimension is not enough as an element for the optical modeling from a previous study [4]. This reason is due to the phenomenon that the electric field is absorbed by a part in contact with the metal. Therefore, it is necessary to consider that the evanescent field is incorporated into the optical modeling.

In this study, we numerically investigate the influence of the fractal dimension on the optical properties. Moreover, we discuss the optical modeling using the evanescent field.

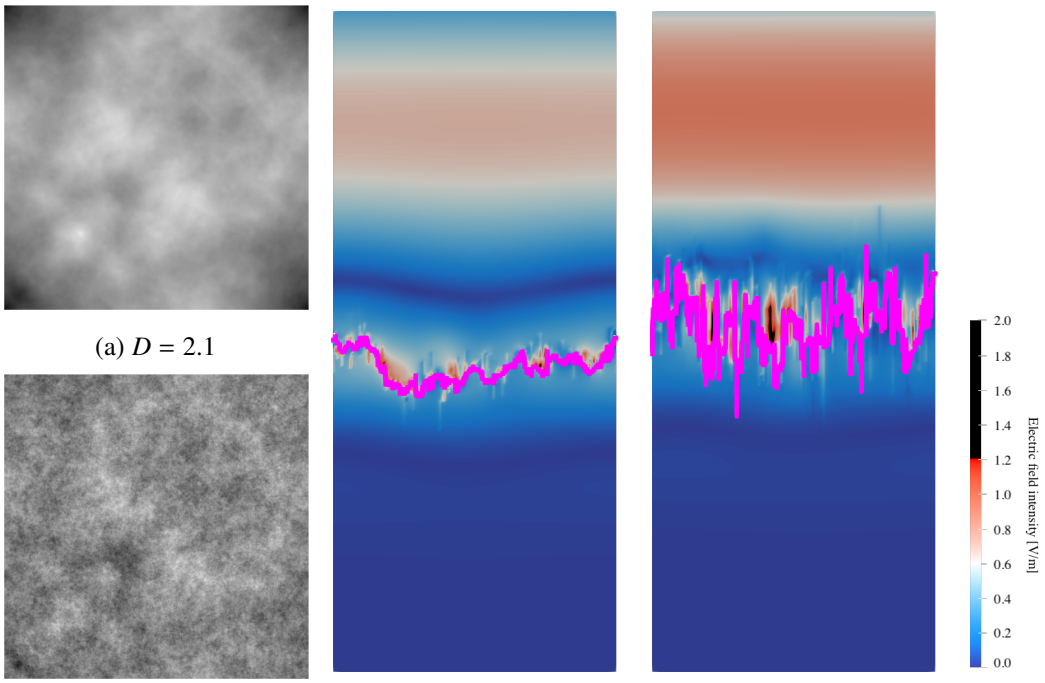

(a) $D = 2.1$ (b) $D = 2.9$ (c) $D = 2.1$ (d) $D = 2.9$

Figure 1: (a), (b) Normalized height map of fractal structure. (c), (d) Spatial distributions of electric field intensity when the electromagnetic wave is injected into (a) and (b), respectively. Here, D denotes the fractal dimension.

2. Numerical Method and Results

In this study, we attempt to model the optical properties by following steps:

I. Generate the arbitrary fractal surface using the mid-point algorithm.

II. Evaluate the optical properties by injecting the electromagnetic wave to a fractal surface.

III. Lead to a relationship between fractal dimension and optical properties.

In order to clarify the relationship, the evanescent field is estimated by calculating the accessible surface area [5].

The fractal structures generated using the mid-point algorithm are shown in Figs. 1(a) and (b). On the one hand, if the fractal dimensions are small, the surface is relatively smooth. On the other hand, as the fractal dimension increases, the surface will be jagged. Then, the electromagnetic wave is injected into the above structure. The simulation result of the electromagnetic wave propagation is shown in Figs. 1(c) and (d). We can see from this figure that the electric field is more concentrated than in the case of the low fractal dimension.

The detailed results will be shown in JSST2021.

References

[1] S. Kajita, T. Yoshida, D. Kitaoka, R. Etoh, M. Yajima, N. Ohno, H. Yoshida, N. Yoshida and Y. Terao: Helium plasma implantation on metals: Nanostructure formation and visible-light photocatalytic response, *J. Appl. Phys.*, 113 (2013), 134301.

[2] S. Kajita, N. Yoshida, N. Ohno and Y. Tsuji: Growth of multifractal tungsten nanostructure by He bubble induced directional swelling, *New J. Phys.*, 17 (2015), 043038.

[3] I. M. Rian and S. Asayama: Computational Design of a nature-inspired architectural structure using the concepts of self-similar and random fractals, *Automat. Constr.*, 66 (2016), 43–58.

[4] Y. Fujita, H. Nakamura, S. Ikuno and S. Nakata: Numerical Analysis of Optical Properties in Metals with Fractal Structures, *Proc. ISPlasma*, (2021), 08P-29.

[5] L. J. Abbott, K. E. Hart and C. M. Colina: Polymatic: a generalized simulated polymerization algorithm for amorphous polymers, *Theor. Chem. Acc.*, 132:1334 (2013).

JSST 2021

Preconditioner for Ill-conditioned Tall and Skinny Matrices

Atsushi Minamihata[1,*], Katsuhisa Ozaki[2], Takeshi Ogita[3], Shin'ichi Oishi[4]

[1]Development of Social Studies, Kansai University of International Studies
[2]College of Systems Engineering and Science, Shibaura Institute of Technology
[3]Division of Mathematical Sciences, Tokyo Woman's Christian University
[4]Faculty of Science and Engineering, Waseda University

[*]a-minamihata@kuins.ac.jp

Abstract. In this talk, we propose a triangular preconditioner for an ill-conditioned rectangular matrix, especially that is called an ill-conditioned tall and skinny matrix. To compute QR factorization of a tall and skinny matrix quickly, some algorithms are proposed which are rich in Blas-3 operations. The algorithms use preconditioner as Cholesky factor, sifted Cholesky factor, or U-factor of LU factorization. A preconditioner based on an R-factor of QR factorization of A^TA is proposed. Numerical results are showing the effectiveness of our proposed preconditioner for ill-conditioned tall and skinny matrices.

Keywords: preconditioner, ill-conditioned rectangular matrix, QR factorization

1. Introduction

In this talk, we propose a triangular preconditioner for an ill-conditioned rectangular matrix, especially that is called an ill-conditioned tall and skinny matrix. Tall and skinny matrix $A \in \mathbb{R}^{m\times n}$ satisfies $m \gg n$ and A^TA is a very small matrix compared with $m \times m$ matrix. A triangular preconditioner is used for solving least squares problems and computing QR factorization. QR factorization plays an important role in solving least squares problems. QR factorization is used for computing approximate solution $\tilde{x}$ of least squares problems and also for computing rigorous error between $\tilde{x}$ and A^+b in [1, 2]. Householder QR, CGS, and MGS algorithms are popular, but not effective algorithms for computing QR factorization of a tall and skinny matrix. Fukaya et al. [3] proposed CholeskyQR2 algorithm on a large-scale parallel system. CholeskyQR2 algorithm is rich in Blas-3 operations and parallelized easily. However, CholeskyQR2 algorithm is often break down when a matrix is an ill-conditioned matrix. To avoid breaks down, Fukaya et al. proposed shiftedCholeskyQR3 algorithm using sifted Cholesky factorization. Terao et al. [4] proposed LU-Cholesky QR algorithms using LU factorization on shared and distributed memory computers. CholeskyQR2, shiftedCholeskyQR3, and LU-Cholesky QR use a preconditioner for computing QR factorization as Cholesky factor, sifted Cholesky factor, and U-factor of LU factorization, respectively. In

this talk, we propose a preconditioner for A using an R-factor of QR factorization of A^TA. This preconditioner isn't effective in some ill-conditioned cases. We modify the R-factor and improve this preconditioner. Numerical results are showing the effectiveness of our proposed preconditioner for ill-conditioned tall and skinny matrices.

References

[1] S.M. Rump. "Improved componentwise verified error bounds for least squares problems and underdetermined linear systems." Numerical algorithms 66.2 (2014): 309-322.

[2] S. Miyajima. "Componentwise enclosure for solutions of least squares problems and underdetermined systems." Linear Algebra and its Applications 444 (2014): 28-41.

[3] T. Fukaya, Y. Nakatsukasa, Y. Yanagisawa, and Y. Yamamoto. "CholeskyQR2: a simple and communication-avoiding algorithm for computing a tall-skinny QR factorization on a large-scale parallel system." 2014 5th workshop on latest advances in scalable algorithms for large-scale systems. IEEE, 2014.

[4] T. Terao, K. Ozaki, and T. Ogita. "LU-Cholesky QR algorithms for thin QR decomposition." Parallel Computing 92 (2020): 102571.

[5] T. Fukaya, R. Kannan, Y.Nakatsukasa, Y. Yamamoto and Y.Yanagisawa. "Shifted Cholesky QR for Computing the QR Factorization of Ill-Conditioned Matrices." SIAM Journal on Scientific Computing 42.1 (2020): A477-A503.

Verified Numerical Computations for a Standard Eigenvalue Problem Without Directed Rounding

Takeshi Terao[1,*], Katsuhisa Ozaki[2], Takeshi Ogita[3], Toshiyuki Imamura[1]

[1]RIKEN Center for Computational Science
[2]Shibaura Institute of Technology
[3]Tokyo Woman's Christian University

[*]takeshi.terao@riken.jp

Abstract. In this paper, we consider verified numerical computations without directed rounding for an eigenvalue problem. Directed rounding for floating-point arithmetic depends on computer environments and sometimes causes difficulty in implementing verification methods. If verification methods are designed without directed rounding, they can be implemented on various computers (e.g., CPU, GPU, and supercomputers). We propose a simple and efficient verification method without directed rounding for a standard eigenvalue problem.

Keywords: Eigenvalue problem, Verified numerical computation, Portable algorithms

1. Introduction

A standard eigenvalue problem for a symmetric matrix $A \in \mathbb{R}^{n\times n}$ is $Ax^{(i)} = \lambda_i x^{(i)}$, where an eigenvalue $\lambda_i \in \mathbb{R}$ and an eigenvector $x^{(i)} \in \mathbb{R}^n$. In this paper, we consider

$$AX = X\Lambda,$$

where a diagonal matrix $\Lambda = \mathrm{diag}(\lambda_1, \ldots, \lambda_n) \in \mathbb{R}^{n\times n}$ and an orthogonal matrix $X = [x^{(1)}, \ldots, x^{(n)}] \in \mathbb{R}^{n\times n}$. Numerical computations produce $\hat{D} \approx \Delta$ and $\hat{X} \approx X$ such that

$$A\hat{X} \approx \hat{X}\hat{D}, \quad \hat{X}^T\hat{X} \approx I,$$

where I is the identity matrix.

The verified numerical computation for an eigenvalue problem gives an error bound for $\hat{\lambda}_i$ using only floating-point arithmetic. The verification methods are proposed in [1, 2, 3, 4, 5, 6]. These employ interval matrix multiplication using directed rounding [7]. However, verification methods without directed rounding for a solution of a linear system have been investigated [8, 9]. Although rounding error analysis is lengthy and complicated, this technique can be applied to verification methods for eigenvalue problems. This study reduces the implementation cost and avoids complicated rounding error analysis and it is improved from [10].

2. The proposed method

Let $A = A^T \in \mathbb{F}^{n\times n}$, where $\mathbb{F}$ is the set of floating-point numbers defined in the IEEE standard 754, and assume that all approximate eigenpairs $\hat{D}$ and $\hat{X} \in \mathbb{F}^{n\times n}$ are obtained for A. $fl(\cdot)$ is a computed result by floating-point arithmetic with rounding to nearest. Define

$$\alpha_1 \geq \|A\hat{X} - \hat{X}\hat{D}\|_1, \quad \alpha_2 \geq \|A\hat{X} - \hat{X}\hat{D}\|_\infty, \quad \beta \geq \|\hat{X}^T\hat{X} - I\|_\infty,$$

where α_1, α_2, and $\beta \in \mathbb{F}$. If $\beta < 1$, then

$$|\lambda_i - \hat{d}_i| \leq fl\left(\sqrt{\frac{\alpha_1 \cdot \alpha_2}{1-\beta}}/(1-4u)\right) \tag{1}$$

is satisfied for $1 \leq i \leq n$ [10], where u is the unit roundoff (e.g., $u = 2^{-53}$ for binary64). For the computation of the upper bounds α_1, α_2, and β, we use only floating-point arithmetic with rounding to nearest based on the following theorem.

Theorem 1. *Let non-negative vectors $v, w \in \mathbb{F}^n$ and a non-negative normalized floating-point number $p \in \mathbb{F}$, and*

$$\rho_{(p,k)} = \frac{p}{1-ku}, \quad ku < 1.$$

If $(n+2)u < 1$, then, all of the following

$$fl\left(\left(\rho_{(p,n+2)}v^T\right)w\right), \quad fl\left(\rho_{(p,n+2)}\left(v^Tw\right)\right), \quad fl\left(v^T\left(\rho_{(p,n+2)}w\right)\right)$$

are upper bounds of pv^Tw.

$\texttt{dot}(p, v, w)$ indicates a computed result of pv^Tw using floating-point arithmetic. Then $pv^Tw \leq \texttt{dot}(\rho_{(p,n+2)}, v, w)$ is satisfied from Theorem 1. Moreover, it is independent of a computational order. Therefore, routines in Basic Linear Algebra Subprograms (BLAS) for various computational environments can be applied to matrix-vector multiplication in the verification methods. Using only Theorem 1 repeatedly, we can obtain α_1, α_2, and β. Thus, the error bound from Eq. (1) can be computed. The numerical examples (shown in the presentation) illustrate the efficiency of the proposed method.

Acknowledgments

This work has been supported by the COE research grant in computational science from Hyogo Prefecture and Kobe City through Foundation for Computational Science.

References

[1] Takeo Hoshi, Takeshi Ogita, Katsuhisa Ozaki, and Takeshi Terao. An a posteriori verification method for generalized real-symmetric eigenvalue problems in large-scale electronic state calculations. *Journal of Computational and Applied Mathematics*, page 112830, 2020.

[2] Shinya Miyajima. Numerical enclosure for each eigenvalue in generalized eigenvalue problem. *Journal of Computational and Applied Mathematics*, 236(9):2545–2552, 2012.

[3] Shinya Miyajima. Fast enclosure for all eigenvalues and invariant subspaces in generalized eigenvalue problems. *SIAM Journal on Matrix Analysis and Applications*, 35(3):1205–1225, 2014.

[4] Siegfried M Rump. Computational error bounds for multiple or nearly multiple eigenvalues. *Linear Algebra and its Applications*, 324(1-3):209–226, 2001.

[5] Shin'ichi Oishi. Fast enclosure of matrix eigenvalues and singular values via rounding mode controlled computation. *Linear algebra and its Applications*, 324(1-3):133–146, 2001.

[6] Tetsuro Yamamoto. Error bounds for computed eigenvalues and eigenvectors. *Numerische Mathematik*, 34(2):189–199, 1980.

[7] Siegfried M Rump, Takeshi Ogita, Yusuke Morikura, and Shin'ichi Oishi. Interval arithmetic with fixed rounding mode. *Nonlinear Theory and Its Applications, IEICE*, 7(3):362–373, 2016.

[8] Takeshi Ogita, Siegfried M Rump, and S Oishi. Verified solution of linear systems without directed rounding. *Advanced Research Institute for Science and Engineering, Waseda University*, 2005.

[9] Yusuke Morikura, Katsuhisa Ozaki, and Shin'ichi Oishi. Verification methods for linear systems using ufp estimation with rounding-to-nearest. *Nonlinear Theory and Its Applications, IEICE*, 4(1):12–22, 2013.

[10] Takeshi Terao, Katsuhisa Ozaki, Takeshi Ogita, and Toshiyuki Imamura. Verification methods for a standard eigenvalue problem for a real symmetric matrix with rounding-to-nearest. *IPSJ SIG Technical Report (HPC)*, 2020(16):1–8, 2020 (in Japanese).

JSST 2021

Acceleration of Iterative Refinement for Symmetric Eigenvalue Decomposition

Yuki Uchino[1,*], Katsuhisa Ozaki[2], Takeshi Ogita[3]

[1]Graduate School of Engineering and Science, Shibaura Institute of Technology, Japan
[2]Department of Mathematical Sciences, Shibaura Institute of Technology, Japan
[3]Division of Mathematical Sciences, Tokyo Woman's Christian University, Japan

[*]mf20013@shibaura-it.ac.jp

Abstract. This study considers a refinement algorithm for the eigenvalue decomposition of a real symmetric matrix. Various numerical algorithms have been developed for standard eigenvalue problems. Recently, Ogita and Aishima proposed efficient refinement algorithms for improving approximate eigenpairs obtained using a numerical algorithm. In this study, we aim to reduce computational cost of those refinement algorithms. Numerical experiments illustrate the efficiency of the proposed algorithm.

Keywords: Iterative refinement, Accurate numerical algorithms, Symmetric eigenvalue decomposition

1. Introduction

Let $A \in \mathbb{R}^{n\times n}$ be a real symmetric matrix, $\lambda_i \in \mathbb{R}$ the eigenvalues of A, and $x_{(i)} \in \mathbb{R}^n$ the normalized eigenvectors of A associated with λ_i. Assume that $\lambda_1 \le \lambda_2 \le \cdots \le \lambda_n$. This study investigates the eigenvalue decomposition of A:

$$A = XDX^T,$$

where

$$D = \mathrm{diag}(\lambda_1, \lambda_2, \ldots, \lambda_n) \in \mathbb{R}^{n\times n}, \tag{1}$$
$$X = (x_{(1)}\ x_{(2)}\ \cdots\ x_{(n)}) \in \mathbb{R}^{n\times n}. \tag{2}$$

Various numerical algorithms have been developed for calculating (1) and (2). The accuracy of approximate eigenvectors obtained using a numerical algorithm decreases with the gap between the associated eigenvalue and its closest one. Therefore, using iterative refinement methods is useful for obtaining the eigenvalue decomposition with high accuracy.

Ogita and Aishima proposed refinement algorithms for the eigenvalue decomposition of A. Those algorithms converge quadratically, provided that an error matrix $E \in \mathbb{R}^{n\times n}$ such

that $X = \hat{X}(I + E)$, where I is the $n \times n$ identity matrix, for an initial guess $\hat{X}$ of X satisfies the following condition [1, Theorem 1, 2]:

$$\begin{cases} \|E\|_2 < \min\left(\dfrac{\min\limits_{1 \le i < j \le n} |\lambda_i - \lambda_j|}{10n\|A\|_2}, \dfrac{1}{100} \right) & \text{(if all eigenvalues are simple),} \\ \|E\|_2 < \dfrac{1}{3} \min\left(\dfrac{\min\limits_{\lambda_i \neq \lambda_j,\ 1 \le i,j \le n} |\lambda_i - \lambda_j|}{10n\|A\|_2}, \dfrac{1}{100} \right) & \text{(otherwise).} \end{cases}$$

The refinement algorithms are constructed via four high-accuracy matrix multiplications $\hat{X}^T\hat{X}$, $\hat{X}^TA\hat{X}$, and $\hat{X}\tilde{E}$. Thus, they may yield high-accuracy results faster than those obtained using multiple-precision arithmetic (See the numerical results in [1, 2]). Ozaki et al. proposed an algorithm for high-accuracy matrix multiplication using error-free transformation [3].

In this study, we design algorithms to obtain almost the same quality of results as refinement algorithms proposed by Ogita and Aishima via three high-accuracy matrix multiplications $A\hat{X}$, $\hat{X}^T(A\hat{X} - \hat{X}\mathrm{diag}(\tilde{\lambda}))$, and $\hat{X}E$, where $\tilde{\lambda}_i$ is an approximation of λ_i. We improve accuracy of approximate eigenpairs provided by MATLAB [4] command `eig` with double-precision arithmetic using these refinement algorithms with high-accuracy matrix multiplications proposed by Ozaki et al. We compare the performance of the proposed algorithms with that of MATLAB command `eig` by Advanpix Multiprecision Computing Toolbox version 4.8.4.14478 [5]. For $n = 5000$, we obtained high-accuracy results 1.8 times faster than that obtained using the original algorithms proposed by Ogita and Aishima and 11 times faster than those obtained using multi-precision arithmetic when the arithmetic precision was set to 34 decimal digits in the first iteration and 48 decimal digits in the second iteration.

References

[1] T. Ogita, K. Aishima: Iterative refinement for symmetric eigenvalue decomposition, *Jpn. J. Ind. Appl. Math.*, **35**:3 (2018), 1007–1035.

[2] T. Ogita, K. Aishima: Iterative refinement for symmetric eigenvalue decomposition II: clustered eigenvalues, *Jpn. J. Ind. Appl. Math.*, **36**:2 (2019), 435–459.

[3] K. Ozaki, T. Ogita, S. Oishi, S.M. Rump: Error-free transformation of matrix multiplication by using fast routines of matrix multiplication and its applications, *Numer. Algorithms*, **59**:1 (2012), 95–118.

[4] MathWorks, `https://jp.mathworks.com/`.

[5] Advanpix: Multiprecision computing toolbox for MATLAB, `https://www.advanpix.com/`.

JSST2021

The mechanical genome

Helmut Schiessel

Cluster of Excellence Physics of Life, Technical University Dresden, Dresden, Germany

helmut.schiessel@tu-dresden.de

Abstract. In addition to the classical layer of genetic information, DNA molecules also carry other layers of information. Two possible layers are discussed. One is a mechanical layer, namely that the base pair sequence influences the mechanical and geometrical properties of the DNA molecules which in turn might guide their packing inside the cell. A second possible layer is the speed of translation in the protein-producing ribosomes where the speed influences the quality of the protein product. We demonstrate that the degeneracy of the genetic code allows for multiplexing of all three layers of information.

Keywords: Monte Carlo simulation, DNA mechanics, genetic information, synonymous mutations, weighted graphs

1. Introduction

As early as 1989 it was suggested by Edward N. Trifonov that DNA could carry several codes in addition to the classical code (the genes which encode for proteins) [1]. One of the suggested layers, a chromatin code, was studied in detail later by Jonathan Widom who claimed that base pair sequences carry a "nucleosome positioning code" [2]. Nucleosomes, DNA-wrapped protein spools, are the first layer of the chromatin complex, the DNA-protein complex that fills the nuclei of our cells. Other scientific communities have focused on other possible layer of information, often ignoring each other. This leads to the question whether DNA molecules could carry several independent layers of information, multiplexed with each other. To address this set of questions we build models of nucleosomes that account for the sequence-dependent DNA elasticity and study them using simulations (introducing the mutation Monte Carlo method) and analytical approaches (transfer matrix method and mapping of base pair sequences on weighted graphs).

2. Nucleosome sequence preferences

Nucleosomes show clear DNA sequence preferences [2]. We wanted to know the physical origin of these sequence preferences. We built a coarse-grained nucleosome model based on the nucleosome crystal structure and found via Monte Carlo simulations that our model reproduces the experimentally known sequence preferences [3]. Since our model only accounts for the sequence dependent elasticity and geometry of the DNA double helix, we conclude that nucleosomes prefer certain positions on the DNA more than others because it requires less DNA bending costs. Using an analytically exactly solvable model we can understand these preferences in detail and can show that nucleosomes prefer DNA that it is intrinsically curved in the right direction [4].

3. Multiplexing of genetic and mechanical signals

The question arises whether DNA sequences have evolved to put mechanical signals on DNA to e.g. position stable nucleosomes at certain places and whether this is even possible on top of genes. We developed methods to demonstrate this by systematically exploring all sequences that encode for the same protein, making use of the degeneracy of the genetic code. Using graph theory we were able to show that, at least within our nucleosome model, we can modify sequences such to position nucleosomes anywhere on the genome of yeast with single base pair precision, without modifying the encoded proteins [5].

4. Is there space for even more layers?

Since it was straightforward to modify the DNA shape or elasticity on top of genes, we checked whether there is space for a third layer: the translation speed in ribosomes. It has been claimed that the speed profile affects the co-translational folding of proteins [6]. We demonstrate using graph theory that this is indeed possible, namely to independently put mechanical signals on genes and control the translational speed at the same time [7].

5. Mechanical cues on real genomes

We studied the genomes of various organisms and found mechanical signals, e.g. around the transcription start sites [8, 9]. Remarkably, unicellular organisms show a signal opposite to that of multicellular life forms and the way these signals are created varies from organism to organism. Why there is such a rich zoo of "mechanical genomes" remains an open question.

References

[1] E. N. Trifonov: *Bulletin of Mathematical Biology*, 51:4 (1989), 417-432.

[2] E. Segal, Y. Fondufe-Mittendorf, L. Chen, A. Thåström, Y. Field, I. K. Moore, J.-P. Z. Wang, J. Widom: *Nature*, 442 (2006), 772-778.

[3] B. Eslami-Mossallam, R. D. Schram, M. Tompitak, J. van Noort, H. Schiessel: *PloS ONE*, 11(6) (2016), e0156905.

[4] M. Zuiddam, R. Everaers, H. Schiessel: *Phys. Rev. E*, 96 (2017), 052412

[5] M. Zuiddam, H. Schiessel: *Phys. Rev. E*, 99 (2019), 012422.

[6] K. C. Stein, J. Frydman: *J. Biol. Chem.*, 294(2) (2019), 2076-2084.

[7] M. Zuiddam, B. Shakiba, H. Schiessel, in preparation

[8] M. Tompitak, C. Vaillant, H. Schiessel: *Biophys. J.*, 112 (2017), 505-511.

[9] J. Neipel, G. Brandani, H. Schiessel: *Phys. Rev. E*, 101 (2020), 022405.

Cooperation of Real-World Modeling with Simulation toward the Problem "What is Life?"

Kenichi Yoshikawa[1,2]

[1]Faulty of Life and Medical Science, Doshisha University
[2]Institute for Advanced Study, Kyoto University

*keyoshik@mail.doshisha.ac.jp

Abstract. All living organisms have complicated but self-organized intracellular structures with various specific functions to maintain their lives. To gain insight into the underlying mechanism of the self-organization of cells, we have been performing cooperative studies of real-world modeling through the cooperation with numerical modeling. We may report; 1) Spontaneous generation of cell-like structure and function under crowding condition with macromolecules. 2) Self-organization of cellular assembly. 3) Occurrence of macroscopic regular motion for the assembly of nano-scaled self-propelling objects.

Keywords: Experimental modeling, Proto cell, Spatio-temporal self-organization

1. Introduction

Living cells on the earth maintain their active lives under highly crowding conditions; the concentrations of macromolecules, such as RNA, proteins and DNA, are 0.3-0.5g/mL. It is well known in polymer physics that a mixed solution of different polymers tends to undergo phase separation because of the minimum contribution of mixing entropy, in contrast to the solution containing different low molecular-weight chemicals. Generally speaking, in crowding polymer solutions, the contribution of conformational entropy coupled with self-avoiding volume effect, or depletion effect, becomes significant instead of mixing entropy. Here, we will demonstrate the real-world experimental models, 4revealing the significant role of such crowding effect on the self-emergence of cell-like structure and also on the appearance of characteristic biological functions.

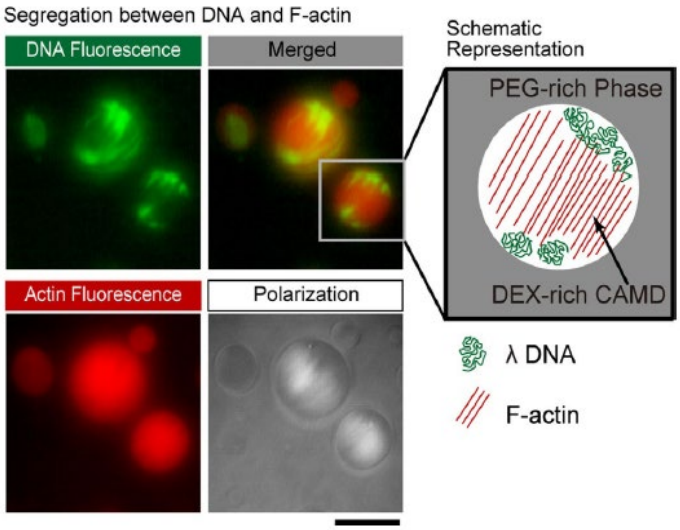

Fig.1 Specific localization of DNA and actin in water/water droplets generated through simple mechanical mixing of binary polymer solution with polyethylene glycol (PEG) and dextran (DEX) containing γ-DNA (49kbp) and F-actin (polymerized actin). [1]

2. Real-world modeling of self-emerging cell-like structure

Fig.1 exemplifies the formation of cell-sized water droplets entrapping DNA and actin (skeletal protein) under the aqueous environmental aqueous solution, where the solutions inside and outside droplets are rich in dextran and polyethylene glycol (PEG), respectively. It is noted that such droplets are generated spontaneously through simple mixing of DNA and actin in an aqueous solution with dextran and PEG. Herein, it is noted that microdroplets caused by simple depletion effects served a simple real-world model of a cellular system. These systems are generated under markedly different physicochemical interactions from that of coacervates, that is, aggregation products through attractive interactions among macromolecules.

3. Numerical modeling on the confinement effect

The snapshots in Figs. 2(a) and 2(b) illustrate that the switching of the localization of a large sphere, depending on its rigidity, hard and soft, respectively. The numerical results indicate that the soft large sphere tends to situate in inner cavity but the rigid large sphere localizes on the periphery. By adapting such kind of numerical model, the following issues were found: the preferential location of the larger particle shifts from the region near the cavity wall to the inner cavity by (1) decreasing the size of the smaller particles at a high enough particle density and (2) increasing the density of smaller particles of a given crowder size. It may be interesting to note that, in living cells, organellar including nuclei and mitochondria exhibits the positioning apart from the prefer of the surrounding membrane. Such kind of general trends in cells is attributable to the depletion effect as described in the present paper.

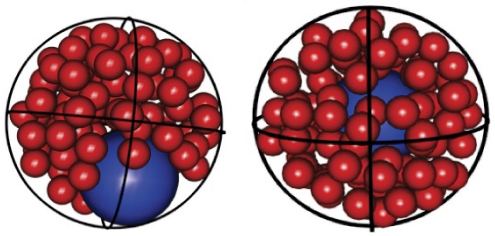

Fig.2 Switching on the spatial positioning of a large sphere depending on its rigidity; hard and soft for left and right pictures. [3]

4. Important role of nonspecific effect in life

Besides the above-mentioned examples, we may show the importance of the depletion effect or crowding effect on the structure and functions in living systems, including the self-organized assembly of multi cellular system as the model of organoids and self-motility of organisms driven by the assembly of fluctuating molecular motors.

References

[1] N. Nakatani, H. Sakuta, M. Hayashi, S. Tanaka, K. Takiguchi, K. Tsumoto, K. Yoshikawa, *ChemBioChem*, 19, 1370-1374 (2018). [2] H. Sakuta, F. Fujita, T. Hamada, M. Hayashi, K. Takiguchi, K. Tsumoto, K. Yoshikawa, *ChemBioChem*, 21, 3323-3328 (2020). [3] C.-Y. Shew, S. Oda, K. Yoshikawa, *J. Chem. Phys.*, 147, 204901/1-12(2017).

Water on the DNA surface: microscopic insight from molecular dynamics simulations

Yoshiteru Yonetani[1*],

[1]National Institutes for Quantum and Radiological Science and Technology (QST),

[*]yonetani.yoshiteru@qst.go.jp

Abstract. Water on the DNA surface exhibits characteristic behavior such as ice-like water network along the narrow groove of DNA. By using molecular dynamics simulations, we obtained detailed picture for such water; our characterization fully describes the water network patterns and their sequence variation [*Biophys. J.* **97**, 1138 (2009)]. Analysis on such water network further revealed microscopic origin of the slow water-exchange kinetics [*Biophys. Chem.* **160**, 54 (2012)]. As another relevant topic, I will also mention a relation with DNA damage production. Our recent study [*Chem. Phys. Lett.* **749**, 137441 (2020)] found that site-dependent water accessibility for DNA backbone is well correlated with the probabilities of DNA damage production by OH radical attacking. This suggests that the site-dependent hydration property is a key factor for DNA damage production.

Keywords: DNA, Hydration water, Hydroxyl radical, Radiation damage, Molecular dynamics

1. Structure and dynamics of DNA hydration water

Water plays an essential role in DNA structure formation and the related biological functions. So far, molecular structures of DNA and the hydration water have been derived from experimental measurements using X-ray and neutron crystallography [1]. However, it is still difficult to obtain more details on the dynamical and sequence-dependent behaviors from the experimental approaches.

Computer simulation can provide such microscopic pictures. In 2007, we started our molecular dynamics (MD) studies on the DNA and hydration water. At first, we calculated spatial distribution of DNA hydration water. The MD result was compared with the experimental data of X-ray crystallography and theoretical RISM calculations [2] to confirm the correspondences between the different methods. After that, we investigated sequence effect using the two typical cases AATT and TTAA [3] and using 136 different sequences [4]. From this systematic comparison, we found that an explicit correlation exists between the DNA structural fluctuation and the hydration patterns in the minor groove.

Water kinetics is also an interesting aspect of DNA hydration. It has been known that water molecules in the narrow minor groove of DNA exhibit long residence times over ~300 ps, depending on the sequence. How does such slow kinetics appear? We found that access of an

additional water molecule is a key step [5]. Such water access triggers the water departure from the DNA surface. Thus, if such an additional water does not access, the residing water does not leave, leading to long residency. In this way, we could explain how water residence times change with the surface environment. We expect that neutron scattering measurements can provide experimental evidence for such dynamical behaviors; experimental studies on DNA and hydration water are carried out with J-PARC facilities in Ibaraki, Japan [6, 7].

2. Water and DNA radiation damage

Water has a significant contribution to radiation-induced DNA damage. Water in a biological cell is highly excited by radiation of X-ray, γ-ray or heavy ion. Such water excitation produces several reactive species; hydroxyl (OH) radical is one of the major products. This attacking to the DNA triggers abstraction of DNA hydrogen, leading to a critical damage of the DNA molecular structure.

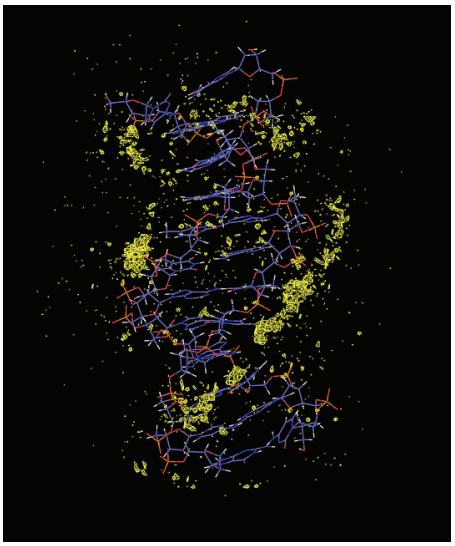

Fig. 1: OH radical distribution. Yellow denotes the region in which OH radicals visit frequently.

To gain the microscopic relationship between the radical attacking and the damage production, we calculated OH radical distribution around DNA [8]. The MD result showed that the OH radical frequently visits the backbone of DNA (Fig. 1). Yet, current statistics of radical distribution is not enough; Instead, water distribution was employed to assess site-dependent accessibility. We found that the result is well correlated with the experimental site-dependent probabilities [9] as to DNA damage production. This suggests that the site-dependent solvent accessibility is key for the DNA damage production.

References

[1] *Oxford Handbook of Nucleic Acid Structure*, edited by S. Neidle (Oxford University Press, New York, 1999).

[2] Y. Yonetani, Y. Maruyama, F. Hirata, H. Kono: Comparison of DNA hydration patterns obtained using two distinct computational methods, molecular dynamics simulation and three-dimensional reference interaction site model theory, *J. Chem. Phys.*, 128 (2008), 185102.

[3] Y. Yonetani, H. Kono, S. Fujii, A. Sarai, N. Go: DNA deformability and hydration studied by molecular dynamics simulation, *Mol. Simul.*, 33 (2007), 103 - 107.

[4] Y. Yonetani, H. Kono: Sequence dependencies of DNA deformability and hydration in the minor groove, *Biophys. J.*, 97 (2009), 1138 - 1147.

[5] Y. Yonetani, H. Kono: What determines water-bridge lifetimes at the surface of DNA? Insight from systematic molecular dynamics analysis of water kinetics for various DNA sequences, *Biophys. Chem.*, 160 (2012), 54 -61.

[6] H. Nakagawa, Y. Yonetani, K. Nakajima, S. Ohira-Kawamura, T. Kikuchi, Y. Inamura, M. Kataoka, H. Kono: Local dynamics coupled to hydration water determines DNA-sequence-dependent deformability, *Phys. Rev. E*, 90 (2014), 022723.

[7] H. Nakagawa, Y. Yonetani, K. Nakajima, S. Ohira-Kawamura, T. Kikuchi, Y. Inamura, M. Kataoka, H. Kono: Sequence-dependent hydration water dynamics of dodecameric DNA, *JPS Conf. Proc.*, 33 (2021), 011101.

[8] Y. Yonetani, H. Nakagawa: Understanding water-mediated DNA damage production by molecular dynamics calculation of solvent accessibility, *Chem. Phys. Lett.*, 749 (2020), 137441.

[9] B. Balasubramanian, W. K. Pogozelski, T. D. Tullius, *Proc. Natl. Acad. Sci USA* 95 (1998), 9738 - 9743.

JSST 2021

Development of an optimal routing system for traveling among farm fields

Takuma Nemoto[1,*], Naoki Niitsuma[2], Norihiro Kamamichi[1,2]

[1]Department of Robotics and Mechatronics, School of Science and Technology for Future Life, Tokyo Denki University
[2]Robotics and Mechatronics, Graduate School of Science and Technology for Future Life, Tokyo Denki University

[*]nemoto@ctrl.fr.dendai.ac.jp

Abstract. This paper presents an optimal routing system for smart agriculture, which is developed to enable inexperienced workers to travel among farm fields via the shortest route. The system provides the shortest route, solving the traveling salesman problem (TSP) with distance data between farm fields included in their road network, and shows the route on a map. The developed system can reduce the traveling distance by 6.89 % in a traveling route for 72 farm fields and has been utilized on trial in an agricultural management entity.

Keywords: Smart agriculture, Optimal routing, Traveling salesman problem (TSP)

1. Introduction

The agricultural population in Japan has been decreasing, and this fact demands to improve the productivity to maintain the domestic agricultural supply. This demand encourages us to save cost and labor through automation and standardization in agricultural work.

One of the causes decreasing the productivity is the time for traveling among farm fields. The time tends to increase, caused by distributed fields in large-scale agricultural management entities. In such entities, inexperienced workers have difficulty to efficiently travel among distributed fields because workers decide traveling routes empirically. The deciding of routes is repeatedly performed since visited fields are changed depending on tasks and situations.

In this paper, we introduce an optimal routing system developed that enables inexperienced workers to travel among farm fields via the shortest route. This system shows the shortest route, solving the traveling salesman problem (TSP) with the road network among farm fields [1], and has some output functionalities.

2. Optimal routing system for traveling among farm fields

The structure of the optimal routing system developed is shown in Figure 1. The system allows us to search the shortest route to travel among farm fields, loading two CSV files: the fields data having the name, number, and coordinate of longitude and latitude of farm fields and the path and distance data between the whole fields included in the fields data [1]. We can get the shortest route, which is provided by solving the TSP with the exact algorithm [2], selecting the farm fields visited from the list constructed with the fields data and then clicking the search button. The shortest route is shown on the map in the main window, and the order of fields traveling on the route is indicated in the display under the map, where the map can be switched to an aerial photo. Moreover, the optimal routing system has the three types of output functionalities: (a) printing the main window, (b) QR code providing a URL to show the shortest route on Google Maps, and (c) file output which generates a HTML file including the shortest route map.

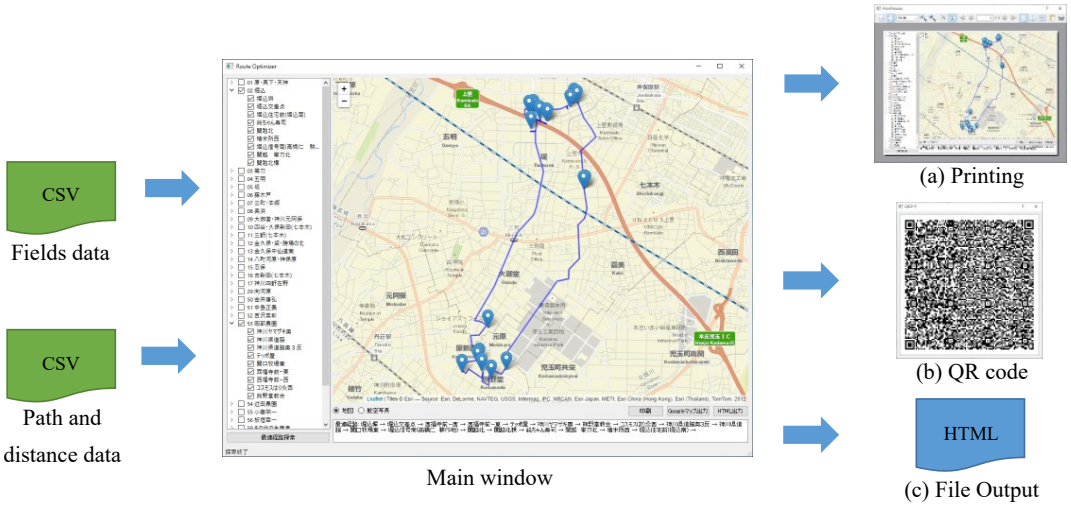

Figure 1: Structure of the optimal routing system.

The effectiveness of the optimal routing system has been demonstrated by comparing the traveling route for 72 farm fields provided by the system to that decided empirically. The experiment shows that the optimal routing system can reduce the traveling distance by 6.89 %.

3. Conclusions

This paper has reported the development of an optimal routing system for traveling among farm fields. The developed system can display on a map the shortest route to visit selected farm fields, solving the TSP with the exact algorithm. The system can also output the route with the printing, QR code, and file generation. Although the system can reduce the traveling distance and has been utilized on trial in an agricultural management entity, it requires detailed road data, such as road width, for more effective optimal routing, which is

discussed in future work.

Acknowledgement

This work was supported by "On-farm demonstration trials of smart agriculture," the Ministry of Agriculture, Forestry and Fisheries (Project number: 露 2C03, Enterprising body: National Agriculture and Food Research Organization).

References

[1] T. Nemoto, N. Niitsuma, N. Kamamichi: Optimal routing with road network information for traveling among farm fields, *Proceedings of the 8th Multi-symposium on Control Systems (MSCS 2021)*, (2021), 1I2-3. (in Japanese)

[2] M. Namiki: Introduction of mathematical optimization with Python, Asakura Publishing Co., Ltd., (2018). (in Japanese)

Elbow Joint Angle Estimation Method Using 1D-CNN with Quantized EMG Generated by SR and Multi-sensor

D. Kashimoto[1,*] and T. Sadahiro[1,*]

[1]Graduate School of Engineering, Oita University

[*]v20e1017@oita-u.ac.jp, sadahiro@oita-u.ac.jp

Abstract. Electromyogram (EMG) is used for a motion estimation as it contains informations of an intended motion. It is possible to estimate human motions in advance using Electromechanical delay (EMD) of EMG. Moreover, a denoising method that uses Stochastic Resonance (SR) and multi-sensor is able to acquire longer EMD than LPF, except the acquired EMG is roughly quantized. In this study, a one-dimensional convolutional neural network (1D-CNN) is used as an estimation model using the roughly quantized EMG to estimate elbow angles. In order to show the advantage of 1D-CNN, the estimation results between 1D-CNN and NDARX model using LPF-processed EMG or SR and multi-sensor-processed EMG were compared.

Keywords: EMG, EMD, Multi-sensor, Stochastic Resonance, CNN

1. Introduction

Electromyogram (EMG) is used for motion estimation as it contains information of human intended motion. EMG has a time-lag between the onset of the EMG production to the actual motion, called Electromechanical delay (EMD). A prior human motion estimation method exploiting EMD has been proposed [1]. In this study, Low Pass Filter (LPF) is used as a preprocess of EMG, yet the acquired EMD is shorter thruough this process.

Recent developments which has been proposed by Sadahiro, et al. [2] revealed that a combination of Stochastic Resonance (SR) and multi-sensor has met with great success for acquiring a longer EMD compared to LPF method. SR is a way to detect the weak signal by adding on appropriate noise to the signal and passing through a hysteresis function. Although SR is helpful to detect early changes in EMG, the EMG acquired after SR becomes the ON-OFF signal. Multi-sensor are used to increase the number of quantization bits of EMG after SR by summing up the all ON-OFF signals obtained from each muscle. EMG made by SR and multi-sensor is a roughly quantized signal. Hence, elbow joint angles estimation results by Multi Input Single Output ARX model with the roughly quantized EMG as inputs were worse than those with LPF-processed EMG as input [3].

The purpose of this study is to estimate elbow joint angles in advance using a one-dimensional convolutional neural network (1D-CNN) with roughly quantized EMG as inputs. 1D-CNN extracts features from the time direction by using convolution layers, and is

preferable for handling time-series data. In order to show the advantage of 1D-CNN, estimation results of 1D-CNN are compared with estimation results of the Nonlinear Delayed ARX (NDARX) model [1].

2. Experimental Method

An experimental equipment that are consisted of BITalino EMG sensors, a goniometer (Biometrics Ltd.), and Arduino Due microcontroller [2]. EMG sensors were attached to biceps brachii (ch1 to ch4) and triceps brachii (ch5 to ch8) as shown in Figure 1. The biceps brachii and the triceps brachii correspond to the elbow flexion and extension, respectively. The goniometer is a device to measure elbow joint angles.

In order to estimate elbow joint angles using EMG, the experiment was conducted such that subject's elbow extensions and flexions were in accordance to the visual information signals provided. The visual information signal was M-sequence signals passed through LPF with a cutoff frequency of 2 [Hz]. Bending angles of the elbow joint were between 0 to 90 [deg], and the straightened elbow was 0 [deg]. One trial on the experiment was set for 10 [sec] and a total of 100 trials was conducted. Eighty trial data were used as training data, and the rest as test data. To eliminate the effects of muscle fatigue as much as possible, a break of 1 [min] was taken after every ten trials.

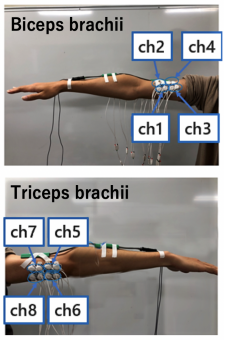

Figure 1: EMG sensors arrangement

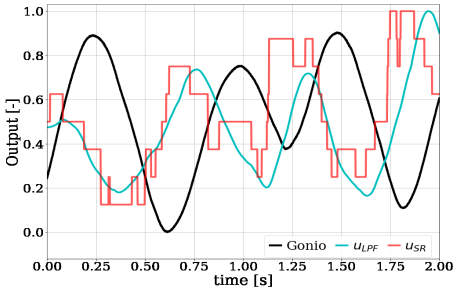

Figure 2: A comparison of u_{LPF} and u_{SR}; Although the experiments were done until 10 [sec], due to the page limitation, variations between 0 to 2 [sec] were shown. The black line shows elbow joint angles measured by the goniometer. The red line shows u_{SR}. The blue line shows u_{LPF}. The graph clearly shows that the wave forms of u_{SR} is a more roughly quantized EMG compared to u_{LPF}. EMD is the time-lag between actual motions and their EMGs. Wave peaks of u_{SR} and u_{LPF} are advanced compared to Gonio. This indicates that u_{SR} and u_{LPF} both possess EMD except for u_{SR} has a longer EMD compared to u_{LPF}.

3. Elbow Joint Angle Estimation

3.1. Preprocessing of EMG [2]

To estimate human motions using EMG, some preprocesses are needed. In general, baseline drift from raw EMG obtained from sensors are removed and the signals are rectified. After these processes, smoothing process are done to reduce noise.

In this study, a second-order Butterworth filter with a cut-off frequency of 2 [Hz] is used as the LPF, which has been widely adopted in the field of EMG preprocessing. In order to use LPF-processed EMG as an input for estimation models, only one channel signal per muscle is needed. Hence, by using the EMGs from biceps brachii of ch1 and triceps brachii of ch5 respectively, the input signal using LPF-processed EMG was defined as

$$u_{LPF} = LPF(\text{ch1}) - LPF(\text{ch5}), \tag{1}$$

where $LPF()$ means the preprocessing by the LPF.

Using SR and multi-sensor is another method to remove noise. SR is a phenomenon to enhance the sensitivity of a weak signal by adding white noise to EMG and passing it through a rectangular hysteresis function. Multi-sensor sums up EMGs after SR for each muscle to increase the number of quantization bits. In this study, the standard deviation of the added white noise to the SR process was 0.05 times **max**, where **max** indicates the maximum value of EMG at each channel. The upper and lower thresholds of the hysteresis function were 0.35 times **max** and −0.1 times **max**, respectively. The inputs made by SR and multi-sensor is defined as

$$u_{SR} = \sum_{i=1}^{4} SR(\text{ch}i) - \sum_{i=5}^{8} SR(\text{ch}i), \tag{2}$$

where $SR()$ means the preprocessing by SR.

A comparison between u_{LPF} and u_{SR} is shown in Figure 2. It shows that u_{SR} is a rougher quantized signal and has advanced wave peaks compared to u_{LPF}. Thus, the EMD obtained through u_{SR} is longer than u_{LPF}.

3.2. Estimation Model

In this study, 1D-CNN was used as an estimation model from EMG to elbow joint angles, as shown in Figure 3. This model extracts temporal features by performing convolution on the input data and maxpooling on the resulted data. The number of filters in each layer was 16, and the filter size was 2. The activation function was ReLu, and the evaluation function was RMSE. Inputs data were $u[k]$, $u[k-1]$, $\hat{y}[k+EMD-1]$ and $\hat{y}[k+EMD-2]$. $u[k]$ is the EMG signal at time k. $y[k]$ is the elbow joint angles measured by the goniometer at time k. $\hat{y}[k]$ is the estimated joint angle at time k. EMD means time steps of EMD. u_{LPF} and u_{SR} were used as $u[k]$. As mentioned in section 2, 80 trial data were used as training data of 1D-CNN. Considering the time lag due to EMD, $y[k+EMD]$ was set to the ground truth for model training when $u[k]$ was used as input. Therefore, it is possible to obtain $\hat{y}[k]$ from $u[k]$, $u[k-1]$, $\hat{y}[k+EMD-1]$ and $\hat{y}[k+EMD-2]$. In this study, the EMD of u_{LPF} was set to 120 and the EMD of u_{SR} was set to 220.

As mentioned in the introduction, the NDARX model is used to compare the results of 1D-CNN. In this study, the number of previous inputs and outputs was two, and the number of divided regions was 10.

3.3. Estimation Results

The estimation results between 1D-CNN and NDARX were shown in Figure 4. Since the estimated signals are the future elbow joint angles, the estimated signals were delayed by the time of EMD. Therefore the estimation signals using u_{LPF} was delayed by 120 [msec], and the estimation signals using u_{SR} was delayed by 220 [msec]. From Figure 4, the 1D-CNN estimation is similar to the actual signal of elbow joint angles compared to the NDARX estimation. This results highlight that the estimation signal of 1D-CNN with u_{SR} is comparable with u_{LPF}. Therefore, 1D-CNN with u_{SR} as inputs can be estimated further in advance compared to the conventional methods.

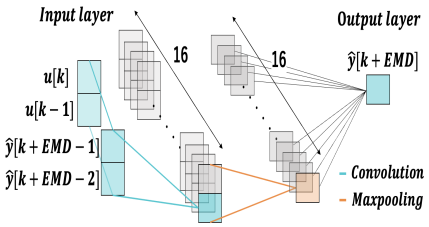

Figure 3: A structure of 1D-CNN; The blue line indicates convolution process. The orange line indicates maxpooling. $u[k]$ is the EMG signal at time k. $\hat{y}[k]$ is the estimated joint angle at time k. EMD means time steps of EMD.

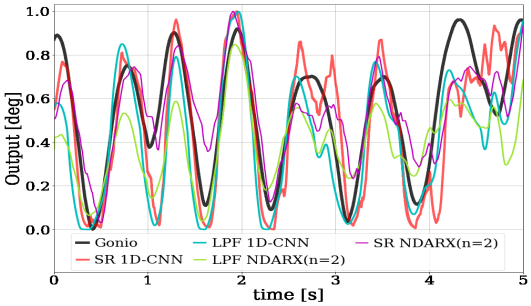

Figure 4: The estimation results of 1D-CNN and NDARX; Although the experiments were done until 10 [sec], due to the page limitation, variations between 0 to 5 [sec] were shown. The black line shows elbow joint angles measured by goniometer. The red line shows estimation result from 1D-CNN with u_{SR}. The blue line shows estimation result from 1D-CNN with u_{LPF}. The green line shows estimation result from NDARX with u_{LPF}. The purple line shows estimation result from NDARX with u_{SR}. In order to compare only their waveforms easily, the estimation results were shifted using the amount of EMD. The result shows that the 1D-CNN estimation is similar to the actual signal than the NDARX estimation. This results highlight that the estimation signal of 1D-CNN with u_{SR} is comparable with u_{LPF}. Therefore, 1D-CNN with u_{SR} as inputs can be estimated further in advance compared to the conventional methods.

4. Conclusion

As a result, 1D-CNN with the roughly quantized EMGs as input is an effective method to estimate elbow joint angles in advance. However, since EMD was determined based on a priori knowledge after measuring the actual motion, it is not suitable for practical applications. Thus, as a future research, we will construct a method to determine actual EMD before completing elbow joint angles acquisition. Additionally, in order to show the statistical significance of the proposed method, to increase the number of subjects is also one of our future works.

Acknowledgement

The authors would like to thank Ms. Nur Hidayah Binti Samijan for carefully proofreading the manuscript. This work was supported by JSPS KAKENHI Grant Number JP18K04071.

References

[1] M. Hayashi, et al.: Development of zero-phase-tracking man-machine interface with electromechanical delay of electromyogram, *Journal of the Robotics Society of Japan*, 30:8 (2012), 767-778 (*in Japanese*).

[2] T. Sadahiro, et al.: Experimental Verification of Obtaining Longer EMD of EMG Using Multisensor and SR Phenomenon, *The 38th JSST Annual International Conference on Simulation Technology*, (2019), 43–46.

[3] D. Kashimoto, et al.: Comparison of elbow angle estimation from rough quantized emg signals using stochastic resonance between different hysteresis functions and number of sensors, *The 39th SICE Kyushu Branch Annual Conference*, (2020), 40–43, (*in Japanese*).

JSST 2021

Elbow Joint Angle Estimation from Smoothed EMG Using Summing Network and Multi-sensor

Naoki Ikeda[1,*] and Teruyoshi Sadahiro[1,*]

[1]Graduate School of Engineering, Oita University

[*]v21e1001@oita-u.ac.jp, sadahiro@oita-u.ac.jp

Abstract. Human motions are performed by muscle contractions, and electrical signals called electromyogram (EMG) produced when a muscle contracts. EMG is used as an input signal for man-machine interface (MMI). Electro Mechanical Delay (EMD) of EMG can improve the responsivity of MMI. A noise reduction method using Stochastic Resonance (SR) and multi-sensor has been proposed to obtain longer EMD compared to the conventional method of low pass filter (LPF). Summing Network (SN) is another method to reduce noise using SR, and finely quantized EMG with longer EMD can be obtained by combining SN and multi-sensor. The purpose of this study is to estimate elbow joint angle from denoised EMG using SN and multi-sensor. Experimental results show that the proposed method has better estimation results compared to the method using EMG made by SR and multi-sensor as inputs.

Keywords: EMG, EMD, Stochastic Resonance, Summing Network

1. Introduction

Human motion are performed by muscle contractions, and an electrical signals called electromyogram (EMG) produced when a muscle contracts. EMG contains various informations about body movements, for example a timing and degree of muscle contraction. One of the features of EMG is Electro Mechanical Delay (EMD). EMD is the time difference of about 30 to 100 msec between the production of EMG and the actual motion.

EMD of EMG can improve the responsitivity of man-machine interface[1]. In general, a denoising process using low pass filter (LPF) is necessary to estimate a motion from EMG. However, LPF makes EMD shorter.

A denoising method that prevents the decrease of EMD has been studied. An example of such method has been proposed by Sadahiro et al.[2], that uses Stochastic Resonance (SR) and multi-sensor. SR is a method to detect a weak signal by adding white noise to the original signal and passing it through a hysteresis function[3]. A denoised EMG using SR and multi-sensor becomes a roughly quantized signal. An estimation accuracy of elbow joint angle using Multi Input Single Output (MISO) ARX model with this roughly quantized EMG as inputs is unsatisfactory compared with denoised EMG using LPF as inputs[4].

Number of quantization bits of the input signals can be made finer by increasing the number of EMG sensors, but it is restricted by surface area limitations of muscles.

The purpose of this study is to estimate elbow joint angle from denoised EMG using Summing Network (SN) and multi-sensors. SN is a method proposed by Collins et al. that can obtain a finer quantized signal compared to SR[5]. denoised EMG using SN is able to obtain finely quantized EMG with longer EMD without increasing the number of sensors[6]. In this paper, estimation results using MISO nonlinear ARX (NARX) with denoised EMG using SN and multi-sensor and using SR and multi-sensor are compared by some experiments.

2. Experiment

An experimental equipment that combined BITalino EMG sensors, goniometer (Biometrics Ltd.) and Arduino Due micro controller were used to measure elbow joint angles and their EMGs[2]. This experimental equipment is shown in Figure 1. EMG sensors for 4 channels were attached to biceps brachii (ch 1 to 4) and triceps brachii (ch 5 to 8), respectively. Figure 2 shows the arm with EMG sensors attached. The biceps brachii corresponds to the flexion of the elbow joint, and the triceps brachii corresponds to the extension of the elbow joint. Goniometer is a device used for measuring elbow joint angles. In this study, the sampling frequency was set to 1 kHz.

Experiments were conducted that subjects bent and stretched their elbow joint following visual instruction signals provided. The straightened elbow was set at 0 deg, and the bending angle was set from 0 to 90 deg. One trial on the experiment was done for 10 s.

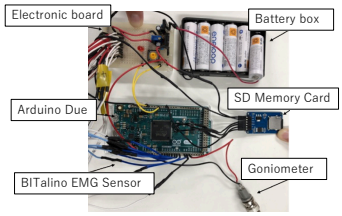

Figure 1: An experimental equipment.

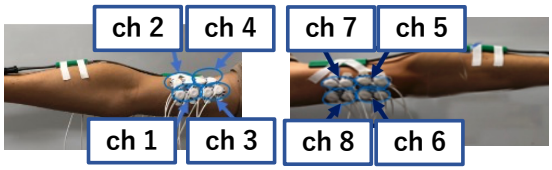

Figure 2: Attached positions of EMG sensors.

3. Denoising Method

3.1. SR and multi-sensor

As mentioned in the introduction, a denoised EMG with a longer EMD can be obtained by using SR and multi-sensor. Before conducting denoising process, drift removing and rectification are done for raw EMG signals as preprocess. The SR process is done by adding white noise to the preprocessed EMG and passing it through a hysteresis function. Denoised EMG of each muscle is obtained by summing up all the SR-processed EMG on each muscle. The standard deviation of the added white noise is 0.03 times MaxEMG, where MaxEMG means the maximum value of a preprocessed EMG. The upper and lower threshold values of the hysteresis function are 0.4 times MaxEMG and −0.05 times MaxEMG, respectively. The hysteresis function binarizes EMG to 1 and 0, while the summed EMG from each muscle are quantized as m-th power of 2, where m means the number of EMG sensors on each muscle.

3.2. SN and multi-sensor

The SN process is done by using N-data of SR-processed EMGs that are processed with different white noises and by summing up their N-data[5]. Denoised EMG of each muscle is obtained by summing up all the SN-processed EMG from each muscle.

3.3. Denoising Results

A denoised EMG using SN and multi-sensor was compared with denoised EMG using LPF and conbination of SR and multi-sensor. In this study, a second-order butterworth filter with cutoff frequency of 2 Hz was used as the LPF. Waveforms of biceps brachii's EMGs using each method are shown in Figure 3. Phase differences and cross-correlations between the denoised EMG using LPF and the denoised EMG using the other methods are shown in Table 1. The phase difference indicates additional EMD compared with denoised EMG using LPF. The cross correlation indicates similarity to denoised EMG using LPF. As mentioned in the previous study[6], Figure 3 and Table 1 show that the denoised EMG using SN and multi-sensor is closer to the denoised EMG using LPF compared to the method of using SR and multi-sensor, although EMDs from each denoised EMG have almost same length.

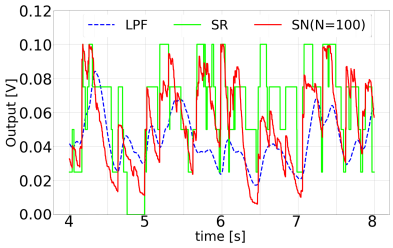

Figure 3: Waveforms of biceps brachii's EMGs using each method; The red solid line indicates denoised EMG using SN (N=100) and multi-sensor. The green solid line indicates Denoised EMG using SR and multi-sensor. The blue dashed line indicates denoised EMG using LPF.

Table 1: Simulation results of phase differences and cross-correlations; Because the added white noises are different for each process, the averages of 10 processes are shown as these results.

Processing method	SR	SN		
Parallel number N	1	5	20	100
Muscle	Biceps brachii			
Cross-correlation	0.6498	0.7878	0.8273	0.8264
Phase difference [ms]	51.3	51.7	52.5	51.9
Muscle	Triceps brachii			
Cross-correlation	0.6928	0.8042	0.8275	0.8238
Phase difference [ms]	53.2	53.1	52.8	53.3

4. An elbow joint angle estimation

4.1. MISO NARX Model

In this study, MISO NARX model was used to estimate an elbow joint angle from EMG. NARX model is a nonlinear ARX model with coefficients that are functions of outputs[7]. Equation of the MISO NARX model with m data inputs and one output is as follows

$$y[j] + a_1(y[j-1])y[j-1] + \cdots + a_n(y[j-1])y[j-n] = b_{11}(y[j-1])u_1[j-1] + \cdots + b_{1n_u}(y[j-1])u_1[j-n_u] + \cdots + b_{m1}(y[j-1])u_m[j-1] + \cdots + b_{mn_u}(y[j-1])u_m[j-n_u], \quad (1)$$

where $y[j]$ and $u_m[j]$ are the output and the mth input at a time step j, respectively. $a_n(y)$ and $b_{mn_u}(y)$ are the coefficient functions of the output and the m-th input, respectively.

4.2. Estimation Results

Experimental results of elbow joint angle estimation by the MISO NARX model for each input were compared. Waveforms of estimation results are shown in Figure 4. Root mean squared errors between estimated values and measurement values by the goniometer are

shown in Table 3. It shows that the proposed method has better estimation results compared to the method using EMG made by SR and multi-sensor as inputs.

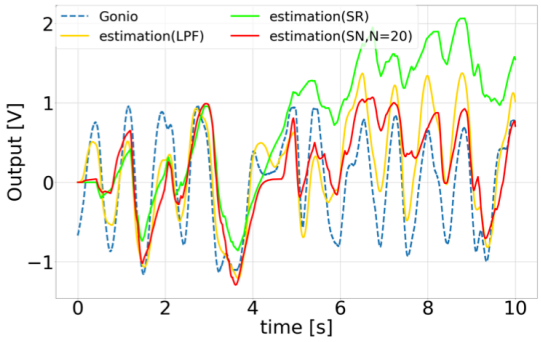

Figure 4: Estimation results; The red, green, and yellow lines indicate estimation results with denoised EMG using SN and multi-sensor, SR and multi-sensor, and LPF, respectively. The blue dashed line indicates the measured value by the goniometer.

Table 2: Root mean squared errors of estimated values using each method; Because the added white noises are different for each process, the averages of 10 processes are shown as below.

Subject	data	LPF	SR	SN(N=5)	SN(N=20)
A	01	0.2108	0.6217	0.4780	0.3687
	02	0.2049	0.8903	0.7011	0.5087
B	01	0.2294	0.9688	0.8628	0.7038
	02	0.4163	0.9213	0.6509	0.5828
C	01	0.2150	3.3631	1.8221	0.9191
	02	0.1905	1.1449	0.8783	0.6280

5. Conclusion

In this study, elbow joint angles were estimated from denoised EMG using SN and multi-sensor. Experimental results show that the proposed method has better estimation results compared to the method using EMG made by SR and multi-sensor as inputs. In this study, the estimation was performed without EMD. Thus, to estimate human motion using a model that is able to deal with EMD is one of our future works.

Acknowledgement

The authors would like to thank Ms. Nur Hidayah Binti Samijan for carefully proofreading the manuscript. This work was supported by JSPS KAKENHI Grant Number JP18K04071.

References

[1] M. Hayashi, et al.: Development of Zero-Phase-Tracking Man-Machine Interface with Electro-Mechanical Delay of Electromyogram, *International Journal of the Robotics Society of Japan*, volume:30 (2012), 767–778. (*in Japanese*)

[2] T. Sadahiro, et al.: Experimental Verification of Obtaining Longer EMD of EMG Using Multi-sensor and SR Phenomenon, *The 38th JSST*, (2019), 43–46.

[3] K. Wiesenfeld, et al.: Stochastic resonance and the benefits of noise: From ice ages to crayfish and SQUIDs, *International Journal of Nature*, volume:373, (1995), 33–36.

[4] D. Kashimoto, et al.: Joint Angle Estimation from Roughly Quantized EMG Signals in Simple Movements, *The Japan Society of Mechanical Engineers Kyushu Student Association*, (2020), 1–4. (*in Japanese*)

[5] J.J. Collins, et al.: Stochastic resonance without tuning, *International Journal of Nature*, volume:376 (1995), 236–600.

[6] N. Ikeda, et al.: An Elbow Joint Angle Estimation Method by a Low-pass less EMG using a Summing Network and Multi-sensors, *The Japan Society of Mechanical Engineers Kyushu Student Association*, (2021), 1–4. (*in Japanese*)

[7] A. Ohata, et al.: Identification of Nonlinear ARX Model with Input and Output Dependent Coefficients, *IEEE International Conference on Control Applications*, (2006), 2577–2582.

Simulation of Team Cooperation Considering Team Cognition – Effect of Mutual Beliefs on Team Performance

Sumie Cho[1], Taro Kanno[1], Daichi Mitsuhashi[1], and Kazuo Furuta[1]

[1]Department of Systems Innovation, School of Engineering, The University of Tokyo

*zhang-chengyue@g.ecc.u-tokyo.ac.jp

Abstract. Computer simulation is an alternative method for investigating the cognitive aspects of human factors in teams. Our previous study developed an agent-based simulation of team cooperation using a team cognition model based on mutual beliefs. We modified that simulation model in the current study to appropriately reflect the meta-cognition behind team cooperation and conducted simulations to examine the effect of mutual beliefs on team performance. Besides, we examined the impact of domain dependence caused by the knowledge structure. The results revealed that regardless of the knowledge structure, communication generated by mutual beliefs improves team performance.

Keywords: Situation Awareness, Agent-based simulation, Team communication

1. Introduction

Several human factor studies explored the cognitive and behavioral factors that affect team performance. Primarily, these studies used verbal protocol analysis and behavior analysis to measure cooperative behavior in team processes. For example, Kiekel et al. [1] developed several automated methods to analyze communication data for measuring team cognition. However, these measurements focus only on observable data, making the precise and efficient extraction of underlying cognitive mechanisms challenging. A promising alternative for exploring cognitive aspects of team cooperation is a computer simulation that can test various hypotheses regarding team cognition. However, the computational approach for team cognitive studies is still in its infancy. Yojima et al. [2] developed an agent-based simulation for cooperative behavior analysis based on a team cognition model proposed by Kanno et al. [3]. It uses the concept of mutual beliefs, explaining the cognitive mechanisms behind dyadic team cooperation. Though the study is yet to conduct multiple simulations with various parameter settings, the simulation was performed with only one domain-specific knowledge. Besides, there was room for improvement in the simulation model as the meta-cognitive operations after communication were inappropriate.

Therefore, in this study, we modified the previous simulation model to investigate the effect of team cognition on team performance and established a new comparative analysis method of the simulation results. Further, we examined the dependence on the knowledge structure.

2. Simulation Model in the Previous Research

Kanno et al. suggest a three-layered structure in their team cognition model: self-cognition, belief about the partner's cognition, and belief about the partner's self-cognition. The previous simulation model [2] used a car diagnosis with two agents collaboratively diagnosing a car's failures. Each agent could see only part of the car; thus, they need cooperation to acquire the correct and complete situation awareness (SA). Each layer of the model is implemented using a Bayesian Belief Network (BBN), representing the agent's domain knowledge structure along with cognitive and inference mechanisms. In the simulation model, agents perform three types of actions: observation (look at) and two types of communication (inform/query). Observation involves obtaining an SA by perceiving the environment, while communication includes resolving contradictions between layers. A "query" is a communicative action to notify the partner about his/her SA of "Unknown" and requesting his/her SA, while "inform" is an action showing the agent's SA to the partner. Table 2 summarizes the conditions for performing each type of communication and action. While taking action, metacognitive operations modeled as interlayer interactions in the simulation model initiate cognition and inference. We evaluate team performance through team accuracy formulated in Equation (1), where U_0 represents a set of states of all nodes in the BBN of the car model, and U_{A1} represents a set of states of all nodes in the BBN of agent A's first layer. Table 1 lists the model parameters used in a previous study [2].

$$Team\ Accuracy = \left(\frac{U_0 \cap U_{A1}}{U_0} + \frac{U_0 \cap U_{B1}}{U_0}\right) \times \frac{1}{2} \quad (1)$$

Table 1 Parameter Setting of Simulation.

Parameter	Definition	Value
Threshold	Threshold of occurrence recognition of an event	0.75
Inter-Layer-Effect	The effect of the inter-layer interaction	0.95
Human Error	Do the agents have wrong SA at the start of the simulation?	True/False
Referenced Layers	The layers the agent refers to when choosing an action	L1/L12/L13/L123

3. Model Modifications

The previous study had an issue of metacognitive processes in communication not being reflected properly in the model. Specifically, whenever agents conduct "inform," there is excessive interlayer interaction, and the second layer is updated almost every time. To fix this

problem, we divided "inform" into two types based on the motivation to tell the partner his/her SA. Type 1 is notifying when the partner does not seem to have the correct SA, and Type 2 is activated when the partner appears to misunderstand his/her SA. The modified communication rules are also shown in Table 2. According to this reconfiguration, the inter-layer interactions for each type of "inform" were modified. We also performed simulations using different BBNs to examine the dependence of cooperative behavior on knowledge structure. Using the two types of knowledge structures and the parameter settings shown in Table 1, we performed a simulation with the modified model and conducted a comparative analysis of the simulation results. Specifically, we repeated the simulation 100 times under the same conditions, sorting the obtained team accuracy in ascending order and making a scatter plot of Team Accuracy with the same rank against those obtained when referencing the L1 layers. The new comparative analysis by removing the effect of parameters other than the reference layers helps in observing whether communication generated by the mutual belief improves team performance and to what extent.

Table 2 Communication Rules.

Let S_1, S_2 and S_3 be the states of corresponding nodes in the first, second, and third layer of an agent. The first row represents the case of a conflict in the states between the first (*Unknown*) and second layer. When this case occurs, the agent will observe the car parts first, and then, if the conflict is not resolved, will query the partner about the state of the node in his/her first layer.

Condition	Action (In Previous Research)	Action (After Modification)
$S_1 \neq S_2 \; and \; S_1 = Unknown$	Look at → Query	Look at → Query
$S_1 \neq S_2 \; and \; S_2 = Unknown$	Inform	Inform (Type 1)
$S_1 \neq S_2$	Look at → Query	Look at → Query
$S_1 \neq S_3 \; and \; S_1 = Unknown$	Look at → Query	Look at → Query
$S_1 \neq S_3 \; and \; S_3 = Unknown$	Inform	Inform (Type 2)
$S_1 \neq S_3$	Inform	Inform (Type 2)

4. Results and Discussions

Fig. 1 shows the results of the simulation with the modified model. The horizontal axis represents team accuracy when referring only to the first layer, and the vertical axis represents the team accuracy obtained when referring to the first and second layers (L12), first and third layers (L13), and all three layers (L123). A plot above the dotted line indicates an improvement in team performance by mutual beliefs and inter-layer interactions triggered by meta-cognition. Table 2 shows the rate of the plot above the dotted line and the average number of actions taken by the two agents before and after model modifications. Team accuracy showed improvement when communication was generated by referring to the second layer or/and the third layer. Using different BBNs in the simulation showed similar improvement. A comparison of the results obtained by different layer combinations revealed that the team performance obtained with L123 was slightly better than that with other combinations. These findings suggested that mutual belief is one of the major factors and driving force for better team cooperation. Moreover, we observed that the number of actions increased after the model modification, suggesting that this modification realized appropriate interlayer interactions to generate constructive actions

for enhancing team performance.

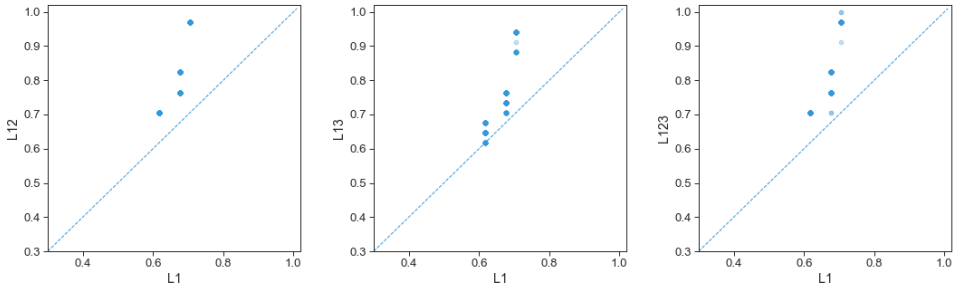

Fig. 1. Comparative Analysis of Results

Table 1. The Number of Total Actions and Rate of Improvement in Team Accuracy

	The Total Number of Actions				Rate of Improvement			
	L1	L12	L13	L123	L1	L12	L13	L123
Before Model Modifications	2.20	5.17	10.24	6.47	-	1.000	0.994	0.984
After Model Modifications	2.20	7.91	15.01	11.31	-	1.000	0.946	1.000

5. Conclusion

To investigate the effect of cooperative behavior generated by mutual beliefs on team performance, we modified the simulation model of the previous study and conducted a comparative analysis of the simulation results under different layer combinations and knowledge structures. We found that mutual beliefs played an important role in improving team performance regardless of domain knowledge and structure. Although further improvements and sophistication are necessary, we believe that our simulation is a promising method to compensate for the limitations of conventional human factor methods and exploring cognitive aspects of team cooperation.

References

[1] Kiekel, P. A., Cooke, N. J., Foltz, P. W., Gorman, J. C., & Martin, M. J.: Some Promising Results of Communication-Based Automatic Measures of Team Cognition, *Proceedings of the Human Factors and Ergonomics Society Annual Meeting,* 46:3(2002), 298–302.

[2] Yojima, S., Kanno, T., Furuta, K.: Simulation of Team Communication and Shared Situation Awareness, *18th Asia Simulation Conference Kyoto, Japan/October,* (2018), 27-29

[3] Kanno, T., Furuta, K., & Kitahara, Y.: A model of team cognition based on mutual beliefs, *Theoretical Issues in Ergonomics Science*, 14:1(2013), 38-52.

Agent-based simulation of consumer panic buying: feasible measures for mitigating its effect

Sotaro Kawanishi[1*], Rithika Dulam[1], Kazuo Furuta[1], Taro Kanno[2]

[1]Technology Management for Innovation, School of Engineering, The University of Tokyo

[2]System Innovation, School of Engineering, The University of Tokyo

*kawanishi-sotaro718@g.ecc.u-tokyo.ac.jp

Abstract. Consumer panic buying in disasters makes supplies unavailable to many people and causes supply chain disruption. Our previous research has analyzed the effect of consumer panic buying on the supply chain by conducting agent-based simulation, but there are some problems with the realism of the model and the limited proposed measures. Therefore, the objective of this research is to develop an agent-based simulation model based on our previous research and devise effective/feasible measures that mitigate the effect of consumer panic buying. The results showed that implementing sales restriction, holding additional inventory, and transmitting information are feasible measures that have significant effect, and the disruption of the supply chain could be prevented by combining those measures. Results obtained in this research could help the government and industry take appropriate measures when a disaster occurs.

Keywords: Consumer panic buying, supply chain disruption, agent-based simulation

1. Introduction

Japan is prone to natural disasters such as typhoons, earthquakes, and tsunamis due to its natural conditions. These natural disasters could cause serious damages by not only directly resulting casualty and property loss, but also by causing secondary disasters such as panic buying of food and daily necessities. Typical examples of this secondary disaster are the buying up of toilet paper during the Covid-19 pandemic and the buying up of bottled drinking water after the Great East Japan Earthquake. Under such circumstances, it is necessary to guarantee the stability of supply chain to avoid shortage of necessities. Against this background, Dulam et al. conducted an agent-based simulation to analyze the effect of consumer panic buying on supply chain disruption due to a disaster, and investigated what measures taken by retailers are effective (hereinafter referred to as the previous study) [1]. In the previous study, two measures were considered: sales restriction and rationing. The results showed that the implementation of sales restriction did not have a significant impact on preventing the disruption of the supply chain, and the implementation of rationing was considered very effective. From these results, the implementation of rationing was recommended. However, rationing requires extensive

government intervention and is impractical at present in Japan. Therefore, it is necessary to devise new measures that are both effective and feasible. In addition, the scale of the model used in the previous study is too small and is too simple, so the model should be extended.

2. Method

2.1 Overview of the model

The model based on the previous study consists of two parts: the supply chain model and the consumer model. The target product assumed in the model is bottled water. The supply chain model includes five types of supply chain agents (SCAs): manufacturers, distributors, individual retailers, chain heads, and chain stores. These SCAs take a hierarchical structure, as shown in Figure 1. The basic actions of the SCAs are placing orders and selling to the customers down the hierarchy, managing their inventory to maximize their revenue efficiently. In the consumer model, each consumer agent represents a household, and they each make purchase action to maintain their stock at a certain level. The variables of each consumer agent, such as the amount of daily water consumption and the frequency of purchase, are distributed based on a questionnaire survey.

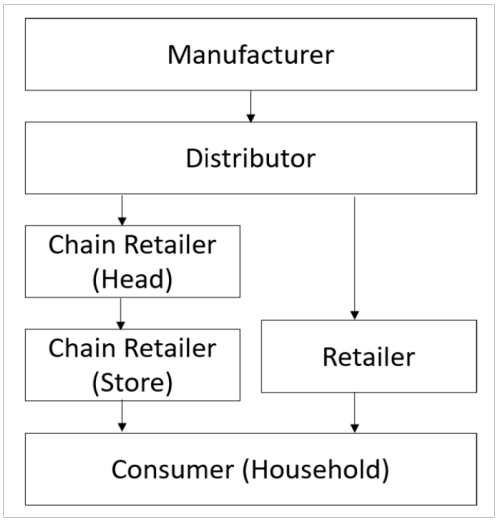

Figure 1: Model structure

2.2 Model improvements

The model used in the previous study is very simple, consisting of 2,000 consumer agents, four retailers, and other SCAs. There are no limitations put to the purchase action of the consumer agents, and consumer agents were able to visit every store in each timestep, in the order of their preference. To increase the scale, the number of consumer agents and retail stores was increased tenfold. Since the number of stores increased, it is unrealistic for consumer agents to be able to visit every store. Thus, the consumer agents' purchase action was restricted. More specifically, a distance-based constraint was set to the consumer agents, and each agent could only visit three retail stores in one timestep. By making this modification, the supply chain model was more complicated, enabling more sophisticated strategies that could be taken to prevent the disruption of the supply chain.

2.3 Measures

Three measures that could be taken simultaneously with sales restriction proposed. The first measure was holding emergency safety stock. The more inventory there is, the easier it is for the supply chain to respond to sudden increases in demand. Therefore, holding extra inventory was considered based on the study conducted by Nahleh et al. [2] The second measure is sharing inventory information among SCAs. Since SCAs order (or produce) inventories based on their average sales, there will be a lead time between the time retailers run out of stock and the time SCAs in higher tiers increase their orders (or production). To eliminate this lead time, the average sale of a certain SCA is compared with the total sales of the related retailers, and the larger number was used as the order (manufacturing) quantity. The third measure is provision

of retail store inventory information to consumers. Consumer agents provided with information on inventory of nearby retailers, consumer agents will change their store preference, and will visit the retailers in the order of their inventory. This will prevent situations in which consumers could not purchase products while some retail stores within their distance limit are not stock out.

2.4 Simulation settings

To evaluate the effectiveness of the proposed methods, simulations were conducted for five different scenarios: normal case, disaster case, sales restriction case, rationing case, and sales restriction combined with the three proposed measures case (hereinafter referred as the combination case). Same random numbers were used to compare the results under the same conditions. The simulation was run for 100 timesteps where one timestep is a day, and the disaster was set to occur in the 70th timestep. Countermeasures were taken from the 71st timestep, right after the disaster occurred. The two main objectives of the measures are to prevent supply chain disruption and make supplies available to more consumers. The former could be evaluated by reviewing the changes in inventory ratio to sales in each supply tier. If the ratio > 1, the supply tire has sufficient inventory, and if the ratio < 1, the supply tier could be considered stock out. If multiple supply tiers are continuously stock out, the supply chain is deemed disrupted. The effect to consumer satisfaction could be evaluated by reviewing the changes in the number of satisfied consumers. Consumer satisfaction for each consumer agent is the average of inventory satisfaction (one if satisfied, and zero if not satisfied) and purchase satisfaction (purchase quantity divided by required purchase quantity). By dividing the consumers into five categories according to the size of the satisfaction level, the overall consumer satisfaction level could be shown by counting the number of agents in each category.

3. Results

Figure 2 shows the changes in the inventory sales ratio in the sales restriction case, rationing case, and the combination case. The results show that the supply chain is disrupted and does not recover in the sales restriction case, while the supply chain recovers around the 90th timestep in the rationing case and the combination case. In addition, the supply chain is recovered from disruption around the 75th timestep in the combination case. This positive effect is attributed to the increase in the amount of inventory in circulation due to the immediate increase in manufacturing quantity and stockpiling of emergency safety stock.

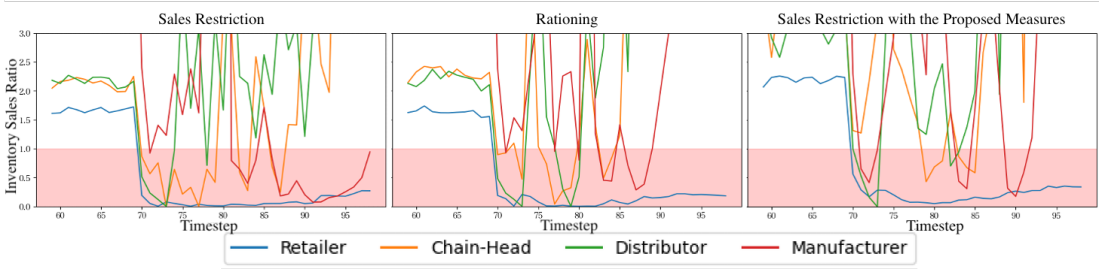

Figure 2: Inventory sales ratio of SCAs

Figure 3 shows the changes in the number of consumer agents in each satisfaction category. In the sales restriction case, consumers with zero satisfaction continue to exist until the 85th

timestep. In the rationing case, the number of unsatisfied consumers is smaller than in the sales restriction case, but they do not disappear. However, there are no consumers with zero satisfaction in the combination case, excluding the 70th timestep when the disaster occurs. In addition, consumers with medium satisfaction decreases, and consumers with high satisfaction increases compared to the rationing case. From this result, the combination case is clearly superior to the rationing case from the consumers' perspective. This is because the amount of inventory in circulation increased as mentioned above, and consumer agents were able to access to them efficiently due to the provision of retailers' inventory information.

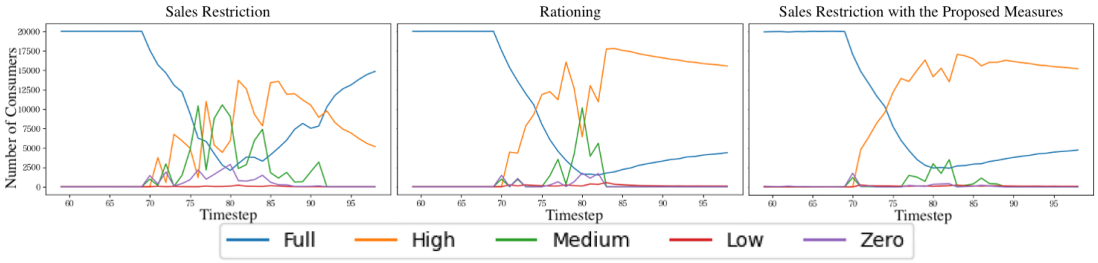

Figure 3: Consumer satisfaction

To conclude, it can be said that combining sales restriction with the proposed methods is superior to rationing in terms of effectiveness from both consumer and supply chain perspectives.

4. Conclusion

This research focused on analyzing the effect of consumer panic buying, which is a major issue in recent years. A simulation model based on previous studies was developed, and feasible measures were devised to mitigate the effects of consumer panic buying. Simulation results showed that the impact of panic buying could be effectively mitigated by combining sales restriction with emergency safety stock, share inventory information among SCAs, and provision of retail store inventory information to consumers. These simulation results could be used to help the government take appropriate measures when a disaster occurs. In the future, the model could be developed by considering price and transportation time.

References

[1] R. Dulam, K. Furuta, T. Kanno: Development of an agent-based model for the analysis of the effect of consumer panic buying on supply chain disruption due to a disaster, *Journal of Advanced Simulation in Science and Engineering*, Volume 7 (2020), Issue 1, 102-116.

[2] Y. Nahleh, A. Hakimi, A. Kumar, F. Daver: Improving Order Quantity Model with Emergency Safety Stock (ESS), *International Journal of Mechanical, Industrial Science and Engineering*, Volume 7 (2013), Issue 12, 688-693.

JSST2021

Comprehending and mitigating the implications of consumer panic buying

Rithika Dulam[1*], Kazuo Furuta[2], Taro Kanno[3]

[1,2]Technology Management for Innovation, School of Engineering, University of Tokyo

[3] Systems Innovation, School of Engineering, University of Tokyo

[*]rithika.dulam@gmail.com

Abstract. Consumer panic buying has been seen to occur frequently with the increasing number of disasters in recent years. Panic buying during the COVID-19 pandemic has seen the disruption of even the most efficient supply chains. In order to develop optimal mitigation measures, it is important to understand consumer behavioral changes and their implications. In our effort, we have developed a model to assess the impact of panic buying on the supply chain and consumer satisfaction. The current work focuses on the application of this model while examining the effectiveness of popular mitigation measures, such as the quota policy.

Keywords: Decision-making, Agent-based model, Panic buying, Consumer behavior, Disaster

1. Introduction

Supply chain (SC) management has come a long way from the traditional techniques to the optimized and efficient ones with the help of advanced technology. However, they are often susceptible to several risks, such as natural disasters, inaccurate forecast. The recent COVID-19 pandemic exposed the drawbacks that led the organizations to reassess their risk management approaches. Severe movement restrictions, transportation disruptions, and panic buying led to shortages of products in almost every sector, with panic buying being a major cause. The incompetency of SC to cope with the situation during the pandemic has explicitly put forward a lack of expertise and research to mitigate the risk of panic buying during emergencies.

Human nature is guided by emotions; especially with a sense of anxiety during disasters. Performing some action over the risk provides a sense of control over the situation. Likewise, a consumer also undertakes the precautionary action of stockpiling as a safety measure against having no stock. A large number of people indulging in stockpiling leads to panic buying, in turn disrupting SC, initiating further panic buying, which converts into a vicious circle. Essential commodities, such as food or water are typically at higher risk and might lead to chaotic situations. Given the study on panic buying is meagre, there is a lack of a predictive consumer model in disaster or SC disruption due to consumer behavior [1]. To bridge the gap, we aimed to build a model that can support in predicting and mitigating the various consequences of large-scale panic buying. Dulam et. al. [2] developed a model to analyze both the consumer panic buying of bottled water and the response of the SC in the disaster aftermath using an agent-based model. The enhanced consumer model assesses the panic purchase intention of a consumer in an uncertain situation based on the factors that play a significant role during crises [3]. This model can help to understand the aftereffects, such as expected panic buying, the

possible SC disruption, and the outcomes of the mitigation measures, which could help industries and the government. The current paper discusses the application and usefulness of the model to elevate the importance and benefits of such tools.

2. Methodology

The model (Fig.1) mainly comprises of a consumer model and an SC model, influenced by the consequences of the Great East Japan Earthquake. Panic buying of food and drinking water occurred, following the notice from the government due to radiation contamination. Analysis of such situations helps us identify potential problems associated with panic buying. Hence, we used the consequences of the triple disaster as a reference for identifying the key parameters of the model.

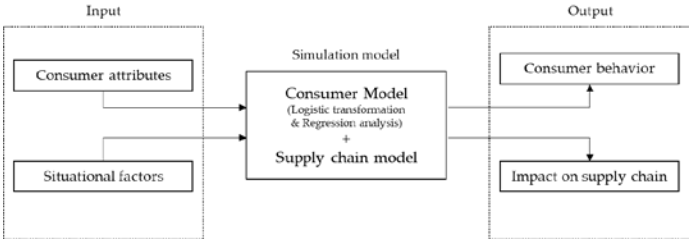

Fig 1. An overview of the model.

The consumer model involves the process leading to the purchase of essential commodities in disaster aftermath, influenced by several factors, such as personal, social, individual, psychological, and situational. The model is built using a six-step decision-making process viz., need recognition, information search and processing, factor valuation, decision, purchase, and purchase evaluation. The household agent (consumer) makes the purchase decision based on its available resources. The decision-making criteria are different in the pre-and post-disaster phases. Pre-disaster decision-making is based on the available inventory and the consumption of the household. However, the post-disaster scenario unveils a multitude of psychological and situational factors as a consequence of the disaster. Hence, post-disaster decision-making was developed based on a logistic transformation model, using a multiple regression analysis of a questionnaire survey. The SC model implements the key functions of the SC members required for sustaining their businesses. The main action of the SC agents (SCAs) is to maintain sufficient inventory and satisfy the customer demand in every interval.

3. Results and Analysis

We conducted simulations by varying several key parameters of the model in a virtual 100x100 grid, with 2000 households and 4 stores. The simulation is run for 60 intervals, with the disaster in the 30^{th} interval and the strategy is initiated in the 31^{st} interval. The following four disaster and mitigation cases have been considered. Normal scenario; Disaster without strategy; Disaster with sales restrictions; Disaster with rationing. In the sales restrictions strategy, the consumers can make multiple purchases, while the consumer's purchase is limited to one purchase per interval in the rationing strategy.

3.1 Effect of strategy on consumer satisfaction:

Consumer satisfaction (S_f) is calculated based on product sufficiency and outcome of the purchase action with equal weightage to both factors, to measure the impact of the disaster or strategy on consumers. Fig.2 shows the number of consumers in each category for the four cases. It can be seen that 100% of consumers have been satisfied in the normal case. While, in the disaster without strategy case, the number of zero satisfaction consumers have increased.

The implementation of restrictions can be seen to reduce both the number of zero satisfaction consumers and the number of intervals with the presence of such consumers. It can be seen that the number of zero satisfaction consumers has reduced drastically, indicating that rationing can help increase the product reach.

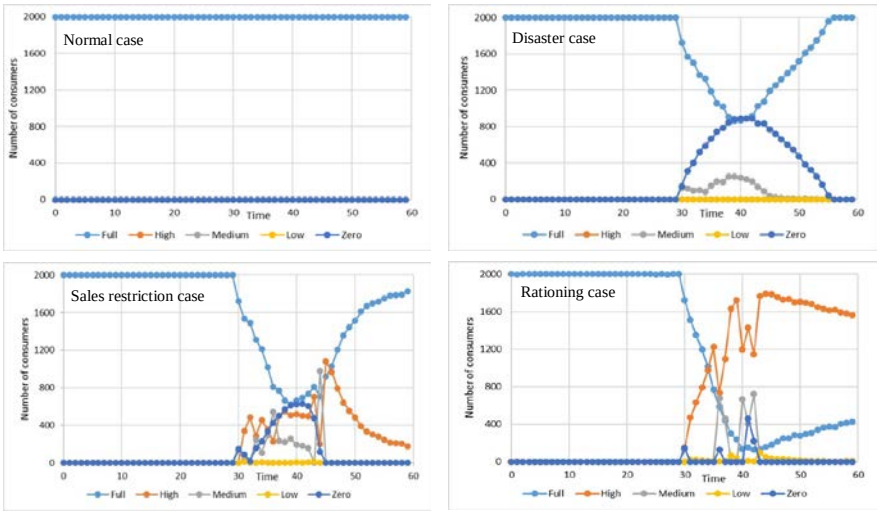

Fig 2. Consumer satisfaction in the four scenarios.

3.2 Effect on supply chain performance:

SC performance (SCP), which is one of the key outcomes indicating the efficiency of the SCA, can be evaluated using Inventory–Sale ratio (R_{IS}). It is a ratio of inventory to sale, where the sale is the sum of sale and lost sale (after stockout). If $R_{IS} > 1$, the white region in Fig.3, the SCA in a safe condition, and if $R_{IS} < 1$, the red region, the SCA is in the stockout zone.

In Fig.3, all SCAs are in the safe zone in normal case. However, in the disaster case, due to high demand, all the SCAs are in the stockout zone, indicating an SC crash. The sales restrictions have helped in averting the SC crash but could not avoid the disturbances, while rationing was effective in avoiding the SC disruption.

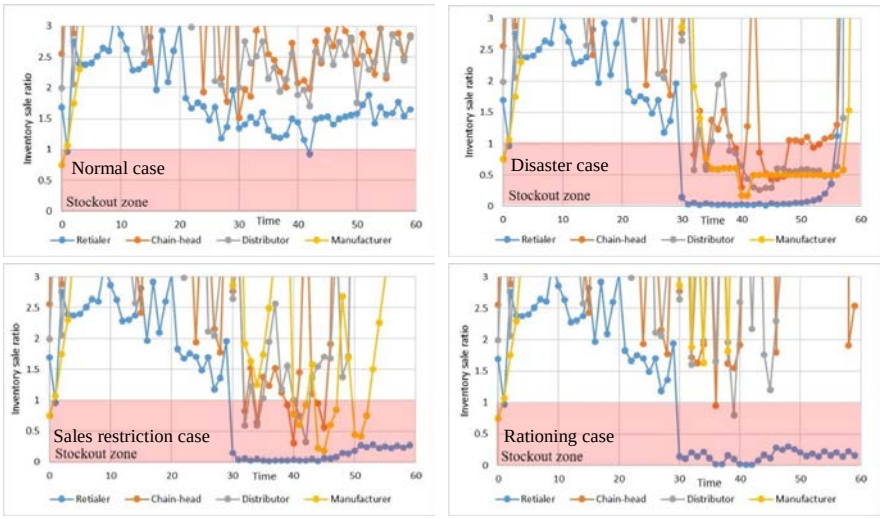

Fig 3. SCP in the four scenarios.

Stockoutness: This parameter indicates the stockout condition of the agent. It is a cumulative R_{IS} in the stockout zone as shown below.

$$Stockoutness = \sum Stockoutness_i$$

$$Stockoutness_i = \begin{cases} 1 - R_{ISi}, & if\ R_{ISi} < 1 \\ 0, & if\ R_{ISi} > 1 \end{cases}$$

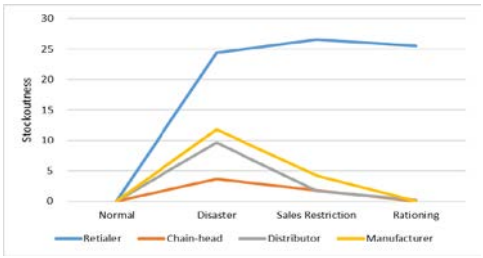

Fig 4. Stockoutness of the SC tiers

The SC stockoutness in the four cases is depicted in Fig.4. It can be observed that the strategies have allowed the stockoutness of the SC to reduce, while rationing brings the stockoutness to almost zero. Stockoutness can be used to compare the SCP among the scenarios.

3.3 Effect of time variation of the strategy:

We have conducted simulations to understand the effect on SCP by varying the interval in which the strategy is initialized, useful for disasters that can be known beforehand, such as typhoons. Five cases were considered with the strategy initialized in different intervals with respect to the disaster interval: D-3 (three intervals before the disaster), D-1, D+1, D+5, and D+10.

The stockoutness, for the five cases and the case without any strategy, was calculated and is shown here. Fig.5 shows that stockoutness increases as the initialization of the strategy is delayed. This indicates that the early employment of sales restrictions by stores could avoid a possible SC disruption. The SCP is improved immediately with the help of rationing at any point in time, as can be seen in Fig.6; the effectiveness of rationing is evident, as stockoutness is greatly reduced in all cases when compared with the case without any strategy.

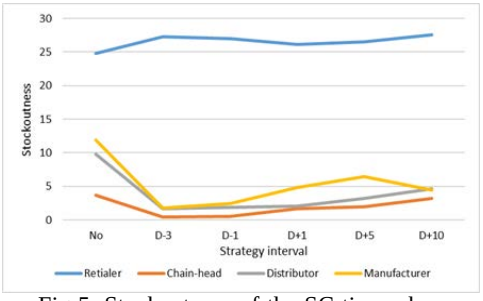

Fig 5. Stockoutness of the SC tiers when initialization of sales restrictions is varied.

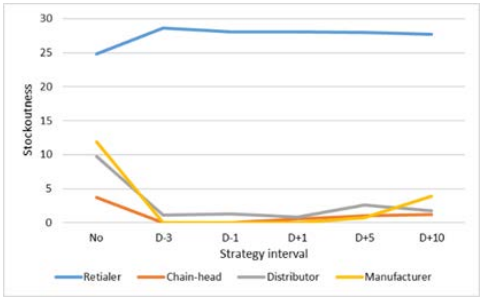

Fig 6. Stockoutness of the SC tiers when initialization of rationing is varied.

4. Conclusions

We developed a multi-agent model of consumer panic buying and supply chain in the disaster aftermath that can be used to study consumer panic buying consequences and its mitigation approaches. The paper shows the application of the simulation model to test various scenarios and strategies that might be beneficial in avoiding SC disruptions. Rationing was found to be a more effective measure than sales restrictions. Similarly, several other scenarios can be studied to understand the outcomes and identify the solutions. The tool could be useful in helping industries and government to analyze consumer behavioral changes and guiding them in developing optimal measures for a resilient SC and in tackling chaotic post-disaster situations.

References

[1] K. F. Yuen, X. Wang, F. Ma, and K. V. Li: The psychological causes of panic buying following a health crisis, *International Journal of Environmental Research and Public Health*, Volume 14, Issue 1:3513, 2020.

[2] R. Dulam, K.Furuta, T.Kanno: Development of an agent-based model for the analysis of the effect of consumer panic buying on supply chain disruption due to a disaster. *Journal of Advanced Simulation in Science and Engineering*, Vol. 7, No. 1, 102-116, 2020.

[3] R. Dulam, K. Furuta, T. Kanno: Quantitative decision-making model to analyze the post-disaster consumer behavior, *International Journal of Disaster Risk Reduction*, 2021, 102329.

Visualization of dose rate distribution around Fukushima Daiichi Nuclear Power Plant using artificial neural networks

Miyuki Sasaki[1,*] and Yukihisa Sanada[1]

[1]Sector of Fukushima Research and Development, Japan Atomic Energy Agency

[*]sasaki.miyuki@jaea.go.jp

The full paper of this paper has been published in Journal of Advanced Simulation in Science and Engineering (JASSE).

DOI: https://doi.org/10.15748/jasse.9.30

Estimation of distribution of Uranium as shielding body using machine learning

Yamazaki Haruka*, Kondo Yuto, Yamaguchi Katsuhiko

Faculty of Symbiotic Systems Science, Fukushima University

*s2070027@ipc.fukushima-u.ac.jp

Abstract. Using machine learning, the position of shielding body and radiation source distribution are estimated from gamma-ray energy spectrum. In this study, Cs-137 was set up as radiation source and uranium as shielding body. Training data was made by simulation, instead of time-consuming actual survey, because a large quantity of training data is required for machine learning. As a result, position of shielding body was estimated roughly, although estimation of distribution of source was not carried out well.

Keywords: Machine Learning, Monte Carlo method, Fukushima Daiichi Nuclear Power Station

1. Introduction

Fukushima Daiichi Nuclear Power Station accident happened in 2011, and it brings necessary for decommissioning work and decontamination. In order to advance these works, it is helpful to estimate the radiation source and some material around source. We have studied estimation of radiation source and shielding body using machine learning[1]. Using this method, a large amount of gamma-rays energy spectra data and various condition such as position of radiation source and shielding body are used as training data, and estimation is carried out.

In this study, uranium and Cs-137 is treated. Uranium is one of radioactive material that is included in fuel debris, but there are few radiation dose from uranium. So uranium was treated as shielding body. And Cs-137, one of the fission products, was set up as radiation source.

2. Simulation Method

To make training data we used PHITS(ver.3.220)[2]. PHITS (Particle and Heavy Ion Transport code System) is a general purpose Monte Carlo particle transport simulation code developed by JAEA. A scheme is a 10cm square plane separated by a 1 cm x 1 cm mesh was set up for simulation to create training data for machine learning. The sources were randomly placed on the plane. The uranium block was randomly placed too. A plane with a height of 1 cm was set as a detection surface, and the γ rays with energy that passed through the detection surface were recorded. This detection surface was divided into a 10×10 mesh, and each of the

count number and the energy distribution are recorded. Recorded energy spectra are divided into 14 parts and all data are normalized.

Fig.1 shows the schema of the machine learning. The spectra input to Input layer as training data, and they are multiplied by the weight and input to the Output layer via Hidden layer. After that the value that output from Output layer are compared to the answer data, namely, distribution of Cs-137 and uranium. Then weight were corrected to approximate output value to answer value. As a result, if spectra which is not learnt by the network are used as input data, output value will be almost the same as answer data.

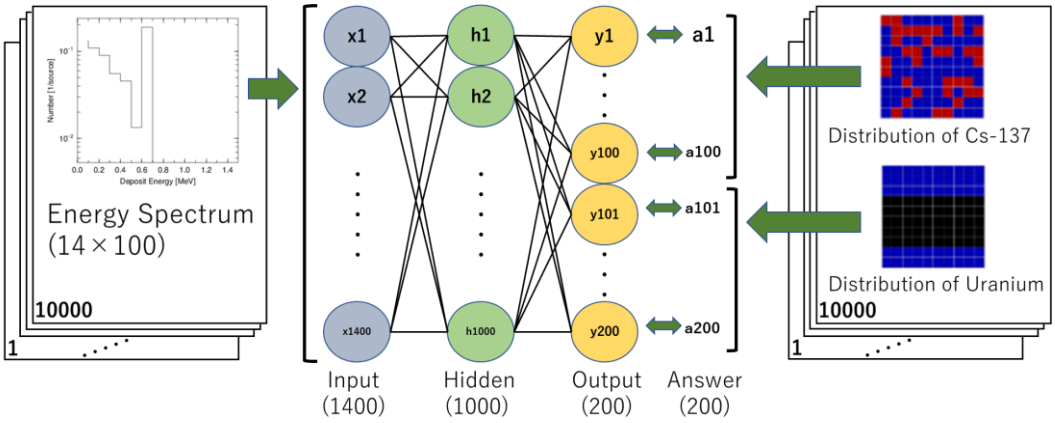

Fig.1 Schema of machine learning

3. Result

Fig.2 shows the dependence of epoch for loss function. The value of loss is calculated one by one when training data are input. The loss means the error when input the training data. On the other hand, the valloss means one when input the data that is not used as training data. In this study, the value of loss was less than 0.1 and one of valloss was about 0.3. Fig.3 shows one of the estimation result. As a result of estimation of radiation source, the value of error was 1.10×10^{-1}. When we estimate position of uranium, the value of the error was 2.88×10^{-2}.

Our previous study was estimate the position of lead block. That result of error was about 10 times less than that one when we estimate the position of uranium. Possible cause is covering most of γ ray with uranium, because the density of uranium is higher than that of uranium.

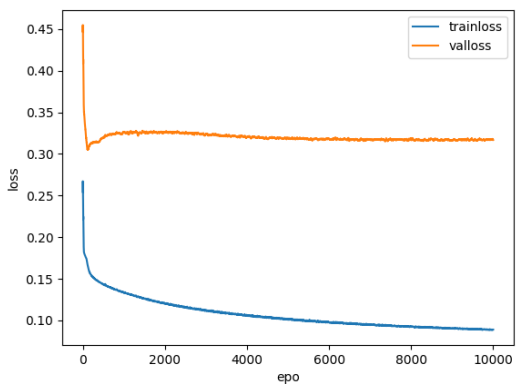

Fig.2 dependence of epoch for loss function

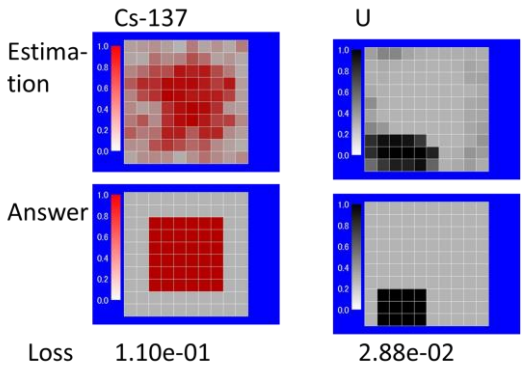

Fig.3 example of the result of estimation

References

[1] Takero Uemura, Katsuhiko Yamaguchi: Estimation of radiation source distribution using machine learning with γ ray energy spectra, J. Adv. Simulat. Sci. Ecg. Vol. 7, No. 1, 71-81(2020)

[2] Tatsuhiko Sato et al.: Features of Particle and Heavy Ion Transport code System (PHITS) version 3.02, J. Nucl. Sci. Technol. 55(5-6), 684-690 (2018)

JSST 2021

Application of Multilayered Division Method to Scattering by Slanted Gratings

Hideaki Wakabayashi[1,*], Masamitsu Asai[2], Jiro Yamakita[1]

[1]Faculty of Computer Science and Systems Engineering, Okayama Prefectural University
[2]Faculty of Biology-Oriented Science and Technology, Kindai University

[*]waka@c.oka-pu.ac.jp

Abstract. In the analysis of electromagnetic scattering by slanted gratings, the multilayer division method has been often used. The method has a disadvantage of high computational cost to keep a high accuracy of approximation for the profile. This paper presents the improvements to reduce the computational cost.

Keywords: slanted grating, electromagnetic scattering, matrix eigenvalues method, multilayer division method

1. Introduction

In the electromagnetic analysis, slanted gratings have often been treated by dividing a grating layer into stratified thin grating layers [1] and by transforming the coordinates [2]. The former is called the multilayer division method (MDM). The MDM has a big advantage that it can be applied to any profiled grating, but has a disadvantage of high computational cost to keep a high accuracy of approximation for the profile. Authors have treated a slanted grating as a grating having a tilted grating vector where the MDM is not used, and have formulated the matrix eigenvalues method (MEM) in consideration of a grating vector [3]. The formulation starts with Maxwell's equations, derives the first-order matrix differential equation directly, and reduces it into the eigenvalue problem for a coefficient matrix.

This paper incorporates the MDM into the MEM without using a grating vector for the analysis of electromagnetic scattering by a slanted grating. The slanted region is approximated by dividing into stratified thin layers. When the division number increases, the number of times to calculate the eigenvalues and eigenvectors increases. Moreover, the dimension of a linear equation to be solved becomes large. In order to reduce the computational cost, we present two improvements of calculation procedure in the MEM to which the MDM is applied. From some numerical examples, we show the effectiveness.

2. Analytical Theory

Let us consider the three-dimensional scattering problem of a slanted grating illuminated by a plane wave having an incident angle θ from the $-x$ direction, an azimuthal angle ϕ from

the $+y$ direction. The slanted region having the thickness d is tilted at a slant angle ψ and is divided into K stratified thin layers with the relative permittivities ε_1 and ε_2, as shown in Fig. 1. The grating has the width W and the periodicity Λ in the tilted direction. The relative permittivities in the incidence and substrate regions are denoted by ε_a and ε_s, respectively. From Maxwell's equations, we obtain the differential equation for the tangential fields as

$$\frac{\mathrm{d}}{\mathrm{d}x}\boldsymbol{F}_\mathrm{t}(x) = j\,[\boldsymbol{C}]\,\boldsymbol{F}_\mathrm{t}(x), \quad \boldsymbol{F}_\mathrm{t}(x) = \begin{bmatrix}\boldsymbol{e}_y(x) & \boldsymbol{e}_z(x) & \boldsymbol{h}_y(x) & \boldsymbol{h}_z(x)\end{bmatrix}^\mathrm{T} \tag{1}$$

where $[\boldsymbol{C}]$ is the coefficient matrix, and $\boldsymbol{e}_{y(z)}$ and $\boldsymbol{h}_{y(z)}$ have $(2M+1)$ spatial harmonics. Using an eigenvectors matrix $[\boldsymbol{T}]$ and a diffraction amplitude vector $\boldsymbol{g}(x)$, the solution of Eq. (1) is

$$\boldsymbol{F}_\mathrm{t} = [\boldsymbol{T}][\boldsymbol{U}(x)]\,\boldsymbol{g}(x), \quad [\boldsymbol{U}(x)] = \begin{bmatrix}[\delta_{ln}e^{-j\xi_l(x-\dot{x})}] & \boldsymbol{0}] \\ [\boldsymbol{0}] & [\delta_{ln}e^{j\xi_l(x-\ddot{x})}]\end{bmatrix} \tag{2}$$

with $l, n = 1, 2, \ldots, 2(2M+1)$. δ_{ln} is the Kronecker's delta, $\mp\xi_l$ is the lth eigenvalue, and $\dot{x}$ and $\ddot{x}$ are the phase reference positions. Putting $[\boldsymbol{A}_k] = [\boldsymbol{T}_k][\boldsymbol{U}_k(x_k)]$ and $[\boldsymbol{B}_{k+1}] = -[\boldsymbol{T}_{k+1}][\boldsymbol{U}_{k+1}(x_k)]$, we have the boundary condition at $x = x_k$ as

$$\begin{bmatrix}\boldsymbol{A}_k\end{bmatrix}\begin{bmatrix}\boldsymbol{g}_k^+(x_{k-1}) \\ \boldsymbol{g}_k^-(x_k)\end{bmatrix} + \begin{bmatrix}\boldsymbol{B}_{k+1}\end{bmatrix}\begin{bmatrix}\boldsymbol{g}_{k+1}^+(x_k) \\ \boldsymbol{g}_{k+1}^-(x_{k+1})\end{bmatrix} = \begin{bmatrix}\boldsymbol{0} \\ \boldsymbol{0}\end{bmatrix} \tag{3}$$

with $k = 1, 2, \ldots, K$. The symbol $\pm$ denotes for the waves traveling in the $\pm x$ directions. We rewrite Eq. (3) using a matrix form as

$$\begin{bmatrix}
[\boldsymbol{A}_0] & [\boldsymbol{B}_1] & & & & & \\
 & [\boldsymbol{A}_1] & [\boldsymbol{B}_2] & & & & \\
 & \cdots & \cdots & \cdots & \cdots & & \\
 & & [\boldsymbol{A}_{k-1}] & [\boldsymbol{B}_k] & & & \\
 & \cdots & \cdots & \cdots & \cdots & & \\
0 & & & [\boldsymbol{A}_{K-1}] & [\boldsymbol{B}_K] & & \\
 & & & & [\boldsymbol{A}_K] & [\boldsymbol{B}_{K+1}]
\end{bmatrix}\begin{bmatrix}\boldsymbol{g}_0 \\ \boldsymbol{g}_1 \\ \vdots \\ \vdots \\ \boldsymbol{g}_K \\ \boldsymbol{g}_{K+1}\end{bmatrix} = \begin{bmatrix}\boldsymbol{0} \\ \vdots \\ \boldsymbol{0}\end{bmatrix}. \tag{4}$$

It is high computational cost to solve Eq. (4) directly to obtain the mth diffraction amplitudes $\boldsymbol{g}_0^- = \begin{bmatrix}\left\{{}^\mathrm{E}g_m^{\mathrm{a}-}\right\} & \left\{{}^\mathrm{M}g_m^{\mathrm{a}-}\right\}\end{bmatrix}^\mathrm{T}$ and $\boldsymbol{g}_{K+1}^+ = \begin{bmatrix}\left\{{}^\mathrm{E}g_m^{\mathrm{s}+}\right\} & \left\{{}^\mathrm{M}g_m^{\mathrm{s}+}\right\}\end{bmatrix}^\mathrm{T}$. The superscripts E and M denote TE and TM waves, respectively. We present the following two improvements to reduce the cost.

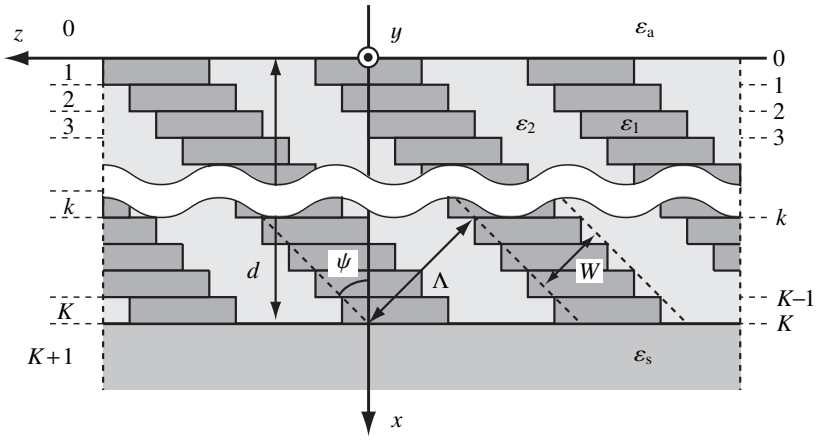

Figure 1: Multilayer division for a slanted grating.

① **The procedure to calculate eigenvalues and eigenvectors**
For the slanted case, the matrix $[\boldsymbol{C}_k]$ of the kth layer can be expressed by

$$[\boldsymbol{C}_k] = \left[\overline{N}_{\mathrm{K}}\right][\boldsymbol{C}_1]\left[\overline{N}_{\mathrm{K}}\right]^{-1}, \quad \left[\overline{N}_{\mathrm{K}}\right] = \begin{bmatrix} [\overline{n}_{\mathrm{K}}] & & & 0 \\ & [\overline{n}_{\mathrm{K}}] & & \\ & & [\overline{n}_{\mathrm{K}}] & \\ 0 & & & [\overline{n}_{\mathrm{K}}] \end{bmatrix}, \quad [\overline{n}_{\mathrm{K}}] = \left[e^{jm\, n_k z_k}\delta_{mn}\right] \tag{5}$$

with $n_{\mathrm{K}} = \lambda/\Lambda_z$ and $\Lambda_z = \Lambda/\cos\psi$. the diagonal matrix $[\overline{\boldsymbol{\kappa}}_k]$ of eigenvalues is the same as $[\boldsymbol{\kappa}_1]$ in the 1st layer, and $[\boldsymbol{T}_k]$ is derived by shifting the phase of $[\boldsymbol{T}_1]$ as

$$[\overline{\boldsymbol{\kappa}}_k] = [\overline{\boldsymbol{\kappa}}_1], \quad [\boldsymbol{T}_k] = \left[\overline{N}_{\mathrm{K}}\right][\boldsymbol{T}_1]\,. \tag{6}$$

We can get $[\boldsymbol{\kappa}_k]$ and $[\boldsymbol{T}_k]$ in all stratified layers by numerical calculation only once.

② **Successive elimination to solve linear equation**
We solve Eq. (4) without using inverse matrix. Using forward elimination successively, we eliminate the unknown amplitudes $\boldsymbol{g}_1,\ \boldsymbol{g}_2, \ldots, \boldsymbol{g}_K$ as follows :

$$\begin{bmatrix} [\boldsymbol{P}^{(k-1)}] & [\boldsymbol{Q}^{(k-1)}] & [\boldsymbol{0}] \\ [\boldsymbol{0}] & [\boldsymbol{A}_k] & [\boldsymbol{B}_{k+1}] \end{bmatrix} \Longrightarrow \begin{bmatrix} [\boldsymbol{A}_0^{(k)}] & [\diagdown] & [\boldsymbol{C}^{(k)}] \\ [\boldsymbol{P}^{(k)}] & [\boldsymbol{0}] & [\boldsymbol{Q}^{(k)}] \end{bmatrix} \tag{7}$$

where $k = 1, 2, \ldots, K$, $[\boldsymbol{P}^{(0)}] = [\boldsymbol{A}_0]$ and $[\boldsymbol{Q}^{(0)}] = [\boldsymbol{B}_1]$. Comparing with Eq. (4), the working memory for Eq. (7) becomes small. We finally have the two medium boundary problems as

$$[\boldsymbol{P}^{(K)}]\begin{bmatrix} \boldsymbol{g}_0^+ \\ \boldsymbol{g}_0^- \end{bmatrix} + [\boldsymbol{Q}^{(K)}]\begin{bmatrix} \boldsymbol{g}_{K+1}^+ \\ \boldsymbol{g}_{K+1}^- \end{bmatrix} = \boldsymbol{0}\,. \tag{8}$$

3. Numerical examples and discussions

This section considers the effectiveness of the above two improvements for a slanted grating case. First, we compare the computational times using the improvements ①, ② and the combination of ① and ② with the case ⓪ without using these improvements. Figure 2 shows the required time to calculate a set of diffraction efficiencies against the division number K by PC (CPU : Intel Xeon W-2145 3.70 GHz, Memory : 128 GB, OS : Windows 64 bit) under $2M + 1 = 31$. We can see that the effect of ② is large. It is worth noting that ② can be applied not only to a slanted grating but also to surface profiled gratings.

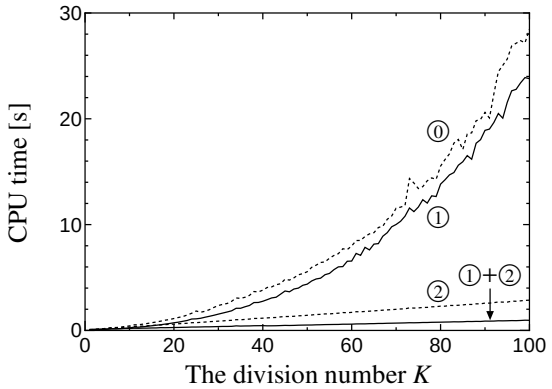

Figure 2: The calculation time against division number.

Next, Fig. 3 compares the numerical results by the MDM and by the method of Ref. [3] using a tilted grating vector for TE and TM incidences having $\theta = 60°$ and $\phi = 90°$ in planar mounting case. Calculation parameters were chosen as $2M + 1 = 31$, $\Lambda/\lambda = 0.4$, $W/\Lambda = 0.5$, $\varepsilon_a = \varepsilon_1 = 1.0$, $\varepsilon_2 = \varepsilon_s = 1.5^2$ and $d/\Lambda_x = 3.0$ with $\Lambda_x = \Lambda/\sin\psi$. Figure (a) plots the -1st reflected diffraction efficiencies η^r_{-1} against the division number K at slant angles $\psi = 45°$ and $75°$. When the division number K increases, the results by the MDM are in good agreement with the results $\overline{\eta}^r_{-1}$ by the method of Ref. [3], which are the dotted lines in the figure. So, we confirmed the validity of the MDM. Figure (b) calculates the relative errors $\left|\eta^r_{-1} - \overline{\eta}^r_{-1}\right| / \overline{\eta}^r_{-1}$. As ψ becomes large, the error increases. This means that applying the MDM to the analysis of surface profiled gratings, a division size should be determined according to the gradient of the grating shape.

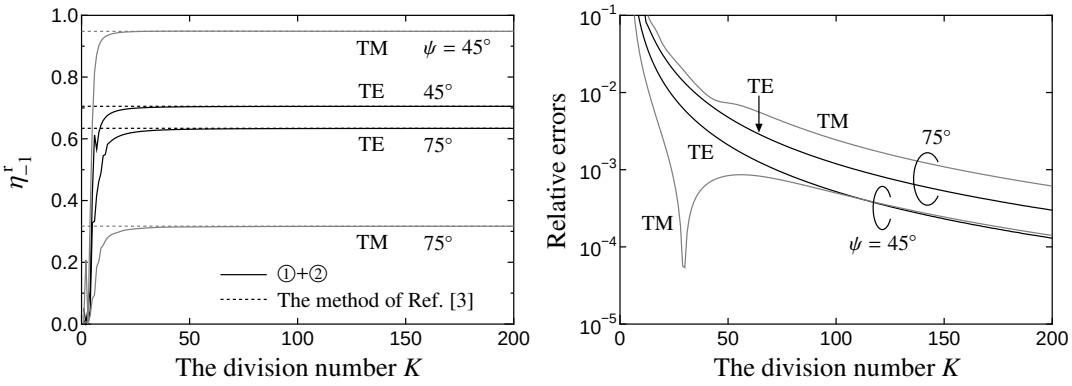

(a) The diffraction efficiencies (b) The relative errors

Figure 3: The comparisons of results by the MDM and the method of Ref. [3].

4. Conclusions

This paper has targeted the analytical method of electromagnetic scattering by slanted gratings. In order to reduce the computational cost, we have improved calculation procedure in the MEM that incorporates the MDM. Some numerical results have shown that our proposed improvements are successful. Using the successive elimination and the division size according to the grating shape, it is expected that the computational cost can be reduced in the analysis of scattering by various surface profiled gratings.

References

[1] S. Campbell, L. C. Botten, R. C. Mcphedran and C. Martijn de Sterke, Modal method for classical diffraction by slanted lamellar gratings, *Journal of the Optical Society of America A*, 25 (2008), pp. 2415–2426.

[2] G. Granet, M. H. Randriamihaja and K. Raniriharinosy, Polynomial modal analysis of slanted lamellar gratings, *Journal of the Optical Society of America A*, 34 (2017), pp. 975–982.

[3] H. Wakabayashi, M. Asai and J. Yamakita, Three-dimensional analysis of structural coloration by a slanted dielectric grating, *Journal of the Optical Society of America A*, 37 (2020), pp. 1539–1547.

On the Regular Tetrahedral Layout of Helices for a Quasi-Isotropic Chiral Particle

Masamitsu Asai[1*], Hideaki Wakabayashi[2], Jiro Yamakita[2]

[1]Department of Computational Systems Biology, Kindai University
[2]Okayama Prefecture University

*asai@waka.kindai.ac.jp

Abstract. The regular tetrahedral layout of thin-wire conducting helices is presented as the structure of a quasi-isotropic chiral particle. This work is done as part of pursuit of particle structure under the trade-off between the simplification of structure and the quality of isotropy and chirality. Effective constitutive parameters of the medium composed of the particles with the presented structure are analyzed by the quasi-static Lorentz theory combined with the method of moments to investigate the quality of isotropy and chirality. The extent of cancellation of electric quadrupole moments is also checked as a criterion for isotropic chirality.

Keywords: Artificial medium, chiral medium, electromagnetic theory, medium design.

1. Introduction

Metamaterials for electromagnetic waves have been of great interest in the fields of radio science, optics, and acoustics etc. They are composed of artificially-fabricated particles in background matrices or are fabricated by working matrices into fine mosaics. They are designed to show required macroscopic characteristics. The size and spacing of each particle or roughness is to be much smaller than the wavelength. The Pasteur medium i.e. a reciprocal isotropic chiral medium was first developed as a metamaterial. It was considered as the magnified scale model of the organic compounds by which K. F. Lindman investigated the optical activity in the microwave frequency in 1914 through 1922. Artificial bi-isotropic and bi-anisotropic media and artificial magnetic and dielectric media also have been studied [1]. The term ‘metamaterials’ has been given to those artificial media since the negative index of refraction in a left-hand material was realized by J. B. Pendry, D. R. Smith et al. in around 2000 [2]. Research on the artificial chiral medium has been intensively reported not only on the optical activity but on the biomimetic functions and the medical effects such as suppression of cancer proliferation etc. [3],[4]. Convensional isotropic chiral media are composed of random or homogeneous distributions of randomly-oriented chiral particles. In the practical design however, it is actually very hard to have the orientations and positions of particles perfectly random, then the isotropy with high accuracy is hard to realize. It is on the other hand more realistic and practical to design a three-dimensional periodic array of quasi-isotropic chiral particles. Each particle should be close to electromagnetically isotropic and should be downsized to around a

tenth of wavelength that is known to be adequate granularity for chiral media. Authors have presented the cubic layout of helices that has twelve helical or double-helical thin wires considering rotational symmetry and granularity. The resultant medium has shown high quality of isotropy and chirality [5]. Although it is still necessary to pursue optimal structure of particles, it is also important to simplify the structure for cost reduction and simplicity of fabrication under the trade-off with the quality of isotropy and chirality.

In this work, the regular tetrahedral layout of thin-wire conducting helices is presented as the structure of a quasi-isotropic chiral particle. Compared to the cubic layout, the number of helical or double-helical wires is reduced by half that is likely to sacrifice the quality of isotropic chirality. To investigate the quality of isotropy and chirality of the medium composed of the particles with the presented structures, the effective constitutive parameters are numerically analyzed by the quasi-static Lorentz theory [7] combined with the method of moments for thin-wire approximation [5],[6]. The electric and magnetic dipole moments and the electric quadrupole moments are taken into account in the analyses [8],[9]. The extent of cancellation of the electric quadrupole moments is also checked as a criterion for the isotropic chirality.

2. Structure and Analysis

The regular tetrahedron with edge length L is shown in Fig. 1. The center of gravity is on

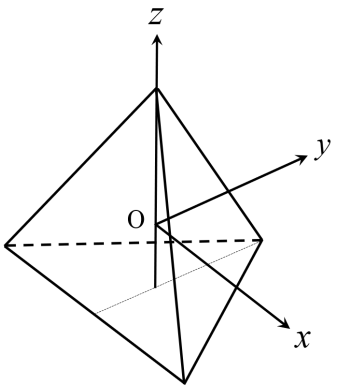

Fig. 1 Regular tetrahedron

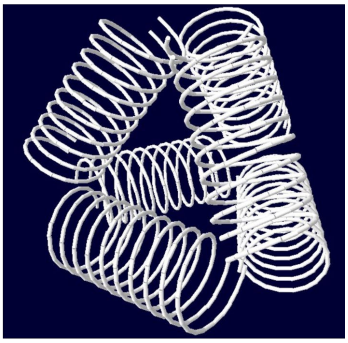

Fig. 2 Particle structure

the origin of Cartesian coordinate. One of the apices is on z-axis that is a perpendicular line and one of the edges is parallel to x-axis. A right-handed single or a double helix is located at the center of each edge of the regular tetrahedron to form a particle and each helical axis is on each edge as shown in Fig. 2. The single helix (that also composes a double helix) is a five-turn perfectly-conducting helical thin wire with wire radius r, wire length l, and axis length h. The particle can be rotated clockwise in the order of toward x, and toward z-axis for θ and ϕ degrees respectively. The medium is composed of three-dimensional periodic array of the particles along the coordinates in free space. The periodicity along each coordinate axis is identically d. Fig. 3 shows the normalized chirality constant at frequencies of 8.0 through 11.0 GHz where double helix is used for each element, and l=18.75mm, r=0.03mm, h/l=0.14, L/h=1.8, d=2L, θ =27° , ϕ =0° . Three diagonal elements of the chirality tensor, averaged absolute values of non-diagonal elements, and the averaged absolute values of the electric quadrupole components of each element are plotted. It can be seen that at around 8.5 through 9.0 GHz and higher

than around 10.5 GHz, three diagonal elements have almost the same values, and non-diagonal elements and the quadrupole components are very small compared to the diagonal elements, that shows almost perfect isotropic chirality.

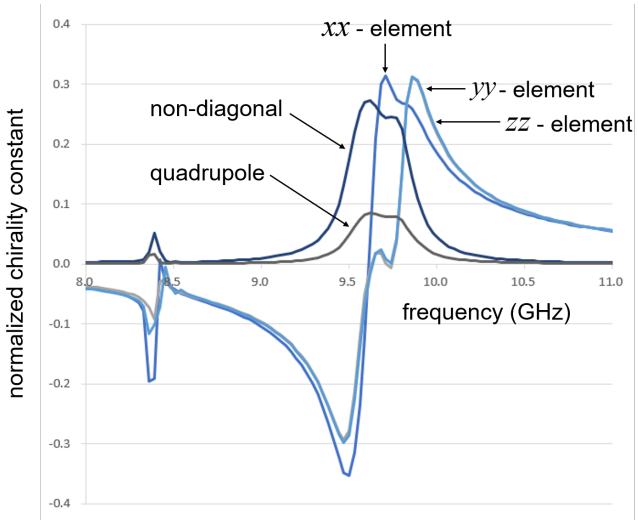

Fig. 3 Chirality constant for the case of double heilx

3. Conclusion

The number of helices was reduced at the present particle structure by half compared to that of our previous work i.e. the cubic case. The present simplified particle turned out to be available as an almost isotropic chiral one for the limited requirements of frequency region and magnitude of chiral constant. Pursuing the simpler structures that can coexist with the high quality of isotropy and chirality will be our future work.

References

[1] I. V. Lindell el al., Artech House, (1994), pp. 1-18, 193-243.

[2] D. R. Smith et al., *Physical Review Letters*, Vol. 84, No. 18 (2000), pp. 4184-4187.

[3] M. Asai et al., *Materials Integrations,* Vol. 25, No. 12 (2012), pp. 31-37.

[4] S. Motojima et al., *Applied Physics Letters*, Vol. 56, No. 4 (1995), pp.321

[5] M. Asai et al., *Proc. of JSST Int. Conf. Sim. Tech*, Vol. 1 (2019)

[6] M. Asai et al., *Proc. of ISAP*, Vol. 1, (2016), pp. 2C2-20584.

[7] A. Ishimaru et. al., *IEEE Trans. Antennas Propag*., Vol. 51, No. 10, (2003), pp. 2550-2557.

[8] A. D. Buckingham et al., *J. Chem. Soc.A*, (1971), pp. 1988-1991.

[9] I. P. Theron et al., *J. Electromag. Waves App*. Vol. 10, No. 4 (1996), pp. 539-561.

An investigation of deflated ICCG method for finite element analysis of eddy current problem

Kota Watanabe*, Wataru Kotani

Graduate School of Engineering, Muroran Institute of Technology

*k-wata@muroran-it.ac.jp

Abstract. A fast liner solvers for Finite Element Analysis (FEA) using a deflation technique is discussed. A deflated Incomplete Cholesky Conjugate Gradient (ICCG) method is introduced so as to reduce the cost of FEA for electromagnetic devices such as motors. The deflation technique decomposes the solution into fast and slowly components. The slowly components can be solved by direct methods with low computational cost due to small dimensions. Therefore, the deflated ICCC method can improve the convergence. The deflated method is applied to a FEA of eddy current problem as well as magnetostatic problem. Numerical results show that the present method can reduce the computational cost of FEA of a synchronous motor.

Keywords: Conjugate gradient method, Deflation method, Eddy current problem

1. Introduction

Finite Element Analyses (FEA) is widely used to evaluate performance of electromagnetic devices such as motors. Fast linear solvers are an important factor to reduce computational cost of FEA. Therefore, it is important to reduce the computational cost in solver process by introducing fast linear solvers.

The deflation technique that replaces small eigenvalues with zeros in the system matrix can improve the convergence of incomplete Cholesky conjugate gradient (ICCG) method [1][2]. The deflated ICCG requires eigenvectors that have high computational cost to obtain. To solve this difficulty, simple quasi vectors instead of eigenvectors are introduced. The authors have applied the present method to FEA of magnetstatic problem. The numerical results show that the present method has good convergence property in comparison with the conventional ICCG method. In this study, the present method is applied to a eddy current problem.

2. Formulation

Let us consider a system of linear equations $A\boldsymbol{x} = \boldsymbol{b}$ with n DoF (Degree of Freedom) obtained by a FEA where A is coefficient matrix, $\boldsymbol{x}$ and $\boldsymbol{b}$ are solution and right hand side vector respectively. The solution $\boldsymbol{x}$ is decomposed into slowly and fast components as

$$\boldsymbol{x} = W\boldsymbol{y} + (\boldsymbol{x} - W\boldsymbol{y}) \quad (1)$$

where $W = [\boldsymbol{w}_1\ \boldsymbol{w}_2\ \ldots\ \boldsymbol{w}_k]\Re \in^{n\times k}$, $\boldsymbol{w}_i\ (i = 1,2,\ldots,k) \in^{n\times k}$ is the eigenvector corresponding to the i-th eigenvalue. A-orthogonality is imposed on the vectors $\boldsymbol{w}_i$ to $\boldsymbol{x}$ – W$\boldsymbol{y}$ results in $W^tAW\boldsymbol{y} = W^tA\boldsymbol{x}$. The slowly converging component W$\boldsymbol{y}$ can be expressed as

$$W\boldsymbol{y} = W(W^tAW)^{-1}W^tA\boldsymbol{x} \equiv Q\boldsymbol{x} \quad (2)$$

where$Q \in^{k\times n}$. Moreover, let us introduce the matrix P given by, $P = I - Q = I - W(W^tAW)^{-1}W^tA$. Consequently, the solution $\boldsymbol{x}$ can be expressed as $\boldsymbol{x} = P\boldsymbol{x} + Q\boldsymbol{x}$. The fast converging component $P\boldsymbol{x}$ can be obtained by solving $AP\boldsymbol{x} = P^tA\boldsymbol{x} = P^t\boldsymbol{b}$. The slowly component $Q\boldsymbol{x}$ is obtained from $Q\boldsymbol{x} = W(W^tAW)^{-1}W^t\boldsymbol{b}$. The huge computational cost is requires to obtain the eigenvectors $\boldsymbol{w}_i$. To solve this difficulty, quasi eigenvectors $\boldsymbol{w}_i^*$ which are similar to $\boldsymbol{w}_i$ are introduced [1].

3. Results

The present method is applied to an Interior Permanent Magnet (IPM) motor based on the IEEJ D model. The FEA of non-linear magnetstatic problem is performed on a 1/4 model due to symmetry. A Newton-Raphson method is used to solve non-linear equation. Table I shows a result for convergence of present method. The result show that the present method has good convergence in comparison with ICCG method. Results in the eddy current problem are shown in the conference.

Table I Comparison of convergence in magnetostatic problem

Method	ICCG	deflated ICCG with $k = 4$
Number of total iterations	446	283

References

[1] H. Igarashi, K. Watanabe: Deflation Techniques for Computational Electromagnetism: Theoretical Considerations, *IEEE Trans. Magn.*, 47:5 (2011), 1438-1441.

[2] Y. Saad, M. Yeung, J. Erhel, F. Guyomarch: A deflated version of the conjugate gradient algorithm, *SIAM J. Sci. Comput.*, 21:5 (2000), 1909-1926.

JSST 2021

Eulerian coupling simulation method for dynamics of air and shock-absorbing structure

Ryohei Katsumata[1,*], Koji Nishiguchi[1], Tokimasa Shimada[2,3], Hiroya Hoshiba[1], Junji Kato[1]

[1]Department of Civil Engineering, Graduate School of Engineering, Nagoya University
[2]Department of Computational Science, Graduate School of System Informatics, Kobe University
[3]RIKEN Center for Computational Science, RIKEN

[*]katsumata.ryohei@k.mbox.nagoya-u.ac.jp

Abstract. The purpose of this study is to analyze the large deformation of a fracture-prevention floor with a shock-absorbing structure made of rubber-resin mixtures. However, to analyze the coupled phenomena between the structure with large deformation and the air, it is necessary to consider the interface discontinuity of the mass density and velocity field at the interface between the solid and the fluid. This paper proposes an Eulerian fluid-structure interaction analysis method that can be used stably even in a field where the interface is discontinuous and verify its validity and effectiveness.

Keywords: Eulerian fluid-structure interaction, Finite volume method, Large deformation

1. Introduction

To reduce the number of bone fractures caused by falls among the elderly, which has become a major social problem in recent years, floor structures that absorb the impact of falls made of rubber-resin mixtures are being explored. To design a more effective structure for absorbing the impact of falls, it is necessary to consider the dynamic structural analysis of large deformations and the interaction with air. However, conventional structural analysis using the finite element method suffers from the failure of the Lagrangian mesh due to large deformations, the time and cost of mesh generation and computation, and the difficulty of fluid-structure interaction analysis considering the effect of air.

In this study, fluid-structure interaction analysis is performed using the Eulerian finite volume method based on the Building Cube Method (BCM) [1]-[4], which has been developed by the authors. However, the problem of discontinuities in the mass density and velocity fields at the interface between solid and fluid has remained an open issue in previous studies.

Against this background, the purpose of this study is to develop and validate a unified Eulerian fluid-structure interaction analysis scheme that can take into account interfacial

discontinuities in the mass density and velocity fields and verify the effectiveness of this method by massively parallel simulations of shock-absorbing structures for preventing fall fractures.

2. Numerical method

In this study, the governing equations are the continuity equation and the equation of motion, which are the basic equations in continuum mechanics, volume-averaged in the control volume [1]. We assume an incompressible neo-Hooke solid as the constitutive equation for a solid and an incompressible Newtonian fluid as the constitutive equation for a fluid [3].

Define the velocity vector at the cell center and discretize it using the finite volume method. In this case, the stress is divided into pressure and deviation stress, and the velocity and pressure fields are computed separately using the fractional step method [2][3]. To avoid numerical diffusion due to advection of the interface and internal variables of the solid, Lagrangian marker particles are used, which not only represent the solid domain explicitly but also serve to compute the physical quantities of the solid.

Previous studies have used the same mass density between solids and fluids, but in this study, we use an equation that smoothes out the discontinuity in mass density at the interface by averaging it by volume fraction. In addition, while previous studies have used a second-order central difference scheme for the spatial discretization of the advection term, in this study, we use a fifth-order WENO scheme, [5], which has higher accuracy to stably solve the discontinuous velocity field at the interface.

3. Numerical examples

First, to verify the validity of the method, we analyze the two-dimensional push-in problem shown in Figure 1. Push the upper rigid body into the deformed body in the plane strain state without slipping. The physical properties of the solid and fluid are given in Table 1.

A finite element solution using the commercial solid analysis code LS-DYNA with a sufficiently fine mesh to which the numerical solution has converged is prepared as a reference solution. Figure 2 compares the deformation diagram and Mises stress distribution at $t = 0.30$ ms. From this figure, it can be confirmed that the solution by the present method is in general agreement with the reference solution.

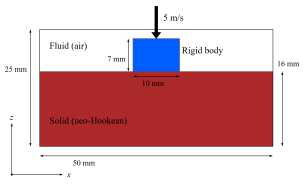

Figure 1: Two-dimensional push-in problem with rigid bodies.

Table 1: Physical properties in a two-dimensional push-in problem.

Solid: incompressible neo-Hookean solid	
Mass density ρ_s [kg/m^3]	1.0×10^3
Young's modulus E [Pa]	1.0×10^6
Viscosity μ_s [Pa · s]	0
Fluid: incompressible Newtonian fluid	
Mass density ρ_f [kg/m^3]	1.2
Viscosity μ_f [Pa · s]	1.8×10^{-5}

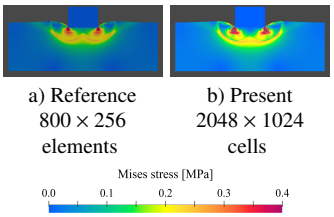

a) Reference 800×256 elements

b) Present 2048×1024 cells

Figure 2: Mises stress distribution in a push-in problem. ($t = 0.30$ ms)

Figure 3 is a graph showing the strain energy time history of the solutions by the present method using meshes with different spatial resolutions and the reference solution by the finite element method. From this figure, it can be confirmed that the solutions by the present method have lower values than the reference solution. The stresses and strains were lower than the actual values due to the overlap of deformed particles in the rigid region.

The next is to analyze the deformation of the fracture prevention floor shown in Figure 4. Push the upper rigid body into the deformed body without slipping. The solid is assumed to be a rubber-resin mixture and the fluid is assumed to be air at 20°C. The properties shown in Table 2 are given. A hierarchical Cartesian mesh with a minimum cell size of about 0.35 mm and a total cell number of 11,190,272 is used, and the analysis time is up to 1.8 ms.

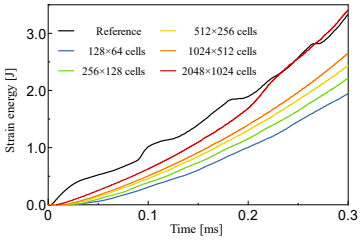

Figure 3: Time history of strain energy.

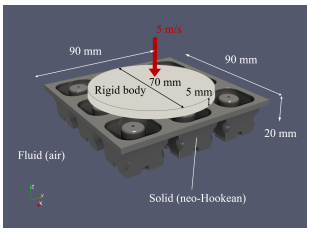

Figure 4: Analysis of fracture prevention floor.

Table 2: Physical properties in the analysis of fracture prevention floor.

Solid: incompressible neo-Hookean solid	
Mass density ρ_s [kg/m^3]	1.0×10^3
Young's modulus E [Pa]	3.0×10^7
Viscosity μ_s [Pa · s]	1.8×10^{-5}
Fluid: incompressible Newtonian fluid	
Mass density ρ_f [kg/m^3]	1.2
Viscosity μ_f [Pa · s]	1.8×10^{-5}

Figure 5 shows the deformation and Mises stress distribution in the deformation analysis of a fracture prevention floor. It can be confirmed that the coupled problem between the air and the structure, which undergoes large deformation, can be computed stably. Figure 6 is the distribution of the velocity field. It can be confirmed that air with a velocity about 10 times faster than the pushing velocity of the rigid body is flowing out from the gap of the deformed body. Figure 7 is the distribution of the pressure field. It can be confirmed that there are areas where high pressure of more than 1 MPa is generated. Considering the thickness of the structure (about 2-3 mm) and Young's modulus (30 MPa), these effects cannot be neglected, suggesting that the interaction between the structure and the air is a strong phenomenon.

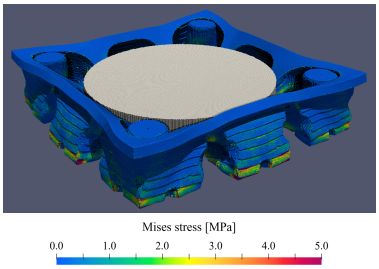

Figure 5: Deformation and Mises stress distribution. (t = 1.8 ms)

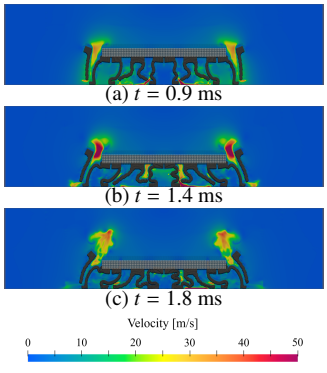

Figure 6: Distribution of the velocity field.

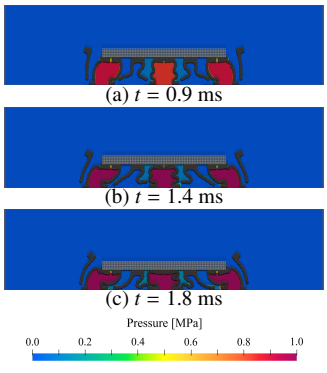

Figure 7: Distribution of the pressure field.

4. Conclusion

In this study, we proposed a unified Eulerian fluid-structure interaction analysis method that takes into account the interfacial discontinuities in the mass density and velocity fields by modifying the volume averaging of the mass density and the spatial discretization scheme of the advection terms. Then, the validity of this method was verified through a two-dimensional push-in problem, and the effectiveness of this method was verified through the analysis of a fracture prevention floor. Future work includes modification of the velocity boundary condition with a rigid body and quantitative comparison of the load-displacement curves with experiments.

References

[1] Nishiguchi, K., Okazawa, S., Tsubokura, M.: Multimaterial Eulerian finite element formulation for pressure-sensitive adhesives, *International Journal for Numerical Methods in Engineering*, 114:13 (2018), 1368-1388.

[2] Nishiguchi, K., Okazawa, S., Tsubokura, M.: Fully Eulerian solid-fluid interaction analysis using hierarchical Cartesian mesh method for large-scale parallel computing, *Journal of Japan Society of Civil Engineers, Ser. A2 (Applied Mechanics)*, 73:2 (2017), 153-163.

[3] Nishiguchi, K., Bale, R., Okazawa, S., Tsubokura, M.: Full Eulerian deformable solid-fluid interaction scheme based on building-cube method for large-scale parallel computing, *International Journal for Numerical Methods in Engineering*, 117:2 (2019), 221-248.

[4] Nishiguchi, K., Okazawa, S., Tsubokura, M.: Implicit particle-in-cell formulation for incompressible solid-fluid interaction problem, *Journal of Japan Society of Civil Engineers, Ser. A2 (Applied Mechanics)*, 74:2 (2018), 253-263.

[5] Liu, X.D., Osher, S., Chan, T.: Weighted essentially non-oscillatory schemes, *Journal of Computational Physics*, 115:1 (1994), 200-212.

JSST 2021

Coupled analysis for active control and energy harvesting from flow-induced vibration

Shigeki Kaneko[1,*] and Shinobu Yoshimura[1]

[1]Department of Systems Innovation, School of Engineering, The University of Tokyo

[*]s_kaneko@save.sys.t.u-tokyo.ac.jp

The full paper of this paper has been published in Journal of Advanced Simulation in Science and Engineering (JASSE).

DOI: https://doi.org/10.15748/jasse.9.1

Finite element approach to fluid-structure interaction with contact

Tomohiro Sawada[1*], Junichi Matsumoto[1]

[1]Continuum Simulation Team, Research Center for Computational Design of Advanced Functional Materials, National Institute of Advanced Industrial Science and Technology

*tomohiro-sawada@aist.go.jp

Abstract. Fluid-structure interaction with contact of structures is one of the challenging issues in computer simulation. We present a direct numerical simulation method for the FSI with contact based fully on a finite element method. Two applications to the sedimentation and mixing of elastic capsules are shown.

Keywords: Computer simulation, Finite element method, Fluid-structure interaction, Contact

1. Introduction

Fluid-structure interaction (FSI) that involves contact of structures is one of the challenging issues in computer simulation. It is still good if there are few structures, but if there are many, it is necessary to compute multiple contacts between structures while computing fluid flow between the structures. Furthermore, structures may be deformed by fluid and contact forces. This paper presents a method based on a finite element method (FEM) that can handle all of these problems. The present method is a method that incorporates implicit contact computation into the interface-reproducing capturing (IRC) method for FSIs proposed in [1-4]. Section 2 briefly describes the computational method. Section 3 shows two examples of computing the sedimentation and mixing of elastic particles/capsules by the method.

2. Method

The present method is summarized as follows:

- Motion of the structures including deformation is computed with Lagrangian meshes that track the structures. Flow of the fluid is computed with a Eulerian mesh fixed in space.
- By applying the extended finite element method (XFEM [5,6]) to the fluid elements at interface between fluid and structures, requisite discontinuities at the interface are reproduced, and thus the overall spatial convergence is enhanced [1-4].
- Equilibrium at the fluid-structure interfaces is computed by a novel *stabilized* Lagrange-multiplier method embedded on surface of the structures with a stabilization term.
- Contacts of the structures in the fluid are computed by a two-pass approach based on a penalty method that inserts nonlinear springs at structural elements near contact.
- After finite element discretization, a nonlinear monolithic matrix equation is obtained. We

solve the monolithic equation as monolithic. The Newmark-β method is employed to the equation for a time integration scheme, and the Newton-Raphson method is employed to find a numerical solution of the nonlinear equation [3,4].

We adopted the completely implicit and monolithic method so that it can solve hard contact problems.

3. Applications

Figure 1(a) shows a two-dimensional application to finite element simulation of sedimentation of eighteen very soft capsules under gravity in a usual incompressible viscous water [7]. Figure 1(b) shows another application to mixing of nine very soft capsules in a shear flow of a very thick Bingham fluid [7].

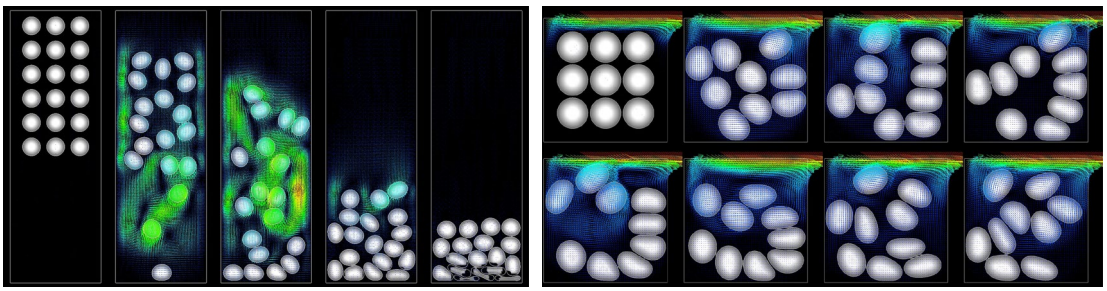

(a) Sedimentation of eighteen elastic capsules. (b) Mixing of nine elastic capsules.

Fig.1 Two applications of the proposed method to fluid-structure interaction with contact.

Reference

[1] T. Sawada, A. Tezuka: High-order Gaussian quadrature in X-FEM with the Lagrange-multiplier for fluid-structure coupling, *Int. J. Numer. Meth. Fluids*, 64 (2010), 1219-1239.

[2] T. Sawada, A. Tezuka: LLM and X-FEM based interface modeling of fluid-thin structure interactions on a non-interface-fitted mesh, *Comput. Mech.*, 48 (2011), 319-332.

[3] T. Sawada: Interface-Reproducing Capturing (IRC) Technique for Fluid-Structure Interaction: Methods and Applications, In: T. Tezduyar (eds), *Frontiers in Computational Fluid-Structure Interaction and Flow Simulation*, Modeling and Simulation in Science, Engineering and Technology, Birkhäuser, Cham, (2018).

[4] T. Sawada, M. Kondo, J. Matsumoto: Computation of Fluid Inertial Term in XFEM for Fluid-Structure Interaction, *Transactions of JSCES*, Paper No. 20200004 (2020), 1-15 (in Japanese Language).

[5] N. Moës, J. Dolbow, T. Belytschko: A finite element method for crack growth without remeshing, *Int. J. Numer. Meth. Engng.*, 46:1 (1999), 131-150.

[6] T. Belytschko, N. Moës, S. Usui, C. Parimi: Arbitrary discontinuities in finite elements, *Int. J. Numer. Meth. Engng.*, 50:4 (2001), 993-1013.

[7] T. Sawada: Direct Numerical Simulation Techniques for Fluid-Structure Interactions, *Journal of Japanese Society of Tribologists*, 65:11 (2020), 672-677 (in Japanese Language).

JSST 2021

Locomotion Control of Snake-like Robot utilizing Friction Forces: Feasibility Verification via Two Wheeled Robot

Shunsuke Nansai[1,*] and Hiroshi Itoh[1]

[1]Department of Advanced Machinery Engineering, School of Engineering, Tokyo Denki University

[*]nansai@mail.dendai.ac.jp

The full paper of this paper has been published in Journal of Advanced Simulation in Science and Engineering (JASSE).

DOI: https://doi.org/10.15748/jasse.9.113

JSST 2021

Degradation diagnosis of Lithium-ion batteries considering operation temperature

TODA Kousuke[1], ODAGAKI Yuuki[1,*], KAMAMICHI Norihiro[1], IWASE Masami[1], SATOH Yasuyuki[1]

[1]Department of Simulation, School of Technology, Tokyo Denki University

[*]odagaki@ctrl.fr.dendai.ac.jp

Abstract. This paper proposes a simulation method for a fractional derivative system representing the dynamics of lithium-ion batteries. The transfer function of the general lithium-ion battery dynamics has non-integer derivative terms. Therefore the fractional calculus is introduced for the simulation method. As a result, a fractional-order state-space representation is derived reducing the modeling approximation. In the representation, the system order may change according to the batteries' operation, and it causes the system matrix size change. Therefore we propose a method to determine α that reduces the size of the system matrix when deriving a fractional state-space model.

Keywords: Computer simulation, Li-ion-Battery, temperature, State-Of-Charge

1. Introduction

Lithium-ion batteries have a risk of accidents due to ignition as they deteriorate, so it is necessary to predict and diagnose deterioration in advance in a non-destructive manner. However, since the characteristics of LIB change depending on the temperature, it has a great influence on the deterioration diagnosis. Therefore, in this study, the change characteristics due to temperature are evaluated using a detailed LIB model. At the same time, the effect on deterioration is analyzed.

Fractional calculus is an extension of integer calculus to real calculus, and the expression of fractional calculus can be used to give solutions to actual physical problems, or conventional calculus can be modeled. It is known that it is possible to model what was difficult [1]. The electrical response of LIB is affected by the ion diffusion phenomenon as a concentration overvoltage, and the model derived from this equivalent circuit can also be modeled by a fractional derivative system.

Zhang et al. Confirmed that the parameters of the equivalent circuit model change with temperature [2]. From this, the fractional model changes depending on the temperature, which may affect the time response.

2. Real time respnse simulation

The real-time response simulation method and results for a temperature of LIB are described.

2.1. Fractional derivative system

Frequency transfer function of LIB contains Constant Phase Elements(CPE) index α, which is non-integer number and Warburg impedance $\frac{1}{\sqrt{j\omega}}$, which is fractional value. From this, it sure that transfer function of LIB is expressed as fractional derivative system instead of usual differentiation system.
In order to simulate the real-time response of this fractional derivative system, in the previous research, LIB was represented by a fractional state-space model using Caputo's fractional calculus. The fractional state-space model is represented

$$D^{\frac{1}{m}}x(t) = Ax(t) + Bu(t) \tag{1}$$
$$y(t) = Cx(t) + Du(t). \tag{2}$$

And this solution orbit is

$$x(t) = E_{\frac{1}{m},1}(At^{\frac{1}{m}})x(0) + \int_0^t (t-\tau)^{\frac{1}{m}-1}E_{\frac{1}{m},\frac{1}{m}}(A(t-\tau)^{\frac{1}{m}})u(\tau)d\tau. \tag{3}$$

Next, in order to consider the exogenous input, consider a spreading system that adds a state to the input, and let it be

$$D^{\frac{1}{m}} = \bar{A}\bar{x}(t). \tag{4}$$

Satisfy the following conditions. $\bar{x}, \bar{A}$ are

$$\bar{x}(t) = \begin{bmatrix} x(t) \\ u(t) \end{bmatrix}, \bar{A} = \begin{bmatrix} A & B \\ 0 & 0 \end{bmatrix}. \tag{5}$$

The solution orbit of this expansion system is

$$\bar{x}(t) = E^{\rho}_{\frac{1}{m},1}(\bar{A}t^{\frac{1}{m}})\bar{x}(0). \tag{6}$$

However, $E_{\alpha,\beta}(z)$ is a 3-parameter Mittag-Leffler function. The function is a generalization of the exponential function. That function can be expressed as

$$E^{\rho}_{\alpha,\beta}(z) = \sum_{k=0}^{\infty} \frac{(\rho)_k}{\Gamma(\alpha k+\beta)}\frac{z^k}{k!}. \tag{7}$$

It is necessary to apply the 3-parameter matrix Mittag-Leffler function after transforming it into the Jordan normal form since this system has duplicate eigenvalues.The function is

$$E_{\alpha,\beta}(z) = \boldsymbol{P}\mathrm{diag}(\mathrm{E}_{\alpha,\beta}(\boldsymbol{J_1})), (\mathrm{E}_{\alpha,\beta}(\boldsymbol{J_2})), \cdots, (\mathrm{E}_{\alpha,\beta}(\boldsymbol{J_s}))\boldsymbol{P^{-1}}. \tag{8}$$

It is possible to simulate without divergence by the exact calculation of the infinite series of $E_{\alpha,\beta}(\boldsymbol{J_k})$.

2.2. Derivate a fractional state-space model of LIB

We derivate a fractional state-space model of LIB. The fractional order is determined from the least common multiple of CPE index α and $\frac{1}{\sqrt{j\omega}}$, which is the denominator of Warburg impedance. The CPE index α at 10 degrees Celsius and the value when approximated to a fraction are as $\alpha = 0.572 \fallingdotseq \frac{3}{5}$.

2.3. Simulation

It was confirmed that the calculation time changed significantly because the system matrix changed due to the change in the differential structure. The size of the system matrix and the simulation time for the value of α are as follows. Under condition $\alpha = \frac{3}{4}$, 1 hour and 6 minutes or more. 37 hours or more under condition $\alpha = \frac{2}{3}$. The execution did not end and the simulation did not complete under condition $\alpha = \frac{3}{5}$.

In this study, in order to solve this problem, we propose a method to fix the differential structure. The fractional order is determined by approximating the CPE index, which is a decimal, to some extent. Therefore, we think that the same differential structure can be used by expanding the allowable range of approximation. This time, in order to reduce the size of the system matrix, the real-time response is simulated with the CPE index $\alpha = \frac{3}{4}$. The fractional state-space model can be derived as

$$A = \begin{bmatrix} 0 & 1 & 0 & 0 & 0 \\ 0 & 0 & 1 & 0 & 0 \\ 0 & 0 & 0 & 1 & 0 \\ 0 & 0 & 0 & 0 & 1 \\ 0 & 0 & \frac{1}{TR_1} & 0 & 0 \end{bmatrix}, B = \begin{bmatrix} 0 \\ 0 \\ 0 \\ 0 \\ 1 \end{bmatrix}, C = \begin{bmatrix} \frac{\sqrt{2}\sigma}{TR_1} \\ 0 \\ \frac{1}{T} \\ \sqrt{2}\sigma \\ 0 \end{bmatrix}^T, D = \begin{bmatrix} R_0 \end{bmatrix}. \tag{9}$$

2.4. Simulation results at 10 degrees Celsius

The real-time response simulation results of the state x and the output y at 10 degrees Celsius are shown in Fig. 1, Fig. 2. The simulation time was 0.5 s and the sampling time was 0.025 s.

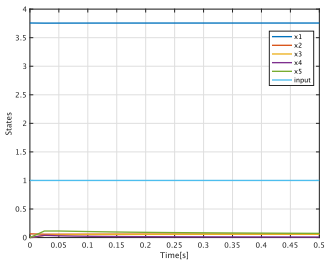

Figure 1: Real-time response simulation of state x

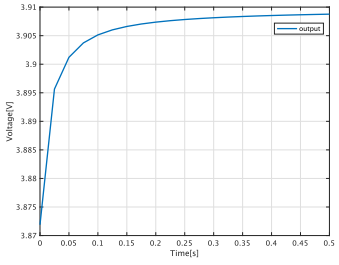

Figure 2: Real-time response simulation of output y

From Fig. 1, it can be confirmed that the input is 1, so it is a step response. It was confirmed that the change in state x_5 was the largest among the states. From Fig. 2, it can be confirmed that the step response can be output. Here, we compare the real-time response obtained in the previous section with the simulation. A comparison is shown in Fig. 3.

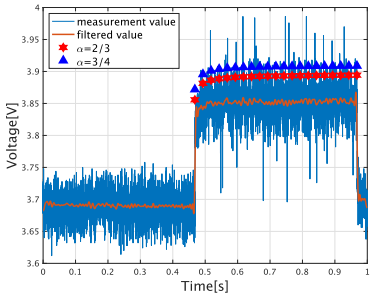

Figure 3: Real-time response and simulation of output voltage

As shown in Fig. 3, it can be confirmed that the real-time response and the rise time of the simulation are similar. However, there is a difference of about 0.05 V for the steady-state value, which shows that the simulation is higher. It can also be confirmed that there is a difference of about 0.01V from the steady value of $\alpha = \frac{3}{4}$.

3. conclusion

It was confirmed that the size of the system matrix of the fractional derivative system of LIB changes depending on the value of α. It was confirmed that there is a problem that the calculation time becomes long when the size of the system matrix is large. As a solution to this problem, we proposed a method of deriving a fractional state-space model by deciding on α to reduce the size of the system matrix. As a result of simulating the real-time response, the steady-state deviation was larger than that of the previous research method. Let us consider the cause of this.
The possible cause is that the initial values of the fractional terms are different from the actual model. The initial values of the fractional-order terms of the current fractional-order state-space model are all set to 0 for simulation. The reason is that it is possible to give physical meaning to terms of integer order, but it is difficult to give physical meaning to terms of fractional order. Although this problem has not been solved, we think that we can derive an integer derivative system from the real-time response of LIB and identify the initial value of the fractional state-space model from that system.

References

[1] Igor Podlubny: Fractional Differential Equations, 198:1 (1999), 41-75.

[2] S.S.Zhang, K.Xu,T.R.Jow: Electrochemical impe-dance study on the low temperature of Li-ion batteries, 49:Issue 7 (2004), 1057-1061.

JSST2021

Analysis of electrostatically induced current in humans when in contact with a stepladder under power transmission lines

Yuta Ishida[1*], Shoji Hamada[1]

[1]Kansai University

k616258@kansai-u.ac.jp

Abstract. We numerically analyzed the short-circuit current flowing from the bare feet of a voxel human model to the ground when standing under power transmission lines and in contact with an ungrounded conductive stepladder model with its left hand. A 50 Hz AC electric field of 3 kV/m was vertically applied to the model, and the short-circuit current was analyzed for different heights of the stepladder, ranging from 2–10 m. In addition, the stepladder height was estimated when the short-circuit current exceeded the reference levels specified in the international guidelines for the general public and occupational workers.

Keywords: Electrostatically induced current, Voxel model, Human model, Short-circuit current

1. Introduction

When a human body is in close proximity with high-voltage equipment such as power transmission lines, short-circuit currents are electrostatically induced in the body from exposure to commercial frequency AC electric fields [1], [2]. The induced currents could cause anxiety and discomfort in the general public, and health issues in occupational workers. Therefore, to prevent such situations, the International Commission on Non-Ionizing Radiation Protection (ICNIRP) guidelines have specified reference levels of such as contact currents [3]. To maintain the currents below the specified reference levels, induced currents have been widely studied through numerical analysis using numerical human models. We have previously analyzed the current induced in simple human voxel models holding a conductive umbrella, bat, plate, fishing rod, and so on [4]. In this study, we analyzed the currents induced in a human model standing under power transmission lines in contact with an ungrounded conductive stepladder with its left hand. To estimate the maximum short-circuit current value, we assumed the human model to be standing barefoot on the ground. The short-circuit current was analyzed for different heights of the stepladder, varying from 2–10 m. Furthermore, we estimated the stepladder heights when the short-circuit current reached the reference levels specified in the ICNIRP guidelines. Note that we only investigated the steady-state AC currents and not transient currents.

2. Methods

Figures 1 (a) and (b) show the two analysis models of this study. The 165.6 cm tall human voxel model is grounded and in contact with the stepladder voxel model with its left hand, and is exposed to a uniform electric field of 3 kV/m (= regulation value of the electric field under transmission lines in Japan) generated by the transmission lines present several tens of meters above the ground. The voxel size was set to 0.9 cm, and the model shapes were expressed in

spheres, cylinders, and partial cylinders. Further details are listed in Table 1. The shape of the top board of the stepladder is shown in Figure 1 (c), and a three-view drawing of the stepladder in Figure 1 (a) is shown in Figure 1 (d). The stepladder voxel model was a combination of cylinders with a diameter of 5.4 cm, excluding the top board. The stepladder was assumed to be floating 9 cm (= 10 voxels) above the ground to simulate ungrounded conditions. The height of the stepladder (from the ground to the top board) was changed from 2 m to 10 m in 1 m increments, and the corresponding short-circuit current values were calculated. The 10 m tall stepladder had a width and depth of 1.75 m and 5.50 m, respectively, and the vertical separation between the rungs was 28.8 cm for all stepladders. The short-circuit current was calculated using the voxel-based fast multipole surface charge simulation method [2], [5]. The reference level of the 50 Hz contact current is 500 μA and 1000 μA for the general public and occupational workers, respectively [3].

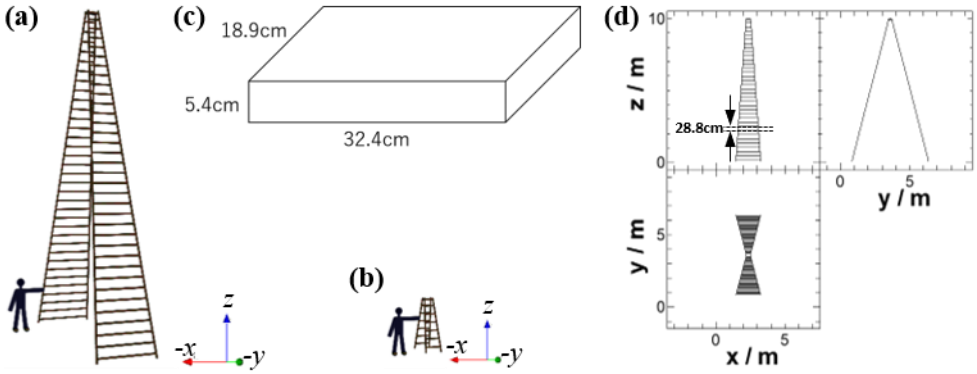

Fig. 1. (a) The human model next to a 10 m stepladder, (b) The human model next to a 2 m stepladder, (c) The dimensions of the top board of the stepladder, and (d) The three-view of the stepladder in (a).

Table 1. Shape of body parts, dimensions, and coordinates of the human voxel model.

Model	Approximate spatial shapes	Radius / cm	Sphere's center of gravity or coordinates at both ends of cylinder (x,y,z) / cm
Head	Sphere	14×0.9	(145.8, 433.8, 170)×0.9
Neck	Cylinder	6×0.9	(145.8, 433.8, 110) ×0.9 ~ (145.8, 433.8, 170) ×0.9
Right arm	Cylinder	8×0.9	(104.8, 433.8, 68) ×0.9 ~ (129.8, 433.8, 138) ×0.9
Left arm	Cylinder	8×0.9	(161.8, 433.8, 138) ×0.9 ~ (235.8, 433.8, 138) ×0.9
Right leg	Cylinder	8×0.9	(124.8, 433.8, 0) ×0.9 ~ (135.8, 433.8, 76) ×0.9
Left leg	Cylinder	8×0.9	(165.7, 433.8, 0) ×0.9 ~ (155.8, 433.8, 76) ×0.9
Right sole	Partial cylinder	8×0.9	(124.8, 413.8, 0) ×0.9 ~ (124.8, 433.8, 0) ×0.9, z>0
Left sole	Partial cylinder	8×0.9	(165.7, 413.8, 0) ×0.9 ~ (165.7, 433.8, 0) ×0.9, z>0
Body	Partial cylinder	18×0.9	(145.8, 433.8, 74) ×0.9 ~ (145.8, 433.8, 146) ×0.9, |y|< 10×0.9

3. Results

The calculated electric field distribution, and short-circuit currents versus the height of the stepladder, H, are shown in Figures 2 and 3, respectively. The distribution of the absolute electric field $|\boldsymbol{E}|$ is depicted on the x-z cross-section at y = 3.6 m, and on the y-z cross-section at x = 2.34 m. The red region indicates a strong electric field, and the upper section of the stepladder falls under this region, owing to the electric charges induced on the upper surface of the stepladder and the human model. Conversely, the electric field distribution under the stepladder or near the ground becomes weaker than the applied electric field. In Figure 3, the black circles represent the currents calculated using the surface charge simulation method, and the solid curve represents the currents calculated by the quadratic function obtained from the least squares fitting, represented as

$$I[\mu A] = 22.64 + 17.14H + 11.16H^2. \quad \cdots (1)$$

The difference between the numerical analysis and the fitting curve, indicated by black dots and solid lines in Figure 3, respectively, ranged from -1.13% to 0.54%. It is known that the

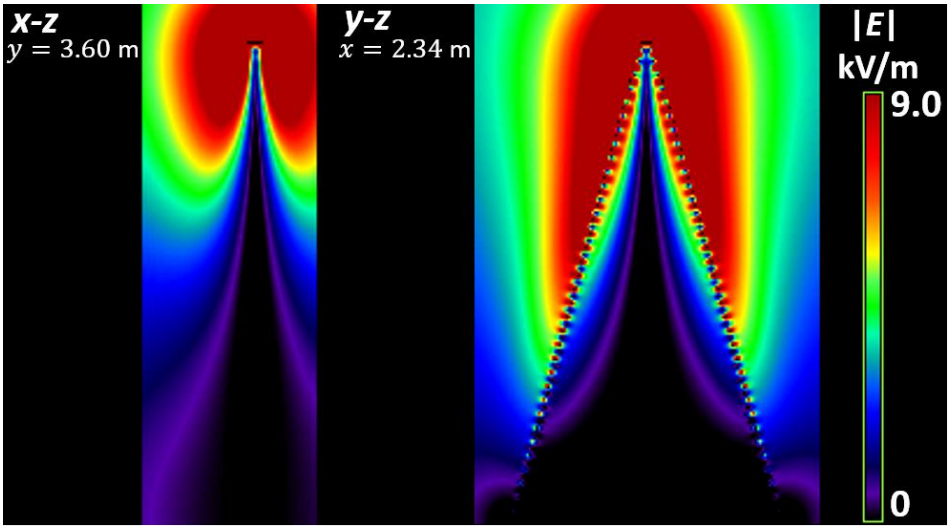

Fig. 2. Electric field distribution around the 10m stepladder.

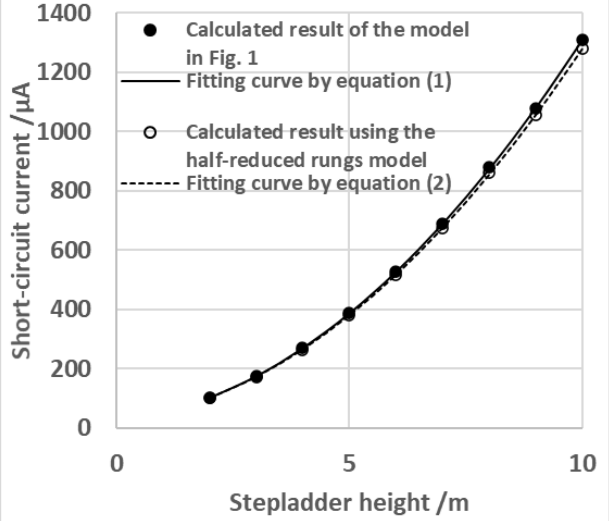

Fig. 3. Short-circuit current versus the height of the of the stepladder.

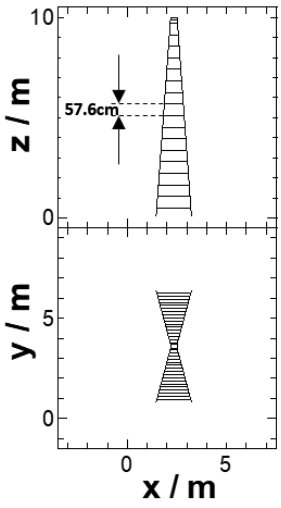

Fig. 4. Half-reduced rungs model.

short-circuit current running through the human model is proportional to the square of the human's height when the model is exposed to a vertical uniform electric field [1]. Therefore, a similar relationship appears in the stepladder model, as seen in Figure 3. According to the fitting equation (1), the ground current reaches 500 μA and 1000 μA when H is 5.81 m and 8.62 m, respectively. Futhermore, we calculated the short-circuit current when the spacing of stepladder rungs was doubled as shown in Figure 4. The calculated short circuit currents are plotted as white circles and a dashed line in Figure 3. The white circles are 1.06% to 2.20% smaller than the black circles. Similar to the fitting equation (1), the dashed line is represented as

$$I[\mu A] = 22.62 + 17.22H + 10.87H^2. \quad \cdots (2)$$

The fluctuation of the short circuit current at the actual rung spacing would be smaller than these fluctuation levels. Therefore, the dependence of the short circuit current on the rung spacing is much less than its dependence on the height.

4. Summary

In this study, we quantitatively calculated the short-circuit current of a grounded human model in contact with an ungrounded conductive stepladder model with its left hand when exposed to a 50 Hz uniform AC electric field of 3 kV/m under transmission lines. The calculated short-circuit current was approximated by a quadratic equation of the stepladder height H, and the fitting coefficient was calculated using the least squares method. The quadratic equation could express the short-circuit current within a difference of -1.13% to 0.54%. The height of the stepladder was 5.81 m and 8.62 m when the short-circuit current reached the reference levels of contact current for the general public and occupational workers, respectively, specified by ICNIRP. The estimated short-circuit currents can be proportionally altered in different frequencies and applied electric fields. In future research, we plan to consider the non-uniformity of the electric field distribution and to use detailed anatomical human models to analyze the short-circuit current.

References

[1] H. Tarao, N. Hayashi, K. Isaka, Estimation of short-circuit current induced by ELF uniform electric fields in grounded humans with different body shapes based on a semi-ellipsoidal model, *Biomed. Phys. Eng. Express*, 6 (2020), 055012.

[2] S. Hamada, Calculation of electrostatically induced electric fields in human models using a two-step process method of voxel-based fast multipole surface charge simulation method, *IEEJ Trans. FM*, 140:10 (2020), 481-490 (in Japanese).

[3] International Commission on Non-Ionizing Radiation Protection Guidelines for limiting exposure to time-varying electric and magnetic fields (1 Hz to 100 kHz), *Health Phys.*, 99 (2010), 818-836.

[4] Y. Ishida, S. Hamada, Short-circuit current analysis of simple human voxel model holding conductive plate and rod, *2020 annual conference of FM IEEJ*, 2-C-p2-3 (2020), (in Japanese).

[5] S. Hamada, T. Kobayashi, Analysis of electric field induced by ELF magnetic field utilizing fast-multipole surface-charge-simulation method for voxel data, *IEEJ Trans. FM*, 126:5 (2006), 355-362 (in Japanese).

JSST 2021

Effects of the number of observations on 4D-Var data assimilation: preliminary experiments

Yasuyoshi Horibata

Faculty of Science and Engineering, Hosei University

*horibata@hosei.ac.jp

Abstract. This paper presents preliminary numerical experiments for effects of the number of observations on 4D-Var data assimilation. A simple equation of thermal conduction is considered. The source program which simulates the heat conduction is differentiated in reverse mode by automatic differentiation tool to generate the adjoint program. In optimization, the gradient of a cost function is computed by the adjoint program.

Keywords: Variational data assimilation, Automatic differentiation, Adjoint program, Optimization

1. Introduction

Four-dimensional variational (4D-Var) data assimilation is an extension of the three-dimensional variational (3D-Var) data assimilation; it allows for observations distributed within a time interval. The cost function is a summation over time of the cost function for each observational increment computed with respect to the model integrated to the time of the observation. The control variable (the variable with respect to which the cost function is minimized) is the initial state of the model. The optimization algorithm requires the gradient of the cost function with respect the control variable. The adjoint program is used in order to compute the gradient efficiently.

In [1], we considered 4D-Var meteorological data assimilation. We improved the differentiability of the source program that simulates the three-dimensional atmospheric flow, and differentiated it by the automatic differentiation tool TAPENADE [2]. The generated tangent and adjoint program were validated by the dot product test. Numerical experiments ware presented for data assimilation for a downburst; the downburst is a strong downdraft which induces an outburst of damaging winds on or near the ground.

In the present paper, we present preliminary numerical experiments for effects of the number of observations on 4D-Var data assimilation. We deal with a simple heat equation where temperature varies only in one space dimension. For the sake of simplicity, we assume no observation and background errors.

2. Heat equation

We consider the heat equation

$$\frac{\partial T}{\partial t} = \alpha \frac{\partial^2 T}{\partial x^2} \qquad (0 < x < L, t > 0) \tag{1}$$

This governs the time-dependent temperature distribution in a homogeneous constant property solid under conditions where the temperature varies only in one space dimension. Consider a large wall of thickness L. The faces of the wall continue to be held as 0°C.

The spatial derivative is approximated using the central-difference scheme and the grid is uniform in x-direction. The explicit Euler method is used in order to integrate it. The new temperature value, T_i^{n+1}, is:

$$T_i^{n+1} = dT_{i-1}^n + (1 - 2d)T_i^n + dT_{i+1}^n \tag{2}$$

where

$$d = \alpha \frac{\Delta t}{(\Delta x)^2} \tag{3}$$

Let $L = 1\text{m}$, $\alpha = 0.02\text{m}^2/\text{h}$. We use $\Delta x = 5 \times 10^{-3}$ m and $\Delta t = 2.25$ sec. Figure 1 shows the obtained evolution of the temperature field.

We use some values of the temperature field as observations.

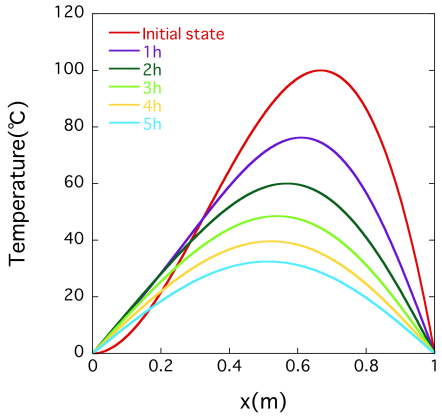

Figure 1: Evolution of the temperature field.

3. Data assimilation

We generate the adjoint program of the simulation program by using TAPENADE.

We use 8 time levels as observation times: 37.5 min ($1000\Delta t$), 75 min ($2000\Delta t$), 112.5 min ($3000\Delta t$), 150 min ($4000\Delta t$), 187.5 min ($5000\Delta t$), 225 min ($6000\Delta t$), 262.5 min ($7000\Delta t$), and 300 min ($8000\Delta t$). Using the observations $T_{i,o}^{1000*k}$, the cost function is defined as

$$J = \frac{1}{2} \sum_{k=1}^{8} \sum_i \left(T_i^{1000*k} - T_{i,o}^{1000*k} \right)^2 \tag{4}$$

Three cases are considered for the number of observation points: 199 ($i = 1, 2, \ldots, 199$), 9 ($i = 20, 40, 60, 80, 100, 120, 140, 160, 180$), and 2 ($i = 65, 135$) grid points.

Usually, in 4D-Var data assimilation, the optimization problem has thousand or millions control variables [1]. Hence, we use the modified L-BFGS-B algorithm [3] in order to solve the problem. Stating from the initial guess, the algorithm repeats search until it reaches the optimal point. Figure 2 shows the initial guess. Figures 3, 4, and 5 show the convergence histories of the optimization and the estimated fields for 199, 9, and 2 grid points, respectively.

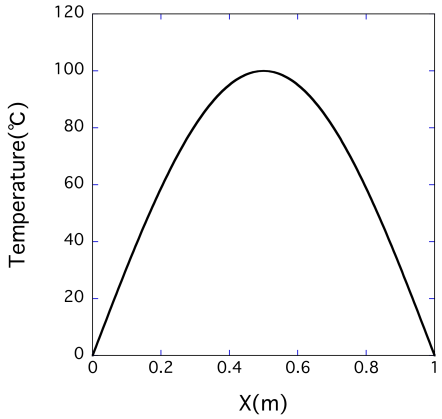

Figure 2: The temperature field of the starting point used for the optimization.

4. Conclusions

We use observations at 8 time levels and 199, 9, 2 grid points. The estimate obtained from observations at 199 grid points is almost identical with the truth. The estimates obtained from observations at 9 and 2 grid points agree reasonably with the truth. The cost functions decrease unsatisfactorily in both cases. More efficient algorithm is required for solving large optimization problems.

References

[1] Yasuyoshi Horibata, Y.: Validation of differentiated programs and their application to data assimilation, Proceedings of the 6th European Conference on Computational Mechanics (ECCM 6) and 7th European Conference on Computational Fluid Dynamics (ECFD 7), June 11-15, 2018, Glasgow, UK, Edited by: Roger Owen, René de Borst, Jason Reese and Chris Pearce (2018), 1325-1339.

[2] Laurent Hascoet, Valerie Pascual: TAPENADE 2.1 user's guide, INRIA, France, 2004.

[3] J. L. Morales, J. Nocedal: Remark on Algorithm 778: L-BFGS-B: Fortran subroutines for large-scale bound constrained optimization, *ACM Transactions on Mathematical Software*, 38 (2011), Article 7.

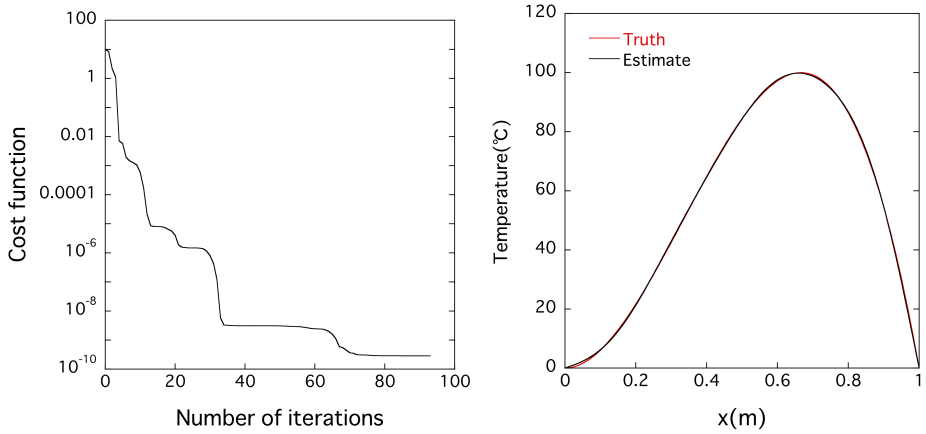

Figure 3: Convergence history of the optimization (left) and the estimated temperature field (right) for 199 grid points.

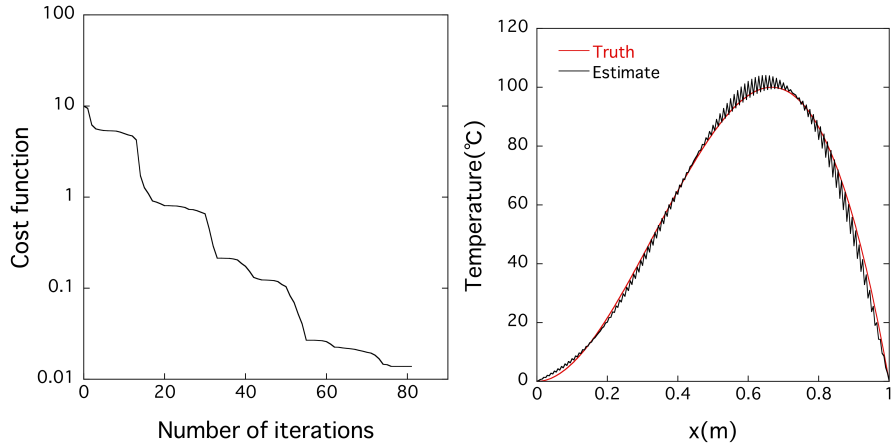

Figure 4: Convergence history of the optimization (left) and the estimated temperature field (right) for 9 grid points.

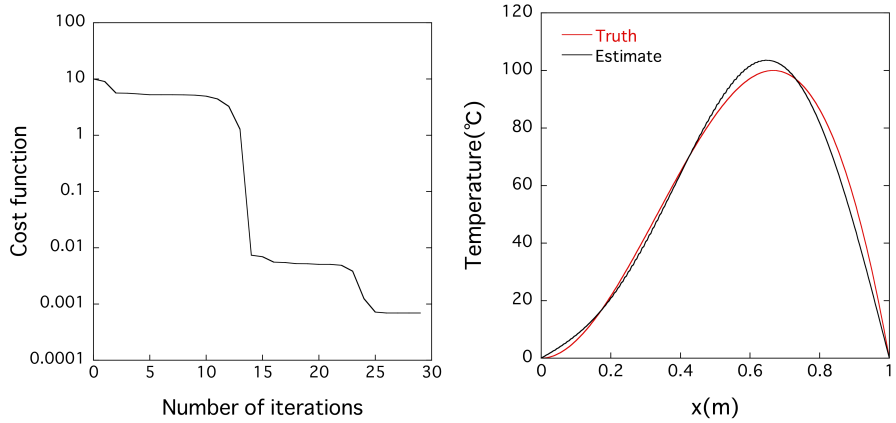

Figure 5: Convergence history of the optimization (left) and the estimated temperature field (right) for 2 grid points.

Rate of double strand breaks of genome-sized DNA in tritiated water: dependence on tritium concentration, water temperature, and DNA concentration

Yuji Hatano[1,*], Hiroto Shimoyachi[2], Tatsya Asano[2], Takahiro Kenmotsu[3], Takuro Wada[4], Yasuhisa Oya[4], Hiroaki Nakamura[5], Susumu Fujiwara[6]

[1]Hydrogen Isotope Research Center, University of Toyama
[2]Graduate School of Science and Engineering, University of Toyama
[3]Faculty of Life and Medical Sciences, Doshisha University
[4]Graduate School of Integrated Science and Technology, Shizuoka University
[5]National Institute for Fusion Science
[6]Faculty of Materials Science and Engineering, Kyoto Institute of Technology

[*]hatano@ctg.u-toyama.ac.jp

The full paper of this paper has been published in Journal of Advanced Simulation in Science and Engineering (JASSE).

DOI: https://doi.org/10.15748/jasse.9.198

Tritium-induced damage on polymers and biopolymers: Molecular dynamics simulations and theoretical calculations

Susumu Fujiwara[1*], Haolun Li[1], Ryuta Kawanami[1,2], Kazushi Terakawa[1], Tomoko Mizuguchi[1], Hiroaki Nakamura[3,4], Yoshiteru Yonetani[2], Kazumi Omata[5,6], Seiki Saito[7], Takuo Yasunaga[8], Ayako Nakata[9], Tsuyoshi Miyazaki[9], Takao Otsuka[10], Takahiro Kenmotsu[11], Yuji Hatano[12], Shinji Saito[13]

[1]Kyoto Institute of Technology
[2]National Institute for Quantum and Radiological Science and Technology
[3]National Institute for Fusion Science
[4]Nagoya University
[5]National Center for Global Health and Medicine
[6]Kumamoto University
[7]Yamagata University
[8]Kyushu Institute of Technology
[9]National Institute for Materials Science
[10]RIKEN Center for Biosystems Dynamics Research
[11]Doshisha University
[12]University of Toyama
[13]Institute for Molecular Science

*fujiwara@kit.ac.jp

Abstract. Molecular dynamics (MD) simulations and theoretical calculations are carried out to study the tritium-induced damage of polymers and biopolymers. We deal with several topics related to the tritium-induced damage: (i) MD simulations of structural change of polymers and DNA by *decay effect* in which chemical bonds break by beta decay of substituted tritium to helium-3, (ii) MD simulations of structural change of DNA by *indirect action* in which tritium-induced or radiation-induced hydroxyl radicals damage DNA, and (iii) theoretical calculations of structural change of polymers by *decay effect* based on the linear response theory. In this paper, we briefly introduce these results.

Keywords: Molecular dynamics simulation, Polymer, Biopolymer, damaged DNA, Tritium

1. Introduction

Tritium is a radioactive isotope of hydrogen and disintegrates to helium-3 by beta decay with emissions of a beta-ray and an antineutrino with a half-life of 12.323 years [1,2]. Beta rays may cause damage on polymers and biopolymers both directly (known as *direct action*) and indirectly (known as *indirect action*). Moreover, if substituted tritium in polymers and biopolymers decays to helium-3, their structure may be changed by breaking chemical bonds, which is called *decay effect*. Tritium-induced damage on polymers and biopolymers include the damage by indirect action of free radicals or active oxygen generated by the tritium beta decay and that by decay effect of substituted tritium of polymers and biopolymers.

2. Our research topics

Our research topics cover several ones related to the tritium-induced damage on polymers and biopolymers:

(i) MD simulations of structural change of polymers and DNA by decay effect in which chemical bonds break by beta decay of substituted tritium to helium-3 [3-6],

(ii) MD simulations of structural change of DNA by indirect action in which tritium-induced or radiation-induced hydroxyl radicals damage DNA,

(iii) theoretical calculations of structural change of polymers by *decay effect* based on the linear response theory.

In the talk, we give a brief introduction to these results.

References

[1] *Tritium: Fuel of Fusion Reactors,* edited by T. Tanabe (Springer Japan, 2017).

[2] P. C. Souers, Hydrogen Properties for Fusion Energy (University of California Press, California, 1986).

[3] S. Fujiwara, H. Nakamura, H. Li, H. Miyanishi, T. Mizuguchi, T. Yasunaga, T. Otsuka, Y. Hatano, S. Saito, Computational strategy for studying structural change of tritium-substituted macromolecules by a beta decay to helium-3, *J. Adv. Simul. Sci. Eng*., 6:1 (2019), 94-99.

[4] H. Li, S. Fujiwara, H. Nakamura, T. Mizuguchi, T. Yasunaga, T. Otsuka, T. Kenmotsu, Y. Hatano, and S. Saito, Structural change of tritium-substituted polymeric materials by a beta decay: A molecular dynamics study, *Plasma Fusion Res.*, 14 (2019), 3401106.

[5] H. Nakamura, H. Miyanishi, T. Yasunaga, S. Fujiwara, T. Mizuguchi, A. Nakata, T. Miyazaki, T. Otsuka, T. Kenmotsu, Y. Hatano, S. Saito: Molecular dynamics study on DNA damage by tritium disintegration, *Japanese J. Appl. Phys*., 59 (2019), SAAE01.

[6] H. Li, S. Fujiwara, H. Nakamura, T. Mizuguchi, A. Nakata, T. Miyazaki and S. Saito, Structural change of damaged polyethylene by beta-decay of substituted tritium using reactive force field, *Jpn. J. Appl. Phys.*, 60 (2021), SAAB06.

Effect of tritium β decay in deoxy-D-ribose on duplex of telomeric DNA

Kento Ishiguro[1,*], Hiroaki Nakamura[1,2], Takuo Yasunaga[3], Susumu fujiwara[4], Tomoko Mizuguchi[4], Ayako Nakata[5], Tsuyoshi Miyazaki[5], Takahiro Kenmotsu[6], Yuji Hatano[7], Shinji Saito[8], Yoshiteru Yonetani[9]

[1]Department of Electrical Engineering, Nagoya University, [2]National Institute for Fusion Science, [3]Kyushu Institute of Technology, [4]Kyoto Institute of Technology, [5]National Institute for Materials Science, [6]Doshisha University, [7]University of Toyama, [8]Institute for Molecular Science, [9]National Institutes for Quantum and Radiological Science and Technology

[*]naka-lab@nifs.ac.jp

Abstract. We confirm the relationship between the number of tritium substitutions for hydrogen in DNA and the occurrence of double strand breaks (DSBs) by using MD simulation. As the result, to induce DSB by the decay effect, it is necessary to damage the DNA with a large number of decays.

Keywords: Molecular dynamics simulation, Double strand break, Telomeric DNA, Tritium

1. Introduction

Tritium is known as a fuel of nuclear fusion power generation. Tritium becomes helium-3 (^{3}He) and β-electron (β-radiation) when it decays. The energy of β-ray, emitted from tritium, is small ($\leq$ 18.6 keV), so there is little effect on the human body from external exposure[1]. Therefore, the main problem is the damage caused by internal exposure.

One of the major damages that DNA suffers from internal exposure to radiation is double-strand breaks (DSBs). It can be repaired, but it can also lead to cell death or cell cancer. In tritium's β-decay, there is three different processes damage DNA, called direct effect, indirect effect, and disintegration effect. In the research by a single molecule observation (SMO), the influence of the disintegration effect has not been clarified. We confirm the relationship between the number of tritium substitutions for hydrogen in DNA and the occurrence of DSBs by using MD simulation[8, 9, 10, 11].

2. Molecular dynamics simulation

By using telomeric DNA (d (TCTAGGGTTAGGGTTAG)$_2$) in 3SJM[2], we prepared the initial structure as (Fig. 1). The size of simulation box is 100 Å $\times$ 100 Å $\times$ 100 Å.

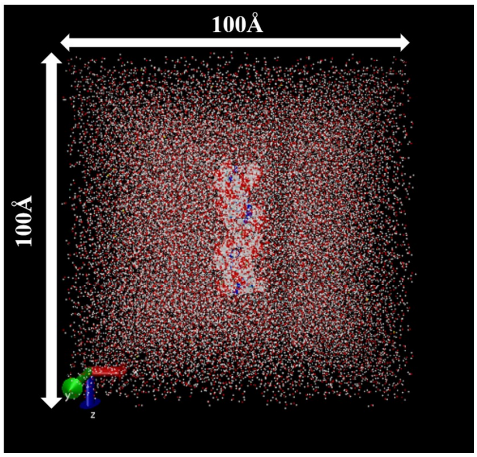

Figure 1: Simulation model. A telomeric DNA structure is surrounded by water molecules and charge neutralized by sodium and chloride ions.

We use Large-scale Atomic/Molecular Massively Parallel Simulator (LAMMPS)[3][5][6] as the MD code, and a kind of reactive force field [4][7]. Under the conditions of 310 K and 1 atm, DNA is shaken around in the box. The hydrogen at the 5' and 5" positions of the main strand was replaced by tritium (Fig. 2), and the decay to helium-3 was simulated as if the replaced hydrogen had been removed.

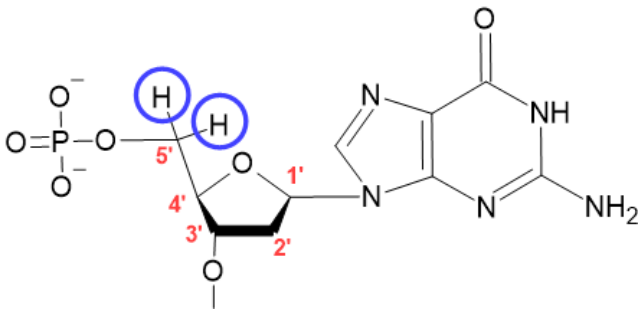

Figure 2: A part of DNA (the base is guanine). Two blue circles indicate the 5' and 5" hydrogens, which are replaced by tritium.

3. Results

As a result, in the case of hydrogen removal at seven bases each in both main strands, it was divided into at least two fragments, and into at least three fragments in the case of removal at all bases (Fig. 3). No cleavage occurred in the case where one base was removed from each of the two main chains, as in the case of removal at no base (Fig. 4).

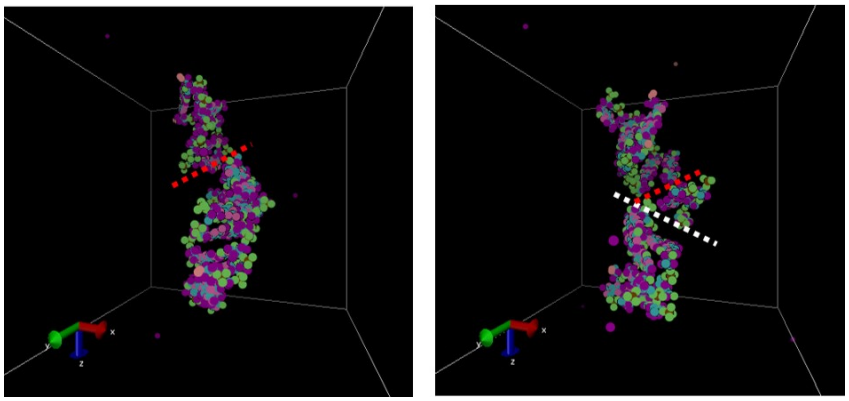

Figure 3: Simulation results. The left figure is the case of hydrogen removal at seven bases in each strand (total 28 hydrogen are removed). DSBs occurs with the red dotted line. The right figure is the case of removal at all bases (total 68 hydrogen are removed). DSBs occur with the red and white dotted line.

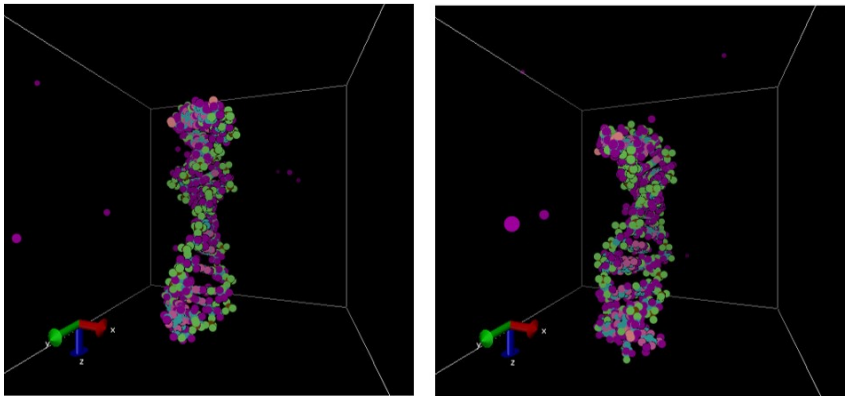

Figure 4: Simulation results. The left figure is the case of hydrogen removal at one base in each strand (total 2 hydrogen are removed). The right figure is the case that no hydrogen is removed. In both cases, DSBs does not occur.

4. Conclusion

In order to induce DSBs by the decay effect, it is necessary to damage the DNA with a large number of decay pairs.

Acknowledgments

The research was supported by Grants-in-Aid for Scientific Research (C), Nos.18K11416, 19K03800 and 21K19845 from the Japan Society for the Promotion of Science, and by the

NIFS Collaborative Research Programs NIFS20KNTS066, NIFS20KNTS070, NIFS20KNSS149, NIFS20KNSS150 and NIFS21KKGS030. The computations were performed using Research Center for Computational Science, Okazaki, Japan.

References

[1] H. Tauchi, T. Umata, and A. Tachibana, J. Plasma Fusion Res. Vol. 88, No. 2, p. 119,2012.

[2] S.K. Nair, S.K. Sliverman, J.H. Chen, and Y. Xiao, Crystal structure analysis of TRF2-Dbd-DNA complex. 2012.

[3] Steve Plimpton, Fast parallel algorithms for short-range molecular dynamics, Journal of Computational Physics, Vol. 117, No. 1, pp. 1–19, 1995.

[4] H. M. Aktulga, J. C. Fogarty, S. A. Pandit, and A. Y. Grama. Parallel reactive molecular dynamics: Numerical methods and algorithmic techniques, Parallel Computing, Vol. 38, pp. 245–259, 2012.

[5] H. M. Aktulga, C. Knight, P. Coffman, K. A. OHearn, T. R. Shan, and W. Jiang, Optimizing the performance of reactive molecular dynamics simulations for multi-core architectures, International Journal of High Performance Computing Applications, toappear.

[6] Adri C. T. van Duin, Siddharth Dasgupta, Francois Lorant, and William A. Goddard.Reaxff: A reactive force field for hydrocarbons, The Journal of Physical Chemistry A, Vol. 105, No. 41, pp. 9396–9409, 2001.

[7] Sung-Yup Kim and Adri C. T. van Duin. Simulation of titanium metal/titanium dioxide etching with chlorine and hydrogen chloride gases using the reaxff reactive force field, The Journal of Physical Chemistry A, Vol. 117, No. 27, pp. 5655–5663, 2013. PMID:23750609.

[8] H. Nakamura, H. Miyanishi, T. Yasunaga, S. Fujiwara, T. Mizuguchi, A. Nakata, T. Miyazaki, T. Otsuka, T. Kenmotsu, Y. Hatano, and S. Saito, Jpn. J. Appl. Phys. 59, SAAE01 (2020). [DOI: 10.7567/1347-4065/ab460d]

[9] H. Li, S. Fujiwara, H. Nakamura, T. Mizuguchi, A. Nakata, T. Miyazaki and S. Saito, Jpn. J. Appl. Phys. 60, SAAB06 (2021). [DOI: 10.35848/1347-4065/abbdc8]

[10] H. Li, S. Fujiwara, H. Nakamura, T. Mizuguchi, T. Yasunaga, T. Otsuka, T. Kenmotsu, Y. Hatano, and S. Saito, Plasma Fusion Res. 14, 3401106 (2019). [DOI: 10.1585/pfr.14.3401106]

[11] S. Fujiwara, H. Nakamura, H. Li, H. Miyanishi, T. Mizuguchi, T. Yasunaga, T. Otsuka, Y. Hatano and S. Saito, J. Adv. Simulat. Sci. Eng. 6(1), 94-99 (2019). [DOI: 10.15748/jasse.6.94]

JSST 2021

Examination of Coil Resistance Measurement during Wireless Power Transfer and Comparison with Finite Element Analysis

Daigo Yonetsu[1,*], Yuji Nakano[1], Naoya Hamano[1]

[1]Department of Electrical and Electronics Engineering, Kansai University

[*]yonetsu@kansai-u.ac.jp

The full paper of this paper has been published in Journal of Advanced Simulation in Science and Engineering (JASSE).

DOI: https://doi.org/10.15748/jasse.9.40

Study on Parallel Coupled Analysis of High-Frequency Electromagnetic Field and Heat Conduction Problems of Numerical Human Body Model

Shin-ichiro Sugimoto[1*], Amane Takei[2], Masao Ogino[3]

[1]Department of Mechanical Engineering, Faculty of Engineering, Hachinohe Institute of Technology

[2]Department of Electrical and System Engineering, Faculty of Engineering, University of Miyazaki

[3]Department of Information Systems, Faculty of Informatics, Daido University

*sugimoto@hi-tech.ac.jp

Abstract. This paper deals with a high-frequency electromagnetic field - heat conduction coupled analysis of a numerical human body model in a parallel environment. The iterative substructuring method has been considered to be an efficient parallel computing method.

Keywords: High-Frequency Electromagnetic Field - Heat Conduction Coupled Analysis, Parallel Computing, Finite Element Method, Hierarchical Domain Decomposition Method, Numerical Human Body Model

1. Introduction

In order to evaluate an effect of cancer treatment by hyperthermia quantitatively, we have been studying its high-frequency electromagnetic field – heat conduction coupled analysis in a parallel environment. In our study, the NICT numerical human body model [1] is analyzed. This model uses a binary data format wherein types of organs are encoded using voxels with a size of 2 mm. However, the boundaries of its different materials are not smooth; thus, unwanted reflection and scattering of electric fields has been observed in numerical simulator results. To reduce this numerical noise, some mesh smoothing techniques with tetrahedral elements have been developed [2]. Furthermore, the diameters of cancers treated with hyperthermia are several millimeters. Therefore, elements must be refined to obtain sufficient accuracy. However, there are approximately 130 billion degrees of freedom (DOFs) provided that the element sizes are 0.25 mm. In addition, smoothing techniques increase the DOFs further.
The efficient parallel computing method for large-scale finite element analysis (FEA) that we

have been studying is the iterative substructuring method in the form known as the domain decomposition method (DDM) based on the iterative method [3]. It is expected to obtain scalable parallel efficiency on distributed memory parallel computers with the implementation of a Hierarchical Domain Decomposition Method (HDDM) [4].

The HDDM has been applied to the large-scale FEA of structural mechanics [5], and heat transfer [6]. In structural analysis, the problem with 100 billion DOFs has been analyzed [7]. In addition, the HDDM has been applied to the large-scale FEA of electromagnetics [8]-[9], too. In recent years, it has been clarified that the conjugate orthogonal conjugate residual (COCR) method [10] is very effective for problems that involve symmetric systems with complex numbers and ill-conditioned systems [11]-[12]. Thus, in the electromagnetic field analysis, high-frequency electromagnetic field problems have been solved with 30 billion DOFs [11] and 130 billion DOFs [13]. These achievements have been implemented as a parallel electromagnetic field analysis module called ADVENTURE_Magnetic [14].

In order to analyze large-scale problems, the parallel analysis of the electromagnetic field problem has been mainly studied. As the next step, a parallel coupled analysis of the high-frequency electromagnetic field and the heat conduction problems is considered. In this paper, the numerical human body model involving 30 million DOFs is analyzed in the parallel environment.

2. High-frequency electromagnetic field – heat conduction coupled problem

Since the hyperthermia heats the human body from normal body temperature (36-37 degrees Celsius) to the temperature at which the cancer dies (42-43 degrees Celsius), the temperature change is only about 5 degrees; thus, changes in physical quantities related to the electromagnetic field analysis due to temperature are negligible. Therefore, in this paper, a one-way coupled analysis using the results of the electromagnetic field analysis for the heat conduction analysis is performed.

The numerical human body model is composed of voxels generated from tomographic images obtained by CT or MRI. Therefore, the boundaries of its different materials are not smooth; thus, unwanted reflection and scattering of electric fields has been observed in numerical simulator results. To reduce this numerical noise, some mesh smoothing techniques with tetrahedral elements will be used in the future; thus, the HDDM based on the finite element method is used for the numerical analysis, in this paper. Since the one-way coupled problem is considered, separate solvers are used for the electromagnetic field and heat conduction analyses. In this paper, ADVENTURE_Magnetic is used for the electromagnetic field analysis, and a parallel heat conduction analysis module called ADVENTURE_Thermal [14] is used for the heat conduction analysis.

In the coupled analysis, E_h which is the electric field approximated by the edge elements is obtained by the high-frequency electromagnetic field analysis, first. Then, the eddy current density Je_h [A/m^2] for each element is obtained as follows:

$$Je_h = \sigma E_h. \tag{1}$$

where σ[S/m] is the conductivity. Here, Je_h is a complex number ($= J_r + iJ_i$), and its amplitude J_m and effective value J_E are obtained as follows:

$$J_m = \sqrt{J_r^2 + J_i^2}, \tag{2}$$

$$J_E = \frac{1}{\sqrt{2}} J_m. \quad (3)$$

Then, the heat generation density $\tilde{f}$[W/m^3] for each element due to heating is obtained as follows:

$$\tilde{f} = \frac{J_E^2}{\sigma} = \frac{J_m^2}{2\sigma} = \frac{J_r^2 + J_i^2}{2\sigma}. \quad (4)$$

In the heat conduction analysis, the temperature distribution in the body is obtained using $\tilde{f}$, and the heat production by muscles.

3. Hierarchical Domain Decomposition Method (HDDM)

In the HDDM, an original domain Ω is divided without overlapping elements. Furthermore, the original domain is hierarchically divided into parts, which are further decomposed into smaller domains called subdomains.

$$\Omega = \bigcup_{i=0}^{N_p-1} \bigcup_{j=0}^{N_s-1} \Omega^{(i,j)}, \quad (5)$$

where $\Omega^{(i,j)}$ denotes the subdomain j in the part i, the superscript (i,j) corresponds to the subdomain $\Omega^{(i,j)}$. N_p and N_s are the number of parts and that of subdomains in each part, respectively. N_s is equal for all parts. In Fig. 1, the original domain is first divided into two parts, and then further decomposed into two subdomains within each part ($N_P = N_s = 2$). The solid circles in the figure are the DOFs shared between parts and subdomains, which are called interface DOFs.

In the HDDM, the interface problem which is obtained by statically reducing DOFs to the interface DOFs is solved by the parallel iterative methods such as the Conjugate Gradient method and COCR method.

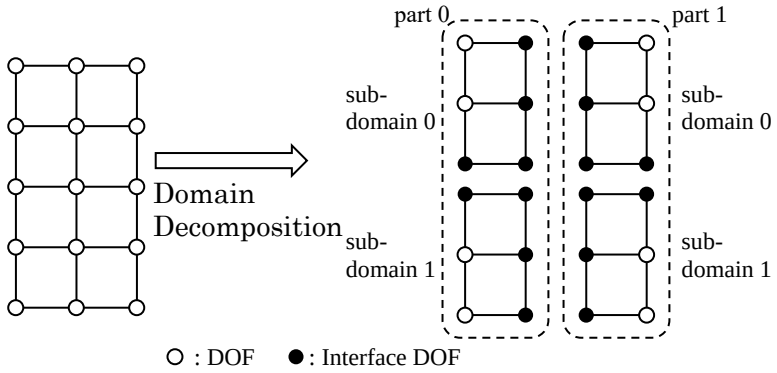

Fig. 1. Hierarchical domain decomposition.

4. Numerical example

The NICT numerical human body model involving 30 million DOFs provided that the element sizes are 4 mm (Fig. 2) is analyzed in parallel environment. Assumption of the treatment of the chest, the electromagnetic waves are emitted from the antenna in front of the chest. The physical quantities of each organ are quoted from [15] and [16].

Fig. 3 and Fig. 4 show the eddy current density and temperature distribution, respectively. It

can be confirmed that the eddy current density around the heart near the antenna is strong, and temperature around the heart is rising.

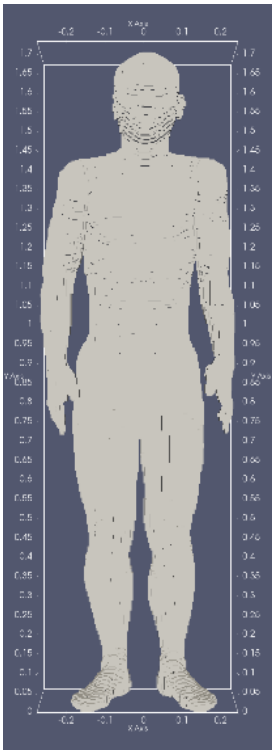

Fig. 2. Numerical human body model with 30 million DOFs.

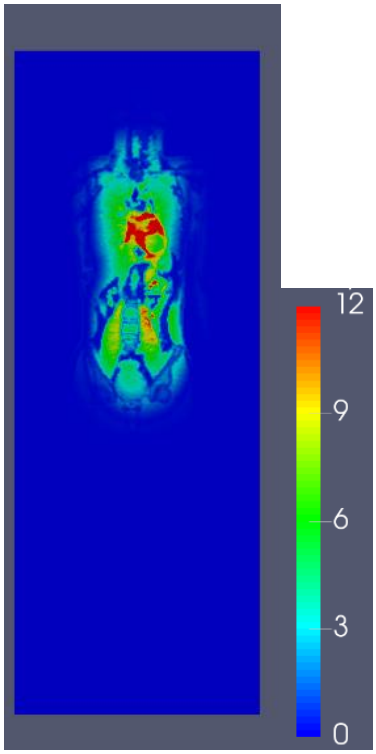

Fig. 3. Result of the electromagnetic field analysis. Eddy current density (real part) [A/m^2]

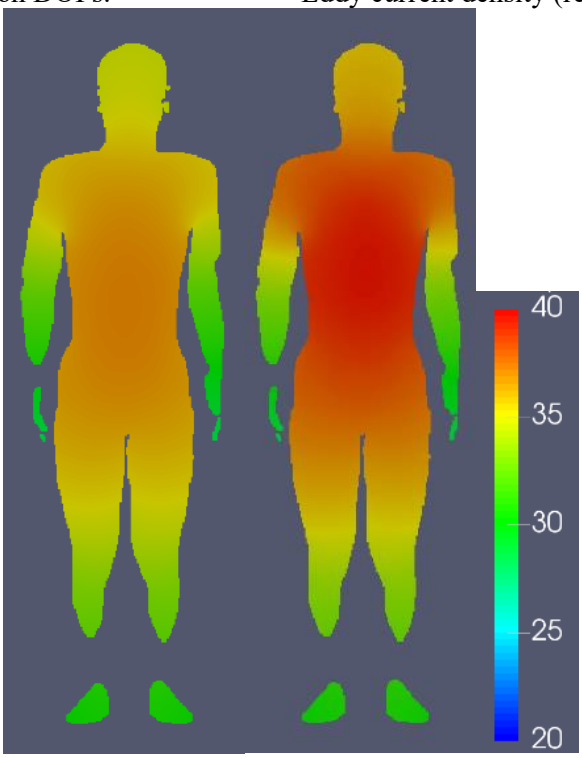

Fig. 4. Results of the heat conduction analysis (body temperature (degrees Celsius)). Left: without heating, Right with heating.

5. Conclusions

In this paper, the high-frequency electromagnetic field – heat conduction coupled analysis of the numerical human body model involving 30 million DOFs provided that the element sizes are 4 mm has been attempted in the parallel environment. In the future, the analysis of larger models and the analysis considering the influence of blood flow will be tried.

Acknowledgment

This work is partially supported by Takahashi Industrial and Economic Research Foundation, JSPS KAKENHI Grant Number 17H02829, and Aomori foundation for promotion of technological education.

References

[1] Electromagnetic Compatibility Laboratory, Applied Electromagnetic Research Institute, National Institute of Information and Communications Technology HP: http://emc.nict.go.jp/index_e.html

[2] A. Takei, K. Murotani, S. Sugimoto, M. Ogino, H. Kawai: High-Accuracy Electromagnetic Field Simulation using Numerical Human Body Models, *IEEE Transaction on Magnetics*, Vol.52, Issue 3, 7402704 (2016), 4p.

[3] A. Quarteroni, A. Valli: Domain Decomposition Methods for Partial Differential Equations, *Clarendon Press, Oxford* (1999).

[4] R. Shioya, G. Yagawa: Iterative domain decomposition FEM with preconditioning technique for large scale problem, *ECM'99 Progress in Experimental and Computational Mechanics in Engineering and Material Behaviour* (1999), pp.255-260.

[5] S. Yoshimura, R. Shioya, H. Noguchi, T. Miyamura: Advanced general-purpose computational mechanics system for large-scale analysis and design, *Journal of Computational and Applied Mathematics*, Vol.149, Issue 1 (2002), pp.279-296.

[6] A.M.M. Mukaddes, M. Ogino, M, H. Kanayama, R. Shioya: A scalable balancing domain decomposition based preconditioner for large scale heat transfer problems, *JSME International Journal Series B Fluids and Thermal Engineering*, Vol,49, No.2 (2006), pp.533-540.

[7] M. Ogino, R. Shioya: Scalable non-overlapping domain decomposition method for finite element simulations with 100 billion degrees of freedom model, *Proceedings of the 1st International Conference on Computational Engineering and Science for Safety and Environmental problems* (2014), pp.96-99.

[8] H. Kanayama, S. Sugimoto: Effectiveness of A-ϕ method in a parallel computing with an iterative domain decomposition method, *IEEE Transactions on Magnetics*, Vol.42, Issue 4 (2006), pp.539-542.

[9] A. Takei, S. Yoshimura, H. Kanayama: Large-scale parallel finite element analyses of high frequency electromagnetic field in commuter trains, *Computer Modeling in Engineering & Sciences*, Vol.31, No.1 (2008), pp.13-24.

[10] T. Sogabe, S.L. Zhang: A COCR method for solving complex symmetric linear systems, *Journal of Computational and Applied Mechanics*, Vol.199, No.2 (2007), pp.297-303.

[11] S. Sugimoto, A. Takei, M. Ogino: Finite Element Analysis with Tens of Billions of Degrees of Freedom in A High-Frequency Electromagnetic Field, *Mechanical Engineering Letters*, Vol.3, p.16-0067 (2017), 10p.

[12] M. Ogino, A. Takei, H. Notsu, S. Sugimoto, S. Yoshimura: Finite element analysis of high frequency electromagnetic fields using a domain decomposition method based on the COCR method, *Theoretical and Applied Mechanics Japan*, Vol.61 (2013), pp.173-181.

[13] S. Sugimoto, A. Takei, M. Ogino: High-Frequency Electromagnetic Field Analysis with 130 Billion of Degrees of Freedom, *The 38th JSST Annual Conference, International Conference on Simulation Technology*, (2017), pp.290-295.

[14] ADVENTURE Project HP: https://adventure.sys.t.u-tokyo.ac.jp/

[15] Human organs property Database for Computer simulation, RIKEN: http://cfd-duo.riken.go.jp/cbms-mp/index.htm

[16] Tissue Properties Database V4.0: https://itis.swiss/virtual-population/tissue-properties/downloads/database-v4-0/

Analysis of electrostatically induced short-circuit current in a human body on a 500 kV transmission tower

Shoji Hamada[1*]

[1]Department of Electrical Electronic and Information Engineering, Kansai University

*shamada@kansai-u.ac.jp

Abstract. We performed the numerical analysis of electrostatically induced steady-state AC short-circuit currents running through a human model on a transmission tower model. The transmission tower model was 80.22 m tall with 500 kV double-circuit three-phase overhead conductors and two ground wires. The NICT TARO model was used for the human model after modifying the posture and resolution. The toe of the left foot of the human model was in direct contact with the bottom cross arm of the tower model, and we analyzed the short-circuit current flowing through the contact point. The model comprised of cubic voxels with a side length of 2 cm, and the overall rectangular region occupied by the model was 27.5 m × 270 m × 165 m, including the mirror image under the ground plane. A voxel-based fast multipole surface charge simulation method was used for the analysis. By applying a single-circuit three-phase voltage of 50Hz, short-circuit AC currents of 441 μA and 500 μA flowed in the standard posture and left-arm-raised posture models, respectively. These currents were about half the reference level of the contact current specified in the international guidelines for occupational workers.

Keywords: Electrostatically induced AC current, Voxel model, Transmission tower, Human body

1. Introduction

High-voltage power equipment electrostatically induces AC electric fields and currents in humans in close proximity [1]-[3]. The induced fields and currents could cause anxiety and discomfort in the general public, and health issues in occupational workers. Therefore, international guidelines have specified basic restrictions of internal electric fields and reference levels of flowing currents [4]. Electrostatically induced electric fields and currents have been widely researched using numerical human models to prevent the fields and currents from exceeding the specified values [2], [3]. In this study, we quantitatively investigated the induced short-circuit contact current flowing through the occupational workers working on a transmission tower through numerical analysis.

2. Numerical calculation method

A two-step process method is known as a method for calculating the electrostatically induced AC current density distribution inside the human body [3], [5]. In the first stage, we calculate the induced electric charge distribution on the body surface while assuming that the human body

is a perfect conductor. This assumption is based on the fact that the electric field inside the body is about 6 to 7 orders of magnitude smaller than the applied electric field outside the body [3], [5]. We can convert this induced charge distribution into the induced conductive current density distribution on the body surface. In the second stage, we calculate the internal body current distribution on the basis of the continuity of the conductive current. Since the short-circuit current flowing through the grounded human body part equals the sum of the current injected through the body surface, we can calculate the short-circuit current using the first stage calculation alone. The first stage requires electrostatic field analysis of the system of conductors, which was performed by the voxel-based fast multipole surface charge simulation method in this study [3], [6]. The voxel surface that forms a boundary between the conductor and the air is regarded as a square surface element, and the surface charge densities on the surface elements are treated as unknown variables. We construct simultaneous linear equations based on the Dirichlet condition of electric potential, which is solved using an iterative solver with the fast multipole method. The amount of calculation required for one step of the iterative solver is O(N), where N is the number of unknowns. Note that $N = O(D^2)$, where D is a representative value of the number of divisions per dimension in the three-dimensional model.

3. Specifications of calculation model

Figure 1 shows a voxel model composed of a human, a transmission tower, six bundled conductors, and two ground wires. The tower was a 500 kV three-phase double-circuit transmission tower. The tower was 80.22 m tall, and the supporting points of the overhead conductors in the A, B, and C phases were 71.52 m, 58.32 m, and 45.12 m tall, respectively. The conductor distance between two-circuits was 18.72 m. The bundled conductors consist of four sub-conductors. The span length, the sag, the bundle spacing, and the radius of the conductor were 400 m, 10 m, 40cm, and 2 cm, respectively. The conductor shape was expressed by a quadratic function. Figure 2 shows the close-up view of the human model on the tower model, simulating a worker who accidentally strays into the live line side. The NICT TARO model was used as the human model, and the posture deformation and smooth resampling were performed using a software tool provided by the NICT [7], [8]. A standard posture model and a left-arm-raised posture model were used in this study. The human model was placed upright with the toe of the left foot in direct contact with the bottom cross arm of the tower. The human body, tower, conductors, and ground wires were regarded as perfect

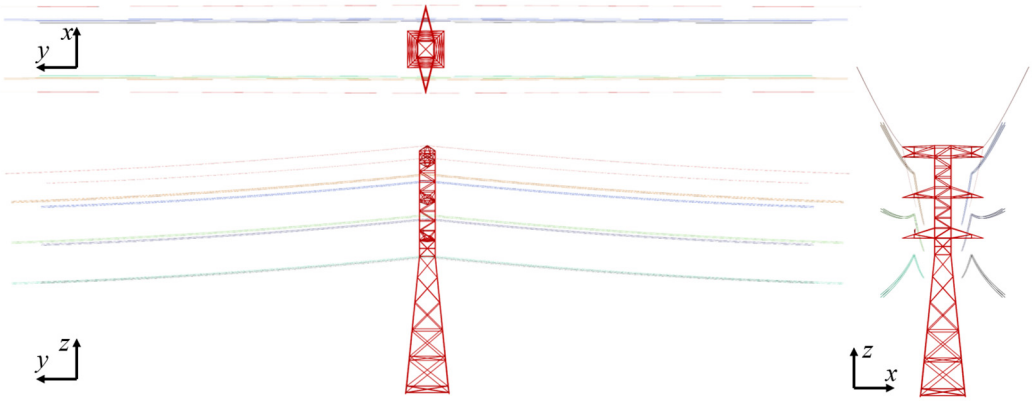

Fig. 1. A model composed of a human, a tower, 6 conductors, and 2 ground wires.

conductors. However, the insulators were ignored, or their relative permittivities were approximated to one. The angle steel of the tower was approximated to a rectangular or a cylinder having cross-sectional width of 20 or 30 cm. To consider the image electric charges, the model above the ground was mirror-inverted and duplicated underground. Cubic voxels with the side length of 2 cm were used. The dimensions of the entire region, including the image model, were 27.5 × 270 × 165 m or 1375 × 13500 × 8250 voxels, and a lossless compression technique was used to handle the voxel model [9]. The number of surface elements (= the number of unknowns in the numerical calculation) was approximately 15 million. A unit voltage was applied to each phase to perform one numerical calculation, and a total of three calculations were performed for the three phases. Then the phasors of all three phases were combined to obtain the maximum value of the induced current.

4. Calculation result

Figure 3 shows the normalized potential distribution when the voltages were –0.5, 1.0, and –0.5 V for phases A, B, and C, respectively, in the standard and left-arm-raised postures. The computer used for the analysis had the following specifications: CPU: AMD Ryzen Threadripper 3990X; main memory: 256 GB. Approximately 27 min were required to generate the model. Whereas the field calculation took approximately 8 min for a single voltage energization and required 6.7GB of memory. A rated voltage of 500 kV means the root mean square value of the line voltage, thus the short-circuit current was also calculated as the root mean square value. When the three-phase 50Hz voltage was applied, short-circuit currents of 441 μA and 500 μA were induced in the standard and the left-arm-raised posture models, respectively. Raising one arm increased the current by 13.4%. The reference level of the contact current in occupational workers specified in the ICNIRP guidelines [4] is 1000 μA. Therefore, the calculated values are approximately half the reference level value. Furthermore, the rms current of 500 μA corresponds to the peak body-surface charge amount of 2.25 μC,

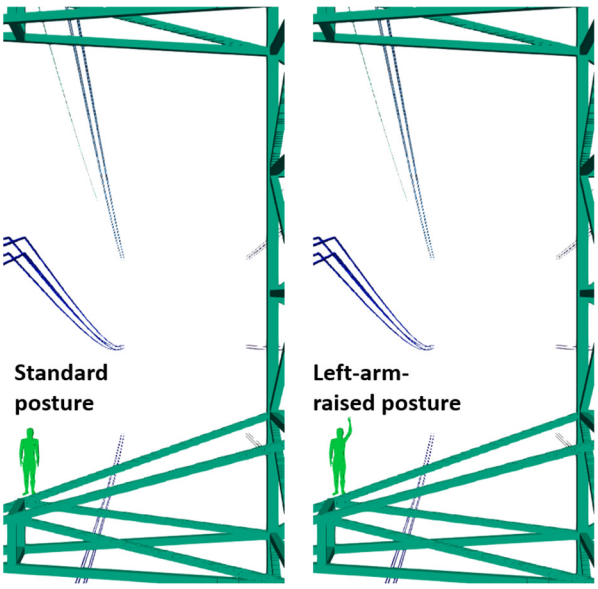

Fig. 2. Close-up view of human models.

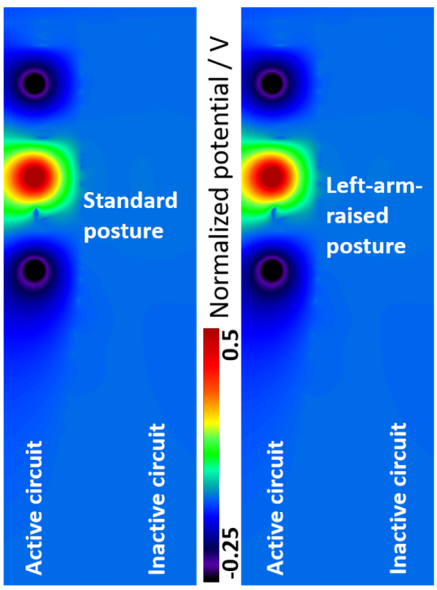

Fig. 3. Potential distribution.

which is approximately 10 times greater than the perception threshold value of 0.2–0.3 μC when stimulated by the transient discharge current due to electrification [10].

5. Summary

We performed the numerical analysis of the 50Hz short-circuit currents electrostatically induced in the voxel human model on the 500 kV transmission tower model. The voxel human model NICT TARO was used after posture deformation and resolution resampling. The model comprised of voxels with a side length of 2 cm and occupied a rectangular region of 27.5 m × 270 m × 165 m. On applying a three-phase voltage, a short-circuit current of 500 μA (rms) was observed when using the left-arm-raised posture model. This current was half the reference level value of the contact current for occupational workers specified in the ICNIRP guidelines. In the future, we plan to reduce the voxel size and analyze the electric field and current in the human body.

References

[1] D. W. Deno: Current induced in the human body by high voltage transmission line electric field - measurement and calculation of distribution and dose, *IEEE Trans. on PAS*, PAS-96:5 (1977), 1517-1527.

[2] H. Tarao, N. Hayashi, and K. Isaka: Estimation of short-circuit current induced by ELF uniform electric fields in grounded humans with different body shapes base on a semi-ellipsoidal model, *Biomed. Phys. Eng. Express*, 6 (2020) 1-12.

[3] S. Hamada: Calculation of electrostatically induced electric fields in human models using a two-step process method of voxel-based fast multipole surface charge simulation method, *IEEJ Trans. FM*, 140:10, (2020) 481-490 (in Japanese).

[4] ICNIRP: Guidelines for limiting exposure to time-varying electric and magnetic fields (1 Hz to 100 kHz), *Health Phys.*, 99:6 (2010) 818-836.

[5] K. Chen, H. Chuang, C. Lin: Quantification of interaction between ELF-LF electric fields and human bodies, *IEEE Trans. on Biomedical Engineering*, BME-33:8 (1986) 746-756.

[6] S. Hamada and T. Kobayashi: Analysis of electric field induced by ELF magnetic field utilizing fast-multipole surface-charge-simulation method for voxel data, *IEEJ Trans. FM*, 126:5, (2006) 355-362 (in Japanese).

[7] T. Nagaoka, S. Watanabe, K. Sakurai, E. Kunieda, S. Watanabe, M. Taki, Y. Yamanaka: Development of realistic high-resolution whole-body voxel models of Japanese adult males and females of average height and weight, *Phys. Med. & Biol.*, 49 (2004) 1-15.

[8] T. Nagaoka, and S. Watanabe: Postured voxel-based human models for electromagnetic dosimetry, *Phys. Med. & Biol.*, 53 (2008) 7047-7062.

[9] S. Hamada: Surface charge simulation method based on lossless compression voxel models, *2021 annual meeting record IEEJ*, 1-024 (2021) 34 (in Japanese).

[10] JNIOSH: Recommendations for requirements for avoiding electrostatic hazards in industry 2007, *JNIOSH-TR-NO*. 42, (2007) (in Japanese)

JSST 2021

Comparative Study of Strongly Coupled Fluid and Structure Systems With Computational Control

Vinay Shankar[1] and Daisuke Ishihara[2,*]

[1,2,*]Department of Intelligent and Control Systems, Kyushu Institute of Technology, 680-4 Kawazu, Iizuka, Fukuoka, 820-8502, Japan

[*]ishihara.daisuke399@mail.kyutech.jp

Abstract. Fluid-structure interaction (FSI) is a typical multi-physics coupled system. The interaction affects the vibration characteristics of coupled system and thus such complex system must be controlled taking into account the interaction. This paper proposes computational control based on the finite element method for strongly coupled analysis of FSI. The vibration characteristics and the effect of direct velocity and displacement feedback (DVDFB) control in FSI for soft and stiff structure will be investigated and the stability of two types of structures will be compared. The results for a soft material show a reduction in displacement and amplitude and more stability compared to the stiff material.

Keywords: Finite element method, Direct velocity and displacement feedback control, Active control, Fluid-structure interaction

1. Introduction

A lot of researches is ongoing for development of insect-like flapping wings based on MEMS technology for micro and nano air vehicles. There are many challenges regarding the design and implementation of the flight mechanism due to coupled systems, such as FSI. Such complex system requires proper control of flapping wings. In computational control, multi-field system interaction with control is simulated [1]. This paper proposes computational control based on the finite element method (FEM) for the coupled analysis of FSI for the stiff and soft structures. Active DVDFB control [2] is employed to investigate the vibration characteristics and the stability of soft and stiff structures is compared.

In this study, FSI is implemented using a monolithic approach. The projection method is employed to solve FSI [3]. Active DVDFB control is incorporated with FSI. Few researchers have applied active control to FSI [2], [4], [5]. Here, we use active DVDFB control to investigate the vibration characteristics and compare the stability of soft and stiff structures. FSI with active control have potential application in sensors and actuators such as energy harvesters which control the flapping of wings to fly freely.

2. Methodology

A FEM for FSI with DVDFB control is proposed. The monolithic equations for the FSI system is split into its subsystem algebraically [3].

$$ {}_{\mathrm{L}}\mathbf{M}^{t+\Delta t}\mathbf{a}^{(k)} + \mathbf{C}^{t+\Delta t}\mathbf{v}^{(k)} + \mathbf{N} + \mathbf{q}^{t+\Delta t}\mathbf{u}^{t}(k) - \mathbf{G}^{t+\Delta t}\mathbf{p}^{(k)} = \mathbf{g}, \qquad {}_{\mathrm{T}}\mathbf{G}^{t+\Delta t}\mathbf{v}^{(k)} = 0, \qquad (1a, 1b) $$

where $\mathbf{M}$ is the mass matrix, $\mathbf{C}$ is the diffusion matrix, $\mathbf{N}$ is the convective term vector, $\mathbf{G}$ is the divergence operator matrix, $\mathbf{g}$ is the external force vector, $\mathbf{q}$ is the internal force vector, $\mathbf{a}$, $\mathbf{v}$, $\mathbf{u}$ and $\mathbf{p}$ are the acceleration, velocity, displacement and pressure vectors at time $t + \Delta t$, respectively. Control force will be added to the translational degree of freedom of the structural external force in Eq. (1a). The control force equation can be written as [2],

$$ \mathbf{F}_{\mathrm{c}} = -\mathbf{K}_{\mathrm{d}}\mathbf{u} - \mathbf{K}_{\mathrm{v}}\dot{\mathbf{u}}, \qquad (2) $$

where $\mathbf{F}_{\mathrm{c}}$ is the control force, $\mathbf{K}_{\mathrm{d}}$ is the displacement proportional gain, $\mathbf{K}_{\mathrm{v}}$ is the velocity proportional gain, ${}^{t}\mathbf{u}$ and ${}^{t}\dot{\mathbf{u}}$ are the displacement and velocity at previous time step, respectively. $\mathbf{K}_{\mathrm{v}}$ adds damping and $\mathbf{K}_{\mathrm{d}}$ adds stiffness to the system. By varying $\mathbf{K}_{\mathrm{v}}$ and $\mathbf{K}_{\mathrm{d}}$, we can control the damping and stiffness to stabilize the system.

3. Numerical control of soft and stiff structures with FSI

3.1. Soft structure

a. Problem setup

In Fig.1, we perform a numerical simulation of the suppression of vibration characteristics and compare the stability of soft and stiff structures by active DVDFB control. Mok and Wall proposed a flexible flap in a fluid channel which is also regarded as a benchmark problem [6]. The material properties of soft structure can be referred from [3].

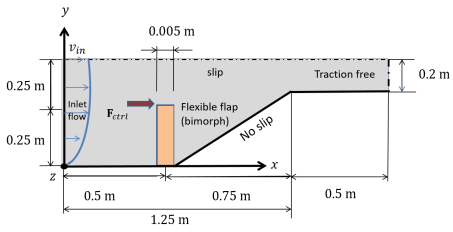

Figure 1: Flexible flapping in converging fluid channel with control

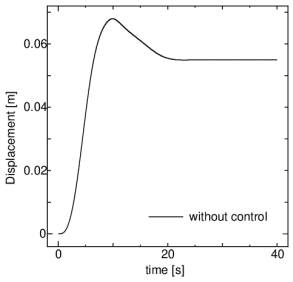

Figure 2: Displacement without control

b. Results and discussion

Figure 2 shows the displacement result obtained using rubber in [3] without DVDFB control. When the control force is applied to the soft structure, there is a significant reduction in

displacement with k_d, as shown in Fig.3. A larger k_d does not produce instability. In previous research [2], when k_d was over 10, it led to numerical instability.

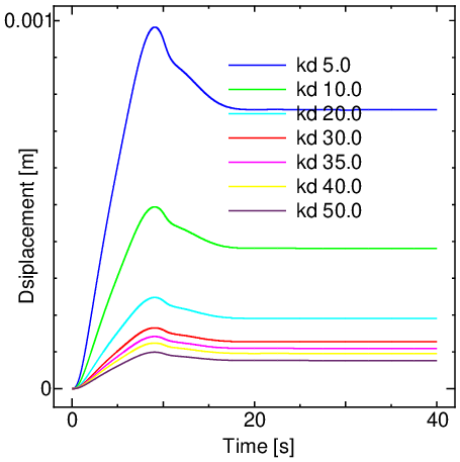

Figure 3: Displacement feedback control k_d for rubber structure

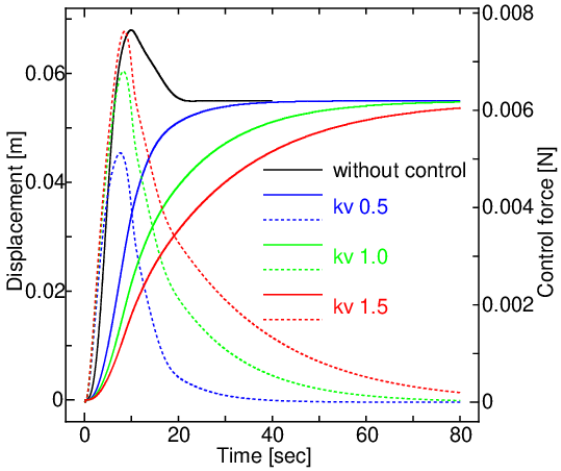

Figure 4: Velocity feedback control and control force k_v for rubber structure

With k_v, there is a significant reduction in amplitude, as shown in Fig. 4. When $k_v > 1.5$, it produces instability. The response of the control force is also shown in Fig. 4. The instability can be removed by using a finer time step.

3.2. Stiff structure

a. Problem setup

In this problem setup, PVDF is used as a stiff structure and the piezoelectric effect of PVDF is neglected. The flexible solid beam in Fig. 1 is replaced with a stiff material, for which the material density, Young's modulus, and Poisson's ratio are $\rho^s = 1800\text{kg/m}^3$, $E^s = 2.0\text{GPa}$, and $v^s = 0.29$, respectively. DVDFB control is applied at the tip of the stiff structure.

b. Results and discussion

We performed a numerical simulation of a stiff structure with DVDFB control. The results in Fig. 5 show a reduction in displacement because of k_d. When $k_d > 27.5$, the large control force produces instability.

In another simulation, k_v is used. The results in Fig. 6 show no reduction in displacement. When $k_v > 4.9$, the control fails and produces instability. The control force is also shown in Fig. 6. There is no instability and no reduction in amplitude because PVDF is a stiff structure. A comparison of the results for PVDF and rubber indicates that better system stability is obtained with rubber. PVDF has a very high stiffness and thus the control force cannot act properly. Rubber is soft and flexible and thus the DVDFB control is more stable.

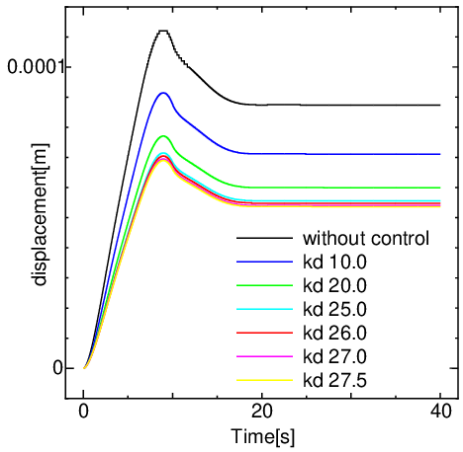

Figure 5: Displacement feedback control k_d for PVDF structure

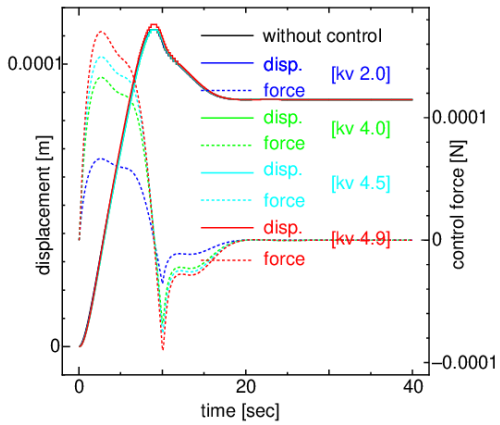

Figure 6: Velocity feedback control and control force k_v for PVDF structure

4. Conclusions

This paper proposed a computational control based on FEM for the FSI of stiff and soft structures. The vibration characteristics were investigated and stability of system with stiff and soft structures were compared with DVDFB control. For a stiff material, namely PVDF, there was a reduction in displacement due to k_d but k_v had no effect. A large control force led to instability. For a soft material, namely rubber, there was a reduction in displacement and amplitude. A larger control force also led to instability, but it was less than that for PVDF. The results show that the proposed computational control algorithm is more stable compared with previous studies.

5. Acknowledgements

This research was supported by the Japan Society for the Promotion of Science under KAKENHI Grant Nos. 19F19379, and 20H04199.

References

[1] A. Mini et al.: *PAMM*, (2016), 15–18.

[2] S. Kaneko et al.: *Computational Mechanics*, (2017), 49–558.

[3] D. Ishihara, T. Horie: *CMES*, 101 (2014), 421–440.

[4] L. Chirco and S. Manservisi: *Fluids*, (2020), 87–102.

[5] A. Mehmood et al. *J. Vib. Control*, (2014), 1137–1147.

[6] D. P. Mok et al.: *Trends in Computational Structural Mechanics*, (2001), 689–698.

Passive motions and aerodynamic performance of insect's flapping wings simulated using the pixel wing model and the strong coupling method

Minato Onishi [1*], Daisuke Ishihara [2]

[1]Department of Computer Science and Systems Engineering, Kyushu Institute of Technology

[2]Department of Intelligent and Control Systems, Kyushu Institute of Technology

*oonishi-m@solid.mse.kyutech.ac.jp

Abstract. In this study, the relationship between the passive motions and the aerodynamic performance in insect's flapping wings is investigated. For this purpose, the pixel wing model flapped in air is analyzed by the strong coupling method for the fluid-structure interaction (FSI). The pixel wing model can deform due to the aerodynamic pressure to produce the passive feathering and cambering motions. Hence, the FSI analysis simulates the aderodynamic forces produced by these passive motions. The aerodynamic force coefficients are evaluated for a variety of wing parameters, and the aerodynamic performance enhancement due to these passive motions is demonstrated.

Keywords: Fluid-structure interaction, Insect's flapping wing, Passive motion, Feathering, Cambering, Pixel wing model, Strong coupling method

1. Introduction

The elastic deformations observed in insect flapping wings are generated by the aerodynamic force from the surrounding air, because insect's wings lack interior muscle [1]. Especially, the feathering and the cambering contribute to the improvement of the aerodynamic performance. As far as we know, there is no study that simulates the feathering and the cambering passively, whose magnitudes are close to those of actual insects. Therefore, the relationship between these passive motions and the aerodynamic performance is still unclear. Hence, in this study, this relationship is investigated using the fluid-structure interaction (FSI) analysis of the pixel wing model flapped in air.

2. Modeling of the insect flapping wing

Fig. 1 shows the employed pixel wing model. The fundamental concept of this model is based on the Ref. [2]. The complicated network of veins is simplified by the leading edge, the cen-

ter vein, and the root vein using the structured shell element. The different mechanical role of the membrane and veins are represented using the different set of the pseudo-elastic material properties. The Young's modulus of the leading edge and root vein are determined based on the flexural ridgidity along the span-wise direction G_s and the chord-wise direction G_c, respectively. The Young's modulus of the center vein is determined such that the flexural rigidity is equal to that of a most significant vein in the center domain of an actual insect's wing. The Young's modulus of the wing membrane E_m is determined from an actual insect's cuticle. Fig. 2 shows the schematic of the flapping motion. Φ and φ are the stroke angle and the angular displacement of flapping motion, respectively. The time history for dφ/dt based on an observation as shown in Fig. 3 is applied to the leading edge. T_φ is the flapping period, and the acceleration and deceleration time t_φ is set to $T_\varphi/8$, which is a typical value. The feathering and the cambering can be simulated from the interaction between the wing and surrounding fluid. The feathering motion can be described using the feathering angular displacement θ as shown in Fig. 4, which is positive in the counter-clockwise direction about the torsional axis. The magnitude of the camber is defined as the ratio of the wing's height C_h to the wing's chord length C_l as shown in Fig. 4, and the sign of the camber is positive if the shape of the camber is concave along the direction of the flapping translation [3].

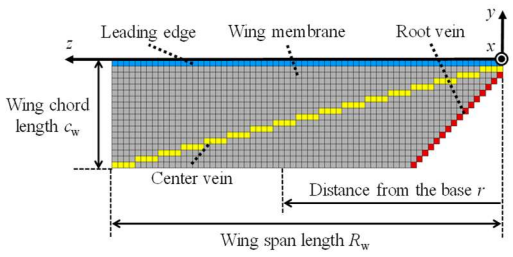

Figure 1: Employed pixel wing model.

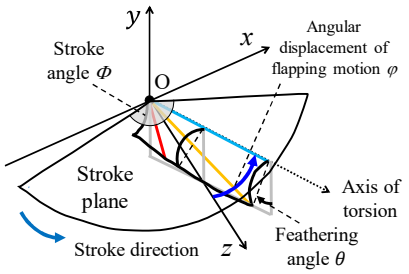

Figure 2: Schematic of flapping motion.

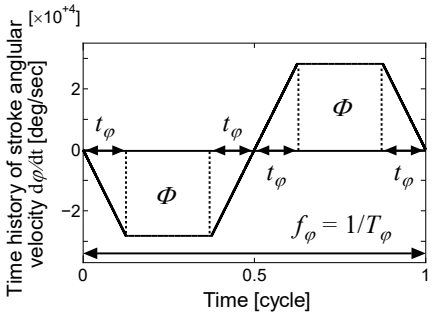

Figure 3: Time history of angular flapping velocity.

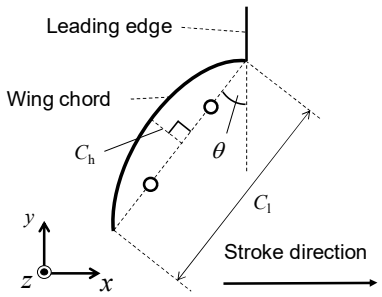

Figure 4: Definition of the feathering angle and the camber.

3. Fluid-structure interaction analysis of the pixel wing model

The finite element discretized equation of the incompressible viscous fluid and the equilibrium equation of the elastic body are combined using the interface conditions, and the monolithic equation systems of FSI is derived as follows:

$$ {}_{\mathrm{L}}\mathbf{Ma}+\mathbf{Cv}+\mathbf{N}+\mathbf{q}(\mathbf{u})-\mathbf{Gp}=\mathbf{g}\,,\ {}_{\tau}\mathbf{Gv}=\mathbf{0}\,, \qquad (1a, b) $$

where the matrices **M**, **C**, and **G** are the mass, diffusive, and divergence operator, respectively, the vectors **a**, **v**, **N**, **q**, **u**, **p**, and **g** are the acceleration, velocity, convective term, elastic inertial force, displacement, pressure, and external force, respectively. The subscripts L and τ denote lumping and transpose, respectively. Eq. (1) is solved using a projection method [4].

4. Numerical result

The parameters used in this study are given based on actual insect's data [5-10] as follows: The wing span length R_w = 0.0113m, the wing chord length c_w = 0.00311 m, the wing's thickness t = 2.0 μm, the flexural rigidity of along the wing's span-wise direction G_s = 4.0 μNm^2, the flexural rigidity of along the wing's chord-wise direction G_c = 0.35 μNm^2, the flexural rigidity of the most significant center vein = 0.26 nNm^2, Poisson's ratio ν = 0.49, Φ = 71°, the flapping frequency f_φ (= $1/T_\varphi$) = 148 Hz, the fluid mass density ρ^f = 1.205 kg/m^3, the fluid viscosity μ^f = 1.822×10^{-5} Pa s, the time increment $\Delta t = T_\varphi/150000$. For the purpose of evaluating the relationship between passive deformation and the aerodynamic performance, the Young's modulus of wing membrane E_m was varied from 7.0 to 13.0 GPa. The normalized position r/R_w is defined, where r is the distance from the wing base.

Fig. 5 shows the comparison of the lift coefficient C_L for various E_m. Fig. 6 shows the relationship between the E_m and average lift coefficient. Fig. 7 shows the the comparison of the cross section for r/R_w = 0.5 at 0.25 cycle. Fig. 8 shows the distribution of the camber along the wing's span-wise direction for the various E_m. C_L increases as E_m decreases and the average lift coeficient are monotonically proportional to E_m as shown in Fig. 5 and 6. This is because that the passive feathering and cambering increases as E_m decreases as shown in Fig. 7 and 8. Therefore passive deformations such the feathering and cambering can improove the aerodynamic performance.

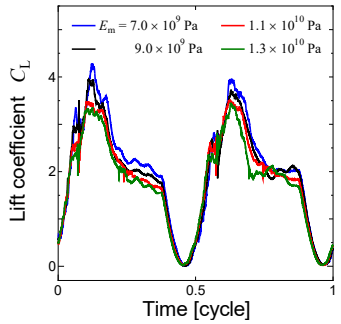

Figure 5: Time history of the lift coefficient for various E_m.

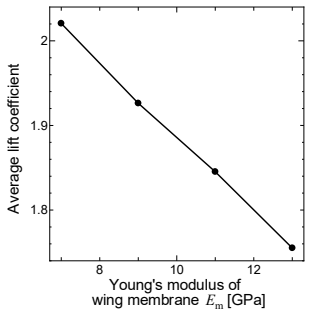

Figure 6: Relationship between the E_m and average lift coefficient.

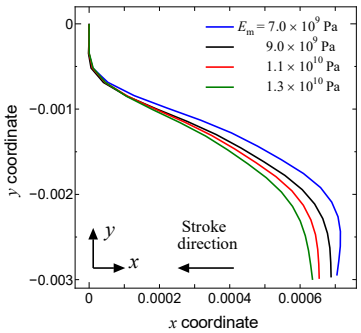

Figure 7: Comparison of the cross section for r/R_w = 0.5 at 0.25 cycle.

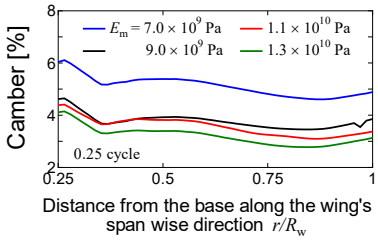

Figure 8: The distribution of the camber along the wing's span-wise direction.

5. Concluding remarks

The relationship between the passive motions and the aerodynamic performance is investigated using the FSI analysis of the pixel wing model flapped in air. The lift coefficient increases as the Young's modulus of the wing membrane decreases. This is because the passive feathering and cambering increase as the Young's modulus of wing membrane decreases. Therefore, these passive motions enhance the aerodynamic performance. In our future work, the passive mechanism of the feathering and cambering will be revealed.

Acknowledgments

This work was supported by JSPS KAKENHI Grant number 20H04199.

References

[1] R. J. Wooton, R. C. Herbert, P. G. Young, K. E. Evans: Approaches to the structural modeling of insect wings. *Philosophical Transactions of the Royal Society of London B*, 358, pp. 1577-1587, 2003.

[2] M. Onishi, D. Ishihara: Modeling the cambering of the flapping wings of an insect using rectangular shell finite elements, *Journal of Advance Simulation in Science and Engineering*, 7, 1, pp. 181-188, 2020.

[3] S. M. Walker, A. L. R. Thomas, G. K. Taylor**:** Deformable wing kinematics in free-flying hoverfly, *Journal of the Royal Society Interface*, 7, pp. 131–142, 2010.

[4] D. Ishihara and T. Horie: "A projection method for the monolithic interaction system of an incompressible fluid and a structure using a new algebraic splitting", *Computer Modeling in Engineering and Sciences*, 101, pp. 421-440, 2014.

[5] H. Tanaka, R. J. Wood: Fabrication of corrugated artificial insect wings using laser micromachined molds, *Journal of Micromechanics and Microengineering*, 20, 075008, 2010.

[6] S. A. Combes, T. L. Daniel: Flexural stiffness in insect wings I. Scaling and the influence of the wing venation. *The Journal of Experimental Biology*, 206, pp. 2979-2987, 2003.

[7] S. A. Wainwright, W. D. Biggs, J. D. Currey, J. M. Gosline: *Mechanical Design in Organism*, Princeton University Press, 1982.

[8] J. F. V. Vincent and U. G. K. Wegst: "Design and mechanical properties of insect cuticle", *Arthropod Structure & Development*, 33, pp. 187-199, 2004.

[9] C. P. Ellington: The aerodynamics of hovering insect flight III. Kinematics, *Philosophical Transactions of the Royal Society of London B*, 305, 1122, pp. 41-78, 1984.

[10] A. R. Ennos: The kinematics and aerodynamics of the free flight of some Diptera. *The Journal of Experimental Biology*, 142, pp. 49-85, 1989.

Comparative study on partitioned iterative algorithms for coupled multiple phenomena in piezoelectric energy harvesters

Naoto Takayama[1*], Daisuke Ishihara[2*], Prakasha C Ramegowda[2], Shunsuke Nozaki[1]

[1]Department of Computer Science and Systems Engineering, Kyushu Institute of Technology

[2]Department of Intelligent and Control Systems, Kyushu Institute of Technology

*ishihara.daisuke399@mail.kyutech.jp

Abstract. Various coupled algorithms are possible for the structure-piezoelectric-circuit interaction in piezoelectric bimorph energy harvesters. Hence, in this study, we propose a partitioned iterative algorithm using an explicit time marching method for the electric circuit, and compare it to that using an implicit time marching method for solving the electric circuit in terms of accuracy, computational cost, and numerical stability in a typical benchmark problem of piezoelectric energy harvesters.

Keywords: Piezoelectric Bimorph, Direct Piezoelectric Effect, Inverse Piezoelectric Effect, Electric Circuit, Partitioned Iterative Method, Block Gauss-Seidel Method, Finite Element Method

1. Introduction

In the piezoelectric energy harvesters, direct and inverse piezoelectric effects and electric circuit are strongly coupled, and this interaction determines the frequency response characteristics. Hence, the accurate prediction of this coupled problem using the numerical approaches is necessary for the design process of these devices. In Ref. [1], the monolithic approach was used for the direct numerical modeling of the structure–piezoelectric–circuit interaction in the piezoelectric energy harvester. The partitioned approach has been also used to simulate this coupled problem. However, the majority of previous studies on this approach used simplified numerical modeling such as the one-way coupling, the structural elements, and the circuit elements. On the contrary, we have been developing the partitioned approach using the direct numerical modeling [2], where the fully implicit algorithm was used. However, various algorithms are possible because of multiple and hierarchical natures of this coupled problem. Hence, the purpose of this study is to propose a new hybrid approach using hierarchical decomposition

for the coupled multiple phenomena. Some partitioned iterative algorithms given by this approach are compared to each other in terms of accuracy, computational cost, and numerical stability, and the effectiveness of this approach is demonstrated.

2. Materials and Methods

The spatially discretized equations of motion of linear piezoelectricity in the global coordinate system are derived using the variation principle with the standard procedure of the finite element method as

$$\mathbf{M}_{uu}\ddot{\mathbf{u}} + \mathbf{K}_{uu}\mathbf{u} + \mathbf{K}_{u\varphi}\boldsymbol{\varphi} = \mathbf{F}, \quad \mathbf{K}_{u\varphi}^{\mathrm{T}}\mathbf{u} + \mathbf{K}_{\varphi\varphi}\boldsymbol{\varphi} = \mathbf{q}_{\mathrm{ext}} + \mathbf{q}_{\mathrm{c}}, \tag{1a, b}$$

where $\mathbf{M}_{uu}$ is the global mass matrix of the structure, $\mathbf{K}_{uu}$ is the global mechanical stiffness matrix of the structure, $\mathbf{K}_{u\varphi}$ is the global piezoelectric stiffness matrix of the piezoelectric continuum, $\mathbf{K}_{\varphi\varphi}$ is the global dielectric stiffness matrix of the piezoelectric continuum, $\mathbf{u}$ is the nodal global vector of the mechanical displacement, $\boldsymbol{\varphi}$ is the nodal global vector of the electric potential, $\mathbf{F}$ is the global equivalent vector of the mechanical external force, $\mathbf{q}_{\mathrm{ext}}$ is the global equivalent vector of the external surface charge, $\mathbf{q}_{\mathrm{c}}$ is the global equivalent vector of the surface charge supplied from the integrated electric circuit, and the right-hand superscript T denotes the transpose of the matrix. We consider the electrical resistance load as the circuit. A SDOF governing equation of this circuit can be derived using Kirchhoff's law as

$$R\dot{Q} + V_{\mathrm{p}} = V_{\mathrm{e}}, \tag{2}$$

where R, Q, V_{p}, and V_{e} are the electrical resistance, the electric charge, the electric potential difference given by the piezoelectric oscillator, and the electric voltage given by the external electric power supply, respectively. The continuities of the electric potential and the electric charge are satisfied at the interface between the piezoelectric continuum and the electric circuit. The electric circuit is connected to the piezoelectric oscillator via electrodes. Here, let S_{+}^{c} and S_{-}^{c} denote the areas of the electrodes where the electric circuit is connected with the subscripts + and − corresponding to the positive and negative poles defined in the general circuit expression. Then, the continuity conditions imposed on the interface can be formulated as

$$V_{\mathrm{p}} = \varphi_{+}^{*} - \varphi_{-}^{*}, \quad \mathbf{q}_{\mathrm{c}} = \int_{S_{+}^{\mathrm{c}}} \mathbf{N}_{\varphi}\left(Q / S_{+}^{\mathrm{c}}\right) dS - \int_{S_{-}^{\mathrm{c}}} \mathbf{N}_{\varphi}\left(Q / S_{-}^{\mathrm{c}}\right) dS \tag{3a, b}$$

where φ_{x}^{*} (x is + or −) denotes the electric potential at the point in $S_{\mathrm{x}}^{\mathrm{c}}$ where the circuit is connected and $\mathbf{N}_{\varphi}$ is the global assemblage of the interpolation functions used for the electric potential. Note that the formulation of Eq. (3a) assumes that the charge from the electric circuit is distributed uniformly and instantaneously throughout each electrode.

References

[1] Ravi S, Zilian A. Time and frequency domain analysis of piezoelectric energy harvesters by monolithic finite element modeling. Int J Numer Meth Eng 2017;112:1828–47.

[2] Ishihara D, Takata R, Ramegowda PC, Takayama N. Strongly coupled partitioned iterative method for the structure–piezoelectric–circuit interaction using hierarchical decomposition, Comput Struct 2021;253:106572.

JSST 2021

Simulation of Cable-Laying Snake-like Robot Locomotion on Cable Rack

Hayato Nagae[1*], Junta takarabe[1], Koji Uchiyama[1], Yasuyuki Sato[1], Masami Iwase[1]

[1]Department of Robot Mechatronics, School of Science and Technology for Future Life, Tokyo Denki University

[*]nagae17@ctrl.fr.dendai.ac.jp

Abstract. We aim to develop a snake-like robot towing a lead cable for reducing the workload in cable laying. For the purpose, it is essential that the snake-like robot can propel while towing the lead cable on a cable rack. Therefore, in this paper, we develop a simulator which mimics the motion of the snake-like robot moving on a cable rack toward laying a cable. Then, on the simulator, we design a motion pattern of the snake-like robot propelling on the cable rack, and verify its effectiveness. We propose two patterns of motion for propulsion, spiral and longitudinal wave. Evaluating the two patterns on a simulator using MATLAB Simscape, it is confirmed that the longitudinal wave motion is effective for propulsion on the cable rack.

Keywords: Snake-like robot, Cable rack, Pitch angle serpenoid motion, Spiral motion, Computer simulation, MATLAB Simscape

1. Introduction

Cable laying is one of the interior works at building construction, and as buildings has more IT devices and apparatus, the number of cables to be laid increases. It leads to enhance research and development on labor-saving methods. In the general cable laying, cables should be laid on a rack which hangs from the ceiling. It is common for workers to ride on stepladders or aerial platforms for manually laying cables. However, the number of aged workers increases, and the total number of workers is decreasing from the peak [1]. Therefore, it is expected that cable laying is automated by robots to save labor.

We propose a snake-like robot that has a long and slender body without limbs for the purpose. The robot is possible to promote a narrow space such as inside a pipe [2]. The locomotive ability is expected to adapt to cable-laying on a cable rack or on the narrow space between laid cables. Also, the ability of the robot to move while pulling a thin lead-in wire is required for cable laying. A snake-like robot can be expected to meet two requirements.

In previous our research, the authors have developed a prototype snake-like robot for moving on a rack and towing a lead cable [3]. The robot has compact passive wheels on

each body segment. The wheels play a important role in locomotion on rough terrain such as sandy and gravel roads. Each joint of the robot is driven by a servomotor. Also, each body segment is composed of alternating pitch-rotating joint and yaw-rotating joint driven by the servomotor. Since the robot is designed having joints with a range of motion of ±90 deg, it can realize various movement even in a narrow space. So, we use the robot with some modification, and design propelling motion of the robot that can move on a cable rack.

As a related study of the movement algorithm, there is a spiral motion of a snake-like robot at Carnegie Mellon University [5]. The spiral motion gives the robot propulsion over cylinders that overhang in a comb shape. We compare mobility efficiency of the spiral motion and the proposed longitudinal wave motion on a cable rack in a simulator. The simulator including a snake-like robot reproduces the precise shape and motion of the robot by importing its CAD data. The simulator is effective to verify the proposed motion to move on the cable rack towing the lead-cable.

2. Robot Configuration

The configuration of the snake-like robot used in this research is shown. Our robot is presented in Fig. 1, and each parameter of the robot is shown in Table 1. The robot consists of 16 links and 15 joints. The coordinates of the robot is set as shown in Fig. 2.The pitch is taken around the x-axis. The body axis is around the y-axis. The yaw is around the z-axis. Each link consists of two passive wheels and two servomotors. The servo motors can rotate in the pitch or yaw directions with the range of motion of ±90 deg. A web camera is built into the robot's head to watch the target environment.

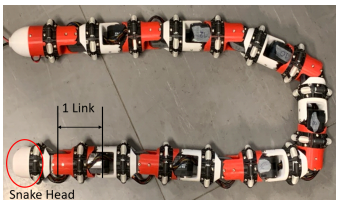

Figure 1: Snake-like robot

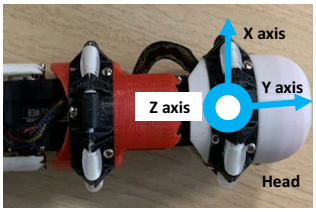

Figure 2: Coordinate axes

Table 1: Parameters

parameters	variable
Link number[-]	i
1 link length[m]	l_i
Yaw angle[rad]	ψ_j
Pitch angle[rad]	θ_j
Amplitude[m]	A
Phase[rad]	P
Number of motors[-]	j

3. Pitch Angle Serpenoid Motion Simulation

We simulate a movement of the snake-like robot, and try to design a motion for moving on a cable rack, which is considered as a pitch-angle serpenoid motion. In the previous research, we have demonstrated the serpenoid motion on the flat floor generated by the yaw-axis servomotors. The serpenoid motion is represented by (2).

$$\phi_i = A\sin(t - P(i-1)) \tag{1}$$

By controlling the pitch angle according to (2), the snake-like robot can realize the pitch-angle serpenoid motion. We set $A = \pi/2$ m, and $P = 2\pi/3$ rad in (2). The result is shown in Fig. 3. It can be confirmed that the snake-like robot is moving on the cable rack due to the motion of pitch angle serpenoid. The motion is easily implemented to the robot for controlling the corresponding servomotors.

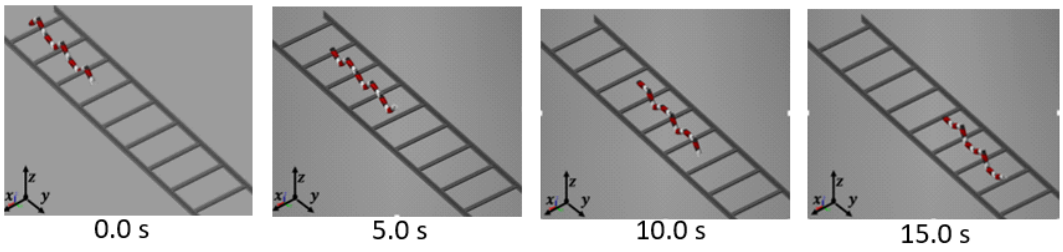

Figure 3: Pitch angle serpenoid motion on the cable rack

4. Comparison with Spiral Motion

We compare and verify the effectiveness of the proposed pitch-angle serpenoid motion by comparing it with the spiral motion by CMU. For the comparison and verificatoin, we first need to design the attitude angle to give the spiral shape of the serpentine robot. Assuming that x, y, z is each coordinate axis respectively, we set and a, b are constants which decide the shape of the normal spiral. The relationship is represented by (2) [5].

$$(x(t), y(t), z(t)) = (a\sin t, a\cos t, bt) \tag{2}$$

A normal spiral can be formed by shifting the phases in the yaw and pitch direction by ±90 deg. Based on (2), the attitude angles determined to form a spiral shape in consideration of the period and phase are given in (3) and (4) as shown in [6].

$$\psi_j = A\sin\left(\frac{-(\frac{j}{2}-1)\pi}{P}\right) - A\sin\frac{-\frac{j\pi}{2}}{P} \tag{3}$$

$$\theta_j = -A\cos\left(\frac{-(\frac{j}{2}-1)\pi}{P}\right) + A\cos\frac{-\frac{j\pi}{2}}{P} \tag{4}$$

Next, in the simulator developed by using Simscape, we input (3) in the yaw direction of the servomotor and (4) in the pitch direction as commands. The result is shown in Fig. 4. It can be confirmed that the snake-like robot cannot propel on the cable rack by the spiral motion. The fact leads to a conclusion where pitch-angle serpenoid motion is more effective than the spiral motion for propulsion on the cable rack.

5. Concludion

We developed a simulator for developing a snake-like robot towing a thin lead-wire toward cable laying. In the simulator, the propulsion of a serpentine robot by pitch angle

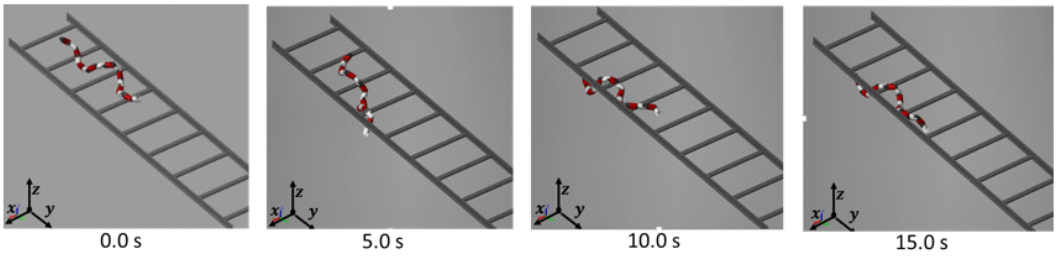

Figure 4: Spiral motion on the cable rack

serpenoid motion on a cable rack model was investigated. As a result, it was found that the snake-like robot can move by the proposed motion. After that, we also simulated the movement of the snake-like robot on the rack due to the spiral motion, and compared it with pitch angle serpenoid motion. The comparison result said that the snake-like robot could not propel on the cable rack in the spiral motion. Therefore, it was confirmed that pitch angle serpenoid motion is more effective than spiral for propulsion of the snake-like robot on the cable rack. We will verify the actual propulsion on the cable rack by the pitch angle serpenoid motion of the snake-like robot.

References

[1] Japanese Statistics Bureau: Labor force survey, (2021).

[2] Selvarajan, A.; Kumar, A.; Sethu, D.; bin Ramlan, M. A.: Design and Development of a Snake-Robot for Pipeline Inspection, *2019 IEEE Student Conference on Research and Development (SCOReD)*, (2019), 237-242.

[3] Dal Corso Francesco, Zini Stefano, Takumi Yamato, Masami Iwase: Design modeling and control of a snake-like robot, *2019 MSCS*, (2019).

[4] CMU Biorobotics Lab: Modular Snake Robots,(2020), http://biorobotics.ri.cmu.edu/projects/modsnake/pipes.html

[5] Keener, James P. , Tyson, John J.: Spiral waves in the Belousov-Zhabotinskii reaction, *Physica D: Nonlinear Phenomena , Vol. 21, No. 2-3 Elsevier*, (1986), 320-322.

[6] Takumi Yamato, Dal Corso Francesco, Zini Stefano, Shoshiro Hatakeyama, Masami Iwase: Helical Rotary Propulsion of Snake-like Robot on Gravel Road, *2020 MSCS*, (2020).

JSST 2021

Path tracking flight of engine-driven multicopter for forest inventory

Yuto Terada[1,*], Kazuya Sato[1], Naoki Masuda[1], Masami Iwase[1], Yasuyuki Sato[1]

[1]Department of Simulation, School of Technology, Tokyo Denki University

[*]terada17@ctrl.fr.dendai.ac.jp

Abstract. The purpose of this study is to conduct a highly accurate and efficient forest inventory using a multicopter equipped with a laser sensor. To achieve this purpose, we solve three problems. The first is to realize an altitude maintenance control of the multicopter. The second is to realize long flight of the multicopter. The third is to achieve collision avoidance by the multicopter with standing rees. For the purpose, we develop a simulator for the flight control of a multicopter to avoid obstacles. Using the simulator an algorithm is designed to fly in the forest, and is confirmed for the autonomous flight.

Keywords: Forestry, Drone, Forest survey, Trajectory generation

1. Introduction

About two-thirds of Japan's land area is covered forest. The forest has multiple functions; such as forest conservation of national land, prevention of global warming, forest including wood product supply. In order to keep these functions sustainably, people hope that forest operations become more efficient. Therefore, it is important to accurately grasp the condition of forest and evaluate the value of forest correctly. In the direction, it is necessary to survey forest in detail and to measure each tree conditions; height, stem circumference, bend of each tree and so on. Current general survey method is a kind of sample plot surveys. However, since the sample survey takes only a part sample of a standard land representing the interest forest, it does not provide an understanding of the topography of the entire forest. It sometimes leads to additional survey is required to perform forest management. For these reasons, decline in profitability for forestry become a problem. In order to solve the problems, we propose to develop an engine-driven multicopter equipped with a laser sensor flying and scanning forest. It can be used toward a substitute field surveys by workers [1]-[2].

This method enables safe surveying even on steep slopes because users only operate the drone far from the survey area. In addition, the multicopter flies for long time during forest suvey. Using the laser sensors efficiently measuring single-tree unit data, the multicopter provides well-rich information for forest management planning. To realizethis system, it is necessary to develop a flight control system of the multicopter. Toward the purpose, we

Figure 1: Engine-driven multicopter

should solve the following three problems. The first is to realize an altitude maintenance control of the multicopter. Because the measurement of each tree by laser sensors requires stable hovering. The second is to extend the continous flight time of the multicopter. The multicopter in this system uses a gasoline engine as the power source because it is required for the multicopter to have both a high payload to carry the laser sensors and the long flight time. The third is to achieve collision avoidance of multicopter with standing trees When the multicopter flies in the forest, there is a possibility that the multicopter will collide with trees. Therefore a collision avoidance system is needed to enable non-professional operators to fly multicopters in the forest. To realize collision avoidance, we implement Simultaneous Localization and Mapping, and generate the trajectory for collision avoidance.

In this paper, We aim to develop simulator that takes the flight path into account.

2. trajectory generation

In this section, we describe simulation of the flight path of a multirotor flying in a forest. The multicopter is able to follow the generated flight path by position control.In this study, the Lidar mounted on a multicopter is used to measure standing trees, and the speed of the Lidar is kept constant to facilitate the measurement. As shown in the Figure 3, the

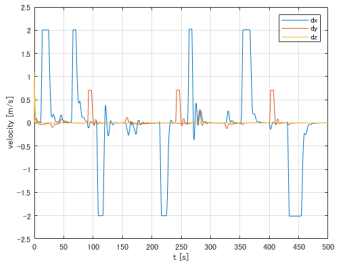

Figure 2: velocity

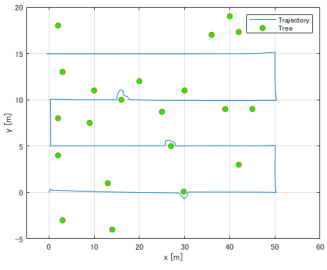

Figure 3: Path tracking flight

multicopter flies over a field of trees randomly placed at intervals of 2.0 m or more. If there is a tree in the middle of the flight path, it is necessary to avoid the collision between the tree and the multicopter, so the multicopter fly as shown in Figure 3. As this time, the distance

between the tree and the multicopter was set to 0.3 m or more. However in this algorithm, a new target value is set and the flight is performed when the target value reached each time. Therefore, the trajectory when avoiding the trees became irregular. So, we propose a new algorithm for collision avoidance flight.

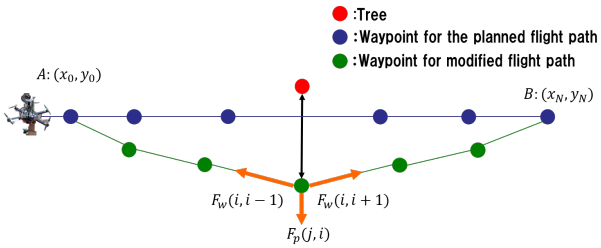

Figure 4: New collision avoidance flight proposal

As shown in Figure 4, the multicopter flies along the trajectory interpolated from the Waypoints set on the generated flight path. When an obstacle on this path is detected by Lidar during flight, the path is changed appropriately. We think we can change the route by hypothetically assuming that the line connecting the waypoints has a spring-like elastic force, and that there is a repulsive force between the point cloud detected by Lidar and the waypoints. We denote by $F_p(j,i)$ the repulsion force that the i-th Waypoint receives from the j-th point group, $F_w(i,i-1)$ the force that the i-th Waypoint receives from the previous Waypoint, and $F_w(i,i+1)$ the force that the i-th Waypoint receives from the subsequent Waypoint. $F_p(j,i)$, $F_w(i,i-1)$ and their combined force are represented by the following equations.

$$F_p(j,i) = \frac{h}{\left\|w_i - p_j\right\|^2} \cdot \frac{w_i - p_j}{\left\|w_i - p_j\right\|} \tag{1}$$

$$F_w(i,i-1) = k\,(w_{i-1} - w_i) \tag{2}$$

$$\sum_j F_p(j,i) + F_w(i,i-1) + F_w(i,i+1) = 0 \tag{3}$$

We use the Newton-Raphson method to search for waypoints where these resultant forces are zero. We define a vector X with the coordinates of the waypoint to be changed aligned vertically.

$$X = \begin{bmatrix} w_2 \\ \vdots \\ w_{N-1} \end{bmatrix} \tag{4}$$

In this case, the waypoints at both ends to be changed are fixed. Therefore, if w_1 and w_N are fixed as Waypoint$w_1, w_2, \cdot, w_N$, the Waypoint that can be changed is $w_2, \cdot, w_{N-1}$. The vector X is updated according to the Newton-Raphson method with the initial value of X^0 as shown in the following equation.

$$X^{k+1} = X^k - \frac{\partial H(X^k)}{\partial X} \times H(X^k) \tag{5}$$

By moving the waypoints to these equilibrium points, the appropriate flight path is generated to avoid collisions between the multicopter and each trees. We have verified the proposed algorithm by simulation.

The simulation is shown in Figure 5.

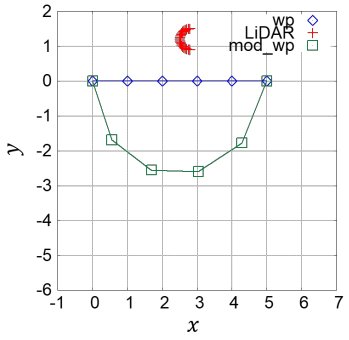

Figure 5: Path generation for collision avoidance flight

As shown in Figure 5, the path that the multicopter is planning to fly is indicated by the blue waypoints. When the multicopter is flying at position (0,0), the Lidar detected half of a tree. As a result, green Waypoints, which is a path that avoids collisions with the tree, was generated. We confirmed that a new flight path that avoids collisions with the tree can be generated from the point cloud detected by Lidar.

3. Conclution

This study aims to develop a path-following flight of an engine-driven multicopter for surveying in forest. For this purpose, we confirmed the flight control of the multicopter and created simulation of the flight path. The simulated flight path was unstable due to irregular spacing when avoiding collisions between the multicopter and trees. Therefore, we proposed an algorithm in which Lidar detects obstacles and generates a new route to avoid collisions. The effectiveness of the proposed algorithm was confirmed by simulations, which generated a new flight path that avoided collisions with trees based on the point cloud detected by Lidar.

In the future, we will confirm the path generation in the forest considering the collision avoidance algorithm by simulation and verify it on the actual machine of multicopter.

References

[1] A. Masato KATOH, B. Songqiu DENG, C. Yuki TAKENAKA, D. kwaion CHEUNG, E. Masahiro HORISAWA, F. Katsumasa OONO, G. Takaaki ITO: *Smart Precision Forestry Using Laser Sensing*, 85:3 (2019), 232–235.

[2] A. Naoki Muroki, B. Takayuki I: *Estimating a stand volume using UAV-aerial images and terrestrial laser scanning*, 52:2 (2019), 83–88.

JSST2021

Angular momentum of electromagnetic wave radiated from a relativistic electron moving on a spiral orbit

Elham Salehi*

UVSOR, Institute for Molecular Science, National Institutes of Natural Sciences

*elham@ims.ac.jp

Abstract. We give an analytic expression for the vector potential of the electromagnetic wave radiated from a relativistic electron moving on a spiral orbit. Based on this expression, we show that the electromagnetic wave has a spiral wave front and carries angular momentum which is combined with spin and orbital angular momentum.

Keywords: Electromagnetic wave, Relativistic electron, Angular momentum, Optical vortex

1. Introduction

Twisted photon beams (optical vortices) have attracted enormous interests because of their applications [1, 2, 3]. A twisted beam forming an helical wave-front structure exhibits two intrinsic degrees of freedom associated angular momentum; an orbital angular momentum (OAM) anda spin angular momentum (SAM).

In the helical undulator, electrons run on a spiral orbit. The spiral motion of the electrons can be separated into a drift motion along the undulator axis and a circular motion around it. In the moving reference frame with the drift velocity, the radiation field should be that from the circular motion. Its Lorentz transformation to the laboratory frame is the helical undulator radiation. Therefore, the origin of the peculiar characteristics of the radiation field from helical undulators should be found in the radiation from the circular motion as shown in [4, 5]. In this paper, we derive the analytic expression directly from the spiral electron motion and discuss the spatial structure and angular momentum of the radiation emitted from this electron.

2. Analytic Expersion for Radiation Field and Angular Momentum

The vector potential of the radiation from an electron on a helical orbit in the spherical coordinate system may be expressed as follows [6];

$$\vec{A}(t) = \int_{-\infty}^{+\infty} A(t) e^{i\omega t} dt = e\frac{e^{i\frac{\omega}{c}r}}{r}\int_{-\infty}^{+\infty} e^{i\omega\left(t+\frac{\vec{n}\cdot\vec{r}}{c}\right)} d\vec{r}_e + o\left(\frac{1}{r^2}\right) \equiv \vec{A}_{\omega}^{(1)} + o\left(\frac{1}{r^2}\right) \qquad (1)$$

Here, $A_{\omega}^{(1)}$ shows the vector potential of the first order of $1/r$. By the vector potential we can obtain the fourie components of the electric and magnetic fields. It should be noted that the non-zero terms of longitudinal component of the electromagnetic fields starts from the

second order of $1/r$ which is usually neglected in the radiation field calculation, contributes to angular momentum.

The number of photons carried by the *m*-th harmonic of the radiation can be obtained by dividing the energy of the radiation to the energy per photon, $\hbar\omega_m(\theta)$, as follows;

$$\frac{dN^m}{dt} = \int \frac{1}{4\pi\hbar c} r^2 d\Omega \omega_m(\theta) \left(A_\theta^{m(1)} A_\theta^{m(1)*} + A_\varphi^{m(1)} A_\varphi^{m(1)*} \right) + o\left(\frac{1}{r}\right) \quad (2)$$

The angular momentum component parallel to the axis of the helical motion carried by *m*-th harmonic of the radiation field may be expressed as follows:

$$\frac{dJ_z^m}{dt} = \int cr^2 j_z^m d\Omega = \frac{m}{4\pi} \int \frac{\omega_m(\theta)}{c} \left(A_\varphi^{m(1)} A_\varphi^{m(1)*} + A_\theta^{m(1)} A_\theta^{m(1)*} \right) r^2 d\Omega + o\left(\frac{1}{r}\right) \quad (3)$$

Eqs. (2) and (3) may be summarized as follows;

$$\frac{dJ_z^m}{dt} = m\hbar \frac{dN^m}{dt} \quad (4)$$

which indicates that *m*-th harmonic component carries angular momentum, $m\hbar$ per photon. Here, we have obtained the same result as obtained in the previous work [4] which the angular momentum was calculated for a circular motion. This work verifies the treatment in the previous work.

Here, we present the numerical results to show typical spatial structures of the phase and intensity of the radiation emitted from an electron in a spiral motion for the positive helecity of the second harmonic $m = 2$ in Fig. 1. The donut-shaped of intensity (left) and phase structure (right) of the radiation show that the radiation carries OAM, $(m-1)\hbar = \hbar$. The degree of circular polarization indicates 100% circular polarization with positive helicity.

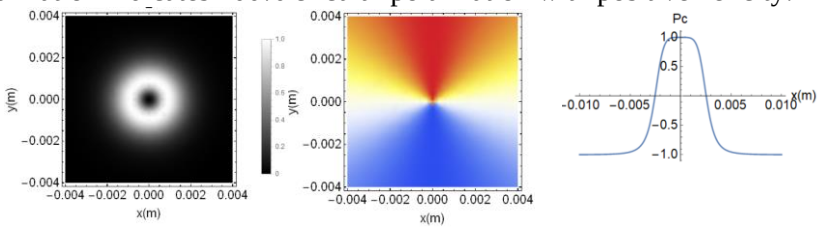

Figure 1: Spatial structure of the 2nd harmonic component

3. Conclusion

We have shown analyticaly and numerically that the electromagnetic field radiated from a free electron running on a spiral orbit carries angular momentum and possesses a helical phase structure, depending on the harmonic number and the helicity. Such a physical situation, in which relativistic free electron are running on spiral orbits, can be found in laboratories and nature, such as in particle accelerators, nuclear fusion plasma, astrophysical objects and so on.

References

[1] *e.g.* G. Molina-Terriza, J. P. Torres, and L. Torner, *Nat. Phys.* 3 (2007), 305-310.
[2] *e.g.* R. W. Bowman, M. J. Padgett, *Nat. Photon.*, 5 (2011), 343-348.
[3] *e.g.* Y. Shen *et al*.: Optical vortices 30 years on, *Light: Sci. & Appl*., 8:90 (2019) (29 Pages).
[4] M. Katoh *et al*., *Phys. Rev. Lett.* 118:9 (2017), 094801 (5 Pages).
[5] H. Kawaguchi, M. Katoh, *Prog. Theor. Exp. Phys.* 2019 (2019), 083A02 (18 Pages).
[6] E. Salehi, M. Katoh, *J. Adv. Simulat. Sci. Eng.,* 8:1 (2021), 87-97

JSST 2021

Structure formation of chiral needles by modeled force fields with helical phase using molecular dynamics simulation

Shu Habu[1*] and Hiroaki Nakmaura[1,2]

[1]Department of Electrical Engineering, Graduate School of Engineering, Nagoya University
[2]National Institute for Fusion Science, National Institute of National Sciences

*naka-lab@nifs.ac.jp

Abstract. We fabricate the helical nano-scaled metal needle (nanoneedle) structure of tantalum using classical molecular dynamics simulation. Since the force on atoms due to the external field is too complex, we simplified it so that the force is proportional to the external electric field. It was found that the nanoneedle structure depends on the topological structure of the external field.

Keywords: Orbital angular momentum, Molecular dynamics simulation, chiral structure

1. Introduction

Laguerre-Gaussian (LG) beams carry orbital angular momentum (OAM) around its beam axis [1]. The component of angular momentum flux in the direction of the EM-wave propagation is $J = \varepsilon_0\omega(l + \sigma_z)/2$, where $l(= 0, \pm1, \cdots)$ is the azimuthal mode index, and $\sigma_z\,(= 0, \pm1)$ is the polarization of the beam.

Omatsu group demonstrated that when the polished tantalum (Ta) target which was ~2 mm in thickness was irradiated with LG beam, the helical nanoneedle was fabricated on the surface of the Ta target [2]. According to their result [2], on the surface of the target Ta irradiated with the LG beam, which has the non-zero orbital angular momentum ($l \neq 0$), the helical needle structures were observed.

Therefore, we investigate the mechanism of the helical nanoneedle structural formation by the EM-wave with the OAM using molecular dynamics (MD) [3, 4].

2. Molecular dynamics simulation

As the MD code, we adopted Large-scale Atomic/Molecular Massively Parallel Simulator (LAMMPS) code [5]. In this classical MD simulation, the body-centered cubic (BCC) Ta

crystal at 300 K was prepared as the initial structure of the target. We used the interatomic potential, embedded atom method (EAM) potential force field of Ta [6]. The canonical ensemble with the Langevin thermostat [7] was also used to control the temperature of the system T. Assuming that the LG beam is irradiated to Ta during 30 ps, we set the external force field to the target instead of calculating the interaction between the EM-wave and the material. This external force described by Eq. 1 depends on the l (the azimuthal mode index of the beam), and σ_z (the polarization of the beam). In the case of $l \neq 0$, it has the helical phase distribution. Then, we continued the simulation with no external force to get the target in the equilibrium state at 300 K. We carried out the above procedure in the nine cases, $l = 0, \pm 1$ and $\sigma_z = 0, \pm 1$, respectively.

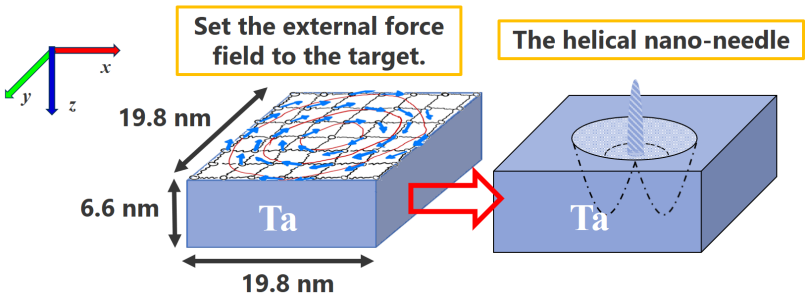

Figure 1: Simulation model. The tantalum BCC crystal was prepared as the initial structure of the target. Assuming that the EM-wave is irradiated from the $-z$ direction to the target, the external force field described by Eq. 1 was set to the target. The nanoneedle structure was generated on the surface of the target.

The external force $\boldsymbol{F}_{l,\sigma_z}$ set to the target is proportional to the electric field of LG beam in the simple form (radial mode index is 0) $\boldsymbol{E}^{\mathrm{LG}}_{0,l,\sigma_z}$, which has the following form:

$$\begin{aligned}\boldsymbol{F}_{l,\sigma_z}(r,\phi,z,t) &\propto \boldsymbol{E}^{\mathrm{LG}}_{0,l,\sigma_z}(r,\phi,z,t)\\ &= \frac{E_0}{2}\left\{\frac{\boldsymbol{e}_x + \boldsymbol{e}_y \mathrm{e}^{\mathrm{i}\frac{\pi}{2}\sigma_z}}{\sqrt{2}}\widetilde{u}^{LG}_{0,l}(r,\phi,z)\right.\\ &\quad \left. + \boldsymbol{e}_z \frac{\mathrm{i}}{\sqrt{2}k}\left[\frac{\partial \widetilde{u}^{LG}_{0,l}(r,\phi,z)}{\partial x} + \mathrm{e}^{\mathrm{i}\frac{\pi}{2}\sigma_z}\frac{\partial \widetilde{u}^{LG}_{0,l}(r,\phi,z)}{\partial y}\right]\right\}\mathrm{e}^{\mathrm{i}(kz-\omega t)} + \mathrm{c.c.}, \qquad (1)\end{aligned}$$

where the $\boldsymbol{k}$ direction of the EM-wave propagation is set to the $-z$ direction, and the unit vector of the z axis is defined by $\boldsymbol{e}_z$. The x and y axes are set in the transverse plane, and their unit vectors are defined by $\boldsymbol{e}_x$ and $\boldsymbol{e}_y$. The function of LG beam $\widetilde{u}^{LG}_{0,l}$ is defined in the cylindrical coordinate (r,ϕ,z) as follows:

$$\begin{aligned}\widetilde{u}^{LG}_{0,l}(r,\phi,z) := &\sqrt{\frac{2}{\pi|l|!}}\frac{w_0}{w(z)}\left(\frac{r}{w(z)}\right)^{|l|}\exp\left[-\frac{r^2}{w^2(z)}\right]\\ &\times\exp\left[\mathrm{i}l\phi + \mathrm{i}\frac{r^2 z}{w^2(z)z_R} - \mathrm{i}(|l|+1)\tan^{-1}\left(\frac{z}{z_{\mathrm{R}}}\right)\right], \qquad (2)\end{aligned}$$

where the Rayleigh length z_R and the radius of the beam $w(z)$ are given by $z_R = kw_0^2/2$ and $w(z) = w_0\sqrt{1 + (z/z_R)^2}$. The constant w_0 is set to unity.

3. Results

We succeeded in the helical nanoneedle fabrication in the cases of $(l, \sigma_z) = (1, 1)$ and $(-1, -1)$ shown in Fig. 2. Furthermore, we found that the direction of the helical needle structure turns on l. However, the nanoneedle was not fabricated in other cases of $l \neq 0$ that the external force field has the helical phase distribution. The problem may exist in the energy transfer from EM-wave to the material (Ta). we also need to improve the modeling of the external force field. It is said that the optical force of the radial and azimuthal components of the external force field are significant to the helical needle fabrication, which collect the Ta particles to the center of the axial core and produce the orbital motion of the particles about the axial core [2, 8, 9].

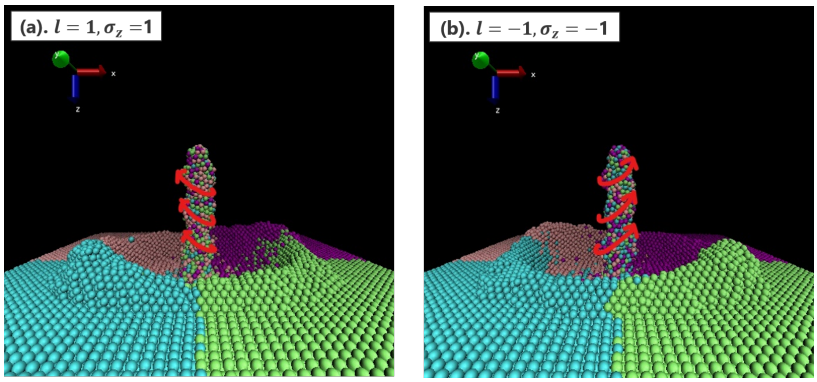

Figure 2: Simulation results. The twisted nanoneedle structure is fabricated in silico by MD simulation. In the bellow figures, the red lines show the helical structures of the nanoneedle, the directions of the helical structures are opposite.

4. Conclusion

In this paper, we have demonstrated the fabrication of the chiral needle using the MD with the modeled external force. In the future work, we will introduce the radiation force formula to improve this model [10].

Acknowledgments

The research was supported by Grants-in-Aid for Scientific Research (C), Nos.18K11416 and 19K03800 from the Japan Society for the Promotion of Science, and by the NIFS Collaborative Research Programs NIFS20KNTS066, NIFS20KNSS150 and NIFS20KKGS028.

The computations were performed using the JFRS-1 supercomputer system at Computational Simulation Centre of International Fusion Energy Research Centre (IFERC-CSC) in Rokkasho Fusion Institute of QST (Aomori, Japan) , Research Center for Computational Science (Okazaki, Aichi, Japan) , and "Plasma Simulator"(NEC SX-Aurora TSUBASA) of NIFS (Toki, Gifu, Japan) .

References

[1] L. Allen, M. W. Beijersbergen, R. J. C. Spreeuw, and J. P. Woerdman. Orbital angular momentum of light and the transformation of laguerre-gaussian laser modes. *Phys. Rev. A*, Vol. 45, pp. 8185–8189, Jun 1992.

[2] Kohei Toyoda, Fuyuto Takahashi, Shun Takizawa, Yu Tokizane, Katsuhiko Miyamoto, Ryuji Morita, and Takashige Omatsu. Transfer of light helicity to nanostructures. *Phys. Rev. Lett.*, Vol. 110, p. 143603, Apr 2013.

[3] Hiroaki Nakramura, Shu Habu, Seiki Saito, and Shin Kubo. Molecular dynamics simulation on structural formation of chiral nanoneedle by optical vortex. In *The 38th JSST Annual International Conference on Simulation Technology*, Miyazaki, Japan, 11 2019. The Japan Society for Simulation Technology.

[4] Shu Habu and Hiroaki Nakmaura. MD Simulation on Chiral Needle Fabrication in Radiation Force Field of Laguerre-Gaussian Beams. In *The 29th International Toki Conference on Plasma and Fusion Research*, Gifu, Japan, 10 2020. National Institute for Fusion Science.

[5] Fast parallel algorithms for short-range molecular dynamics. *Journal of Computational Physics*, Vol. 117, No. 1, pp. 1–19.

[6] R. Ravelo, T. C. Germann, O. Guerrero, Q. An, and B. L. Holian. Shock-induced plasticity in tantalum single crystals: Interatomic potentials and large-scale molecular-dynamics simulations. *Phys. Rev. B*, Vol. 88, p. 134101, Oct 2013.

[7] T. Schneider and E. Stoll. Molecular-dynamics study of a three-dimensional one-component model for distortive phase transitions. *Phys. Rev. B*, Vol. 17, pp. 1302–1322, Feb 1978.

[8] Takashige Omatsu, Keisuke Chujo, Katsuhiko Miyamoto, Masahito Okida, Kazuki Nakamura, Nobuyuki Aoki, and Ryuji Morita. Metal microneedle fabrication using twisted light with spin. *Opt. Express*, Vol. 18, No. 17, pp. 17967–17973, Aug 2010.

[9] Kohei Toyoda, Katsuhiko Miyamoto, Nobuyuki Aoki, Ryuji Morita, and Takashige Omatsu. Using optical vortex to control the chirality of twisted metal nanostructures. *Nano Letters*, Vol. 12, No. 7, pp. 3645–3649, 2012. PMID: 22690654.

[10] James P. Gordon. Radiation forces and momenta in dielectric media. *Phys. Rev. A*, Vol. 8, pp. 14–21, Jul 1973.

JSST 2021

The study on the stability of DNA structure by steered molecular dynamics simulations

Tomoko Mizuguchi[1,*], Naoto Fukushima[1], Takashi Aoki[2], Masato Hashimoto[1], Susumu Fujiwara[1]

[1]Faculty of Materials Science and Engineering, Kyoto Institute of Technology
[2]Department of Biobased Materials Science, Kyoto Institute of Technology

[*]mizuguti@kit.ac.jp

The full paper of this paper has been published in Journal of Advanced Simulation in Science and Engineering (JASSE).

DOI: https://doi.org/10.15748/jasse.9.160

Reactive molecular dynamics study on damaged polyethylene after hydrogen abstraction by radiation

Haolun Li[1*], Susumu Fujiwara[2], Hiroaki Nakamura[3,4], Tomoko Mizuguchi[1],

Ayako Nakata[5], Tsuyoshi Miyazaki[5], Shinji Saito[6], Wataru Sakai[1]

[1]Graduate School of Science and Technology, Kyoto Institute of Technology

[2]Faculty of Materials Science and Engineering, Kyoto Institute of Technology

[3]National Institute for Fusion Science

[4]Nagoya University

[5]National Institute for Materials Science

[6]Institute for Molecular Science

*d0871005@edu.kit.ac.jp

Abstract. One of the effects that radiation causes on polymeric materials is the hydrogen abstraction reaction, which induces radicalization and the subsequent structural changes such as de-crystallization, cross-link and chain scission. However, at a nanoscale, the changes of the entire chain and the reaction paths on local segments are difficult to be completely caught by experiment. In this research, we investigate the structural change of hydrogen-removed polyethylene by means of reactive molecular dynamics simulations using two kinds of ReaxFF force field parameter sets, called CHO-2006 and CHO-2016. And to compare the two parameter sets, atomic forces of the final configurations are calculated by density functional theory. Our results suggest that CHO-2006 is a better parameter set for treating damaged hydrocarbons. Furthermore, during simulations using the CHO-2006 parameter set, de-crystallization, formation of C=C double bond, cyclic structure and conjugated bond and chain scission were observed.

Keywords: Molecular dynamics simulation, Polyethylene, Structural change, Reactive force field

1. Introduction

After exposure to radiation within a high energy or for a long time, polymeric materials are radicalized from the surface to the interior, leading to structural changes and chemical bond rearrangements. Among the effects caused by radiation on polymeric materials, hydrogen abstraction (H-abstraction) reaction is one of the most possibly occurred effect. For the reason that H-abstraction reaction occurs on random position of polymer chains, it is difficult to study the structural change of polymers induced by H-abstraction at a nanoscale through experiment. In our former research, coarse-grained molecular dynamics (MD) simulations were employed to treat a hydrogen-removed polyethylene chain with a folding structure and the results shows that if more hydrogen atoms are removed from polyethylene chain, the crystallinity decreases

more [1-2]. However, it is extremely possible that losing hydrogen on the polyethylene cause chemical bond rearrangements, but the classical MD methods are not able to treat chemical reactions. Thus, we introduce a reactive force field, ReaxFF, which is developed by van Duin and able to treat the break and the formation of chemical bonds. In this research, we predict the structural change of hydrogen-removed polyethylene by MD simulations using ReaxFF force field. As there are two parameter sets (called CHO-2006 [3] and CHO-2016 [4]) available for treating damaged hydrocarbons, we also employed density functional theory (DFT) calculations to compare the appropriateness of the two parameter sets.

2. Simulation models and methods

Hydrogen-removed polyethylene models were made by the following steps. In step (*i*), an all-atom polyethylene model ($C_{300}H_{602}$) was cooled in 100 K by classical force field and formed a chain-folding structure (Fig. 1(a)). In step (*ii*), we randomly removed hydrogen atoms from the model. The ratio of removed hydrogen atoms to carbon atoms (f_H) is set to 0, 0.01, 0.05, 0.1, 0.2, and the number of removed hydrogen atoms is 0, 3, 15, 30, 60, respectively. In step (*iii*), the models of each f_H with the same initial configuration were kept 100 K for 1.3 ns (13,000,000 time steps, 1 fs per time step) in a vacuum simulation box by ReaxFF MD simulations using two parameter sets, CHO-2006 and CHO-2016 respectively. After the simulations, DFT calculations were done to calculate atomic forces of the final configuration. Furthermore, to study the structural change in a high temperature, the models were heated from 100 K to 400 K at a heating rate of 100 K/ns for 3 ns (30,000,000 time steps). In all simulations, NVT ensemble is employed and the size of the vacuum simulation box is set to 400 Å × 400 Å × 400 Å. The Nosé–Hoover method is applied to control the temperature. The simulation software used is LAMMPS.

3. Results and discussions

For the step (a) in ReaxFF MD simulations, the structures of models at 100 K visualized are shown in Fig. 1. To quantify the time dependence of structural change, we also calculate the global orientational order parameter and the root mean square deviation of the carbon atoms. The results suggest that during simulations using either parameter set, the models of $f_H = 0$ keep a chain-folding crystal structure and the models of $f_H = 0.2$ become less ordered after the simulations of 1.3 ns at 100 K.

To compare the two used parameter set CHO-2006 and CHO-2016, DFT calculations are introduced as a reference and classical force field calculations are also employed for a comparison. In DFT calculations, ReaxFF MD simulations and classical force field calculations, the atomic forces of all atoms of the final configuration (CHO-2006 model and CHO-2016 model, respectively) are calculated. The magnitude of forces (F) calculated by different methods is compared in Tables I and II. In Table I and II, the average F in CHO-2006 case and CHO-2016 case derived by ReaxFF MD simulations and DFT calculations is in the same level. However, the average F derived by both classical force field calculations is much higher in CHO-2016 case than in CHO-2006 case and higher than those derived by ReaxFF MD simulations and DFT calculations. It means that the structure configured by CHO-2006 is more stable for classical MD simulations, while that by CHO-2016 is unstable and not in an equilibrium state for classical MD simulations. By this reason, the CHO-2006 is suggested to be the more suitable parameter set to treat damaged polyethylene than CHO-2016.

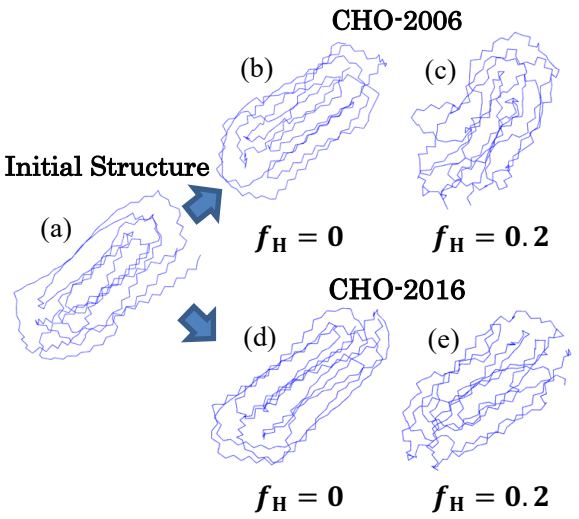

Fig. 1 Snapshots of the structure of polyethylene chains: (a) initial structure before simulation, (b) and (c) structures of $f_H = 0$ and 0.2 after simulation using CHO-2006, respectively, (d) and (e) structures of $f_H = 0$ and 0.2 after simulation using CHO-2016, respectively, where hydrogen atoms are not shown.

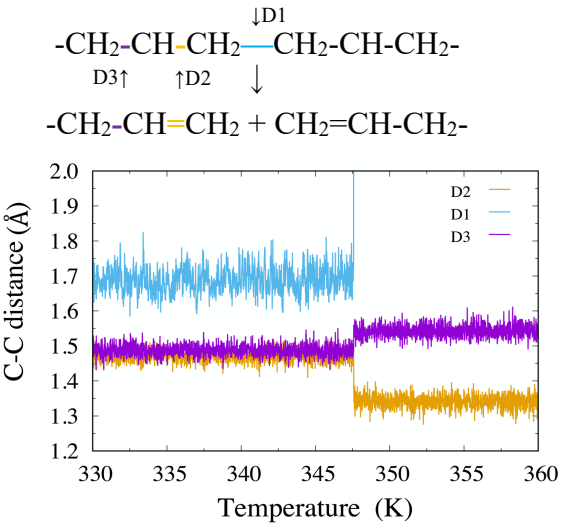

Fig. 2 The reaction formula of chain scission and temperature dependence of the distance of different C-C pairs. At about 348 K, the unstable blue bond breaks, violet C-C single bond becomes stable, and the brown one changes from a unstable C-C single bond to a stable C=C double bond.

Table I. The average F (unit: a.u.) of all atoms for all f_H's derived from four kinds of calculations where the models are configured by CHO-2006.

f_H	0	0.01	0.05	0.1	0.2
DFT	0.02584	0.02539	0.02481	0.02424	0.02316
CHO-2006	0.01816	0.01832	0.01786	0.01901	0.01850
OPLS-AA	0.02107	–	–	–	–
DREIDING-AA	0.02317	–	–	–	–

Table II. The average F (unit: a.u.) of atoms for all f_H's derived from four kinds of calculations where the models are configured by CHO-2016.

f_H	0	0.01	0.05	0.1	0.2
DFT	0.02624	0.02699	0.02709	0.02651	0.02580
CHO-2016	0.01859	0.01805	0.01829	0.01762	0.01788
OPLS-AA	0.03510	–	–	–	–
DREIDING-AA	0.05008	–	–	–	–

During the simulations using CHO-2006, several kinds of chemical reactions were observed on specific segments. Chain scissions (C-C bond break) occur at a high temperature. The temperature dependence of one chain scission is shown as Fig. 2. A unstable bond breaks at about 348 K. And at the same time, the adjacent four C-C bonds changes to be stable or form a C=C double bond, respectively. During simulations at 100 K, formations of C=C double bonds, cyclic bonds and conjugated bonds were also found in specific positions. The reaction formulas are shown in Fig. 3.

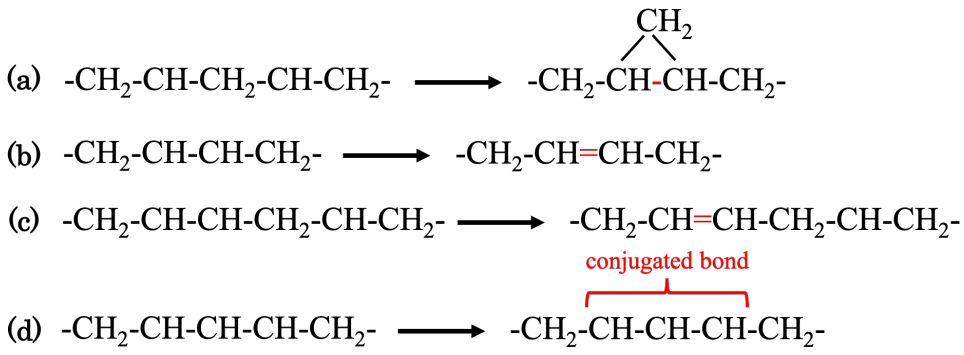

Fig. 3 The reaction formulas (a)-(d) corresponding to situations (1)-(4), respectively. In formula (a), the average length of new C-C bond is 1.51 Å. In formulas (b) and (c), the average length of new C=C double bond is 1.35 Å. In formula (d), the average length of conjugated bond is 1.40 Å. Red parts represent newly formed bonds.

4. Conclusions

In this research, structural change of hydrogen-removed polyethylene is studied by ReaxFF MD simulations using two kinds of parameter sets and DFT calculations are employed to compare the two used parameter sets. Based on our simulation results, we found that losing more hydrogen atoms leads to a higher decrease of crystallinity. After the comparison of atomic forces, the CHO-2006 is suggested to be more suitable to treat damaged hydrocarbons. And during the simulations, chemical reactions at specific segments occurred, including formations of C=C double bonds, cyclic bonds and conjugated bonds at 100 K and chain scissions at a high temperature.

References

[1] S. Fujiwara, H. Nakamura, H. Li, H. Miyanishi, T. Mizuguchi, T. Yasunaga, T. Otsuka, Y. Hatano, S. Saito: Computational Strategy for Studying Structural Change of Tritium-Substituted Macromolecules by a Beta Decay to Helium-3, *J. Adv. Simulat. Sci. Eng.*, 6-1 (2019), 94-99

[2] H. Li, S. Fujiwara, H. Nakamura, T. Mizuguchi, T. Yasunaga, T. Otsuka, T. Kenmotsu, Y. Hatano, S. Saito: Structural Change of Tritium-Substituted Polymeric Materials by a Beta Decay: A Molecular Dynamics Study, *Plasma Fusion Res.*, 14 (2019), 3401106

[3] K. Chenoweth, A. van Duin, W. A. Goddard: ReaxFF Reactive Force Field for Molecular Dynamics Simulations of Hydrocarbon Oxidation, *J. Phys. Chem. A*, 112 (2008), 1040-1153.

[4] C. Ashraf, A. van Duin: Extension of the ReaxFF Combustion Force Field toward Syngas Combustion and Initial Oxidation Kinetics, *J. Phys. Chem. A*, 121 (2017), 1051-1068.

Comparison of beam-wall interaction models using boundary element method

Kazuhiro Fujita[1*]

[1]Department of Information Systems, Faculty of Engineering, Saitama Institute of Technology

*kfujita@sit.ac.jp

Abstract. The electromagnetic interaction of a relativistic particle beam with resistive pipes is of great interest in accelerator physics. There are perturbative and nonperturbative models for this beam-wall interaction. We present direct comparison of frequency domain simulations for both models in the context of boundary element method.

Keywords: Accelerator beam pipe, resistive wall, perturbation theory, boundary element method

1. Introduction

The electromagnetic interaction of a relativistic charged particle beam with vacuum chamber beam pipes with walls of finite conductivity is of great interest in accelerator physics [1]. As a result of this interaction, electromagnetic fields, known as wake fields [1], can be excited due to the existence of resistive wall. The boundary element method (BEM) [2].[3] is one of promising numerical approaches for this subject. The so-called perturbative theory [1], where it is assumed that the magnetic field on the wall is the same as in the case of perfect conductivity, is often used. However, no comparison of perturbative and nonperturbative models in the framework of BEM is shown in [2],[3]. The main purpose of this work is to show direct comparison of perturbative and nonperturbative simulations using the 2-D BEM [4].

2. Modeling

In the nonperturbative model, a boundary integral representation of magnetic field **H** for infinitely long resistive pipe with the cross-section C can be derived as [4]

$$\mathbf{H} = \mathbf{H}_s - j\omega \boldsymbol{F} + \frac{1}{\mu}\nabla \times \mathbf{A},\ \ \mathbf{A} = \mu \int_C G(\mathbf{r},\mathbf{r}')\mathbf{K}(\mathbf{r}')d\mathbf{r}',\ \ \mathbf{F} = \varepsilon \int_C G(\mathbf{r},\mathbf{r}')\mathbf{M}(\mathbf{r}')d\mathbf{r}' \quad (1)$$

$$G(\mathbf{r},\mathbf{r}') = \frac{1}{2\pi}K_0(k_r|\mathbf{r}-\mathbf{r}'|),\quad \mathbf{n}\times\mathbf{H} = \mathbf{K},\quad \mathbf{M} = Z_s\mathbf{K}\times\mathbf{n} \quad (2)$$

where $\mathbf{H}_s$ is the self-field of a relativistic charged particle beam moving with constant velocity $v\boldsymbol{e}_z$ in the z direction and the beam current I, G is the Green function, **K** and **M** are the electric and magnetic surface current on the pipe wall, respectively, Z_s is the surface impedance, K_0 is the modified Bessel function, $k_r=k/\gamma$, $k=\omega/v$, γ is the Lorentz factor and $\omega=2\pi f$ is the angular

frequency. According to the conventional BEM procedure, Eq.(1) is solved for **K**. After **K** is given as boundary values, the longitudinal electric field E_z is obtained from **M**.

In the perturbative model, it is assumed that the magnetic field on the wall is the same as in the case of perfect conductivity. Eq.(1) is solved with Z_s=0, and then E_z is obtained from **M**.

3. Numerical result

We assume here that a particle is highly relativistic (γ=10000) and moves in the center of an infinitely long resistive pipe, for comparison with the perturbation theory [1],[5]. Using both models, we numerically calculate "coupling impedances" $Z=-E_z/I$ for round and square pipes with wall conductivity $\sigma=5.8\times10^7$ S/m and a=2.5mm as in Fig.1. For the round pipe, the theory is valid for $(|Z_s|\omega a)/(2cZ_0)<<1$ with $c=1/(\mu_0\varepsilon_0)^{1/2}$ and $Z_0=(\mu_0/\varepsilon_0)^{1/2}$, $Z_s=(1+j)(Z_0\omega/2c\sigma)^{1/2}$, i.e. $f<<11$ THz. Fig.1 shows comparison of the nonperturbative (black) and perturbative (red) coupling impedances (real part) for both pipes. As expected, for low frequencies $f<1$ THz, both models are in good agreement. Larger discrepancies are observed as f increases.

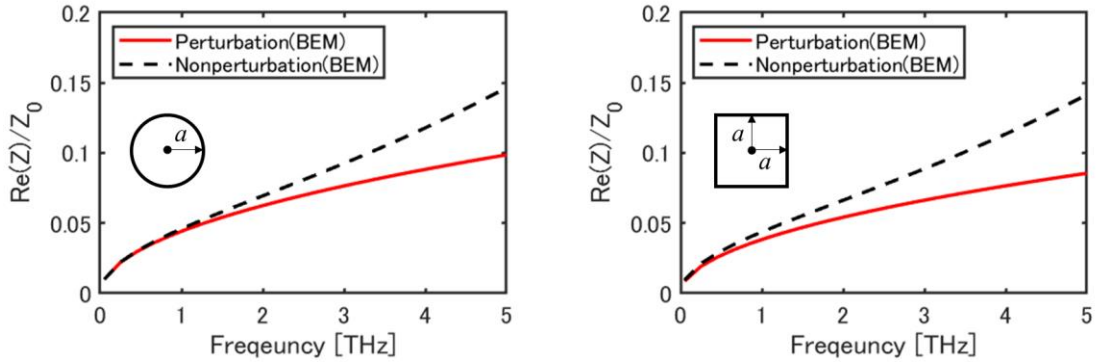

(a) Circular pipe (b) Square pipe

Figure 1: Comparisons of perturbative and nonperturbative coupling impedances (a=2.5mm)

4. Conclusion

The nonperturbative and perturbative beam-wall interaction simulations using BEM have been presented. Direct comparisons of the nonperturbative and perturbative coupling impedances for the round resistive pipe and the square one are clearly shown in the BEM context. A limitation of the perturbation theory is confirmed in our simulations.

References

[1] G. Stupakov, Wake and impedance, *SLAC-PUB-8683*, 2000.

[2] K. Yokoya, Resistive wall impedance of beam pipes of general cross section, *Part. Accel.*, vol.41(1993), pp.221-248.

[3] A. Macridin, et al., Nonperturbative algorithm for the resistive wall impedance of general cross-section beam pipes, *Phys. Rev. ST Accel. Beams*, vo.16 (2013), 121001.

[4] K. Fujita, A study on boundary element analysis of accelerator beam pipes with walls of finite conductivity, *IEICE Technical Report*, EMT2021-27 (2021), pp.105-108.

[5] K. Bane et al., The short-range resistive wall wake fields, *SLAC-PUB-95-7074*,1995.

Design study of BiCG-Stab matrix solver circuit for FIT scheme based on dataflow architecture

Chenxu Wang, Seiya Ota, Hideki Kawaguchi

Division of Information and Electronic Engineering, Graduate School of Engineering,
Muroran Insititute of Technology, Japan

*kawa@mmm.muroran-it.ac.jp

Abstract. In order to achieve high-performance computation for the Finite Integration Technique (FIT) based on the BiCG-Stab method for 2D magnetostatic field simulation, this paper discusses a method of dedicated computer with dataflow architecture for magnetostatic field simulations. In particular, we design the integer arithmetic circuit of the BiCG-Stab matrix solver for FIT scheme based on the dataflow architecture.

Keywords: Dedicated computer, Dataflow architecture, BiCG-Stab matrix solver

1. Introduction

In the last half century, computer performance has progressed remarkably and now performance of the highest-end supercomputer reaches to 400 petaflops. However, such the high performance computation is achieved by vary large supercomputer system based on von Neumann architecture with over 10 millions cores, and 10 megawatts power consumption. Authors have been working in a development of dedicated computers based on the dataflow architecture, to aim to achieve a portable, low power consumption, low cost and green high-performance computing for electromagnetic field simulations[1]. In this work, we propose the dedicated hardware circuit based on the dataflow architecture of finite integration technique (FIT) scheme for magnetostatic fields.

2. Design of BiCG-Stab matrix solver circuit

Two dimensional magnetostatic field is described by the vector Poisson equation for *z*-component of the magnetic vector potential **A**. FIT discretization of the vector Poisson equation can be expressed as follows:

$$c_{i,j}^{(0)}A_{i,j} - c_{i,j}^{(1)}A_{i,j-1} - c_{i,j}^{(2)}A_{i+1,j} - c_{i,j}^{(3)}A_{i,j+1} - c_{i,j}^{(4)}A_{i-1,j} = I_{i,j}$$

$$c_{i,j}^{(0)} = c_{i,j}^{(1)} + c_{i,j}^{(2)} + c_{i,j}^{(3)} + c_{i,j}^{(4)}, c_{i,j}^{(1)} = \frac{1}{2\mu_{i,j-1}} + \frac{1}{2\mu_{i-1,j-1}},$$

$$c_{i,j}^{(2)} = \frac{1}{2\mu_{i,j-1}} + \frac{1}{2\mu_{i,j}}, c_{i,j}^{(3)} = \frac{1}{2\mu_{i,j}} + \frac{1}{2\mu_{i-1,j}}, c_{i,j}^{(4)} = \frac{1}{2\mu_{i-1,j}} + \frac{1}{2\mu_{i-1,j-1}} \qquad (1)$$

where $A_{i,j}$, $I_{i,j}$ and $\mu_{i,j}$ are the magnetic vector potential, externally applied current and permeability at the *i*-th, *j*-th grid in the 2D grid space. We can obtain the distribution of the magnetic vector potential $A_{i,j}$ to construct a matrix equation of (1) for all grid point and to solve the marix equation. Accordingly, in the development of the dedicated computer for the 2D magnetostatic field computation, a main task is a design of the hardware circuit of the matrix solver for (1). Then, the use of floating-point calculations in the hardware circuit requires large size hardware, in addition, large numbers of clock cycles. In order to achieve hardware circuits of the matrix solver with a smaller size hardware and shorten clock cycle, we consider to use fixed-point arithmetic with integer format instead of floating-point arithmetic for matix solver hardware circuits. In the implementation of the matrix solver scheme such as the BiCG-Stab method using the fixed-point arithmetic with integer format, we need to carefully treat individual arithmetic operation between unknown values to avoid truncations and accuracy degrations[2]. Figure 1 depicts a conceptual design of hardware circuits for a single unit grid of the FIT sheme which include the BiCG-Stab matrix solver circuit based on multiple precision fixed-point arithmetic with integer format. All of unknown values are stored in registers at each grid. These registers are connected each other via arithmetic circuits which execute the BiCG-Stab matrix solver scheme. By allocating this unit circuit all over grid space, the magnetostatic field can be simulated automatically.

References

[1] H. Kawaguchi et.al, IEEE Trans. Magn, Vol.51, Issue 3, 7202404, 2015.

[2] T. Kuroki et.al, Trans. IEEJ, vol.129, No.10, pp.687-692, 2009.

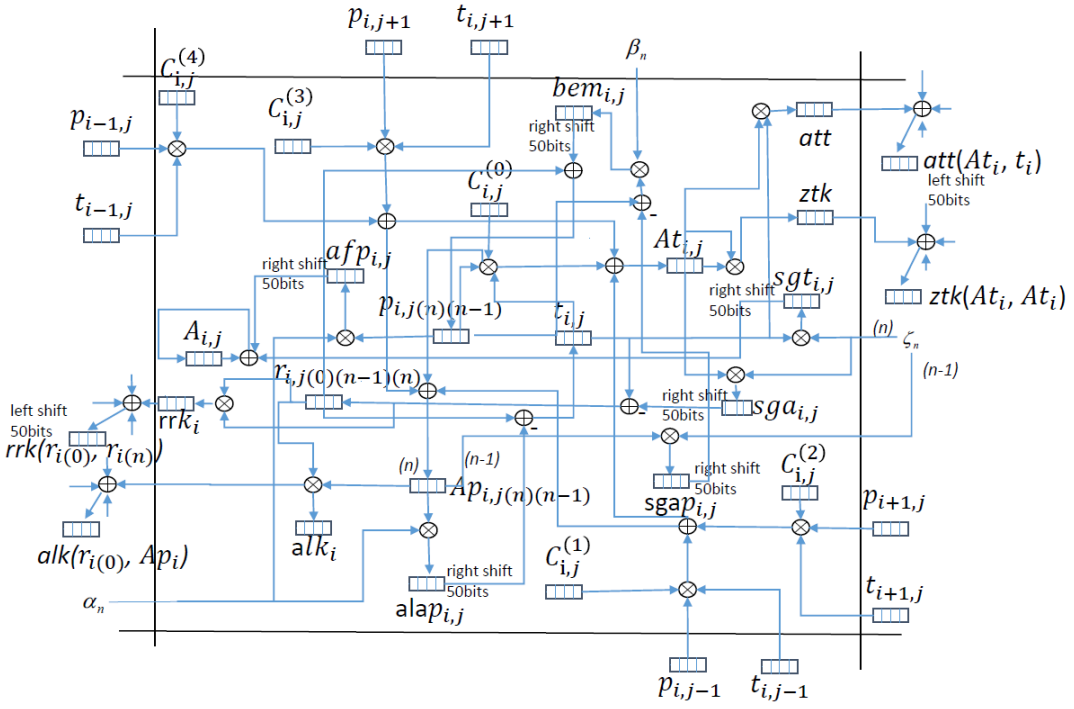

Figure 1. BiCG-Stab matrix solver unit grid circuit for FIT shceme of 2D magnetostatic field

Importance of 3-D piezoelectric coupled analysis in evaluation of thin piezoelectric bimorph deformation

Shoichi Aikawa[1], Daisuke Ishihara[2*], Naoki Iwamaru[1], Prakasha C. Ramegowda [2]

[1]Department of Computer Science and Systems Engineering, Kyushu Institute of Technology

[2]Department of Intelligent and Control Systems, Kyushu Institute of Technology

*ishihara.daisuke399@mail.kyutech.jp

Abstract. Thin piezoelectric bimorphs are often used as actuators and sensors in advanced electromechanical systems. Therefore, it is necessary to accurately evaluate their electromechanical behavios. In this study, the finite element analysis results for the deflection of piezoelectric bimorphs are compared with the analytical solutions based on the beam theory, and it is shown that three-dimensional piezoelectric-inverse piezoelectric coupled analysis is important if the electromechanical coupling coefficient and the width of the bimorph are large.

Keywords: Piezoelectric Bimorph, Finite Element Analysis, Coupled Analysis

1. Introduction

Piezoelectric materials can work as sensors using the accumulation of electric charge in response to mechanical strain or the direct-piezoelectric effect, while as actuators using the change in the size in response to an applied electrical potential or the inverse-piezoelectric effect. Most recently, piezoelectric devices are increasingly employed throughout the field of vibration control, energy harvesting, and nano-aerial vehicles [1]. These piezoelectric devices are usually fabricated as thin cantilevered composite structures with one or more piezoelectric layers, typically, thin cantilevered piezoelectric bimorphs. Their electromechanical behavior has been extensively studied using a variety of numerical approaches [2-5].

This study considers the thin cantilevered piezoelectric bimorph. As seen in the previous studies, this configuration allows various simplified models including closed-form solutions. However, as shown in Ref. [3], the thin cantilevered piezoelectric bimorph beam operating in the sensor mode can present the complicated three-dimensional electric field, which requires the direct numerical modeling for the accurate prediction of the electrical behavior. Similarly, in the thin cantilevered piezoelectric bimorph actuator, a correct understanding of the cases that require the direct numerical modeling is very important. Hence, for the purpose of this understanding, the direct and inverse piezoelectric interaction and the three-dimensional (3-D) geometrical configuration are investigated quantitatively in the mechanical behavior of the thin cantilevered piezoelectric bimorph actuator. Their direct numerical modeling is necessary for the accurate prediction of the thin cantilevered piezoelectric bimorph actuator deformation.

2. Materials and Methods

The spatially discretized equilibrium equations of linear piezoelectricity in the global coordinate system are derived using the variation principle with the standard procedure of the finite element method as

$$\mathbf{K}_{uu}\mathbf{u} + \mathbf{K}_{u\varphi}\boldsymbol{\varphi} = \mathbf{F}, \quad \mathbf{K}_{u\varphi}^{T}\mathbf{u} + \mathbf{K}_{\varphi\varphi}\boldsymbol{\varphi} = \mathbf{q}, \tag{1a, b}$$

where $\mathbf{K}_{uu}$ is the global mechanical stiffness matrix of the structure, $\mathbf{K}_{u\varphi}$ is the global piezoelectric stiffness matrix of the piezoelectric continuum, $\mathbf{K}_{\varphi\varphi}$ is the global dielectric stiffness matrix of the piezoelectric continuum, $\mathbf{u}$ is the nodal global vector of the mechanical displacement, $\boldsymbol{\varphi}$ is the nodal global vector of the electric potential, $\mathbf{F}$ is the global equivalent vector of the mechanical external force, $\mathbf{q}$ is the global equivalent vector of the external surface charge, and the right-hand superscript T denotes the transpose of the matrix.

In the strong coupling method, $\mathbf{u}$ and $\boldsymbol{\varphi}$ that satisfy Eqs. (1a, b) accurately are obtained using the block Gauss-Seidel method, while, in the weak coupling method, as the first step, Eq. (1b) with $\mathbf{u} = \mathbf{0}$ is solved to get $\boldsymbol{\varphi}$, and, as the next step, Eq. (1a) with $\boldsymbol{\varphi}$ obtained in the first step is solved to get $\mathbf{u}$. The strength of coupling is measured using the electromechanical coupling coefficient $k_{31} = d_{31}/(\varepsilon_{33} s^{E}_{11})^{0.5}$, where d_{31} is the piezoelectric strain constant, ε_{33} is the dielectric constant, and s^{E}_{11} is the elastic compliance constant. The relative difference between the weak coulpling analysis result and the theoretical solution is less than 0.1% iresspective of k_{31} for the actual PZT materials considered here. On the contrary, the relative difference between the strong coulpling analysis result and the theoretical solution reaches 8% for the maximum k_{31}.

References

[1] Ishihara D, Ohira N, Takagi M, Horie T. Fluid-structure interaction design of insect-like micro flapping wing. Proceeding of the VII International Conference on Computational Methods for Coupled Problems in Science and Engineering 2017:870–5.

[2] Ramegowda PC, Ishihara D, Niho T, Horie T. A novel coupling algorithm for the electric field-structure interaction using a transformation method between solid and shell elements in a thin piezoelectric bimorph plate analysis. Finite Elem Anal Des 2019;159:33–49.

[3] Ramegowda PC, Ishihara D, Takata R, Niho T, Horie T. Finite element analysis of thin piezoelectric bimorph with a metal shim using solid direct-piezoelectric and shell inverse-piezoelectric coupling with pseudo-piezoelectric evaluation. Compos Struct 2020;245:112284.

[4] Ramegowda PC, Ishihara D, Takata R, Niho T, Horie T. Hierarchically decomposed finite element method for a triply coupled piezoelectric, structure, and fluid fields of a thin piezoelectric bimorph in fluid. Comput Meth Appl Mech Eng 2020;365:113006.

[5] Ishihara D, Takata R, Ramegowda PC, Takayama N. Strongly coupled partitioned iterative method for the structure–piezoelectric–circuit interaction using hierarchical decomposition. Comput Struct 2021;253:106572.

JSST 2021

Comparative study on linear and quadratic solid direct-piezoelectric solvers with shell inverse-piezoelectric solver to analyze a thin piezoelectric bimorph device

P.C. Ramegowda[1,*] and D. Ishihara[1]

[1]Department of Intelligent and Control Systems, Kyushu Institute of Technology, Iizuka, Fukuoka, Japan

[*]prakasha@solid.mse.kyutech.ac.jp

Abstract. The successful design of a thin piezoelectric bimorph device for sensor and actuator applications requires an efficient and accurate finite element modeling (FEM) of direct and inverse piezoelectric effects. In this work, a partitioned iterative method utilizing the best features of the solid elements for the direct-piezoelectric field and MITC shell elements for the inverse-piezoelectric field is employed. A comparative study of linear and quadratic elements for the approximation of the electrical potentials in the solid direct-piezoelectric solver is presented. Numerical results are compared with analytical results. Quadratic solid piezoelectric elements significantly outperform linear solid piezoelectric elements in terms of solution accuracy and computational efficiency.

Keywords: Linear solid piezoelectric element, quadratic solid piezoelectric element, MITC4 shell inverse-piezoelectric solver, partitioned iterative method, thin piezoelectric bimorph.

1. Introduction

Piezoelectric materials exhibits two types of electromechanical coupling effects, namely, direct-piezoelectric effect and inverse-piezoelectric effect. Authors in their early works [1, 2] had proposed a novel FE method wherein the combination of 3D solid and MITC shell elements are employed to solve direct-piezoelectric and inverse-piezoelectric fields, respectively, to overcome the demerits of these elements to solve both the direct and inverse-piezoelectric effects in a single framework reported in the works of Benjeddou [3]. Shell elements are efficient for analyzing the deformation of a thin-layered piezoelectric device. However, the electric potential distribution within the piezoelectric continuum is still significantly three-dimensional even though the structure is thin [1, 4] and it is quadratic through-thickness [5]. Therefore, 3D solid elements are necessary for analyzing the electric potential distribution in the piezoelectric material. The electromechanical coupling is only partial if the potential is assumed to vary linearly through the thickness [3]. Quadratic variation of the electric potential through the thickness direction can be achieved using linear 3D solid

elements by increasing the density of the mesh in the thickness direction which leads to an increase in the computational cost. Therefore, this work presents a comparative study of linear and quadratic elements for the approximation of the electrical potentials to solve the direct-piezoelectric field. Numerical results are compared with analytical results. Quadratic solid piezoelectric elements significantly outperform linear solid piezoelectric elements in terms of solution accuracy and computational efficiency.

2. Finite element equations and coupling strategy

Eqs.(1) and (2) represents the general FE coupled inverse-piezoelectric and direct-piezoelectric effect of a piezoelectric material.

$$\mathbf{M}_{uu}\ddot{\mathbf{u}} + \mathbf{K}_{uu}\mathbf{u} + \mathbf{K}_{u\phi}\phi = \mathbf{F}, \tag{1}$$

$$\mathbf{K}_{\phi u}\mathbf{u} + \mathbf{K}_{\phi\phi}\phi = \mathbf{q}, \tag{2}$$

where $\mathbf{M}_{uu}$ is the constant mass matrix, $\mathbf{K}_{uu}$ is the mechanical stiffness matrix, $\mathbf{K}_{u\phi}$ is the piezoelectric coupling matrix, $\mathbf{K}_{\phi\phi}$ is the dielectric stiffness matrix, $\mathbf{F}$ is the external force vector, and $\mathbf{q}$ is the external electric charge vector. Employing shell elements for inverse-piezoelectric equation (1) and solid elements for direct-piezoelectric equations (2), ignoring the inertial effect ($\mathbf{M}_{uu} = 0$), we obtain Eqs.(3) and (4). The kinematic coupling between the shell and solid is done using a transformation method [1] in a Block Gauss-Seidel (BGS) iterative loop [4]. The Eqs.(3) and (4) can be written as Eqs.(5) and (6).

$$\mathbf{K}_{uu}^{\text{shell}}\mathbf{u}^{\text{shell}} + \mathbf{K}_{u\phi}^{\text{solid}}\phi^{\text{solid}} = \mathbf{F}^{\text{shell}} \tag{3}$$

$$\mathbf{K}_{\phi u}^{\text{solid}}\mathbf{u}^{\text{solid}} + \mathbf{K}_{\phi\phi}^{\text{solid}}\phi^{\text{solid}} = \mathbf{q}^{\text{solid}} \tag{4}$$

$$\mathbf{K}_{uu}^{\text{shell}}\mathbf{u}^{\text{shell}} = \mathbf{F}^{\text{shell}} + {}^{\text{e}}\underline{\mathbf{F}}^{\text{shell}} \tag{5}$$

$$\mathbf{K}_{\phi\phi}^{\text{solid}}\phi^{\text{solid}} = \mathbf{q}^{\text{solid}} + {}^{\text{e}}\mathbf{q}^{\text{solid}} \tag{6}$$

The transformation of the quantities from shell to solid and solid to shell are represented using the transformation matrix ${}^{\text{e}}\mathbf{T}$ and ${}^{\text{u}}\mathbf{T}$, respectively. Eqs.(7) and (8) represents the nodal electric force and the nodal electric charge given by the solid direc-piezoelectric solver, respectively.

$${}^{\text{e}}\mathbf{F}^{\text{solid}} = -\mathbf{K}_{u\phi}^{\text{solid}}\phi^{\text{solid}} \tag{7}$$

$${}^{\text{e}}\mathbf{q}^{\text{solid}} = -\mathbf{K}_{\phi u}^{\text{solid}}\mathbf{u}^{\text{solid}} \tag{8}$$

$${}^{\text{e}}\underline{\mathbf{F}}^{\text{shell}} = \left[{}^{\text{e}}\mathbf{F}^{\text{shell}}, {}^{\text{e}}\mathbf{M}^{\text{shell}}\right] = {}^{\text{e}}\mathbf{T}\,{}^{\text{e}}\mathbf{F}^{\text{solid}} \tag{9}$$

$$\mathbf{u}^{\text{solid}} = {}^{\text{u}}\mathbf{T}\,{}^{\text{e}}\mathbf{u}^{\text{shell}} \tag{10}$$

${}^{\text{e}}\mathbf{F}^{\text{solid}}$ is transformed to the equivalent forces ${}^{\text{e}}\mathbf{F}^{\text{shell}}$ and moments ${}^{\text{e}}\mathbf{M}^{\text{shell}}$ acting on the shell mesh from the solid mesh. Eqs.(11) and (12) represents the equivalent force and moments on the shell from linear solid mesh, while Eqs.(13) and (14) represents the equivalent force and moments on the shell from quadratic solid mesh [1].

$${}^{\text{e}}\mathbf{F}^{\text{shell}} = \sum_{n_r=1}^{N_r} {}^{\text{e}}\mathbf{F}_{n_{\text{r}}}^{\text{solid}} \tag{11}$$

$${}^{\text{e}}\mathbf{M}^{\text{shell}} = \sum_{n_r=1}^{N_r} \left(\mathbf{d}_{n_r} \times {}^{\text{e}}\mathbf{F}_{n_{\text{r}}}^{\text{solid}}\right) \tag{12}$$

$${}^{\text{e}}\mathbf{F}^{\text{shell}} = \sum_{n_r=1}^{N_r} {}^{\text{e}}\mathbf{F}_{n_{\text{r}}}^{\text{solid}} + \sum_{n_s=1}^{N_s} {}^{\text{e}}\mathbf{F}_{n_{\text{s}}}^{\text{solid}}/2 \tag{13}$$

$${}^{\text{e}}\mathbf{M}^{\text{shell}} = \sum_{n_r=1}^{N_r} \left(\mathbf{d}_{n_r} \times {}^{\text{e}}\mathbf{F}_{n_{\text{r}}}^{\text{solid}}\right) + \sum_{n_s=1}^{N_s} \left(\mathbf{d}_{n_s} \times {}^{\text{e}}\mathbf{F}_{n_{\text{s}}}^{\text{solid}}/2\right) \tag{14}$$

3. Piezoelectric bimorph sensor analysis

3.1. Problem setup

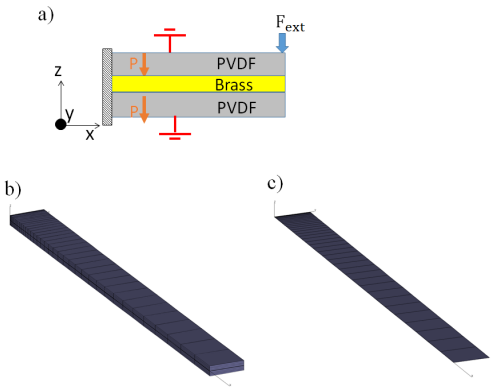

Figure 1: a) Short circuit bimorph sensor with external force $\mathbf{F}_{ext} = \mathbf{1.0mN}$. b) Solid mesh for the piezoelectric analysis. c) Shell mesh for the inverse-piezoelectric analysis.

Fig. 1(a) shows the short circuit sensor mode of the piezoelectric bimorph. The length and the width of the bimorph are 250mm and 20mm, respectively, the thicknesses of the piezoelectric and shim layers are 5mm and 0.5mm, respectively. The materials of the piezoelectric and shim layers are PVDF and brass, respectively. Fig. 1(b) shows the solid mesh used in the direct-piezoelectric analysis. Fig. 1(c) shows the shell mesh used in the inverse-piezoelectric analysis. The solid elements are hexahedral elements (8-node element for linear and 20-node element for quadratic), while the shell elements are MITC4 elements [6].

3.2. Results and Discussions

Fig. 2 shows the electric potential distribution at the fixed end of the bimorph through the thickness for various mesh densities. As shown in Fig. 2(a), the red curve shows a smooth quadratic variation than the blue curve. On the contrary, a smooth quadratic distribution through the thickness is achieved using 20-node solid elements, as shown in the magenta curve in Fig. 2(b). The solution obtained with the 20-node solid is very close to that of the theory. The theoretical solution is 3.524×10^{-1} V. The error is 1.61%. The solution accuracy in Fig. 2(a) are very bad. The green curve shows a solution accuracy (6.64%) close to that of the magenta curve in Fig. 2(b). This indicates that quadratic solid-piezoelectric solver is computationally efficient and solutions are very accurate than linear solid-direct piezoelectric solvers

4. Conclusions

A comparative study of linear and quadratic elements for the approximation of the electrical potentials in the solid direct-piezoelectric solver, while shell elements for inverse-piezoelectric solver are presented. Numerical results are compared with analytical results. Quadratic solid piezoelectric elements significantly outperform linear solid piezoelectric elements in terms of solution accuracy and computational efficiency.

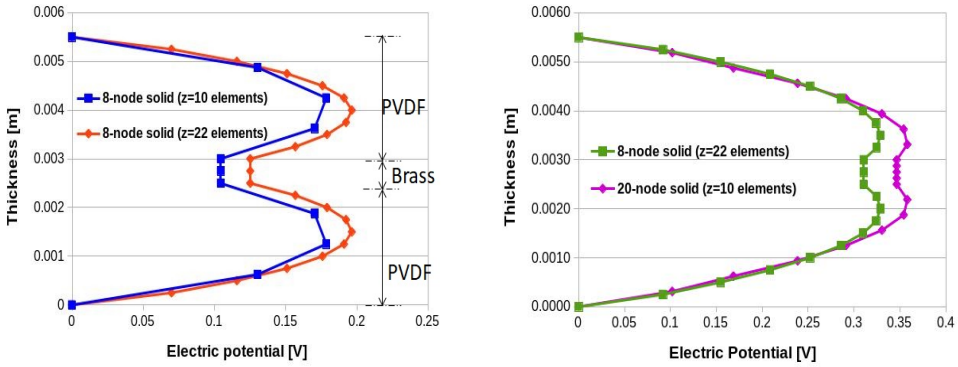

(a) (b)

Figure 2: Induced electric potentials through the thickness: blue curve (8-node solid; mesh division along the length, width, and thickness are 50,1, 10 respectively), red curve (8-node solid; mesh division along the length, width, and thickness are 50,1, 20 respectively), green curve (8-node solid; 4646 number of nodes; mesh division along the length, width, and thickness are 100, 1, and 22, respectively), magenta curve (20-node solid; 3803 number of nodes; mesh division along the length, width, and thickness are 50, 1, and 10, respectively.)

Acknowledgments

The present study was supported by JSPS KAKENHI Grant No. 19F19379

References

[1] P.C. Ramegowda, D. Ishihara, T. Niho, T. Horie: A novel coupling algorithm for the electric field–structure interaction using a transformation method between solid and shell elements in a thin piezoelectric bimorph plate analysis, *Finite Elements in Analysis and Design*, 159 (2019), 33–49.

[2] P.C. Ramegowda, D. Ishihara, R. Takata, T. Niho, T. Horie: Finite element analysis of thin piezoelectric bimorph with a metal shim using solid direct-piezoelectric and shell-inverse piezoelectric coupling with pseudo-piezoelectric evaluation, *Composite Structures*, 245 (2020), 112284.

[3] A. Benjeddou: Advances in piezoelectric finite element modeling of adaptive structural elements: a survey, *Computers & Structures*, 6 (2000), 347–363.

[4] P.C. Ramegowda, D. Ishihara, T. Niho, T. Horie: Performance evaluation of numerical finite element coupled algorithms for structure–electric interaction analysis of MEMS piezoelectric actuator, *International Journal of Computational Methods*, 16 (2019), 1850106.

[5] S. Ravi, A. Zilian, *International Journal for Numerical Methods in Engineering*, 112 (2017), 1828–1847.

[6] E.N. Dvorkin, K.J. Bathe, *Engineering Computation*, 1 (1984), 77–88.